Ru(II) Polypridyl Complexes Investigated from the Pico to the Micro Second Domain.

William Henry

Submitted towards the degree of Ph.D.

Supervisor:

Prof. Johannes G. Vos.

School of Chemical Sciences,

Dublin City University.

July 2006.

I hereby certify that this material, which I now submit for assessment on the programme of study leading to the award of Ph.D. is entirely my own work and has not been taken from the work of others save and to the extent that such work has been cited and acknowledged within the text of my work.

Signed: _____ (Candidate)

ID No.: 52156052

Date: 25/9/2006

Dedicated to my parents,

Padraic and Kay.

Many people have contributed to the writing of this thesis. Every attempt is made to thank them all but any omission is the error and with the apologises of the author. And anyway, don't take it personally because, as usual, I'm doing this at the last minute.

Firstly I have to thank Han. At all times you were supportive, helpful and ready to offer a joke whenever things were getting tough. I am grateful to have worked with you for the past four years and you were an excellent mentor. Plus, no longer will I think of the Dutch as just those people who always knock us out of football tournaments. I must also thank John McGarvey for allowing me the privileged to work with you and for so expertly advising me in all things Raman. At this point I have to thank Wes. For explaining, re-explaining, going through the basics and telling me again I will be forever grateful. I even think I learnt a few things. In return for all your hard work I have never once tried to kill you, although I did think about it once or twice!!

Next I have to thank my parents for supporting me in all I have done through the years and for their continued support and constant understanding. The pride you have shown in all my achievements, no matter how small, has given me the confidence to try anything without fear of failure. I also have to thank my wonderful girlfriend, Maria, for all her hard – work (am I really that much work?), caring, understanding and patience (nearly forgot that one!).

I have been lucky enough to collaborate with a number of fine people through my work. In Queen's University of Belfast I have to thank all those who explained, demonstrated, aligned and then re-aligned. The head – honcho Kate (I'll always remember you before you were a nerd), Clare, Louise, Mutu, Renne, Lyndsey and Stephen; sorry I made it all so difficult. I think I get it now. To all those in Jena, especially Sven, Bernhard and Wolfgang, I give to my sincerest gratitude. I also have to thank the people I

worked with in Amsterdam (Luisa, Anthony, Benedeck and many more), R.A.L. (Pavel, Mike and Tony) and all those in Susana.

I have also had the pleasure to work with a variety of characters during my time in D.C.U. If I said the work was always a pleasure we'd all know I was lying. But you have all made four years of seemingly endless slog as much fun as could possibly be. From the old (sorry, Adrian) to the young (the newbies; Laura and Yvonne), the crazy (Tia's group) and the cool (Johnnie) I thank you all. Special praise has to be given to the members of the HVRG, past and present, and "them from the old lab" – Mary's group. There seems too many of you to mention but I 'll try: Noel (I've forgiven you for Brussels), Dec, Stefi, Balducci (Sitting Tarus), Helen, Sabine, Fiona, Johan, Rob, Lynda, Elena (of the short arms), Fiona, Claire and of course Tony, Nikki and Steph.

ABSTRACT

Ru(II) Polypridyl Complexes Investigated from the Pico to the Micro Second Domain.

William Henry

The present work probes the ground and excited state energy structures of a variety of Ru(II) complexes to better understanding the factors which affect their photo – chemical and – physical properties.

In the picosecond domain, ultrafast time resolved resonance Raman spectroscopy has been used to investigate the rate of formation of the thermally equilibrated excited (THEXI) state in $[Ru(bpy)_3]^{2+}$. These studies have shown that evolution of the THEXI state persists into the picosecond time range and is not complete on the femtosecond timescale, as previously suggested. These studies have also been extended to cover heteroleptic complexes and the effects of deuteriation and solvent.

Ru(II) complexes containing a 1,2,4 – triazole moiety have been investigated using a variety of techniques, including time correlated single photon counting, resonance Raman and transient absorption. At room temperature studies have shown the ability to control the electrochemical and photophysical properties through substitution of the triazole and alternating the symmetrical NN ligands.

Low temperature emission and single photon counting (on the microsecond timescale) measurements have shown the presence of two emissions for the 1,2,4 – triazole complexes containing a pyrazine moiety. These studies have highlighted the importance of electron delocalisation and excited state dipole, as well as the relative energies of the ligands, when controlling the excited state location.

Throughout the work deuteriation have been employed to considered effect with its application of particular importance to the Raman and excited state lifetime studies. Computational studies have also been used to augment the experimental work. These studies have reveal details about the energy level structures of dual emissive complexes while also highlighting some limitations of calculations preformed in an isolated environment.

Chapter 1

Introduction

The first chapter serves as an introduction to the work which follows. The area of supramolecular chemistry and the potential for the future is discussed. The chemistry of Ruthenium complexes is reviewed, with a more detailed account of $[Ru(bpy)_3]^{2+}$ *and complexes containing a 1,2,4 – triazole ligand provided. A theoretical background for the experimental and computational techniques used is also given.*

This thesis uses a variety of techniques to probe the excited state processes in Ru(II) polypyridyl complexes. These processes are probed over three time ranges; picosecond resonance Raman spectroscopy is used to probe the formation of the thermally equilibrated excited state of $[Ru(bpy)_3]^{2+}$ in Chapter 3 while the nano- and micro-second timescale is investigated via temperature dependent lifetime studies in Chapters 4 and 5. In order for the reader to better appreciate the results obtained, this introductory chapter gives an overview of the techniques employed and their theoretical background. In this introduction an attempt has been made to devote extra space to the techniques which the reader may be less familiar with. At the beginning of each of the subsequent chapters a short introduction is presented which is more specific to the work contained therein.

1.1 Supramolecular Chemistry.

Supramolecular chemistry is a difficult area to define succinctly. It can be thought of as "chemistry beyond the molecule". However, as synthetic versatility increases and the ability to control the properties and structures of entities is broadened, the boundaries of single molecules begin to blur. The difference between a large molecule and a supermolecule is best defined by the degree of interaction between the constituent parts in a molecular structure. When the degree of interaction between the subunits is small in comparison to other relevant parameters, the chemical entity may be described as a supramolecular species. On the other hand an entity with a large amount of interaction between the subunits is best described as a large molecule. The degree of interaction can be seen via the excited states of the molecules and examples of the distinction are given below in FIGURE 1.1. The subunits of a supermolecule may each have their own properties, however, the overall properties of the molecule may not be simply a superimposition of these properties.

In the case of a supramolecular species the excited state formed is localised on one of the subunits of the species. ~ indicates a bond between the units in a supramolecular species and a large molecule. Initially, supramolecular chemistry was thought of as hydrogen and ionic bonds between the subunits, but once the synthetic versatility and analytical accuracy to include coordination compounds and covalent bonds was achieved, the area of supramolecular chemistry began to flourish.

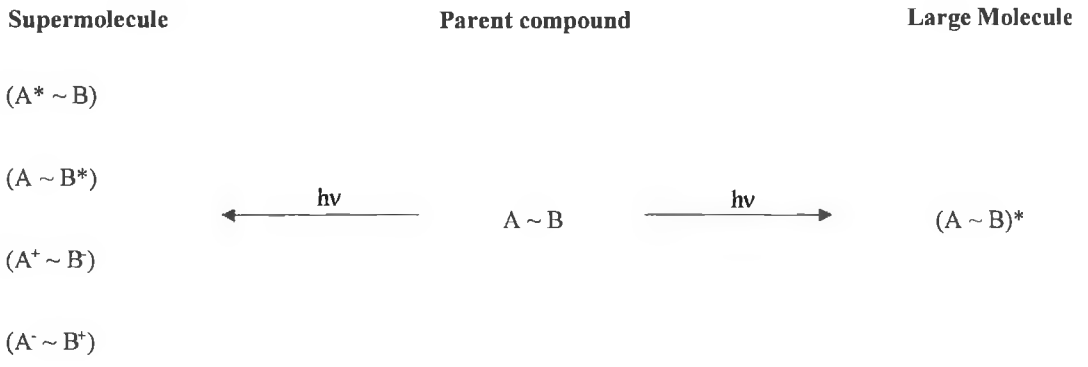

FIGURE 1.1: DISTINCTION BETWEEN SUPERMOLECULE AND LARGE MOLECULE.

The increased complexity involved in the synthesis and characterisation of supramolecular species represents an exciting challenge for chemists. Although the area generates enough theoretical and synthetic challenges to be of considerable academic interest it is the various potential applications[1,2,3] that have generated considerable fervour in both the media and industry.

The definition of supramolecular chemistry tends to be somewhat loose and the subject area is perhaps best defined with a number of examples which show the potential applications. FIGURE 1.2 gives structures of a variety of supramolecular entities. The ability for molecular recognition of both anions and cations has provoked considerable interest. The recognition of alkali cations has been achieved using polyethers and crown ethers[4] while anions can form non – covalent bonds with polyammonium macrocycles.[5] For the ether based macrocycles, the lone pairs on the oxygen atoms interact with the

postive charge on the cation. For the anion receptors, protonation of the ammonium groups of the macrocycles forms an ellipsodial cavity which allows binding to electron rich substrates of suitable size, such as the azide anion. The increased binding ability of macrocycles compared to similar acyclic molecules is referred to as the macrocyclic effect. Another highly important area is supramolecular catalysis. This work also deals with molecular recognition as the reactants form supramolecular entities before catalysis occurs. Examples of artificial metalloenzymes are those based on cyclodextrins[6] and porphyrins.[7] The hydrophobic cavity of the cyclodextrins are able to bind appropriate substituents and position the another part of the molecule at a catalytic site which is attached to the outer OH groups, resulting in orders of magnitude reaction rate increases.

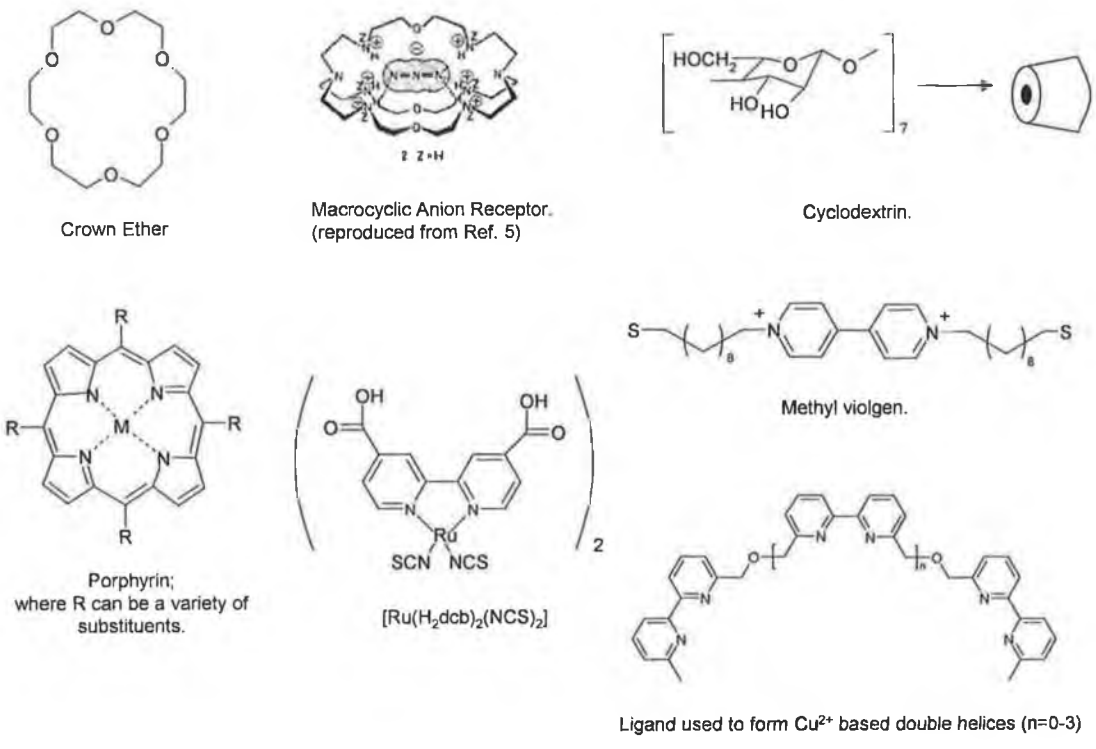

FIGURE 1.2: EXAMPLES OF STRUCTURES IN SUPRAMOLECULAR CHEMISTRY.

Of particular interest for the current work is light – driven electron transfer processes. The electron transfer processes of $[Ru(H_2dcb)_2(NCS)]$ (where dcb is 2,2′-bipyridyl, 4,4′-carboxylate and NCS is a thiocyanate group) upon attachment to TiO_2 surfaces have been the subject of intense research. These hetero – supramolecular systems show charge injection on the femtosecond timescale upon irradiation, with charge recombination occurring via an external circuit.[8] Organic electron transfer process studies have seen a large number of publications based on viologen systems.[9] The electron tunnelling between a nanoparticle and a substrate bound by a dithiolated viologen system has been controlled using an applied potential and monitored using Scanning Tunnelling Microscopy.[10] The area of self – processing has received considerable attention in mainstream media[11] due to the potential to produce self – replicating and self – assembling devices. This work is charged with designing systems which can create themselves once the correct building blocks are in place. One example is the double helix structure created based on bipyridine blocks in the presence of Cu^{2+}.[12] The most comprehensive tome on the area of supramolecular chemistry is the book of the same title by Jean – Marie Lehn and the interested reader is directed there for more information on the subject and for elaboration on the examples given above.[13]

1.2 Principles of Photophysics.

The interaction of light with matter is a fundamental process which underpins a wide variety of natural phenomena. This section serves as an introduction to photophysical processes and the electronic structure of inorganic complexes. Where possible mathematical formulae are kept to a minimum for ease of reading and also because a more rigorous mathematical treatment is required in the section on computational chemistry (section 1.5). The initial step in the formation of an excited state is the absorption of light which is dealt with in the next section.

1.2.1 Absorption and Formation of the THEXI state.

FIGURE 1.3 gives an overview of the processes involved in the formation of an excited state. On the left hand side is a diagram of the potential energy surfaces of the various states possible. The potential energy surface is a plot of the energy of the complex relative to the nuclear positions of its constituent atoms. Since different electronically excited states have different equilibrium nuclear positions the position of the minima are shifted depending on the excited state. On the right hand side is a Jablonski diagram. This is another way to represent the electronic energy structure of a complex.

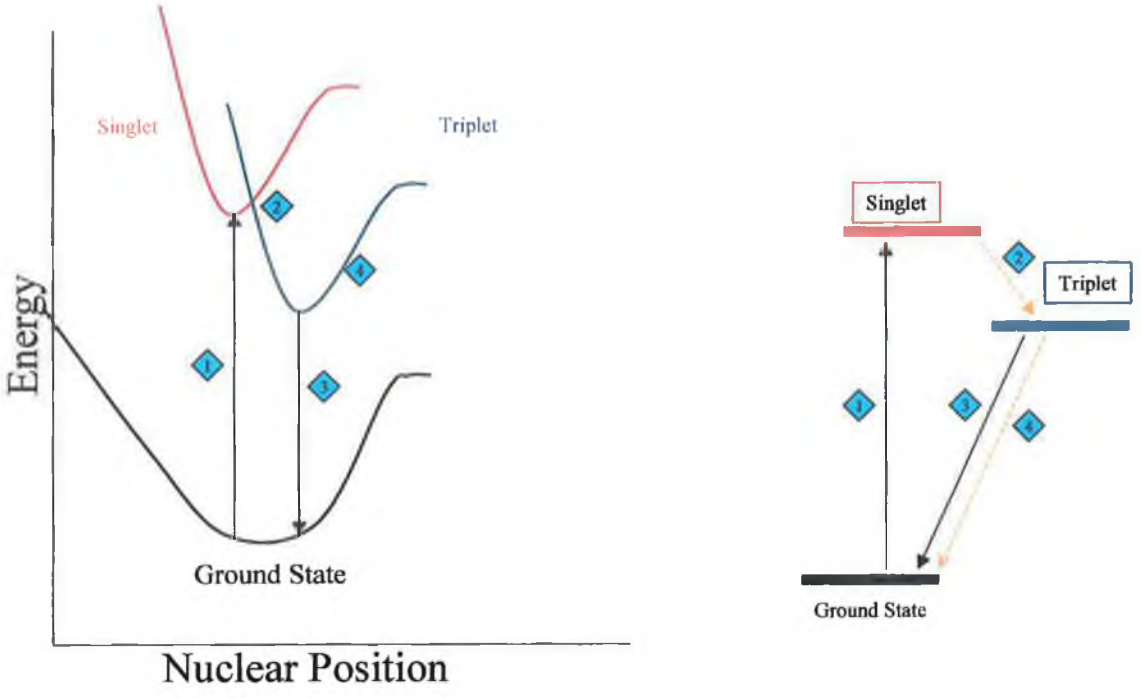

FIGURE 1.3: FORMATION OF AN EXCITED STATE IN AN INORGANIC COMPLEX, (LEFT) POTENTIAL ENERGY SURFACE AND (RIGHT) JABLONSKI DIAGRAM.

The absorption of light is an instantaneous process (1). The excited state formed from this instantaneous absorption leads to an excited state in which the positions of the nuclei are identical to the ground state. In general these positions are not the equilibrium positions in the excited state and therefore the molecule is said to be vibrationally excited. The initially formed excited state is referred to as the Franck – Condon state. The vibrational levels can be seen in the absorption and emission spectra in low temperature (2-10K) studies.[14] The difference in the structure of the excited and ground state leads to a shift in the absorption and emission spectra as the vibrationally hot states dissipates energy non-radiatively before reaching equilibrium. This is known as the Stokes shift[15] and may also be used as a measure of the distortion of the excited state geometry relative to that of the ground state.

If a molecule is not excited into the state from which it is to emit, it may then covert into this state via two processes.[15] Radiationless conversion between states of different multiplicity is known as intersystem crossing (ISC), while

radiationless conversion between states of the same multiplicity is referred to as internal conversion (IC). Since the conversion shown in FIGURE 1.3 is between two state of different multiplicity, process ◆ is ISC.

Upon conversion to the lowest excited state and vibrational cooling to the equilibrium position, the molecule may then be referred to as being in the THEXI (or thermally equilibrated excited) state. It is from this state that the majority of emissive processes (◆) occur. By analogy with radiationless deactivation, emission between two states of different multiplicity is referred to as phosphorescence while it is called fluorescence between states of the same multiplicity. THEXI states do not last very long with the longest known lifetime of a coordination compound in the ms range at room temperature. Deactivation may also occur by non – radiative processes (◆) such as ISC to the ground state or IC to the non – emissive triplet metal centred state (not shown). The deactivation process, energy and lifetime of the THEXI state is dependent on the nature of the ground and excited state orbitals.

1.2.2 Electronic Configurations and Emission.

FIGURE 1.4 presents the electronic structure of an octahedral inorganic complex. The structure is derived from the energy levels of the free metal (left) and ligand (right) orbitals. The ligand orbitals are:

i) strongly bonding, ligand centred σ_L orbitals

ii) bonding, ligand centred π_L orbitals

iii) ligand-centred, anti-bonding π^*_L orbitals

The contribution of the free metal is made up of the orbitals:

iv) nonbonding $\pi_M(t_{2g})$ metal-centred, predominantly d orbitals

v) anti-bonding $\sigma^*_M(e_g)$ metal-centred, predominantly d orbitals

vi) strongly anti-bonding, metal-centred σ^*_M orbitals.

The electronic structure obtained is dependent on the relative energies of the metal and ligand orbitals. The free metal d orbitals are seen to split into $\pi_M(t_{2g})$ and $\sigma^*_M(e_g)$ states due to the octahedral field of the ligands. In the present example the energy of the ligand π^* orbitals is lower than that of the metal σ^*, as is the case for the majority of Ru(II) polypyridyl complexes. However, for other choices of ligands and metal ion the lowest occupied orbitals (HOMO) may be ligand based or the lowest anti-bonding unoccupied orbitals may be based on the metal (LUMO).

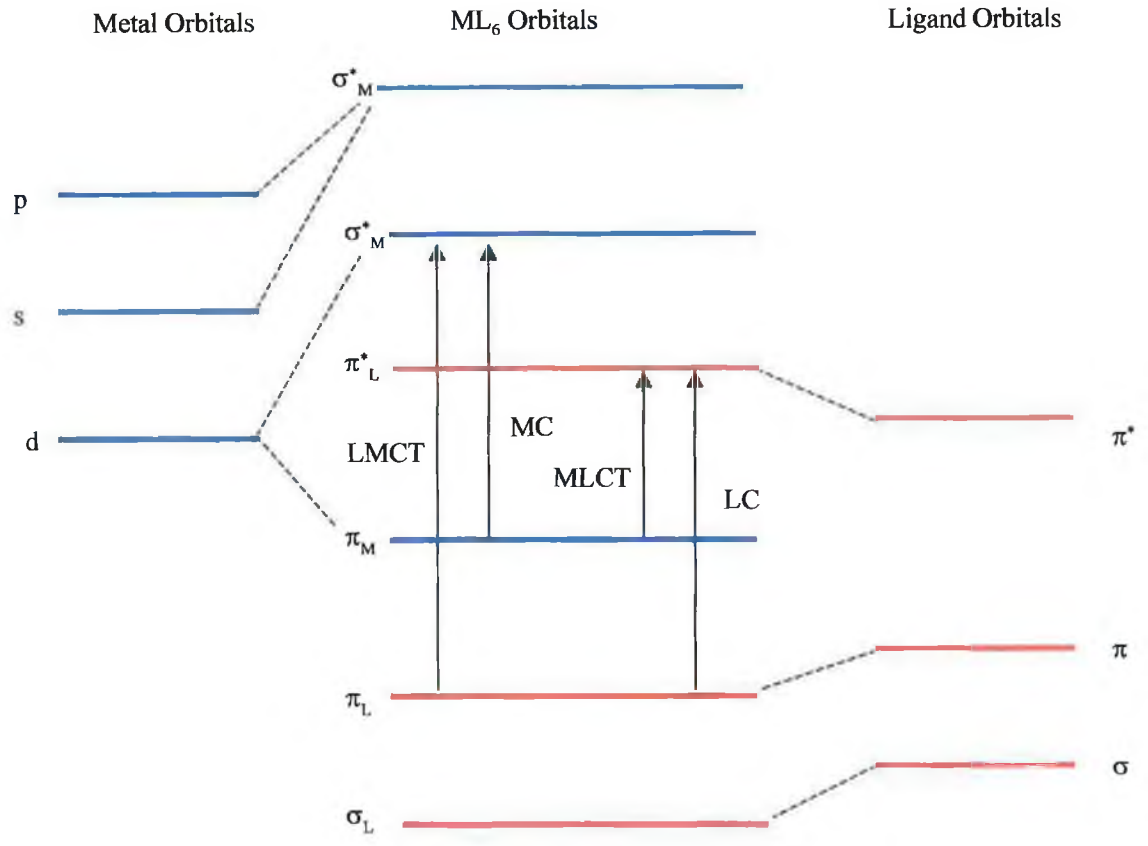

FIGURE 1.4: ELECTRONIC CONFIGURATION OF AN OCTAHEDRAL INORGANIC COMPLEX.

The transitions between these orbitals are defined based on the nature of the initial and final orbitals, such as metal centred (MC) iv) → v), ligand centred (LC) ii) → iii), Ligand to Metal Charge Transfer (LMCT) ii) → v) and Metal to Ligand Charge Transfer (MLCT) iv) → iii). The nature of these transitions is represented in FIGURE 1.4. The nature of the transition uses the same label for both absorptions and emissions. Resonance Raman spectroscopy may be used to investigate the nature of the absorption (see section 1.4). The nature of the THEXI state can be examined using emission (both time resolved and steady state) spectroscopy. From these experiments the following generalisations can be made:

- MLCT emission: At low temperature the emission is intense and highly structured, often with the presence of a vibrational progression. Luminescence is often also observed at room temperature and is seen to show a solvent dependency.[16]

- MC emission: The emission is broad, structureless and rarely observed in solution. The quantum yield is low but may be increased by deuteriation.[16]

- LC emission: The emission is highly structured at low temperature and is seen to resemble the energy of the free ligand. Little solvent dependency is observed in the excited state.[16]

- LMCT emission: LMCT emission is rare and not well characterised. By analogy with MC states it is expected to be broad, structureless and have a large Stokes shift.[16]

1.2.3 Other Excited State Processes.

A number of processes may be involved in the deactivation of the excited state. FIGURE 1.5 gives an overview of these processes. Electron transfer can lead to the storage of excited state energy if the charge separation can be maintained. This is the basis for the development of artificial photosynthetic / solar energy devices.[17] Non – radiative deactivation results in the re-formation of the ground state molecule with the dissipation of the absorbed energy as heat. Photochemistry produces a transformation in the initial molecule into products. This can again lead to the storage of energy if the final products are at higher energy than the starting materials.[18] In this way light can be looked at as a catalyst in a reaction that would not (or would occur slowly) otherwise. Bimolecular quenching results in the transfer of energy to a second species. Already the quenching process has resulted in a number of important applications. The disappearance of an emission signal can used as a probe for the presence of a second, non – emissive species.[18] Energy transfer also allows potential photochemical reactions to occur even if the reactants are unable to absorb light. In this instance the molecule may act as a photosensitiser to absorb light and then transfer energy to the reactants.[18]

This is the basis of the potential photocleavage of H_2O to H_2 and O_2 for energy storage.[18]

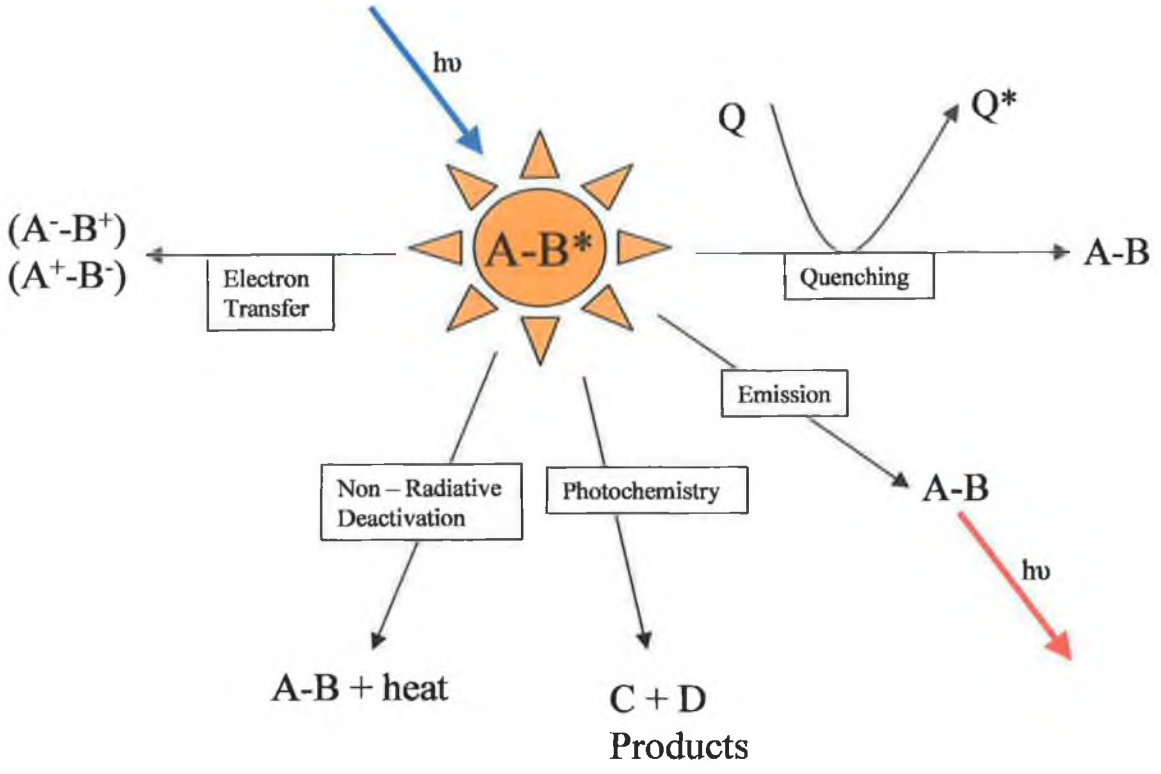

FIGURE 1.5: PROCESSES LEADING TO THE DEACTIVATION OF THE EXCITED STATE.

Each of these processes have an associated rate, *k*. The excited state lifetime of a complex, τ, is related to the sum of all these processes by the following equation:

$$\frac{1}{\tau} = \sum (k_r + k_{nr}) \qquad \text{EQN. 1.1}$$

where k_r and k_{nr} are all the radiative and non – radiative processes, respectively and τ is the excited state lifetime.

This leads to the concept of quantum yield, Φ_{em}, which is the proportion of absorbed light that is re – emitted.

$$\phi_{em} = \frac{k_r}{\sum(k_r + k_{nr})}$$ EQN. 1.2

Inorganic photophysical studies have focussed considerable attention on the properties of Ru(II) polypyridyl complexes, which will be dealt with in the next section.

1.3 Ru(II) Polypyridyl Complexes.

The complexes of Fe, Ru and Os are the most extensively studied of all the transition metal complexes. One of the main advantages of Ru(II) over the other elements in row 8 is its reactivity. Although Fe(II) complexes are more easily synthesised they are overly photolabile, while complexes of Os(II) are less reactive and show weaker emission than Ru(II). The electronic configuration of Ru(II) complexes give them a favourable mix of properties such as synthetic versatility, photostability, room temperature luminescence and moderate excited state lifetime such as to be of considerable interest for a range of applications.[18]

1.3.1 $[Ru(bpy)_3]^{2+}$.

$[Ru(bpy)_3]^{2+}$ is the most widely studied of all Ru(II) complexes. Although it has a variety of the above mentioned favourable properties, research is ongoing into alternative complexes with properties specifically tailored for applications. In all these complexes, however, their properties are still compared to those of $[Ru(bpy)_3]^{2+}$, the paradigm and best understood species.

1.3.1.1 Structure and Bonding.

Ru^{2+} is a d^6 system. $[Ru(bpy)_3]^{2+}$ is a low spin system with all the π_m (t_{2g}) orbitals filled. The uncoordinated 2,2′ - bipyridine ligands are colourless, possessing σ-donor orbitals localised on the nitrogen atoms and π – donor and π^* – acceptor orbitals more or less delocalised on the aromatic rings. $[Ru(bpy)_3]^{2+}$ possesses roughly D_3 symmetry with a Ru-N bond length of 2.05 Å.[19] This is shorter that the 2.10 Å obtained for $[Ru(NH_3)_6]^{3+}$ and indicates significant backbonding into the π^* bpy orbitals.

1.3.1.2 Redox Properties

Oxidation of $[Ru(bpy)_3]^{2+}$ involves a metal centred orbital, with the formation of a Ru(III) complex that is inert to ligand substitution. Reduction occurs in three one electron steps all of which are reversible. Low temperature cyclic voltammetry (CV) measurements have allowed the formation of the highly reduced complex, $[Ru(bpy^{2-})_3]^{4-}$. The orbitals involved in the reduction processes are the same ones that are involved in MLCT and MC transitions, according to Koopman's Theorem[20]. Thus the reversibly of the first reduction step, indicating a ligand centred LUMO, also implies that the lowest excited state is MLCT(*vide infra*).

TABLE 1.1 gives the electrochemical properties of $[Ru(bpy)_3]^{2+}$, with $[Os(bpy)_3]^{2+}$ included for comparison. The lower oxidation potential of the Os complex indicates that the electrons in the 5d orbitals are weaker bound than that of the 4d in Ru. The lower reduction potential of $[Os(bpy)_3]^{2+}$ is due to reduced backbonding from the Os centre. There is significant experimental data which shows the correlations between redox potentials and emission energies.[21] This is compelling evidence for the assignment of absorption bands as MLCT. A pronounced substituent effect on redox properties is observable based on its electron donating / withdrawing properties.

Complex	Oxidation (V vs. SCE)	Reduction (V vs. SCE)
$[Ru(bpy)_3]^{2+}$	1.26	-1.35
$[Os(bpy)_3]^{2+}$	0.83	-1.28

TABLE 1.1: ELECTROCHEMICAL PROPERTIES OF $[Ru(bpy)_3]^{2+}$.

1.3.1.3 Absorption Spectrum.

FIGURE 1.6 gives the absorption spectrum of $[Ru(bpy)_3]^{2+}$ in acetonitrile. Bands at 185 nm (not shown – log ε = 4.95) and the intense band at 285 nm (log ε = 4.94) have been assigned as Ligand Centred $\pi \rightarrow \pi^*$ by comparison with

the free bpy ligand. The remaining intense bands at 240 and 450 nm (log ε = 4.47 and 4.26, respectively) are assigned as d → π* MLCT transitions. Absorption in any of these bands leads to the formation of the excited state.

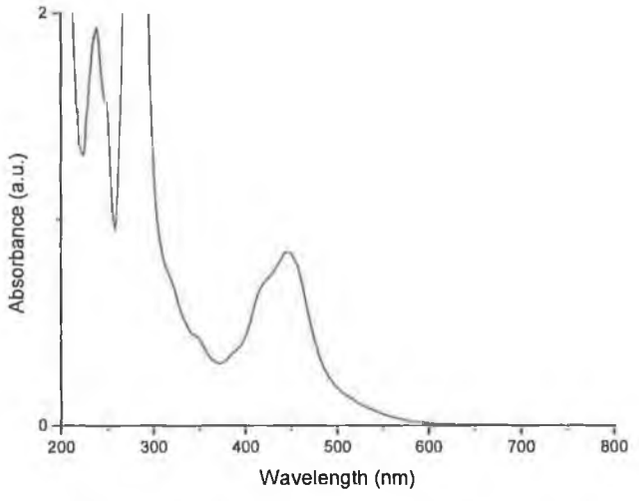

FIGURE 1.6: ABSORPTION SPECTRUM OF $[Ru(bpy)_3]^{2+}$ IN ACETONITRILE.

1.3.1.4 Excited State Properties.

The lowest excited state of $[Ru(bpy)_3]^{2+}$ is ^{3}MLCT. In fact, the excited state is a cluster of 3 MLCT states all predominately triplet in character. Meyer *et al.* produced a model of this cluster of excited states based on low temperature – dependent behaviour.[22] The energy gaps and quantum yields are shown in FIGURE 1.7 with the results obtained for $[Os(bpy)_3]^{2+}$ included for comparison. Not shown in the diagram is the "4th" MLCT that is populated at higher temperatures for $[Ru(bpy)_3]^{2+}$. This has been omitted as it is of significantly more singlet character (as much as 90%) and as such is not part of the triplet manifold.[22]

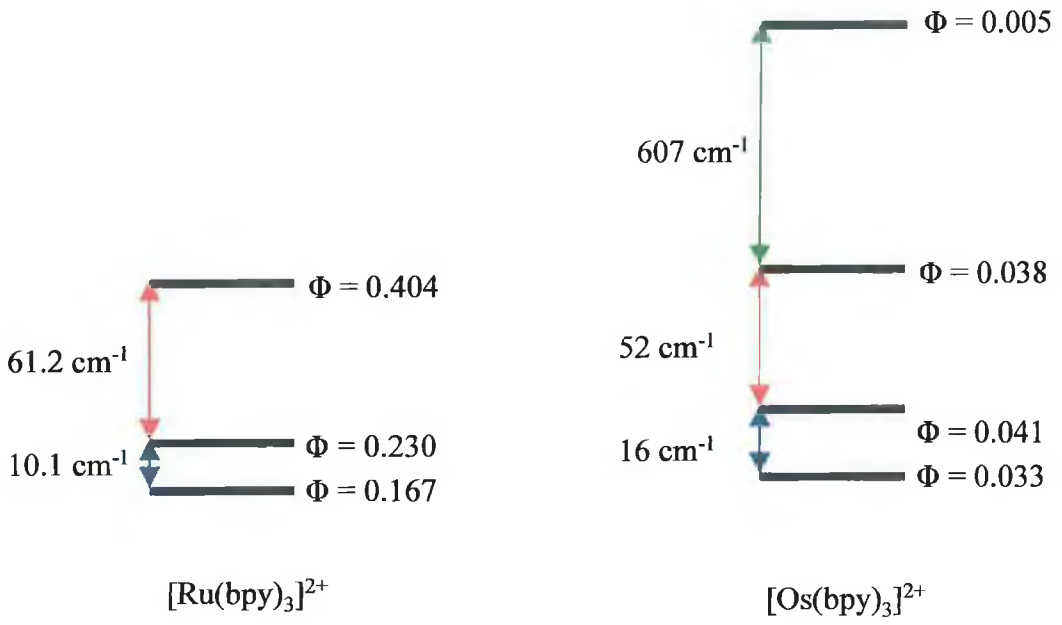

FIGURE 1.7: ENERGY LEVELS OF THE CLUSTER OF ^{3}MLCT EXCITED STATES FOR $[Ru(bpy)_3]^{2+}$ AND $[Os(bpy)_3]^{2+}$.

In acetonitrile solution, emission is at 611 nm at room temperature, with emission blue – shifted to 582 at 77K in an ethanol:methanol (4:1) glass. Excited state lifetime is 168 ns in aerated acetonitrile, and although results are known to vary greatly, the value for the degassed sample is ~ 1μS. For many years it was thought that excitation of the complexes in any of its absorption bands resulted in the formation of a ^{3}MLCT excited state with near unity efficiency. However, recent studies with a variety of techniques have shown an appreciable emission from the ^{1}MLCT excited state (see Chapter 3).[23]

The MC (metal centred) excited state of $[Ru(bpy)_3]^{2+}$ is strongly displaced with respect to the ground state geometry along the metal – ligand vibrational coordinates.[16] Population of the MC is via coupling with the ^{3}MLCT. It is possible to make the lowest excited state MC by judicious choice of ligand, however, in these complexes it undergoes fast radiationless deactivation to the ground state and/or ligand dissociation.[24] Potential photolability is one of the drawbacks in the application of $[Ru(bpy)_3]^{2+}$ as a solar energy catalyst and, as such, considerable interest has been shown in increasing the ^{3}MLCT – ^{3}MC energy gap.

In the excited state $[Ru(bpy)_3]^{2+}$ is both a better reducing and oxidising agent. FIGURE 1.8 provides an overview of the redox potentials in the excited state.

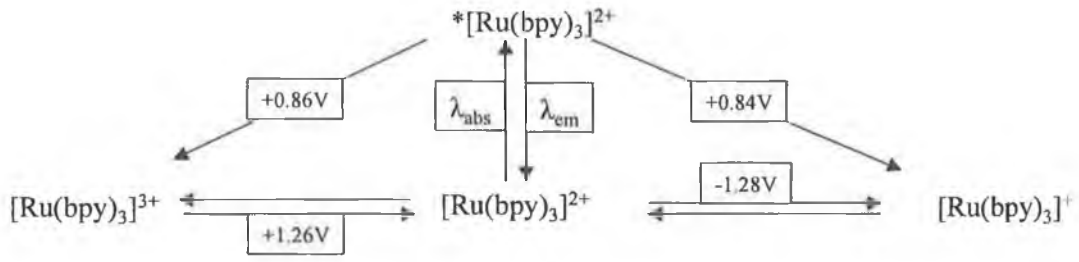

FIGURE 1.8: EXCITED STATE OXIDATION AND REDUCTION POTENTIALS.

The increased reducing and oxidising ability of $[Ru(bpy)_3]^{2+}$ in the excited state offers the possibility that it may act as a sensitiser. As a light absorption sensitiser (LAS) $[Ru(bpy)_3]^{2+}$ can absorb light energy and transfer a portion of this energy to another molecule by a redox process. This allows a molecule which does not absorb large amounts of light energy to undergo photoredox processes, with $[Ru(bpy)_3]^{2+}$ acting as an intermediary.[25] This may also be thought of as an example of light energy being used to catalyse a reaction.

1.3.1.5 Localised versus Delocalised Excited State.

Considerable interest has been focused on the extent of localisation of the excited state electron in $[Ru(bpy)_3]^{2+}$. EQN 1.3 shows the different possible excited state structures based on the degree of localisation.

$$[Ru(bpy)_3]^{2+} + h\nu \rightarrow [Ru^{3+}(bpy^{-})(bpy)_2]^{2+}$$
$$[Ru(bpy)_3]^{2+} + h\nu \rightarrow [Ru^{3+}(bpy^{-\frac{1}{3}})_3]^{2+}$$

EQN. 1.3

The Electron – Ion Coupling model, proposed by Crosby *et al.*, consists of three levels. The lowest energy level has D_3 symmetry and is formed from the lowest anti-bonding orbitals of each ligand, which led to a delocalised excited state model.

In the localized picture, the Ru-LL unit is proposed to be of C_{2v} symmetry. However, a drawback of this model is that the LL and Ru-LL units would be essentially independent and therefore dual emission (*vide infra*) would be expected for complexes such as $[Ru(bpy)_3]^{2+}$.

A variety of techniques have been used to determine whether the excited state is localised or delocalised. Although the issues remains complex, it is now believed that the localised model with electron hopping between ligands on the picosecond timescale is a more accurate description. This is based on resonance Raman studies of the saturated MLCT state which show bands due to both bpy^0 and $bpy^{-\bullet}$.

1.3.2 Triazole containing Complexes

1,2,4 – triazole containing complexes have shown considerable promise in the construction of practical molecular devices. Properties such as photochemical stability, pH dependent behaviour and synthetic versatility which are present that lead to the possibility of a wide range of applications.[26] The triazole ligand is a strong σ-donor and can be coupled with pyrazine, pyridine and quinoline moieties of varying σ-donor / π-acceptor strength. Variation of the symmetrical diimine ligands by the use of 1,10 – phenanthroline, 4,7-diphenyl-1,10 – phenanthroline and 2,2′-biquinoline increases the synthetic possibilities as well as the photophysical and photochemical properties on offer.[27,28] Coordination isomers are possible due to the asymmetry of the triazole ligands. The N2 and N4 isomers are seen to have different properties due to the stronger σ-donor properties of the N2 nitrogen.[29] The ability to substitute the ring selectively has increased the number of complexes for study and has also aided in the tailoring of their properties.

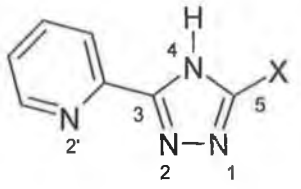

FIGURE 1.9: NUMBERING SCHEME FOR TRIAZOLE.

Two synthetic schemes for the formation of a substituted triazole ligand are shown in FIGURE 1.10. It is important to note the versatility available through the choice of the starting material. This leads to the possibility of coordination isomers through the synthesis of asymmetric ligands, as well as dimer formation.

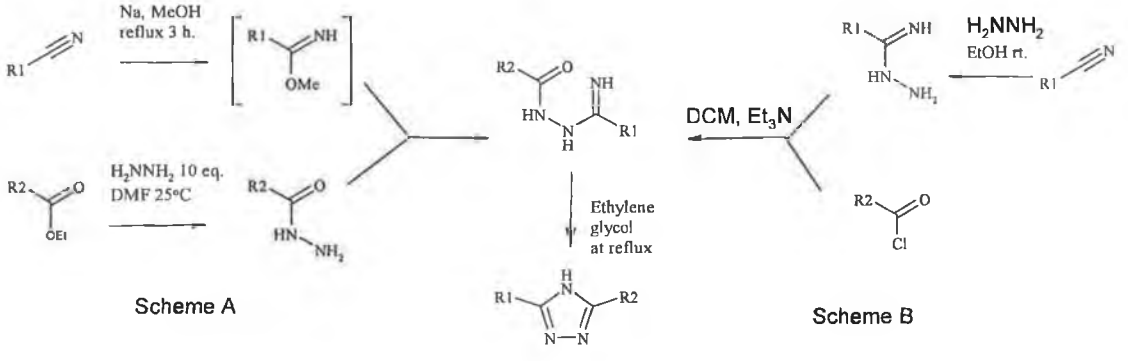

FIGURE 1.10: SYNTHESIS OF A SUBSTITUTED 1,2,4-TRIAZOLE.

The use of 1,2,4 – triazole ligands in ruthenium complexes was first reported by Vos and co-workers.[30] The numbering scheme of the triazole is shown in FIGURE 1.9. It is important to note the position of the N2 and N4 nitrogens. In these early studies the triazole acted as monodentate ligands. Triazoles were first employed as bidentate ligands in homoleptic Ru(II) complexes with pyridine used as the second chelating moiety.[31] Triazole ligands were then incorporated into the heteroleptic $[Ru(bpy)_2(pytr)]^+$, where pytr is 2'-(1,2,4-triazol-3-yl)-pyridine, and characterised by NMR, electronic spectroscopy and

electrochemistry.[32] This is an analogue of the thoroughly studied complex $[Ru(bpy)_3]^{2+}$ with one of the pyridine groups replaced with the triazole.

The absorption and emission properties of Ru(II) complexes containing a triazole ligand are seen to be similar to those of $[Ru(bpy)_3]^{2+}$.[33] However, the strong σ-donating triazole group leads to a red shifting of the absorption and emission maxima as compared to $[Ru(bpy)_3]^{2+}$. This is due to the increased electron density on the metal core, which raises the energy of the ground state and decreases the energy gap for electronic transitions. The red shift observed for the N4 isomer is less then that for the N2 isomer and reflects the decreased σ-donor ability of the N2 position.[29]

The application of HPLC techniques has also been highlighted in the study of the reactions of Ru polypyridyl complexes. The N2 and N4 coordination isomers were separated by semi-preparitative chromatographic techniques.[34] The presence of the free nitrogen in the monomeric complexes leads to the possibility of acid/base chemistry.[35] This has been extensively studied[36] for both $[Ru(bpy)_2(pytr)]^+$ and $[Ru(bpy)_2(3\text{-Methyl-pytr})]^+$. Protonation leads to a blue shifting of the absorption and emission maxima. The acid / base behaviour of the complex in the excited state can also be used to detect the location of the excited state. If the excited state is located on the ligand that is involved in the absorption and emission process, the complexes should be more basic in the excited state. $[Ru(bpy)_2(pytr)]^+$ shows increased acidity in the excited state, indicating that the excited state is bpy – based, which is also confirmed by resonance Raman data. Isomerisation of the coordination mode can be achieved by both photochemical and thermal means.[37] The protonation state of the complex has also been shown to affect the photochemistry.[28]

Symmetrical substituted pyridyl triazole ligands were first synthesized in the form of the bis-pyridyl triazole (bpt). The synthesis of this ligand led to the formation of the first dinuclear Ru(II) complexes containing a 1,2,4-triazole moiety.[38] Dinuclear complexes were of particular interest because of the

possibility of transferring two electrons and the formation of mixed valence compounds. Mixed valence compounds have the added photophysical property of an intervalence transition. The first mixed metal dinuclear complex synthesised and characterised[39] was $[(bpy)_2Ru(bpt)Os(bpy)_2]^{3+}$. In this complex it is seen that the oxidation potential changes depending on whether the Os or Ru moiety is bound to the N1 position of the triazole. In these complexes intense intervalence transition bands are observed suggesting a moderately strong interaction between the metal centres. The energy of these bands are correlated to the oxidation potentials of the centres. Complexes containing other symmetrical diimine ligands such as 1,10-phenanthroline[40] (phen), 2,2′-biquinoline[41] (biq) and 4,4′-dimethyl-2,2′-bipyridyl (dmbpy)[42] have also been investigated. Biq is a good π-acceptor complex which leads to a red shifting of the absorption and emission maxima. For $[Ru(phen)_2(bpt)]^+$ the absorption is blue-shifted compared to the bpy containing analogue, while the room temperature emission and redox properties are little changed. These studies also showed that the bpy-based ^{3}MLCT is lower than that of the phen. The synthesis of multinuclear complexes was also extended to tri[43]-, tetra[44]- and hexa[45]-nuclear complexes.

The pyrazinyl-substituted triazole complex, $[Ru(bpy)_2(pztr)]^+$, where pztr is 2′-(1,2,4-triazol-3-yl)-pyrazine, was also synthesised and its acid / base properties investigated.[29] For this complex the coordination mode (N2 or N4) is seen to effect the physical properties. The N4 coordinated isomer is more acidic, has a higher energy ^{3}MLCT emission and a higher oxidation potential. This again confirms the stronger σ-donor ability of the N2 position. The location of the excited state in this complex was seen to switch from bpy to pyrazinyl-triazole depending on the protonation state. This led to extensive investigation of the temperature dependent emission from N2 isomer of the complex.[46] A temperature dependent dual emission was observed in the temperature range from 140K-200K. The pyrazine moiety is a stronger π - acceptor and hence there is a red shift of the absorption and emission maxima as compared with the pyridine containing analogue. The effect of protonation

of the triazole is similar to that for the pyridine-containing complex. The presence of a free nitrogen on the pyrazine leads to the further possibility of pH dependent behaviour. This nitrogen is protonated at negative pH and it leads to a quenching of emission.[35]

More recent work has concentrated on dinuclear complexes with a variety of bridging ligands. The pyrazinyl – triazole moiety has been used in the construction of dinuclear complexes with some examples given in FIGURE 1.11.[47,48,49,51] These studies have encompassed metal centres coordinated in both monodentate and bidentate fashions. A variety of triazole substituents have been used as bridges in dinuclear complexes.[49] The extent of interaction is dependent on the protonation state of the triazole and the bridging moiety selected.[50] The first published computational studies of Ru(II) complexes containing a triazole moiety were performed on a dinuclear complex with pyrazine as the bridging moiety.[51] This work showed the ability of Density Functional Theory (DFT) to accurately predict properties such as location of excited state and the effect of protonation. DFT studies have also been performed on simple molecules dyads containing a pyrazine triazole ligand.[52] These results have been used to gain a greater understanding of the role of bridging ligands in dinuclear complexes. Recently a publication reviewing the area of excited state structure and intercomponent interaction has been produced which covers the application of a variety of techniques to mono – and di – nuclear systems.[53]

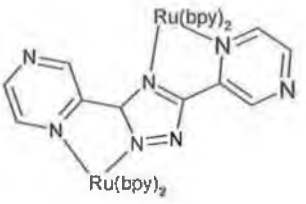

3,5-bis(pyrazin-2-yl)-1,2,4-triazole (bpzt)

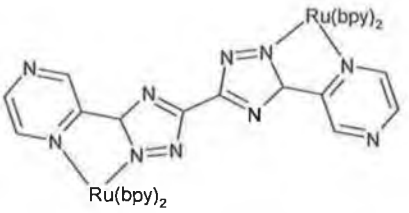

5,5'-bis(pyrazin-2"-yl)-3,3'-bis(1H-1,2,4-triazole)) (bpzbt)

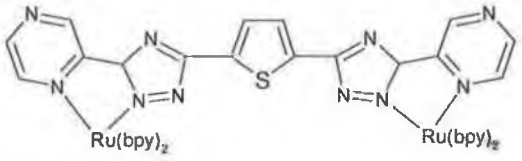

2,5-bis-[5-pyrazinyl-1H-1,2,4-triazol-3-yl]thiophene ($(pztr)_2th$)

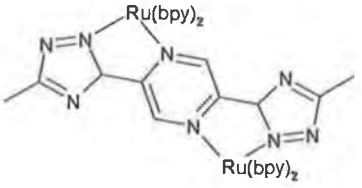

2,5-bis-(5-methyl-1H-[1,2,4]triazol-3-yl)-pyrazine ($H_2(Metr)_2pz$)

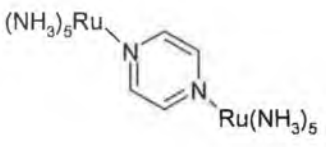

Creutz - Taube ion

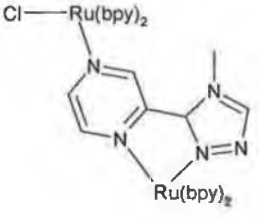

1-methyl-(pyrazin-2-yl)-1,2,4-triazole (1Mepztr)

FIGURE 1.11: EXAMPLES OF DIMERS FORMED USING PYRAZINE CONTAINING LIGANDS. ALSO INCLUDED ARE THE NAMES OF THE LIGANDS AND THE COMMON ABBREVIATIONS USED.

1.3.3 Previous Reports of Dual Emission.

Kasha's rule states that emission from organic molecules originates from the lowest excited state of a given multiplicity. The first example of an exception to this rule was seen in the dual fluorescence of azulene.[54] This statement was refined by Demas and Crosby in 1970 for transition metal complexes to include emission from those states that achieve a significant Boltzmann population. There are a number of differences between the emission observed in transition metal complexes and organic compounds. In transition metal complexes the predominant form of emission is phosphorescence, which often occurs at room temperature with substantial efficiency. Also the emission quantum yields show an excitation wavelength dependency that indicates anisotropic non-radiative coupling between states of different orbital origin.

The first dual emission from a transition metal complex was reported from $[Rh(bpy)_2(phen)]^{3+}$ and $[Rh(bpy)(phen)_2]^{3+}$ at 77K. In these complexes two emissions and lifetimes could be observed which were the same as those seen in the homoleptic parent complexes.[55] These emissions have been categorized as being spatially isolated, ligand centred and are not thermally equilibrated. The emissions in these complexes are not equilibrated because of the lack of an efficient acceptor mode to aid in energy transfer.

Another type of multiple emission has been observed. These emissions occur from states of different orbital parentage i.e. d-d* and d-π^* or d-d* and π-π^*. This was first observed[56] for $[Ir(phen)_2Cl_2]^+$ at 77K. In this complex the dominant emission is d-π^* in nature while the second emission is d-d in nature which persists up to 230 K. The complex $[Ir(5,6\text{-Mephen})_2Cl_2]^+$ shows one emission of π-π^* nature and while again the second emission is of d-d orbital parentage.

Dual emission was also reported for a Cu(I) complex at low temperatures. In $[Cu(dmp)_2]^+$ both emissions are MLCT based, however, one is from a singlet excited state, while the other emissive excited state is a triplet.[57]

The complex $[Ir(LL)(LL')_2]^+$ (where LL=bpy or phen and LL'=2-phenylpyridine or benzo[h]quinoline) was also seen to show dual emission at 77 K. Again in these complexes the excited states are spatially isolated.[58] However, thermal equilibration is also thought to be hindered by the viscosity dependent Franck-Condon barrier to energy transfer between states which show a large geometric difference. In these complexes the excited states are both ^{3}MLCT and based on different ligands. Above the glass transition temperature only a single emission occurs, indicating that the energy transfer is efficient in fluid environments. Dual emission of this type is similar in nature to that observed in ruthenium pyrazinyl-triazoles that is discussed in this report.

Finally, dual emission can also occur from dinuclear complexes. An example of this is the complex $[Ru(bpy)_2(bpyen)Re(CO)_5(py)]^{3+}$, where bpyen is 1,2-bis(4'-methyl-2,2'-bipyridyl-4-yl)ethane, which emits at both 610nm and 540nm.[59] The absorption spectrum of the complex could be modelled with a 1:1 mixture of the monomeric analogues, however, the emission spectra requires a 9:1 Ru:Re mixture. This indicates that there is some communication via the bridging ligands in the excited state but not enough to fully deactivate the Re excited state.

1.3.4 Emission Lifetime Temperature Dependence.

Low temperature studies in the 1.8 – 77K range have shown that luminescent from Ru(II) polypyridyl complexes originate from a cluster of three closely lying levels which are in Boltzmann equilibrium.[60] The rate of radiative transition is generally governed by spin and symmetry factors, while the radiationless rate constant is generally seen to increase as the temperature is raised. The temperature dependent terms are associated with two different forms of deactivation.

The deactivation of the excited state by vibrational modes due to the melting of the frozen environment[61] is expressed by the following equation:

$$k_{nr} = \frac{B_i}{1 + e^{[C_i(\frac{1}{T} - \frac{1}{T_{B_i}})]}}$$

This describes stepwise behaviour centred on a temperature T_{Bi}, with C_i related to the smoothness of the step and B_i the value of k at $T >> T_{Bi}$.

An Arrhenius equation may be used to describe the activated surface crossing from the ^{3}MLCT to another excited state. This may be to the ^{3}MC state or may result in coupling of a weakly coupled fourth ^{3}MLCT state.[62]

$$k = Ae^{-\frac{\Delta E_i}{RT}}$$

where k is the rate, A is the prefactor, ΔE is the activation energy and T is the temperature.

FIGURE 1.12 gives an overview of the potential energy diagrams for an electron transfer reaction. ΔE_i is the free activation energy of the electron transfer (ΔG* in the figure). This is related to the energy differences between the initial and final states and the reorganisation energy (inner and outer sphere). The prefactor has contributions from the average nuclear frequency factor, v_N, and the transmission co – efficient, κ. When this is strong electronic interaction between the initial and final states, 2H is large and κ = 1. This is referred to as the adiabatic limit. In this limit the rate limiting step is the nuclear motion which leads to the transiton state. In contrast when 2H is small, the rate limiting step is electron transfer once the transition state geometry is attained.

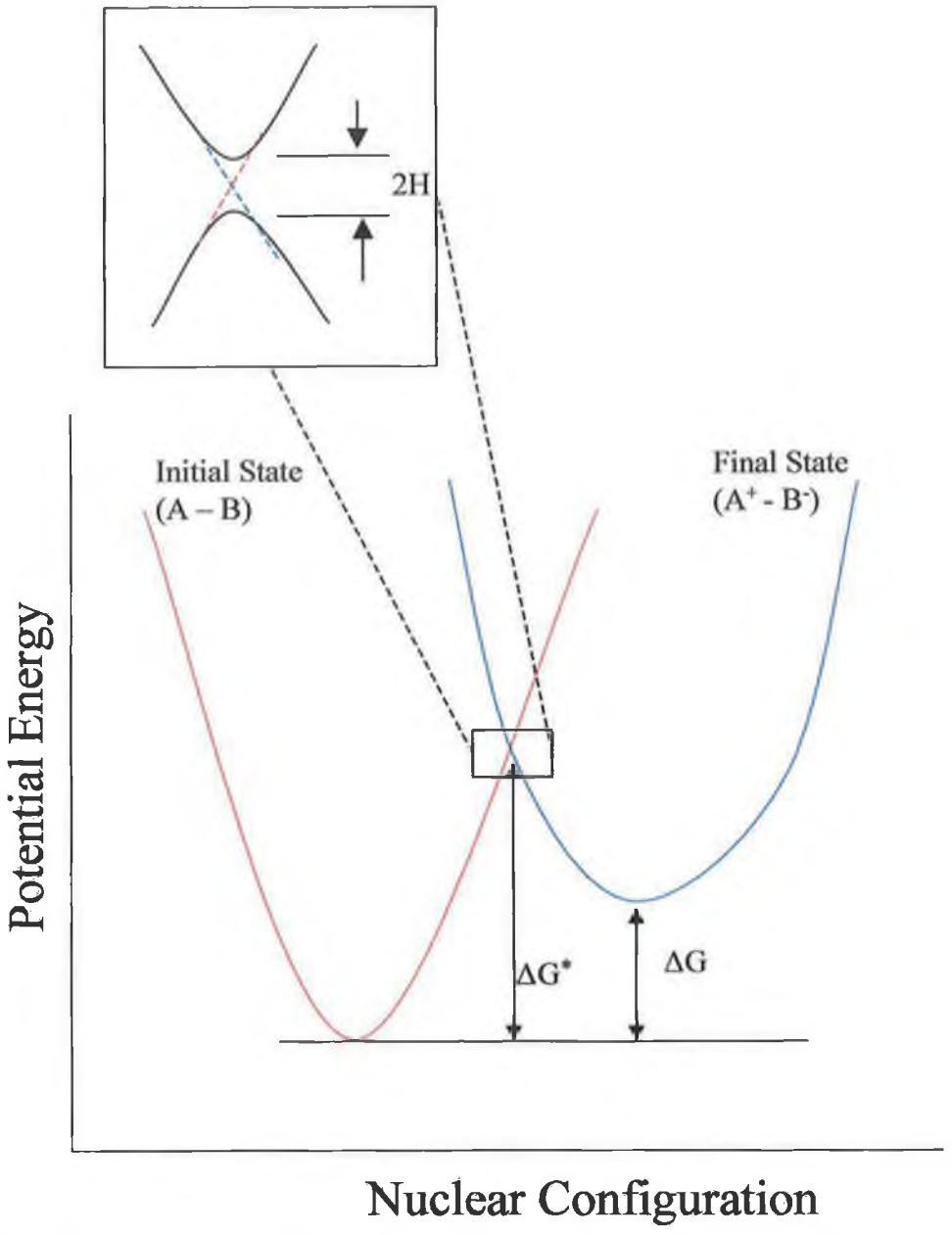

FIGURE 1.12: POTENTIAL ENERGY CURVES FOR AN ELECTRON TRANSFER REACTION.

1.3.5 Deuteriation.

In the present work, deuteriation has been applied to vibrational spectroscopy and in the measurements of excited state lifetimes. The exchange of hydrogen for deuterium can be achieved by a number of methods. Deuteriated starting materials can be used in the synthesis of selectively deuteriated molecules. This has been employed in the synthesis of partially deuteriated triazole containing ligands (see APPENDIX D) and dipyridophenazine (dppz).[63] It is also possible to exchange labile acidic hydrogens by dissolving the sample in a deuteriated protic solvent.[64] The method which has been applied in the current work is that developed by Vos *et al.*[65] This method employs 10% Pd/C catalyst and D_2O with exchange occurring under pressure and high temperatures. Repeated exchange reactions are required to ensure complete deuteriation. This method is often used to synthesise deuteriated starting material for the preparation of selectively deuteriated complexes.

Deuteriation is seen to affect the vibrational spectra and excited state lifetime of a variety of complexes. An extensive review of the effect of deuteriation on the excited state lifetimes of platinum and lanthanide group complexes has been produced by Browne and Vos.[66] The classical expression for vibrational frequency[67] is shown below:

$$\upsilon = \frac{1}{2\pi c}\sqrt{\frac{k}{\mu}} \qquad \text{WHERE} \qquad \mu = \frac{1}{m_1} + \frac{1}{m_2} \qquad \text{EQN. 1.4}$$

k is the force constant, c is the speed of light and ν is the frequency. μ is known as the reduced mass of the system, while m_1 and m_2 are the masses of the two bodies. On the basis of this simple reduced mass system deuteriation results in a decrease in the frequency of a vibration. When applied to vibrational spectroscopy, in general, selective deuteriation leads to the shifting of the bands due to this ligand to lower frequencies, thus allowing assignment of the bands.

As shown in Eqn. 1.1 the excited state lifetime of a complex is dependent on the sum of the radiative and all the non – radiative processes. The rate of radiative decay (sometimes referred to as the intrinsic lifetime) is dependent on the cube of the emission energy.[68] A variety of processes contribute to the non – radiative deactivation of the excited state such as photochemical reaction or bimolecular quenching (see section 1.2.3). Deuteriation affects the coupling of the excited and ground states. Jortner *et al.* proposed two limiting cases for coupling, the strong and weak coupling limits (FIGURE 1.13).

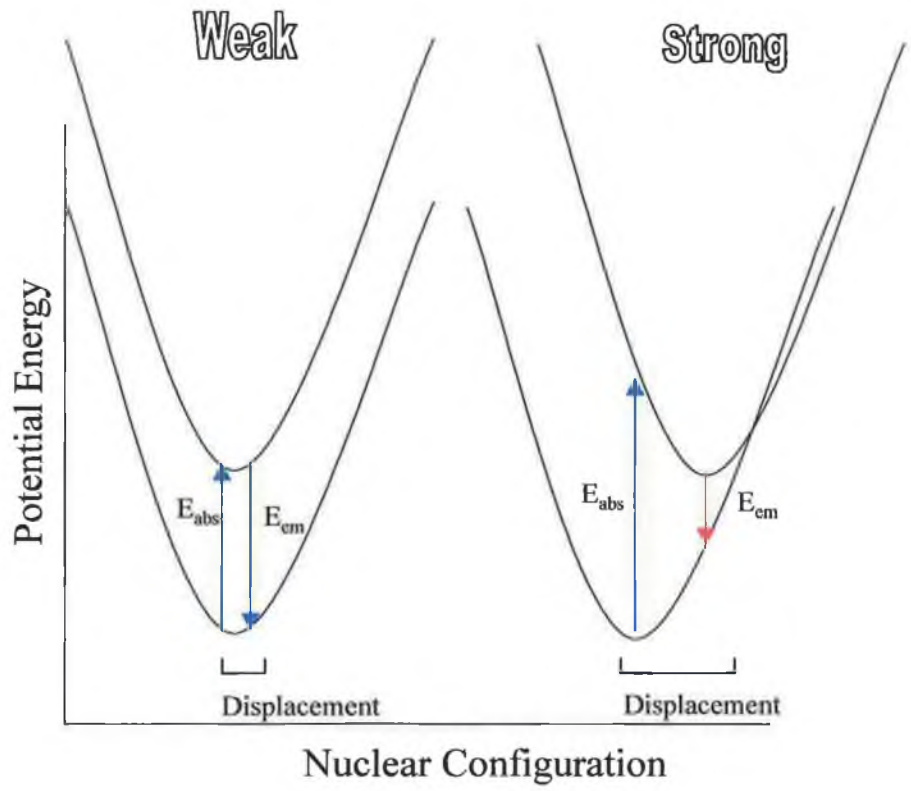

FIGURE 1.13: WEAK AND STRONG COUPLING LIMIT, AND THE EFFECT ON EMISSION ENERGY.

Weak coupling occurs when the excited state has a similar nuclear configuration to that of the ground state, for example in ligand centred excited states. In contrast, strong coupling occurs when the ground and excited states have different structures, such as in charge transfer excited states. The Stokes shift can be used as a measure of the relative displacements of the ground and excited states and it can be seen that in the strong coupling limit that there is a large difference in the absorption and emission energy. The effect of

deuteriation is reduced in the strong coupling limit due to possibility of all vibrational modes accepting energy, rather than simply those of the type C-H.

The rate of non – radiative deactivation due to vibrational modes is give in Eqn. 1.5.

$$k_{x-H} = (\frac{2\pi}{\eta})\rho JF(E) \qquad \text{EQN. 1.5}$$

where p is the weighted sum of the energy gap between vibrational states, J is the electronic coupling and F(E) is the Franck – Condon sum of the products of the overlap integrals. As show by Eqn. 1.4 the vibrational frequency is reduced by deuteriation while the amplitude is also reduced. This reduction in the rate of non – radiative deactivation leads to an increase in the excited state lifetime of a complex on ligand deuteriation if the ligand is involved in the excited state. This effect has been used previously to aid in the assignment of the location of the excited state.[65]

Deuteriation has been applied to aid in the photophysical studies of a wide variety of molecules. Its first application was in the study of the excited state decay of organic molecules. The effect of ligand and solvent deuteriation on $[Ru(bpy)_3]^{2+}$ lifetimes was investigated by Watts *et al.*[69] The first use of deuteriation in Ru(II) complexes containing a triazole ligand was performed by Vos and co – workers.[65] Since then it has been applied to aid in synthetic[70], photochemical, vibrational[52] and computational studies (see APPENDIX D).

1.4 Raman Spectroscopy.

Raman spectroscopy is an rapidly - growing field of physical chemistry whose ability to elucidate distinct structural characteristics in a variety of media has led to intensive studies and a renewed interest in its industrial analytic application.

1.4.1 Historical Development.

The Raman effect is based on the inelastic scattering of light from molecules with the first spectra recorded in 1928.[71] During the 1950's and 1960's the growth in infrared spectroscopy as a vibrational structure probe led to a decrease in the use of Raman spectroscopy. However, the development of lasers and the subsequent production of intense monochromic light sources have led to a rediscovery of the applicability and versatility of the Raman technique. As laser technology progressed the number of accessible wavelengths increased leading to the possibility of vibrational probing over a wide spectral range.

More recently Raman spectroscopy has been applied to a variety of practical problems. The non – destructive nature of Raman measurements means that the technique is ideal for *in vivo* studies and testing of evidence in criminal cases. Studies of the inactive ingredients and the degree of hydration of active MDMA in seized ecstasy tablets have shown the potential to identify a common manufacturer of a range of tablets.[72] Other work has also raised the possibility to quickly and accurately identify other hazardous substances such as anthrax spores[73] and nicotine.[74]

1.4.2 Stokes and Anti-Stokes Radiation.

The signals obtained in Infra Red Spectroscopy are due to the absorption of energy and the transition between two distinct vibrational levels in the sample molecules. The selection rule for an IR transition is that, in order for a transition to occur, it must lead to a change in the polarity of the molecule under investigation. By contrast, Raman spectroscopy does not result from the absorption and re-emission of a photon but is a single photon process. The collision of the probe photon results in the formation of a virtual excited state and the excess energy obtained in this state is then lost to produce a signal. The selection rule for a Raman signal is that it must produce a change in the polarisability of the molecule.[75] Shown in FIGURE 1.14 are the differences between Rayleigh, Stoke and Anti-Stokes Radiation.

Rayleigh radiation is due to the formation of a virtual excited state and then the re-attainment of the vibrational ground state. There is no shift in the frequency of the radiation and it remains the same as that of laser excitation source. This can be used as a reference line for the Stokes and anti-Stokes radiation. While re-attaining the ground state structure a proportion of the molecules may first relax to a vibrationally excited state. The emerging photon would, therefore, be of lower energy that that of the excitation source and this leads to a shifted signal. This is known as Stokes radiation. The shift of this signal is generally reported in reference to the Rayleigh line and is indicative of the vibrational structure of the molecule in question.

Anti-Stokes radiation occurs when the molecules form the virtual excited state from a state that is not in the vibrational ground state and then re-attains the ground state configuration. This is due to the Boltzmann distribution of molecules that are in a vibrationally excited state due to thermal energy. Anti-Stokes radiation leads to a signal that is at higher frequency (and hence energy) than the Rayleigh line.

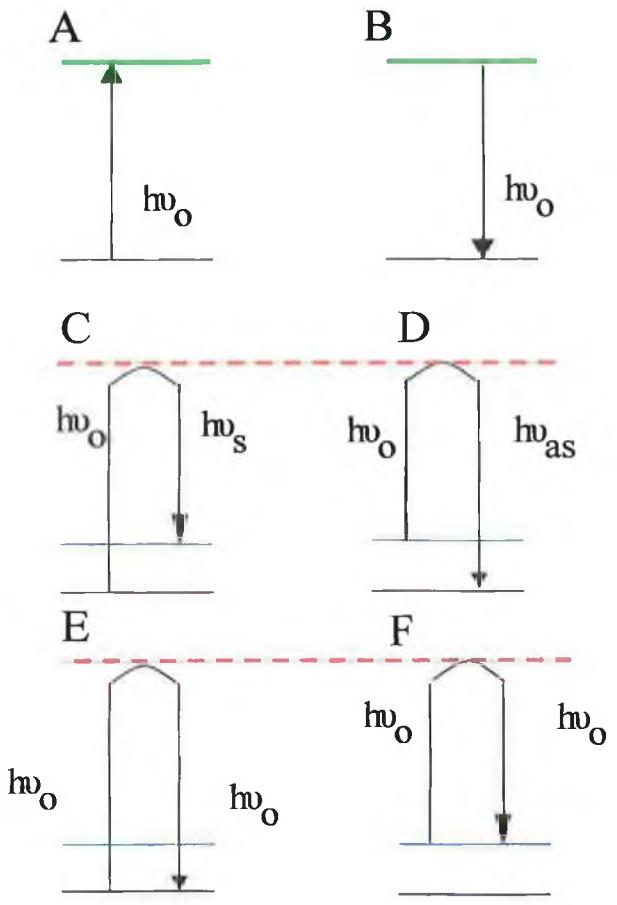

FIGURE 1.14: DIAGRAMS ILLUSTRATING (A) ABSORPTION, (B) EMISSION, (C) STOKES RAMAN SCATTERING, (D) ANTI-STOKES RAMAN SCATTERING, (E) AND (F) RAYLEIGH SCATTERING FROM THE TWO DIFFERENT LEVELS. NOTE THAT THE GREEN LINES REPRESENT ELECTRONIC ENERGY LEVELS, THE RED LINE VIRTUAL STATES AND THE BLUE LINES VIBRATIONAL STATES.

1.4.3 Resonance Raman Spectroscopy.

The signals obtained from Stokes and anti-Stokes radiation are quite weak ($\sim 10^{-6}$ of the intensity of the Rayleigh radiation). However, when the excitation energy of the probe pulse is chosen to coincide which an absorption band of the molecule an enhancement of the Stokes and anti-Stokes signals is produced.[75] The signals that are enhanced to the greatest extent are those that are associated with the absorption band on which the probe energy is coincident.

1.4.4 Other Raman Techniques.

Surface Enhanced Resonance Raman spectroscopy (SERRS) is the study of samples which have been adsorbed onto roughened metallic surfaces. This adsorption results in a enhancement of up to 5 orders of magnitude of the Raman signal. This technique allows the detection of small quantities of sample (even on the part per billion scale[74]). The observation of a surface enhanced Raman signal was first made by Fleischmann *et al.*,[76] however, the true nature of the effect was not identified until work by Creighton *et al.*[77] Two mechanisms of enhancement have been identified, the electromagnetic model and the charge transfer model. The electromagnetic model proposes that the Raman signal is enhanced by interaction with the surface plasmons. These plasmons, which are particularly associated with nanoparticles, are thought to radiate a portion of their energy at roughened surfaces and enhance the Raman signal when it is at resonant energies. In the second theory, called the electromagnetic model, the incident radiation is thought to excited a surface electron into the LUMO of the adsorbed sample. This excited sample emits an enhanced Raman photon while the electron tunnels back to the surface.

Scissors or Shifted Subtracted Raman Spectroscopy (SSRS) is a techniques which was developed by Bell and co-workers.[78] A common problem encountered in the collection of Raman data is the presence of a strong fluorescent background. The use of lower energy excitation can reduce fluorescence however this method is not applicable in all cases. In order to subtract this fluorescent background from Raman data a large number of accumulations is required to reduce the random noise in the measurements. However, differences in the sensitivities of individual pixels in the CCD detector used becomes significant at large accumulations. These differences can be compensated for by use of the SSRS method which takes two spectra focussed on different parts of the detector. Therefore in the two spectra different pixels are used to accumulate the data points of the spectra. These spectra can now be subtracted, which removes the fluorescent background, and using a

specially designed algorithm the original spectra reconstructed. This technique has been investigated used dye – treated cyclohexane[78a] and applied to problems such as that of document analysis.[78b]

1.5 Computational Chemistry.

This section serves as an introduction to the field of computational chemistry. The advent of relatively cheap, fast and easy to use computers has led to a considerable growth in the practicality of undertaking computational studies. The added processing power of next – generation computers has been particularly important for transition metal complexes were the computational power needed to accurately account for the d orbital electrons is now within the reach of the average research group. Firstly, molecular orbital theory is explained, as the basis on which the other methods were developed, followed by the important principles of Density Functional Theory – which has been used for the studies in this work. An overview of the other available techniques is also provided along with a selection of publications on Ru(II) complexes.

1.5.1 Molecular Orbital Theory.

At the dawn of the 20th century physicists began to discover the limitations of classical mechanics to explain phenomena such as black – body radiation and atomic spectra. The ability of wave mechanics to approximate the observed quantized systems made it suitable theory for application in the investigation of atomic particles. Thus from wave mechanics was born the fundamental postulate of quantum mechanics, the Schrödinger Equation (Eqn. 1.6)

$$H\Psi = E\Psi \qquad \text{EQN. 1.6}$$

where H is an operator called the Hamiltonian operator which returns the energy, E, of the system defined by the wavefunction, ψ. The basic Hamiltonian has the form shown in Eqn. 1.7;

$$H = -\sum_i \frac{\eta^2}{2m_e}\nabla_i^2 - \sum_k \frac{\eta^2}{2m_k}\nabla_k^2 - \sum_i \sum_k \frac{e^2 Z_k}{r_{ik}} + \sum_{i<j} \frac{e^2}{r_{ij}} + \sum_{k<l} \frac{e^2 Z_k Z_l}{r_{kl}} \quad \text{EQN. 1.7}$$

where i and j run over electrons, k and l run over nuclei, $\hbar$ is Planck's constant divided by 2π, m_e and m_k are electron and nuclear mass respectively, ∇^2 is the Laplacian operator, e is the charge on the electron, Z is an atomic number and r_{ab} is the distance between particles a and b. Note that the first two terms relate to the kinetic energy of the system while the last three relate to the potential energy.

For a real system the correlated motion of all the associated particles make it extremely difficult to obtain an accurate wavefunction. At this point the Born – Oppenheimer Approximation is applied, which allows separation of the relative motion of the nuclei and electrons. Since the nuclei are far more massive than the electrons the system can be treated as if the nuclei are static and the electrons react instantaneously to any changes in nuclei positions. With this assumption the Hamilton is simplified (technically it returns only the electronic energy of the system) and also the idea of a "Potential Energy Surface" is derived.

Although it is now possible to use operators to obtain various properties of the system we still do not know how to construct an appropriate wavefunction to describe the system. However, from the Variational Principle we obtain Eqn. 1.8

$$\frac{\int \Phi H \Phi dr}{\int \Phi^2 dr} \geq E_0 \quad \text{EQN. 1.8}$$

where Φ is the wavefunction constructed from any number of orthonormal wavefunctions and E_0 is the ground state energy. The Variational Principle states that the set of appropriate wavefunctions is bounded from below and

that the most accurate wavefunction will have the lowest energy. We may now construct a "guess" wavefunction and use Eqn. 1.8 to evaluate its accuracy. It is also important to note that the correct wavefunction is at the lowest possible energy and therefore we can apply the techniques of calculus which are particularly useful in the location of extremes.

The guess wavefunction is constructed from a linear combination of atomic wavefunctions. To obtain the energy of this guess we use the Variational Principle (Eqn. 1.8) and obtain Eqn. 1.9.

$$E = \frac{\int (\sum_i a_i \varphi_i) H (\sum_j a_j \varphi_j) dr}{\int (\sum_i a_i \varphi_i)(\sum_j a_j \varphi_j) dr} \qquad \text{EQN. 1.9}$$

where φ_i is an atomic wavefunction and a_i is the corresponding co-efficient (collectively they are referred to as the basis set). From the above equation, we can derive the following equation:

$$E = \frac{\sum_{ij} a_i a_j H_{ij}}{\sum_{ij} a_i a_j S_{ij}} \qquad \text{EQN. 1.10}$$

where H_{ij} is called the resonance integral and S_{ij} is the overlap integral. As the Variational Principle showed, the most accurate guess wavefunction was obtained when the energy was at a minimum. Therefore by differentiation of Eqn. 1.10 with respect to all free variables and setting the answer to zero we can produce the lowest energy wavefunction. From this we get:

$$\sum_{i=1}^{N} a_i (H_{ki} - E S_{ki}) = 0 \qquad \forall k \qquad \text{EQN. 1.11}$$

where k represents all the free variables. This is a set of N equations involving N unknowns. To solve these equations the determinant of the co-efficients is formed and set equal to zero.

$$\begin{vmatrix} H_{11}-ES_{11} & \Lambda & \Lambda & H_{1N}-ES_{1N} \\ \mathrm{M} & \mathrm{O} & & \mathrm{M} \\ \mathrm{M} & & \mathrm{O} & \mathrm{M} \\ H_{N1}-ES_{N1} & \Lambda & \Lambda & H_{NN}-ES_{NN} \end{vmatrix} = 0 \qquad \text{EQN. 1.12}$$

Eqn. 1.12 is known as the Secular Equation. From this is obtained N roots with an associated energy, E, and each energy gives rise to different co-efficients which define a wavefunction. The co-efficients associated with the lowest energy wavefunction would then define the ground state while the orbitals with higher energies are the excited states.

The above method derives the molecular orbitals based on a single – electron formalism. A method to deal with multi – electron systems was developed by Hartree and furthered by Fock, and as such became known as the Hartree – Fock (HF) theory. Hartree proposed that the Hamilton is separable (under certain conditions) into a summation of one – electron Hamiltonian's, h_i. The interelectronic repulsion is then included in these one – electron Hamiltonians which is given in Eqn. 1.13.

$$h_i = -\frac{1}{2}\nabla_i^{\,2} - \sum_{k=1}^{M}\frac{Z_k}{r_{ik}} + \sum_{j\neq i}\int\frac{\rho_j}{r_{ik}}dr \qquad \text{EQN. 1.13}$$

where ρ_j is the electron (probability) density of electron j. However, since the square of the wavefunction is equal to the probability density, the wavefunction must be known before the electron probability density (and hence the third term) can be calculated. In order to circumvent this problem, Hartree guessed the initial wavefunction for all molecular orbitals and produced one – electron operators and resultant wavefunctlons based on the

initial guess. These results were then used as the guess to calculate the next set of operators and wavefunctions. This iterative procedure was called the "Self – Consistent Field" (SCF) method and was repeated until certain criteria were met (such as the change in energy between two of the steps).

Fock further extended Hartree's work by incorporating Slater determinants (which take into account anti – symmetry and electron spin). Fock replaced the one – electron Hamiltonian with the Fock operator, f_i, and again constructed the secular equation (this time containing F_i to F_N instead of the resonance integral). From this secular equation is derived the energies and corresponding co-efficients required to construct the molecular orbitals. It should also be noted that elements of the Fock operator, F, are weighted by a density matrix, P, which is related to the co-efficients of the wavefunctions. Again this produces a paradox as the co-efficients are only known once the secular equation has been solved. To solve this an iterative method is used in which an initial guess at the density matrix is used to find the co-efficients which are used for the next step. The importance of these initial guesses cannot be underestimated and one of the most significant improvements of the computational software Gaussian 03 over earlier versions is said to be the quality of the initial guess.

1.5.2 Density Functional Theory.

Although the early foundations of Density Functional Theory (DFT) was laid by Thomas, Fermi and Slater its great potential for dealing with chemical problems was not realized until the work of Hohenberg, Kohn and Sham. The main difference with DFT in comparison to Hartee – Fock theory described above is that electron density replaces the wavefunction as the central element in the construction of the Hamilitonian. The electron density was chosen to describe the kinetic and potential energies of the system as integration of the density over all space gives the number of electrons present, while their positions are found in the area of local density maxima. The early

work provided the equations for the potential and kinetic energy of the system based on the electron density, shown in Eqn 1.14 and Eqn 1.15.

$$V_{ne}[\rho(r)] = \sum_{k}^{nuclei} \int \frac{Z_k}{|r - r_k|} \rho(r) dr \qquad \text{EQN. 1.14}$$

$$V_{ee}[\rho(r)] = \frac{1}{2} \int\int \frac{\rho(r_1)\rho(r_2)}{|r_1 - r_2|} dr_1 dr_2$$

$$T[\rho(r)] = \frac{3}{10}(3\pi^2)^{\frac{2}{3}} \int \rho^{\frac{5}{3}}(r) dr \qquad \text{EQN. 1.15}$$

Note that the energies are a function of the electron density while this itself is a function of the coordinates, r. This "function of a function" is known as a functional, hence the name of the theory.

The work of Hohenberg and Kohn (for which Kohn won the 1998 Nobel Prize for chemistry) provided a Variational Principle and the Hohenberg - Kohn Existence Theorem. The Variational Principle is similar to that given in section 1.5.1 and states that the calculated energy is greater than or equal to the true ground state energy. As such the most accurate result can be obtained by minimising the energy. The Hohenberg – Kohn Existence Theorem dictates that the Hamilton constructed from the electron density functionals not only defines the energy of the electrons but also the energy of the external potential (i.e. the nuclei). This, therefore, proved that the energy of the system could be accurately modeled using only the electron density.

This method uses a system with non – interacting electrons that have the same density as the system if they were interacting, as this simplifies the equation for their kinetic energies. At this point the energy of the system can be successfully obtained from the electron density using Eqn 1.16:

$$E[\rho(r)] = T_{ni}[p(r)] + V_{ne}[p(r)] + V_{ee}[p(r)] + \Delta T[p(r)] + \Delta V_{ee}[p(r)] \qquad \text{EQN. 1.16}$$

where the terms on the r.h.s. are the kinetic energy of the non – interacting electrons, the nuclear – electron interaction, the classical electron – electron interaction, the correction due to electron interaction and all non – classical corrections to electron – electron interaction, respectively. The correction terms (ΔT and ΔV_{ee}) are grouped together and are known as the exchange – correlation energy, E_{xc}. As in Hartree – Fock theory, one – electron operators are now constructed, however, with the electron density as the variable:

$$h_i^{KS} = -\frac{1}{2}\nabla_i^2 - \sum_k^{nuclei} \frac{Z_k}{|r_i - r_k|} + \int \frac{\rho(r')}{|r_i - r'|} dr' + \frac{\delta E_{xc}}{\delta \rho} \qquad \text{EQN. 1.17}$$

It is from these one – electron (Kohn – Sham) operators that the secular equation is produced and the iterative process for obtaining the lowest energy begins.

At this point the only term which is not known exactly is the exchange – correlation energy, E_{xc}. However, no function of p has yet been obtained for E_{xc} and it is with this term that DFT has to approximate. A variety of approximations are available for the exchange – correlation energy, such as the Local Density Approximation[79], Density Gradient Corrections[80] and Adiabatic Correction Method[81], and the reader is directed towards the appropriate references for more information.[82]

1.5.3 Other Techniques.

There are a variety of computational techniques available to the modern scientists each with their own benefits depending on the size and nature of the system and the practical computational expense.

Molecular mechanics methods use classical expressions for a range of forces to predict the energy of a structure. Examples of the forces used are bond

stretching, angle bending, torsions and van der Waals interactions. These forces can be subdivided into valence and non - valence terms, with the first three examples given being valence type and the last interaction being a non-valence type. The extent to which each type is employed is based on the make – up of the model used. The expressions used are parameterized using experimental data, generally from spectroscopy or more recently electronic structure methods, and as such this technique is also referred to as the empirical force field method. The main advantage of molecular mechanics is the low computational cost and hence the ability to treat large systems such as DNA or proteins. However, the calculations are dependent on the quality of the parameters available and these are often difficult to obtain.

Semi – empirical methods are closely related to the HF theory presented in section 1.5.1. This method reduces the computational time compared to HF theory using a number of shortcuts. The main assumption in semi – empirical calculations neglects all products of basis functions which are located on different atoms. This is known as the Zero Differential Overlap (ZDO) approximation.[83] This allows the one – and two – electron integrals of more than two centres to be ignored and the remaining integrals are parameterized in compensation. A number of models have been derived using the ZDO approximation as a basis such as NDDO, CNDO and INDO. Semi – empirical methods are similar to molecular mechanics in that they use experimental data to aid in the calculations. As such they are subject to the same advantages and disadvantages as that method, namely increased computational efficiency and reliance on parameters, respectively. However, it should be noted that since semi – empirical methods do result in the construction of an electronic wavefunction there is the ability to calculate a variety of properties (such as molecular polarizability) which are not available to the force field methods.

1.5.4 Calculations on Ru(II) Complexes.

This section intends to give an overview of previous publications on Ru(II) complexes. As with all areas of computational chemistry, huge strides have occurred over the last decade due to the advent of high – performance, reasonably priced computers. This review is therefore intended to only highlight publications of particular interest to the current work and some of the background.

The first investigations of Ru(II) polypyridyl complexes were, unsurprisingly, carried out on $[Ru(bpy)_3]^{2+}$. Geometry optimisation was carried out by Daul *et al.* using the LDA and GGA functionals.[84] These results showed best agreement for the LDA functional due to the slight overestimation of the bond length by GGA. DFT was first used to investigate the electronic properties of $[Ru(bpy)_3]^{2+}$ by Baerends *et al.*[85] This work attempted to model the MLCT excited state manifold. Although reasonable agreement with experiment was obtained, it was still not possible to describe the fine structure. The work by Daul *et al.* also calculated the energy of the ^{3}MC with the calculated value being 1.5 times that of the ^{3}MLCT.[84] From this it was concluded that vibrational relaxation in the ^{3}MLCT state occurred before any population of the ^{3}MC.

Time – Dependent DFT (TD-DFT) studies were used by Amini *et al.* to investigate the excitation energy of the lowest energy excited state, again with good agreement obtained.[86] The first published TD – DFT studies on Ru(II) complexes containing a triazole ligand also been used to investigated the properties of dinuclear complexes. These studies showed the ability of DFT to predict the location of the HOMO and LUMO as observed in electrochemical studies. They also highlighted the importance of solvent environment on calculations. The electron density difference maps of the ground state absorption obtained did not agree with the experimental Raman results. This was suggested as due to the calculations being performed in an isolated

environment while the Raman measurements were in H_2O. The first DFT studies of the vibrational spectra of Ru(II) homoleptic complexes were carried out by Dines *et al.*[87] These studies allowed a satisfactory fit of the experimental and calculated spectra using LanL2Dz model, although, ab initio calculations using the 3-21G theory produced unrealistic scaling factors. Work in our group also showed good agreement between the Raman spectra Ru(II) complexes containing a 1,2,4 – triazole and calculated values.[52] These results also highlighted the effect of deuteriation on calculated Raman spectra and the ability to approximate the location of the ground and excited state electron density based on the HOMO and LUMO isosurfaces. Previously studies on the vibrational spectra of transition metal complexes of polypyridyls were carried out by Gordon.[88] These studies show good agreement between the calculated and experimental vibrational spectra for both the ground and excited state species. The excited state was modelled using the reduced complex $[Cu(phen^{\cdot-})(PH_3)_2]^+$. The calculation of Raman spectra has also been used to aid analytical work. In a study by Bell *et al.* the fitting of calculated spectra to those obtained by experiment allows the identification of two rotational isomers for a selection of fatty acid methyl esters.[89] A useful introduction to DFT and vibrational spectroscopy can be found on the personal website of Dr. Roma Oakes.[90]

1.6 Aim of Thesis.

This thesis is concerned with the photophysics of Ru(II) polypyridyl complexes. The processes leading to the formation and deactivation of the THEXI state are investigated on different timescales. At low temperature the excited state deactivation of Ru(II) complexes occurs on the microsecond scale. This process has been investigated using temperature dependent single photon counting. Also investigated was the formation of the THEXI state in a number of complexes at room temperature, a process which is complete on the

picosecond timescale. The excited state decay of these complexes occurs on the nanosecond timescale at room temperature and, as such, information on the photophysical processes has been obtained on 3 timescales.

Firstly, Chapter 3 looks at the picosecond time resolved resonance Raman(TR^3) spectra of $[Ru(bpy)_3]^{2+}$ as well as two heteroleptic complexes. Although $[Ru(bpy)_3]^{2+}$ is a paradigm complex in the study of inorganic photophysics and is the most well understood of all the Ru(II) complexes, a number of issues still remain outstanding. These TR^3 studies are used to investigate the rate of formation of the THEXI state. The effect of change in the overall charge of the molecule and the electron density on the metal centre is investigated through the study of a triazole containing complex which shows pH dependent photophysics. The effect of electron withdrawing groups is also investigated through the study of $[Ru(bpy)_2(Hdcb)]^+$ (where dcb is 2,2'-bipyridyl, 4,4'-carboxylate). The photophysical properties of dcb containing complexes are the subject of intense study in their own right as they have the potential for electron injection (and hence charge separation) upon binding to TiO_2 surfaces.

Chapter 4 and 5 investigate the photophysical properties of Ru(II) complexes with triazole containing ligands. Chapter 4 studies complexes of both pyridine and pyrazine triazole ligand which are substituted at the C-5 positions. This work is particularly interesting as the C-5 position may act as a bridge between metal units in dinuclear complexes. In order to better understand the interaction of units inside di – and multi – nuclear systems a comprehensive characterisation of the monomers components is required. This is achieved through the use of a variety of techniques such as Raman spectroscopy, fluorescence measurements and computational studies.

Chapter 5 looks at the properties of pyrazine triazole complexes with a selection of LL ligands (where the complexes are $[Ru(LL)_2(pztr)]^+$). Previous studies on $[Ru(bpy)_2(pztr)]^+$ (*vide supra*) containing complexes have shown

the presence of emissions from two non – equilibrated ligands at low temperatures. This work investigates the robustness of this dual emissive behaviour. The complexes investigated have been selected in order to vary the σ – donor / π – acceptor properties and the extent of delocalisation in the excited state.

During the preparation of the thesis a wide range of studies have been undertaken, many in collaboration with other institutes. Appendices D,E and F give an overview of this work. APPENDIX D lists the complexes for which vibrational spectra were calculated. Finally APPENDIX E contains the publications which have been contributed to. APPENDIX F shows the structures of all the complexes studied during the course of this thesis.

1.7 Bibliography.

1 Balzani, V., Scandola, F., Supramolecular Photochemistry, Ellis Horwood, **1991**.

2 Balzani, V., Juris, A., Venturi, M., Campagna, S., Serroni, S., *Chem. Rev.*, **1996**, *96*, 759.

3 Balzani, V., Supramolecular Photochemistry, *Tetrahedron*, **1992**, *48*, 10443.

4 Gokel, G., Crown Ethers and Cryptands, R.S.C.,Cambridge, **1989**.

5 Lehn, J.-M., Sonveaux, E., Willard, A.K., *J. Am. Chem. Soc.*, **1978**, *100*, 4914.

6 Breslow, R., Zhang, B., *J. Am. Chem. Soc.*, **1992**, *114*, 5882.

7 (a) Breslow, R., Brown, A.B., McCullough, R.D., White, P.W., *J. Am. Chem. Soc.*, **1989**, *111*, 4517. (b) Croves, T., Neumann, R, *J. Am. Chem. Soc.*, **1987**, *109*, 5045.

8 Hagfeldt, A., Gratzel, M., *Acc. Chem. Res.*, **2000**, *33*, 269 – 277.

9 Grimaldi, J.J., Boileau, S., Lehn, J.M., *Nature*, **1977**, *265*, 229.

10 Gittins, D.I., Bethell, D., Schriffrin, D.J., Nichols, R.J., *Nature*, **408**, *200*, 67. Gittins, D.I., Bethell, D., Nichol, R.J., Schriffrin, D.J., *J. Mat. Chem.*, **2000**, *10*, 79.

11 (a)http://news.bbc.co.uk/2/hi/uk_news/3883749.stm,
(b)http://news.bbc.co.uk/2/hi/science/nature/2758191.stm.

12 Harding, M.M., Koert, U., Lehn, J.-M., Marquis-Rigault, A., Piquet, C., Siegel, J., *Helv. Chim. Acta*, **1991**, *74*, 594.

13 Lehn, J.-M., Supramolecular Chemistry: Concepts and Prespectives, VCH, **1995**.

14 Elfring Jr., W.H., Crosby, G.A., *J. Am. Chem. Soc.*, **1981**, *103*, 2683.

15 Hoffman, M.Z., *J. Chem. Ed.*, **1983**, *60*, 10, 784.

16 Kalyanasundaram, K., Photochemistry of Polypyridine and Porphyrin Complexes, Academic Press, **1996**.

17 Meyer, T.J., *Acc. Chem. Res.*, **1989**, *22*, 163.

18 Juris, A., Balzani, V., Barigelletti, F., Campagna, S., Belser, P., von Zelewsky, A., *Coord. Chem. Rev.*, **1988**, *84*, 85.

19 Rillema, D.P., Jones, D.S., Woods, C., Levy, H.A., *Inorg. Chem.*, **1992**, *31*, 2935.

20 Koopmans, T., *Physica*, **1933**, *1*, 104.

21 DeArmond, M.K., Carlin, C.M., *Coord. Chem. Rev.*, **1981**, *36*, 325.

22 Kober, E.M., Meyer, T.J., *Inorg. Chem.*, **1984**, *23*, 3877.

23 Browne, W.R., Coates, C.G., Brady, C., Matousek, P., Towrie, M., Botchway, S.W., Parker, A.W., Vos, J.G., McGarvey, J.J., J. Am. Chem. Soc., **2003**, *125*, 1706.; Bhasikuttan, A.C., Suzuki, M., Nakashima, S., Okada, T., J. Am. Chem. Soc., **2002**,*124*, 8398.

24 Crosby, G.A., *Acc. Chem. Res.*, **1975**, *8*, 231.

25 Rillema, D.P., Dressick, W.J., Meyer, T.J., *Chem. Commun.*, **1980**, 274.

26 Fanni, S.; Keyes, T.E.; O'Connor, C.M.; Hughes, H.; Wang, R.; Vos, J.G., *Coord. Chem. Rev.*, **2000**, *208*, 77.

27 Hughes, H.P., Martin, D., Bell, S., McGarvey, J.J., Vos, J.G., *Inorg. Chem.*, **1993**, *32*, 4402.

[28] Keyes, T.E., Vos, J.G., Kolnaar, J.A., Haasnoot, J.G., Reedijk, J., Hage, R., *Inorg. Chim. Acta*, **1996**, *245*, 237.

[29] Hage, R., Haasnoot, J.G., Nieuwenhuis, H.A., Reedijk, J., Wang, R., Vos, J.G., *Dalton Trans.*, **1991**, 3271.; Keyes, T.E., Vos, J.G., Kolnaar, J. A., Haasnoot, J.G., Reedijk, J., Hage, R., *Inorg. Chim. Acta*, **1996**, *245*, 237.

[30] Vos, J.G., Haasnoot, J.G., *Inorg. Chim. Acta*, **1983**, *71*, 155.

[31] Hage, R., Haasnoot, J.G., Reedijk, J., Vos, J.G., *Inorg. Chim. Acta*, **1986**, *118*, 73.

[32] (a)Hage, R., *Dalton Trans.*, **1987**, 1389. (b) Buchanan, B., McGovern, E., Harkin, P., Vos, J.G., *Inorg. Chim. Acta.*, **1988**, *154*, 1; (c) Buchanan, B.E., Wang, R., Vos, J.G., Hage, R., Haasnoot, J.G., Reedijk, J., *Inorg. Chem.*, **1990**, *29*, 3263; (d) Hage, R., Haasnoot, J.G., Stufkens, D.J., Snoek, T.L., Vos, J.G., Reedijk, J., *Inorg. Chem.*, **1989**, *28*, 1413.

[33] Barigelletti, F., De Cola, L., Balzani, V., Hage, R., Haasnoot, J.G., Reedijk, J., Vos, J.G., *Inorg. Chem.*, **1991**, *30*, 641.

[34] Buchanan, B.E., Wang, R., Vos, J.G., Hage, R., Haasnoot, J.G., Reedijk, J., *Inorg. Chem.*, **1990**, *29*, 3263.

[35] Nieuwenhuis, H.A., Haasnoot, J.G., Hage, R., Reedijk, J., Snoeck, T.L., Stufkens, D. J., Vos, J.G., *Inorg. Chem.*, **1991**, *30*, 48.

[36] Vos, J.G., *Polyhedron*, **1992** *18,* 2285.

[37] Buchanan, B.E., Degn, P., Velasco, J.M.P., Hughes, H., Creaven, B.S., Long, C., Vos, J.G., Howie, R.A., Hage, R., van Diemen, J.H., Haasnoot, J.G., Reedijk, J., *Dalton Trans.*, **1992**, 1177.; Wang, R., Vos, J.G., Schmehl, R.H., Hage, R., *J. Am. Chem. Soc.*, **1992**, *114*, 1964.

[38] Hage, R., Dijkhuis, H.J., Haasnoot, J.G., Prins, R., Reedijk, J., Buchanan, B.E., Vos, J.G., *Inorg. Chem.*, **1988**, *27*, 2185.

[39] Hage, J.G., Haasnoot, J.G., Nieuwenhuis, H.A., Reedijk, J., De Ridder, D. J.A., Vos, J.G., *J. Am. Chem. Soc.*, **1990**, *112*, 9245.

[40] Hughes, H.P., Martin, D., Bell, S., McGarvey, J.J., Vos, J.G., *Inorg. Chem.*, **1993**, *32*, 4402.

[41] Keyes, T.E., Vos, J.G., Kolnaar, J.A., Haasnoot, J.G., Reedijk, J., Hage, R., *Inorg. Chim. Acta*, **1996**, *245*, 237.

[42] Ryan, E.M., Wang, R., Vos, J.G., Hage, R., Haasnoot, J.G., *Inorg. Chim. Acta*, **1993**, *208*, 49.

[43] de Wolf, J.M., Hage, R., Haasnoot, J.G., Reedijk, J., Vos, J.G., *New. J. Chem.*, **1991**, *15*, 501.

[44] Serroni, S., Vampagna, S., Denti, G., Keyes, T.E., Vos, J.G., *Inorg. Chem.*, **1996**, *35*, 4513.

[45] Lempers, H.E.B., Haasnoot, J.G., Reedijk, J., Hage, R., Weldon, F., Vos, J.G., *Inorg. Chim. Acta*, **1994**, **225**, 67.

[46] Keyes, T., O'Conner, C.M., O'Dwyer, U., Coates, C.G., Callaghan, P., McGarvey, J.J., Vos, J.G., *J. Phys. Chem. A*, **1999**, *103*, 8915.

[47] Hage, R., Lempers, H.E.B., Haasnoot, J.G., Reedijk, J., Weldone, F.M., Vos, J.G., *Inorg Chem.*, **1997**, *36*, 3139.

[48] Hage, R., Haasnoot, J.G., Reedijk, J., Wang, R., Vos, J.G., *Inorg. Chem.*, **1991**, *30*, 3263.

[49] Browne, W.R., Weldon, F., Guckian, A., Vos, J.G., *Collect. Czech. Chem. Commun.*, **2003**, *68*, 1467.

[50] Browne, W.R., Weldon, F., Guckian, A., Vos, J.G., *Collect. Czech. Chem. Commun.*, **2003**, *68*, 1467.

[51] Browne, W.R., O'Boyle, N.M., Henry, W., Guckian, A.L., Horn, S., Fett, T., O'Connor, C.M., Duati, M., De Cola, L., Coates, C.G., Ronayne, K.R., McGarvey, J.J., Vos, J.G., *J. Am. Chem. Soc.*, **2005**, *127*, 1229.

[52] Henry, W., Browne, W.R., Ronayne, K.L., O'Boyle, N.M., Vos, J.G., McGarvey, J.J., *J. Mol. Struct.*, **2005**, *735*, 123.

[53] Browne, W.R., O'Boyle, N.M., McGarvey, J.J., Vos, J.G., *Chem. Soc. Rev.*, **2005**, *34*, 1.

[54] Beer, M., Longuet-Higgins, H.C., *J. Chem. Phys.*, **1955**, *23*, *8*, 1390.

[55] Halper, W., DeArmond, M.K., *J. Lumin.*, **1972**, *5*, 225.

[56] Watts, R.J., Griffith, B.G., Harrington, J.S., *J. Am. Chem. Soc.*, **1975**, *97*, 6914.

[57] Blaskie, M.W., McMillin, D.R., Inorg. Chem., 1980, 19, 3519.; Everly, R.M., McMillin, D.R., *J. Phys. Chem.*, **1991**, *95*, 9071.

[58] Watts, R.J., Brown, M.J., Griffith, B.G., Harrington, J.S., *J. Am. Chem. Soc.*, **1975**, *97*, 6029.

[59] Vanwallendael, S., Rillema, D.P., *Chem. Commun.*, **1990**, *16*, 1081.; Vanwallendael, S., Rillema, D.P., *Coord. Chem. Rev.*, **1991**, 297.

[60] Harrigan, R.W.; Crosby, G.A., *J. Phys. Chem.*, **1973**, *59*, 3468; Hager, G.D.; Crosby, G.A., *J. Am. Chem. Soc.*, **1975**, *97*, 7031.

[61] Barigelletti, F.; Juris, A.; Balzani, V.; Belser, P.; von Zelewsky, A., *J. Phys. Chem.*, **1987**, *91*, 1095.

[62] Van Houten, J.; Watts, R.J., *J. Am. Chem. Soc.*, **1976**, *98*, 4853.

[63] Caotes, C.G., Callaghan, P.L., McGarvey, J.J., Kelly, J.M., Kruger, P.E., Higgins, M.E., *J. Raman Spectro.*, **2000**, *31(4)*, 283.

[64] Frink, M.E., Ford, P.C., *Inorg. Chem.*, **1985**, *24*, 1033.

[65] Keyes, T.E., Weldon, F., Muller, E., Pechy, P., Grätzel, M., Vos, J.G., *Dalton Trans.*, **1995**, *16*, 2705.

[66] Browne, W.R., Vos, J.G., *Coord. Chem. Rev.*, **2001**, *219-221*, 761-787.

[67] The Schrödinger Equation for the motion of two atoms is:

$-\frac{\eta^2}{2\mu}\frac{d^2\psi}{dx^2}+V\psi=E\psi$ which also includes the reduced mass of the system.

[68] Strickler, R.J., Berg, R.A., *J. Chem. Phys.*, **1962**, *37*, 814.

[69] van Houten, J., Watts, R.J., *J. Am. Chem. Soc.*, **1975**, *97*, 3843.

[70] Henry, W., Browne, W.R., Passaniti, P., Gandolfi, M.T., Ballardini, R., O'Connor, C.M., Maestri, M., Coates, C.G., Brady,C., McGarvey, J.J., Vos, J.G., *Inorg. Chim. Acta*, In press.

[71] Smekal, A., *Naturwissenschaften*, **1923**, *11*, 873.

[72] Bell, S.E.J., Barrett, L.J., Burns, D.T., Dennis, A.C., Speers, S.J., *Analyst*, **2003**, *128*, 1331.

[73] Bell, S.E.J., Mackle, J.N., Sirimuthu, M.S., *Analyst*, **2005**, *130*, 545.

[74] Bell, S.E.J., Sirimuthu, N.M.S., *Analyst*, **2004**, *129*, 1032.

[75] Czernuszewicz, R.S.; Spiro, T.G., Ch.7. Inorganic Electronic Structure and Spectroscopy. Volume I: Methodology; Wiley, **1999**.

[76] Fleischmann, M., Hendra, P.J., McQuillan, A.J., *Chem. Phys. Lett.*, **1974**, *26*, 163.

[77] Albrecht, M.G., Creighton, J.A., *J. Am. Chem. Soc.*, **1977**, *99*, 5216.

[78] (a) Bell, S.E.J., Bourguignon, E.S.O., Dennis, A.C., *Analyst*, **1998**, *123*, 1729.; (b) Bell, S.E.J., Bourguignon, E.S.O., McGarvey, J.J., Fields, J.A., Seddon, K.R., *Anal. Chem.*, 2000, *72*, 234.; Bell, S.E.J., Bourguignon, E.S.O., O'Grady, A., Villaunie, J., Dennis, A.C., *Spectroscopy Europe*, **2002**, *14*, 17.

[79] Vosko,S.J., Wilk, L., Nusair, M., *Can.J. Phys.*, **1980**, *1980*, 1200.

[80] Becke, A.D., *Phys. Rev.*, **1988**, *38*, 3098.

[81] Stevens, P.J., Devlin, J.F., Chabalowski, C.F.,Frisch, M.J., *J. Phys. Chem.*, **1994**, *98*, 11623.

[82] Koch, W., Holthausen, M.C., A Chemist Guide To Density Functional Theory, Wiley, **2000**.

[83] Cramer, C.J., Essentials of Computational Chemistry, Wiley, **2002**.

[84] Buchs, M., Daul, C., *Chimia*, **1998**, *52*, 163.

[85] Daul, C., Baerends, E.J., Vernooijs, P., *Inorg. Chem.*, **1994**, *33*, 3538.

[86] Amini, A., Harriman, A., Mayeux, A., *Phys. Chem. Chem. Phys.*, **2004**, *6*, 1157.

[87] Alexander, B.D., Dines, T.J., *Inorg. Chem.*, **2004**, *43*, 342.

[88] Howell, S.L., Gordon, K.C., *J. Phys. Chem. A*, **2004**, *108*, 2536-2544.

[89] Oakes, R.E., Beattie, J.R., Moss, B.W., Bell, S.E.J., *J. Mol. Struct. Theochem.*, **2002**, *586*, 91.

[90] http://home.btconnect.com/reoakes/index.html.

Chapter 2

Experimental Techniques

Chapter 2 introduces the various experimental techniques used to investigate the photophysical properties of the Ru(II) complexes in this thesis. A broad spectrum of techniques has been employed including Raman, Time Correlated Single Photon Counting and Electronic Spectroscopy. Technological advances now allows investigation into the sub picosecond time scale and the techniques used here range from the steady state into the picosecond range.

Experimental techniques have been complimented by computational calculations. These calculations have been used to gain an insight into the experimentally observed results and to enhance the theories proposed.

2.1 Steady State Electronic Spectroscopy.

Throughout this thesis electronic spectroscopy is used to investigate the photophysical properties of transition metal complexes. Steady state spectroscopy refers to measurements which occur under constant illumination and observation, and only energy and intensity of the excited state is probed. The two techniques used here are UV/Vis absorption and emission spectroscopy.

2.1.1 UV/Vis Absorption Spectroscopy.

Absorption spectroscopy measures the transition of atoms and molecules between electronic states. Generally, it is concerned with the absorption of light in the visible or ultraviolet region of the spectrum, as the energy of infrared and microwave radiation is too small to cause changes in the electronic structure.

The Beer – Lambert Law relates the intensity of light absorbed, Abs, to the path length of the light, l, and the concentration of the species, c.

$$Abs = \log_{10}(I_o / I_t) = \varepsilon c l \qquad \text{EQN. 2.1}$$

I_o and I_t are the incident and transmitted intensities respectively. ε is referred to as the molar absorptivity or molar extinction coefficient. The molar absorptivity is a measure of the strength of the transition between the ground and the excited state. A large value for ε indicates that a transition is almost fully allowed, such as MLCT transition in $[Co(NH_3)Br]^{2+}$ where ε_{max} = 20,000 $M^{-1}cm^{-1}$. By comparison, the ligand field transition of the same complex at 550 nm[1] is a Laporte forbidden transition and has ε_{max} = 50 $M^{-1}cm^{-1}$. In some transition metal complexes the effect of the heavy metal leads to large molar absorptivity for transitions that are formally forbidden. A more complete

overview of the states involved in these transitions and the absorption spectra of Ru(II) complexes is given in Chapter 1.

Accurate measurements require that the absorption, Abs, is between 0.2 and 1.2. A low Abs value leads to a situation were the signal to noise ratio is a significant source of error. On the other if the Abs value is too high all the light is absorbed and the amount available for measurement is insufficient.

Unless otherwise stated, UV.Vis spectra were recorded on a Shimadzu UV.Vis/NIR 3100 spectrophotometer interfaced with an Elonex-466 PC using UV.Vis data manager or a Varian Cary 50 Scan spectrometer interfaced with a Dell optiplex GXI PC using Win UV Scan Application 2.00. Samples were held in 0.1 or 1 cm pathlength quartz cuvettes.

2.1.2 Emission Spectroscopy.

Emission spectroscopy probes the relaxation of a complex from its excited state via the irradiation of energy as light. After the absorption of light a complex relaxes to a thermally equilibrated state (THEXI) state which may have a lifetime from ns to ms. The formation of the THEXI state in transition metal complexes occurs on the sub-nanosecond time scale.[2] Steady state emission spectroscopy is used to probe this steady state via the energy and the intensity of the emitted light.

As with absorption spectroscopy the concentration of samples measured via emission spectroscopy must be moderated. Highly concentrated samples can be seen to reabsorb the emitted light leading to a decrease in the emission intensity. This is known as the inner filter effect. Weakly concentrated samples produce signals of such low intensity that the signal to noise ratio is troublesome.

Temperature dependence is used in both the emission and lifetime measurements throughout this thesis. It is used to investigate the effect of the solvent environment on the excited state of the complex. Ridigochromatic studies involve varying temperature so as to limit the ability of the solvent to rearrange to accommodate the excited state. Studies have also used the rigidochromatic effect as a temporal probe as the evolution of solvent with temperature can be used as a model for the ultrafast relaxation of the solvent.[3]

Excitation wavelength dependence can also be used to probe the nature of the excited state. In general the coupling between excited states in transition metal complexes is isotropic.[4] Therefore, excitation in any of the absorption bands should lead to the formation of the THEXI state. However, in some cases this does not occur which may indicate the presence of more that one emitting state or other modes of excited state deactivation.

Solvatochromatic measurements investigate the effect of solvent on the emission energy and intensity. The emission energy of a complex is dependent on the ability of the solvent to stabilise the newly - formed excited state. Solvatochromatic studies are used to probe the nature of the emitting state as charge transfer states (such as MLCT or LMCT), are greatly affected by solvent environment due to the large change in dipole on excited state formation.[5] Metal and ligand centred states show a smaller effect as the electron is not displaced to the same extent.

Unless otherwise stated, emission spectra were recorded at all temperatures using a Perkin-Elmer LS50-B Luminescence spectrophotometer interfaced with an Elonex-466 PC using Windows 3.1 based fluorescence data manager software. Emission and excitation slit widths were typically 3, 5 or 10 nm depending on the conditions. Measurements at 77 K were carried out in liquid nitrogen filled glass cryostat, with the sample held in a NMR tube. Measurements between 80 K and 280 K were carried out using an Oxford

Instruments liquid nitrogen cooled cryostat model 39426 controlled with an Oxford ITC601 unit. Samples were held in a home-made quartz or glass cuvette. Spectra are uncorrected for photomultiplier response.

2.2 Time Resolved Emission Techniques.

Time resolved measurements were undertaken in addition to steady state measurements. It is important to understand the relationship between steady state and the time resolved measurements. The intensity of a steady state emission, I_{ss}, is given by EQUATION 2.2.

$$I_{ss} = \int I_o e^{\frac{-t}{\tau}} dt = I_o \tau \qquad \text{EQN. 2.2.}$$

where I_0 is the illumination intensity of a single pulse and τ, the lifetime. It should be noted that I_{ss} is the intensity under constant illumination and, as such, has arbitrary units while the pulsed irradiation has units of arbitrary units per second.

Steady state measurements are, therefore, an average of the time – resolved phenomena over the intensity decay of the sample.[6] Hence, extra information can be obtained from the time – resolved measurements. While the control of excited state lifetime is now a goal in itself for catalytic and sensor applications, the lifetime and number of decays present in a sample provides valuable information on the processes occurring. The majority of time – resolved measurements are undertaken using Time Correlated Single Photon Counting.

2.2.1 NanoSecond Time Resolved Single Photon Counting.

An overview of the system is given in FIGURE 2.3. The system consists of two main parts – the excitation source and the detection system. The excitation source is a nf900 nanoflash lamp which uses N_2 as its filler gas. The characteristic spectral output from N_2 gas is shown in FIGURE 2.1.

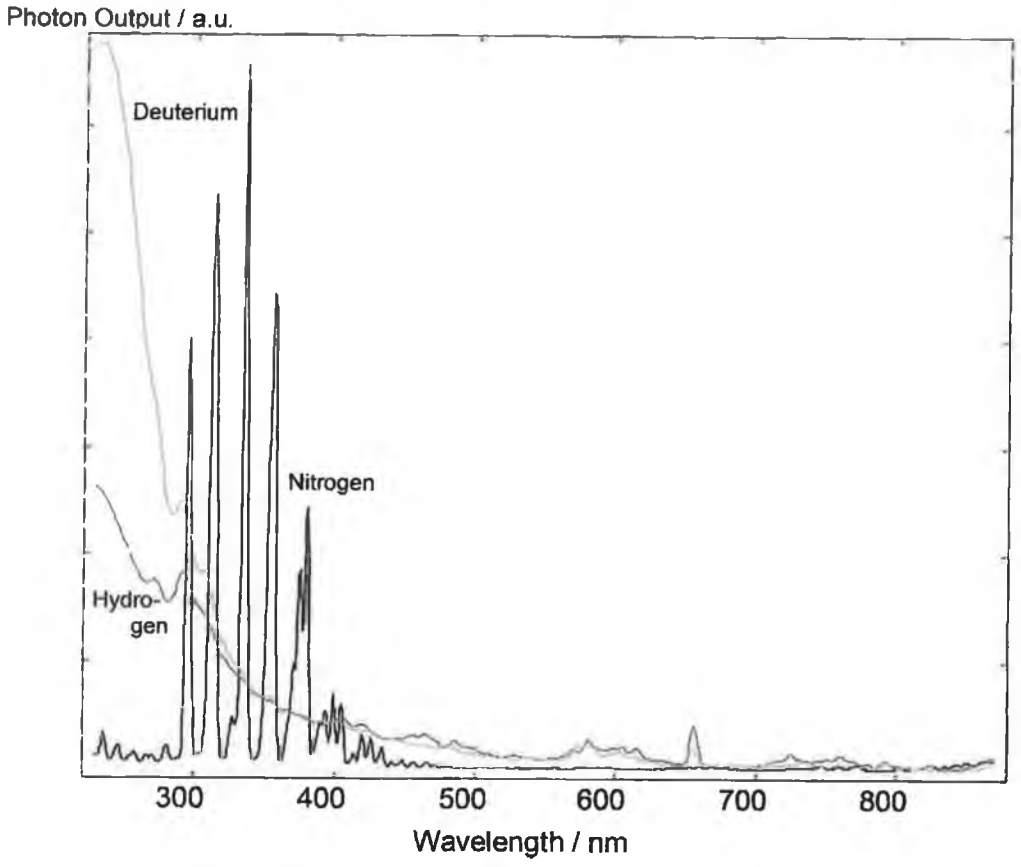

FIGURE 2.1: SPECTRAL OUTPUT OF N_2 FILLER GAS. INCLUDED FOR COMPARISION ARE THE SPECTRA OF H_2 AND D_2.

FIGURE 2.2 shows the electrical circuit of the flashlamp. A highly positive charge is applied to the anode of the spark gap by charging resistors R_1 and R_2. The cathode of the spark gap is connected to the anode of the thyratron and has a similar potential due to resistor R_3. The thyratron uses hydrogen gas as its switching medium. A gating pulse is sent to the grid of the thyratron which causes it to switch to its conducting state. The cathode of the spark gap is therefore grounded causing a large intergap voltage, which leads to a spark discharge. When the capacitance is discharged the anode current falls below its minimum holding value and the thyratron returns to its non-conducting state. The repetition rate is dependent on the time required for the thyratron and the spark gap to recover after conduction. As the intergap resistance increases the energy per flash and the flash duration increase, therefore this

capacitance is kept at a minimum to ensure a high repetition rate. The typical pulse width (FWHM) obtainable using N_2 filler gas is 1ns allowing measurements as low as 100ps after deconvolution.

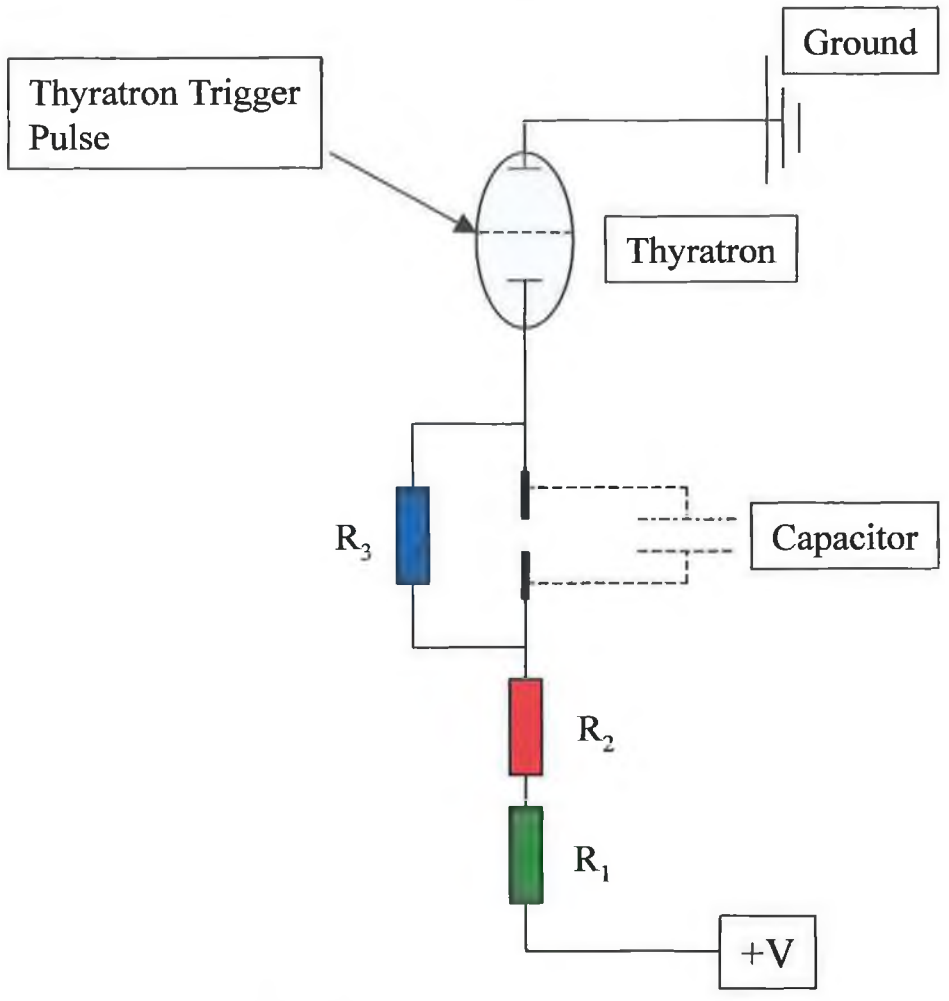

FIGURE 2.2: ELECTRICAL CIRCUIT OF NANOSECOND FLASHLAMP.

Low temperature samples were dissolved in a 4:1 ethanol/methanol solution (Uvasol grade) to give a concentration ~10^{-5} M and cooled to 77K in a simple cryostat of in-house design.

The mechanism of operation of the Single Photon Counter is described below and in FIGURE 2.3. A photon of light from the flashlamp travels via optical cable to the START detector. Upon receiving a signal at the START detector the TAC (Time to Analogue Converter) initiates a voltage ramp. Simultaneously, another photon of light passes through the excitation monochromator to select the excitation wavelength. Light at the selected wavelength is then absorbed

by the sample. The re-emitted photon passes first through a filter and then through an emission monochromator to select the wavelength at which the lifetime is to be monitored.

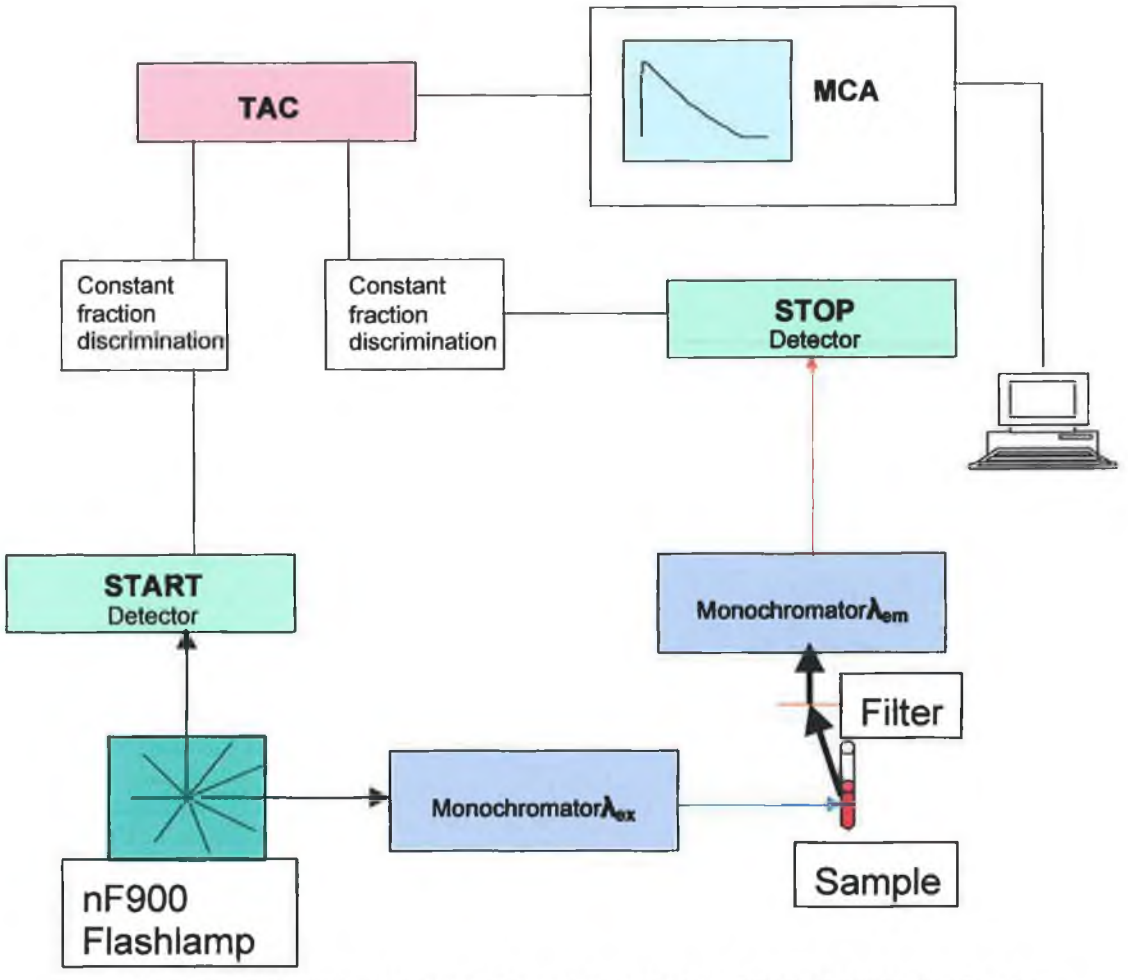

FIGURE 2.3: NANO SECOND TIME CORRELATED SINGLE PHOTON COUNTING SETUP.

The voltage ramp is halted when the STOP detector receives a photon of emitted light from the sample. Both the START and STOP detectors contain signal amplifiers, which may be varied to adjust the sensitivity of the instrument. These signal amplifiers are related to the potential bias applied to the photomultiplier tubes and the lifespan of the tube may be reduced if too high a voltage is applied. The time range is split into 1024, 2048 or 4096 channels depending on the chosen settings. Each of these channels is assigned a range of voltages corresponding to a certain time range. The multi channel analyser (MCA) records the number of times a specific voltage is

obtained in each of the channels. A spectrum of voltages, and hence time differences, is produced by the MCA memory and the experiment is terminated when a sufficient number of counts are collected. The number of counts collected depends on a number of factors:

- The signal to noise ratio.
- The number of decays in the sample.
- The presence of scatter from the sample.

Typically 1000 counts in the peak channel is sufficient to obtain a fit of good quality after data analysis(*vida infra*).

The spectrum of voltages is directly related to the emission decay allowing for measurement of the lifetime. An initial time delay can be introduced to the measurement via a series of optical cable inside the TAC.

The STOP detector contains red sensitive S900-R photomultiplier. It has a working range of 160-870nm due to the use of quartz glass for its side window. This version is generally operated within a Peltier element cooled housing at 50 K below ambient temperature, so as to reduce the presence of dark counts.

2.2.2 Analysis of TCSPC Data.

Two methods of data analysis are available using the F900 program Version 6.24, provided with the Edinburgh Instruments CD/nF900. Reconvolution fit takes into account the finite nature of the excitation pulse and the fact that the sample decay may be convoluted with this initial rise time. The convolution integral (EQUATION 2.3) provides the mathematical relationship between the sample response function (X(t)), the instrument response function (E(t)) and the sample decay model(R(t));

$$X(t) = \int_0^t E(t')R(t-t')dt' \qquad \text{EQN. 2.3.}$$

Reconvolution fit can be used to fully describe the data, apart from noise, including the rise of the signal, the initial part of the decay and the tail.

The second method of data analysis is the tail fit. When the tail fit method is used X(t) is considered equal to R(t). This method is only suitable for the region where there is no further sample signal growth, for example, by excitation pulse or excimer generation. Since the majority of the excited state lifetime measurements in this thesis are at low temperature, where the measured lifetime is far greater than the excitation pulse width, tail fit has been used unless otherwise stated. Tail fitting proved better able to cope with the scatter observed from the solvent at low temperature. This was done by reducing the range of the fitting to exclude scattered photons.

Once the method of fit has been decided, the lifetime of the excited state are obtained by fitting experimental decay to the equation;

$$R(t) = A + B_i e^{-(\frac{t}{\tau_i})} \qquad \text{EQN. 2.4}$$

where R(t) is the sample decay model, B_i is the pre-exponential factor, τ_i is the characteristic lifetime and A is an additional background. The Marquardt-

Levenberg algorithm is used to search for the best values of B_i and τ_i. This iterative procedure minimises the value of the "goodness of fit", χ_g^2, which is defined as

$$\chi_g^{\,2} = \sum_k w_k^{\,2}(X_k - F_k)^2 \qquad \text{EQN. 2.5}$$

where k is the index of individual data points, F_k is the raw experimental data and w_k is the weighting factor for each data point. Data obtained by TCSPC is seen to obey Poisson noise statistics with the well-defined weighting factor of $w_k = \frac{1}{\sqrt{F_k}}$.

The quality of the lifetime data obtained is judged primarily by two criteria: the reduced Chi-squared, χ^2, and the random nature of the residuals plot. The χ^2 value is obtained by dividing the goodness of fit by the number of free parameters, n (which is approximately the number of fitted points divided by the number of lifetime parameters used in the fit) and is shown in EQUATION 2.6. Poisson distributed data have a theoretical limit of 1.0. Values above unity indicate a bad fit result, while χ^2 values below unity indicate a poor choice of fitting range. The F900 program also provides a graphical distribution of the residuals of this fitting procedure. These residuals are the difference between the fitted curve and the original data. This is inspected visually to ensure that the residual curve only contains random noise.

$$\chi^2 = \sum_k w_k^{\,2} \frac{[X_k - F_k]^2}{n} \qquad \text{EQN. 2.6.}$$

A value for the Durbin-Watson parameter is also provided by the software. It is calculated using EQUATION 2.7.

$$DW = \frac{\sum_{t=nL+1}^{nH}(X_t - X_{t-1})^2}{\sum_{t=nL}^{nH} X_t^{\,2}} \qquad \text{EQN. 2.7.}$$

where nH and nL are the lower and upper limit of the fitting range respectively. Acceptable values vary for the number of exponentials investigated, with DW values of less than 1.7 and 1.75 indicative of poor fits to single and double exponentials, respectively.

2.2.3 PicoSecond Time Resolved Single Photon Counting.

Picosecond time resolved Single Photon Counting measurerments were undertaken at Rutherford Appleton Laboratories, Abingdon, UK.[7] The principles of measurement and data analysis have already been explained for the nanosecond studies.

2.3 Raman Spectroscopy.

Raman spectroscopy is a highly valuable analytical technique which uses laser radiation to probe the vibrational structure of molecules. Resonance Raman spectroscopy is particularly useful in inorganic chemistry as it exploits the resonance enhancement effect to investigate the moieties involved in electronic transitions. A more thorough description of the Raman spectroscopy and its theoretical background is provided in Chapter 1.

2.3.1 Ground State Resonance Raman Spectroscopy.

A schematic showing the experimental setup employed for the ground state measurements using the Ar^+ or Ti:Sapph lasers is shown below in FIGURE 2.4. For all experiments the Raman signal was collected at 180^0 to the incident beam and focused onto the entrance slit of a single-stage Jobin-Yvon HR640 Spectrograph containing a holographic grating. (For experiments in the visible and ultraviolet spectral region, a 1200 l/mm grating was used.) A holographic notch filter (Kaiser Optics) was used to exclude Rayleigh (elastic laser light) scattering. The spectrograph was coupled to an Andor Technology open-electrode CCD detector (DV420-OE) thermoelectrically cooled to -45 ^{0}C to minimise any electronic background signal due to dark current in the silicon sensor. The Raman signal incident on the detector was observed on a PC which allowed the camera setting to be controlled by means of a PCI controller.

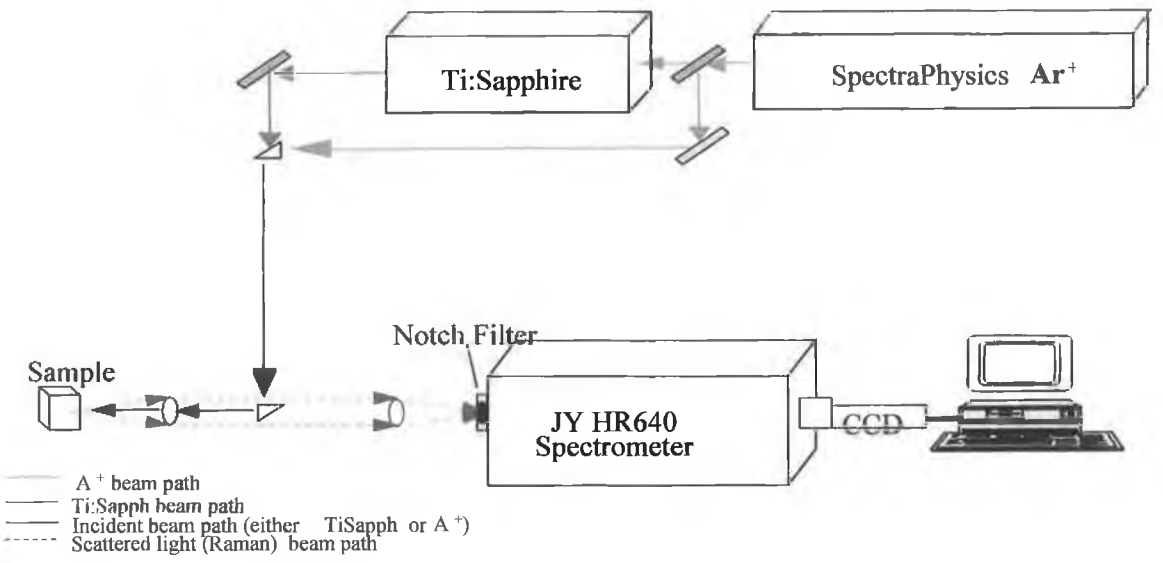

FIGURE 2.4: GROUND STATE EXPERIMENTAL RAMAN SETUP.

2.3.2 Excited State Resonance Raman Spectroscopy.

Two pulsed laser systems were used singly or in tandem for the nanosecond excited state work presented here:

- Spectra Physics Q-switched Nd:YAG (Neodymium Yttrium Aluminium Garnet) laser, DCR-2
- Spectra Physics Q-switched Nd:YAG laser, GCR-3

Both lasers produce a fundamental output at 1064 nm (300 mJ max) with a 10 ns pulse width at a repetition rate of 10 Hz. The optics produce a filled in circular beam cross-section with a smooth intensity profile which is almost Gaussian in appearance, ideal for uniform irradiation of sample. The DCR-2 (Diffraction Coupled Resonator) was used as a pump laser in two-colour resonance Raman experiments. The GCR-3 (Gaussian Coupled Resonator), which has an additional amplifier stage and thus a higher maximum power output, was used as the excitation source for transient resonance Raman (TR^2) and the probe for time-resolved resonance Raman (TR^3) experiments (*vide infra*).

Non-linear optical processes were used to generate wavelengths which were in resonance with the absorption bands of the excited Ru(II) complexes. Frequency doubling to 532 nm occurred by passing the 1064nm beam through a crystal of potassium dideuterium phosphate (KDP). This was then mixed with the fundamental wavelength to obtain a beam at 355 nm. These wavelengths are then separated by a prism harmonic generator (FIGURE 2.5). The collinear beams are first passed through a Pellin-Broca prism which disperses the beams according to wavelength, a rooftop prism then turns the beams before a movable prism is used to select the desired wavelength.

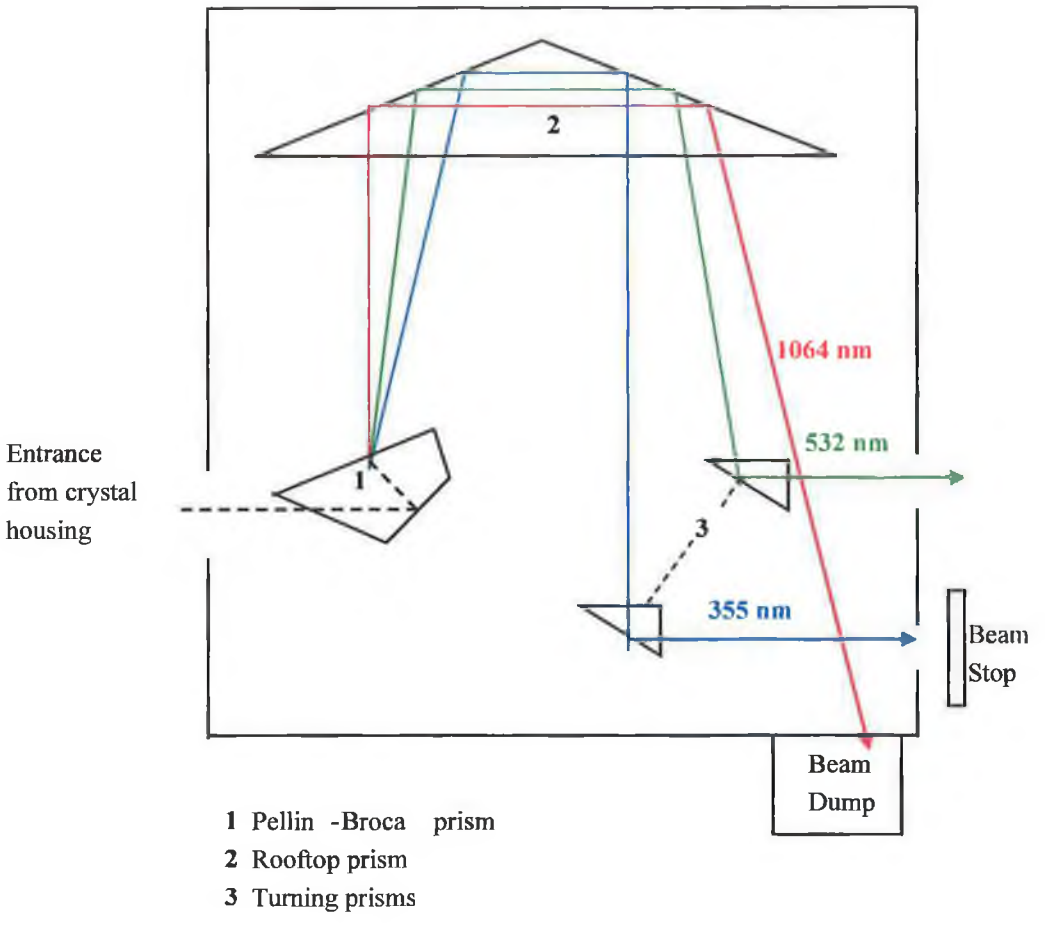

FIGURE 2.5: PRISM HARMONIC SEPARATOR.

The same apparatus was employed for the TR^2 and TR^3 experiments carried out for this work as shown in FIGURE 2.6 with only one laser being used in the transient resonance Raman experiments, and both being used for the time resolved measurements.

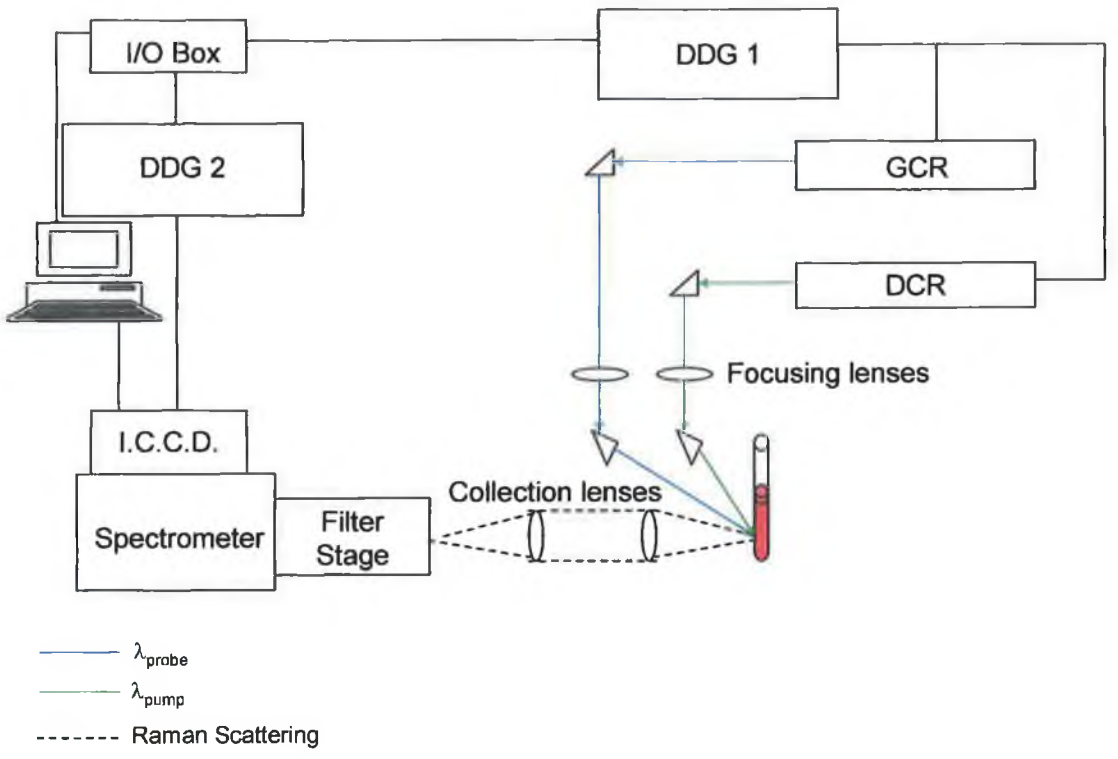

FIGURE 2.6: EXCITED STATE EXPERIMENTAL RAMAN SETUP.

TR^2 is often referred to as single-colour excited state Raman as only one beam is used to excite and probe the sample under study. It is usually applied to a system which has some ground and excited state electronic absorption at the excitation laser wavelength, so the leading edge of the laser pulse can populate the excited state and the resonance Raman of this excited state can be probed by the trailing edge of the pulse. Photodecomposition of samples can be avoided by spinning the sample tube or for particularly photo-unstable complexes, a flow cell of in-house design (*vide infra*) is utilised ensuring that each pulse encounters a fresh volume of sample. Typically the solutions were approx. 1×10^{-3} - 5×10^{-4} M as this ensured a good signal to noise ratio while avoiding unduly long accumulation time.

The excitation source for the single-colour experiments was the Spectra-Physics GCR-3 pulsed laser operating at λ_{ex} = 355 nm. For photostable compounds the sample was contained in a quartz NMR tube mounted in an air powered spinner. Measurement of photolabile complexes were done in a modified quartz NMR tube with a hole at the base and a small sample reservoir

at the top which was used to allow continuous flow of the solution. A 45^0 scattering geometry (*vide infra*: FIGURE 2.7) was employed and the scattered radiation was passed through two focussing lenses and a polarisation scrambler before dispersion through a double spectrograph in which a filter stage was used to remove the Rayleigh line. The signal was then passed through a slit (set at 100 μm for normal acquisitions, at 30 μm for calibration and 150 μm for signal optimisation) into a Spex 1870 single spectrograph which dispersed the Raman signal onto the Andor Technology ICCD detector (DH501).

2.3.3 Nanosecond Time Resolved Resonance Raman Spectroscopy.

TR^3 or two-colour excited state Raman employs both the GCR and DCR lasers to pump and probe the sample. The wavelength of the pump beam is chosen to create a significant excited state population which may be probed after a variable time delay by a second beam which is selected to lie within an excited state electronic transition. Spatial overlap of the pulses at the sample was achieved using an aqueous solution of $[Ru(bpy)_3]Cl_2$ which was highly fluorescent under both pump and probe beams ensuring the pump beam was slightly more diffuse and that the probe beam waist is contained within the pump beam. A small portion of each beam was split off to a photodiode coupled to a Tektronix digital oscilloscope (TDS 350) and the beams were aligned in time by using a Stanford Instruments digital pulse delay generator (DG-535) (DDG 1 in FIGURE 2.6). The time-delay between pump and probe pulses was also controlled using this delay generator for time-resolved studies.

2.3.4 Sample Geometry.

As mentioned above, a 45^0 scattering geometry was employed for these studies. This novel geometry, first devised by Dr. C.G. Coates of the Queen's University of Belfast laser Raman group, was favoured over a conventional 180^0 or 90^0 arrangement as it allowed more flexibility than the 180^0 or backscattering setup. This was due to the use of separate focusing optics for the incident beams and scattered radiation, while a relatively high sample concentration could be adopted (relative to that required for the 90^0 method) because in this case re-absorption of scattered light is not critical.

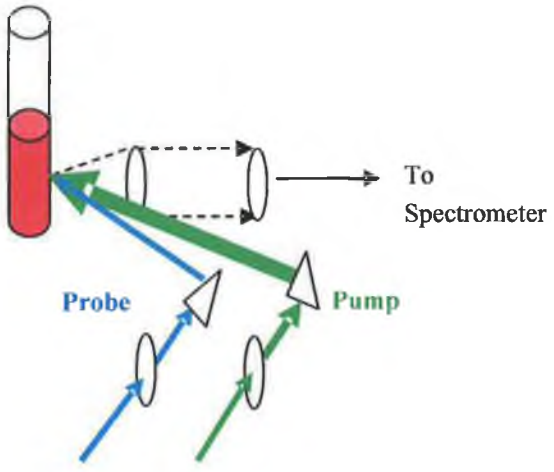

FIGURE 2.7: SAMPLE GEOMETRY.

For studies involving photosensitive materials (such as $[Ru(biq)_2(Hpztr)]^{2+}$ studied in Chapter 5), a flow-cell was used in order to avoid sample decomposition. This was a quartz NMR tube with a wide reservoir at the top to store fresh solution and a narrow opening at the base to allow the solution to flow into a collection beaker below. The reservoir was topped-up as required throughout the accumulation.

2.3.5 Picosecond Time Resolved Resonance Raman Spectroscopy.

Picosecond time resolved resonance Raman measurements were carried out at the Rutherford Appleton Laboratories. A schematic of the apparatus is shown below and a comprehensive description of the set-up may be found in literature.[8]

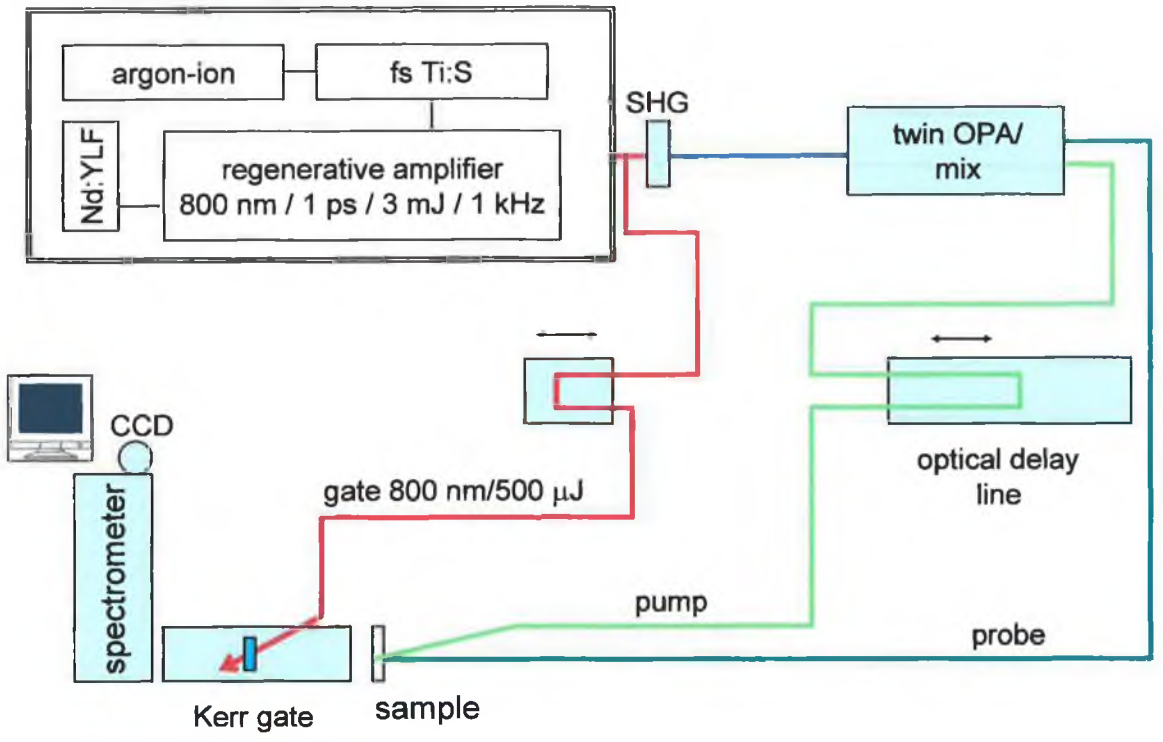

FIGURE 2.8: PICOSECOND TIME RESOLVED RESONANCE RAMAN SETUP.

A regenerative amplifier system supplies a 1 ps, 800 nm pulse with power 3 mJ at a rate of 1 kHz which is frequency doubled to 400 nm. This pulse pumps the optical parametric amplifiers which are independently tuneable over a range of visible wavelengths. A software controlled optical delay line was used to vary the path length of the pump laser to provide time resolution. The Kerr gate, a 2 mm cell of CS_2 was used to reject sample fluorescence. A residual 800 nm pulse induces a transient anisotropy of the Kerr medium giving rise to fast gating propertieswith a ~4 ps open/close time. The sample was continuously flowed so that the laser was incident on an open jet of 500 μm diameter, requiring large sample volumes (~20 mL). As evaporation of the

solvent used often occurred over the accumulation times, it was necessary to "top-up" the sample volume between cycles. The number of cycles recorded was varied and the time delays were randomised in order to check for photo-degradation of the sample over the acquisition cycles.

2.4 Time Resolved Absorption Techniques.

Time resolved absorption techniques have been used to investigate the formation of the THEXI state. These measurements provide information on the evolution of the excited state with time, while also giving the absorption spectra of the excited state complex to be probed by transient Raman measurements. These data help to interpret the TR^2 and TR^3 data in terms of resonance and pre-Resonance Raman spectroscopy.

2.4.1 Nanosecond Transient Absorption.

The setup used for these experiments has been described previously.[9] Excitation source for the samples was a continuously tunable (420nm-710nm) Coherent Infinity XPO laser, with an output power of typically less than 5mJ/pulse and a repetition rate of 10Hz. The excited state was probed using a low pressure, high power EG&G FX-504 Xe lamp as a white light source. Probe light from both the signal and reference were collected by optical fibres and connected to a Acton SpectraPro-150 spectrograph coupled with a Princeton Instruments ICCD-576-G/RB-EM gated intensified CCD camera. For these measurements the optical density of the sample was near 1 at the excitation wavelength of 355 nm.

2.4.2 Femtosecond Transient Absorption.

Sub-picosecond transient absorption spectroscopy experiments were performed on a Spectra-Physics Hurricane Titanium:Sapphire regenerative amplifier system at the University of Amsterdam. An overview of the system is given in FIGURE 2.9. The optical bench assembly of the Hurricane includes a seeding laser (Mai Tai), a pulse stretcher, a Titanium:Sapphire regenerative amplifier, a Q-switched pump laser (Evolution) and a pulse compressor. The 800 nm output of the laser is typically 1 mJ/pulse (130 fs) at a repetition rate of 1 kHz. A full-spectrum setup based on an Optical Parametric Amplifier (Spectra-Physics OPA 800) as pump and residual fundamental light (150 μJ/pulse) from the pump OPA was used for white light generation, which was detected with a CCD spectrometer. The white light generation was accomplished by focusing the fundamental (800 nm) into a H_2O flow-through cell (10 mm).

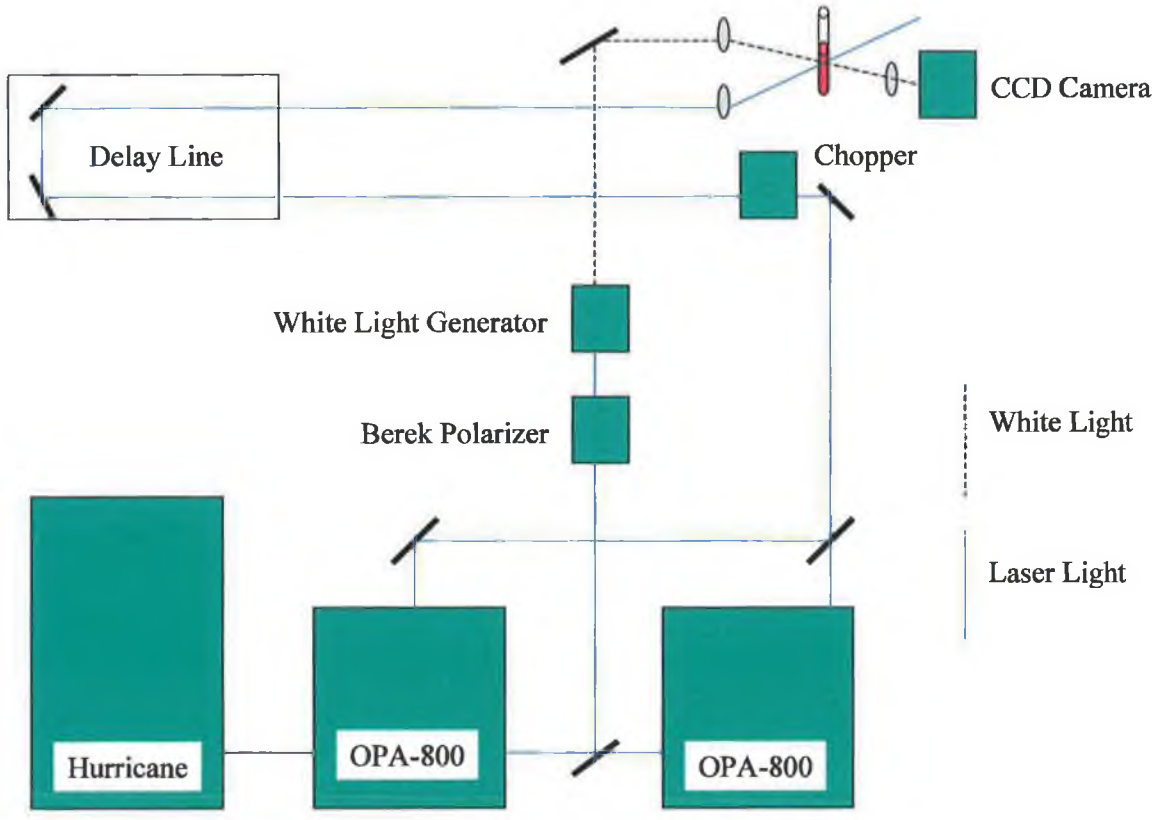

FIGURE 2.9: SUB-PICOSECOND TRANSIENT ABSORPTION SET-UP.

2.5 Computational Details.

2.5.1 Hardware and software.

Calculations were carried out on an Intel Pentium IV 2.8GHz desktop computer with 1GB DDR RAM running Windows XP. Gaussian 03W[10] was used to carry out all DFT calculations. Jobs were prepared and results were inspected using GaussView 3.0[11]. GaussSum[12] was used to monitor jobs, calculate density of states spectra, Raman spectra and calculate group contributions to molecular orbitals.

2.5.2 Density functional.

Becke's 3-parameter hybrid functional[13] was used along with the correlation functional of Lee, Yang and Parr.[14,15] This combination is denoted by B3LYP (see Section 1.1.4). The functional is described by the following equation:

$$E_{xc}^{B3LYP} = (1-a)E_x^{LSDA} + aE_x^{HF} + b\Delta E_x^{B} + (1-c)E_c^{LSDA} + cE_c^{LYP} \qquad \text{EQN. 2.7}$$

Becke chose values for a, b and c (0.20, 0.72, and 0.81) that minimised the least-squares fit to 56 atomisation energies, 42 ionisation potentials and 8 proton affinities of the G1 set of atoms and molecules. Although in his original paper Becke used the correlation functional PW91[16], Stevens *et al.*[17] modified Becke's functional to use LYP instead, while retaining the original values of a, b and c.

2.5.3 Basis set.

Most modern computational codes use the 'Basis Set Approximation' to solve the Schrödinger equation. This involves expressing the molecular orbitals as a linear combination of a set of mathematical functions called the basis set. An infinite basis set will give the best possible result for a given level of theory although, in practice, only a finite basis set is possible. A larger and more

flexible basis set is better able to describe the electron density of a molecule, and hence gives more accurate results. Generally, a trade-off between speed and accuracy is necessary, as there is a N^4 dependence on the basis set size. In a system of the size of a ruthenium polypyridyl complex, a reasonable compromise is to use the LanL2DZ basis set and electron-core potential of Dunning, Hay and Wadt.

For the atoms C, H and N, LanL2DZ uses the Dunning/Huzinaga[18] valence double-ζ basis set. Following the usual notation for basis sets, H, C and N are described by (10s5p/4s)[3s2p/2s].

The treatment of heavy atoms (third row and lower) by LanL2DZ involves the use of a pseudopotential or effective core potential (ECP) for the core electrons.[19] The ECP is an analytical function which is used to account for the effect of the combined nuclear-electronic core on the remaining electrons. This approach is justified by the fact that the inner electrons of a heavy atom are unimportant, in a chemical sense – their spatial distribution and energies are largely unchanged when they form a chemical bond. In addition, relativistic effects, which are important for atoms as heavy as ruthenium, can be 'worked into' the ECP. These effects would otherwise be neglected. The LanL2DZ ECP accounts for the innermost 28 electrons of Ru ($[Ar]3d^{10}$). The remaining 16 electrons ($4s^2 4p^6 4d^7 5s^1$) are treated using a double-ζ basis set. The name LanL2DZ comes from the fact that it uses the Los Alamos National Laboratory (LANL) ECPs along with a double-ζ (DZ) basis set.

2.5.4 Symmetry.

The use of symmetry constraints is extremely useful in the computational study of inorganic complexes. The symmetry of a molecule can be constrained at the start, or the symmetry detected by Gaussian, can be used to reduce the effective degrees of freedom of a molecule and hence the number of steps required in a geometry optimisation. The calculation of energy is also speeded up as some integrals will be equal due to symmetry, while others will be zero due to the orthogonality of the irreducible representations. However, since all calculations in this thesis concern the asymmetric pyridinyl or pyrazinyl triazole ligand symmetry constraints have not been imposed. The symmetry calculated by Gaussian 03 has been used, which has been C1 unless otherwise stated.

2.5.5 Geometry optimisation.

The Berny algorithm is the default geometry optimisation algorithm for Gaussian 03. This algorithm is based upon a program by Schlegel[20], although it has been considerably enhanced (see under keyword *OPT* in Ref. [21], and references therein). The optimisation takes place in redundant internal coordinates regardless of the input format (Z-matrix or Cartesian coordinates). Redundant internal coordinates include all sets of internal coordinates (bond distances, angles and torsions) between atoms within bonding distance. In general, the number of such internal coordinates will be greater than the minimum of 3N-6 required to specify the structure of the molecule – hence the name 'redundant'.

After each calculation of the energy, the algorithm moves the atoms slightly, based upon an analysis of the gradient vector (the vector of first derivatives of the energy with respect to each of the internal coordinates) and the Hessian (the matrix of second derivatives of the energy with respect to the internal coordinates). The energy is calculated again, and the cycle continues until a local minimum is found. Gaussian 03 concludes that a local minimum has been found if each of the following four criteria are met:

1. the maximum force is less than 0.000450 hartrees/bohr
2. the RMS force is less than 0.000300 hartrees/bohr
3. the maximum displacement is less than 0.001800 bohr
4. the RMS displacement is less than 0.001200 bohr

Alternatively, if the forces are two orders of magnitude smaller than the threshold value, the geometry is considered to have converged irrespective of criteria 3 and 4. This facilitates optimisation of large molecules which may have a very flat potential energy surface around the minimum.

The threshold values listed above for each of the criteria are defaults. It is possible to specify tighter thresholds (Gaussian keyword *OPT=TIGHT*) for which the values are 0.000015 hartrees/bohr, 0.000010 hartrees/bohr, 0.000060 bohr and 0.000040 bohr respectively. Use of the tighter thresholds is recommended for calculation of low frequency vibrational modes.[21] When tight thresholds are specified for DFT calculations an ultrafine grid should also be used (see Section 2.5.6).

Difficulties in geometry convergence are often due to a poor guess for the Hessian, or force constant, matrix. In this case, calculation of the force constants by means of a frequency calculation can greatly reduce the number of steps required to reach an energy minimum. The Gaussian keywords, *OPT=CALCFC* (calculate the force constants for the initial geometry optimisation step), *OPT=CALCALL* (calculate the force constants before every step), and *OPT=READFC* (read in the force constants from a frequency calculation, usually at a lower level of theory) are useful in this regard.

2.5.6 Integration grid.

The exchange-correlation energy is calculated numerically by integration using a quadrature grid. The default, or 'fine', grid was used in most instances. This is a pruned (75,302) grid; that is, it is equivalent to having 75 radial shells and

302 angular points per shell. Pruned grids are optimised to use the minimal number of points required to achieve a given level of accuracy – this grid uses about 7000 points per atom (instead of about 23000).

In some cases, either where the SCF or geometry had difficulty in converging or where tight thresholds were used for the geometry optimisation, an 'ultrafine' grid was used (Gaussian keyword *INT=ULTRAFINE*). This is a pruned (99,590) grid, recommended for computing very low frequency modes of systems (see the discussion of *OPT=TIGHT* in Section 2.5.5).

The same integration grid should be used when comparing the energies of two molecules, and also when performing frequency calculations after a geometry optimisation.

2.5.7 GaussSum.

GaussSum is a program written by Noel O'Boyle of the Han Vos Research Group to parse the output of two popular computational chemistry programs, Gaussian[10] and GAMESS.[22] In addition to rearranging the computed data into a more accessible format, it performs calculations on the data and can convolute spectra. GaussSum provides a graphical user interface to all of its functions and runs on Windows, Linux and MacOSX. It is written in Python and uses the plotting program Gnuplot[23] for drawing graphs. GaussSum is open-source and is available for free from http://gausssum.sourceforge.net. Since January 2004, there have been more than one thousand downloads of GaussSum 0.8.

GaussSum may be used to:

- monitor the progress of the self-consistent field (SCF) convergence
- monitor the progress of geometry optimisation
- display all lines in the log file containing a particular phrase
- extract molecular orbital information

- calculate contributions of groups of atoms to each molecular orbital using Mulliken Population Analysis
- plot the density of states spectrum (and the partial density of states, in the case of groups of atoms)
- calculate and plot the crystal orbital overlap population (COOP)
- extract information on electronic transitions and plot the UV-Vis spectra
- calculate the change in the charge density corresponding to a particular UV-Vis transition
- create an electron density difference map, which can be used to visualise the change in electron density corresponding to a particular UV-Vis transition
- extract information on IR and Raman vibrations
- plot the IR and Raman spectra, which may be scaled using general or individual scaling factors

Throughout the computational studies carried out in this thesis, GaussSum has been used to monitor the progress of SCF and Geometry Optimisation. It has also been invaluable in the processing of the output data. Further information on GaussSum and its applications can be obtained from the website above and in the thesis of Noel O'Boyle.[24]

2.6 Bibliography.

[1] Porter, G.B., *J. Chem. Ed.*, **1983**, *60,* 785.

[2] Adamson, A.W., *J. Chem. Ed.*, **1983**, *60,* 797.

[3] McCusker, J.K., Damrauer, N.H., *Inorg. Chem.*, **1999**, *38*, 4268.

[4] Kasha, M., *Discuss. Faraday Soc.*, **1950**, *9*, 14.

[5] Demas, J.N., Turner, T.F., Crosby, G.A., *Inorg. Chem.*, **1969**, *8*, 674.

[6] Lakowicz, J.R., Principles of Fluorescence Spectroscopy, **1999**, Kluwer Acedemic.

[7] A schematic diagram of the experimental set-up can be found at http://www.clf.rl.ac.uk/Facilities/LSF/LML/confocal/resources/spc.htm.

[8] a) Towrie M., Parker A.W., Shaikh W., Matousek P., *Meas. Sci. Technol.,* **1998,** *9*, 816;
b) Matousek P., Towrie M., Stanley A., Parker A.W., *Appl. Spectrosc.*, **1999,** *53*, 1485.

[9] Kleverlaan, C.J., Stufkens, D.J., Clark, I.P., George, M.W., Turner, J.J., Martino, D.M., van Willigen, H., Vlcek, J., *J. Am. Chem. Soc.*, **1998**, *120*, 10871.

[10] Gaussian 03, Revision B.04, M. J. Frisch, G. W. Trucks, H. B. Schlegel, G. E. Scuseria, M. A. Robb, J. R. Cheeseman, J. A. Montgomery, Jr., T. Vreven, K. N. Kudin, J. C. Burant, J. M. Millam, S. S. Iyengar, J. Tomasi, V. Barone, B. Mennucci, M. Cossi, G. Scalmani, N. Rega, G. A. Petersson, H. Nakatsuji, M. Hada, M. Ehara, K. Toyota, R. Fukuda, J. Hasegawa, M. Ishida, T. Nakajima, Y. Honda, O. Kitao, H. Nakai, M. Kiene, X. Li, J. E. Knox, H. P. Hratchian, J. B. Cross, C. Adamo, J. Jaramillo, R. Gomperts, R. E. Stratmann, O. Yazyev, A. J. Austin, R. Cammi, C. Pomelli, J. W. Ochterski, P. Y. Ayala, K. Morokuma, G. A. Voth, P. Salvador, J. J. Dannenberg, V. G. Zakrzewski, S. Dapprich, A. D. Daniels, M. C. Strain, O. Farkas, D. K. Malick, A. D. Rabuck, K. Raghavachari, J. B. Foresman, J. V. Ortiz, Q. Cui, A. G. Baboul, S. Clifford, J. Cioslowski, B. B. Stefanov, G. Liu, A. Liashenko, P. Piskorz, I. Komaromi, R. L. Martin, D. J. Fox, T. Keith, M. A. Al-Laham, C. Y. Peng, A. Nanayakkara, M. Challacombe, P. M. W. Gill, B. Johnson, W. Chen, M. W. Wong, C. Gonzalez, J. A. Pople, Gaussian, Inc., Pittsburgh PA, **2003**.

[11] GaussView 3.0, Gaussian Inc., Pittsburgh PA, **2003**.

[12] O'Boyle, N.M., Vos, J.G., GaussSum 0.8, Dublin City University, **2004**. Available at http://gausssum.sourceforge.net.

[13] Becke, A.D., *J. Chem. Phys.*, **1993**, *98*, 5648.

[14] Lee, C., Yang, W., Parr, R.G., *Phys. Rev. B*, **1988**, *37*, 785.

[15] Miehlich, B., Savin, A., Stoll, H., Preuss, H., *Chem. Phys. Lett.*, **1989**, *157*, 200.

[16] (a) Perdew, J.P., Wang, Y., *Phys. Rev. B*, **1992**, *45*, 13244. (b) Perdew, J.P., Chevary, J.A., Vosko, S.H., Jackson, K.A., Pederson, M.R., Singh, D.J., Fiolhais, C., *Phys. Rev. B*, **1992**, *46*, 6671.

[17] Stevens, P.J., Devlin, J.F., Chabalowski, C.F., Frisch, M.J., *J. Phys. Chem.*, **1994**, *98*, 11623.

[18] Dunning Jr., T.H., Hay, P.J., *Modern Theoretical Chemistry*, Ed. Schaefer III, H.F., Vol. 3, 1-28, Plenum, New York, **1976**.

[19] (a) Hay, P.J., Wadt, W.R, *J. Chem. Phys.*, **1985**, *82*, 270. (b) Wadt, W.R., Hay, P.J., *J. Chem. Phys.*, **1985**, *82*, 284. (c) Hay, P.J., Wadt, W.R, *J. Chem. Phys.*, **1985**, *82*, 299.

[20] Schlegel, H.B., *J. Comp. Chem.*, **1982**, *3*, 214.

[21] Frisch, A., Frisch, M.J., Trucks, G.W., *Gaussian 03 User's Reference*, Gaussian, Inc., Carnegie, PA., **2003**.

[22] Schmidt, M.W., Baldridge, K.K., Boatz, J.A., Elbert, S.T., Gordon, M.S., Jensen, J.H., Koseki, S., Matsunaga, N., Nguyen, K.A., Su, S., Windus, T.L., Dupuis, M., Montgomery, J.A., *J. Comput. Chem.*, **1993**, *14*, 1347.

[23] Gnuplot – An interactive plotting program, Version 3.7.3, Williams, T., Kelley, C., http://www.gnuplot.info/.

[24] O'Boyle, N.M., Ph.D. Thesis, Dublin City University, **2004**.

Chapter 3

Early-Stage Photophysics of Homo and Heteroleptic Ru(II) Polypyridyl Complexes

The photophysical properties of $[Ru(bpy)_3]^{2+}$ and a number of similar complexes have been investigated using pico-second resonance Raman spectroscopy. These results show that the electronic structure of $[Ru(bpy)_3]^{2+}$ is still evolving up to 50ps after initial excitation. This is not affected by deuteriation of the ligands and is also observed for the heteroleptic complexes $[Ru(bpy)_2(phpytr)]^+$ and $[Ru(bpy)_2(Hdcb)]^+$. These results do not agree with the conclusions reached from other studies and highlight the extremely complicated nature of early stage processes in transition metal complexes. The results presented here are discussed in relation to those obtained in other studies, with an overview of the issues which remain outstanding.

3.1 Introduction.

The favourable photophysical properties of Ru(II) complexes lead to the possibility that they may play key roles in the construction of supramolecular systems.[1] These systems, it is hoped, will be able to perform useful photo – and/or redox – triggered processes such as light harvesting or information storage. The properties which show most promise are broad light absorption in the visible spectrum, stability in both the reduced and oxidised states and long – lived charge transfer excited states at room temperature. The complex $[Ru(bpy)_3]^{2+}$ has been the subject of the majority of the studies in this area and is therefore the best understood of the Ru(II) complexes.

In recent years, interest has focussed on the complex $[Ru(phen)_2(dppz)]^{2+}$ (where dppz is dipyrido-[3,2-a:2′,3′-c]phenazine). The source of this interest is its unusual "light – switch" properties. This term refers to the fact that the complex is strongly emissive in non – aqueous solvents while the emission virtually completely quenched in H_2O. Also of great interest is the ability of this complex to intercalate with DNA. This leads to strong phosphorescence, even in aqueous conditions, and hence has potential as a DNA sensor device. A large body of work has been dedicated to the investigation of the photophysical structure which leads to these emissive properties. Recent work has shown that solvent co-ordination and relaxation are involved in controlling the relative rates of radiative and non-radiative relaxation. Resonance Raman studies[2] on this complex supported a previously proposed three state model (subsequently extended[3,4]) to explain the solvent-dependent excited state dynamics. For these studies $[Ru(bpy)_3]^{2+}$ was used as a reference with which the results of $[Ru(phen)_2(dppz)]^{2+}$ could be compared. However, during the course of this work several observations suggested that the early picosecond photophysics associated with $[Ru(bpy)_3]^{2+}$ should be re - examined.[5] The work on dppz containing complexes is also highlighted here as the work was carried out simultaneously with that of $[Ru(bpy)_3]^{2+}$ and it helps to emphasise

the importance of resonance Raman spectroscopy in probing ultrafast processes. It is also an example of a heteroleptic complex in which there is the possibility of emission from two chromphores like $[Ru(bpy)_2(phpytr)]^+$, which has been studied in the present work (*vide infra*).

$[Ru(bpy)_3]^{2+}$ has long been regarded as a paradigm species with respect to the spectroscopy and photophysics of transition metal complexes, and continues to be the subject of a considerable number of publications.[6] Until relatively recently the majority of studies have focussed on the lowest thermally equilibrated excited (THEXI) state (i.e. ^{3}MLCT manifold).[7] Over the last decade, advances in laser technology and analytical techniques have lead to a resurgent interest in complexes that, previously, were considered to be fully understood. The photophysical behaviour of the emitting triplet state is well understood (see section 1.3.1.4), but much less is known about the events that lead to its formation. The processes, which occur in the time interval between excitation to the Frank-Condon state and relaxation to the THEXI states, have received an increasing amount of attention,[8] not least due to the recognition that significant photochemical processes such as charge injection in photovoltaic cells[9] (*vide infra*) and energy transfer in multinuclear complexes can occur via states lying higher than the THEXI states.[10] Understanding the factors which influence these early processes can therefore lead to greater control in the formation of long-lived charged separated species. Investigations into the early time photophysical properties of $[Ru(bpy)_3]^{2+}$ and its analogues have been undertaken using a variety of techniques.[8,11,12] Due to the relevance of these results to the present study, these studies are thoroughly reviewed in the discussion, section 3.4. The results in the present chapter primarily concern the ultrafast photophysics of $[Ru(bpy)_3]^{2+}$, however the complexes $[Ru(bpy)_2(phpytr)]^+$ and $[Ru(bpy)_2(Hdcb)]^+$ (where phpytr is 2,-(5′-phenyl-4′-[1,2,4]triazole-3′-yl)pyridine and dcb is 4,4′-dicarboxy 2,2′-bipyridine) are also investigated.

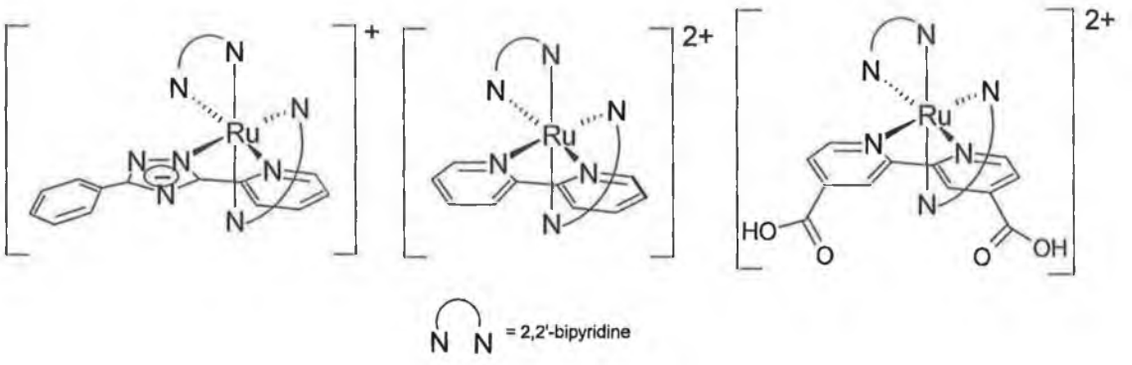

FIGURE 3.1: STRUCTURES OF THE COMPLEXES DISCUSSED IN THE TEXT.

The properties of Ru(II) complexes containing a triazole moiety has been an area of intense research by Vos and co-workers. An extensive review of the chemistry of complexes of this type is presented in Chapter 1, however an overview of the photophysics is presented here. Triazole containing complexes are analogous to $[Ru(bpy)_3]^{2+}$ with one pyridine moiety substituted for a triazole. The greater σ – donor properties of the triazole leads to an increase in the ^{3}MLCT – ^{3}MC energy gap, while the enhanced electron density of the triazole results in a splitting of the degeneracy of the ligand orbitals.[13] This has resulted in a number of interesting photophysical properties, such as the dual emission[14] observed for $[Ru(bpy)_2(pztr)]^+$ (where pztr is 2'-(1,2,4-triazol-3-yl)-pyrazine), and the pH dependent photostability of $[Ru(biq)_2(pytr)]^+$ (where biq is 2,2'-biquinoline and pytr is 2'-(1,2,4-triazol-3-yl)-pyridine).[15] Triazole containing complexes offer a range of synthetic possibilities due to the ability to substitute the ligand with a variety of moieties at various positions.[13] The presence of a free nitrogen on the triazole moiety also allows for pH dependent photo – physical and – chemical properties. The present work represents the first studies of the ultrafast photophysics in complexes of this type. The main reason for the inclusion of the triazole containing complex in the present study is that the ability to control the ^{3}MC – ^{3}MLCT energy gap (and the subsequent changes in excited state lifetime) via pH allows the investigation of the effect of this property on the ultrafast photophyiscs of the Ru(II) complex.

Ru(II) complexes containing pendant carboxylate groups have been a source of interest for many research groups due to their potential application in solar cells. The ability of the carboxylate groups to attach to TiO_2 surfaces leads to long – lived, light – driven charge separation.[16] After light absorption a charge separated excited state is formed, however in solution phase emission of a photon results in charge recombination on the nanosecond time scale. When a photoactive molecule is attached to a surface there is the potential for charge injection into the surface. This charge injection isolates the oxidised metal centre and the electron, and hence results in the harvesting of the light energy. Studies on the rate of charge transfer to surfaces have shown that this process occurs on the sub picosecond time scale.[16] In order to optimise the light harvesting ability of the complexes of interest, data are required on their electronic states at these very early times. These charge injection processes most likely occur from the Franck – Condon states in the excited molecules and not from the thermally equilibrated MLCT structures. The investigation of $[Ru(bpy)_2(Hdcb)]^+$, on the pico – and femto – second time scale have allowed increased understanding of the factors which serve to increase the efficiency of the injection process and reduce the rate of charge recombination. The present work uses picosecond time resolved Raman spectroscopy to probe these processes in free solution to gain further insight into the early processes which may be linked to the charge injection.

In the present work, as in much of the other photophysical studies of this thesis, deuteriation plays a significant role. The effect of deuteriation on vibrational spectroscopy was first highlighted by Yersin.[17] Deuteriation of ligands causes a shift and change in intensity of the bands due to these ligands. Not only does this sometimes (though not always) result in the simplification of the spectra but may also facilitate the assignment of vibrational bands. However, as we have noted in other studies (see Chapter 4), deuteriation also appears to occasionally cause a reduction in the signal / noise ratio of the spectra. Deuteriation has proved a valuable synthetic tool as

^1H – NMR silent ligands aid in the interpretation of complex spectra, particularly for multi – nuclear asymmetric complexes.

3.2 Experimental.

$[Ru(bpy)_3](PF_6)_2$, $[Ru(bpy)_3]Cl_2$, and their deuteriated analogues were obtained from Complex Solutions, Dublin City University, Glasnevin, Dublin 9 and were used without further purification. $[Ru(bpy)_2(phpytr)]^+$ and $[Ru(bpy)_2(Hdcb)]^+$ were obtained from Dr. Wesley Browne, Dublin City University.

Resonance Raman spectra were calibrated using an acetol (acetonitrile: toluene 1:1) solution. The prominent peaks in these spectra were compared to those in a reference spectrum. A graph of pixel number vs wavenumber was drawn and a calibration line in the form of y = mx + c obtained. The correct wavenumber in each spectrum was then calculated using this formula. A separate calibration line was constructed for each probe wavelength used. This processing was performed using Microsoft Excel with the spectra then saved with the .prn extension. These spectra were converted to .spc files using a DOS-based program SpectroCalc. All subtractions were carried using out GRAMS /32 version 5.03, unless otherwise stated. In a number of spectra a calibration error has occurred leading to the spectra being shifted to a lower frequency by approx. 77 cm^{-1}. The captions of these spectra are followed by an asterix(*). A comparison of the intensity profile of a sample spectra of $[Ru(bpy)_3]^{2+}$ and a related complex ($[Ru(bpy)_2(bpt)]^+$) is provided in APPENDIX A-10, with a table of the band shifts shown in APPENDIX A-11.

Spectral subtractions involved in the first instance subtraction of the solvent only spectra (where available) at the corresponding pump and probe wavelength. The ground state (-20 ps) sample spectra were then subtracted to leave the excited state only spectra. It is important to note that the presence of ground state bands due to neutral bpy^0 bands in the localised $[Ru(III)(bpy^0)_2(bpy^{-\bullet})]^{2+}$ excited state may lead to the over-subtraction of the ground state spectra. To account for this, a note was kept of the ration of

subtraction of each spectra and this ratio was matched for spectra were possible. In some cases the spectra which represented the fully evolved THEXI state (such as at 300 ps) were also subtracted. These subtractions are referred to as excited state subtractions and were done in an attempt to uncover any bands due to a precursor state. This approach proved to be particularly effective in the investigation of the excited state photophyiscs of $[Ru(phen)_2(dppz)]^{2+}$.[2]

The results were obtained during a number of visits to Rutherford Appleton Laboratories, Abingdon, England by investigators of the John McGarvey Research Group (JMcGRG) of the Queen's University of Belfast. Previous work on the processing of the spectra has been carried out by other researchers in the JMcGRG (mostly Dr. Colin Coates) and some of these results have been incorporated into the present work. Such data are presented as black and white spectra and are clearly identified by (DCC) at the end of the caption. Where possible the spectra have been re-processed to ensure consistency in the methods employed.

3.3 Results.

The primary focus of this chapter concerns the ultrafast photophysics of $[Ru(bpy)_3]^{2+}$ and its deuteriated analogues as observed by Time Resolved Resonance Raman (TR^3) spectroscopy. Studies have also been carried out on the Time Resolved Luminescence (TRL) of this complex and these results are included to support the TR^3 measurements. The generality of the effects observed for polypyridyl transition metal complexes is explored in two heteroleptic ruthenium complexes, $[Ru(bpy)_2(LL)]^+$ (where LL is phpytr and Hdcb).

3.3.1 Overview of Picosecond Time Resolved Luminescence (ps-TRL) Spectroscopy Results.

Previous work by the JMcGRG showed a high energy emission at 520 nm from the complex $[Ru(bpy)_3]^{2+}$, which was seen to decay within < 3 ps.[5] FIGURE 3.2, which is reproduced from the published work, shows the time resolved luminescence spectra observed for $[Ru(bpy)_3]^{2+}$ in acetonitrile. The presence of an emission at 520 nm is clearly observable as is the lower energy emission (at 610nm) which persists into the nanosecond time scale. These studies also showed that deuteriation of the ligands on the complexes led to an increase in the lifetime to beyond 200 ps. As pointed out in a later communication, further studies carried out on complexes synthesised by a different method have, however, shown that this increased lifetime is not due to emission from the complex but from another source.[18] Although these results confirm the presence of a high energy emission (< 520 nm), they raise doubts about the effect of deuteriation. Extensive studies have been carried out in order to confirm the nature of the deuteriation dependent emission, however so far they have not been successful. Interestingly, recent work by McFarland *et al.*[12] has also noted the observation of a similar 'unidentified' emission, with a lifetime comparable to that observed in our studies. Studies have been carried

out on corresponding Fe(II) and Os(II) tris homoleptic complexes, as well as the free ligand and it has been confirmed that these are not the source of the emission. Due to the susceptibility of luminescence measurement to small impurities every effort has been made to minimise this possibility by repeated purification steps and the use of samples from independently produced batches.

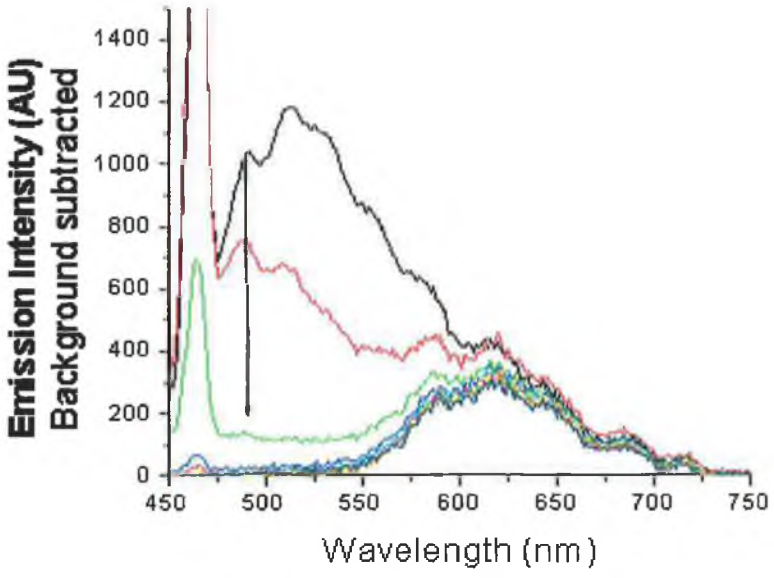

FIGURE 3.2: TIME RESOLVED LUMINESCENCE OF $[Ru(bpy)_3]^{2+}$ IN ACETONITRILE. REPRODUCED FROM REFERENCE.[5]

3.3.2 Overview of Picosecond Time resolved resonance Raman (ps-TR^3) Results.

Pico-second time resolved resonance Raman spectroscopy has been used to investigate the early photophysical properties of transition metal complexes. The majority of the studies have been carried out on $[Ru(bpy)_3]^{2+}$ as it is a paradigm for the study of other complexes and its orbital structure is better understood than its counterparts. The Raman spectroscopy of $[Ru(bpy)_3]^{2+}$ is presented first. The effect of solvent and counter – ion have also been investigated. Anti – Stokes measurements have also been attempted (for more information see SECTION 3.3.3.3). The effect of deuteriation on $[Ru(bpy)_3]^{2+}$ is investigated in SECTION 3.3.3.4. Next the time resolved spectra of the

heteroleptic complexes are presented. Firstly, the spectra of $[Ru(bpy)_2(phpytr)]^+$ are given followed by the spectra of $[Ru(bpy)_2(Hdcb)]^+$. For the complex $[Ru(bpy)_2(phpytr)]^+$ the triazole moiety in the asymmetric ligand of this complex can be protonated and therefore spectra have been recorded in both basic and acidic conditions. For the complex $[Ru(bpy)_2(Hdcb)]^+$ there is the possibility of the carboxylic acid moiety to be protonated or deprotonated. These measurements have been recorded in solutions at pH 2, which is the monoprotonated form in both the ground and excited states.[19] Studies of the ultrafast Raman spectroscopy of $[Fe(bpy)_3]^{2+}$ and $[Os(bpy)_3]^{2+}$ have also been carried out. As these results were found not be directly related to the discussions regarding the photophysics of the Ru(II) complexes they can be found in APPENDIX A. These results have, however, confirmed that the results presented here are not due to experimental artifacts.

3.3.3 ps-TR^3 on $[Ru(bpy)_3]^{2+}$.

The ps-TR^3 spectra of $[Ru(bpy)_3]^{2+}$ were recorded using several combinations of pump and probe wavelengths to investigate the effect of pumping on excited state formation and resonance at each probe wavelength with the excited state formed. The pump and probe wavelengths used where 255/390, 390/390, 400/350, 410/475, 400/530 nm respectively. Also investigated were the effects of deuteriation and the counterion, and the anti – Stokes spectra.

3.3.3.1 Effect of Pump and Probe Wavelength.

FIGURE 3.3 shows $[Ru(bpy)_3]^{2+}$ with pump at 400 nm, probe at 350 nm and with acetonitrile as the solvent. Both solvent and ground state are subtracted in the spectra. The kinetics of the peaks observed at 1145, 1220 and 1468 cm^{-1} have also been plotted. The grow-in of all three bands occur on the picosecond timescale. The bands are seen to grow in intensity up to 50 ps, with no change in intensity observed after this time. It is difficult to accurately determine the time taken for the excited state bands to be fully formed. This is due to the number of points available for the kinetics and also the variation in the signal to noise ratio between sets of spectra. The time taken for formation of the steady state spectra is seen to be approximately 50 ps, however, this figure is not definitive. It is an attempt to reflect the overall trends of the kinetics and that time taken is longer than the femtosecond timescale but appears shorter than 100's of picoseconds time range.

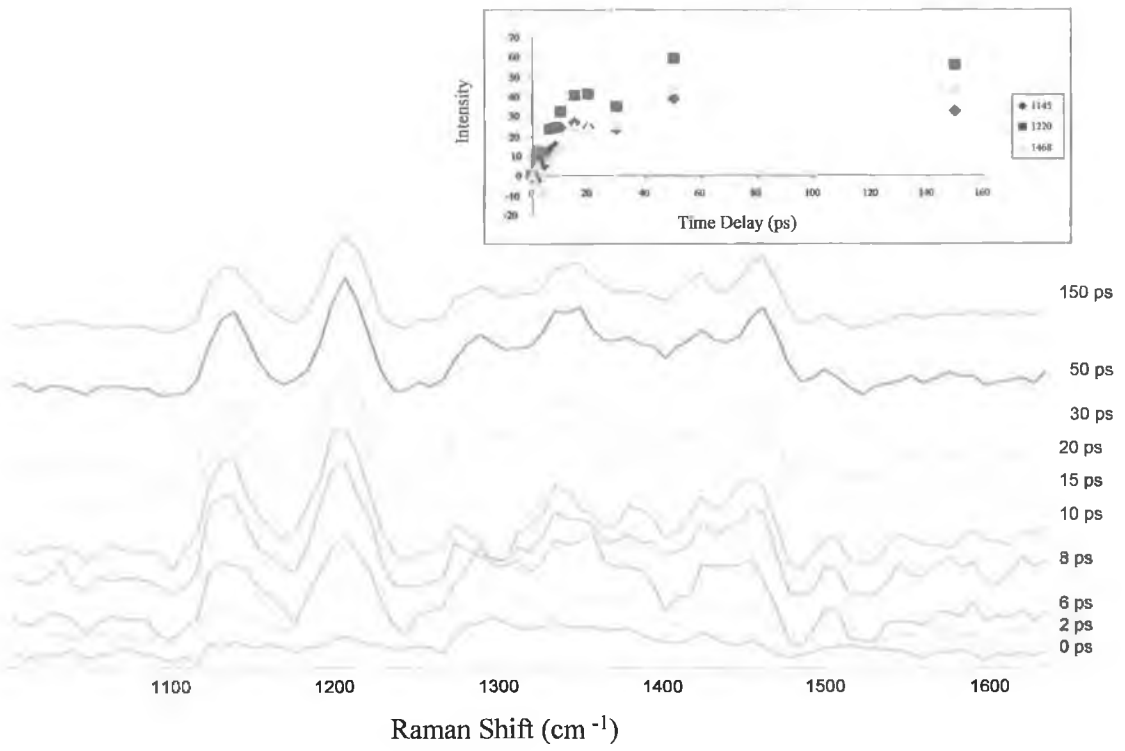

FIGURE 3.3: $[Ru(bpy)_3]Cl_2$ IN ACETONITRILE WITH PUMP AT 400 NM AND PROBE AT 350 NM. THE INSET SHOWS THE KINETICS OF BANDS AT 1145, 1220 & 1468 CM^{-1}. *

Shown in APPENDIX A-1 are the spectra of $[Ru(bpy)_3]^{2+}$ in H_2O with the same pump and probe combination. These spectra again show a growth of the steady state spectrum on a 50 ps timescale.

Spectra were also recorded using a 475 nm probe wavelength, in order to be in resonance with the lower energy transition of ^{3}MLCT (FIGURE 3.4). From previous experience[20] with ns-TR^3, a less rich excited state spectrum of the ^{3}MLCT state at this wavelength, the most prominent $bpy^{\cdot-}$ feature appearing at ~ 1500 cm^{-1}. The corresponding spectra in D_2O are given in APPENDIX A-2. The most prominent feature observed is around 1500 cm^{-1}, as expected. The kinetics of this band are also shown and indicate that the grow in of the steady state spectrum occurs over the first 20 - 50 ps. Subtraction of the –20 ps spectra yields pure excited state spectra with a good signal to noise ratio. Also apparent is a band at very early times at 1476 cm^{-1}(*vide infra*) . This is quite apparent at 2 ps, before the characteristic 1500 cm^{-1} appears at 4 ps. This feature is also illustrated in the excited state subtracted spectra in FIGURE 3.5.

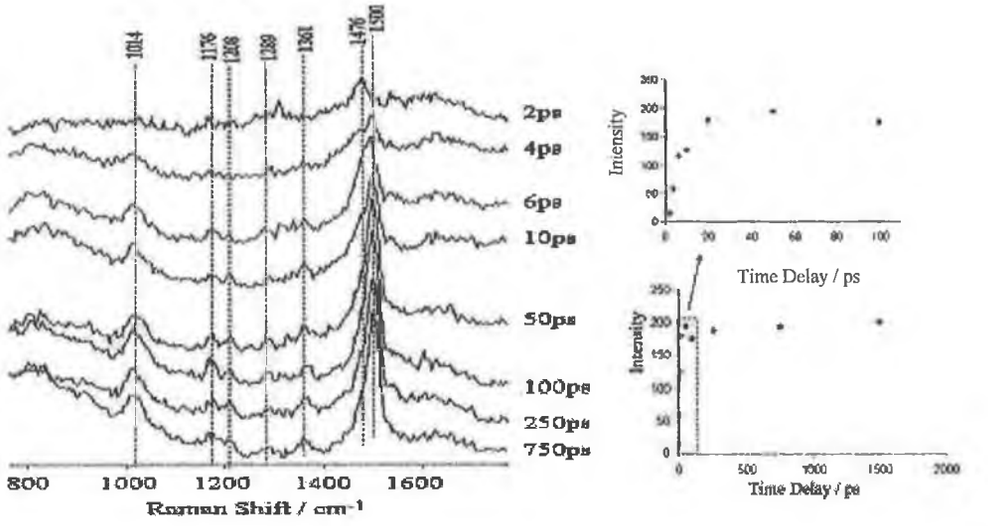

FIGURE 3.4: (LEFT) SPECTRA OF $[Ru(bpy)_3]^{2+}$ WITH PUMP AT 400 NM AND PROBE AT 475 NM IN H_2O AND (RIGHT) KINETICS BETWEEN (TOP) 0 – 100PS AND (BOTTOM) 0 – 1500 PS. (DCC)

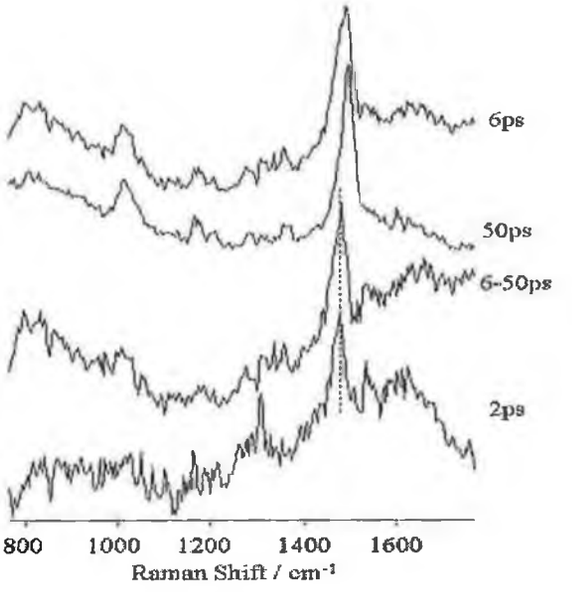

FIGURE 3.5: EXCITED STATE SUBTRACTED SPECTRA FOR $[Ru(bpy)_3]^{2+}$ WITH PUMP AT 400 NM AND PROBE AT 475 NM IN H_2O. (DCC)

FIGURE 3.5 highlights the pure excited state spectra in the early time range of $[Ru(bpy)_3]^{2+}$ and also gives the spectra after excited state (50 ps) subtraction. A band is observed at 1472 cm^{-1} which appears earlier than the grow – in of

the steady state. This band appears to be an artefact of the system, however, as it is not present in other spectra (see FIGURE 3.6 for example).

It is known through nanosecond transient absorption studies and time resolved resonance Raman, that there is a further distinct ^{3}MLCT transition of $[Ru(bpy)_3]^{2+}$ in the wavelength region beyond 500 nm.[8,21] Spectra were therefore measured with 530 nm probe wavelength and a 400 nm pump. These spectra are shown in APPENDIX A-3. The signal to noise ratio of the spectra was quite poor indicating either ineffective pumping (although pump wavelength is same as before) and/or relatively weak resonance with the excited state(s) at this probe wavelength. However, it is possible to make out a profile change over early time, which seems to reflect that which was observed at 475 nm probe (FIGURE 3.5).

The pump wavelength was next moved to the red so as to see the effect of reduced energy in the ^{1}MLCT in the Franck – Condon state. This results in the excited state having less vibrational energy when it is initially formed. At this pump wavelength the excited state is formed with less excess energy due to the reduced energy of the excitation photon.

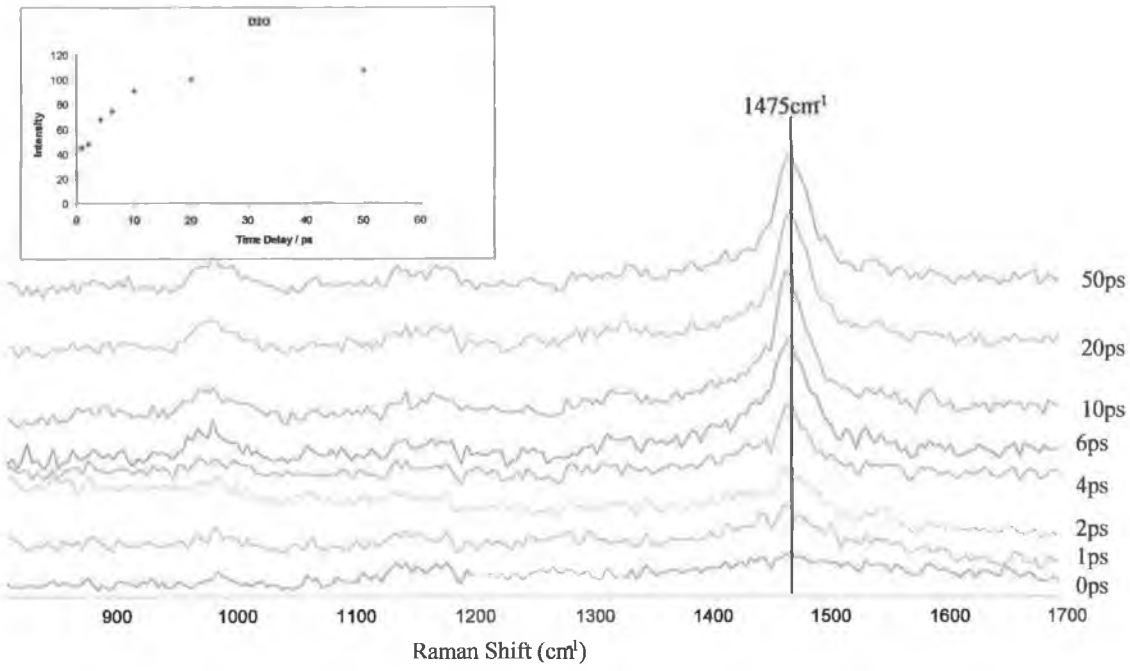

FIGURE 3.6: $[Ru(bpy)_3]Cl_2$ WITH PUMP AT 410 NM AND PROBE AT 475 NM IN D_2O. ALSO SHOWN AT THE KINETICS OF BAND AT 1475CM^{-1}. *

FIGURE 3.6 shows the excited state spectra of $[Ru(bpy)_3]^{2+}$ with the pump wavelength at 410 nm and probe wavelength at 475 nm. The most intense band in the spectra is observed at 1475 cm^{-1}. The kinetics of this band show that no further growth is apparent after 50 ps. Further spectra of $[Ru(bpy)_3]^{2+}$ in D_2O with pump at 410 nm and probe at 475 nm are given in APPENDIX A-2 and the results are in agreement with those shown in FIGURE 3.6.

Spectra were also recorded with 390 nm pump and probe. Due to overlap between the pump and the probe pulses the earliest time which could be considered was 4 ps (outside the cross-correlation time). These spectra are given in FIGURE 3.7.

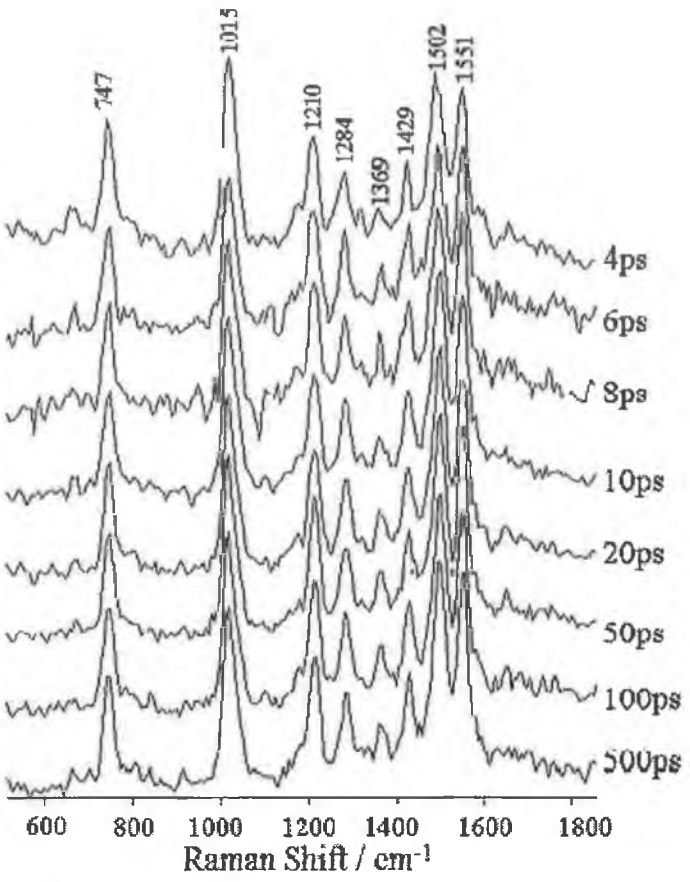

FIGURE 3.7: PURE EXCITED STATE $[Ru(bpy)_3]^{2+}$ IN H_2O WITH PUMP AND PROBE AT 390 NM. (DCC)

Further spectra recorded with a 265 nm pump and a 400 nm probe are given in APPENDIX A-5. At this wavelength a poor signal – to – noise ratio is found and little conclusion can be drawn about the rate of THEXI state formation.

Solvent Dependence of $[Ru(bpy)_3]^{2+}$

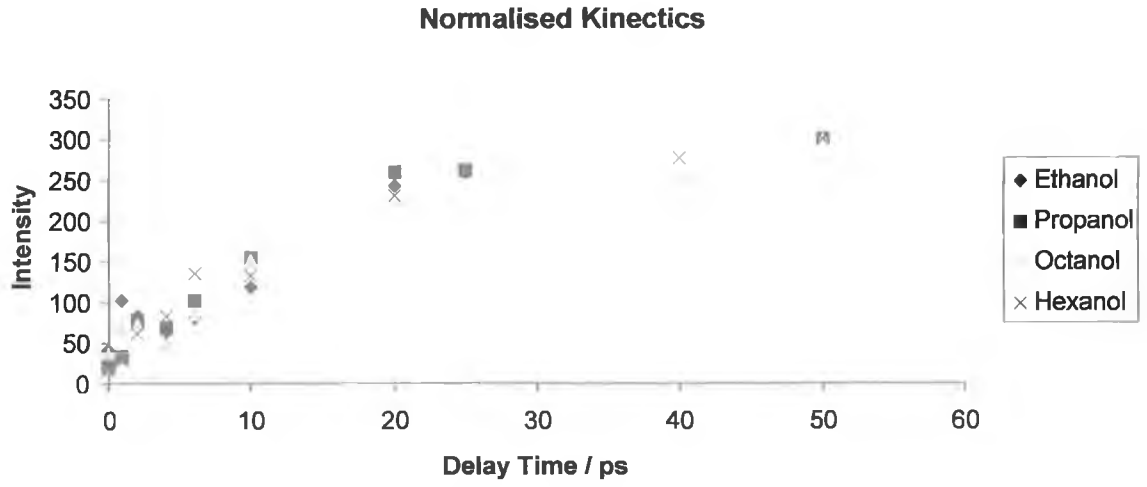

FIGURE 3.8: KINETICS OF BAND AT 1473 CM^{-1} IN A SERIES OF ALCOHOLS.

The solvent dependence of the time required for the formation of the steady state (THEXI) spectra were investigated for a series of alcohols, acetonitrile and deuteriated solvents. FIGURE 3.8 shows the kinetics of excited state grow-in of $[Ru(bpy)_3]^{2+}$ in 4 alcohols with pump at 410 nm and probe at 475 nm. It is apparent that over the series of alcohols that the rise time of this signal is approximately constant despite the very different viscosities, dielectric constants and thermal diffusivities.[22]

FIGURE 3.9 and FIGURE 3.10 give an example of the spectra and kinetics obtained in hexanol. As shown in FIGURE 3.10 the formation of the steady state is complete by 50 ps.

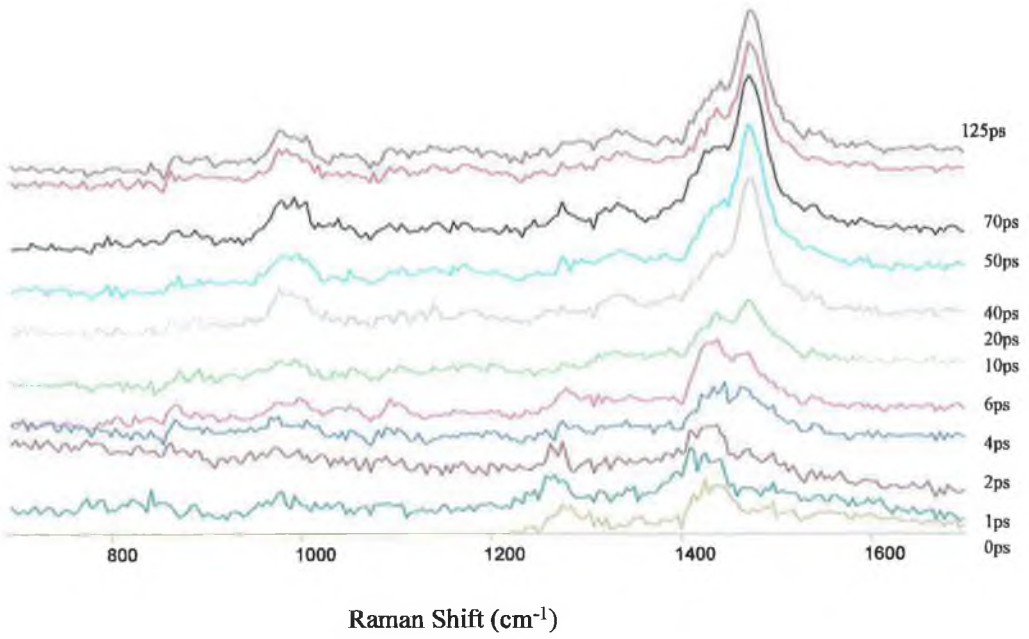

FIGURE 3.9: TIME RESOLVED EXCITED STATE RESONANCE RAMAN OF $[RU(BPY)_3]^{2+}$ IN 1-HEXANOL; PUMP AT 400NM, PROBE AT 475NM. *

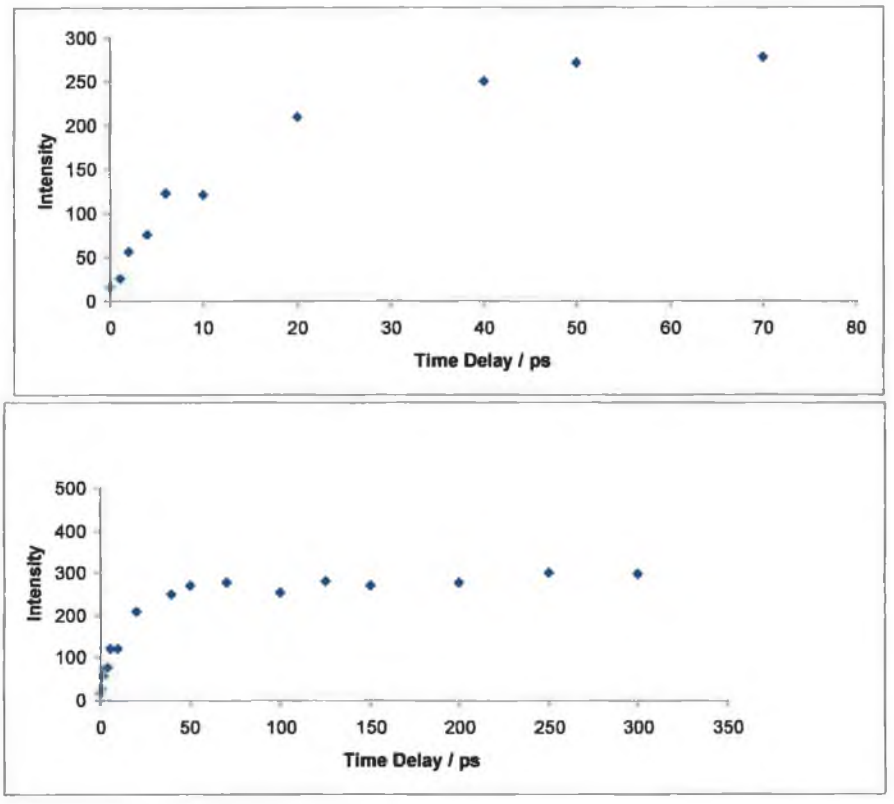

FIGURE 3.10: KINETICS OF EXCITED STATE FORMATION AT 1475 CM^{-1} IN 1-HEXANOL. TOP SHOWS THE FIRST 80 PS AND BOTTOM GIVES THE TIME RANGE FROM 0 – 300 PS.

APPENDIX A-3 shows the non-normalised pure excited state spectra and corresponding kinetic plot of the excited state ^{3}MLCT grow-in over early times,

recorded for $[Ru(bpy)_3]^{2+}$ in hexanol solvent. This is useful in comparison to FIGURE 3.9 and FIGURE 3.10 which are also in 1-hexanol but using a different probe wavelength.

FIGURE 3.11 shows the TR^3 spectra of $[Ru(bpy)_3]^{2+}$ in acetonitrile and H_2O with pump at 400 nm and probe at 350 nm.

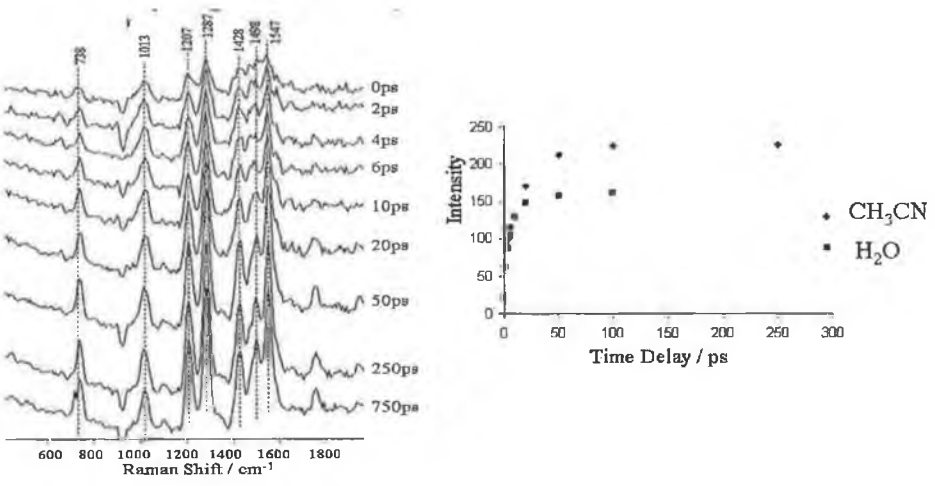

FIGURE 3.11: (LEFT)SPECTRA OF $[Ru(bpy)_3]^{2+}$ IN ACETONITRILE WITH PUMP AT 400 NM AND PROBE AT 350 NM AND (RIGHT) THE RESULTANT KINETICS IN ACETONITRILE AND H_2O. (DCC)

These kinetics show that the time required to reach maximum intensity is approximately the same for the two solvents.

3.3.3.2 Counterion Dependence of $[Ru(bpy)_3]^{2+}$ Photophysics.

The effect of counter-ion on early photophysics was also investigated. $[Ru(bpy)_3]^{2+}$ was prepared with chloride and hexafluorophosphate counter ions. FIGURE 3.12 compares Cl and PF_6 counterions, albeit in different solvents. The grow-in process is again complete after 50 ps, irrespective of the counterion. Therefore, no significant counter ion dependence was observed on the kinetics of the grow-in of the ^{3}MLCT state. The results suggest that significant ion – pairing effects are not involved in the processes observed.

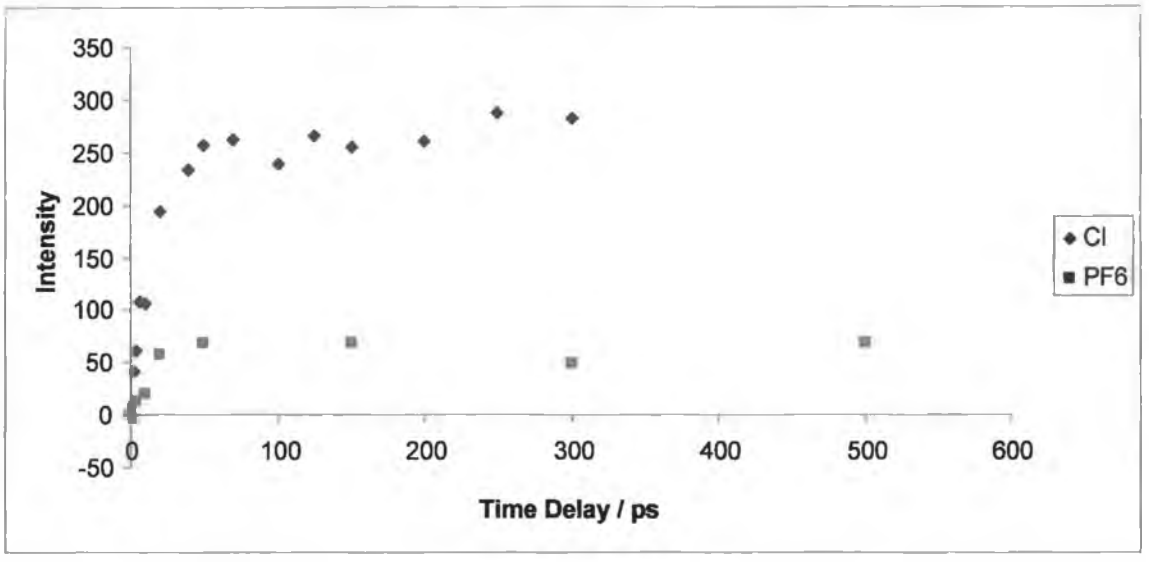

FIGURE 3.12: KINETICS OF $[Ru(bpy)_3]Cl_2$ IN HEXANOL AND $[Ru(bpy)_3](PF_6)_2$ IN D_3-ACN WITH PUMP AT 410 NM AND PROBE 475 NM.

3.3.3.3 Anti - Stokes of $[Ru(bpy)_3]^{2+}$.

In order to examine the time taken to obtain the steady state spectra further, anti-Stokes measurements were attempted. It was hoped that the growth of the Stokes bands would be mirrored by a concomitant decrease in anti – Stokes bands. This would provide strong support for a vibrational cooling mechanism on the picosecond timescale as anti – Stokes bands occur from

vibrationally excited states. These states would be depleting as the lowest vibrational state (from which the Stokes bands occur) is being formed. However, due to the weak nature of anti-Stokes bands and the overlap of anti-Stokes bands with pump Stokes bands, the quality of the spectra were insufficient to provide further information. The overlap of Stokes bands from the pump laser with the anti – Stokes bands from the probe is an important experimental consideration when planning two – colour anti – Stokes measurements.

3.3.3.4 $[Ru(d_8\text{-}bpy)_3]^{2+}$.

The spectra of the fully deuteriated analogue of $[Ru(bpy)_3]^{2+}$ were also investigated. The effect of deuteriation on vibrational spectra is well known[17] and is a useful probe in photophysical measurements. Briefly, the increased mass of deuterium relative to hydrogen leads to a shift in the location of bands due to the deuteriated ligand in vibrational measurements. In general, a shift to lower wavenumbers is expected on the basis of a simple reduced mass effect. In excited state lifetime measurements, deuteriation leads to a reduction in the contribution of high frequency C – H vibrations of the ligand.[23] Deuteriation of the ligand on which the excited state is based results in a reduction in the rate of non – radiative deactivation and hence the excited state lifetime increases. Deuteriation of a spectator ligand has no effect on the excited state lifetime and therefore selective deuteriation can be used to aid in the investigation of the location of the excited state energy.

$[Ru(d_8\text{-}bpy)_3]Cl_2$ was investigated with the pump at 410 nm and a probe wavelength of 470 nm. The results are presented in APPENDIX A-6 with the ground state (-20 ps) subtracted to show the pure excited state spectra. The grow – in of a band at 1445 cm^{-1} is visible, however due to the large fluorescent background observed in the spectra accurate kinetic data was unobtainable.

Further measurements of the photophysical properties of $[Ru(d_8\text{-}bpy)_3]Cl_2$ where carried out using a pump wavelength of 400 nm and a probe at 350 nm. The resulting pure excited state spectra in d_3-acetonitrile are give in FIGURE 3.13.

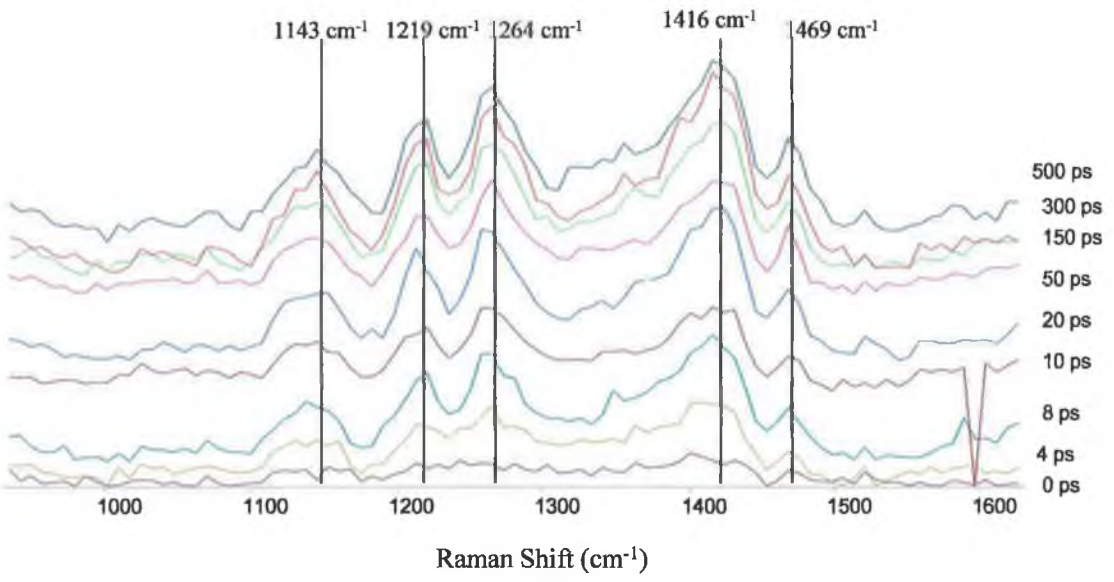

FIGURE 3.13: EXCITED STATE SPECTRA OF $[Ru(D_8\text{-}BPY)_3]Cl_2$ IN D_3-ACN WITH PUMP AT 400 NM AND PROBE AT 350 NM. *

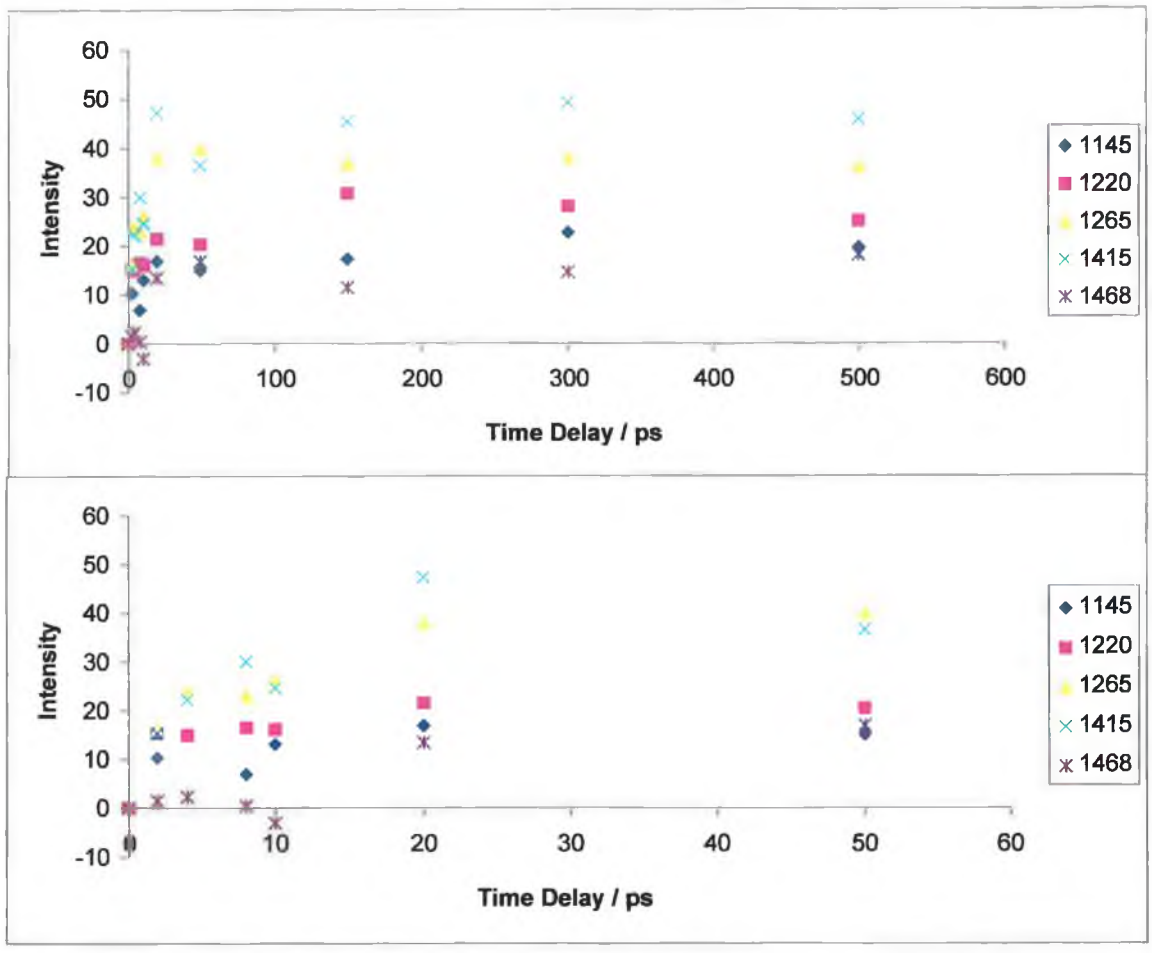

FIGURE 3.14: KINETICS OF $[Ru(D_8\text{-BPY})_3]Cl_2$ IN D_3-ACN PUMP AT 400 NM / PROBE AT 350 NM. THE TOP PICUTRE IS BETWEEN 0 AND 600 PS WHILE THE BOTTOM SHOWS THE 0 – 60 PS TIME FRAME.

A number of bands are visible at 1469, 1416, 1265, 1219 and 1143 cm^{-1}. The kinetics of these peaks are given in FIGURE 3.14. The majority of the bands appear to have reached maximum intensity after 50 ps. This is especially clear in the kinetics of the 1265 cm^{-1} band (the yellow triangle).

The spectra of $[Ru(d_8\text{-bpy})_3](PF_6)_2$ were also investigated in d_3-acetonitrile with pump at 400 nm and a probe wavelength of 350 nm, and in D_2O with pump at 410 nm and probe at 470 nm. However in both of these sets of spectra there was a strong fluorescent background and it was not possible to obtain any information about the complex (for example see APPENDIX A-6).

The spectra of the complex $[Ru(d_8\text{-}bpy)_2(bpy)]^{2+}$ was investigated with a pump at 410 nm and a probe at 470 nm. FIGURE 3.15 shows the kinetics of the two bands observed at 1440 and 1461 cm^{-1} Again it is seen that the growth in intensity is completed after 50 ps.

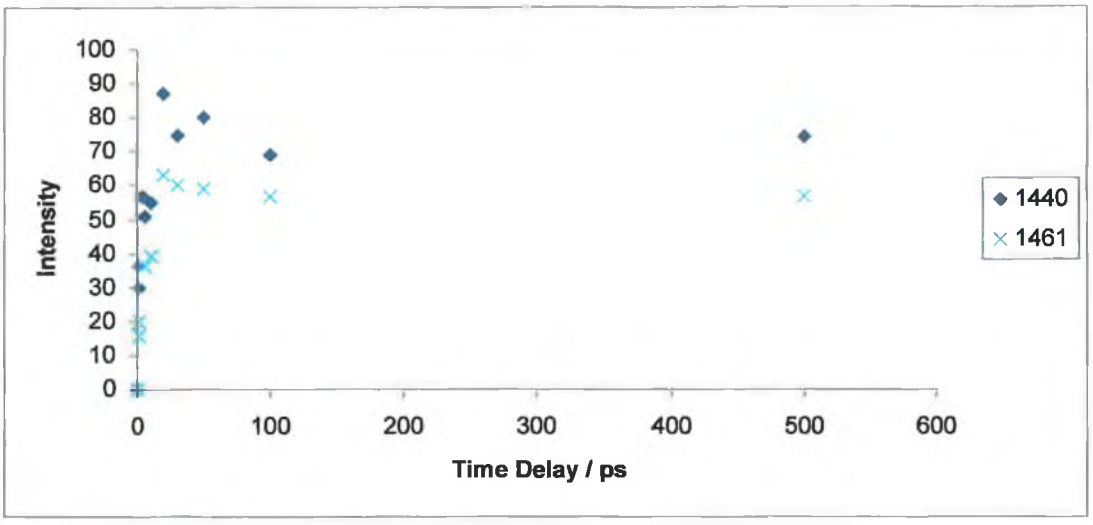

FIGURE 3.15: KINETICS OF $[Ru(D_8\text{-}BPY)_2(BPY)]$ IN D_2O WITH PUMP AT 410 AND PROBE AT 470 NM.

FIGURE 3.16 shows the spectra of $[Ru(d_8\text{-}bpy)(bpy)_2]^{2+}$ in H_2O with pump at 400 nm and probe at 350 nm. The kinetics of the grow in of the steady state spectrum is given in FIGURE 3.17. Again it is apparent that the grow in occurs within 50 ps.

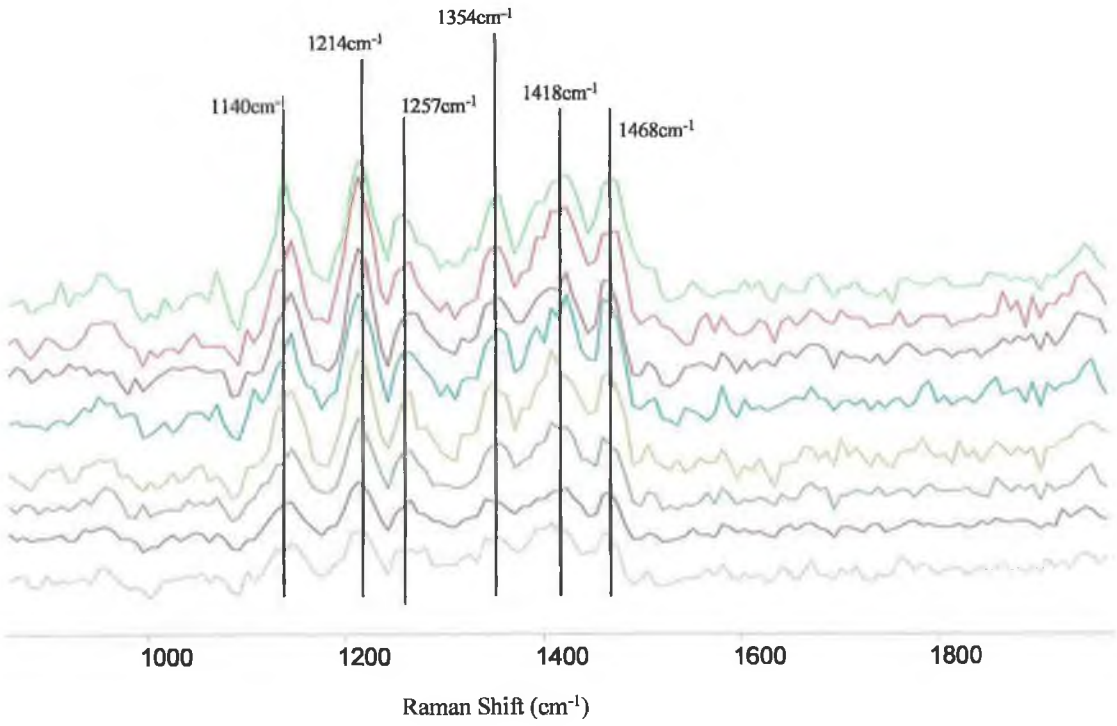

FIGURE 3.16: SPECTRA OF $[Ru(D_8\text{-}BPY)(BPY)_2]^{2+}$ IN H_2O WITH PUMP AT 400 NM AND PROBE AT 350 NM.*

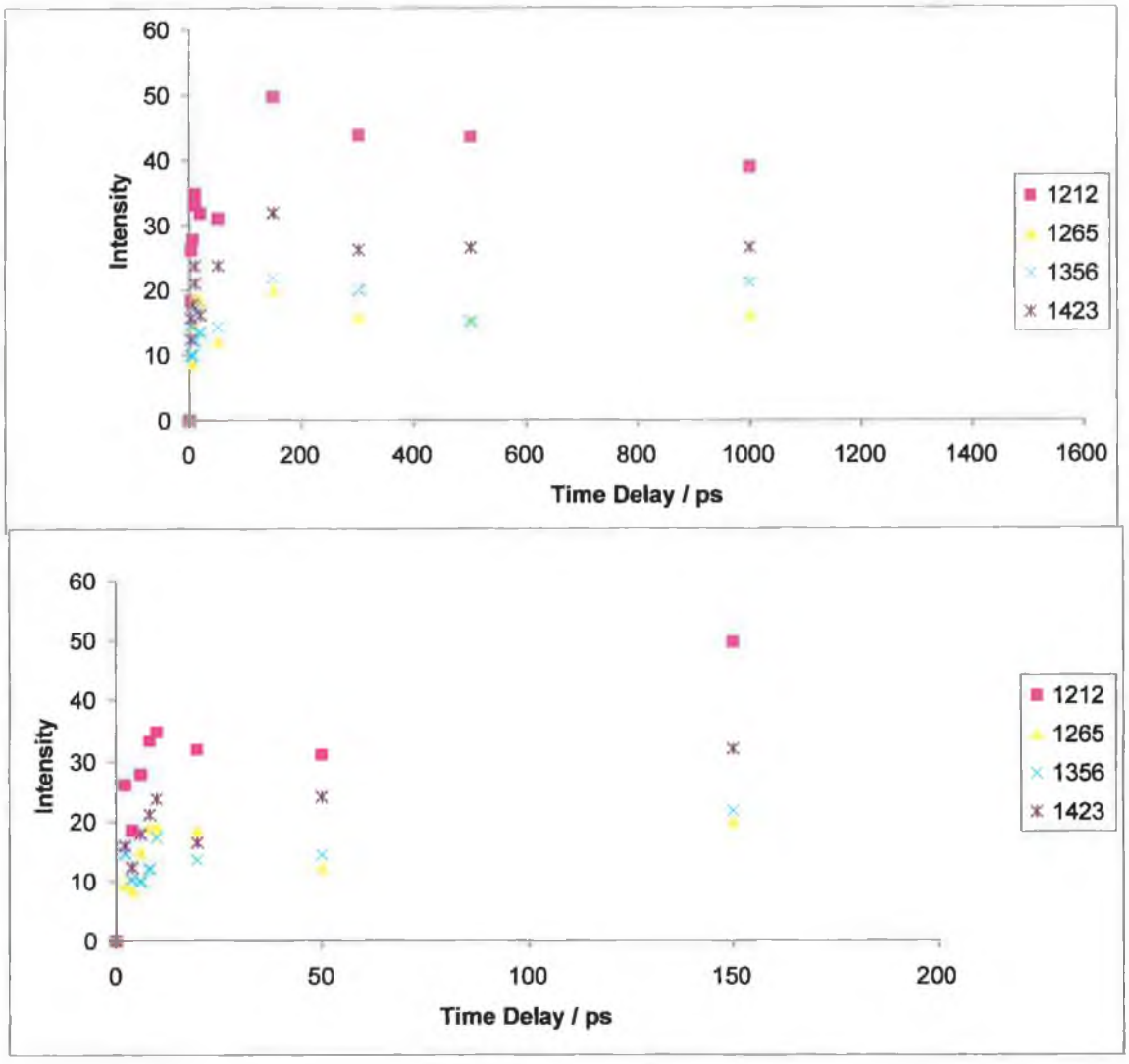

FIGURE 3.17: KINETICS OF BANDS OBSERVED FOR $[Ru(D_8\text{-}BPY)(BPY)_2]^{2+}$ IN H_2O WITH PUMP AT 400 NM AND PROBE AT 350 NM.

3.3.4 $[Ru(bpy)_2(phpytr)]^{n+}$.

Picosecond time resolved resonance Raman measurements have also been used to investigate the early stage photophysics of Ru(II) complexes with a triazole containing ligand. The strong σ – donor ability of the triazole moiety leads to interesting photophysics in complexes of this type.[14] This σ – donor ability also changes the energy gap between the ^{3}MLCT and ^{3}MC, and the effect of these changes can be used to gain further insight into the nature of the ultrafast processes occurring. The presence of a free nitrogen on the triazole moiety allows pH dependent photo – physics and chemistry to occur.

Firstly, the spectra of the deprotonated pyridine triazole complex were investigated with a pump wavelength of 400 nm and a probe wavelength of 350 nm. FIGURE 3.18 and 3.18 show the excited state spectra and kinetics of $[Ru(bpy)_2(phpytr)]^+$ in H_2O and acetonitrile. The ^{3}MLCT state of this complex is bpy-based, hence characteristic $bpy^{-\bullet}$ features are observable at 1213, 1287 and 1503 cm^{-1}. Also observed is the grow-in of the excited state features at early times, analogous to that observed for $[Ru(bpy)_3]^{2+}$. Plotting of the relative intensity of the 1288 cm^{-1} peak shows a grow-in which is complete within ~ 50 ps.

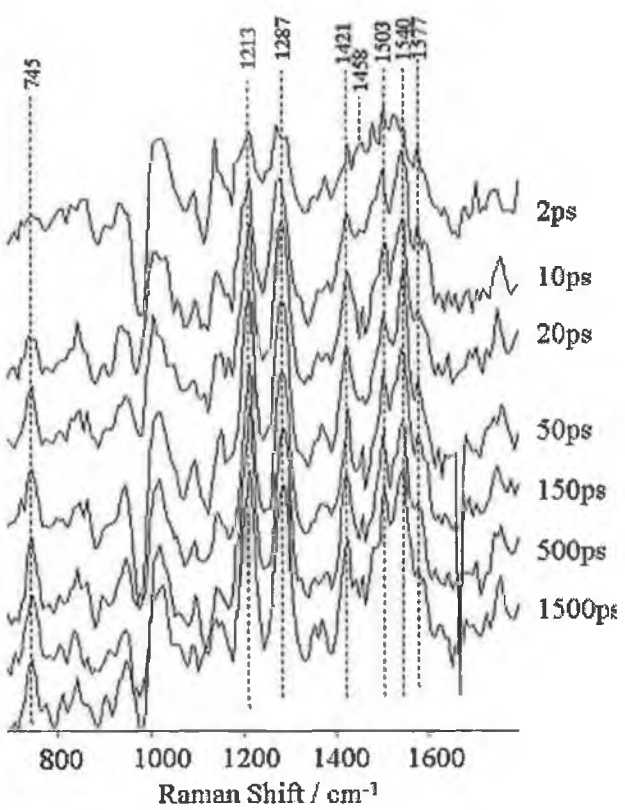

FIGURE 3.18: RESONANCE RAMAN SPECTRA AND KINETICS OF $[Ru(bpy)_2(phpytr)]^+$ IN H_2O WITH PUMP AT 400 NM AND PROBE AT 350 NM. (DCC)

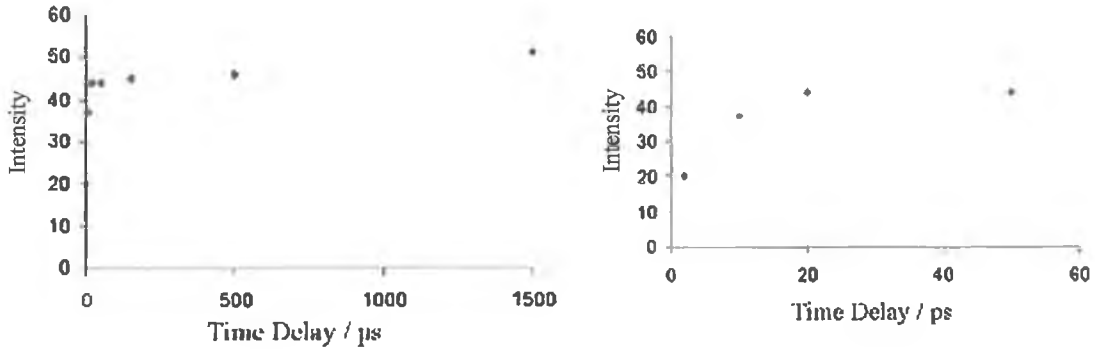

FIGURE 3.19: KINETICS OF $[Ru(bpy)_2(phpytr)]^+$ IN H_2O WITH PUMP AT 400 NM AND PROBE AT 350 NM., (LEFT) BETWEEN 0 AND 1500 PS AND (RIGHT) BETWEEN 0 AND 50 PS. (DCC)

Subtractions of the fully evolved excited state spectra (150 ps) from that of the early times were also made to investigate the presence of a precursor state. However the results did not conclusively show any changes, other than in intensity, over the time scale of the experiment.

Next the complex was protonated by the addition of trifluoroacetic acid and the spectra re-measured with the pump at 400 nm and the probe at 350 nm. These results are given in FIGURE 3.20. The kinetics show that the rise time of the bands remain unaffected and growth is complete by 50 ps. However, a decay in the bands can also be observed in experiments over a 3 ns time range. This is due to the reduction in the excited state lifetime in complexes containing a pyridine triazole ligand upon protonation.[24,#]

[#] The accuracy of the intensities obtained in the nanosecond time range are not wholly reliable due to he potential for instrumental drift. However, this decrease in excited state lifetime has been previously observed in our laboratory by time correlated single photon counting.

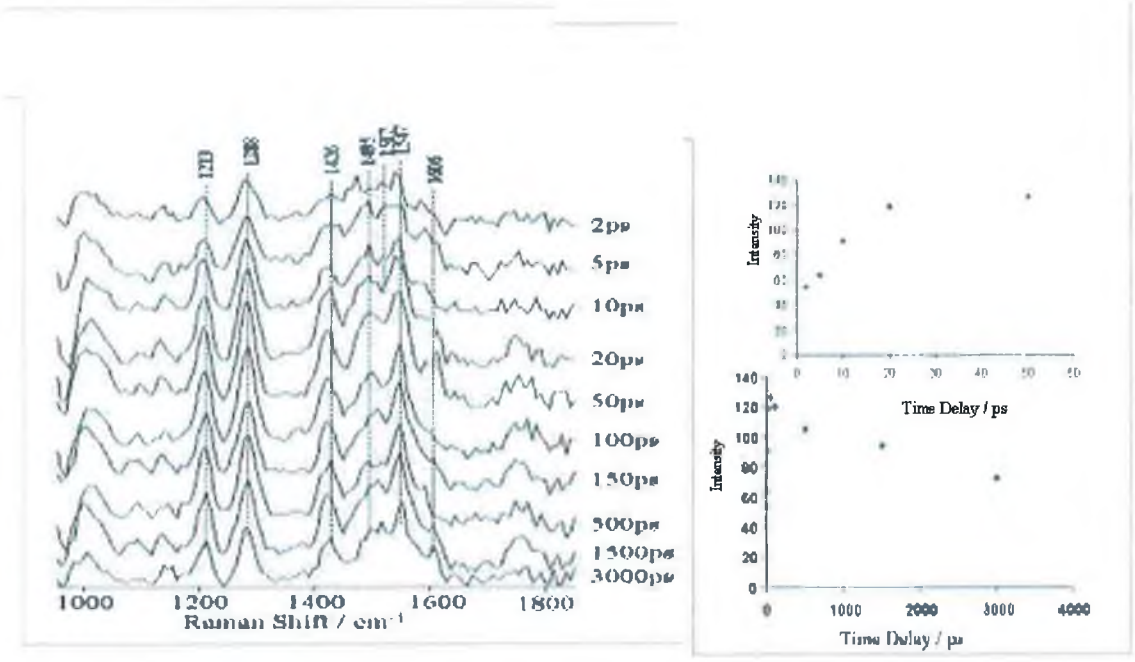

FIGURE 3.20: SPECTRA(LEFT) AND KINETICS (RIGHT) OF $[Ru(bpy)_2(Hphpytr)]^{2+}$ IN CD_3CN WITH PUMP AT 400 NM AND PROBE AT 350 NM. THE RIGHT TOP KINETICS GIVES THE 0 – 50 PS TIME RANGE WHILE THE RIGHT BOTTOM KINETICS ARE BETWEEN 0 AND 3000 PS.(DCC)

The deuteriated analogue of the complex investigated above was also investigated with a 400 nm and 350 nm pump and probe wavelength, respectively, in d_3-acetonitrile. APPENDIX A-7 shows the kinetics of 1339 cm^{-1} band of $[Ru(d_8\text{-bpy})_2(phpytr)]^+$ in acetonitrile. Again these spectra show a grow – in of the steady state spectrum on the picosecond timescale. Further results for this complex are presented in FIGURE 3.21 and FIGURE 3.22.

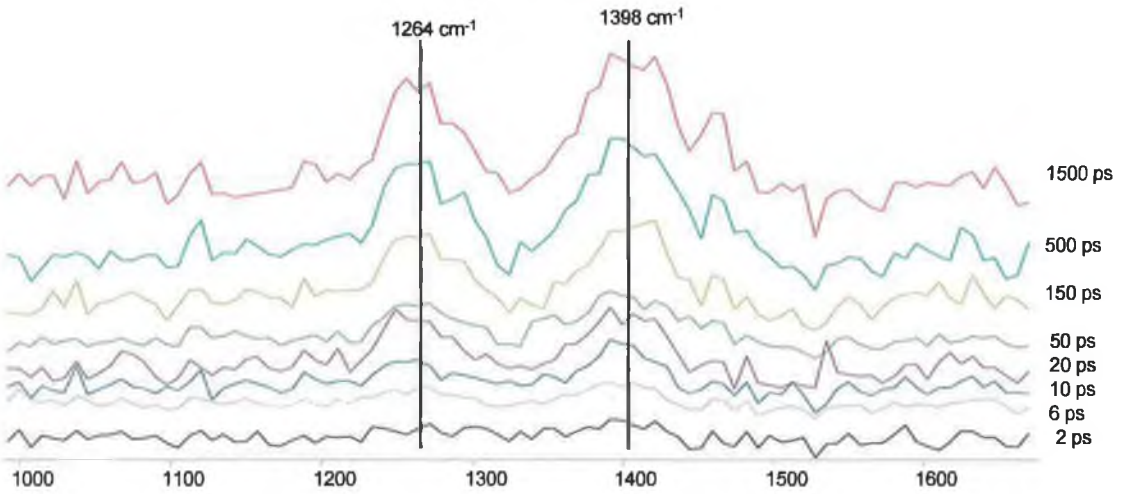

FIGURE 3.21: $[Ru(D_8\text{-}BPY)_2(PHPYTR)]^+$ IN D_3-ACN WITH PUMP AT 400 NM AND PROBE AT 350 NM. *

FIGURE 3.21 shows the spectra of $[Ru(d_8\text{-}bpy)_2(phpytr)]^+$ in acetonitrile with pump at 400 nm and probe at 350 nm. Two peaks are visible in the spectra of at 1256 and 1399 cm^{-1} (FIGURE 3.21). The kinetics of these peaks are shown in the FIGURE 3.22 below. The results again show no clear change in the time required for formation of the steady state spectrum. Again it should be noted that the final point on the graph (in the nanosecond time range) may be subject to experimental drift.

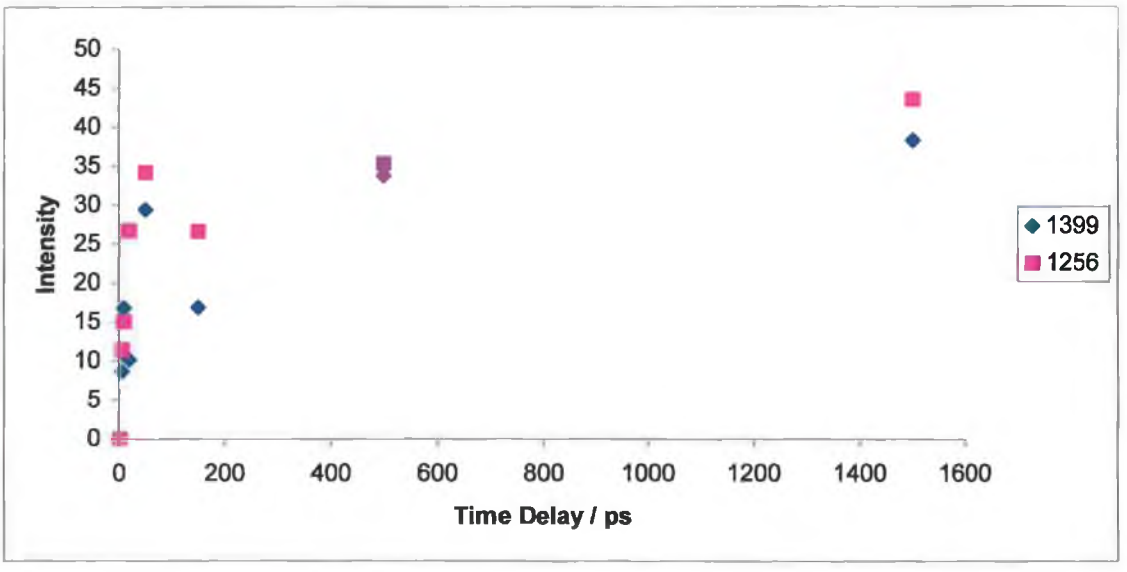

FIGURE 3.22: KINETICS OF PEAKS AT 1399 AND 1256CM^{-1} FOR $[Ru(D_8\text{-}BPY)_2(PHPYTR)]^+$ IN D_3-ACN PUMP 400 / PROBE 350.

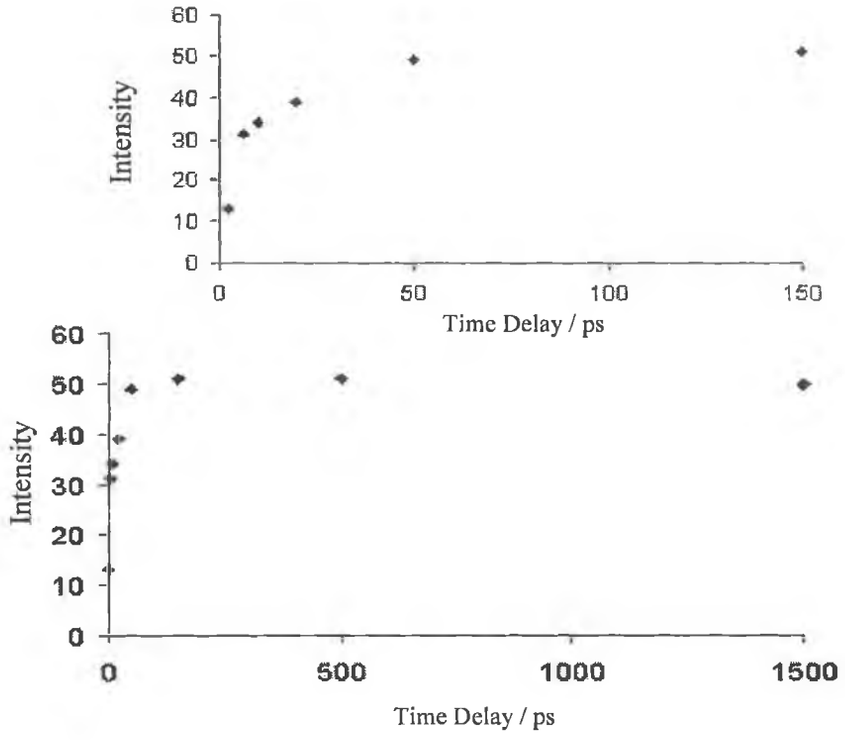

FIGURE 3.23: $[Ru(D_8\text{-BPY})_2(HPHPYTR)]^{2+}$ IN D_3-ACN WITH PUMP AT 400 NM AND PROBE AT 350 NM. (TOP) BETWEEN 0 AND 150 PS AND (BOTTOM) BETWEEN 0 AND 1500 PS. (DCC)

FIGURE 3.23 shows the kinetics of the protonated complex, $[Ru(d_8\text{-bpy})_2(Hphpytr)]^{2+}$, with pump at 400 nm and probe at 350 nm. In these spectra little change is observed between 50 and 150 ps. Note that over the time range studied there is no decay observed in the spectra. This is in contrast to the results observed in FIGURE 3.20, for the perprotio complex. This may be said to tentatively reflect the increase in lifetime that occurs when the excited state is localised on the ligand which is deuteriated, however no firm conclusions should be drawn from measurements at this timescale.

The probe wavelength was then moved to 470 nm to investigate the lower energy absorption of the heteroleptic complex.

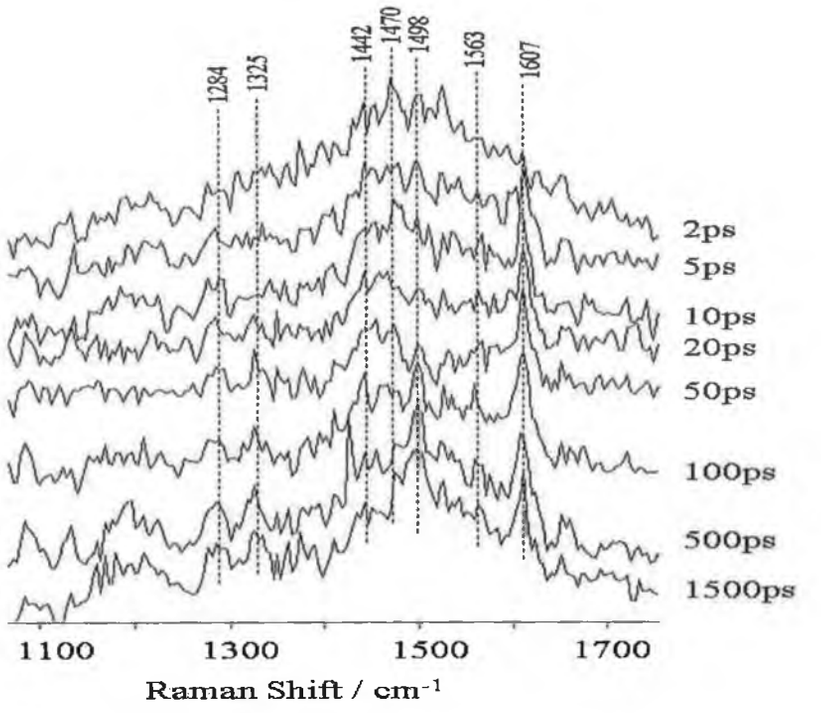

FIGURE 3.24: PURE EXCITED STATE SPECTRA OF $[Ru(bpy)_2(phpytr)]^+$ IN CD_3OD WITH PUMP AT 400 AND PROBE AT 470 NM. (DCC)

FIGURE 3.24 shows the spectra of the deprotonated complex, $[Ru(bpy)_2(phpytr)]^+$, in d_3-acetonitrile. Subtraction of ground state yields relatively weak excited state spectra. Although a grow-in at 1498 cm^{-1} can be clearly discerned, accompanied by a decay of the 1470 cm^{-1} feature the spectra are too weak for accurate kinetics to be obtained.

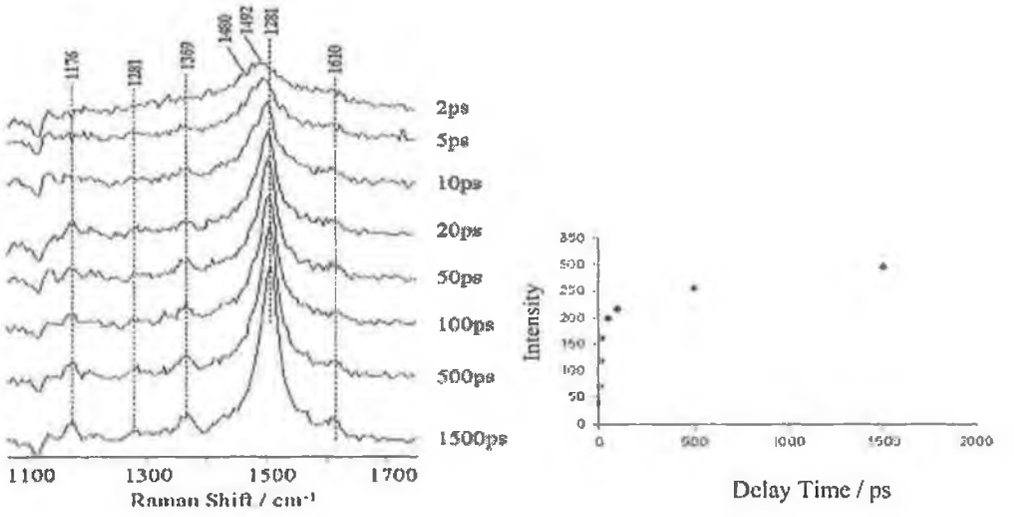

FIGURE 3.25: SPECTRA (LEFT) AND KINETICS (RIGHT) OF $[Ru(D_8\text{-}BPY)_2(HPHPYTR)]^{2+}$ IN ACETONITRILE PUMP AT 400 NM AND PROBE AT 470 NM. (DCC)

In FIGURE 3.25, the spectra and kinetics of $[Ru(d_8\text{-}bpy)_2(Hphpytr)]^{2+}$ in acetonitrile with a pump and probe wavelength of 400 and 470 nm, respectively, are shown. At this wavelength the spectra of the protonated complex are more prominent than those shown above for the deprotonated complex. There is a band at 1500 cm^{-1} which can be attributed to $bpy^{\cdot-}$ with an early rise time apparent. The kinetics of this band appear to show no clear change in the grow – in time of the steady state.

3.3.5 $[Ru(bpy)_2(Hdcb)]^+$

FIGURE 3.26 shows the kinetics of the single peak at 1440 cm^{-1} observed for $[Ru(bpy)_2(Hdcb)]^+$ at pH2 with pump at 410 nm and probe at 470 nm. Although there is some fluorescent background (see APPENDIX A-8) the kinetics again show that no further growth in the peak is observed after 50 ps.

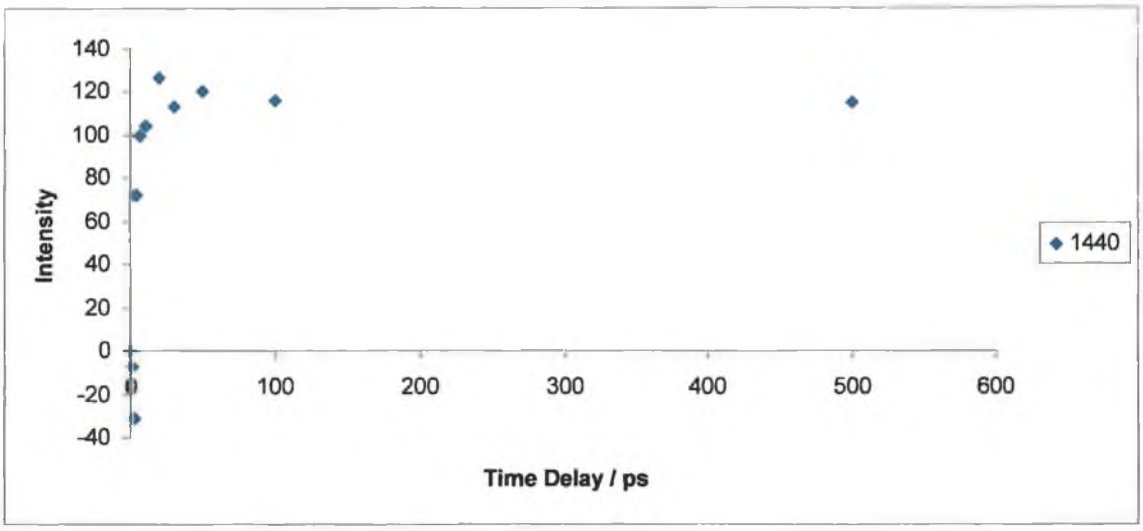

FIGURE 3.26: KINETICS OF PEAK AT 1440CM^{-1} FOR $[RU(BPY)_2(HDCB)]^+$ IN D_2O WITH PUMP 410 NM AND PROBE 470NM.

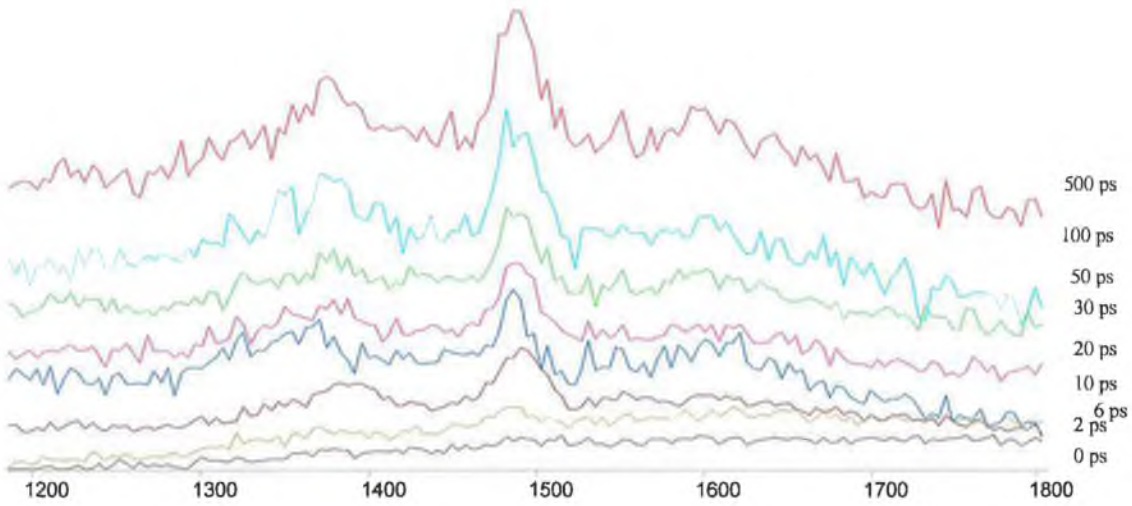

FIGURE 3.27: RESONANCE RAMAN SPECTRA OF $[RU(D_8\text{-}BPY)_2(D_6\text{-}HDCB)]^+$ IN D_2O WITH PUMP AT 410 NM AND PROBE AT 470 NM. *

The deuteriated analogue, $[Ru(d_8\text{-}bpy)_2(d_6\text{-}Hdcb)]^+$, of the complex above was also studied, with the spectra shown in FIGURE 3.27. A single peak was observed at 1486cm^{-1}, with the grow – in again complete after 50 ps.

3.4 Discussion.

The discussion will first focus on the experimental results obtained. This is followed by a discussion of the results produced by other researchers and the theories proposed. Finally the current work is placed in context of the previous studies.

3.4.1 Results Obtained.

FIGURE 3.2 shows the ultrafast luminescence obtained for $[Ru(bpy)_3]^{2+}$. The rate of the emission observed at 520 nm is instrument limited and therefore is < 4 ps. This emission can be related to that observed by Okada and co – workers[25](*vide infra*) by fluorescent upconversion spectroscopy and is due to emission for the ^{1}MLCT. This shows that the intersystem conversion efficiency to the ^{3}MLCT is not unity, as previously suggested.

Our picosecond time resolved resonance Raman spectroscopy measurements have used a variety of pump and probe wavelengths. The energy of the pump wavelength dictates the amount of excess energy in the initially created Franck-Condon excited state. As suggested by Papanikolas *et al.* (vide infra)[11] the amount of energy required to be dissipated to reach the THEXI state can lead to changes in the rate and route of ^{3}MLCT equilibration. The energy of the probe beam interrogates a specific region of the excited state absorption and can also affect the relative intensity of bands.

FIGURE 3.3 gives the spectra of $[Ru(bpy)_3]^{2+}$ in acetonitrile with the pump energy at 400 nm and the probe at 350 nm. Bands are observed at 1145, 1220 and 1468 cm^{-1}. These bands can be assigned as $bpy^{-\bullet}$ by comparison with nanosecond time range spectra (when allowing for the calibration error). All bands undergo a grow – in on the picosecond time scale. This is in contradiction to the results of transient absorption studies which suggest that the THEXI state is fully formed after 300 fs.[8] FIGURE 3.5 gives the spectra after

subtraction of the complete spectra at 150 ps. This is the spectrum which persists into the nanosecond time domain. These subtractions are used to investigate if there are any changes in the early time spectra or if there are two states simultaneously present which interconvert. Such subtractions have been used to great effect in the studies of the excited state structure of $[Ru(phen)_2(dppz)]^{2+}$ and led, in that case, to the proposal of a three state model (*vide infra*).[2,3] However, in the present study the subtracted spectra are very noisy, making it difficult to draw firm conclusions. APPENDIX A-4 shows the spectra of $[Ru(bpy)_3]^{2+}$ with pump at 400 nm and probe at 530 nm. The low signal to noise ratio for these spectra also indicates that the excited state is only weakly resonant at this wavelength. FIGURE 3.6 shows the excited state spectra with the pump wavelength shifted to 410 nm, corresponding to a formal reduction of the energy of the Franck – Condon state by 610 cm^{-1}. From the spectra we see that the THEXI state is still attained on the picosecond time range. This, therefore, suggests that equilibration of the Franck – Condon state on the ^{1}MLCT potential energy surface is not the rate limiting step in THEXI formation. This is consistent with the lifetime of 40 fs observed by Okada *et al.* for the fast component of the ^{1}MLCT emission.[25] FIGURE 3.7 gives the spectra with both the pump and probe wavelength at 390 nm. This results in an increase in Franck – Condon state energy by 1250 cm^{-1}. The signal to noise ratio in these spectra is high, indicating both good pumping and strong resonance of the excited state absorption with this wavelength. Again it is seen in these spectra that the grow – in occurs on the picosecond time scale. This is further evidence that the energy of the initial Franck – Condon state apparently does not influence the rate of formation of the equilibrated THEXI state. It should be noted that the spectra in Figure 3.4 and Figure 3.6 use a probe wavelength of 475 nm resulting in rich spectra on both occasions. This, therefore, indicates that the excited state formed is in resonance with the 475 nm probe wavelength. APPENDIX A-5 gives the spectra obtained with a pump wavelength at 265 nm and a probe at 400 nm. The spectra obtained at these wavelengths are weak and may be due to ineffective pumping at 265 nm or a lack of resonance with the excited state absorption at

400 nm. Since good quality spectra were obtained with both 390 and 475 nm probe wavelengths, this would suggest that the poor spectra are due to ineffective pumping at 265 nm.

Also studied was the effect of counter ion on the spectra of $[Ru(bpy)_3]^{2+}$. As can be seen from FIGURE 3.12 the counter ion has little effect on the rate of formation of the thermally equilibrated excited state.

FIGURE 3.8 highlights the effect of solvent on the excited state grow – in. Again the process occurs on the picosecond timescale, with all evolution essentially complete after 50 ps. This series of solvents was chosen due to the range of dielectric constant and viscosities available. The dielectric constant[26] (or relative permittivity) of the solvents used varied from 3.4 for octanol to 25.3 for ethanol and as high as 80.1 for H_2O while the viscosity of the solvents increased with molecular weight. The negligible effect of both dielectric constant and viscosity indicates that solvent reorganisation to facilitate excited state formation does not play a significant role in the rate of THEXI formation. The ability of the solvent to remove heat from the excited molecule is related to its thermal conductivity.[22] These values vary between 0.152 Wm^{-1} for 1-hexanol to 0.5562 Wm^{-1} for H_2O (values quoted at 25°C).[26] The solvent reorganisation time of acetonitrile has been estimated as 200 fs[27] which further indicates that this process is completed on a different time scale to excited state evolution.

Anti – Stokes measurements were attempted, however the overlap of the Stokes lines from the pump with the anti – Stokes lines of the probe meant that no bands were observable. In these measurement it was hoped that it would be possible to observe the decay of the anti – Stokes bands from the upper excited states as the complex cooled. The time scale of this process would have given further evidence of vibrational cooling on the picosecond timescale.

The effect of ligand deuteriation was next investigated. Deuteriation of the ligands on which the excited state energy is localised generally leads to an increase in the observed excited state lifetime. This is due to a reduction in the intensity of the C-H vibrations on the replacement of hydrogen with deuterium. Simply, this can be explained by a reduced mass effect which results in a reduction in the intensity of vibration upon doubling the mass of one of the bodies. The extent to which deuteriation effects the excited state lifetime depends on the coupling between the ground and the excited state.[23] Two coupling limits dominate; strong and weak coupling limits. The displacement of the excited state along the potential energy co-ordinate dictates the coupling limit (FIGURE 3.28). For Ru(II) polypyridyl complexes estimation of the coupling limit from the Stokes shift is problematic as the direct absorption into the excited state is spin forbidden.

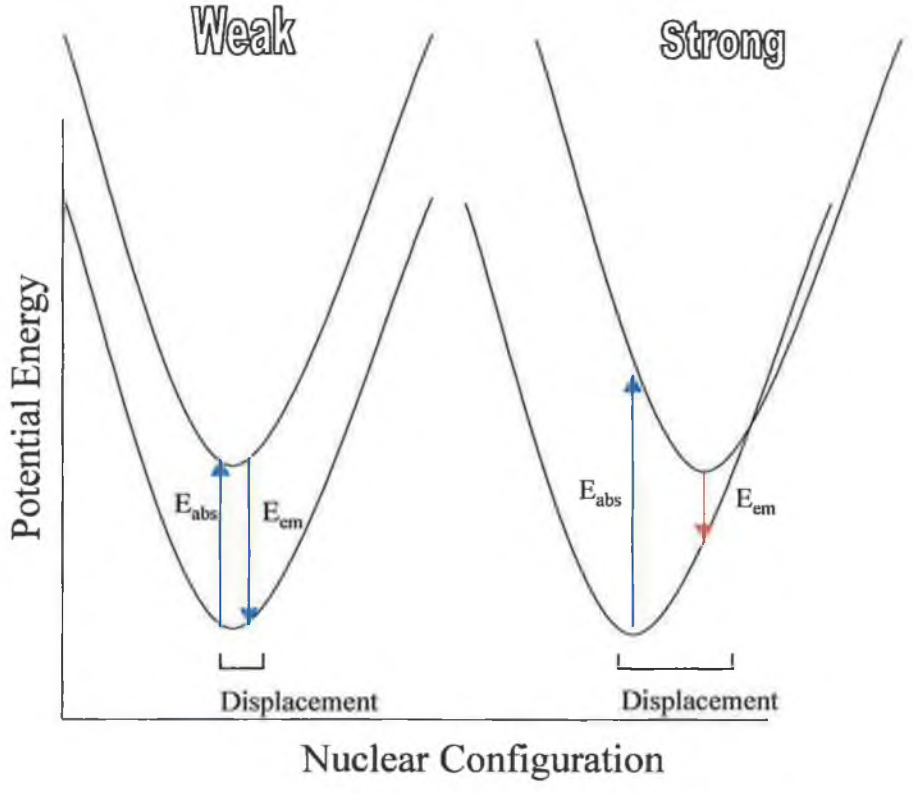

FIGURE 3.28: STRONG AND WEAK COUPLING LIMITS.

C-D vibrations are of lower amplitude and frequency than the equilivalent C-H vibrations.[23] This leads to a reduction in the overlap between the ground and

excited state and hence a reduction in the radiationless deactivation. The reduced frequency of the vibrational energy level also results in an increase in the density of vibration levels in both the ground and excited states. This is represented in FIGURE 3.29.

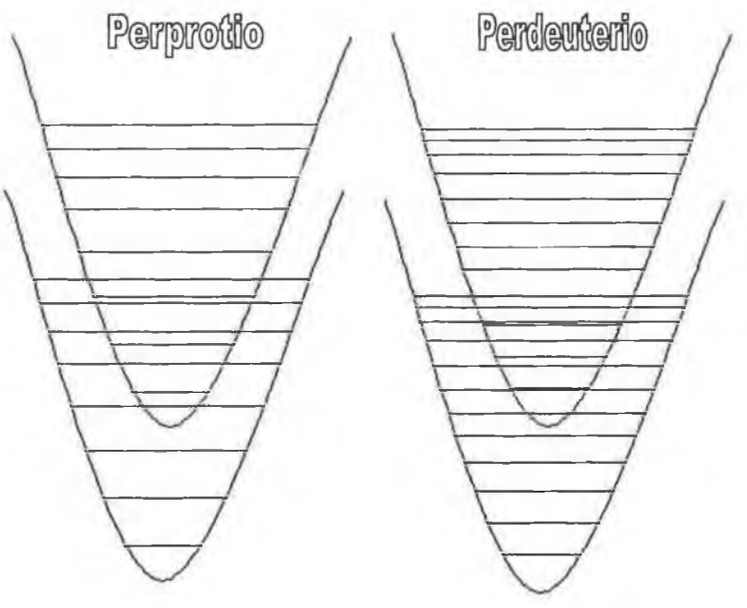

FIGURE 3.29: DENSITY OF VIBRATIONAL LEVELS IN PERPROTIO AND PERDEUTERIO MOLECULES.

FIGURE 3.13 and FIGURE 3.14 show the effect of deuteriation on the time resolved resonance Raman spectra of $[Ru(d_8\text{-}bpy)_3]^{2+}$ in H_2O. From the kinetics observed it is seen that there is no change in the time scale for evolution of the long lived spectrum. This indicates that C-H vibrations are not important in the rate of formation of THEXI state. The effect of coupling between the excited state can also be discounted as the rate remains unchanged on the decrease in coupling on deuteriation. It is also important to note the effect of solvent deuteriation. FIGURE 3.3 and FIGURE 3.13 give the spectra of $[Ru(bpy)_3]^{2+}$ and $[Ru(d_8\text{-}bpy)_3]^{2+}$ in acetonitrile and d_3-acetonitrile respectively. Previous studies[28] have shown the effect of solvent deuteriation

due to the suppression of solvent acceptor modes. Again no effect is observed due to deuteriation. This suggests that the mode of energy dissipation for THEXI state formation is not due to high frequency C-H vibrations, but may have significant contributions from ring breathing modes.

FIGURE 3.18 gives the resonance Raman spectra and kinetics of $[Ru(bpy)_2(phpytr)]^+$ in acetonitrile with pump at 400 nm and probe at 350 nm. It is seen from the kinetics of these spectra that the grow – in of the steady state spectra is complete after 50 ps, as observed for $[Ru(bpy)_3]^{2+}$ and its deuteromers. $[Ru(bpy)_2(phpytr)]^+$ is a less symmetrical molecule than $[Ru(bpy)_3]^{2+}$ which leads to changes in the excited state energy structure. The electron density of the negative triazole moiety increases the energy of the phpytr ligand such that this ligand is at higher energy than the two bipyridine ligands. Also the strong σ – donor properties of the triazole leads to an increase in the energy gap between the ^{3}MLCT and metal centred ^{3}MC states. Another important point to note is the overall 1+ charge on this molecule due to the negative triazole moiety. This modifies the dipole of the molecule in both the ground and excited states (the magnitude of the dipole is significantly reduced in the excited state) and therefore indicates that solvent reorganisation in order to stabilise that excited state dipole does not contribute to the rate of THEXI formation. For the deprotonated complex there is a negative charge on the triazole which opposes the excited electron based on the bpy and hence reduces the dipole. This is in agreement with the results of the solvent studies (*vide supra*) which show that varying the solvent does no effect the rate of grow – in of the steady state spectrum. FIGURE 3.20 gives the spectra and kinetics of the protonated complex $[Ru(bpy)_2(Hphpytr)]^{2+}$, which again shows grow – in of the THEXI state on the picosecond timescale. The energy structure of this complex is similar to that of $[Ru(bpy)_3]^{2+}$ as it is 2+ and the magnitude of the σ – donor properties of the triazole are reduced on protonation. As shown by the kinetics of the protonated complex over the longer time range (FIGURE 3.20, right bottom) the excited state bands begin to decay within 5 ns although, also note previously, no firm conclusions should be

drawn from these measurements on this timescale. The ability to control the excited state lifetime of these complexes with pH is a feature of these triazole containing complexes and show that the rate of THEXI formation is not related to the lifetime. FIGURE 3.26 gives the resonance Raman spectra of $[Ru(bpy)_2(Hdcb)]^+$ in D_2O. Again little change is observed in the rate of THEXI formation due to the presence of the electron withdrawing COOH groups. At pH 2 a single carboxylic group is protonated, with the pK_a of the second carboxylic group at 1.75. In the excited state, the complex is monoprotonated as its pK_a* is estimated to be lower than 0.2.[19] The time which is taken for the formation of the steady state spectra (FIGURE 3.26 and FIGURE 3.27) is important for studies on dye – based solar devices. Previous work has suggested that charge injection occurs on the femtosecond time scale and from a level above the THEXI state. The present results are in agreement with these studies as they suggest that $[Ru(bpy)_2(Hdcb)]^{2+}$ is not vibrationally cold on this timescale.

3.4.2 Results from Other Studies.

The first observation of slow Raman intensity grow – in and centre wavenumber shifting was for aromatic cation radicals by Nishi *et al.*[29] These studies investigated the ultrafast Raman spectra of biphenyl, trans-stilbene and naphthalene with the cations formed via two photon ionisation. A solvent dependence was observed in the rise time of the long – lived Raman spectra; in ethyl acetate and other polar solvents spectral evolution was completed within the instrument limit of < 5 ps. However, in acetonitrile the maximum intensity of the bands is not reached until 40 – 60 ps after excitation. Band shifting and narrowing is also observed for the cationic radicals with time scales reported between 10 – 20 ps in all solvents investigated. Nishi *et al.*[29] proposed that after initial excitation the excess energy is transferred to the surrounding solvent. The first solvent shell is therefore disturbed by this excess energy and is unable to stablise the solute until the energy is transferred to the bulk solvent. This energy transfer occurs on the picosecond

time scale and as the solvation structure of the radical is affected, so to is its electronic transition moment. Similarily the ability of the solvent to conduct energy away from the first solvation shell is suggested to cause the band shifting and narrowing observed in the radical spectra.

A number of points must be noted when comparing the results obtained by Nishi *et al.*[29] with those in the present study. Firstly, ionisation results in the formation of a cation in a previously neutral species. This is in contrast to MLCT excited states in which overall molecular charge is preserved. Secondly, on ionisation electron solvation is required, whereas the electron remains confined to the molecule in our studies. The studies by Nishi *et al.* also observed the excited state S_1 bands of the neutral molecules. These bands showed instantaneous instrument limited grow – in which was unaffected by solvent. This indicates that the S_1 state which is due to the neutral molecule is formed < 5 ps and is a good reference for the formation of thermalised Raman bands on the picosecond timescale.

This work's initial interest in the ultrafast photophysical properties of $[Ru(bpy)_3]^{2+}$ was as a model complex in the investigation of $[Ru(phen)_2(dppz)]^{2+}$ and $[Ru(bpy)_2(phpytr)]^{+}$. A large amount of research has been undertaken on $[Ru(phen)_2(dppz)]^{2+}$ due to its emissive behaviour referred to as the "light – switch" mechanism.[30] Studies have shown that in non – protic solvents the complex is strongly luminescent, however in water and other protic solvent this emission is largely quenched. Another interesting property is the strong luminescence observed in water for this complex in the presence of DNA. This is due to the interaction of the complex with the helical cavity of the DNA[31], and may lead to the use of $[Ru(phen)_2(dppz)]^{2+}$ or its derivatives in sensor applications. The excited state structure has been investigated by absorption, emission and Raman measurements. Transient absorption and time correlated single photon counting measurements by Barbara *et al.* led to the description of the excited state properties as due to two excited states.[32] In non – aqueous solvents the lowest energy excited

state (referred to as MLCT') dominates with a long lived lifetime (660 ns in acetonitrile). In H_2O the MLCT' rapidly converts to a lower lying MLCT" state. This state is non – emissive and is non – radiatively deactivated in 250 ps. The 3 ps conversion between the MLCT' and MLCT" states is faster than solvent dynamics for H_2O but closer to the rate of hydrogen bond formation.[32] It was therefore suggested that the MLCT" state was due to a $dppz^{\bullet -}$ excited state which was lower in energy in protic solvent due to H – bonding. McGarvey *et al.* used TR^3 measurements to further probe the excited state structure.[3] Their investigations revealed a third distinct excited state which also had a solvent dependence. Although this "precursor" state is non – emissive and could not be resolved in aqueous environments, subtractions of the 400 ps spectra from the 10 ps spectra in acetonitrile and methanol show differences in the transient profiles with time. This is indicative of an early state that is formed and then converts into a longer lived moiety. Onfelt *et al.* used picosecond time correlated single photon counting (TCSPC) measurements in glycerol to investigate the excited state lifetimes of the various states.[3] The increased viscosity of glycerol hinders the ability to reorientate and form H – bonds, therefore, the lifetime was longer than that observed in water, but still short compared to monohydric alcohols. Singular – Value Decompostion (SVD) analsysis of the excited state lifetimes between 550 nm and 820 nm produced values of 0.30, 1.85 and 8.06 ns. A kinetic model was proposed with decay based on the MLCT" state at 20°C but with the backward process to repopulate the MLCT' state becoming increasingly prominent as the temperature is increased. The similarity of the first two lifetimes with that of $[Ru(phen)_3]^{2+}$ in glycerol and $[Ru(phen)_2(dppz)]^{2+}$ in ethanol, respectively, allowed the proposition of structures for the three states formed. FIGURE 3.30 gives an overview of the electron locations and the relative energtics of the levels described above. Note that the green arrows represent H – bonding by the solvent.

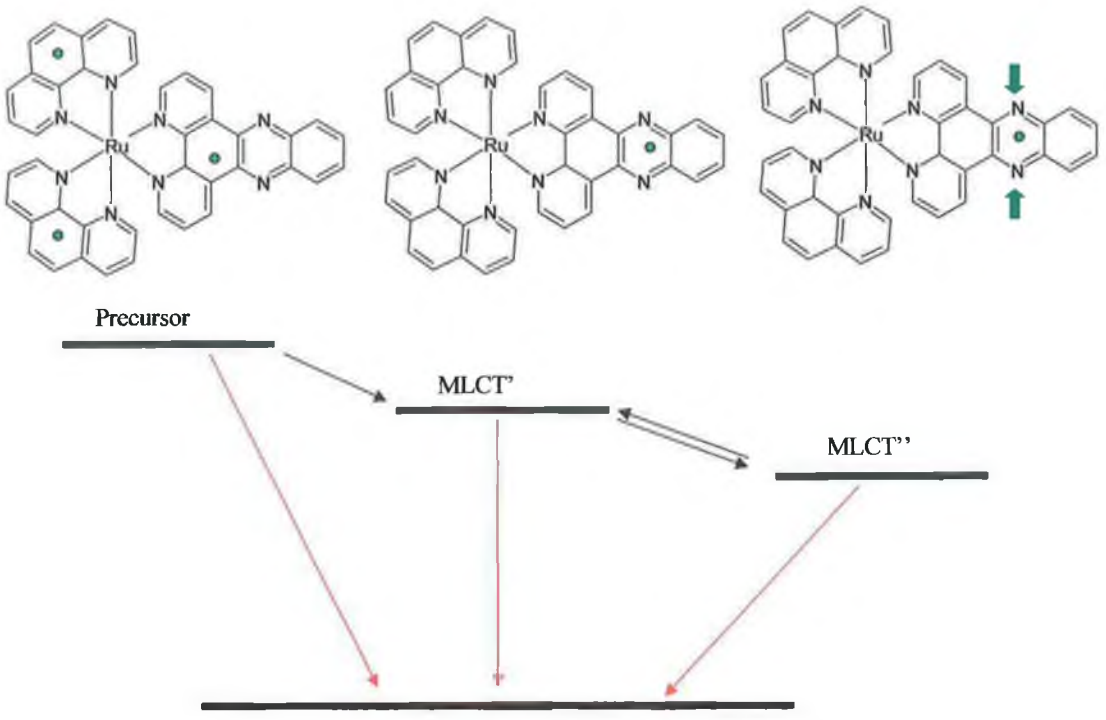

FIGURE 3.30: ENERGY LEVEL SCHEME WITH ELECTRON LOCALISATION FOR $[Ru(phen)_2(dppz)]^{2+}$.

Investigations by McClusker *et al.*[8] into the femtosecond transient absorption gave the first insight into the ultrafast photophysics of $[Ru(bpy)_3]^{2+}$ in acetonitrile. These studies have shown that the observable changes in the excited state absorption spectra is complete after 300fs. The transient absorption spectra obtained at this time appears to correspond to that found using nanosecond techniques. Although the depletion of the ground state bands are instantaneous, the formation of the excited state features should not be completed until the final thermalised state is reached. The effect of the molecular dynamics of CH_3CN on this process is thought to occur on the 100fs time scale.[27] The rate of intramolecular vibrational relaxation (IVR) is assumed to be the fastest process occurring, followed by internal conversion (IC) and finally inter system crossing (ISC), which is thought to be the slowest of the processes. However the rate of the process observed by transient absorption indicates that IVR is occurring concurrently with solvent reorganisation while ISC may also contribute to the changes in the spectra. The transformation from initial to final state may not be regarded as a stepwise process through various states but a constantly evolving direct transition. Although

intermediate levels may be present, the excited state wave packet only becomes stationary once it has reached the lowest energy vibronic state.

When considering the implications of the above results it is worth contemplating the source of the transient absorption signal. Transient absorption spectroscopy looks at the evolution of the excited state where bands are observed due to the depletion of the ground state and the grow – in of the excited state absorption. As with steady state absorption spectroscopy, the broad spectral bands observed are due to the overlap of many vibrational states on the potential energy surface. As a molecule relaxes from a vibrationally hot state, changes in the absorption spectra are observed as band narrowing, as opposed to shifting or intensity changes. However, the magnitude of the change which would be observed for cooling from the vibrationally hot state to the thermallised structure, especially on the picosecond timescale, suggests that the lack of further evolution of the spectra do not necessarily indicated that the molecule has reached the THEXI state.

Okada *et al.* have used femtosecond upconversion spectroscopy[25] to investigate $[Ru(bpy)_3]^{2+}$ in acetonitrile. The signal obtained using this technique is due to radiative coupling back to the ground state. This allows direct observation of the singlet state as any change in spin greatly effects the resultant signal. This work has led to the first direct observation of emission from the singlet excited state. Steady state measurements using laser excitation and CCD accumulated monitoring allows the observation of a weak band in the 500 nm region with a quantum yield estimated at 9×10^{-5}. Time resolved upconversion measurements were monitored at 500, 575 and 620 nm. FIGURE 3.31 gives an overview of the processes observed. Fitting of the results at 500 nm showed a single decay process with a time constant of 40 ± 15 fs. At 575 nm two decay signals are present with time constants of 40 ± 15 fs and 630 ± 50 fs. At 620 nm a single emission is again observed with a time constant of 600 ± 50 fs, however a rise time of 40 ± 15 fs is seen. The slower decay at 575 nm is solvent dependent, with decay fastest in propionitrile and

slowest in propanol, while the faster decay is seen to be solvent independent. The slower decay constant shows a linear dependence on the thermal diffusivity indicating vibrational cooling effects. It has been surmised from this work that the fast decay is due to inter system crossing from the ^{1}MLCT to a vibrationally hot triplet manifold while the solvent dependent slower component is due to vibrational cooling to the long – lived ^{3}MLCT.

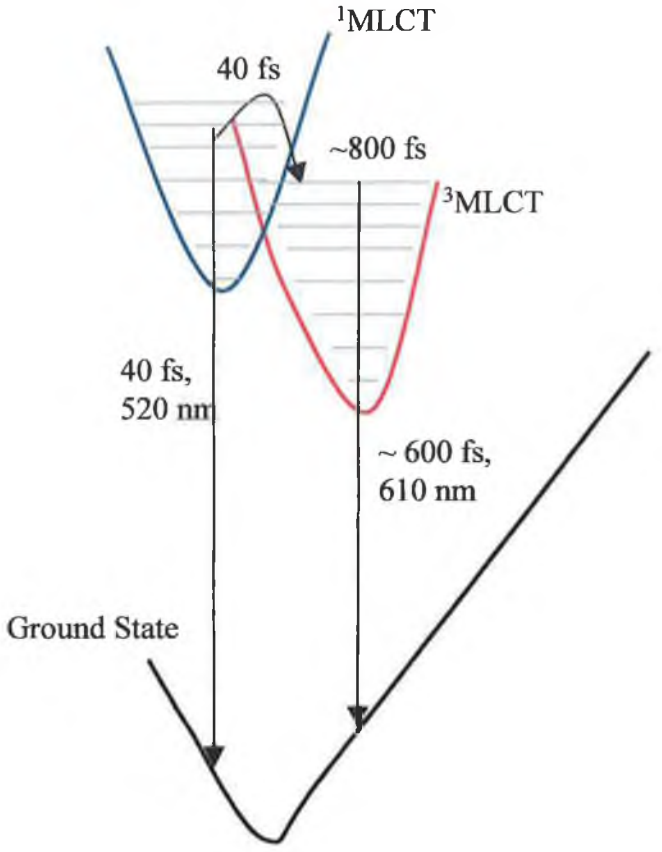

FIGURE 3.31: EMISSION FROM VIBRATIONALLY HOT BANDS AS DESCRIBED BY OKADA *ET AL.*

Although the fluorescent upconversion experimental method allows observation of the ^{1}MLCT emission, and hence the singlet excited state, it does not interrogate the ^{3}MLCT directly. Therefore, while the time constant obtained for the singlet emission is reliable, the time constant and nature of the longer – lived process is not directly investigated.

Papanikolas *et al.* have extensively investigated the ultrafast photophysics of $[Ru(bpy)_3]^{2+}$, $[Os(bpy)_3]^{2+}$ and other heteroleptic complexes. Studies of

$[Os(bpy)_3]^{2+}$ using magic angle and anisotropy excited state absorption measurements have been used to investigated the processes occurring on both the singlet and triplet surfaces.[11] Magic angle measurements reflect changes in intensity and shape of the excited state absorption bands, while anisotropy measurements highlight changes in the transition dipole. Excitation into the ^{3}MLCT of $[Os(bpy)_3]^{2+}$ (at 625, 650, 675 and 693 nm) shows little change in the absorption spectra after 1 ps. By contrast, when the complex is excited into the ^{1}MLCT band reshaping occurs during the first 30 – 45 ps after photoexcitation. This occurs in the form of intensity growth and a blue shift of the $\pi - \pi^*$ absorption. Kinetics analysis reveals two components – a fast component comparable to that observed with triplet excitation, and a slower component with a time scale of approximately 16 ps. It is important to note that the magnitude of the spectral shifting is greater after 440 nm excitation than after 500 nm, although the time scales are similar. Since the time scale of this blue shifting is too long to be due to ISC (it is 100 times slower that observed for $[Ru(bpy)_3]^{2+}$) it is therefore assigned as vibrational cooling. The kinetics can then be described as fast ISC (< 1 ps) followed by vibrational cooling of the ^{3}MLCT on a 16 ps time scale. These rates are in agreement with those observed by Vlcek *et al.*(*vide infra*). Anisotropy measurements produce interesting results for excitation at the high energy side of the ^{3}MLCT band (at 580 and 625 nm). At these excitation energies the fast component of the absorption anisotropy decays are faster (1.2 and 2.5 ps respectively) than those observed at lower energy excitation (~ 3 ps). The fast 3 ps component is thought to be due to Inter Ligand Electron Transfer (ILET).[11] The increase in rate of the fast component at higher energy is suggested to be due to a second process that occurs when the excited state is formed with a large excess of energy (i.e. when excited at the blue edge of the ^{3}MLCT absorption band). This excess energy allows formation of the excited state with an unfavourable solvent configuration. The excess energy is, therefore, in the form of solvent degrees of freedom rather than vibrational energy and the molecule is formed vibrationally cold.

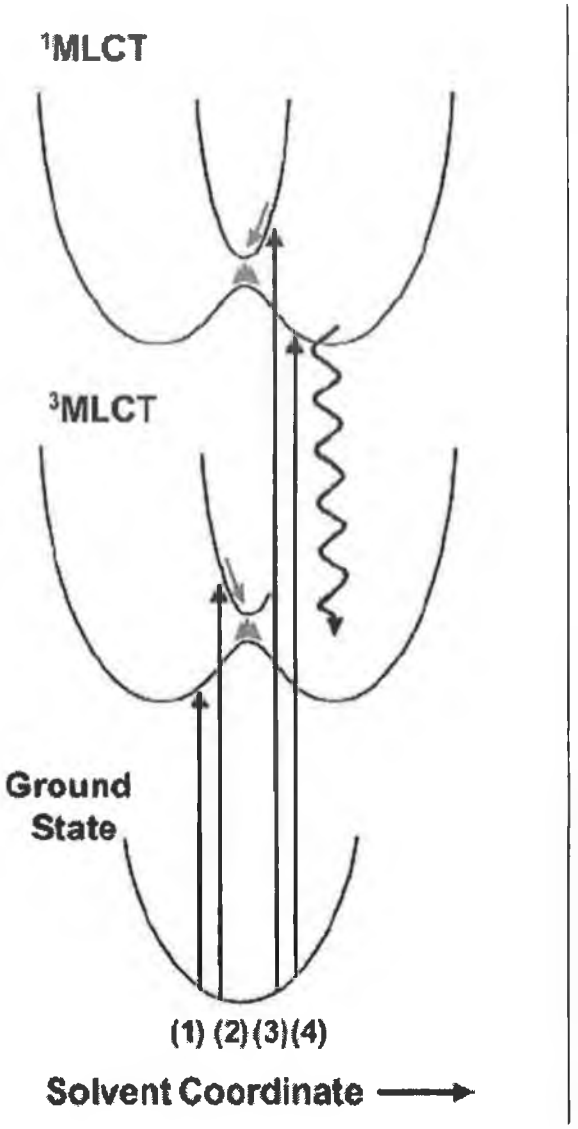

FIGURE 3.32: POTENTIAL ENERGY SURFACE FOR $[Os(bpy)_3]^{2+}$ IN POLAR SOLVENTS. THE DIFFERENT TRANSITIONS OCCUR BASED ON THE EXCITATION ENERGY. REPRODUCED FROM REFERENCE 11.

High photon energy excitation has been used by McFarland *et al.* to investigate the picosecond luminescence of $[Ru(bpy)_3]^{2+}$ and its substituted analogues.[12] For $[Ru(bpy)_3]^{2+}$ instrument limited excited state decay ~ 1 – 5 ps is observed at 500 nm when excited at 388 nm. However, for the 4,4′ – disubstituted complexes, such as $[Ru(dmb)_3]^{2+}$, $[Ru(dmeob)_3]^{2+}$ and $[Ru(dfmb)_3]^{2+}$, a second excited state decay is observed at 500 nm for this excitation wavelength. These samples are seen to have lifetime > 50 ps and this behaviour is specific to the 4,4′ – substituted complexes. On substitution

of the 5,5′ positions of $[Ru(dmb)_3]^{2+}$ and $[Ru(dfmb)_3]^{2+}$ the second emission is seen to disappear. This longer lifetime emission is assigned to a third state, referred to as State C. It may be a higher vibrational level of the ^{3}MLCT, a local minimum or a completely distinct state. It should be noted however that this second emission is only observed when the sample is excited at 388 nm, indicating that the increased energy of excitation is required so that the singlet manifold is capable of accessing state C. These studies are also in agreement with the results provided above (section 3.3.1) that deuteriation does not appear to increase the lifetime of the emission at 500 nm for $[Ru(bpy)_3]^{2+}$.

Again there are a number of points to note when considering the results obtained by McFarland *et al.* in the context of the present study.[12] Firstly, the use of a streak camera in the detection system may lead to some errors in the values obtained. Again the fluorescence observed is instrument limited therefore thought to encompass the processes observed by Okada[25](*vide supra*). The observation of an emission which persists at 500 nm up to 3 ns after excitation is highly surprising.[33] The energy of this emission suggests that it arises from the singlet manifold, however, the time scale on which it persists is contrary to previously observed emissions of this nature. The observation of this emission for the 4,4 substituted complexes but not the 5,5 or unsubstituted complexes is also a cause for concern.

Work of the ultrafast photophysics of $[Re(Etpy)(CO)_3(dmb)]^+$ and $[Re(Cl)(CO)_3(bpy)]$ has been carried out by Vlcek and co-workers.[34] These complexes are partically useful for the understanding of the early stage photophysics as electron localization and hopping is not an issue, since only a single chromophore is present. These studies encompassed time – resolved UV – Vis, resonance Raman and IR spectroscopy. Time resolved IR spectra show that the steady state is not obtained until 50 ps after photoexcitation for $[Re(Etpy)(CO)_3(dmb)]^+$. Before this time, a dynamical shift of band positions and intensity growth can be observed, with biexponential kinetics of 1.3 ± 0.2 and 11.6 ± 2.1 ps for the A′(1) band. A shift of +11.4 ± 0.8 cm^{-1} is also

observed. The time resolved Raman spectra of this complex show a grow-in of a bands over a 20 ps time scale. This growth and narrowing is observed for all the bands in the spectra.

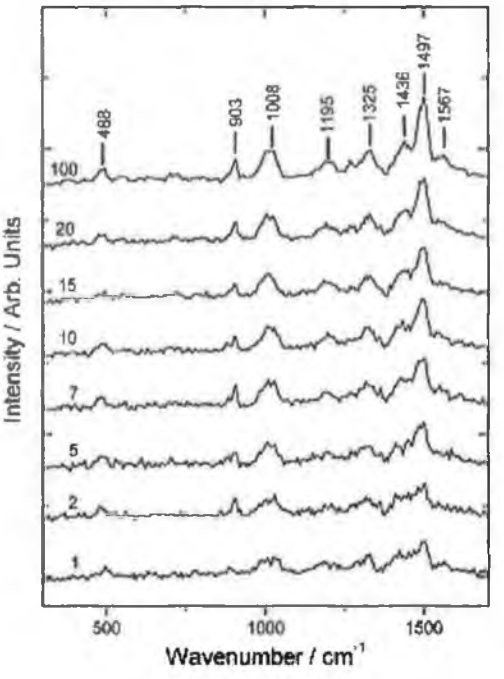

FIGURE 3.33: PICOSECOND TIME - RESOLVED RAMAN SPECTRA OF $[Re(Etpy)(CO)_3(dmb)]^+$ IN ACETONITRILE WITH PUMP AND PROBE AT 400 NM. REPRODUCED FROM REFERENCE 34.

Over the same time scale growth is observed in transient absorption spectra depending on the pump and probe wavelengths used. Anti – Stokes measurements of these complexes were also attempted, however, no excited state bands were observed. This was not due to an experimental artefact and was thought to indicate that excitation of high – frequency dmb localized modes in the ^{3}MLCT state has decayed already after 1 – 5 ps. The growth of bands in this case is attributed to structural relaxation during the vibrational cooling process. The Raman intensity of a transition depends on both the electronic transition moment and the vibrational overlap between the states. As cooling occurs modification of the potential energy surface changes these properties and hence an increase in the band intensity is observed in the Raman spectra.

The results obtained by Vlcek *et al.* appear in agreement with our present study. The growth of the excited state bands indicates that the THEXI state is not formed on the femtosecond time scale, as previously suggested.[8] This also suggests that the picosecond time scale of THEXI formation is not unique to Ru(II) but also occurs for other transition metal complexes. The presence of a single chromophore ligand in the complexes studied by Vlcek *et al.* helps to discount the effect of inter-ligand hopping on the slow Raman grow – in.

Each experimental technique used in the above studies has the ability to investigate a specific process which results in the formation of the thermallised structure of $[Ru(bpy)_3]^{2+}$. Fluorescent upconversion spectroscopy looks at the emission from the ^{1}MLCT and, as such, is able to provide information on the deactivation of the singlet state. Transient absorption spectroscopy examines the changes occurring upon oxidation and reduction of species in the excited state. Raman spectroscopy, on the other hand, is a vibrational technique and, therefore, is most suited to the investigation of vibrational phenomena. It provides direct information on processes which can only be inferred from other techniques. Shown below is a illustration of the time scales obtained from the research carried out (FIGURE 3.34).

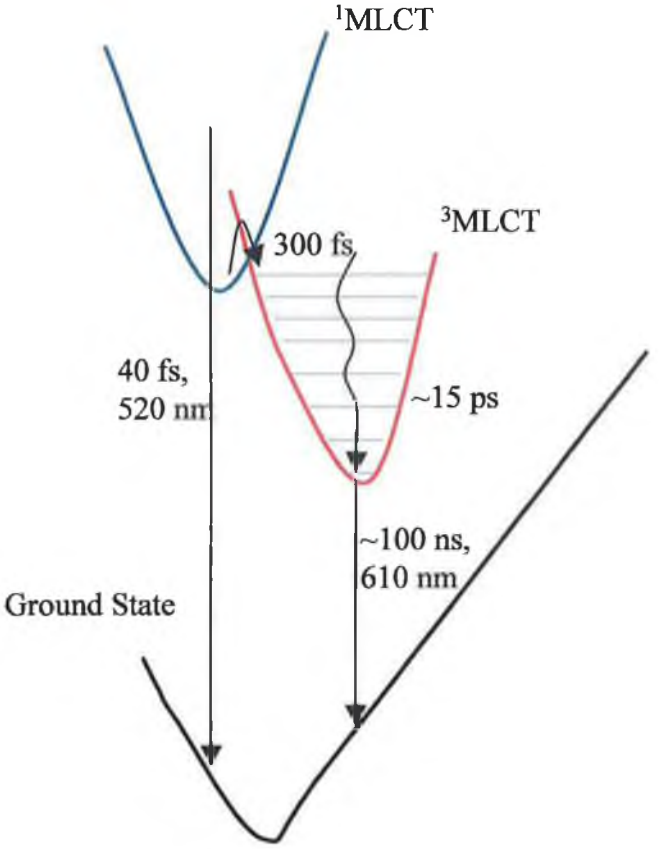

FIGURE 3.34: OVERVIEW OF RESULTS OBTAINED FROM VARIOUS STUDIES FOR $[RU(BPY)_3]^{2+}$.

The excited state lifetime of the singlet MLCT is provided by the fluorescent upconversion work of Okada *et al.*[25] The crossing to the triple state is obtained from the work of McCusker *et al.*[8] The present work investigates the lowest vibrational state of the ^{3}MLCT and as such provides direct evidence of the formation of the THEXI state. The simultaneous use of a variety of probe techniques allows the production of a more complete excited state picture, which is not possible using any single technique.

3.5 Conclusions.

Studies have been carried out on $[Ru(bpy)_3]^{2+}$ using a variety of techniques and, although no technique is able to provide complete information of the early time photophysical processes, slowly a more comprehensive picture is being obtained. The present work looks at the Raman spectroscopy of this paradigm complex and, as such, is best suited to interrogate its vibrational characteristics. From these results we see that the THEXI state is not formed on the femtosecond timescale, as previously suggested, but changes in the vibrational spectra are seen up to 50 ps.

This work is not only relevant in understanding the fundamental properties of the excited state in transition metal complexes but is also vitally important in the design of supramolecular devices. The inclusion of $[Ru(bpy)_2(Hdcb)]^+$ extends this work to cover complexes which have previously been incorporated into molecular light – energy storage devices and is in agreement with studies which say that charge injection occurs from a non – THEXI state. The similarity of the results obtained for this complex and $[Ru(bpy)_3]^{2+}$ also highlights the importance of a complete understanding of the most fundamental of structures. The investigations of the properties of $[Ru(bpy)_2(phpytr)]^+$ are also very interesting and important. Firstly, the agreement of the results obtained for both the protonated and deprotonated complexes highlights the fact that the protonation state, and hence charge, of the complex does not affect the time taken for formation of the THEXI state. Also the ability to control the σ – donor properties and ^{3}MLCT – ^{3}MC energy gap of the triazole containing complex gives an indication of the effect on ^{1}MLCT – ^{3}MLCT coupling of these properties. Again since little change is seen for the triazole containing complex in either protonation state the influence of ^{3}MC coupling during vibrational cooling in the picosecond time range must be seen as negligible.

3.6 Bibliography.

1 Juris, A., Balzani, V., Barigelletti, F., Campagna, S., Belser, P., von Zelewsky, A., *Coord. Chem. Rev.*, **1988**, *84*, 85.

2 Coates, C.G., Olofsson, J., Coletti, M., McGarvey, J.J., Onfelt, B., Lincoln, P., Norden, B., Tuite, E., Matousek, P., Parker, A.W., *J. Phys. Chem. B*, **2001**, *1005*, 12653.

3 Onfelt, B., Olofsson, J., Lincoln, P., Norden, B., *J. Phys. Chem. A*, **2003**, *107*, 1000.

4 Brennanman, M.K., Meyer, T.J., Papanikolas, J.M., *J. Phys. Chem. A*, **2004**, *108*, 9938.

5 Browne, W.R., Coates, C.G., Brady, C., Matousek, P., Towrie, M., Botchway, S.W., Parker, A.W., Vos, J.G., McGarvey, J.J., *J. Am. Chem. Soc.*, **2003**, *125*, 1706.

6 (a) Hu, Y.-Z., Tsukiji, S., Shinkai, S., Oishi, S.; Hamachi, I., *J. Am. Chem. Soc.*, **2000**, *122*, 241. (b) Meyer, T. J. *Acc. Chem. Res.*, **1989**, *22*, 163. (c) O'Regan, B., Grätzel, M. *Nature*, **1991**, *335*, 737. (d) De Cola, L., Belser, P. *Coord. Chem. Rev.*, **1998**, *177*, 301. (e) Bignozzi, C. A., Schoonover, J. R., Scandola, F., *Progr. Inorg. Chem.*, **1997**, *44*, 1. (f) Blanco, M.-J., Jiménez, M. C., Chambron, J.-C., Heitz, V., Linke, M., Sauvage, J.-P., *Chem. Soc. Rev.*, **1999**, *28*, 293.

7 Kober, E.M., Meyer, T.J., Inorg. Chem., **1984**, *23*, 3877.

8 Damrauer, N.H., Cerullo, G., Yeh, A., Boussie, T.R., Shank, C.V., McCusker, J.K., *Science*, **1997**, *275*, 54.

9 Martini, I., Hodak, J.,H., Hartland, G.V., *J. Phys. Chem. B*, **1998**, *102*, 9508.

10 Huynh, M.H., Dattelbaum, D.M., Meyer, T.J., *Coord. Chem. Rev.*, **2005**, *249*, 457.

11 Shaw, G.B., Styers-Barnett, D.J., Gannon, E.Z., Granger, J.C., Papanikolas, J.M., *J. Am. Chem. Soc.*, **2004**, *108*, 4998.

12 McFarland, S.A., Lee, F.S., Cheng, K.A.W.Y., Cozens, F.L., Schepp, N.P., *J. Am. Chem. Soc.*, **2005**, *127*, 7065.

13 Fanni, S., Keyes, T.E., O'Connor, C.M., Hughes, H., Wang, R., Vos, J.G., *Coord. Chem. Rev.*, **2000**, *208*, 77.

14 Keyes, T.E., O'Connor, C.M., O'Dwyer, U., Coates, C.G., Callaghan, P., McGarvey, J.J., Vos, J.G., *J. Phys. Chem. B*, **1999**, *103*, 8915.

15 Keyes, T.E., Vos, J.G., Kolnaar, J.A., Haasnoot, J.G., Reedijk,J., Hage, R., *Inorg. Chim. Acta*, **1996**, *245*, 237.

16 Hagfelt, A., Grätzel, M., *Chem. Rev.*, **1995**, *95*, 49.

17 (a) Yersin, H., Humbs, W., Strasser, J., *Topics Curr. Chem.*, **1997**, *191*, 154. (b) Resen, H., Krauz, E., *Comments Coord. Chem.*, **1995**, *18*, 27.

18 Browne, W.R., Coates, C.G., Brady, C., Matousek, P., Towrie, M., Botchway, S.W., Parker, A.W., Vos, J.G., McGarvey, J.J., *J. Am. Chem. Soc.*, **2004**, *126*, 10190.

19 (a) Nazeeruddin, Md., K., Kalyanasundaram, K., *Inorg. Chem.*, **1989**, *28*, 4251. (b) Shimidzu, T., Iyoda, T., Izaki, K., *J. Phys. Chem.*, **1985**, *89*, 642.

20 Coates, C.G., Ph.D. Thesis, The Queen's University of Belfast, **1996**.

21 McCusker, J.K., *Acc. Chem. Res.*, **2003**, *36*, 876.

[22] Seilmeier, A. Kaiser, W., Ultrashort Laser Pulses and Applications – Chapter 7, Springer Verlag, **1998**.

[23] Browne, W.R., Vos, J.G., *Coord. Chem. Rev.*, **2001**, *219*, 761.

[24] Wang, R., Vos, J.G., Schemhl, R.H., Hage, R., *J. Am. Chem. Soc.*, **1992**, *114*, 1964.

[25] Bhasikuttan, A.C., Suzuki, M., Nakashima, S., Okada, T., *J. Am. Chem. Soc.*, **2002**, *124*, 8398.

[26] Handbook of Chemistry and Physics, Chemical Rubber Company, Chemical Rubber Co. Ltd., **2004**.

[27] Rosnethal, S.J., Xie,X., Du, M., Fleming, G., *J. Chem. Phys.*, **1991**, *95*, 4715.

[28] Freeman, J.J., Crosby, G.A., Lawson, K.E., *J. Mol. Spectro.*, **1964**, *13*, 399.

[29] Nakabayashi, T., Kamo, S., Sakuragl, H., Nishi, N., *J. Phys. Chem. A*, **2001**, *105*, 8605.

[30] Amouyal, E., Homsi, A., Chambron, J.-C., Sauvage, J.-P., *Dalton Trans.*, **1990**, *1990*, 1841.

[31] Friedman, A.E., Chambron, J.-C.,Sauvage, J.-P., Turro, N.J., Barton, J.K., *J. Am. Chem. Soc.*, **1995**, *117*, 4788.

[32] Olson, E.J.C., Hu, D., Hormann, A., Jonkman, A.M., Arkln, M.R., Stemp, E.D.A., Barton, J.K., Barbara, P.F., *J. Am. Chem. Soc.*, **1997**, *119*, 11458.

[33] An emission in this timescale was previously observed in our time resolved luminescence studies but was discounted as being due to free bpy ligand.

[34] Liard, D.J., Busby, M., Matousek, P., Towrie, P., Vlček, A., *J. Phys. Chem. A*, **2004**, *108*, 2363.

Chapter 4

Effect of Substitution at the C-5 Position of the Triazole on Photophysical Properties.

Chapter 4 investigates the complexes $[Ru(bpy)_2(thpztr)]^+$ and $[Ru(bpy)_2(thpytr)]^+$ using Raman and electronic spectroscopy, Single Photon Counting and Computational Chemistry. The effect of substitution at the C5 position of the triazole on the photophysical properties is compared with previously investigated complexes. Complexes containing a pyrazinyl- triazole ligand are seen to emit from two excited states based on different ligands at low temperatures. This behaviour is confirmed by both temperature dependent emission and single photon counting measurements for the thienyl substituted complex. However, for the pyridyl containing complex a single emission, with mono-exponential excited state decay, is observed.

Resonance Raman spectroscopy has been used to investigate the MLCT absorptions of the complexes and the effect of protonation, with isotope labelling employed to further explore the spectra obtained. Computational studies have been applied to gain further insight into the physical phenomena and to investigate the degree of interaction of the thienyl and metal centre in the ground and excited state.

4.1 Introduction.

A clear understanding of the spectroscopic, photophysical and electrochemical properties of metal complexes must precede their application in supramolecular assemblies. Of particular interest in supramolecular chemistry is the ability to direct energy and electron transfer for use in molecular electronic and photonic devices. Transition metal complexes have received considerable attention in this area due to their well defined properties and the synthetic variety available. This synthetic ability also allows the modulation of the ground and excited state properties to suit the particular application.

FIGURE 4.1 shows the structures of the complexes discussed in the text. Triazole ligands containing both a pyridyl and a pyrazinyl moiety are studied in this chapter. While Chapter 5 looks at the dramatic effects of varying the NN ligand in bis-heteroleptic systems, the present chapter looks at the more subtle effect of substitution at the C-5 position of the triazole moiety. The complexes under investigation in this chapter are substituted with a thiophene moiety at the C-5 position. Complexes **1** and **2** are the C-5 thiophene substituted triazole pyridine and pyrazine complexes, respectively, on which the majority on work has been performed. **3** and **4** are the unsubstituted complexes which are used as a reference to compare the effect of the thiophene. **5** and **6** are the dinuclear complexes based on a thiophene bridge. Complexes **1** and **2** have been used to help understand the behaviour of the dinuclear complexes, with results obtained for **1** and **2** interpreted in relation to the results observed for **5** and **6**. In previous work a number of different moieties have been incorporated at the C-5 position, some examples of which are methyl, bromo, phenyl and dimethoxyphenyl[1] groups. This has allowed for the tuning of the electrochemical and photophysical properties of the complexes due to electron withdrawing or donating properties of the substituents.

Thiophene is a planar, unsaturated heterocycle.[2] It is regarded as aromatic when a lone pair from the sulphur is incorporated in to the aromatic sextet. It is an electron – rich molecule, which is resonance stabilised and has a resonance energy about half that of benzene. The ring system exerts a π electron – donating effect and a σ electron – withdrawing effect to substituents at the 2 and 5 positions of the thiophene ring (note that numbering begins at the heteroatom). Thiophene undergoes both electrophilic and nucleophilic substitution reactions. One of the most interesting properties of sulphur is the ability of its lone pair to interact with gold molecules. This has lead to the opportunity to non – covalently bond sulphur containing units with gold surfaces and gold colloidal particles in the production of supramolecular assemblies.[3]

Substitution at the C-5 position of the triazole ligand can have a number of important effects on the properties of the resultant complex. The electron – withdrawing / donating ability of the substituent leads to changes in the emission and absorption maxima[4], and also on the acid / base properties. The ability of the substituent to increase the delocalisation of the excited state can also result in changes to the acid / base properties of the complex. The presence of a large substituent at the C-5 position is seen reduce N2 / N4 isomer interconversion due to steric bulk of the thiophene.[5]

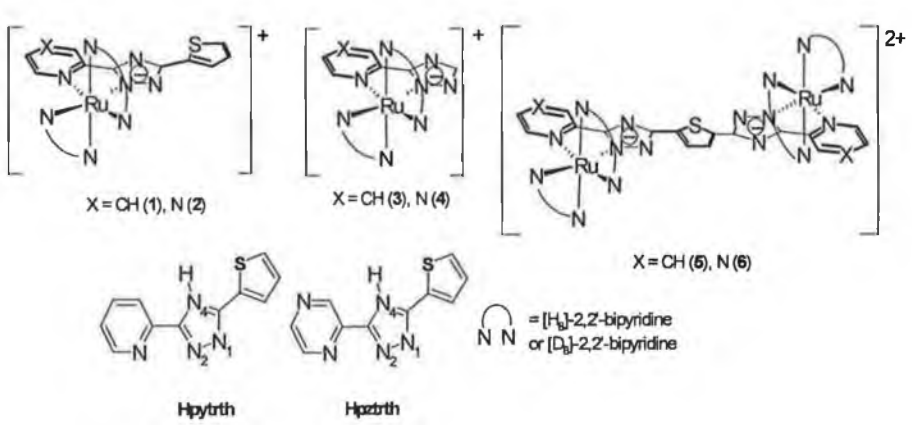

FIGURE 4.1: STRUCTURES OF THE COMPLEXES AND LIGANDS REFERRED TO IN CHAPTER 4.

Previous studies[6] have shown that Ru(II) complexes containing a pyrazine triazole ligand show two emissions at low temperatures. In work by *Keyes et al.*, the complex $[Ru(bpy)_2(pztr)]^+$ (**3** in the present chapter, pztr is 2'-(1,2,4-triazol-3-yl)-pyrazine) produces emissions from two thermally equilibrated excited states between 140K and 200K. Temperature dependent measurements allowed the resolution, via emission and excited state lifetime measurements respectively, of two emissions that are energetically and temporally separate.[6] This dual emission was explained as being due to barriers in the equilibration of the excited state energy, and results in excited states formed on both the pyrazine containing ligand and the symmetric (or NN) ligand.[6] The present chapter further investigates the excited state behaviour of complexes containing a pyrazinyl or pyridyl triazole ligand, and also looks at the effect of substitution at the C-5 position of the triazole ring.

Multinuclear complexes are a source of intense interest due to their ability to transfer electrons and energy between the metal centres.[7] These processes have already lead to the production of potential molecular logic gates[8], although processing of the information and the incorporation of these molecules into larger systems is still non – facile. The starting point of understanding the processes occurring in multinuclear complexes is the investigation of the properties of their isolated units. This chapter looks at the properties of complexes containing a thiophene substituent at the C-5 position, which may act as a bridge between two nuclear centres. The ability of nuclear centres to interact is dependent on the nature of the energy / electron transfer processes. Forster energy transfer is seen as a through space process while Dexter energy transfer can be seen to be through bond.[9] While both processes are seen to be distance dependent, Forster processes are also dependent on the relative orientation of the interacting dipoles. Dexter processes have a dependence on both distance and the ability of the orbitals of the bridging moiety to facilitate the double electron transfer. Hence, the ability to accurately model the molecular orbital structure of the interacting units is vital in the understanding of the communication between units and in the future

design of multinuclear systems. It is in this area that the growth in power and affordability of computational chemistry systems has proved invaluable and these techniques are used in the current chapter to augment the experimental results obtained.

The multinuclear Ru(II) complex that has received most attention is the pyrazine bridged $[(Ru(NH_3)_5)_2pz)]^{2+}$, known as the Creutz – Taube ion.[10] Of particular interest in the current work are multinuclear complexes which include a triazole moiety. It can be seen, from previous work, that the triazole can act as the bridging moiety[4] via its N2 and N4 positions or can support a substituent which bridges two independent complexes.[11] It is complexes of the latter type which are most relevant in the present work and the $[Ru(bpy)_2(thpztr)]^+$ / $[Ru(bpy)_2(thpytr)]^+$ complexes investigated here may be looked on as half a dinuclear complex in which the thienyl group is the bridging moiety.[12] These studies[12] have shown that the nature of the bridging moiety greatly affects the level of interaction between the metal centres with strong and weak interaction reported for thiophene and phenyl bridges, respectively. Studies[12] were carried out on the both mono – and di – nuclear complexes containing a C-5 substituted triazole ligand using electrochemistry, spectroelectrochemistry and UV/Vis-Near IR spectroscopy. Specifically, they showed that the thiophene group is non-innocent in the electrochemistry and electronic spectroscopy of the complexes. Irreversible ligand based oxidations were observed due to the electron rich nature of the thiophene moiety while absorptions at 360 and 500 nm due to the thiophene are also present.[12] Investigation of the mixed valence Ru(II)/Ru(III) proved problematic due to disproportionation of the complexes. The present studies augments the data for the mononuclear complexes with emission and Raman spectroscopy, and computational chemistry data.

Overall the purpose of this chapter is to obtain a more complete understanding of the excited state properties of a set of triazole containing complexes, substituted with a thiophene moiety. This is used to further understand the

biexponential excited state decay (dual emission) previously observed for Ru(II) complexes[6] and the effect of the thiophene moiety upon triazole containing ligands. In this chapter the photophysical properties of the complexes substituted at the C-5 position of the triazole are presented and compared to their unsubstituted analogues. Temperature dependent emission spectroscopy, both time resolved and steady state, is then used to probe the formation of THEXI state and the excited state energy distribution between the triazole containing ligand and the bipyridine ligand. The effect of deuteriation is used to identify the location of the excited state, as the excited state lifetime of a complexes is seen to increase on deuteriation of the ligand on which the excited state is based.[13] Raman techniques are employed to investigate the absorption bands and the effect of protonation on the absorptive properties of the triazole containing complexes. Deuteriation of a ligand is seen to cause a shift in the vibration bands of that ligand in Raman spectroscopy and this effect has been used to assign the various bands. Computational studies are used to supplement the experimental photophysical data. The results obtained are also interpreted in relation to intercomponent interaction that occurs in multinuclear systems and the role of a thiophene bridging ligand in this interaction.

4.2 Experimental Part.

The deuteriated analogues of **1** and **2** (named **1d** and **2d**, respectively) were synthesised to aid in the analysis of the Raman spectra and to increase the resolution of the excited state lifetime measurements. The synthesis of the perprotio complexes (**1p** / **2p**) and the C-5 substituted ligands were previously reported[12], and samples were obtained from Dr. Wesley Browne. D_8-bpy, for use in the synthesis of $Ru(d_8\text{-bpy})_2Cl_2$, and the C-5 substituted pyridine triazole ligand were also obtained from Dr. Browne. 2-(5'-pyrazin-2''-yl)-1'H-1',2',4'-triaz-3'-yl)-thiophene for synthesis of $[Ru(d_8\text{-bpy})_2(thpztr)]^+$, **2d**, was provided by Claire Brennan. CHN analysis of the perdeuterio complexes was not attempted due to the small sample amount obtained and as the perprotio complexes were analysed when the initial syntheses were reported.[12]

All complexes synthesised were characterised by ^1H NMR spectroscopy. An overview of the results are presented below with the spectra for **1d** and **2d** given in APPENDIX B.

$Ru(d_8\text{-bpy})_2Cl_2.2H_2O$

A solution of 2,2' d_8-bipyridine (3.67g, 22.4mmol), $RuCl_3.2H_2O$ (2.71g, 11.1mmol) and LiCl (3.08g, 72.6mmol) was vigorously heated at reflux in 50 cm^3 of DMF for 5 hr, and then allowed to cool. The reaction mixture was added to 200 cm^3 of acetone and left overnight at 4°C to recrystallise. The precipitate was filtered and washed thoroughly with iced water and diethyl ether. Yield: 1.25g (2.3mmol, 20%). ^1H NMR silent.

$[Ru(d_8\text{-bpy})_2(thpytr)]^+$, **1d.**

$Ru(d_8\text{-bpy})_2Cl_2$ (0.40g, 0.8mmol) and Hthpytr (0.18g, 0.9mmol) were heated at reflux in 150 cm^3 of EtOH:H_2O (1:1) for 8hr. The solution was filtered to remove excess ligand and the solvents removed *in vacuo*. The sample was redissolved in H_2O and the pH raised with 1M NaOH. Saturated aqueous

NH_4PF_6 was added and the precipitate was recovered by vacuum filtration. The product was purified twice by column chromatography on neutral alumina (Al_2O_3) with acetonitrile as the mobile phase. Yield: 0.20g(0.24mmol, 30%). ^1H NMR: 8.10(1H,d), 7.88 (1H, dd), 7.49(1H, d), 7.39(1H, d), 7.25(1H, d), 7.12(1H,dd), 7.01(1H,dd).

$[Ru(d_8\text{-}bpy)_2(thpztr)]^+$, **2d**.

$Ru(d_8\text{-}bpy)_2Cl_2$ (0.40g, 0.8mmol) and Hthpztr (0.23g, 1.1mmol) were heated at reflux in 150 cm^3 of EtOH:H_2O (1:1) for 8hr. The solution was filtered to remove excess ligand and the solvents removed *in vacuo*. The sample was redissolved in H_2O and the pH raised with 1M NaOH. Saturated aqueous NH_4PF_6 was added and the precipitate was recovered by vacuum filtration. The product was purified twice by column chromatography on neutral alumina with acetonitrile as the mobile phase. Yield: 0.07g (0.08mmol, 10%). ^1H NMR: 9.21(1H,s), 8.22(1H,d), 7.57(1H,d), 7.42(1H, d), 7.28(1H, d), 7.02(1H, d).

4.3 Results.

A number of techniques are used to probe the THEXI state of C5 substituted pyrazinyl and pyridyl triazole complexes. The structures of the complexes investigated are shown in FIGURE 4.1. $[Ru(bpy)_2(pytr)]^+$, **3**, and $[Ru(bpy)_2(pztr)]^+$, **4**, are used as reference complexes to which the properties of the C-5 substituted complexes are compared. Deuteriatlon of ligands has a number of useful properties. It leads to an increase in the excited state lifetime if the excited state is located on the deuteriated ligand. It also leads to the shifting of vibrational bands associated with the deuteriated ligand. Both of these effects have been exploited in the following sections. Throughout this chapter the postscript **d** refers to a complex in which the bpy ligands are fully deuteriated, while **p** refers to the perprotio complexes. The effect of substitution and protonation on the absorption spectrum has been investigated using ground and excited state Raman spectroscopy. Temperature dependent emission studies, along with Time Correlated Single Photon Counting, have been used to probe the THEXI state and the nature of the processes leading to its deactivation. Computational studies have been used to model the location of electron density in the ground and excited state. Throughout the chapter the results for **1** and **H1** are presented first, followed by those for **2** and **H2**.

4.3.1 Steady State Electronic Spectroscopy.

The visible absorption and emission data for the complexes are shown in TABLE 4.1. The lowest energy absorption feature for all complexes is assigned to several overlapping singlet metal-to-ligand-charge-transfer (^{1}MLCT) transitions ($\log \varepsilon \sim 4$), by comparison with other ruthenium polypyridyl complexes[14] and on the basis of resonance Raman analysis (*vide infra*). All compounds show strong absorptions ($\log \varepsilon \sim 5$) at about 280 nm which are π-π^* in nature. Overall the electronic properties are typical for pyridyl and

pyrazine triazole complexes (*i.e.*, in comparison with complex **3** and **4**).[14,15]

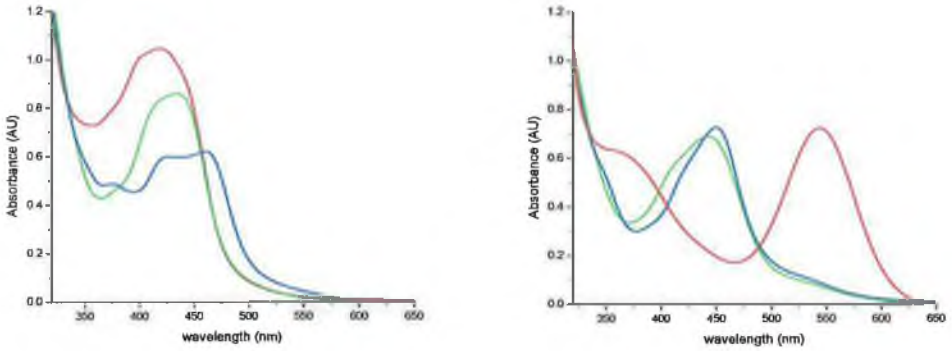

FIGURE 4.2: ABSORPTION SPECTRA FOR 1P (LEFT) AND 2P (RIGHT) IN CONC. H_2SO_4 (RED), PH 1.5 (GREEN) AND PH 7 (BLUE).

For the pyridine-1,2,4-triazole complex, **1p**, the absorption spectra of the protonated and deprotonated species are very different, with a substantial blue shift in the λ_{max} occurring upon protonation (~ 40 nm) (FIGURE 4.2). However, for the pyrazine-1,2,4-triazole based complex, **2p**, only a small blue shift in the λ_{max} of the ^{1}MLCT absorption bands occurs upon protonation (~ 10 nm). Differential absorption spectra, by Dr. Browne, are included in APPENDIX B which show the changes more clearly with a blue-shift in the visible absorption bands upon protonation and a red-shift in the π-π^*_{bpy} transition in UV region. The effects of protonation on the substituted pyridine and pyrazine containing complexes are similar to those of related complexes, **3** and **4**. In strongly acidic solution (*i.e.*, in conc. H_2SO_4), complex **1p** shows no significant change in absorption, whilst in contrast, very dramatic changes are observed in the absorption spectrum of **2p** when compared to **1p**, with a blue-shift in the ^{1}MLCT absorption bands and the appearance of a very strong absorption around 550 nm.

All complexes examined are luminescent in acetonitrile and, weakly, in aqueous solution at room temperature and in EtOH/MeOH glass at 77 K. The complexes emit in the 600 to 700 nm region and a large blue shift is observed

on cooling to 77 K. FIGURE 4.3 shows the emission spectra of **1p**, **H1p**, **2p** and **H2p** in acetonitrile at 293K. As for the absorption spectra, the emission maxima of **1p** (683 nm) and **2p** (664 nm) are close to that of the related complex **3** (677 nm) and **4** (668 nm) respectively. Protonation of **1p** results in a blue shift in the emission while for **2p** protonation results in a modest red-shift.

	λ_{Abs} /nm[A] (log ε)	$E_{1/2}$ (V vs. SCE)[A] Ru(II/III)	λ_{max} 293nm (nm)[A]	λ_{max} 77K (nm)[B]	pK_a[C]	$\tau_{298\,K}$ /ns[A]	$\tau_{77\,K}$ /μs[B]
1	480 (3.93)[12]	0.86(1.62 irr.)[12]	683	610	3.05[16]	110 (135)	3.01 (8.73)
H1	439 (4.03)[12]	1.19(1.67 irr.)[12]	613	575	--	15 (6)	5.76 (7.62)
2	455 (4.15)[12]	0.95(1.55 irr.)[12]	664	610	2.15[16]	82 (184)	7.85 (4.00)
H2	438 (4.18)[12]	1.23(1.55 irr.)[12]	672	630	--	312 (320)	7.34 (7.56)
3[34]	484 (1.10)[17]	0.83	677	611	4.1	145 (250)	--
H3[34]	442 (1.29)	1.14	611	577	--	--	--
4[6]	445 (1.14)[18]	1.01	668	600	3.7	230 (283)	4.45 (7.03)
H4[6]	441 (1.32)[18]	1.25	658	619	--	230 (230)	4.77 (6.00)

TABLE 4.1: PHOTOPHYSICAL DATA OF THE COMPLEXES. A) IN ACETONITRILE B) IN ETOH:MEOH (4:1) C) IN ROBINSON BRITTON BUFFER SOLUTION.

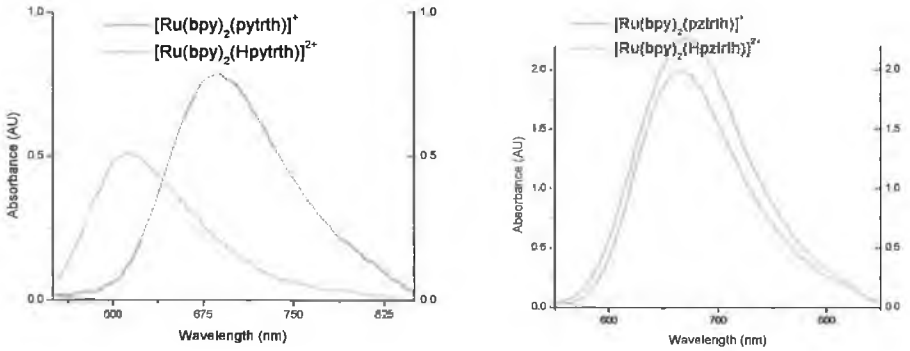

FIGURE 4.3: EMISSION SPECTRA FOR **1P/H1P** (LEFT) AND **2P/H2P** (RIGHT) AT 293K.

The excited state lifetime for all complexes at 77K and 293K are also presented in TABLE 4.1. The lifetimes of the deuteriated analogues are in brackets. Deuteriation of the ligand on which the excited state is located

causes an increase in the lifetime of that complex and hence selective deuteriation allows identification of the location of the excited state energy. At room temperature deuteriation leads to an increase in the excited state lifetime for **1** and **2**. The lifetime of the unsubstituted analogues, **3** and **4**, are also seen to increase on deuteriation. The protonated complexes **H2** and **H4** are seen to remain unchanged on deuteriation. For the protonated pyridyl triazole complexes the lifetimes are very short, and in the case of the **H3** accurate measurement was not possible.

The emissive properties of these pyridyl triazole complexes are seen to be effected by the choice of solvent (solvatochromic behaviour). FIGURE 4.4 shows the emission from **1** and **H1** in acetonitrile and Ethanol:Methanol (4:1). Emission from the deprotonated complex is approximately twice as intense in the alcoholic solvent than in acetonitrile. λ_{max} is also red – shifted by 20 nm in acetonitrile compared to the alcoholic solvents. The excited state lifetime of the complex is also seen to shorter in acetonitrile than in Ethanol:Methanol (4:1). Upon protonation emission in acetonitrile is very weak and the excited state lifetime is very short (2 ns aerated). By comparison, **H1** is still emissive in Ethanol:Methanol (4:1) with a lifetime of 14ns. For **H1** no change is observed in λ_{max} on switching solvents. These results highlight the danger in comparing temperature dependent emission / lifetime results at 293K (usually in acetonitrile) and those at low temperature using a different solvent.

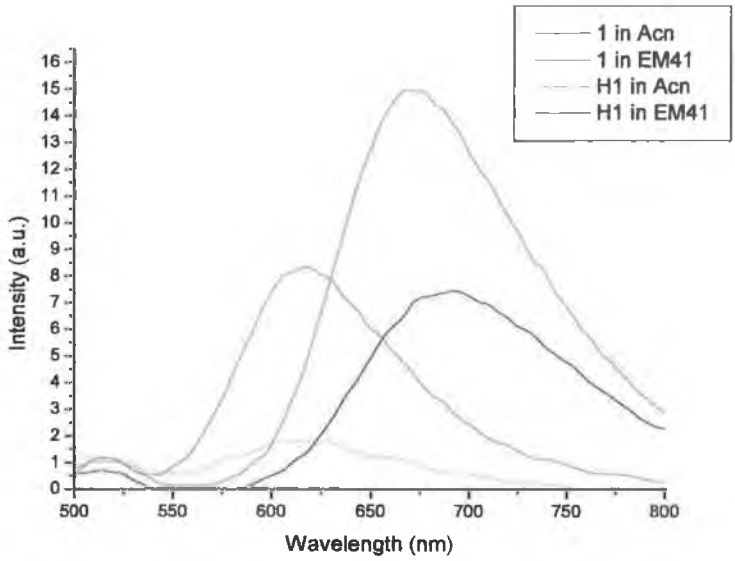

FIGURE 4.4: SOLVATOCHROMIC BEHAVIOUR OF **1** AND **H1**.

The acid dissociation constants (pK_a) for all complexes are also given in TABLE 4.1. The values were obtained from the change in the absorption spectra of the complexes with changing pH. The behaviour observed can be rationalised by protonation/deprotonation of the triazole moiety. Protonation of the coordinated pyrazine ring is possible, however, this occurs at only at negative pH i.e. in concentrated H_2SO_4.[18] The ability of the C-5 position to tune the pH of the complexes is observed by the changes in pK_a of **1** and **2** relative to **3** and **4**, respectively. The acidity of the coordinated triazole ring has been found to be dependent on the nature of the non-coordinated substituent in the C5 position of the 1,2,4-triazole.[19]

4.3.2 Temperature Dependent Spectroscopy.

4.3.2.1 Temperature Dependent Emission Spectroscopy.

Temperature dependent measurements have proved invaluable in probing the excited state of triazole containing complexes. At low temperature solvent reorganisation is slowed in reaction to the formation of an excited state. Therefore, low temperature measurements can be used to model very fast photo-chemical and -physical processes that occur at room temperature, as these processes are also slowed by the delayed solvent reorganisation.[20] Precise control of the solvent temperature also limits the amount of energy available to the complexes for activated processes. This allows the study of the excited state processes which lead to the return of the ground state.[32] Ethanol: Methanol (4:1) is used as the solvent system as it forms a clear glass at low temperature.

FIGURE 4.5 shows the temperature dependent emission spectra of **1p** between 80 and 180K in Ethanol:Methanol (4:1), with the high temperature region highlighted on the right. The glass transition temperature of this solvent is between 130K and 140K. There is a large decrease in emission intensity between 90K and 130K, which is due to softening of the glass matrix. As the temperature is raised above 140K, there is little shifting of the emission maxima as the solvent becomes fluid at this point. The spectra of **1p** shows temperature dependence that is common to most Ru(II) complexes, it is seen to red – shift and decrease in intensity with increasing temperature. The presence of a lower energy band is also common to most Ru(II) complexes and is attributed to the vibronic structure of the complex at low temperature.

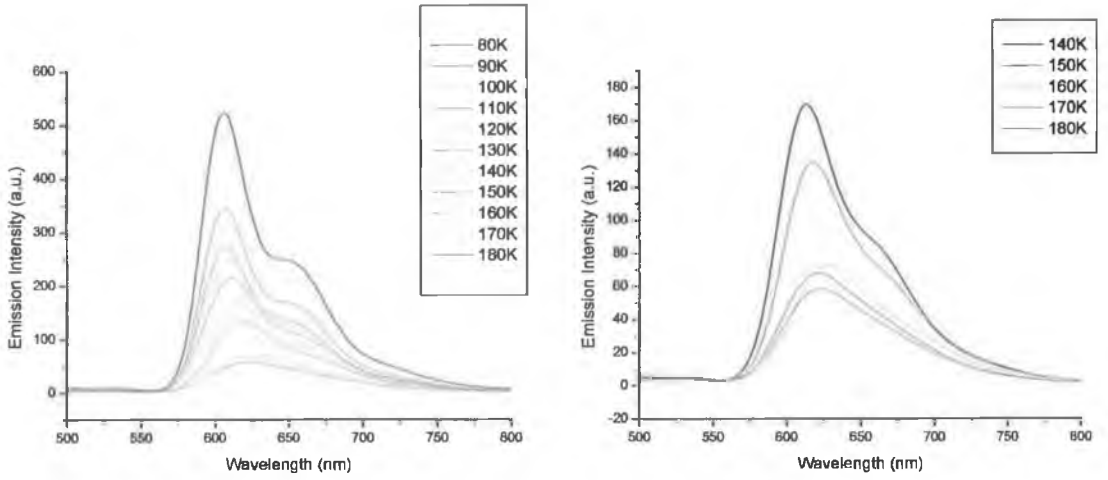

FIGURE 4.5: TEMPERATURE DEPENDENT EMISSION OF 1P (LEFT)80K – 180K AND (RIGHT) HIGHLIGHTING THE REGION BETWEEN 140 – 180K.

The temperature dependent emission of **H1p** has also been investigated. The spectra for **H1p** are shown in FIGURE 4.6. It can be seen in these spectra that the high energy band dominates the spectra. As expected **H1p** is blue shifted with respect to its deprotonated analogue. The protonated complex behaves in the same manner as **1p**, in that it shows "normal" temperature dependence with only one emission observable. It should also be noted that the emission from **H1p** remains strong even at 200K. This result is not surprising when it is considered that the solvatochromic behaviour presented in the previous section shows that the protonated complex, **H1**, is still strongly emissive at room temperature in Ethanol: Methanol (4:1).

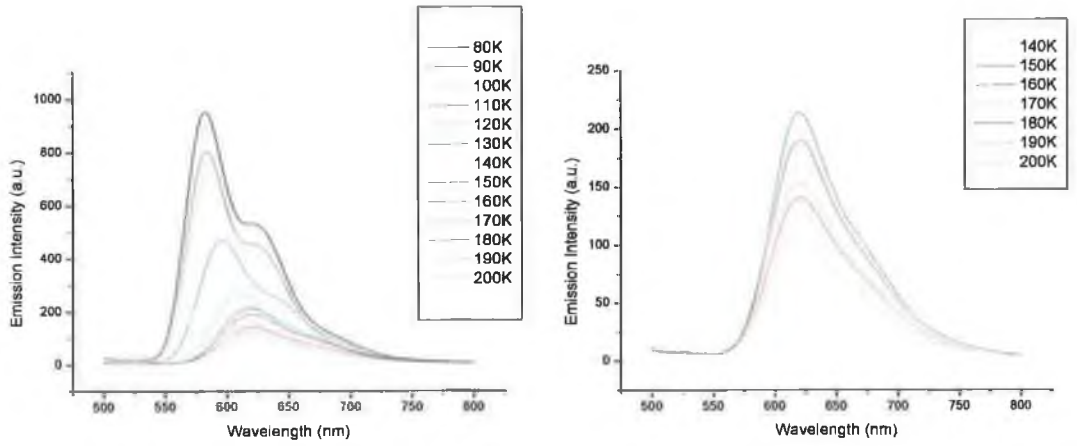

FIGURE 4.6: TEMPERATURE DEPENDENT EMISSION SPECTRA OF H1P BETWEEN (LEFT)80K – 200K AND (RIGHT) BETWEEN 140K AND 200K.

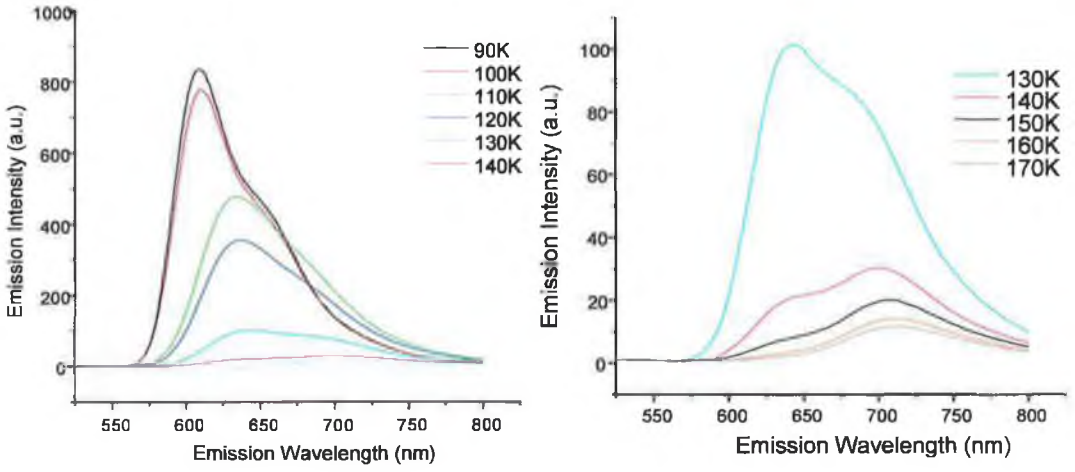

FIGURE 4.7: TEMPERATURE DEPENDENT EMISSION OF 2P IN ETOH:MEOH (4:1).

FIGURE 4.7 shows the temperature dependent emission spectra of **2p** in Ethanol: Methanol (4:1) between 90 and 170K. The spectra on the right highlight the temperature dependent emission between 130 and 170K. It is important to note the presence of one main peak and also a shoulder in the spectra. This shoulder appears similar to a vibronic peak, however, as the temperature is increased the intensity of the lower energy shoulder appears to grow relative to the main peak. In the higher temperature spectra the low energy peak (now centred at 705 nm) is most intense. As the low energy band shows a different temperature dependence to the high energy one it does not

appear to be a vibronic peak of the complex. This suggests that the low energy band is due to a second emission from the complex. To highlight the difference in the temperature dependence of **1p** and **2p** the normalised spectra are shown in FIGURE 4.8. From these spectra it is clear that the low energy peak in **2p** becomes the dominant emission by 140K and is the only emission observable at 180K. These results show that dual emission may be present for this complexes. However, more data is required and this is obtained via temperature dependent lifetime studies in the next section.

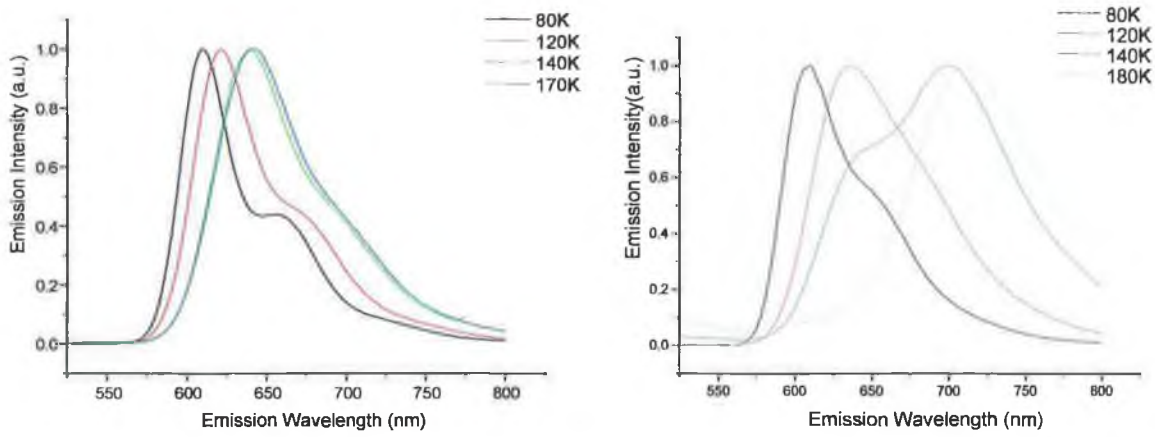

FIGURE 4.8: NORMALISED TEMPERATURE DEPENDENCE OF **1P**(LEFT) AND **2P**(RIGHT).

Previous studies have investigated the temperature dependent emission properties of **3** and **4**.[6,21] These studies have previously found that Ru(II) complexes containing a pyrazinyl triazole ligand also show similar dual emissive behaviour. In contrast complexes containing a pyridyl moiety show singly emissive behaviour. It appears from the present work that this interesting dual emissive behaviour is not specific for **4**, but also occurs for C-5 substituted complexes.

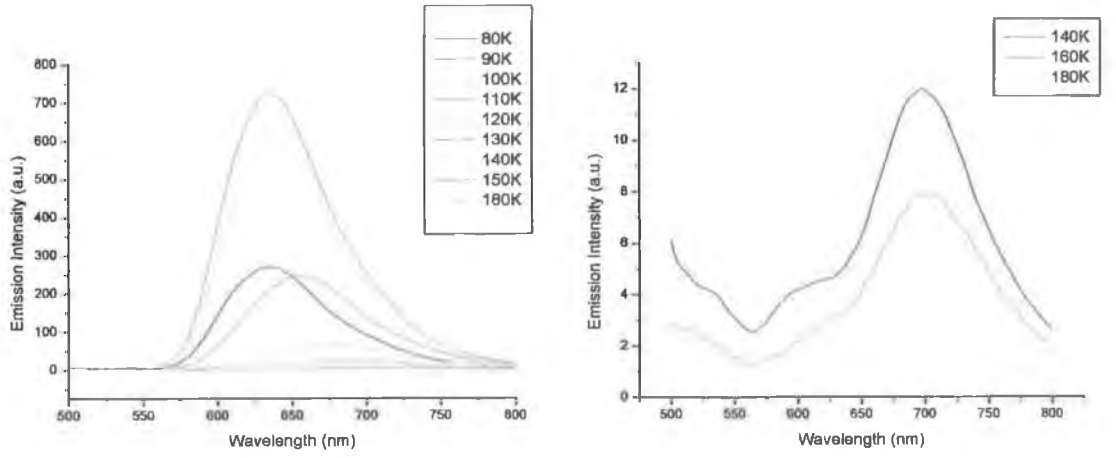

FIGURE 4.9: TEMPERATURE DEPENDENT EMISSION OF H2P IN ETOH: MEOH BETWEEN (LEFT) 80K AND 180K AND (RIGHT) 140K AND 180K.

FIGURE 4.9 shows the temperature dependent emission spectra of **H2p**. In contrast with **1**, the protonated analogue of the pyrazine triazole containing complex is red shifted at low temperatures. The emission intensity is also greatly reduced above the glass transition of the EtOH:MeOH 4:1 solvent system. By 180K no emission is observable. The second emission observed for **2p** is no longer apparent for the protonated complex. It should be noted that the λ_{max} for **H2p** at 140K is very similar to that observed for the low energy emission of **2p** at this temperature. Previous studies have shown that pyrazine triazole containing complexes in which the free nitrogen of the pyrazine is also protonated are non – emissive and hence no spectra were obtained for **$H_2$2p** in the present study.[18]

Temperature dependent emission studies have therefore identified two emissions in the spectra of **2p**, while one is observed for both **1p** and **H1p**. In the case of **H2p** there is a remarkable decrease in the emission intensity of the complex above the glass transition making identification of a second emission difficult.

In order to further understand the emissive behaviour of complexes temperature dependent excited state lifetime measurements were performed, with the results presented in following section. Studies of the deuteriated

complexes were also in agreement with those for the perprotio complexes.

4.3.2.2 Temperature Dependent Excited State Lifetime.

The excited state lifetime of a complex is another important property which can be probed. It provides information on the rate of deactivation and also allows identification of the processes by which the excited states return to the ground state. This information can be used to understand the relative energies of the ^{3}MLCT and ^{3}MC levels.

TABLE 4.2 shows the temperature dependent lifetime results for **1d** between 140K and 250K with 5K steps. Excited state decay measurements of this complex were seen to be mono-exponential at all wavelengths and temperatures investigated. This is in agreement with emission results which show a single excited state. The graph of 1/Temperature vs. Rate (1/Lifetime or $1/\tau$) for this complex is found in APPENDIX B with the results obtained presented in TABLE 4.5.

Temperature (K)	Lifetime (ns)
140	452
145	425
150	398
155	378
160	358
165	340
170	325
175	307
180	293
185	277
190	267
195	251
200	240
205	228
210	216
215	207
220	198

225	188
230	178
235	170
240	162
245	156
250	149

TABLE 4.2: TEMPERATURE DEPENDENT LIFETIMES OF 1D FROM 140K – 250K.

TABLE 4.3 gives the temperature dependent lifetime results for **H1p** between 140K and 170K. These results were also seen to be mono-exponential at the measurement wavelength, as for the deprotonated complex. Comparison of these results with those obtained for **H1d**, in APPENDIX B, shows the effect of deuteriation on excited state lifetime. The graph obtained by plotting 1/temperature vs. ($1/\tau$) for **H1d** is shown in FIGURE 4.10.

Temperature (K)	Lifetime (ns)
140	1589
143	1521
146	1438
149	1408
152	1361
155	1298
158	1247
161	1197
164	1138
167	1067
170	1027

TABLE 4.3: TEMPERATURE DEPENDENT LIFETIMES OF H1P FROM 140K – 180K.

APPENDIX B shows the graph of 1/temperature vs. Rate from which we obtain the results for the prefactor and activation energy(TABLE 4.5). The lifetime of the **1** is shorter than **H1** at low temperatures while at room temperature the lifetime of 1 is longer. This is not surprising, however, as at 77K the lifetime of **H1** is longer than that of **1**, and **H1** has a stronger temperature dependent behaviour (see TABLE 4.5) which means that its lifetime is reduced more rapidly with increasing temperature.

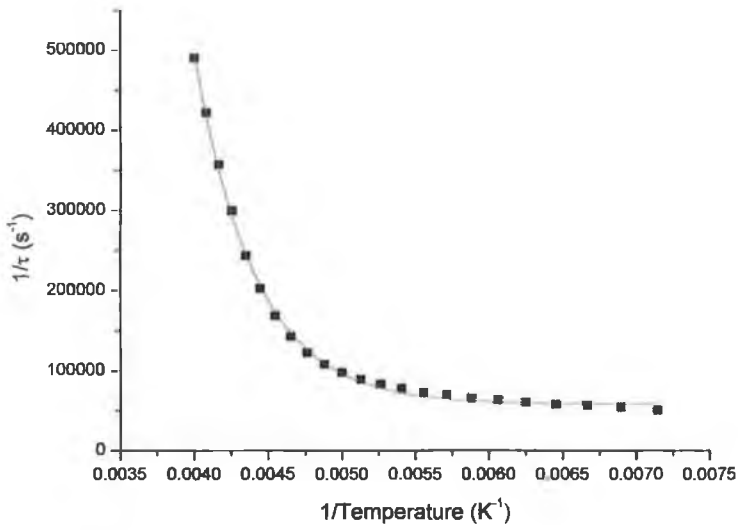

FIGURE 4.10: GRAPH OF 1/TEMPERATURE VS RATE FOR H1D.

Two equations can be used to fit temperature dependent behaviour. EQN. 4.1 shows the Arrhenius type equation. EQN. 4.2 shows the empirical equation. K_0 is the intrinsic lifetime, k′ is the prefactor of the temperature dependent term and ΔE_a is the activaition energy.

$$k_i = k_0 + k' \exp^{(-\frac{\Delta E_a}{RT})} \qquad \text{EQN. 4.1}$$

$$k_i = \frac{B_i}{1 + \exp[C_i(1/T - 1/T_{B_i})]}$$ EQN. 4.2

which describes a stepwise behaviour centred at temperature T_{Bi} and C_i is related to the smoothness of the step. Previous studies have used a both equations to fit the temperature dependent behaviour, however in the present study only EQN. 4.1 was required to get a good fit to experimental results.

The values obtained were $k_0 = 5.81 \times 10^5\ s^{-1}$; $k' = 7.73 \times 10^9\ s^{-1}$ and $t = 4.09 \times 10^{-4}\ K^{-1}$.

Temperature (K)	Lifetime at 580nm (ns)	Lifetime at 700nm (ns)
80	5442	9654
90	5486	10055
100	4952	7215
110	1624	4660
120	1525	4332
130	403	768
140	228	499
142	102	322
145	96	304
147	74	283
150	27	286
152	22	224
155	27	228
157	22	224
160	24	230
162	21	224
165	22	226
167	17	216
170	14	212
172	15	209
175	10	195
177	8	192
180	7	187
190	4	172
200	4	169
210	2	161
220	1	150
230	-	-
240	-	136
250	-	130
260	-	126
270	-	123
280	-	117
290	-	110

TABLE 4.4: TEMPERATURE DEPENDENT LIFETIMES OF $[Ru(bpy)_2(thpztr)]^+$ (2P) IN ETOH:MEOH (4:1).

TABLE 4.4 shows the results obtained for the temperature dependent excited state lifetimes of **2p**. The lifetime was monitored at 2 wavelengths to investigate the emissions centred at these wavelengths. It can be seen from

these results that the two emissions have different temperature dependencies, in agreement with the steady state emission results. The lifetime of the high energy emission decays faster than that of the low energy band. Measurements were also made at 650 nm to monitor both emissions simultaneously. In these measurements biexponential excited state decays were observed, again indicating the presence of two emissions in the complex. In order to investigate further the deactivation processes for each emission, temperature dependent lifetime measurements were taken in 3K steps between 140K and 180K. This range was chosen as it is above the glass transition temperature for Ethanol: Methanol 4:1 (130-140K) and the emission signal was still strong enough to produce satisfactory results.

These results were graphed as 1/temperature against the rate. This graph was fit to EQN 4.1 and from this, the prefactor and activation energy (E_a) for the processes which deactivate the excited state were calculated. The graph is presented in APPENDIX B. The result for the high energy and low energy emissions were calculated separately with the results presented in TABLE 4.5. The two excited states have significantly different prefactors and activation energies. Again, this indicates the difference in the temperature dependence of the two emissions and also that they are deactivated by different processes.

Temperature dependent excited state lifetimes of **H2p** have been recorded at 700 nm, the λ_{max} of the complex at 140K. Little change in the λ_{max} is observed after 140K as the solvent is fluid at this temperature. As seen in FIGURE 4.9 the emission from this complex is very weak above the glass transition. The temperature dependent lifetime results (see APPENDIX B) of this complex appear to be bi-exponential, however the results do not change consistently with increasing temperature. This would indicate that they are not due to emission from the complex but due to noise. Therefore the nature of the emission from **H2p** cannot be confirmed by TCSPC.

TABLE 4.5 summarises the results for the prefactor and activation energy for all complexes. Also included in TABLE 4.5 are the results obtained from previous studies for **3** and **4**. Note that the results for k_0 are not given for **4** and **H4** by Keyes *et al.*[6]

Complex	k_0, (s^{-1})	k', (s^{-1})	E_a (cm^{-1})
1p	2×10^5	8×10^6	490
H1p	6×10^4	1×10^9	1200
H1d	6×10^4	8×10^9	1700
2p High Energy	0	2×10^{12}	1500
2p Low Energy	2×10^5	3×10^6	280
3[34]	1.7×10^6	4.7×10^7	550
H3[34]	1.6×10^6	6.0×10^{10}	1700
4 High Energy[b]	---	2.40×10^{10}	850
4 Low Energy[b]	---	6.52×10^6	80
H4[6]	---	8.2×10^{12}	2610

TABLE 4.5: CALCULATED PREFACTORS AND A_E FOR THE COMPLEXES.

In general, the results for the **1** and **2** are in agreement with those obtained previously for **3** and **4**. The temperature dependent lifetime results highlight two important points regarding the triazole containing complexes. Firstly, protonation of **1** leads to an increase in the prefactor and activation energy of the excited state deactivation process. This is indicative of a process that deactivates via the ^{3}MC (*vide infra*). Secondly, the two emissions observed for **2** show clearly different temperature dependencies and hence deactivate via different pathways.

4.3.3 Transient Absorption Spectra of 1p and 2p.

Excited state absorption spectra are used to investigate the changes in absorption occurring on formation of the excited state. Both time resolved (transient) and steady state measurements are possible. Here time resolved measurements are presented. These measurements allow identification of the source and destination of the excited electron. The source of the excited electron can be identified by the depletion of absorption bands due to this moiety i.e. if an electron is removed from the metal centre on excitation, the transient absorption spectra will see the loss of absorption bands due to the Ru(II) centre. Similarly, the growth of new bands in the transient absorption allow the identification of new moieties formed which may be due to their oxidation or reduction. Transient absorption spectra are also of vital importance in transient resonance Raman measurements (Section 4.3.4.3). Transient resonance Raman (TR^2) spectra probe the nature of the absorption of the excited state molecule. To ensure that resonance enhancement occurs in TR^2 measurements, the laser wavelength used must be coincident with an absorption of the excited state molecule. Therefore, the excited state absorption of the molecule must be known and this information is provided by transient absorption measurements. The spectra are presented with the ground state subtracted to highlight the changes occurring on excited state formation. For these measurements the optical density of the sample was near 1 at the excitation wavelength of 355 nm.

FIGURE 4.11 shows the transient absorption spectra of **1p** in acetone. A bleach in the region between 450 - 480nm is observed due to the depletion of the ground state. The main excited state absorption is at 385nm with a shoulder at 365nm. There is also a long tail in the excited state absorption due to LMCT bands.[22] This band is in resonance with the 785nm excitation used in the Raman studies of the oxidised species.

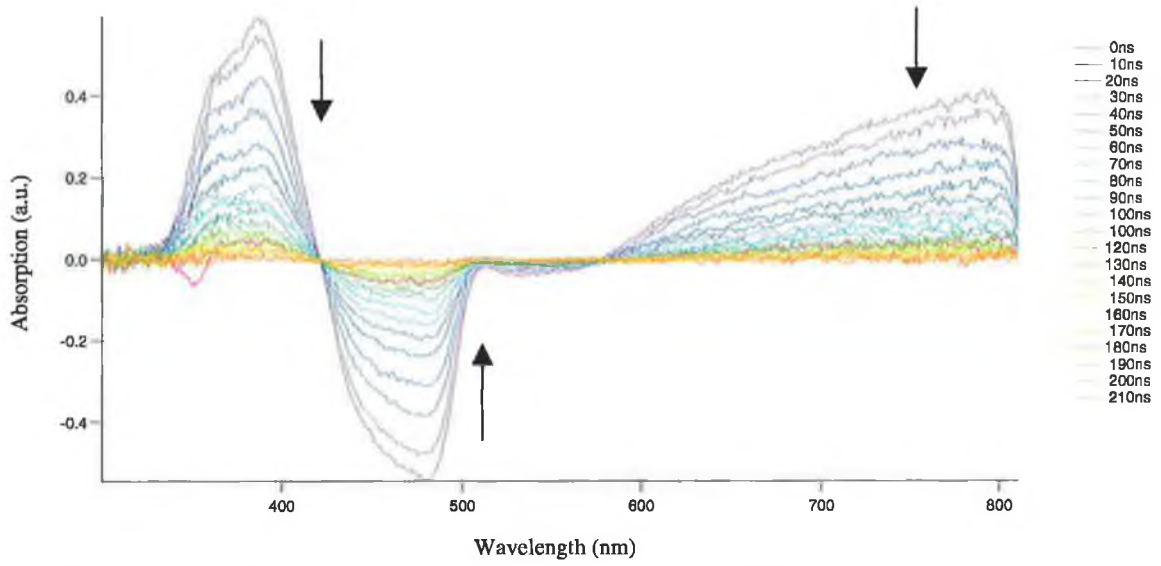

FIGURE 4.11: TRANSIENT ABSORPTION SPECTRA OF 1P IN ACETONE AT 355 NM.

FIGURE 4.12 shows the transient absorption spectra of **2p**. A bleach in the ground state absorption is seen at 465nm while the main excited state absorption is at 375nm. Again the LMCT band is observed.

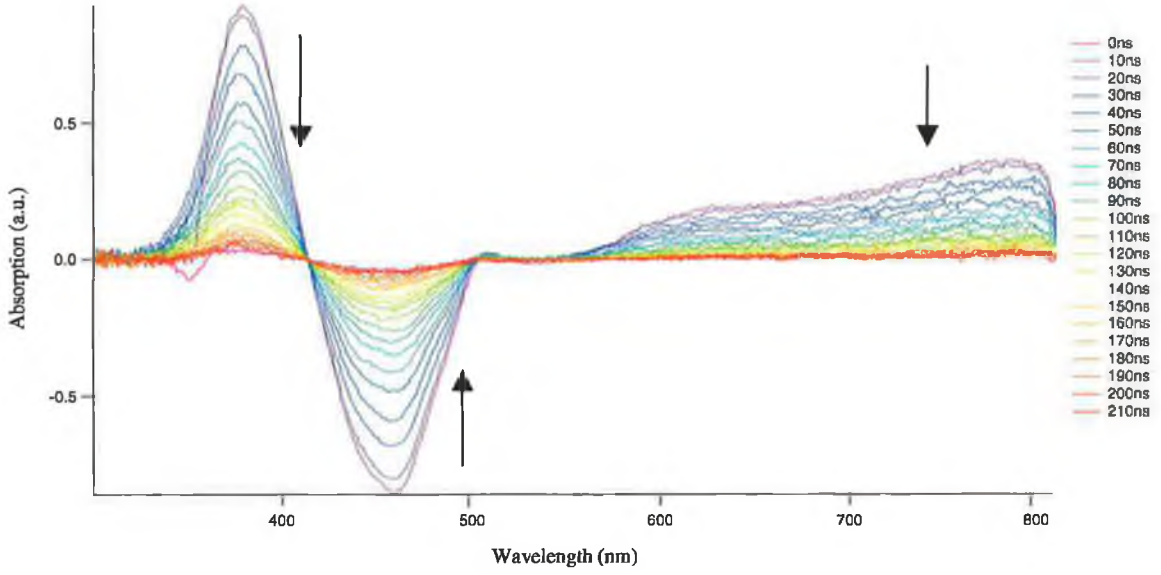

FIGURE 4.12: TRANSIENT ABSORPTION SPECTRA OF 2P IN ACETONE AT 355 NM.

4.3.4 Raman Studies.

Raman spectroscopy is an experimental technique that has seen huge growth in popularity in recent years. Non – resonant Raman spectroscopy is a structural probe that allows observation of the moieties present based on their vibrational characteristics and has a number of practical applications.[23] Resonance Raman measurements are used to investigate the nature of the absorptions in complexes and the location of their excited state. Time resolved techniques have also been developed to allow greater understanding of excited state structures and their evolution with time.

4.3.4.1 Raman Spectra of 1p/d and 2p/d.

Raman spectra of the complexes in the solid state were recorded at 785nm. These spectra differ from those in the following sections in that the excitation energy used is not in resonance with an absorption of the complex. In this case resonance enhancement does not occur and it is possible to obtain a general overview of all the vibrational modes present. In this section all the Raman bands of the complexes are observed and assigned based on their shift on ligand deuteriation. The results are also used for comparison with calculated vibrational spectra in later chapters.

FIGURE 4.13 shows the solid state spectra of **1p**, **2p** and **1d** with 785nm excitation. Deuteriation enables direct assignment of bpy based vibrational bands (at 1601, 1484, 1316, 1269, 1171, 1033, 761 cm^{-1}) and the thpytr (at 1608, 1552, 1515, 1462, 1434, 1388, 1148, 1097, 1012, 949, 646 cm^{-1}) and thpztr (1552, 1460, 1418, 1356, 1143, 1102, 945, 651cm^{-1}) based vibrational bands.[24] $[D_8]$-bpy vibrational bands are observed at 1561, 1417, 1294, 1251, 1226, 1196, 1012 and 982 cm^{-1} for **1d**. This is based on the shifting of the vibrational bands of the ligands which have been deuteriated, while the bands

due to the perprotio ligands remain unaffected.[25] All bands observed are in agreement with results obtained previously for triazole containing complexes.[26]

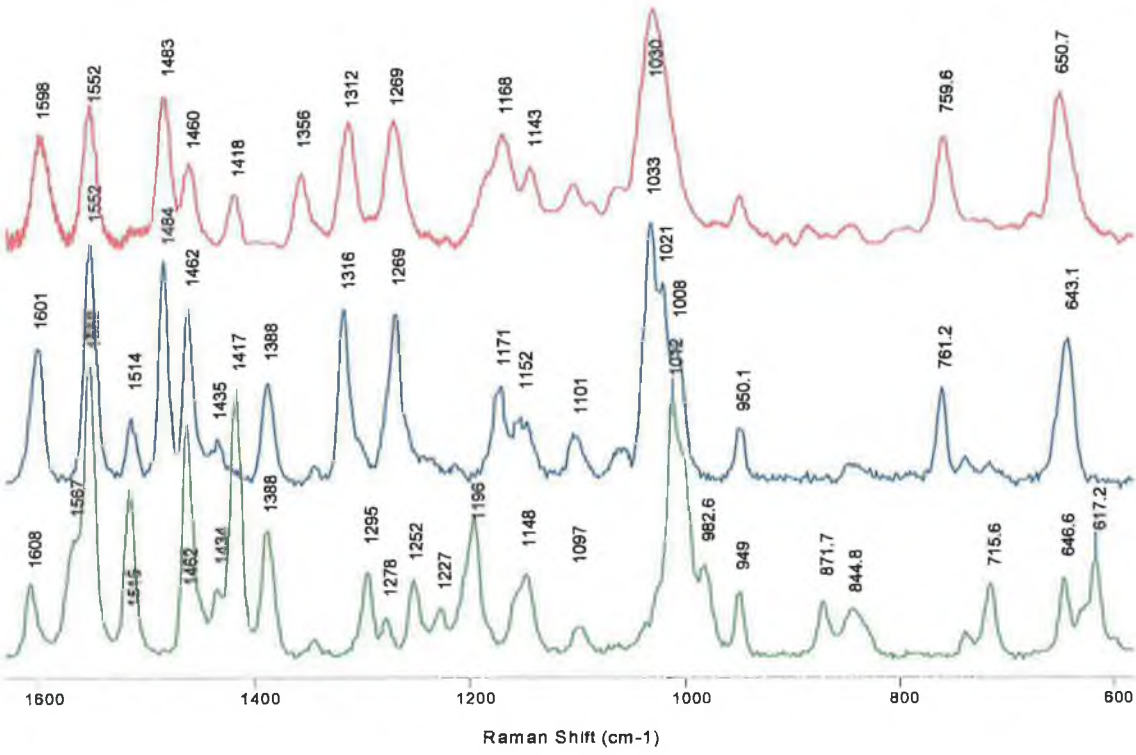

FIGURE 4.13: SOLID STATE RAMAN SPECTRA OF 2P (UPPER), 1P (MIDDLE) AND 1D (LOWER) AT 785 NM.

4.3.4.2 Resonance Raman Studies of 1p/d and 2p/d.

Resonance Raman has been used to investigate the nature of the absorption spectra of the thienyl substituted complexes. In resonance Raman spectroscopy the probe laser wavelength is co-incident with an absorption band of the complex. The resonance enhancement effect causes the bands of the ligand associated with this absorption to be greatly increased ($\sim 10^4 - 10^6$). An overview of the resonance enhancement effect is provided in Chapter 1. This therefore allows the identification of ligands that are populated upon excitation i.e. the singlet excited state. In all the following spectra deuteriation has again been used to assign the nature of the peaks in the spectra.

FIGURE 4.14 shows the resonance Raman spectra of **1p** and **1d** in H_2O with λ_{exc} = 457 nm.

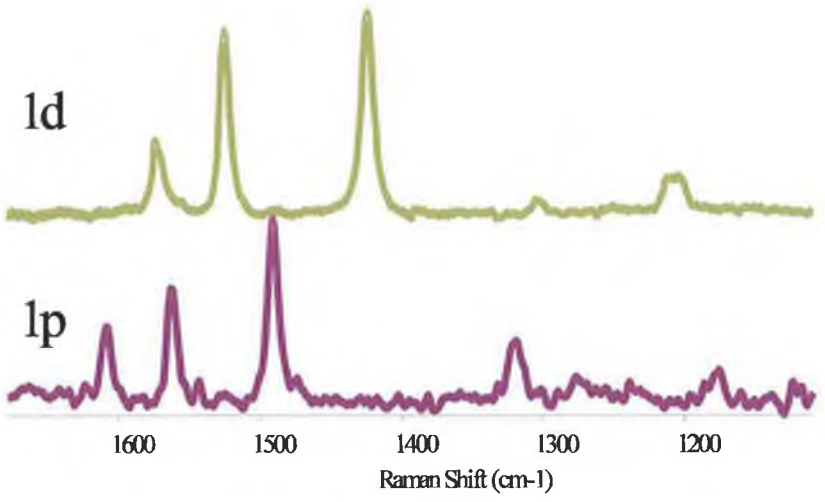

FIGURE 4.14: RESONANCE RAMAN SPECTRA OF 1P AND 1D IN H_2O WITH λ_{EXC} = 457 NM.

FIGURE 4.14 shows that the peaks at 1605, 1563, 1485 and 1320 cm^{-1} shift upon deuteriation and are therefore assigned as bpy peaks. No peaks due to the pyridyl triazole ligand are observed.

FIGURE 4.15 shows the spectra of the protonated pyridyl triazole (**H1p**) complex and its deuteriated analogue. Again deuteriation leads to shifting of all the peaks observed (at 1603, 1561, 1485 and 1320 cm^{-1}) indicating that the ^{1}MLCT absorption for the protonated complex is also bpy based at the high energy side of the absorption.

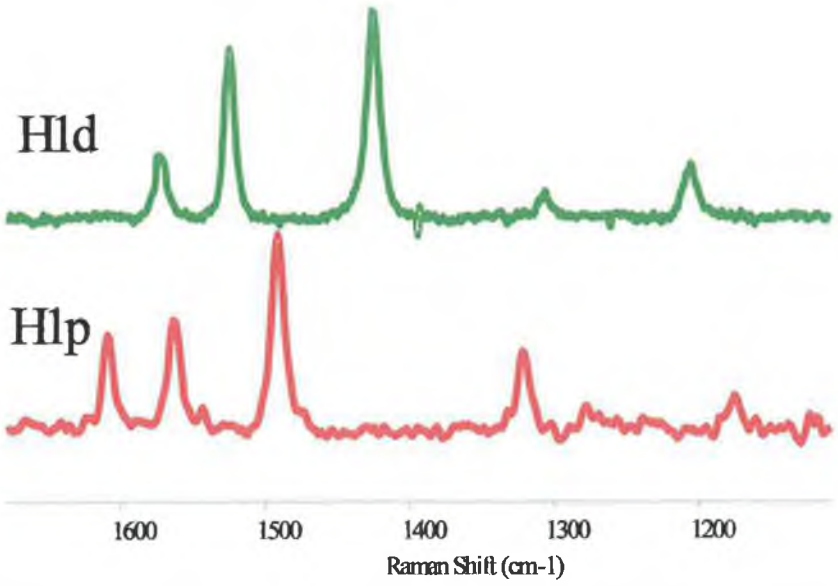

FIGURE 4.15: RESONANCE RAMAN SPECTRA OF H1P AND H1D IN H_2O WITH λ_{EXC} = 457 NM.

Resonance Raman spectra have also been measured at 488 nm excitation. FIGURE 4.16 shows the spectra of 1p and H1p, and their deuteriated analogues (**1d** and **H1d**). It should also be noted that there appears to be a reduction in the spectral quality of the deuteriated complexes at 488 nm excitation.

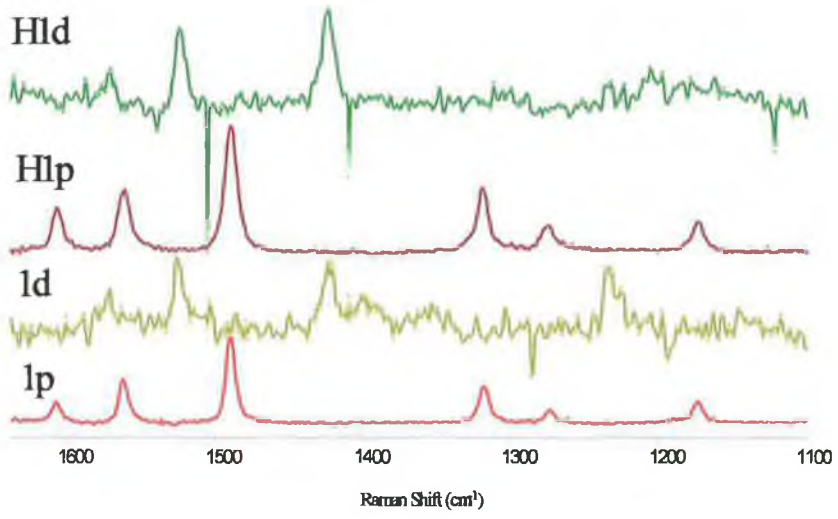

FIGURE 4.16: RESONANCE RAMAN SPECTRA OF 1P, 1D, H1P AND H1D IN H_2O WITH λ_{EXC} = 488 NM.

All the peaks observable in the spectra of **1p** and **H1p** (at 1606, 1561, 1488 and 1318 cm^{-1}) are seen to shift on deuteriation of the bpy ligands. Thus no

contribution from the pyridyl triazole to the absorption band at 488 nm is observed in both the protonated and deprotonated complexes.

Complexes containing a pyrazinyl triazole ligand were also investigated. FIGURE 4.17 shows the resonance Raman spectra of **2p** and **2d** in H_2O with 457 nm excitation.

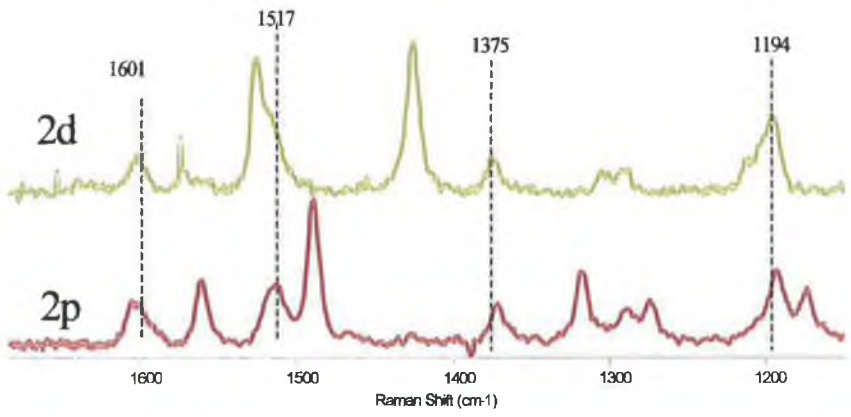

FIGURE 4.17: RESONANCE RAMAN SPECTRA OF 2P AND 2D IN H_2O WITH λ_{EXC} = 457 NM.

Again peaks due to the bpy moiety are observable at 1608, 1564, 1492 and 1320 cm^{-1}. However there are also peaks due to the thpztr moiety at 1601, 1517, 1375 and 1194 cm^{-1}. Their identity is confirmed by their insensitivity to deuteriation.

FIGURE 4.18 shows the spectrum of **H2p** and its deuteriated analogue in H_2O with 457.9 nm excitation. Again bands due to both the bpy ligands (at 1564, 1494 and 1320 cm^{-1}) and the Hthpztr moiety (at 1549, 1517, 1391 and 1192 cm^{-1}) are seen indicating that both ligands are involved in the absorption at that wavelength.

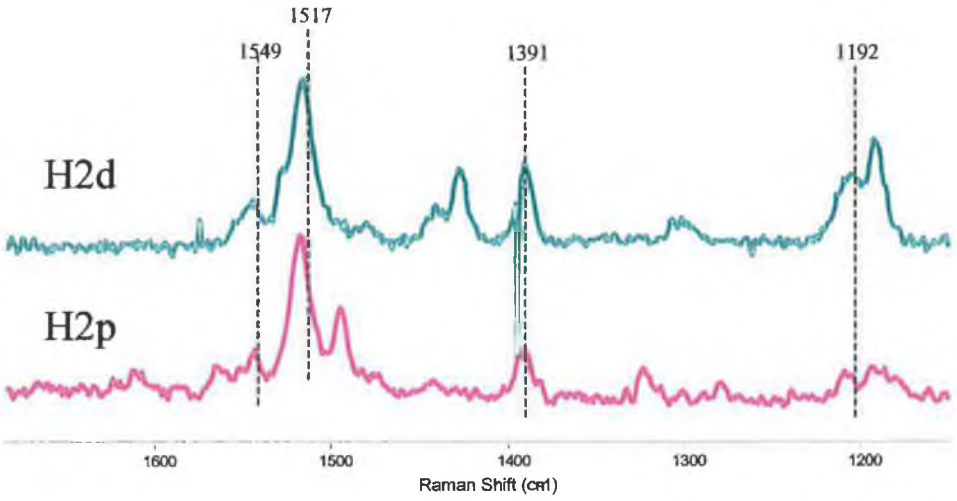

FIGURE 4.18: RESONANCE RAMAN SPECTRA OF H2P AND H2D IN H_2O AT 457 NM EXCITATION.

FIGURE 4.19 compares the deprotonated and protonated complexes at 488 nm excitation. As with Figure 4.16 a reduction of the spectral quality of the deuteriated complexes is observed at 488 nm. For **2p** and **H2p** peaks due to the bpy ligands (at 1562, 1491 and 1320 cm^{-1}) are observable, with peaks due to thpztr (at 1514, 1375 and 1194 cm^{-1}) and Hthpztr (at 1517 and 1387 cm^{-1}) also seen. Resonance Raman therefore indicates the bands of the ^{1}MLCT of **2p/d** and **H2p/d** consists of absorption due to population of both the pyrazinyl triazole and the bpy moieties of the complex.

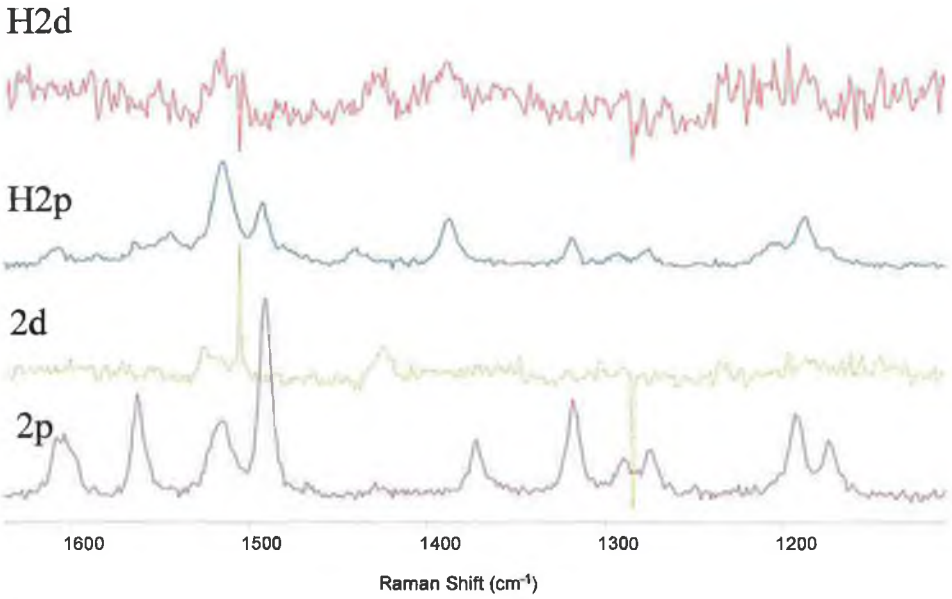

FIGURE 4.19: RESONANCE RAMAN SPECTRA OF 2P, 2D, H2P AND H2D IN H_2O AT 488 NM EXCITATION.

Resonance Raman spectra of the oxidised complexes **1p**$^+$ and **2p**$^+$, in H_2O, (FIGURE 4.20) in contrast to those of **1p**/**2p**, show no characteristic $[H_8]$-bpy features. The samples were oxidised using ammonium cerium(IV) nitrate in H_2O. The excitation wavelength used is in resonance with a strong absorption assigned as a ligand to metal charge transfer (LMCT) band (*vide supra*). The absence of vibrational bands assignable to bpy ligand vibrations is not unexpected since the oscillator strength of LMCT absorptions has been shown to be dependent on the electron donor properties of the ligands.[27] In the present case the electron rich thiophene substituted triazole ligand results in a much more intense LMCT absorption band than expected for this class of complex. Hence the observation of vibrational bands not assignable to the bpy ligand supports the assignment of the absorption to a pyridyl or pyrazinyl triazole -to-metal charge transfer band.

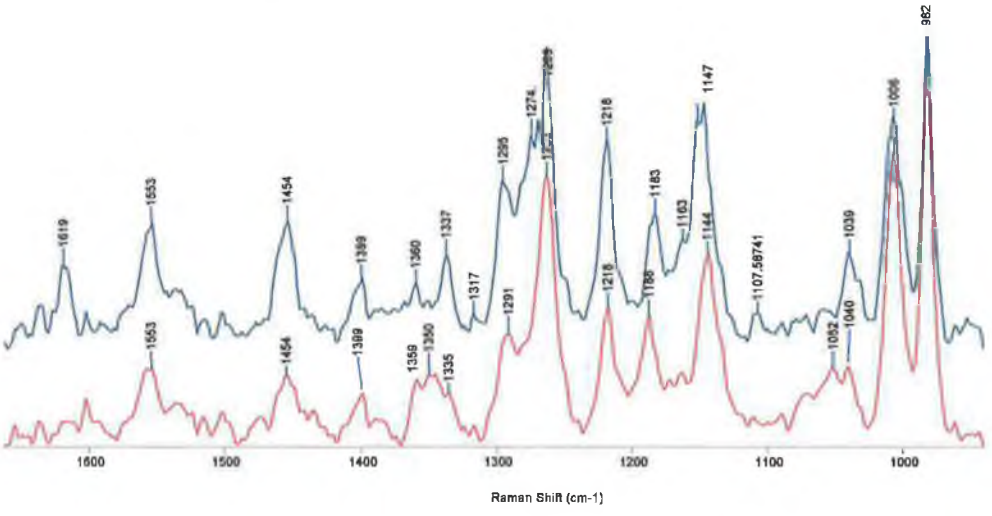

FIGURE 4.20: RESONANCE RAMAN SPECTRA OF (TOP)$1P^+$ AND (BOTTOM)$2P^+$, IN BASIC/H_2O AT 785 NM.

4.3.4.3 Transient Resonance Raman Spectroscopy.

Transient resonance Raman spectra of **1p** and **2p** in CD_3CN, both in a deprotonated and protonated state, are shown in FIGURE 4.21. The observation of strong bands at 1212 and 1285 cm^{-1} in the spectra of **1p**,**H1p** and **2p**, assigned to the bpy anion radical, confirm the assignment of the lowest emissive state as being from a bpy based ^{3}MLCT in these complexes. In the case of **H2p**, there is a notable absence of these bands. It is possible that a

shift in the excited state absorption out of resonance with the 355 nm excitation line is responsible for their absence. However on the basis of transient absorption spectra of the related complexes **3** and **4**, and other similar complexes[22], this is unlikely. Based on earlier transient Raman studies of **4**[6], it can be concluded that for **H2p** the lowest excited state is pyrazine based. Observation of bands due to the pyrazinyl radical is difficult due to overlap with the neutral bpy modes. However, as there are no bpy radical bands and previous studies have shown the excited state to be Hthpztr based, the bands at 1493 and 1431 cm^{-1} are probably due to the pyrazine radical.[6] In aqueous solution, a similar situation is observed. The switching of the location of the excited state is in agreement wit the results observed by emission spectroscopy(section 4.3.2.2) and confirm the ability to switch the location of the excited state by pH control.

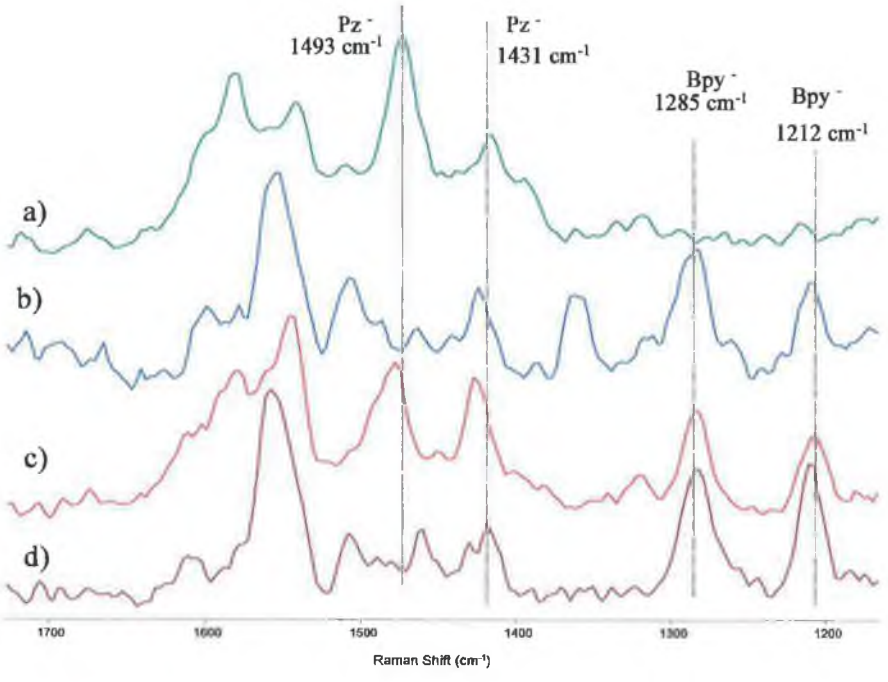

FIGURE 4.21: TRANSIENT RAMAN SPECTRA OF A) H2P, B) 2P, C) H1P AND D) 1P IN CD_3CN (λ_{EXC} 355 NM).

In the spectra of **1p** and **2p** bands assigned to the neutral 1,2,4-triazole based ligands are also observed suggesting contribution from thpytr and thpztr based absorptions at 355 nm.[11]

4.3.5 Density Functional Theory.

4.3.5.1 Electronic Properties.

In order to gain more insight into the electronic properties of the complexes **1/H1** and **2/H2**, DFT calculations were carried using the B3LYP functional and the LanL2DZ basis set. For the protonated complexes a complication arises in regard to the point of protonation, whether it is at N1 or N4 (FIGURE 4.1). Previous studies on the relative reactivity of the nitrogens of a 1,2,4-triazole ring have indicated that the N1 position is slightly less acidic than the N4 position.[28] However, due to the potential to introduce additional steric interactions in protonation at the N1 position, in the present study, the N4 position of the 1,2,4-triazole was protonated for the DFT calculations of **H1** and **H2**. After geometry optimisation with an ultrafine integration grid, the molecular orbitals were described in terms of contributions from various groups in the molecule: for **1** and **H1**: *Ru* – the Ru atom, *py* – the pyridine ring, *(H)tr* – the triazole moiety; *th* – the thiophene moiety; *bpy1* and *bpy2* – the two bipyridines; for **2** and **H2**: *pz* represents the pyrazine ring. Tables of this molecular orbital data are given in APPENDIX B. The isosurfaces for the HOMO-1, HOMO, LUMO and LUMO+1 of **1** / **H1** and **2** / **H2** are shown in FIGURE 4.22 and FIGURE 4.24, respectively. In the frontier region, neighbouring orbitals are often closely spaced. In such cases, consideration of only the HOMO and LUMO may not yield a realistic description of the frontier orbitals. For this reason, partial density of states (PDOS) diagrams, which incorporate a degree of overlap between the curves convoluted from neighbouring energy levels, can give a more representative picture of the nature of the frontier orbitals. The PDOS diagrams obtained for **1** / **H1** are shown in FIGURE 4.23 while those for **2** / **H2** are in FIGURE 4.25.

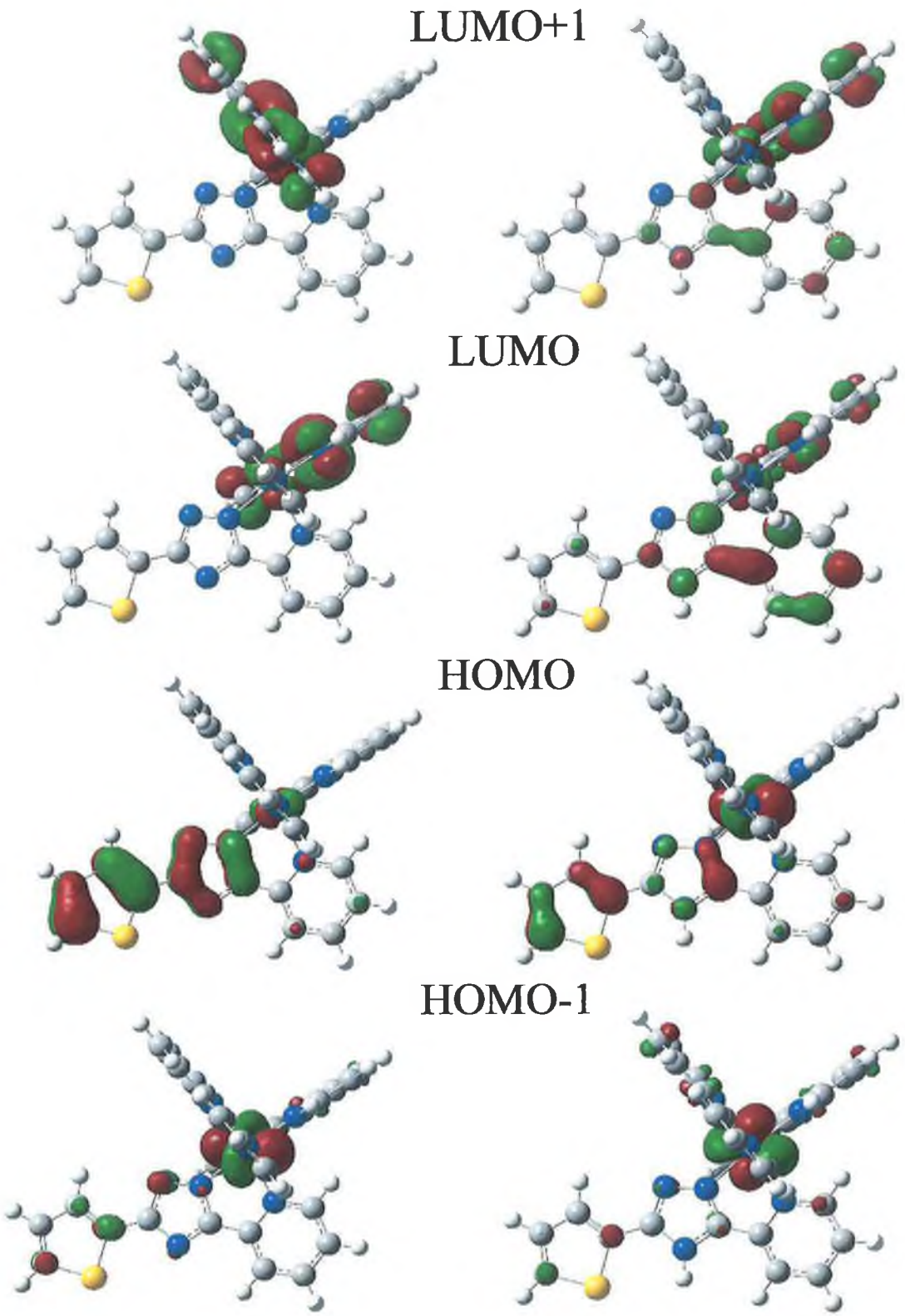

FIGURE 4.22: ISOSURFACES OF HOMO-1, HOMO, LUMO AND LUMO+1 ORBITALS FOR 1P (LEFT) AND H1P (RIGHT).

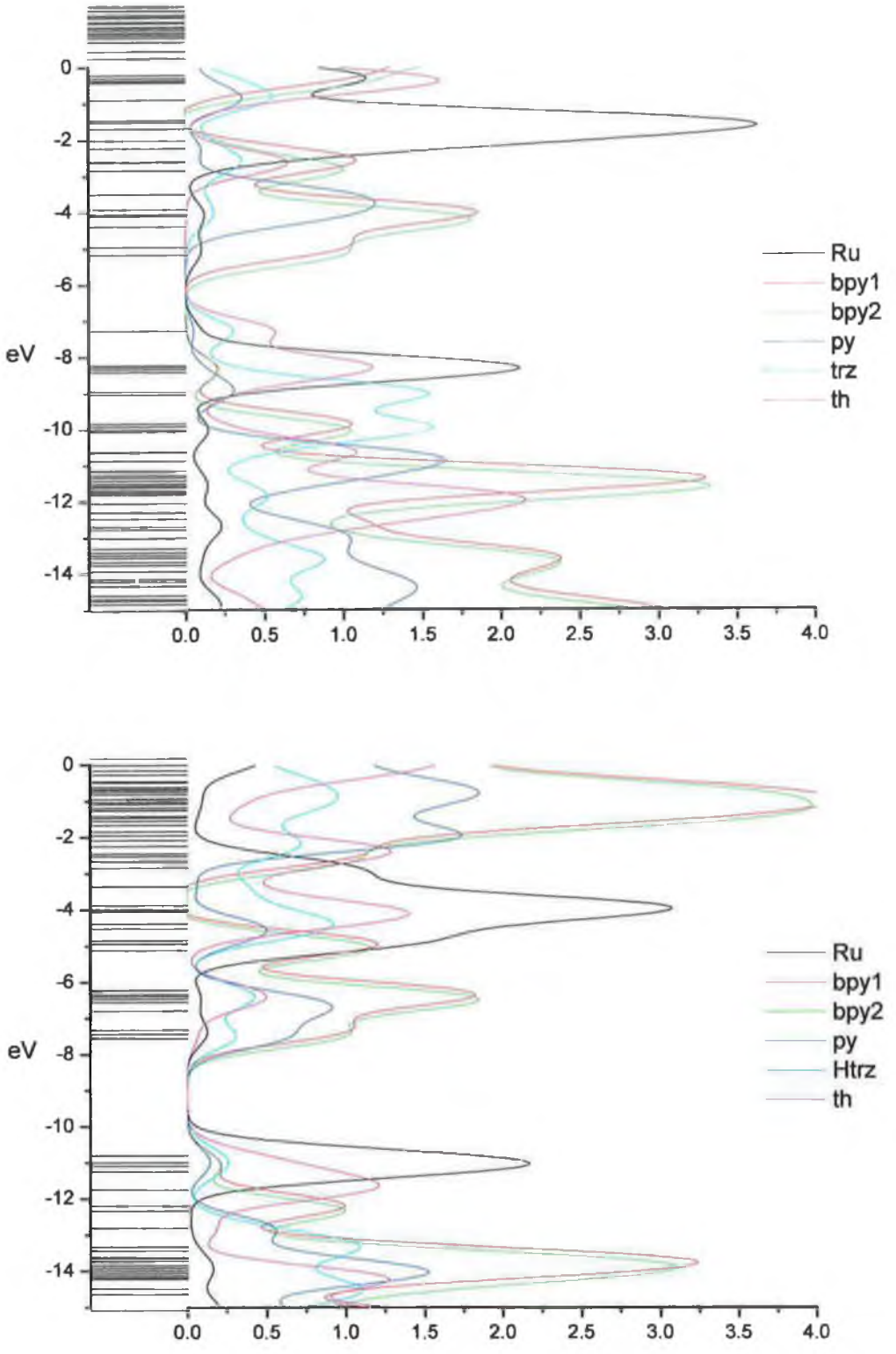

FIGURE 4.23: PDOS DIAGRAMS OF 1P(TOP) AND H1P(BOTTOM).

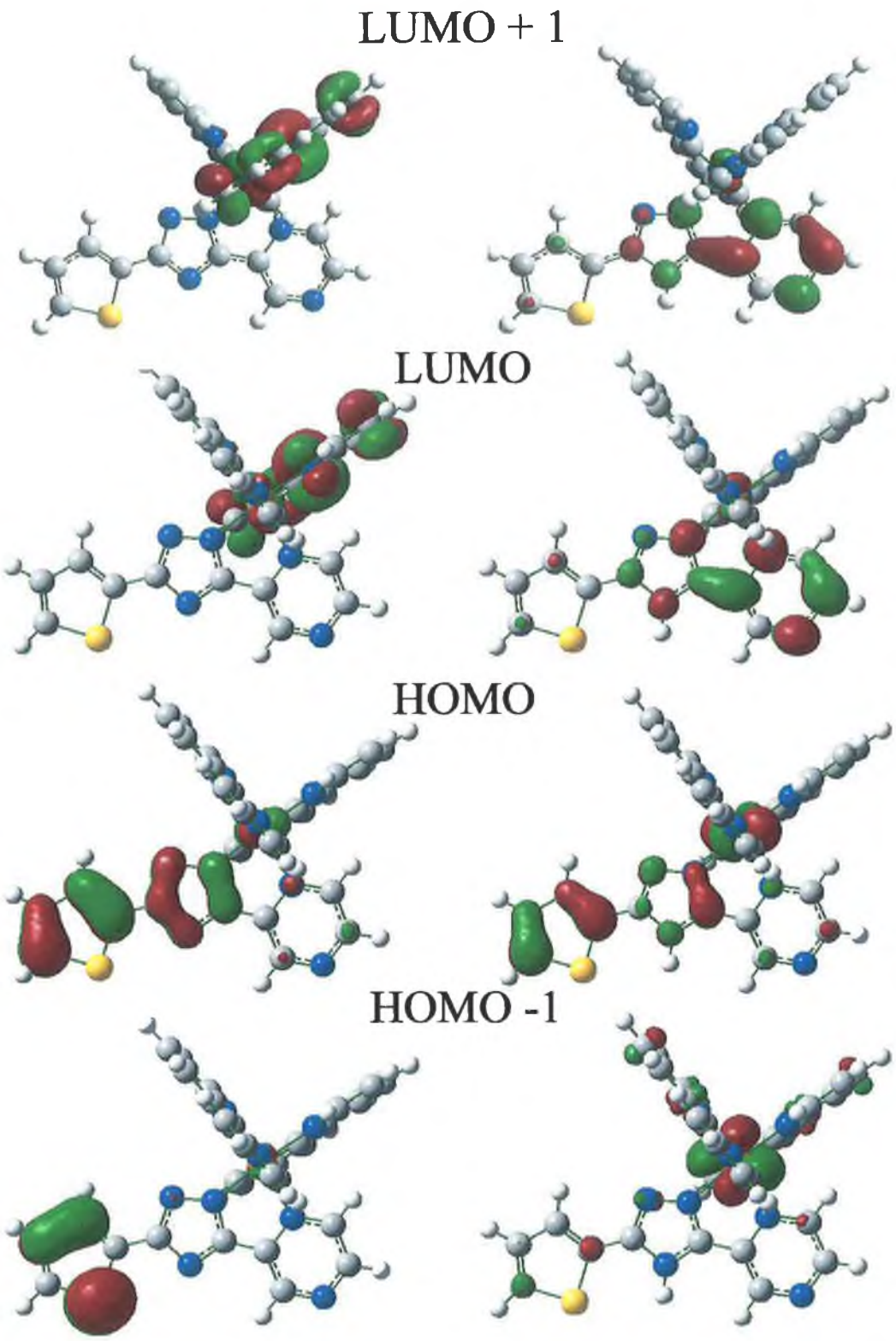

FIGURE 4.24: ISOSURFACES OF HOMO-1, HOMO, LUMO AND LUMO+1 ORBITALS FOR 2P (LEFT) AND H2P (RIGHT).

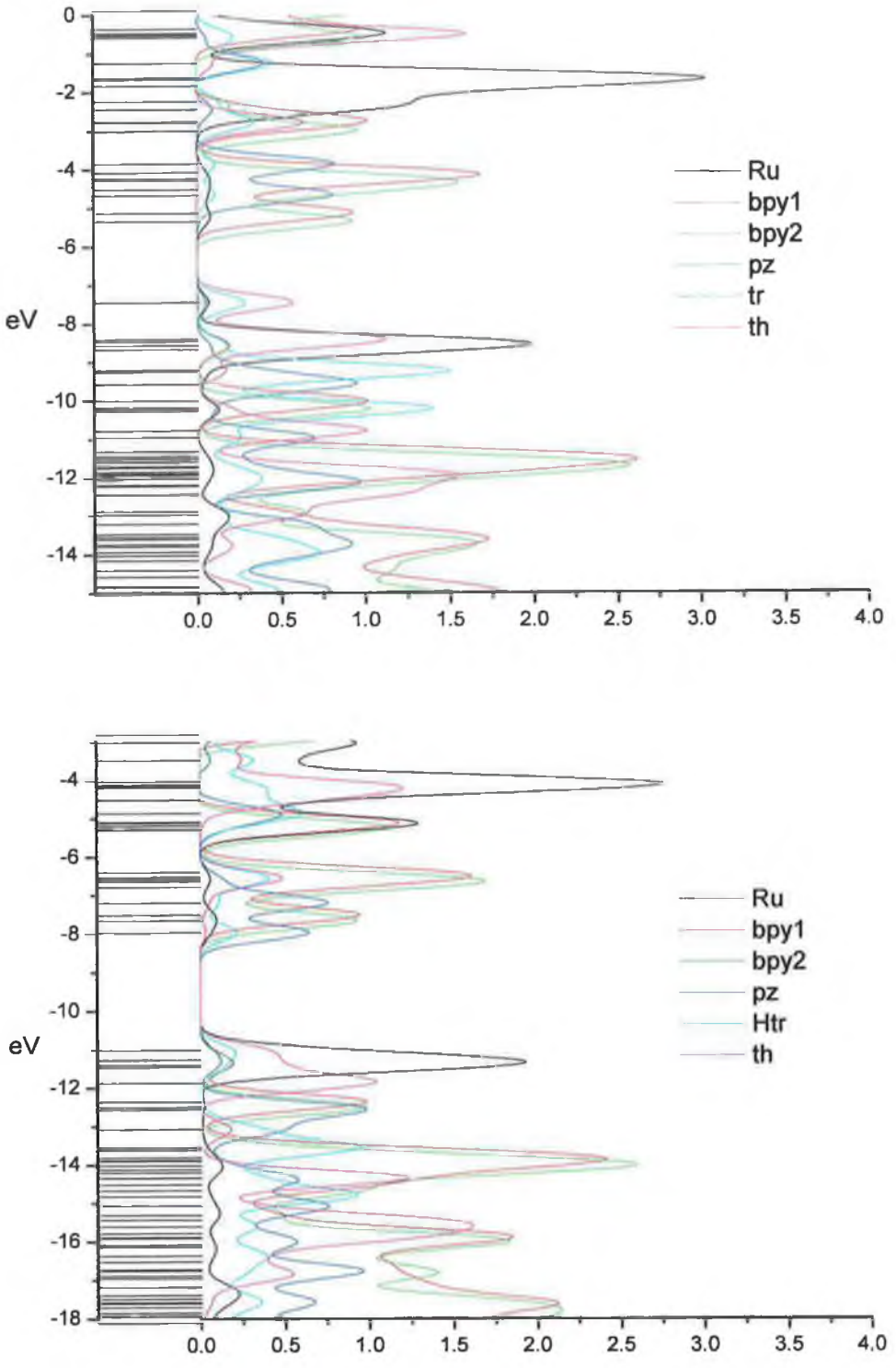

FIGURE 4.25: PDOS DIAGRAMS FOR 2P(TOP) AND H2P(BOTTOM).

the LUMO is on the bpy ligands. However, interesting results are observed for the protonated complex. The LUMO of **H1p** appears to have significant electron density on both the bpy ligands and on the Hthpytr. APPENDIX B also shows the molecular orbital population data for **1p** / **H1p**. From this it is seen that there is a large contribution from the pyridine of the thpytr ligand to the LUMO and the LUMO+3. This somewhat contradicts both the emission and Raman results *(vide supra)* as these suggest that the excited state is based on the bpy ligands for the pyridyl triazole containing complexes, irrespective of protonation state.

FIGURE 4.23 shows the PDOS for **1p** and **H1p**. As expected, protonation leads to a shifting to lower energy, reflecting the increased oxidation potential of the protonated complex (see TABLE 4.1). The energy of the pyridine orbital of the thpytr ligand is also reduced on protonation. It has a significant contribution to the LUMO frontier orbital, however it is not the lowest energy frontier orbital. The molecular orbital data (APPENDIX B) for **1p** shows that the majority of the excited state (LUMO) is located on the two bpy ligands. The PDOS also show a significant contribution to the HOMO frontier orbitals from the thiophene moiety. It is at higher energy than the metal centre for the deprotonated complex and at similar energy for the protonated complex. This does not agree with the electrochemistry results which show the first oxidation on the metal centre and the second (irreversibly) oxidation at 760 and 480 mV lower energy **1p** and **H1p**, respectively. Overall both the PDOS and isosurfaces for **1p** show that the HOMO frontier orbitals have contributions from both the Ru centre and the thiophene moiety. On protonation the energy of the metal centre is reduced, as is that of the thiophene. This leads to a reduced overlap between the Ru and thiophene for the protonated complex.

For **2p**, the HOMO is based on thiophene and triazole, with also a significant contribution from Ru (Figure 4.24). The LUMO is based on one of the bpy ligands. The same information is shown in the PDOS spectrum in Figure 4.25. In addition, the PDOS spectrum for **2p** shows that the π^* orbital of the

pyrazine ligand is at higher energy than that of the bpy. The metal-based frontier orbitals are the HOMO-2 to HOMO-4 (APPENDIX B).

In contrast, the HOMO of **H2p** has an increased contribution from the Ru centre (FIGURE 4.24). The location of the LUMO has changed from bpy to pyrazine. The PDOS spectrum shows the overall changes in electronic structure. In the protonated complex, the metal centre has a large contribution to the first four occupied orbitals (APPENDIX B). The PDOS spectrum of **H2p** is shifted to lower energy by about 3.5eV, compared to that of **2p**. This indicates the increased difficulty in removing an electron from the HOMO of **H2p**, which is due to the increased charge on the complex, in agreement with electrochemical measurements. A comparison of the PDOS spectra of **2p** and **H2p** shows that the π^* orbital of the pyrazine is shifted to lower energy on protonation, so that the LUMO is now pyrazine-based. These results are in agreement with previous emission and Raman[6] results for **4** which show that, at room temperature, the ground state is based on the bpy ligands in the deprotonated complex and switches to the pyrazine triazole ligand on protonation. Protonation also has an effect of the degree of overlap between the Ru and thiophene orbitals in the HOMO frontier orbitals. For **2p** there is a large overlap between these two moieties, however, on protonation the amount of interaction is reduced.

4.4 Discussion.

Electronic spectroscopy is the most fundamental method of investigation of the photophysical properties of a complex. UV / Vis spectroscopy allows observation of the various electron transitions possible in a complex. These can range from intraligand $\pi - \pi^*$ to Metal to Ligand Charge Transfer, which are of particular interest in Ru(II) complexes. These measurements show the energy difference between the ground state and the ^{1}MLCT. By contrast, emission spectroscopy gives information on the energy difference between the thermally equilibrated ^{3}MLCT state and the ground state.

The UV / Vis absorption properties of the complexes **1** and **2** show a close comparison with those of the analogues (**3** and **4**), but are slightly red shifted. This is due to the electron withdrawing nature of the thienyl substituent[2], reducing the electron density on the triazole containing ligand and increasing its π – acceptor ability. Upon protonation, a blue shift in the absorption spectra is observed for both complexes. For **1**, protonation results in large blue shift (~40 nm), in agreement with observations on other mononuclear pyridyl-1,2,4-triazole complexes. For **2**, protonation results in a smaller blue shift of ~ 20 nm. Protonation, for both complexes, leads to a reduction in the σ-donor ability of the triazole ligand. The energy of the metal orbitals are, therefore, reduced leading to the blue shift in the absorption spectra. The reduced shift observed in **2** is due to the increase π – acceptor ability of the pyrazine moiety on protonation of the triazole.

The emission properties again show small effects due to the substituent at the C-5 position. The thienyl group causes a red shift in the spectra due a reduction of the electron density on the thpytr / thpztr ligand. Protonation of **1** leads to a blue shift in the spectra caused by a reduction of the electron density at the metal centre. However, protonation of **2** leads to slight blue shift in the emission maximum. This is due to the switching of the location of

the emissive excited state(*vide infra*). When the excited state is located on the pyrazine triazole ligand (as in **H2**) the electron withdrawing properties of the thiophene reduces the electron density on the pyrazine and hence increases the red shift observed in this complex, relative to **4**.

The acid-base emission properties bear close comparison with related systems. The pK_a values determined for both complexes are lower than for **3** and **4**.[16] This confirms the electron withdrawing nature of the thienyl group. As is typical, the pyrazine complex is more acidic than the analogous pyridine complex, due to the greater electron withdrawing nature of the pyrazine ring.[29]

Temperature dependent spectroscopy investigates the emissive properties of complexes when the temperature is closely controlled. In present studies the temperature region between 80K – 250K is investigated. The results are compared to those obtained for similar triazole containing complexes and for Ru(II) complexes in general.

Temperature dependent emission spectroscopy of **2p** is in agreement with previous results[6] for **4**, that deprotonated complexes containing a pyrazinyl triazole moiety have two emissions at low temperatures. This, therefore, shows that dual emissive behaviour is not limited to **4** but is a feature of complexes containing a deprotonated pyrazinyl triazole ligand. This shows the ability in triazole complexes to tune certain properties, such as pK_a or redox potential, without losing the interesting excited state behaviour observed. Between 140K and 180K it is possible to resolve these emissions spectrally as both emissions are reasonably intense. For **1p** a single emission is observed, along with a vibronic band at ~ 45 nm lower energy. This is common in bpy containing complexes with vibrational progressions assignable to bpy framework vibrations.[30] This is due to an emission from $\nu'_m = 0 \rightarrow \nu_m = 1$ where ν'_m is an excited state vibrational mode and ν_m is the ground state .

For **1**, the increased electron density of the triazole ring raises the energy of the pyridine moiety in the thpytr ligand. This leads to a substantial energy difference between the pyridine triazole ligand and that of the two bpy ligands. Therefore on excitation there is a strong driving force for the THEXI state to be formed on the bpy in **1**. However, in **2** pyrazine is a better π – acceptor than pyridine. This causes the energy of the thpztr ligand to be reduced and to be similar to that of the bpy ligands. This leads to a significant Boltzmann distribution of both the $thpztr^{-\bullet}$ and $bpy^{-\bullet}$ excited states.[6] At low temperatures there is not enough energy to overcome the barrier between the two excited state and hence two THEXI states are observed. This energy barrier is contributed to by both inner and outer sphere effects. Inner sphere effects are due to the changes in nuclear distances of the ligands in the two excited states.[31] Outer sphere effects are due to the orientation of solvent molecules in the excited state.[31] When the excited state is formed on one of the ligands the solvent molecules re-orientate to accommodate this dipole. In order for the excited state to switch to another ligand the solvent would have to change its position to lower the energy of the new dipole. As the temperature is increased the solvent becomes less viscous, reducing the energy required to switch between the ligands.

Triazole complexes are pH sensitive and protonation leads to changes in their emissive properties. For **H1p** / **H1d** the complex is still singly emissive. This is confirmed by both the emission (FIGURE 4.6) and lifetime measurements (FIGURE 4.10 and APPENDIX B). Protonation of the triazole ligand in **1** does not lead to a switching of the excited state as observed for **H2p** in Raman studies. In **H1**, there is still sufficient energy difference between the bpy ligands and the pyridyl triazole ligand such that a single excited state is formed on the bpy. Protonation also leads to a decrease in the molecular dipole in the complex which in turn reduces the outer sphere barrier to thermal equilibration. The effect of the molecular dipole on excited state dynamics is examined in greater depth in Chapter 5.

Temperature dependent excited state lifetime measurements have been used to calculate the activation energies and prefactors for the deactivation of the excited states formed. The results are presented in TABLE 4.5. From these the coupling and deactivation processes can be elucidated. In general the activated processes can be separated into two categories[32]:

Category A: Small activation energies (<800 cm^{-1}) and low prefactors (<10^9 s^{-1}).
Category B: Large activation energies (>2000 cm^{-1}) and large prefactors (>10^{11} s^{-1}).

Complexes with activation energies and prefactors in category A are indicative of deactivation via a state that is only weakly coupled to the ^{3}MLCT manifold. This is similar to a state observed by Meyer and co-workers[33] in photostable Ru(II) polypyridyl complexes. It is attributed to the so called "fourth" MLCT state of increased singlet character. The calculated activation energy is therefore the energy difference between the ^{3}MLCT and the fourth MLCT. Complexes which fall into category B are deactivated via the ^{3}MC. Deactivation via the ^{3}MC may occur by a number of processes, which are outlined in FIGURE 4.26.

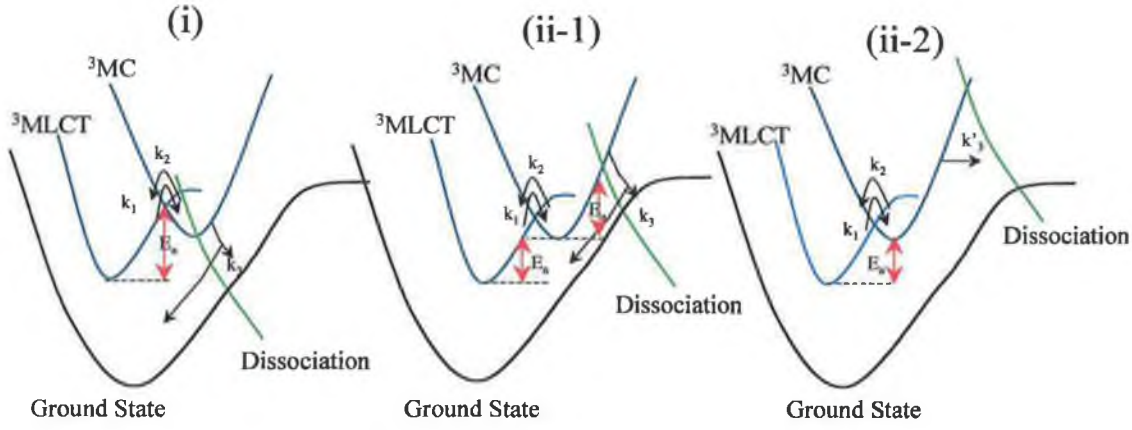

FIGURE 4.26: DEACTIVATION OF ^{3}MLCT VIA ^{3}MC STATE . LEFT SHOWS THE ACTIVATED ^{3}MC DECAY AND RIGHT IS THE NON-ACTIVATED ^{3}MC DECAY.

The processes shown in FIGURE 4.26 were highlighted by *Balzani et al.* for deactivation of the excited state via the ^3MC.[32] k_1 is the rate of crossing from the ^3MLCT to the ^3MC, k_2 is the rate of the backward process and k_3 is made up of all the processes which lead to the deactivation of the ^3MC (i.e. rate of dissociation, rate of radiationless deactivation etc.). When the ^3MC is populated from the ^3MLCT the calculated prefactors and activation energies can represent a number of deactivation pathways. When $k_3 >> k_2$ then the results reflect the surface crossing ^3MLCT to ^3MC surface crossing (Type i) and E_a is the activation energy for ^3MLCT to ^3MC surface crossing.

When $k_2 >> k_3$ then the majority contribution to the deactivation is due to decay of the ^3MC (type ii-1 or 2). There are two processes which can lead to this decay: activated and non-activated decay. For the activated process (type ii-1), the activation energy and prefactor relate the energy required to reach the dissociative state. Note that there are two contributions to the activation energy(red arrows – E_a) in this case. One contribution is the equilibration energy of the ^3MLCT and ^3MC, while the other is for the activation to the dissocative level. For the non-activated process, the activation energy represents the difference between the ^3MLCT and the ^3MC levels, while the prefactor corresponds to the non - activated ^3MC decay.

The emission observed for **1** is seen to fall into category A. Therefore, in the deprotonated state the pyridyl triazole complexes do not decay via the ^3MC, which is consistent with the increased photostability of complexes. This is attributed to the strong σ-donor properties of the triazole moiety leading to an increased ligand field splitting. These results are similar to those obtained previously[34] for **3**, in which a prefactor of 4.7×10^7 s^{-1} and an activation energy of 550 cm^{-1} were obtained.

In contrast to **1**, protonation of the triazole leads to an increase in the prefactor and activation energy of the excited state decay pathway. The

results for **H1** are close to those of category B. Protonation of the triazole leads to a reduction of its σ-donor ability. This, in turn, leads to a reduction in the ligand field splitting and hence the ^{3}MLCT – ^{3}MC energy gap. The results for the deuteriated complex, **H1d**, are within an order of magnitude of results obtained for **H3** in a previous study.[34] The prefactor and activation energy associated with type i and ii-1 are, in principle, high frequency (10^{13} – 10^{14} s^{-1}) vibrations whose activation leads to the ^{3}MLCT – ^{3}MC surface crossing region.[32] As the results for **H1** are lower than this it is thought that the excited state in the protonated complex is deactivated via a non – activated process (type ii-2) and the activation energy is the energy difference between the ^{3}MLCT and ^{3}MC.

The two emissions observed for the **2** have different temperature dependencies as seen by the large differences in their activation energies and prefactors. The lower energy emission of **2** is similar to **1**, in that its calculated properties fall into category A. This emission is, therefore, deactivated via equilibration with the fourth MLCT state of increase singlet character. The activation energy is the energy difference (280 cm^{-1}) between the two states. By comparison with previous results[6] it is though that this state is bpy based.

The second emissive state, at higher energy, has a prefactor and activation energy which leads it to be in the category B. The frequency of the vibrations associated with the prefactor are not sufficiently large to lead to the ^{3}MLCT – ^{3}MC crossing region (as with **H1**). Therefore deactivation of the higher energy of **2p** is via non-activated crossing from the ^{3}MC.

Transient absorption spectra are vital in the interpretation of excited state resonance Raman measurements. They allow selection of the appropriate excitation wavelength in transient resonance Raman measurement so that the excited state absorption is probed. FIGURE 4.11 and FIGURE 4.12 show that **1** and **2** both have an absorption at 355 nm region indicating that the excited states of both complexes are indeed being probed with resonance

enhancement. If there was not a sufficient absorption for resonance enhancement of the excited state, the TR^2 measurements may only produce spectra with ground state bands. This may lead to the misinterpretation that no excited state is formed.

For **1p** the bleach between 440 and 500 nm is due to a loss of the ^{1}MLCT ground state absorption. This is due to excitation from the Ru(II) centre[22] and depletion of this band indicates that there is no Ru(II) present in the excited state. The excited state band centred at 390 nm is due to π to π* absorption of the ligand. The LMCT absorption observed at higher wavelengths is due to bpy to Ru(III) LMCT.[22] This again shows that the Ru(II) metal centre is oxidised on photoexcitation. Results for **2p** are in agreement with those obtained for **1p**, with a bleach observed due to depletion of the ^{1}MLCT absorption and the appearance of absorptions due to ligand based π to π* and LMCT. Again, there is a sufficient absorption in the excited state at 355 nm to allow resonance enhancement in the excited state.

In the present work Raman measurements have been used to overview allowed vibrational bands in the complexes while resonance Raman measurements probe the nature of the absorption bands. When excitation is used that is close in energy to that of an absorption band, the vibrations of the moiety responsible for this absorption are increased by a factor of 10^6. Transient resonance Raman (TR^2) investigates the excited state of the complex as it uses the trailing edge of a laser pulse to probe the excited state which is formed by the leading edge of the same pulse. In TR^2, the resonance effect (*vide supra*) is also used to enhance the bands of the excited state moiety.

Resonance Raman measurements of **1p/d** and **H1p/d** show that the ^{1}MLCT for pyridyl triazole containing complexes is bpy based. This is in agreement with previous results[16] and is due to the added electron density of the triazole moiety increasing the excited state energy level of the ligand. For complexes

2p/d and **H2p/d**, the ^{1}MLCT absorption band is due to an overlap of the pyrazinyl and the bpy based absorptions.[16] The high electron density of the triazole ligand increases the energy of the pyridyl and pyrazinyl moieties attached to it in **1**/**H1** and **2**/**H2**, respectively. However, since the pyrazinyl moiety is a better π – acceptor than the pyridine its energy is still low enough to overlap with the bpy ligands in the absorption spectra.

Transient resonance Raman spectra show bands due to both the excited and ground state of the complexes investigated. The absence of excited state peaks for the thpytr ligands in **1** and **H1** indicate that the excited state is based on the bpy ligands irrespective of protonation state for the pyridyl complexes. For both **1** and **H1** bands for the bpy radical are observed at 1285 and 1212 cm^{-1}. **2** also produces spectra which do not contain any excited state triazole bands, with the bands for bpy^- still present at 1285 and 1212 cm^{-1}. This indicates that the excited state in the deprotonated pyrazinyl triazole complex (**H2**) is also bpy based at room temperature. However, in **H2p** bands due to $Hthpztr^-$ only are observable at 1493 and 1431 cm^{-1}. Although these bands may be overlapping with neutral bpy bands, the absence of the bpy radical bands confirm that the excited state is no longer located on the bpy.[6] This indicates the switching of the excited state from the bpy ligand to the triazole containing ligand on protonation in **H2**. This further indicates the subtle energy balance that is apparent in the pyrazinyl complexes which is not replicated for the pyridine moiety.

Computational methods can be used to investigate a number of properties of chemical interest such as reactivity and hardness.[35] The present studies focus on complimenting experimental work and results are presented for the partial density of states and HOMO-LUMO gap.

DFT calculations highlight the contrast in the degree of interaction between the metal centre and the thienyl moiety in the ground and excited states. In the ground state, **2p** shows contributions from both the thienyl and the Ru in

the levels H-4 to HOMO, which may be considered the occupied frontier orbitals. However, in the excited state the unoccupied frontier orbitals, LUMO to LUMO+4, show contributions from the bpy moieties but little or no contributions from the Ru and thienyl. A similar picture emerges for **1**. The degree of interaction appears to be reduced for **H1** and **H2**, upon protonation of the triazole. On protonation the energy of both the Ru(II) centre and the thienyl containing ligands is reduced, leading to a decrease in the overlap of these moieties in the HOMO frontier orbitals. Previous studies of thienyl bridged mixed valence dimers[12] have suggested that interaction is due to HOMO assisted superexchange. The contribution from the Ru(II) and thienyl moieties to the HOMO frontier orbitals are in agreement with this proposal. This, therefore, suggests that interaction in these triazole bridged dyads occurs via hole transfer mechanism which is promoted by the negative charge on the triazole. The effect of protonation to reduce the level of interaction also suggest that the negatively charged triazole is important for communication in the dyad. The interaction is not solely dependent on the triazole ligands as studies of phenyl[12] and dimethoxyphenyl[1(d)] bridged complexes show weak interaction, in both protonation states, due to the slight electron withdrawing nature of this substituent. It is also important the note that the pyridine / pyrazine which is attached to the triazole is largely a spectator in the HOMO assisted process. This highlights the varying role which ligands play in the ground and excited state and, once again, the importance of treating the ground and excited state complexes as different species.

The frontier orbitals the shown in FIGURE 4.22 – FIGURE 4.25 may also be related to the electrochemistry of the complexes (TABLE 4.1).[12] For the protonated complexes, **H1** and **H2**, there is an overlap between the metal centre and the electron – rich thiophene moiety. This indicates that the metal and ligand oxidation potentials should be similar. However, this does not agree with electrochemical results which shows the irreversible ligand based oxidations at 480 mV and 320 mV higher energy for **H1** and **H2**, respectively. Upon deprotonation the energy of the metal orbitals are seen to decrease due

to the reduced σ – donor ability of the triazole. The energy of the thiophene is seen to remain relatively unchanged and, therefore, appears to be the higher energy moiety in the HOMO. This is not reflected in the electrochemical results (TABLE 4.1) in which the energy difference between the reversible (metal – based) and irreversible (ligand – based) oxidations increases to 760 mV and 500 mV for **1** and **2**, respectively. It therefore appears that DFT calculations do not agree well with the experimental results. The reason for this is unclear, although it is in agreement with previous results[36] in which DFT did not accurately predict the ordering of metal – based oxidation potentials for a series of Ru(II) triazole complexes.

Computational data helps to rationalise the mode of interaction between the Ru(II) centre and the thienyl moiety, and by extension, between two metal centres. The lack of contribution of the thienyl moiety to the frontier orbitals of the LUMO indicates that the presence of C-5 substitution does not effect the excited state properties of the complex, in agreement with emission and lifetime results. Again the computational data aids in understanding how C-5 substitution affects electrochemical, but not temperature dependent emissive, properties.

The calculated isosurfaces for the LUMO and LUMO+1 have been used to approximate the location of the ^{3}MLCT excited state in **1p**, **H1p**, **2p** and **H2p**. There are a number of assumptions which must be borne in mind, namely: that the virtual Kohn-Sham orbitals from the DFT calculations are equivalent to unoccupied orbitals; that the lowest energy transition is to the lowest unoccupied orbitals; and that the ^{1}MLCT is located on the same ligands as the ^{3}MLCT state.

The effect of deuteriation may also be used to predicted the location of the excited state in heteroleptic complexes.[37] If the excited state is located on the ligand which has been deuteriated then the excited state lifetime is seen to increase. For **1p**, **H1p** and **2p** the electron density of the LUMO is based

predominantly on the bpy ligands (see FIGURE 4.22 and FIGURE 4.24). For both **1p** and **2p** deuteriation of the bpy ligands lead to an increase in lifetime of at least 20% (see TABLE 4.1). A reduction in lifetime is observed for **H1p**, however this complex is weakly emissive in acetonitrile at room temperature and, therefore, the result is prone to error. For **H2p**, computational studies predict that the excited state will be based on the pyrazine-triazole ligand. As would be expected, deuteriation of the bpy ligands in this complex has little effect on the excited state lifetime in this case (TABLE 4.1) with the change being well within experimental error(± 5%). Therefore, computational chemistry appears well able to predict the location of excited state electron density and the assumptions proposed in the preceding paragraph are valid.

4.5 Conclusion.

This chapter serves as the first introduction to dual emission in the present work. The results obtained in this chapter offer an increased understanding of the dual emission observed for Ru(II) complexes containing a pyrazinyl triazole ligand and are in agreement with those obtained by Keyes *et al.*[6] The persistence of this phenomenon on substitution of the triazole shows that the behaviour is not confined to the complex $[Ru(bpy)_2(pztr)]^+$. This information allows the possibility to design complexes with emissive and redox properties tailored for specific uses in supramolecular assemblies. The ability to control emissive properties via the ^{3}MLCT – ^{3}MC energy gap, as opposed to simply that of the ^{3}MLCT – ground state as highlighted in the energy gap law, is also investigated via the rate of excited state deactivation. It is also important to note how the temperature dependent emission and lifetime studies are used to compliment one another and gain a more definitive view of the processes occurring. The effect of protonation on both these deactivation pathways is useful as it provides a basis for easily controlled molecular switching. Shown in FIGURE 4.27 is the excited state structure of **1P**. Based on the emission energies at 140K the pyrazine based ^{3}MLCT and the bpy based ^{3}MLCT are separated by 1445 cm^{-1}. This is similar to the activation energy of the obtained from the temperature dependent lifetime studies (1500 cm^{-1}) of the higher energy process. However, it should be remember that since the pyrazine ^{3}MLCT is at higher energy at all times, equilibration of this ^{3}MLCT with that of the bpy is always possible but is restricted by inner and outer sphere effects. The energy difference between the lower bpy based ^{3}MLCT and the ^{3}MC is almost 3000 cm^{-1} (this consists of the ^{3}MLCT bpy to ^{3}MLCT pyrazine energy difference and the activation of the ^{3}MLCT pyrazine process) which would account for the photostability of the deprotonated complex.

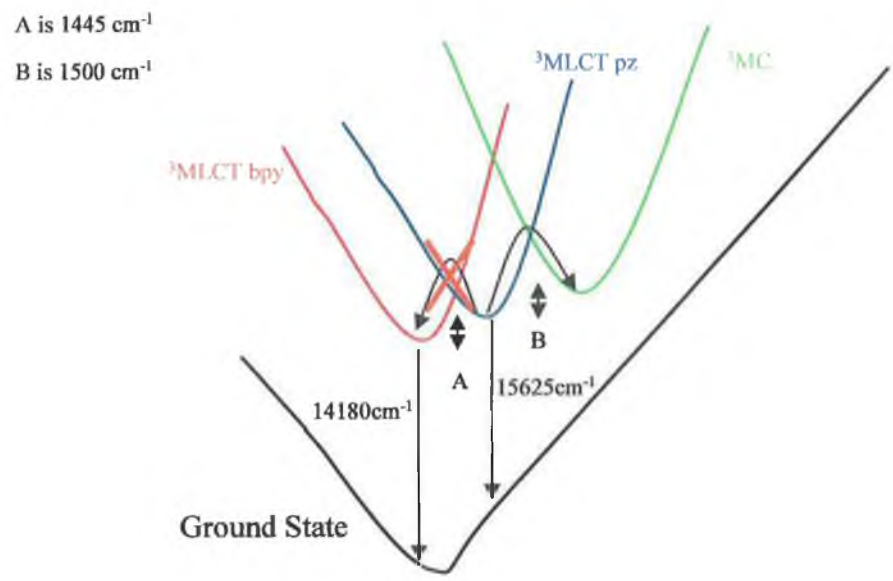

FIGURE 4.27: EXCITED STATE STRUCTURE OF $[RU(BPY)_2(THPZTR)]^+$, 2P.

The results also allow for a more detailed understanding of the nature of the interaction between the thienyl and ruthenium(II) – based components of these complexes, which may also be regarded as simple dyads. Although it is tempting to consider the thienyl group as an innocent part of the Hpytrth and Hpztrth ligands (as is suggested from the temperature dependent emission results), in electronic terms such a simplification is not appropriate for understanding the overall properties of the systems. It is clear that in the ground state there is significant interaction between the metal centre and the thiophene moiety. However, in the excited state the effect of the thiophene is minimised as seen by the emission properties of the complexes. It is clear from examination of the properties of the complexes in their ground and THEXI electronic states that the degree of interaction between the components is critically dependent on the electronic state (*i.e.*, ground or excited) and that extrapolating conclusions based on study of ground state interaction to excited state systems is not always justified. This information is then extended to dinuclear complexes in the hope of further understanding metal – metal communication in systems with the potential to act as modulators of excited state energy.

4.6 Bibliography.

[1] (a) Buchanan, B.E., Vos, J.G., Kaneko, M., van der Putten, W.J.M., Kelly, J.M., Hage, R., de Graaff, R.A.G., Prins, R., Haasnoot, J.G., Reedijk, J., *Dalton Trans.*, **1990**, *8*, 2425. (b) Fanni, S., Murphhy, S., Killeen, J.S., Vos, J.G., *Inorg. Chem.*, **2000**, *39*, 1320. (c) Browne, W.R., Heek, P., Gallagher, J.F., O'Connor, C.M., Killeen, J.S., Aoki, F., Ishida, H., Inoue, Y., Villani, C., Vos, J.G., *Dalton Trans.*, **2003**, 2597. (d) Passaniti, P., Browne, W.R., Lynch, F.C., Hughes, D., Nieuwenhuyzen, M., James, P., Maestri, M., Vos, J.G., *Dalton Trans.*, **2002**, *8*, 1740.

[2] Gilchrist, T.L., Heterocyclic Chemistry, Wiley, **1985**.

[3] (a) Ulman, A., Thin Films: Self – Assembled Monolayer of Thiol (Thin Films), Academic Press, **1998**. (b) Kang, J. F., Liao, S., Jordan, R., Ulman, A., *J. Am. Chem. Soc.*, **1998**, *120*, 9662.

[4] Hage, R., Haasnoot, J.G., Reedijk, J., Wang, R., Vos, J.G., *J. Am. Chem. Soc.*, **1991**, *30*, 3263.

[5] Hage, R., Prins, R., Haasnoot, J.G., Reedijk, J., Vos, J.G., *Dalton Trans.*, **1987**, *6*, 1389.

[6] Keyes, T.E., O'Connor, C.M., O'Dywer, U., Coates, C.G., Callaghan, P., McGarvey, J.J., Vos, J.G., *J. Phys. Chem. A*, **1999**, *103*, 8915.

[7] Balzani, V., Scandola, S., Supramolecular Photochemistry, Ellis Horwood, **1991**.

[8] Low, P.J., *Dalton Trans.*, **2005**, 2821.

[9] Kalyanasundaram, K., Photochemistry Of Polypyridine amd Porphyrin Complexes, Academic Press, **1992**.

[10] Creutz, C., Taube, H., *J. Am. Chem. Soc.*, **1969**, *91*, 3988.

[11] Guckian, A.L., Doering, M., Ciesielski, M., Walter, O., Hjelm, J., O'Boyle, N.M., Henry, W., Browne, W.R., McGarvey, J.J., Vos, J.G., *Dalton Trans.*, **2004**, *23*, 3943.

[12] Browne, W.R., Weldon, F., Guckian, A., Vos, J.G., *Collect. Czech. Chem. Commun.*, **2003**, *68*, 1467.

[13] Browne, W.R., Vos, J.G., *Coord. Chem. Rev.*, **2001**, *219*, 761 and references therein.

[14] Buchanan, B.E., Wang, R., Vos, J.G., Hage, R., Haasnoot, J.G., Reedijk, *Inorg. Chem.*, **1990**, *29*, 3263

[15] Hage, R., Haasnoot, J.G., Nieuwenhuis, H.A., Reedijk, J., Wang, R., Vos, J.G., *Dalton Trans.*, *12*, 1991, 3271.

[16] Henry, W., Browne, W.R., Royayne, K.L., O'Boyle, N.M., Vos, J.G., McGarvey, J.J., *J. Mol. Struct.*, **2005**, *735-736*, 123-134.

[17] Hage, R., Ph.D. Thesis, Leiden University, **1992**.

[18] Nieuwenhuis, H.A., Haasnoot, J.G., Hage, R., Reedijk, J., Snoeck,T.L., Stufkens, D.J., Vos, J.G., *Inorg. Chem.*, **1991**, *30*, 48.

[19] Browne, W.R., O'Connor, C.M., Hughes, H.P., Hage, R., Walter, O., Doering, M., Gallagher, J.F., Vos, J.G., *Dalton Trans.*, **2002**, *21*, 4048.

[20] Damrauer, N.H., McClusker, J.K., *Inorg. Chem.*, **1999**, *38*, 4268 – 4277.

[21] Keyes, T.E., O'Connor, C.M., Vos, J.G., *Chem. Commun.*, **1998**, *8*, 889 – 890.

[22] Creutz, C., Chou, M., Netzel, T.L., Okumura, M., *J. Am. Chem. Soc.*, **1980**, *102*, 1309.; Browne, W.R., O'Boyle, N.M., Henry. W., Guckian, A.L., Horn, S., Fett, T., O'Connor, C.M., Duati, M., De Cola, L., Coates, C.G., Ronayne, K.L., McGarvey, J.J., Vos, J.G., *J. Am. Chem. Soc.*, **2005**, *127*, 1229.

[23] Ferraro, J.R., Introductory Raman Spectroscopy, Academic Press, **1994**.

[24] [H8]-bpy bands observed in the spectrum of [Ru(bpy)2(thpztr)]+, 2p, at 1598, 1483, 1312, 1269 and 1030 cm-1.

[25] (a) Yersin, H., Humbs, W., Strasser, J., *Topics Curr. Chem.*, **1997**, *191*, 154. (b) Resen, H., Krauz, E., *Comments Coord. Chem.*, **1995**, *18*, 27.

[26] (a) Coates, C.G., Keyes, T.E., Hughes, H.P., Jayaweera, P.M., McGarvey, J.J., Vos, J.G., *J. Phys. Chem.*, **1998**, *102*, 501. (b) Danzer, G.D., Kincaid, J.R., *J. Phys. Chem.*, **1990**, *94*, 3976. (c) Danazer, G.D., Golus, J.A., Kincaid, J.R., *J. Am. Chem. Soc.*, **1993**, *115*, 8643.

[27] (a) Nazeeruddin, M. K., Zakeeruddin, S. M., Kalyananundaram, K., *J. Phys. Chem.*, **1993**, *97*, 9607. (b) Kalyananundaram, K., Zakeeruddin, S. M., Nazeeruddin, M. K., *Coord. Chem. Rev.*, **1994**, *132*, 259.

[28] (a) Fanni, S., Murphy, S., Killeen, J.S., Vos, J.G., *Inorg. Chem.*, **2000**, *39*, 1320. (b) O'Boyle, N.M., Ph.D. Thesis, Chapter 3, Dublin City University, **2004**.

[29] Meyer, T.J., *Pure Appl. Chem.*, **1990**, *62*, 1003.

[30] Caspar, J.V., Meyer, T.J., *Inorg. Chem.*, **1983**, 22, 2444.

[31] Cruetz, C., Sutin, N., *J. Chem. Ed.*, **1983**, *10*, 60, 809.

[32] Barigelletti, F., Juris, A., Balzani, V., Belser, P., von Zelewsky, A., *Coord. Chem. Rev.*, **1988**, *84*, 85.

[33] Kober, E.M., Meyer, T.J., *Inorg. Chem.*, **1984**, *23*, 3877.

[34] Wang, R., Vos, J.G., Schmehl, R.H., Hage, R., *J. Am. Chem. Soc.*, **1992**, *114*, 1964.

[35] (a) Parr, R.G., Yang, W.J., *J. Phys. Chem.*, **1984**, *106*, 4049. (b) Tissandier, M.D., Cowen, K.A., Feng, W.Y., Gundlach, M.H., Earhart, A.D., Coe, J.V., Tuttle Jr., T.R., *J. Phys. Chem. A*, **1998**, *102*, 7787.

[36] Ph.D. Thesis, O'Boyle, N.M., Dublin City University, **2004**.

[37] Browne, W.R., Vos, J.G., *Coord. Chem. Rev.*, **2001**, *219*, 761 and references therein.

Chapter 5

Photophysical Investigation of Complexes of the Type [Ru(LL)2(pztr)]+

Chapter 5 investigates the photophysical properties of pyrazine triazole complexes with a variety of LL ligands. Both the emissive and the absorption properties are investigated. The absorption properties are investigated using Raman spectroscopy (both steady state and transient) and transient absorption. Temperature dependent emission and single photon counting studies are used to investigate the emissive properties. Emission from two excited states is seen for deprotonated phenanthroline containing complex at low temperature. In contrast, for the complexes containing the biquinoline and diphenylphenanthroline ligands only a single emission is observed in both the protonated and deprotonated state. The results obtained are compared to those observed for the bipyridine analogues.

Computational studies have also been undertaken to gain further insight into the photophysical processes and the energies of the excited states present in the complexes.

5.1 Introduction.

The ability to tailor the chemical and physical properties of complexes is central to their incorporation into larger supramolecular systems. A wide range of properties are required depending on the overall aim of the molecular device. For example, the antenna or light harvesting portion of a solar energy device would require good absorption over the visible spectrum, while at the reaction centre of a photocatalyst the stability of both the oxidised and reduced states is more important.[1,2] In order to provide maximum control over these properties a variety of mono, bis and tris – chelating ligands have been investigated by photo – chemical and – physical studies. The most extensively used monochelates include chloro, amino and pyridyl ligands. While bischelate ligands are the most predominate of those studied as a number of trischelate ligands such as terpyridine[3] have also been studied. Although investigations into the applications of tris – chelated Ru(II) complexes are ongoing, the photostabilty of the complexes, prompted by the bite angle of the ligands, remains a major drawback.[4]

While $[Ru(bpy)_3]^{2+}$ is by far the most studied and best understood of all the Ru(II) complexes, other homoleptics have also received significant attention.[5] The majority of the ligands used in these investigations are structurally analogous to 2,2′ – bipyridine (bpy) in an attempt to copy its beneficial properties while trying to minimise its shortcomings. The emission studies which have been carried out have not only investigated the electron donating and withdrawing effects of the substituents but also the positional dependence and steric effects.[6] Some of the substituents employed have included chloro[7], methyl[8], bromo[9] and carboxy[10] groups. Table 5.1 shows results obtained for a selection of substituted complexes.[5,11] For the majority of substituents employed the changes are seen to be quite minor.

LL	Absorption (nm)	Emission (nm)	Lifetime (μs)
Bpy[8]	452	615	1.10
3,3′ – Me_2 – bpy[8]	456	625	0.21
4,4′ – Cl_2 – bpy[7]	462	632	0.48
4 – NO_2 – bpy[7]	480	700	0.12
4,4′ – diphenyl - bpy[12]	474	638	0.67[#]
Phen[13]	442	604	0.46

TABLE 5.1: SELECTED PHOTOPHYSICAL PROPERTIES OF $[RU(LL)_3]^{2+}$ COMPLEXES. MEASUREMENTS ARE IN ACETONITRILE OR WATER[#].

The second most widely studied ligand in Ru(II) photochemistry is most probably 1,10-phenanthroline. Homoleptic complexes of this ligand have many of the same photophysical properties as that of bpy (see Table 5.1). Complexes of the type $[Ru(LL)_2(dppz)]^{2+}$ (where dppz is dipyrido-[3,2-a:2′,3′-c]phenazine and LL is bpy or phen) have been thoroughly investigated due to the "light – switch" effect where the complexes are non – emissive in H_2O but are strongly luminescent in aqueous DNA solutions.[14] The addition of a phenyl group at the 4,4′ position of the bpy ligand was shown to have a large effect on the photophysical properties of the homoleptic complex by McCusker[6] *et al.* By comparing $[Ru(dpb)_3]^{2+}$ (where dpb is 4,4′ – diphenyl – 2,2′ – bipyridine) with those that were increasingly sterically hindered, this work showed that the ability of the phenyl rings to move into the plane of the bpy ligand in the excited state and increase the quantum yield and lifetime of this complex.

The increased π – acceptor properties of the biquinoline ligand results in the deep purple colour of the complex $[Ru(biq)_3]^{2+}$ (where biq is 2,2′ – biquinoline). The ability of this complex to absorb over a wide range of the visible spectrum has lead to interest in the incorporation of this ligand in to photo – driven devices. However, the weak σ – donor properties of this ligand also results in reduction of its photostabilty in comparison to other Ru(II) complexes.

Ligands containing a 1,2,4 – triazole moiety have been the focus of attention for the Vos research group for quite some time. The presence of more than one nitrogen makes this ligand suitable as a bridging moiety in multinuclear complexes. In mononuclear complexes the free nitrogens allow the possibility of pH dependent photo – physics and – chemistry. In the deprotonated state the increased electron density of the triazole resulted in an increased ^{3}MLCT – ^{3}MC energy gap and hence photostabilty.

Bis – chelating ligands containing a triazole moiety initially incorporated a pyridine. These complexes showed increased photostabilty compared to their bipyridine analogues and the ability to control their properties with pH.[15] The pyrazine triazole ligand was subsequently studied with the complex $[Ru(bpy)_2(pztr)]^+$ (where pztr is 2-(1,2,4-triazol-3-yl)-pyrazine) showing interesting emissive properties at low temperatures.[19] This complex was shown to emit from both the pyrazine and bipyridine ligands between the 140 and 200K. Due to the similarity in energy of the two ligands there was little driving force for the equilibration of all the excited state energy on a either of the ligands. At low temperatures, there was insufficient thermal energy to overcome the barriers to equilibration. The observation of only a single emission for the protonated complex showed that this effect was not due to experimental artefacts, and also highlighted the temperature and pH dependent photophysics of triazole containing complexes.

Figure 5.1 gives the structures of the ligands discussed in the text of the current chapter.

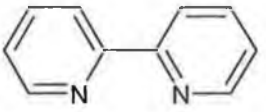

2,2' - bipyridine (bpy)

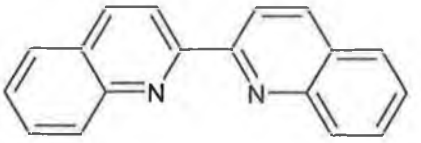

2,2' - biquinoline (biq)

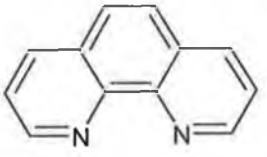

1,10 - phenanthroline (phen)

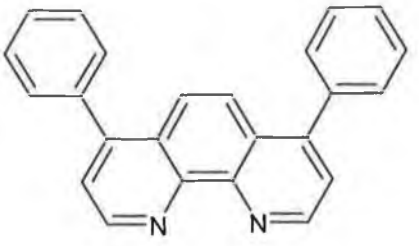

4,7 - diphenyl 1,10 - phenanthroline (dpp)

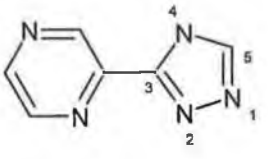

[1,2,4]-triazol-3-yl-pyrazine (pztr)

FIGURE 5.1: STRUCTURE OF LIGANDS DISCUSSED IN THE TEXT.

Throughout this work the previous results obtained for $[Ru(bpy)_2(pztr)]^+$ are presented for comparison. In all sections the results for the biq containing complexes are given first followed by those for phen and finally those of $[Ru(dpp)_2(pztr)]^+$. The sections have been structured in this manner as $[Ru(biq)_2(pztr)]^+$ is seen to be singly emissive and, as such, shows a temperature dependent behaviour which would be more familiar to the reader. Next, the biexponential excited state decay and dual emission of $[Ru(phen)_2(pztr)]^+$ introduces the phenomenon of two non – equilibrated excited states. Finally the results obtained for the dpp containing complex are surprising and raise some interesting points about the causes of dual emissive behaviour.

5.2 Experimental Part.

The complexes $[Ru(biq)_2(pztr)]^+$, $[Ru(phen)_2(pztr)]^+$ and their deutomers were synthesised by Dr. Christine O'Connor. The complete syntheses can be found in her thesis.[16] $[Ru(dpp)_2(pztr)]^+$ and its deuteomers were obtained from Dr. Wesley Browne.[20] CHN analysis and ^1H NMR of the complexes are found in the relavant theses. Deuteriation of ligands was carried out by previously published methods.[17] Briefly perprotio samples were heated to ~ 200 °C under pressure in D_2O in the presence of 10% w/w Pd / C catalyst.

The experimental methods used are outlined in Chapter 2.

5.3 Results.

The work presented in the current chapter seeks to investigate the photophysical properties of complexes containing pyrazine triazole ligands in conjunction with alternative symmetrical diimine ligands (sometimes referred to as LL ligands). The ligands have been selected for a number of reasons. The biq ligand is a stronger π – acceptor and weaker σ – donor than bpy and is, therefore, expected to change the relative energies of the two possible ^{3}MLCT states, and the ^{3}MLCT and ^{3}MC energy gap. In contrast, the phen ligand has very similar donor / acceptor properties to bpy. The dpp ligand has similar donor and acceptor properties as phen (and hence bpy) but previous studies have shown that the ability of the phenyl rings to cant and form a large delocalised excited state has a significant effect on the emissive properties.[6] The intention of this study is to use a variety of techniques to gain an understanding of the processes which lead to the formation and deactivation of the excited state. An overview of the excited state properties is initially presented in the form of steady state electronic spectroscopy. The temperature dependent emission spectroscopy results are then presented so as to observe the effect of the LL ligands on the dual emission phenomenon. The ligands which contribute to the formation of the excited state are then investigated using transient absorption and resonance Raman techniques. Finally, the results of computational studies are given. This work is intended as an *a priori* studies in order to gain further information on the experimental results already obtained. Deuteriation has also been used in this work to a large extent, with it being particularly valuable to aid in the assignment of bands in vibrational spectroscopy studies. Selective deuteriation of ligands also allows prediction of the location of the excited state.[17]

5.3.1 Steady State Electronic Spectroscopy.

TABLE 5.2 provides the photophysical data obtained for the complexes discussed in the text. Also included are the results obtained previously for $[Ru(bpy)_2(pztr)]^+$ for comparison. The lowest energy absorptions reported below are assigned as due to several overlapping metal – to – ligand charge transfer (MLCT) transitions, by comparison with other Ru(II) complexes[18] and on the basis of the Raman spectra obtained (*vide infra*). The spectra of these complexes also show transitions in the 200 – 300 nm range which are $\pi - \pi^*$ in nature. The spectra are comparable to their homoleptic analogues and other pyrazine – triazole complexes. The ground state spectra are given in APPENDIX C-9.

	λ_{Abs} /nm (log ε)[a]	E_{ox} (V vs SCE)	λ_{max} 293K (nm)[a]	λ_{max} 77K (nm)[b]	$\tau_{298\,K}$ (ns)[a]	Reference
$Ru(bpy)_2(pztr)]^+$	445 (3.18)	1.01	668	600	230	16, 19
$Ru(bpy)_2(Hpztr)]^{2+}$	441 (4.12)	1.25	658	619	230	16, 19
$Ru(biq)_2(pztr)]^+$	576 (4.10)	1.02	782	742	220	16
$Ru(biq)_2(Hpztr)]^{2+}$	550 (3.67)	---	746	720	---	16
$Ru(phen)_2(pztr)]^+$	430 (3.68)	0.87	654	587	130	16
$Ru(phen)_2(Hpztr)]^{2+}$	415 (3.79)	---	642	565	---	16
$Ru(dpp)_2(pztr)]^+$	440	0.93	665	610	---	20
$Ru(dpp)_2(Hpztr)]^{2+}$	430	---	650	624	---	

TABLE 5.2: PHOTOPHYSICAL PROPERTIES OF COMPLEXES DISCUSSED IN THE TEXT. A) IN ACETONITRILE, B) IN ETHANOL: METHANOL (4:1).

The absorption spectra of all complexes are seen to undergo a hypsochromic shift on protonation. The energy of the main absorption bands of both $[Ru(phen)_2(pztr)]^+$ and $[Ru(dpp)_2(pztr)]^+$ are quite similar. However the biq containing complex is seen to be red – shifted by ~ 6,000 cm^{-1}.

The complexes are emissive at room temperature in acetonitrile and at 77K in an Ethanol: Methanol glass. Again, the energy of the biq transition is seen to be red – shifted in comparison to both the phen and dpp containing complexes at room temperature and at 77K. At low temperatures all the complexes are

strongly emissive with their emission maxima blue – shifted when compared to 293K.

The oxidation potential of the complexes are also presented. The oxidation potential of the phen and dpp complexes are similar, with the biq containing complexes shifted to a higher potential. The redox potentials of the protonated complexes were not obtained due to problems with deposition on the electrodes in these measurements.

5.3.2 Temperature Dependent Emission Spectroscopy.

Temperature dependent studies have been to be important probes of excited state structure. Early investigations into the manifold of excited states present in $[Ru(bpy)_3]^{2+}$ used the fine structure of very low temperature (< 10K) emission measurements to obtain energy differences and quantum yields between the states.[21] At higher temperatures (77 – 150K) the restriction of solvent reorientation in glass matrices can be used to model ultrafast processes.[22] In the present work temperature dependent studies are used to limit the amount of energy available for molecules to overcome the barriers between difference states and hence obtain more information on the excited state structure.

5.3.2.1 Temperature Dependent Emission Spectroscopy.

As noted in the introduction the complex $[Ru(bpy)_2(pztr)]^+$ was seen to be dual emissive at low temperatures due to two non – equilibrated excited states.[19] This was discovered via temperature dependent emission spectroscopy which showed the presence of two emissions with differing temperature dependencies. The present section investigates the complexes containing the dpp, biq and phen ligands under the same conditions. For $[Ru(bpy)_2(pztr)]^+$ bi-exponential excited state decay was only observed for the deprotonated complex while the protonated complex $(Ru(bpy)_2(Hpztr)]^{2+}$)

showed "normal" mono-exponential decays attributed to a single excited state moiety. In the present study attempts were made to study both the protonated and deprotonated complexes.

The emission spectra given below show red shifting of the excited state emission maxima on increasing temperature, accompanied by a concurrent decrease in emission intensity. This is as expected and is due to the softening of the glass matrix and the subsequent increase of its ability to stabilise the excited state.

FIGURE 5.2 gives the temperature dependent emission spectra of $[Ru(biq)_2(pztr)]^+$ in EtOH: MeOH (4:1) between 80 K and 200 K. The spectra on the right highlight the temperature range between 140 K and 200 K which is above the glass transition temperature for this solvent matrix. Above 140 K it is assumed that the solvent is fluid, the glass matrix is no longer present and the effects of matrix inhomogeneities can be discounted from any results obtained. Matrix inhomogeneities refer to localised differences in solvent configurations which lead to variations in the energies of the excited state formed in molecules at these positions. As noted in the preceding section the emission band of the biq-containing complex is red – shifted compared to that of the phen and dpp complexes. As the temperature is increased its emission intensity decreases and the energy is red – shifted. For this complex a shoulder is not observed on the main band at any temperature. Also observable is an emission at ~ 600 nm at lower temperature which is due to scatter. From these spectra it appears that there is a single emissive excited state in $[Ru(biq)_2(pztr)]^+$.

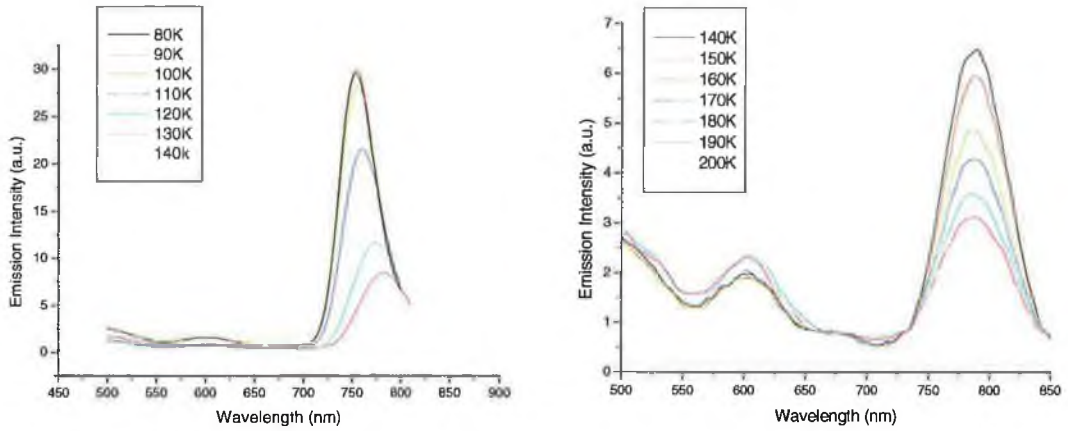

FIGURE 5.2: TEMPERATURE DEPENDENT EMISSION OF $[Ru(biq)_2(pztr)]^+$ IN ETOH: MEOH (4:1) BETWEEN (LEFT) 80K AND 140K, (RIGHT) 140K AND 200K.

FIGURE 5.3 shows the temperature dependent emission spectra of the protonated complex, $[Ru(biq)_2(Hpztr)]^{2+}$. The emission maxima for this complex are blue – shifted compared to the deprotonated complex. Again, increasing temperature results in a red – shift of emission maximum and a decrease in intensity. As with the deprotonated complex no shoulder is observed on the main band at any temperature which indicates a single emissive excited state.

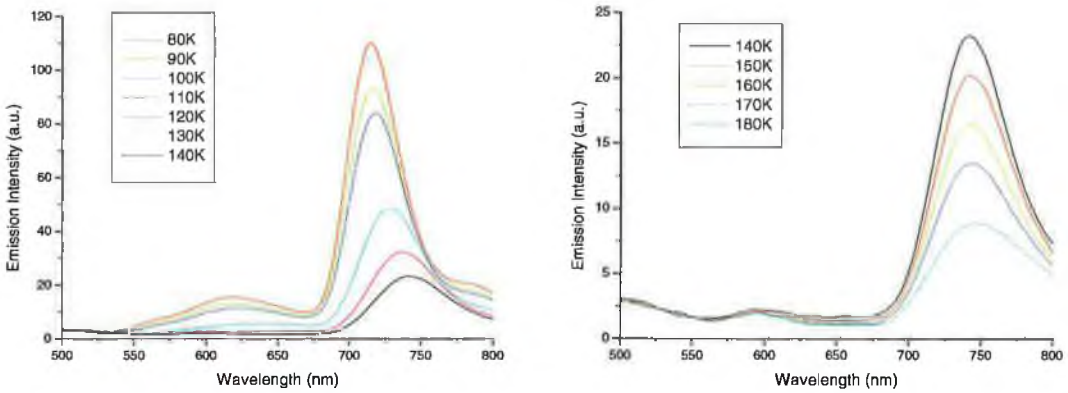

FIGURE 5.3: TEMPERATURE DEPENDENT EMISSION OF $[Ru(biq)_2(Hpztr)]^{2+}$ IN ETOH: MEOH (4:1) BETWEEN (LEFT) 80K AND 140K, (RIGHT) 140K AND 180K.

The temperature dependent emission spectra of $[Ru(phen)_2(pztr)]^+$ in Ethanol: Methanol (4:1) was also obtained and is shown in FIGURE 5.4. As with the other

spectra, the maxima are seen to red – shift and decrease in intensity as the temperature is increased. Again, this is due to ridigiochromatic effects. Particular note should be taken to the spectra on the right of FIGURE 5.4. In these spectra the relative intensity of the emission and its lower energy shoulder (at 630 and 675 nm at 140K, respectively) are seen to change as the temperature is increased. The effects are highlighted in FIGURE 5.5 by the normalised spectra.

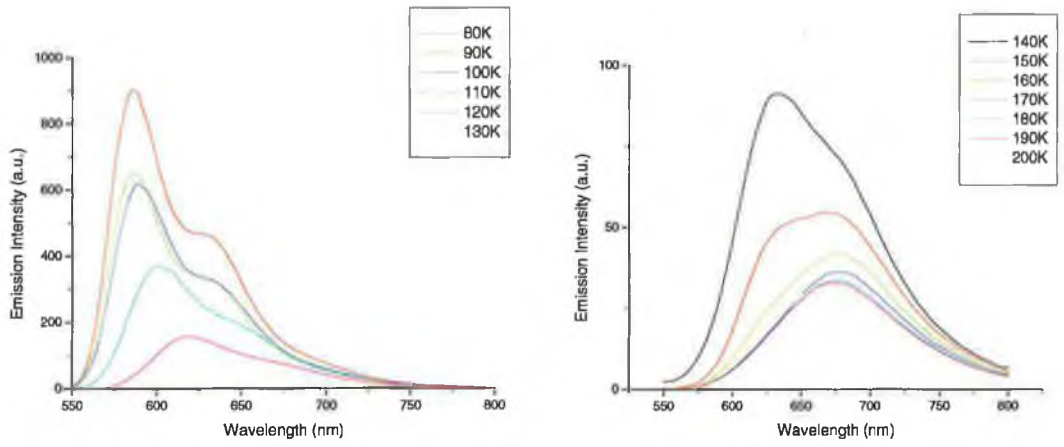

FIGURE 5.4: TEMPERATURE DEPENDENT EMISSION OF $[Ru(phen)_2(pztr)]^+$ IN ETOH: MEOH (4:1) BETWEEN (LEFT) 80 AND 130K, AND (RIGHT) 140 AND 200K.

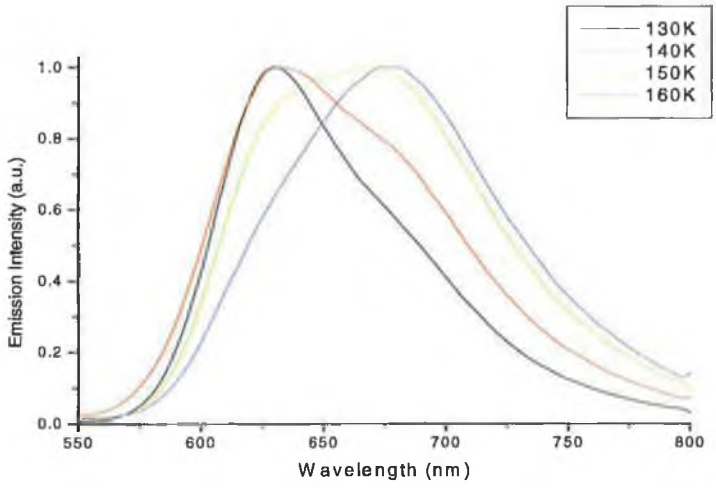

FIGURE 5.5: NORMALISED TEMPERATURE DEPENDENT EMISSION OF $[Ru(phen)_2(pztr)]^+$ BETWEEN 130 AND 160K.

It can be seen in the spectra shown in FIGURE 5.5 that the intensity of the lower energy band (~675 nm) grows relative to that of higher energy as the temperature is increased. At 150K, the low and high-energy emissions are of similar intensity, while at 160K the lower energy emission is dominant. This behaviour is similar to that observed for $[Ru(bpy)_2(pztr)]^+$ previously[19] and indicates the presence of two emitting moieties at low temperatures. The nature of these excited states are further investigated using temperature dependent excited state lifetime measurements in the next section which is also used to confirm the presence of two excited states.

The temperature dependent emission spectra of $[Ru(phen)_2(Hpztr)]^+$ are shown in FIGURE 5.6. In these spectra two bands are observed below the glass transition temperature. As the temperature was increased the band at lower energy is seen to decrease and is no longer visible above 140K. This was observed previously for Ru(II) complexes containing a bpy ligand at low temperature and is known as a vibronic progression. It has been assigned as due to emission to a vibrationally hot ground state.[23] It is due to an emission from $\nu'_m = 0 \rightarrow \nu_m = 1$ where ν'_m is an excited state vibrational mode and ν_m is the ground state

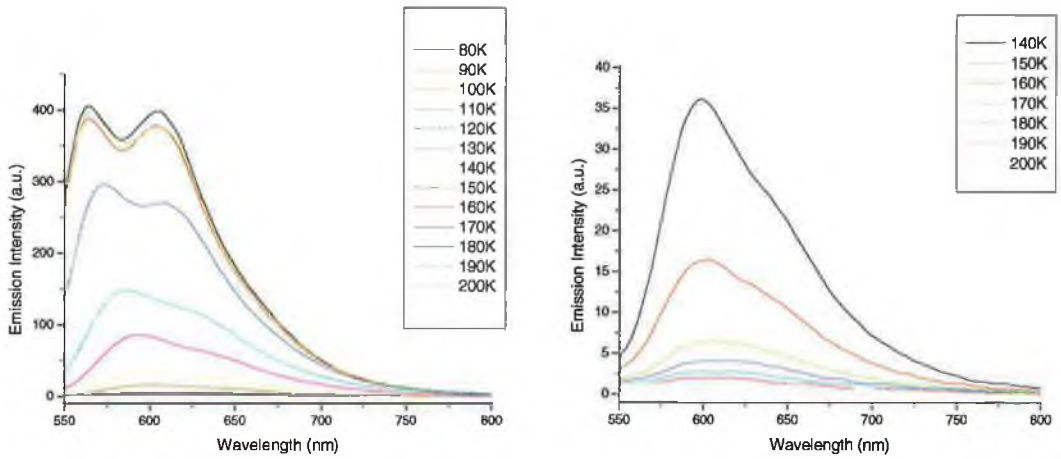

FIGURE 5.6: TEMPERATURE DEPENDENT EMISSION SPECTRA OF $[Ru(phen)_2(Hpztr)]^+$ BETWEEN (LEFT) 80 AND 130 K AND (RIGHT) 140 AND 170K.

FIGURE 5.7 gives the temperature dependent emission spectra of $[Ru(dpp)_2(pztr)]^+$ in EtOH: MeOH between 80K and 200K. At 80K a shoulder is observed on the main emission band at lower energy (~660 nm). This band is seen to reduce, relative to the main band, as the temperature is increased. Again this is behaviour consistent with a vibronic progression. The temperature dependent excited state behaviour observed here differs from that observed for $[Ru(bpy)_2(pztr)]^+$ (and $[Ru(phen)_2(pztr)]^+$ above) in that as the temperature is increased the intensity of the main emission and the lower energy shoulder decrease simultaneously. This indicates that in the excited state for $[Ru(dpp)_2(pztr)]^+$ it is possible for both the emitting states to equilibrate and for emission to occur from a single ligand site.

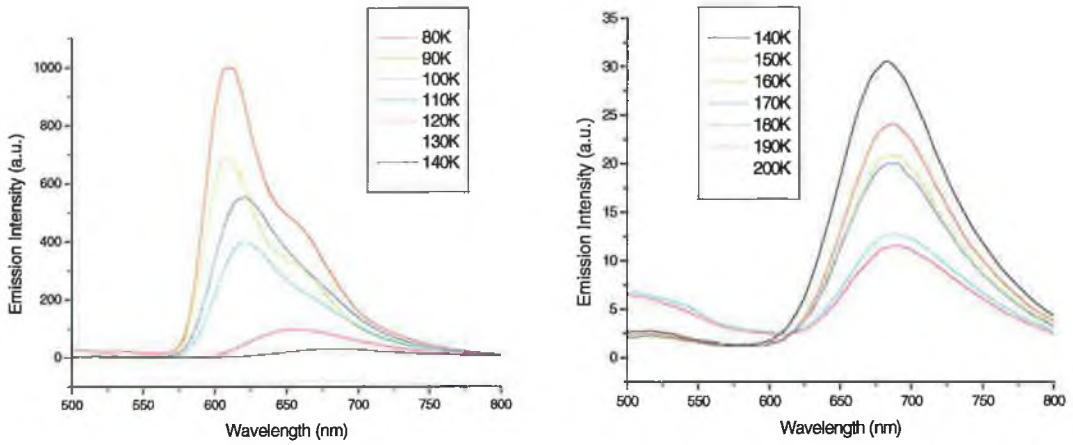

FIGURE 5.7: TEMPERATURE DEPENDENT EMISSION OF $[RU(DPP)_2(PZTR)]^+$ IN ETOH: MEOH (4:1) BETWEEN (LEFT) 80K AND 140K AND (RIGHT) 140K-200K.

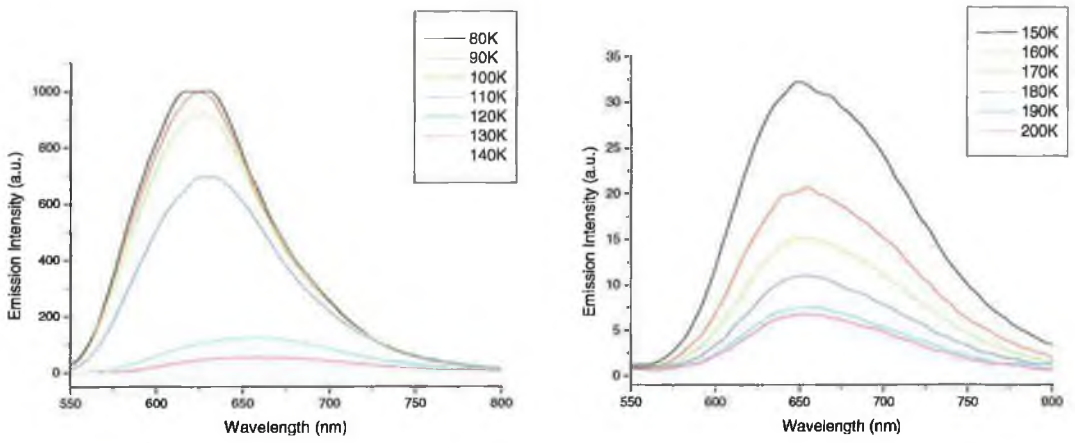

FIGURE 5.8: TEMPERATURE DEPENDENT EMISSION OF $[Ru(dpp)_2(Hpztr)]^{2+}$ IN ETOH: MEOH (4:1) BETWEEN (LEFT) 80K AND 140K AND (RIGHT) 140K-200K.

FIGURE 5.8 gives the temperature dependent emission spectra of $[Ru(dpp)_2(Hpztr)]^{2+}$ between 80 and 200 K. At all temperatures only a single emission is observed.

At this point, it is important to note that the pH dependent emission from pyrazinyl triazole containing complexes is non – facile. FIGURE 5.9 gives the pH dependent emission from $[Ru(phen)_2(pztr)]^+$ and $[Ru(biq)_2(pztr)]^+$ in aqueous Robinson – Britton buffer solution. No change is observed in emission intensity between pH 4 and 11 for $[Ru(biq)_2(pztr)]^+$ and pH 6 and 11 for $[Ru(phen)_2(pztr)]^+$. This is in disagreement with the results of the methylated pyrazine triazole complex, $[Ru(bpy)_2(3\text{-}Mepztr)]^+$, which has an emission maximum at pH 3.2 in acetontrile.[24,25] As the pH is further decreased the emission is seen to decrease. This is due to the protonation of the pyrazine ring and the formation of the non – emissive cationic species.[26] The presence of $[Ru(LL)_2(H_2pztr)]^{3+}$ species is, however, problematic for low temperature studies as its temperature dependent behaviour has not previously been studied. It is for this reason that temperature dependent lifetime studies have not been carried out on the protonated complexes in the following section.

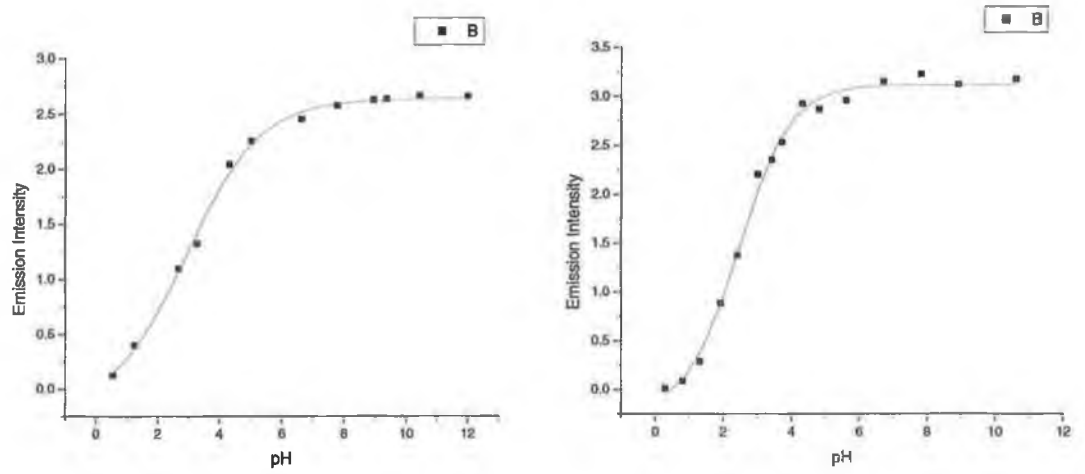

FIGURE 5.9: pH DEPENDENT EMISSION OF (LEFT) $[Ru(phen)_2(pztr)]^+$ AND (RIGHT) $[Ru(biq)_2(pztr)]^+$ IN ROBINSON – BRITTON BUFFER SOLUTION.

5.3.2.2 Temperature Dependent Excited State Lifetime.

Temperature dependent excited state lifetime measurements are used to investigate the deactivation pathways of these complexes. These measurements provide information on the rate of excited state deactivation when the energy available to the molecule is strictly controlled.

Temperature (K)	Lifetime (ns)
240	589
235	604
230	614
225	626
220	638
215	651
210	663
205	676
200	689
195	704
190	727
185	738
180	757
175	777
170	800
165	819
160	839
155	861
150	885

TABLE 5.3: TEMPERATURE DEPENDENT LIFETIMES OF $[Ru(biq)_2(pztr)]^+$ FROM 150 – 240K.

TABLE 5.3 gives the temperature dependent lifetime of $[Ru(biq)_2(pztr)]^+$ between 150 and 240 K. The excited state lifetime in these measurements is seen to decay via a single exponential at all wavelengths and temperatures measured. This indicates that there is a single emissive excited state and is in

agreement with the steady state emission results obtained (see FIGURE 5.2). These results were fit to Eqn. 5.1 where T is the temperature and k is the reciprocal of the lifetime.

$$k = k_o + k' e^{\frac{\Delta E_a}{RT}} \qquad \text{EQN. 5.1}$$

From this graph, the activation energy and prefactors of the excited state deactivation were obtained. The results for all the complexes examined are shown in TABLE 5.6. FIGURE 5.10 shows the graph obtained for $[Ru(biq)_2(pztr)]^+$.

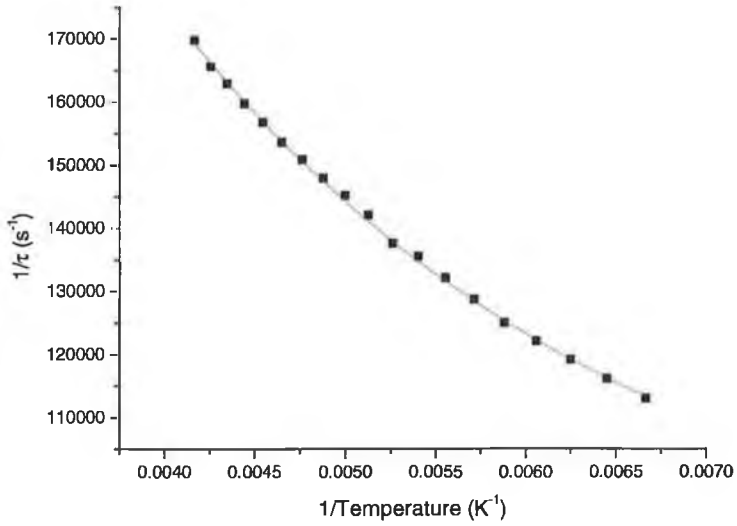

FIGURE 5.10: GRAPH OF 1/TEMPERATURE VS. RATE FOR $[RU(BIQ)_2(PZTR)]^+$.

TABLE 5.4 gives the temperature dependent excited state lifetimes of $[Ru(phen)_2(pztr)]^+$ between 170 and 260K. The excited state of this complex required two exponentials to be accurately fit. However, the results obtained for the shorter decay of the complex did not change in a systematic way. This was due to the overlap of the shorter decay with an intense instrumental response from the flash lamp. FIGURE 5.11 gives an example of the excited state decay of $[Ru(phen)_2(pztr)]^+$ at 4 different temperatures. For the decays

between 140 and 146K two exponentials are required to fit these decays. At 149K only a single exponential is required and the decay appears to show only a single emissive species

Temperature (K)	Lifetime (ns)
260	157
250	191
240	266
230	291
220	301
210	306
200	311
195	314
190	322
185	324
180	331
175	342
170	359

TABLE 5.4: TEMPERATURE DEPENDENT LIFETIME OF [RU(PHEN)2(PZTR)]+ FROM 170 - 260K.

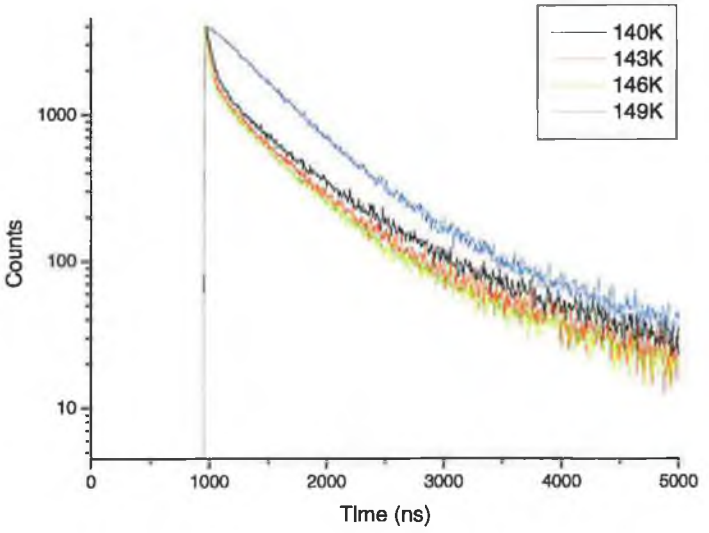

FIGURE 5.11: EXAMPLE OF DECAY OF $[Ru(phen)_2(pztr)]^+$ AT 140 – 149K.

TABLE 5.5 gives the temperature dependent excited state lifetime of $[Ru(dpp)_2(pztr)]^+$ between 140 and 250K. As with the biq containing complex, $[Ru(dpp)_2(pztr)]^+$ is seen to decay with a mono – exponential lifetime at all temperatures.

Temperature (K)	Lifetime (ns)
250	535
240	545
230	555
220	562
210	578
200	594
190	600
180	612
170	629
160	673
150	791
140	986

TABLE 5.5: TEMPERATURE DEPENDENT LIFETIME OF $[Ru(dpp)_2(pztr)]^+$ BETWEEN 140 AND 250K.

FIGURE 5.12 compares the excited state decays of $[Ru(phen)_2(pztr)]^+$ and $[Ru(dpp)_2(pztr)]^+$ at 143K. It can be seen from these decays that two exponentials are required for the phen complexes while the decay of $[Ru(dpp)_2(pztr)]^+$ can be fit using only a single exponential.

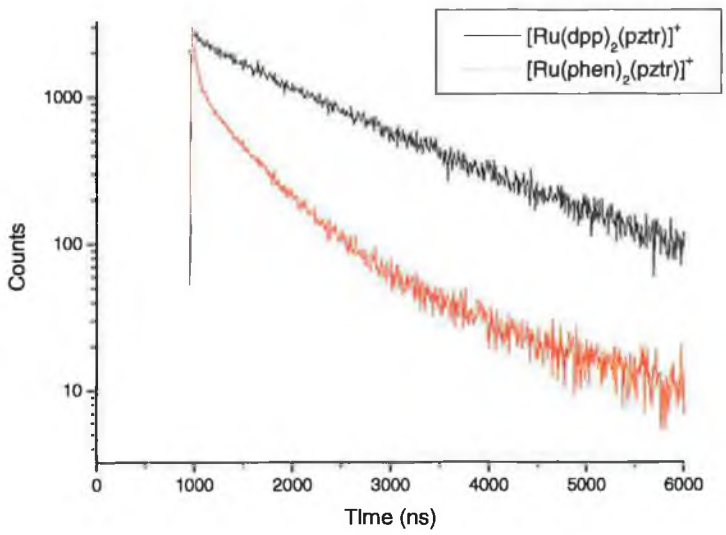

FIGURE 5.12: COMPARISON OF THE EXCITED STATE LIFETIME DECAYS OF $[Ru(phen)_2(pztr)]^+$ AND $[Ru(dpp)_2(pztr)]^+$ AT 143 K.

The results obtained for the prefactors and activation energies of the excited state deactivation are given in Table 5.6.

Complex	k_0 (s^{-1})	k^* (s^{-1})	E_a (cm^{-1})
$[Ru(biq)_2(pztr)]^+$	8×10^4	5×10^5	280
$[Ru(phen)_2(pztr)]^+$	2×10^6	2×10^6	530
$[Ru(dpp)_2(pztr)]^+$	1×10^5	4×10^5	400

TABLE 5.6: CALCULATED ACTIVATION ENERGIES AND PREFACTORS.

5.3.3 Transient Absorption Spectra.

Transient absorption spectroscopy is a useful technique to probe the excited state of a complex and also aids in the interpretation of the excited state Raman spectra. The spectra are presented as differential absorption spectra after subtraction of the spectra due to the complex in the ground state. This makes it possible to view the changes that occur on excited state formation. Transient absorption spectra also provide useful information on the excited

state Raman measurements. These spectra provide the absorption maxima of the excited state and it can therefore be seen if there is sufficient absorption in the excited state for resonance enhancement to occur during the Raman measurements. For these measurements the optical density was near 1 at the excitant wavelength of 355 nm. All the ground state spectra are given in APPENDIX C-9.

Figure 5.13 gives the transient absorption spectra of $[Ru(biq)_2(pztr)]^+$ in acetone. There is a significant bleach of the bands at 350 and 560 nm on excited state formation. This is due to the depletion of the bands of the ^{1}MLCT absorption in the ground state. There is also a grow – in of bands at 400 and 450 nm which is assigned as a $\pi \rightarrow \pi^*$ transition.[27] At wavelengths longer than 600 nm there is an absorption tail which is most likely Ligand – to – Metal Charge Transfer (LMCT).

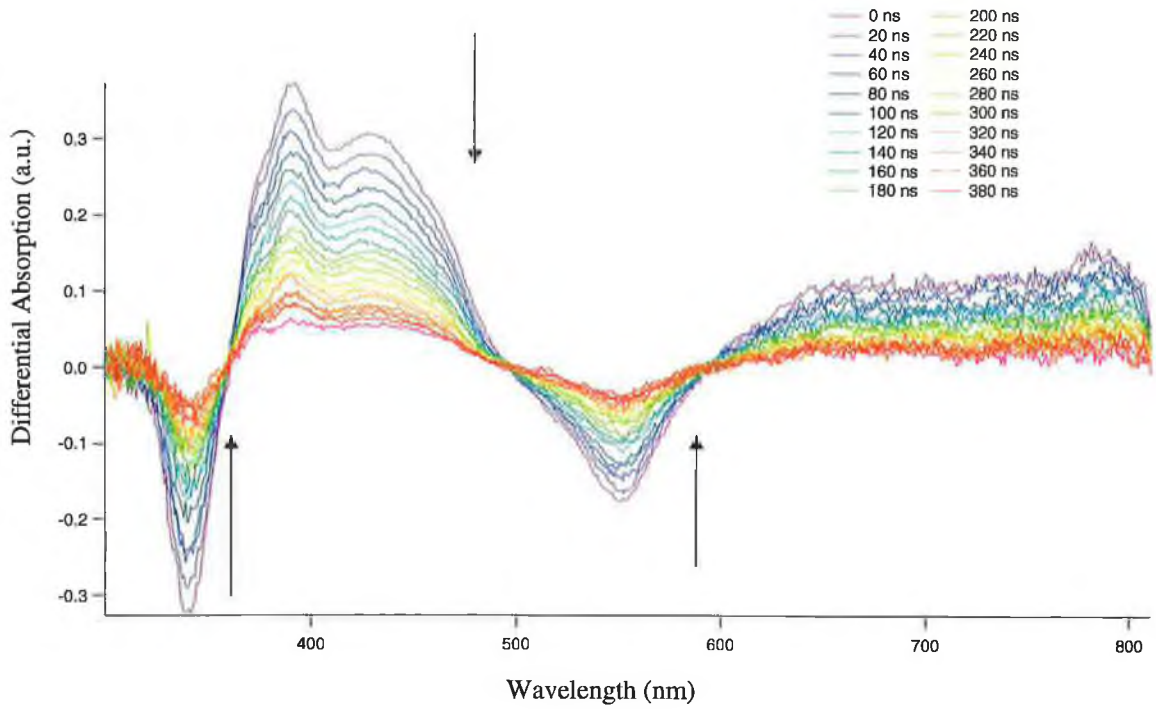

FIGURE 5.13: TRANSIENT ABSORPTION SPECTRA OF $[Ru(biq)_2(pztr)]^+$ IN ACETONE.

Figure 5.14 shows the transient absorption spectra of $[Ru(dpp)_2(pztr)]^+$ in acetone. For this complex a large bleach is observed between 450 and 500

nm. Also observed are absorptions in the excited state at 350 and 600 nm. As with $[Ru(dpp)_2(pztr)]^+$ an absorption tail is observable at wavelengths longer than 600nm, which can be assigned as due to LMCT transitions.

It is important to note that for $[Ru(biq)_2(pztr)]^+$ there is no excited state absorption at 355 nm. However since this is a difference spectrum these results must be compared to the ground state spectra to see if there is an excited state absorption.

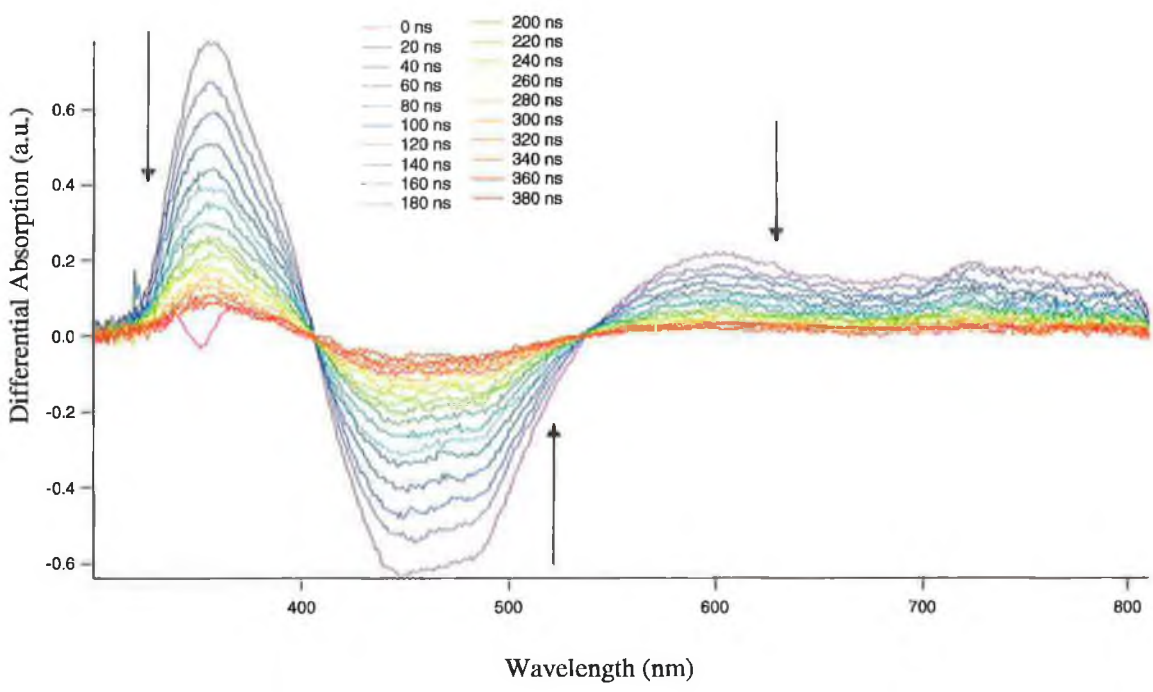

FIGURE 5.14: TRANSIENT ABSORPTION SPECTRA OF $[Ru(dpp)_2(pztr)]^+$ IN ACETONE.

5.3.4 Raman Studies.

Raman spectroscopy is a technique which has seen a resurgence in recent years. In the present work, resonance Raman spectroscopy has been used to investigate the nature of the absorption bands which lead to the formation of the excited state. Transient studies have also been used to probe the location of the excited state.

5.3.4.1 Resonance Raman Spectra.

Figure 5.15 shows the resonance Raman spectra of $[Ru(dpp)_2(pztr)]^+$ and its deuteomer in H_2O with 457.9 nm excitation. The main bands observable in the spectra are highlighted at 1626, 1556, 1515, 1440 and 1261 cm^{-1}. None of the bands are seen to move on deuteriation of the pyrazine triazole ligand and hence are assigned as due to the dpp moiety. This is in agreement with previous results.[29]

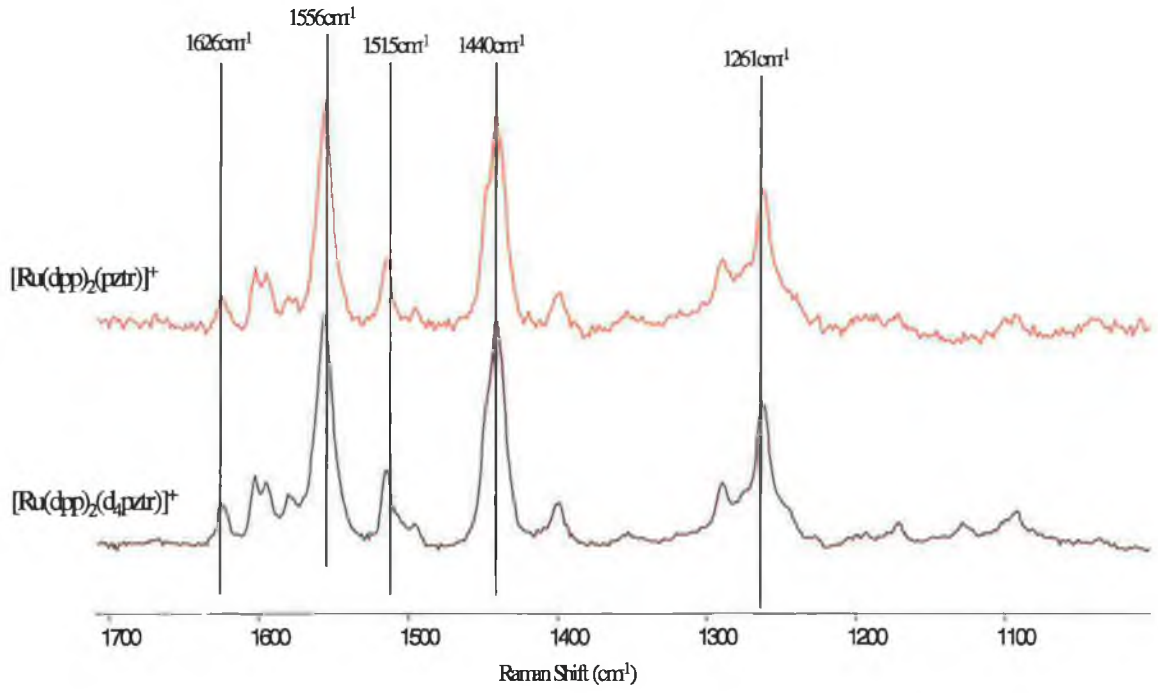

FIGURE 5.15: RESONANCE RAMAN SPECTRA OF $[Ru(dpp)_2(pztr)]^+$ IN H_2O WITH 457.9 NM EXCITATION.

Figure 5.16 shows the resonance Raman spectra of $[Ru(dpp)_2(Hpztr)]^{2+}$ and its deuteomer in H_2O with 457.9 nm excitation. Again none of the bands are seen to move in the spectra of the deuteriated complex. Therefore none of the bands are due to the pyrazine triazole ligand.

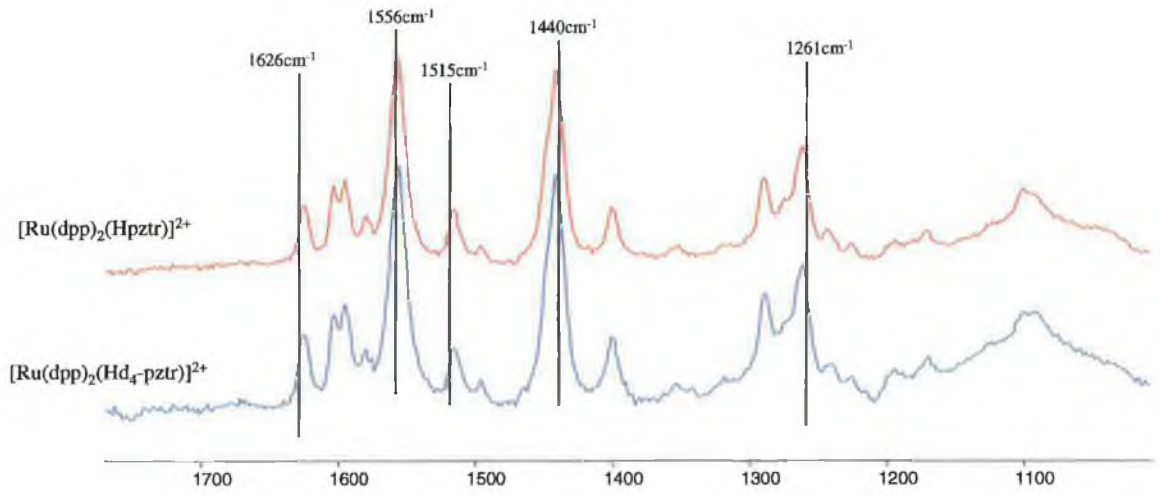

FIGURE 5.16: RESONANCE RAMAN SPECTRA OF $[RU(DPP)_2(HPZTR)]^+$ IN H_2O WITH 457.9 NM EXCITATION.

Figure 5.17 shows the resonance Raman spectra of the deuteomers of $[Ru(phen)_2(pztr)]^+$ in MeOH with 488 nm excitation.

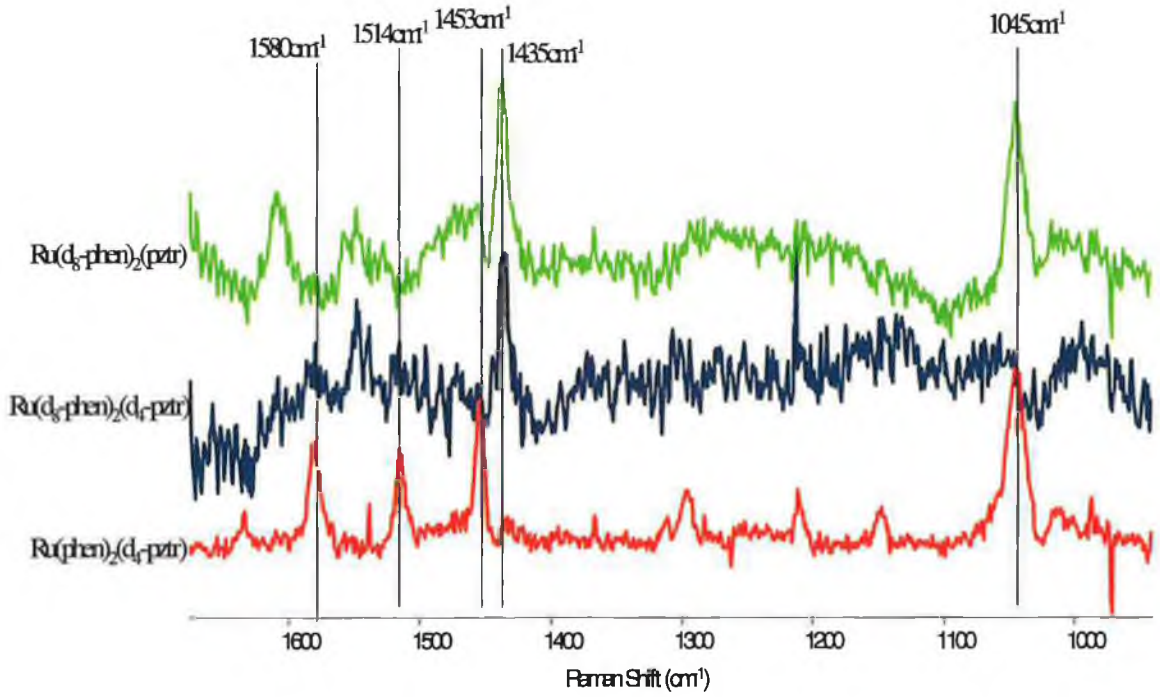

FIGURE 5.17: RESONANCE RAMAN SPECTRA OF $[RU(PHEN)_2(PZTR)]^+$ AND ITS DEUTOMERS IN MEOH WITH 488 NM EXCITATION.

The spectra of $[Ru(phen)_2(d_4\text{-pztr})]^+$ shows bands at 1580 and 1453 cm^{-1} which are assigned as due to the phen moiety by comparison with previous

results.[29] In these spectra there is the possibility of overlap between the pztr and phen bands. A vibration due to both the phen and pztr moieties has been previously observed at 1514 cm^{-1}. At this point deuteriation aids in the assignment of this band. This peak is only observable in the spectrum of $[Ru(phen)_2(d_4\text{-pztr})]^+$ and not $[Ru(d_8\text{-phen})_2(pztr)]^+$, and therefore we can assign the bands in these spectra as being solely due to the phen ligands. The spectrum of $[Ru(d_8\text{-phen})_2(pztr)]^+$ shows a band at 1600 cm^{-1} which is not present in the spectra of the d_4-pztr complexes and is therefore due to the pyrazine moiety.[28] The resonance Raman spectra of the protonated complex $[Ru(phen)_2(Hpztr)]^{2+}$ is given in the APPENDIX C. The signal to noise ratio of the spectra are poor, however, and bands due to the phen ligand only are observable.

Figure 5.18 give the resonance Raman spectra of the $[Ru(dpp)_2(pztr)]^+$ in MeOH with excitation at 488 nm. In the spectrum of $[Ru(dpp)_2(pztr)]^+$ bands are observable at 1630, 1596, 1560, 1455, 1443, 1293 and 1264 cm^{-1}. None of these bands are seen to shift in the spectrum of the deuteromer $[Ru(dpp)_2(d_4\text{-pztr})]^+$ and hence can be assigned as due to the dpp ligands. These bands are in agreement with results obtained by Chang *et al.* for phen.[29]

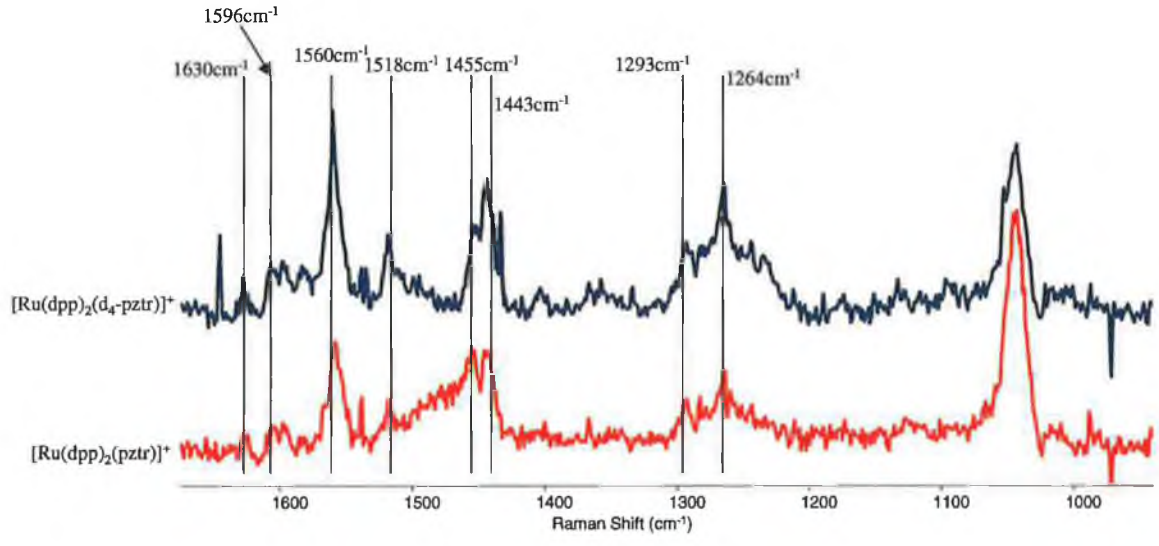

FIGURE 5.18: RESONANCE RAMAN SPECTRA OF $[Ru(dpp)_2(pztr)]^+$ IN MEOH WITH 488 NM EXCITATION.

Next the spectrum of the protonated complex was examined. Figure 5.19 gives the spectra of $[Ru(dpp)_2(Hpztr)]^{2+}$ and its deuteromer in the same conditions as above. Again the bands observed (at 1550 and 1445 cm^{-1}) are seen to be insensitive to deuteriation of the pyrazinyl triazole ligand and are therefore assigned as due to dpp.

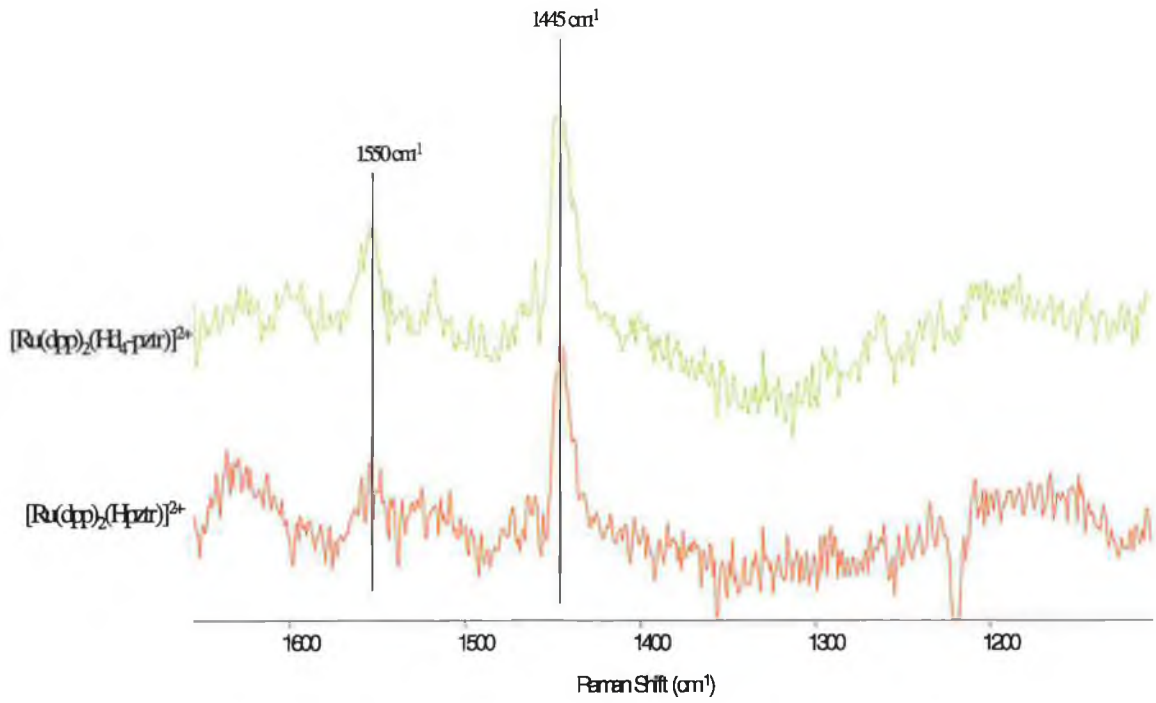

FIGURE 5.19: RESONANCE RAMAN SPECTRA OF $[Ru(dpp)_2(Hpztr)]^{2+}$ IN MEOH WITH 488 NM EXCITATION.

The excitation energy was then shifted to 514 nm to probe the absorption further in the red region. Figure 5.20 gives the spectra of the deuteomers of $[Ru(phen)_2(pztr)]^+$. Bands are observable at 1513 and 1452 cm^{-1} in the spectrum of $[Ru(phen)_2(d_4\text{-pztr})]^+$. A band observed at 1604 cm^{-1} is seen to be only present for the perprotio pztr spectra and is therefore assigned as due to the pyrazine moiety.

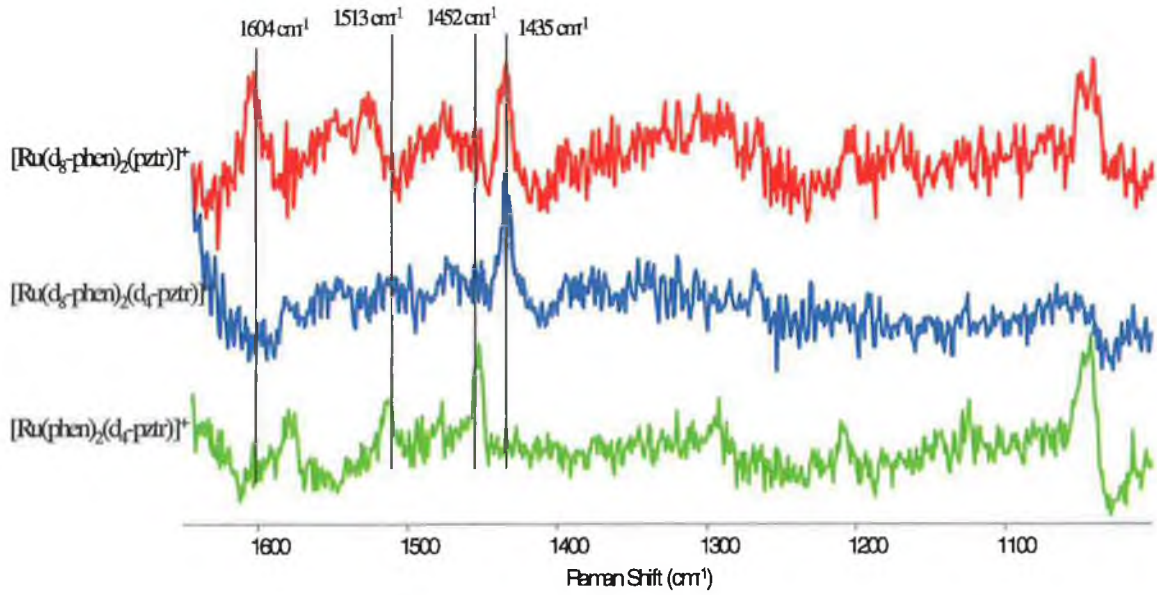

FIGURE 5.20: RESONANCE RAMAN SPECTRA OF $[RU(PHEN)_2(PZTR)]^+$ IN MEOH WITH 514 NM EXCITATION.

Figure 5.21 gives the spectra of $[Ru(phen)_2(Hd_4\text{-}pztr)]^{2+}$ and its deuteomers in methanol with 514 nm excitation. The spectral quality in these measurements is poor. This is reflective of the reduced signal to noise ratio for protonated complexes (*vide supra*) and also on deuteriation of ligands. It also should be noted that the absorption bands of the complexes are quite weak at this energy and therefore the magnitude of the resonance enhancement is reduced. However, a band is observable for $[Ru(phen)_2(Hd_4\text{-}pztr)]^+$ at 1455 cm^{-1} and at 1435 cm^{-1} for $[Ru(d_8\text{-}phen)_2(Hpztr)]^{2+}$. These bands are assigned as due to the phen and Hpztr moiety, respectively, based on previous studies.[18, 29]

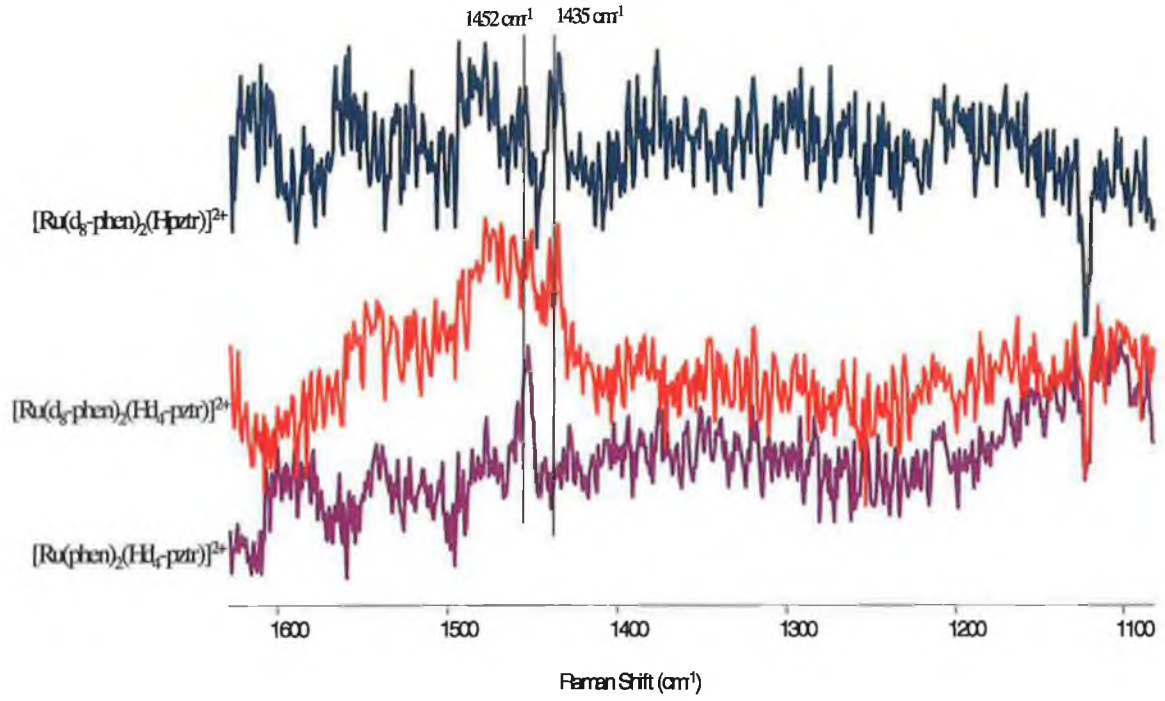

FIGURE 5.21: RESONANCE RAMAN SPECTRA OF $[RU(PHEN)_2(HPZTR)]^{2+}$ IN MEOH WITH 514 NM EXCITATION.

The spectra of the deprotonated complex $[Ru(dpp)_2(pztr)]^+$ was also of poor quality and is given in Appendix C. It shows a number of bands at 1604, 1595, 1556, 1441 and 1263 cm^{-1} which remain unchanged after deuteriation of the pyrazinyl triazole ligand. These are, therefore, assigned as due to the dpp ligands. Spectra of $[Ru(dpp)_2(Hpztr)]^{2+}$ and its deuteomer were also obtained, however, the spectral quality was poor.

5.3.4.2 Transient Resonance Raman.

Transient resonance Raman probes the excited and ground state of the complexes investigated. The pulsed beam acts as both a pump and a probe. In order to probe the excited state, the complex must possess a significant absorption in both the ground and the excited states so that the excited state is formed and the resonance occurs with the probe beam, respectively. The ground state absorption information for these complexes are given in TABLE 5.2 while the excited state absorption spectra are shown in section 5.3.3.

FIGURE 5.22 gives the excited state resonance Raman spectra of $[Ru(biq)_2(pztr)]^{2+}$ with 355 nm excitation with acetonitrile as solvent. The spectrum of $[Ru(biq)_2(pztr)]^+$ shows bands at 1593, 1461, 1373 and 1340 cm^{-1}. These bands appear insensitive to deuteriation of the pztr ligand and are still visible in the spectrum of $[Ru(biq)_2(d_4\text{-pztr})]^+$. Although the transient absorption spectra showed no absorption at 355 nm, this is a difference spectrum and reflects changes from the ground state. The ground state absorption (Appendix C-9) shows a strong absorption at 355 nm and therefore there is also an absorption in the excited state. These bands are therefore assigned as $biq^{-\bullet}$.

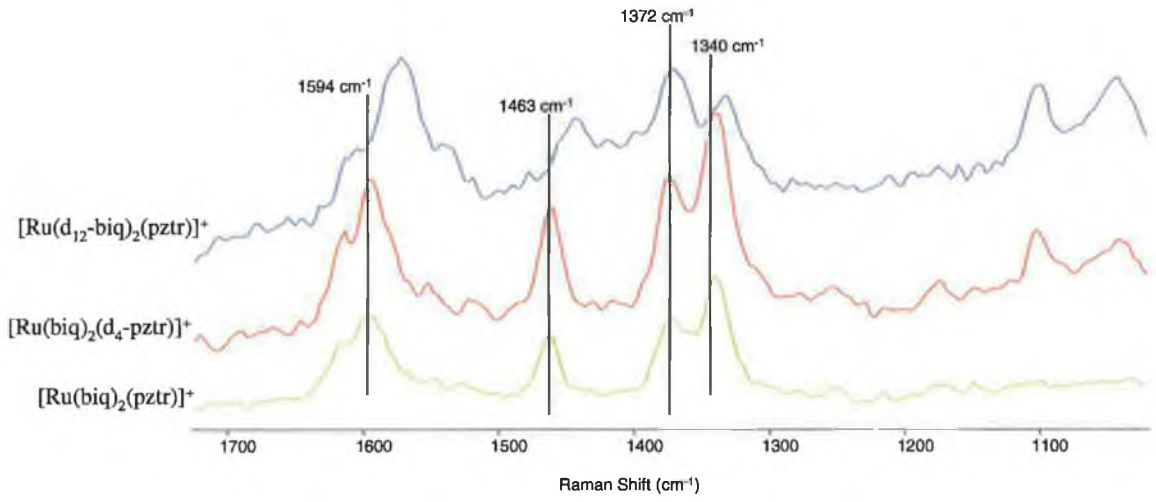

FIGURE 5.22: EXCITED STATE RESONANCE RAMAN SPECTRA OF $[Ru(biq)_2(pztr)]^+$ IN ACETONITRILE WITH 355 NM EXCITATION.

Figure 5.23 gives the spectra of the protonated complex, $[Ru(biq)_2(Hpztr)]^{2+}$, and its deuteomers. A number of bands are observed at 1534, 1512, 1377, 1253 and 1251 cm^{-1}. These bands appear insensitive to the deuteriation of the pztr moiety, as seen in the spectrum of $[Ru(biq)_2(Hd_4\text{-pztr})]^{2+}$, and are therefore assigned as due to the biq ligands. These are the same bands are above, shifted due to an alignment error. This is confirmed by the band shapes and relative intensity of the spectra.

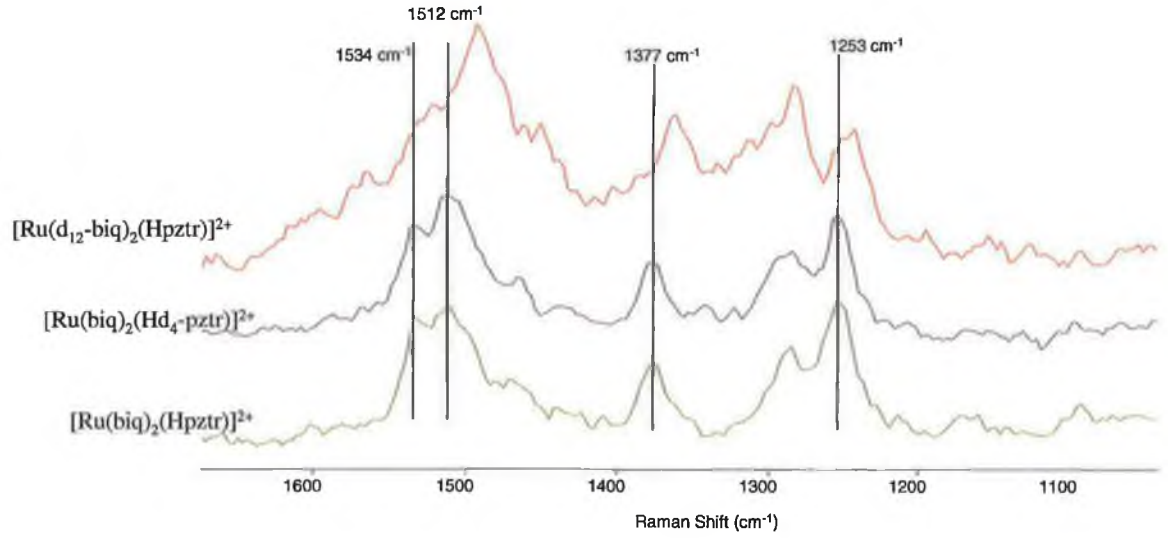

FIGURE 5.23: EXCITED STATE RESONANCE RAMAN SPECTRA OF $[Ru(biq)_2(Hpztr)]^{2+}$ IN ACETONITRILE WITH 355 NM EXCITATION.

Figure 5.24 shows the excited state resonance Raman spectra of the deuteomers of $[Ru(phen)_2(Hpztr)]^{2+}$ in MeOH with 355 nm excitation. Although the spectra are weak, a band is observable at 1436cm^{-1}. This band shifts on deuteriation of the pztr ligand and is therefore assigned as excited state pyrazine, in agreement with previous results.[19,30]

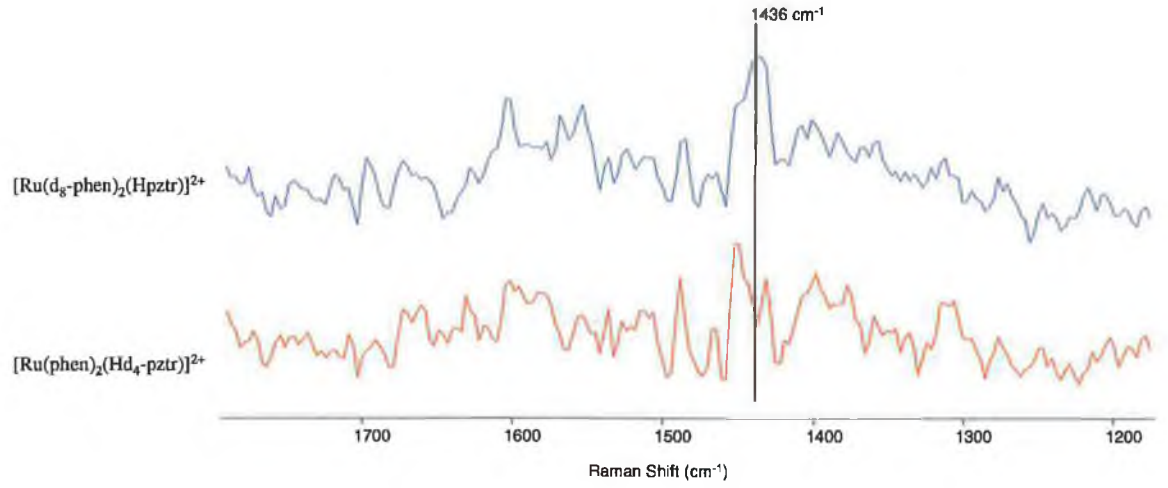

FIGURE 5.24: EXCITED STATE RESONANCE RAMAN SPECTRA OF $[Ru(phen)_2(Hpztr)]^+$ IN MEOH WITH 355 NM EXCITATION.

Figure 5.25 shows the excited state resonance Raman spectra of $[Ru(dpp)_2(Hpztr)]^+$ in methanol with 355 nm excitation. The spectra do not possess any bands which can be assigned to $dpp^{\bullet-}$ or $Hpztr^{\bullet-}$. The spectra of

the tris heretoleptic complex, $[Ru(bpy)(dpp)(Hbpzt)]^{2+}$ (where bpzt is 3,5 - bis (pyrazin-2-yl) - 1,2,4 - triazole), were also obtained. These spectra are of better quality and have been used to approximate the location of the excited state electron in a complex containing both a dpp and pyrazine - triazole type ligand. The spectra at high and low irradiation energy are shown in FIGURE 5.26. In these spectra new bands at 1547 and 1496 cm^{-1} due to the $Hbpzt^{\bullet-}$ can be seen as the irradiation energy is increased.[30]

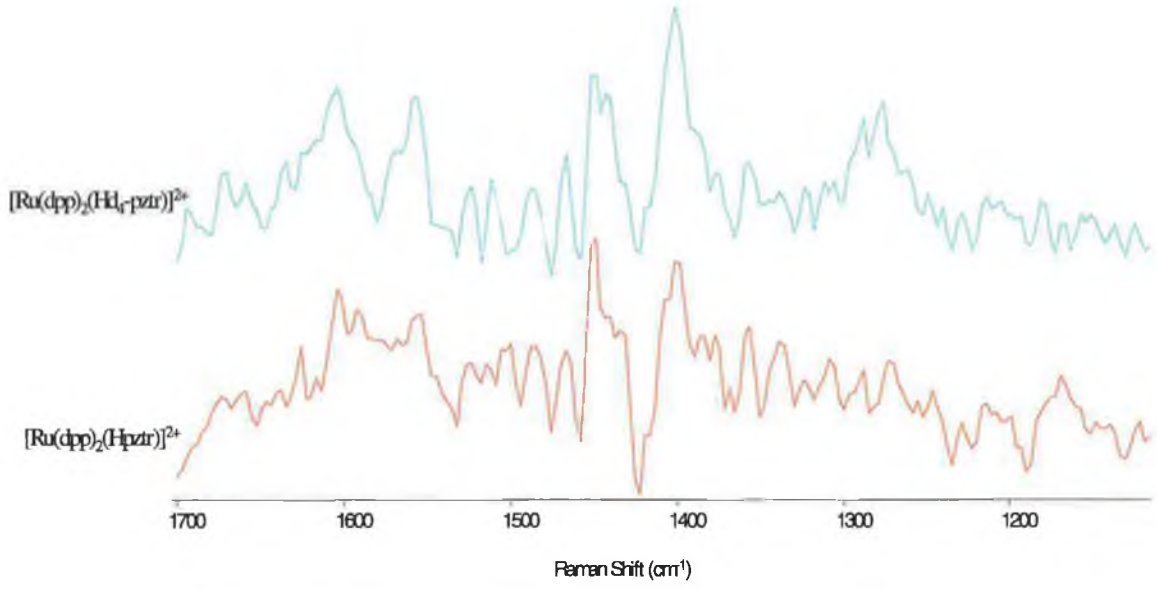

FIGURE 5.25: EXCITED STATE RESONANCE RAMAN SPECTRA OF $[Ru(dpp)_2(Hpztr)]^+$ IN MEOH WITH 355 NM EXCITATION.

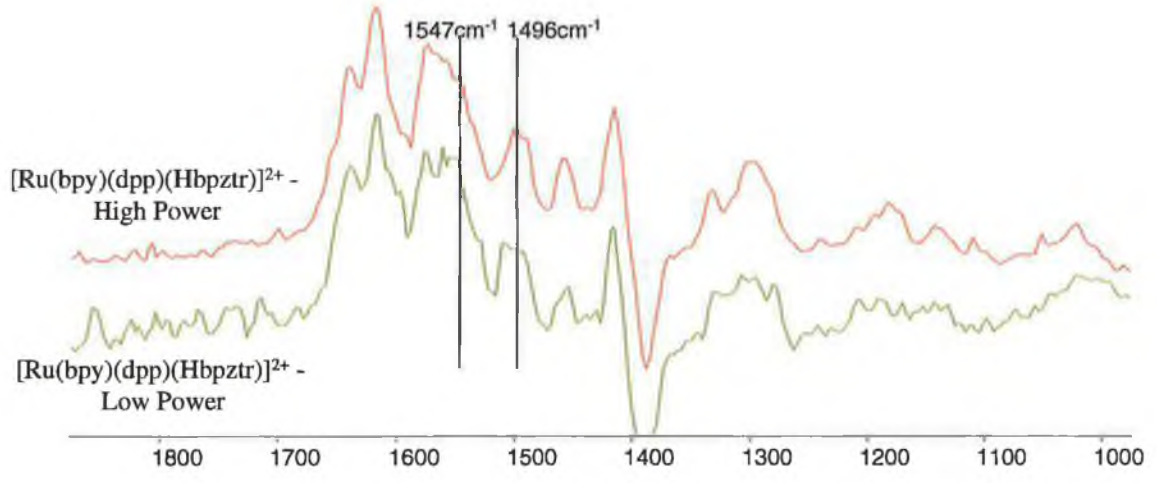

FIGURE 5.26: EXCITED STATE RESONANCE RAMAN SPECTRA OF $[Ru(bpy)(dpp)(Hpztr)]^{2+}$ WITH 355 NM EXCITATION.

5.3.5 Density Functional Theory.

The importance of computational methods has grown rapidly over the last decade. This has been primarily due to the increased affordability of high end computers and the advances in the theoretical background. In the present work the ground state structure of the complexes under investigation have been optimised using the B3LYP functional and LanL2DZ basis set. The complexes were investigated in both protonation states with the proton at the N4 position. The location of the proton is a matter of some debate. Previous studies have shown that the N1 position is slightly more acidic, however, in an effort to reduce the effect of steric hindrance, protonation at the N4 position has been chosen. After geometry optimisation with an ultrafine integration grid, the molecular orbitals were described in terms of contributions from various groups in the molecule: *Ru* – the Ru atom; *LL1* and *LL2* the symmetrical diimine ligand (such as phen1, biq1 or dpp2); *pz* – the pyrazine moiety; *(H)tr* – the triazole ring. Tables of the molecular data obtained are given in Appendix C. The isosurfaces of the complexes are shown in Figure 5.27, Figure 5.29 and Figure 5.31. In the frontier region, neighbouring orbitals are often closely spaced. In such cases, consideration of only the HOMO and LUMO may not yield a realistic description of the frontier orbitals. For this reason, partial density of states (PDOS) diagrams, which incorporate a degree of overlap between the curves convoluted from neighbouring energy levels, can give a more representative picture of the nature of the frontier orbitals. The PDOS diagrams obtained for the complexes are shown in Figure 5.28, Figure 5.30 and Figure 5.32

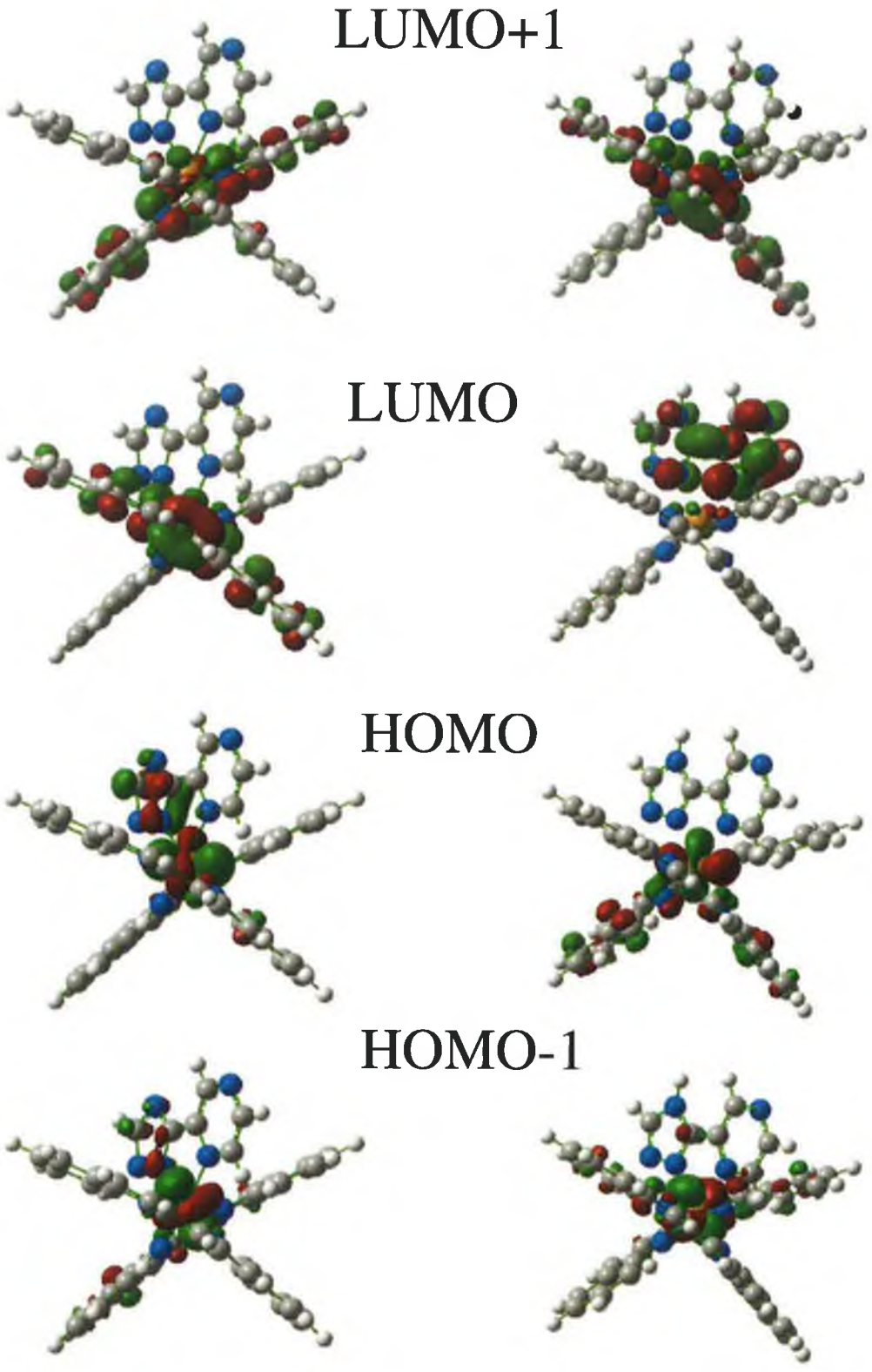

FIGURE 5.27: ISOSURFACES OF HOMO-1, HOMO, LUMO AND LUMO+1 FOR (LEFT) $[Ru(biq)_2(pztr)]^+$ AND (RIGHT) $[Ru(biq)_2(Hpztr)]^{2+}$.

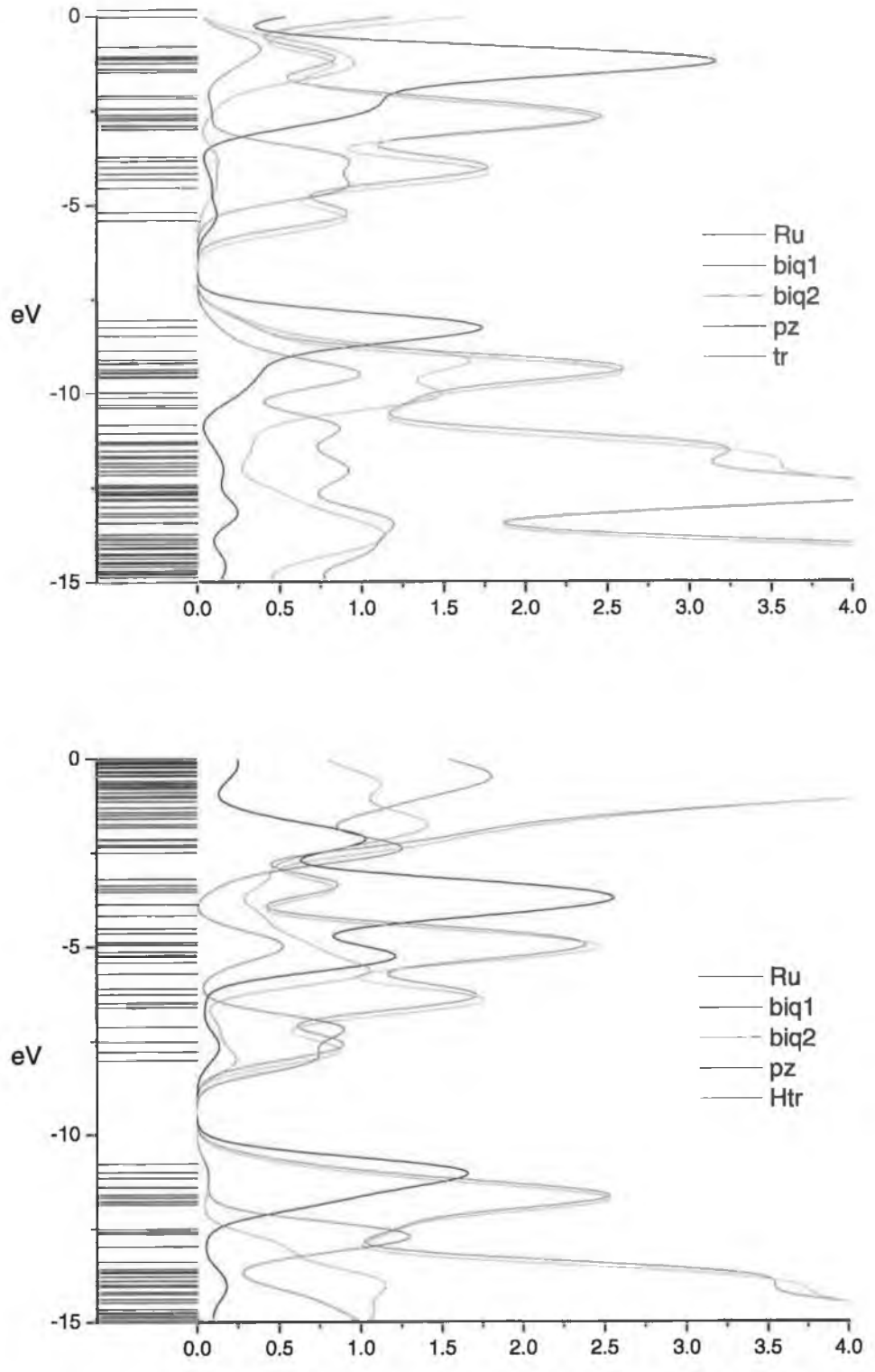

FIGURE 5.28: PDOS DIAGRAMS OF (TOP) $[Ru(biq)_2(pztr)]^+$ AND (BOTTOM) $[Ru(biq)_2(Hpztr)]^{2+}$.

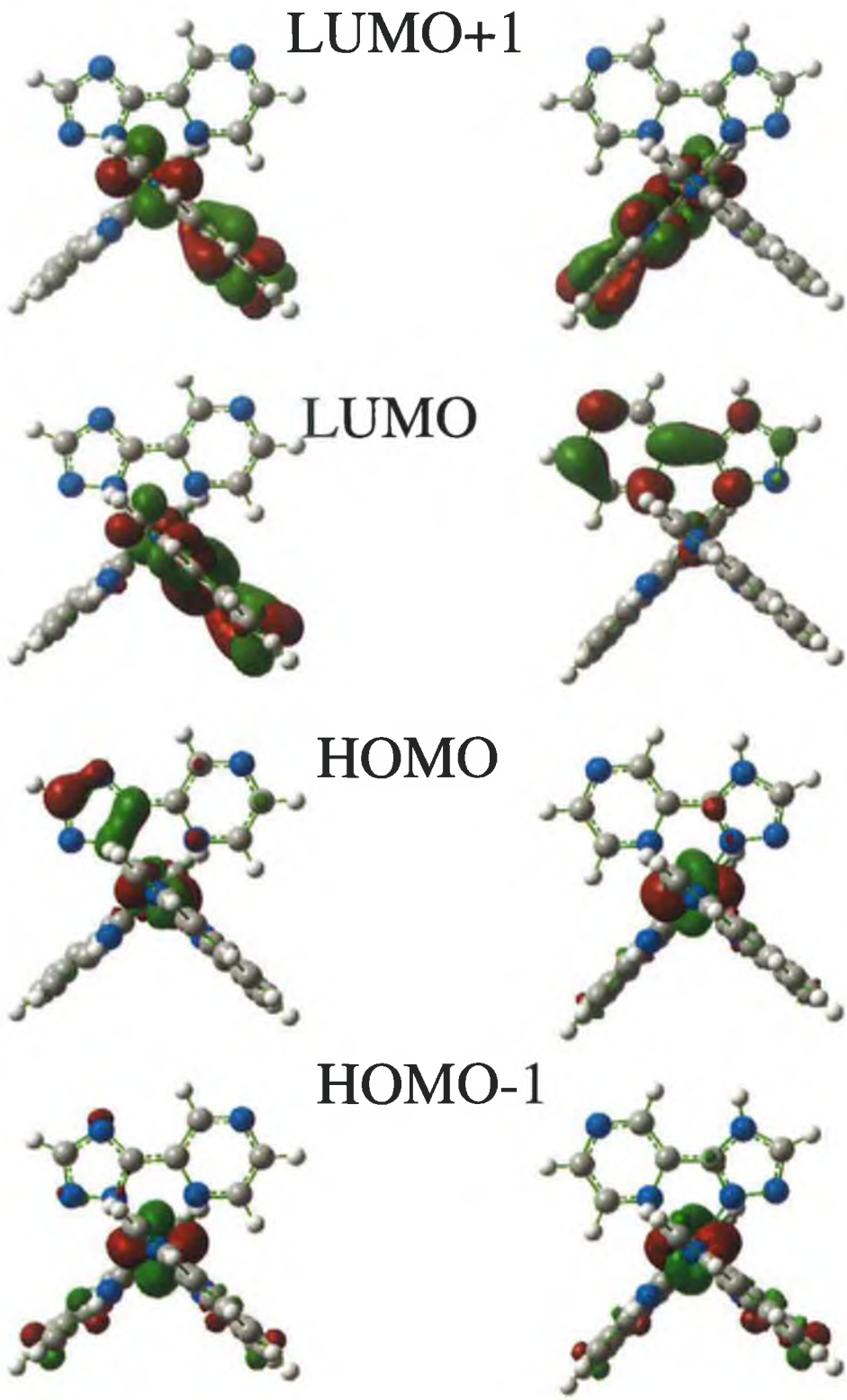

FIGURE 5.29: ISOSURFACES OF HOMO-1, HOMO, LUMO AND LUMO+1 FOR (LEFT) $[Ru(phen)_2(pztr)]^+$ AND (RIGHT) $[Ru(phen)_2(Hpztr)]^{2+}$.

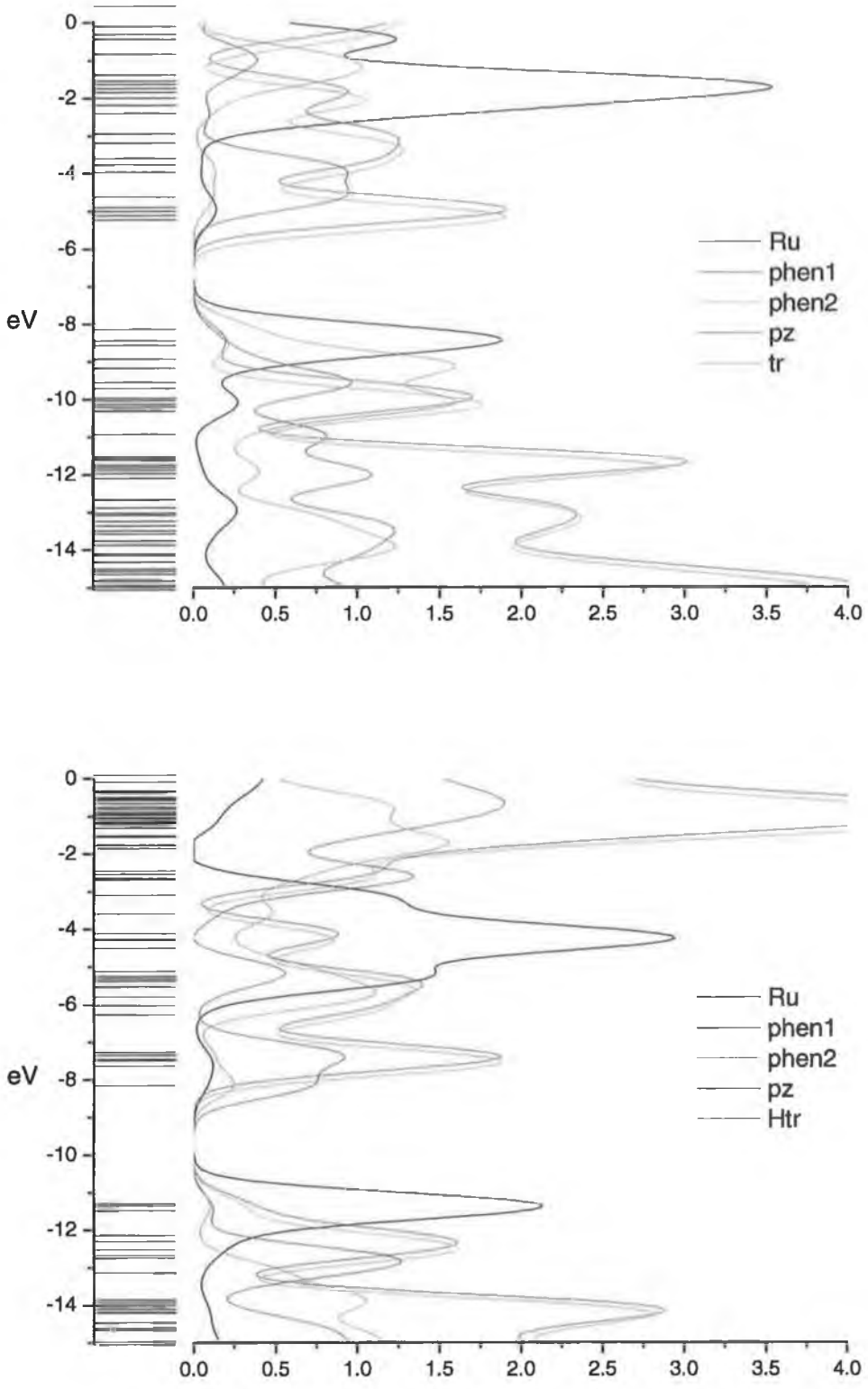

FIGURE 5.30: PDOS DIAGRAMS OF (TOP) $[Ru(phen)_2(pztr)]^+$ AND (BOTTOM) $[Ru(phen)_2(Hpztr)]^{2+}$.

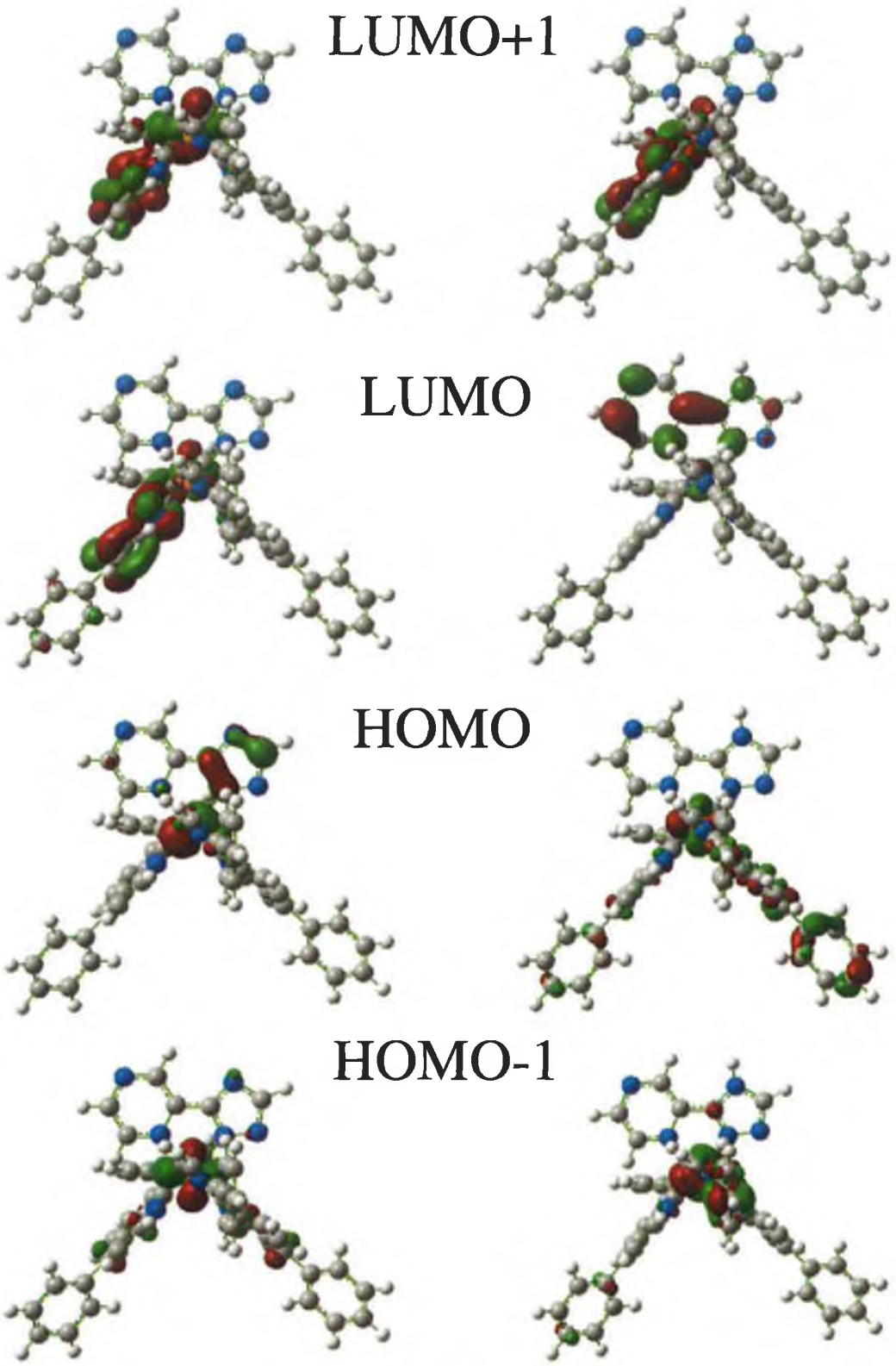

FIGURE 5.31: ISOSURFACES OF HOMO-1, HOMO, LUMO AND LUMO+1 FOR (LEFT) $[Ru(dpp)_2(pztr)]^+$ AND (RIGHT) $[Ru(dpp)_2(Hpztr)]^{2+}$.

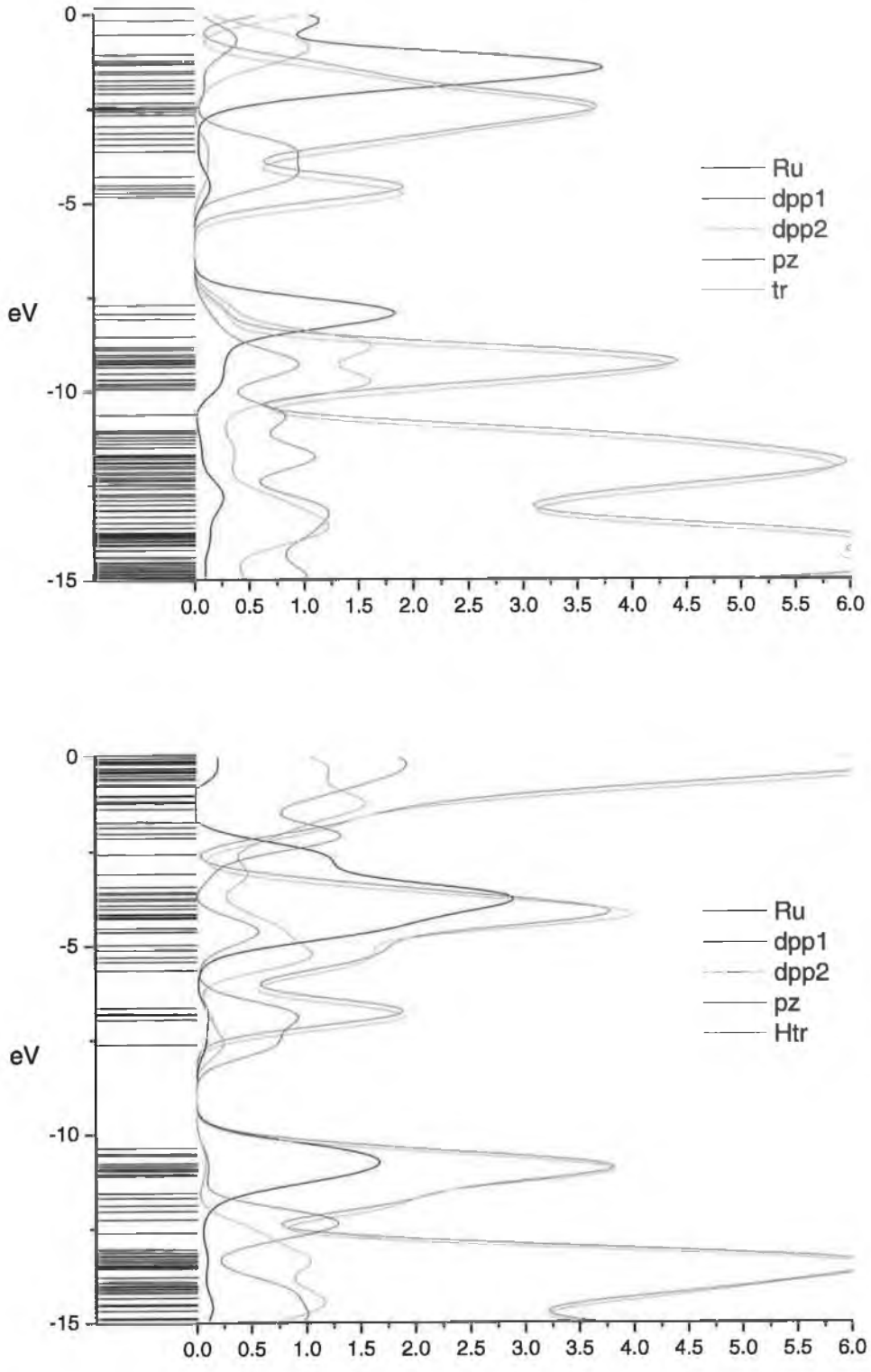

FIGURE 5.32: PDOS DIAGRAMS OF (TOP) $[Ru(dpp)_2(pztr)]^+$ AND (BOTTOM) $[Ru(dpp)_2(Hpztr)]^{2+}$.

FIGURE 5.27 shows the isosurfaces obtained for the frontier orbitals of $[Ru(biq)_2(pztr)]^+$ and $[Ru(biq)_2(Hpztr)]^{2+}$. In both the deprotonated and protonated complexes, the HOMO and HOMO-1 are dominated by the Ru atom. In contrast the LUMO of the protonated complex appears to be based on the pztr ligand. FIGURE 5.28 shows the PDOS spectra of the biq containing complexes. Protonation of the triazole results in a shift to lower energy of the metal orbitals. As observed FIGURE 5.27, protonation also results in a significant increase in the contribution of the triazole containing ligand to the LUMO and LUMO+3 (Appendix C). The overlap of the frontier orbitals for $[Ru(biq)_2(pztr)]^{2+}$ would also suggest the possibility of dual emission as observed for the deprotonated phen complex and $[Ru(bpy)_2(thpztr)]^+$ (see Chapter 4). However, the experimental data presented in section 5.3.2 – Temperature Dependent Emission Spectroscopy – shows only mono – exponential excited state decay.

FIGURE 5.29 shows the isosurfaces of $[Ru(phen)_2(pztr)]^+$ and $[Ru(phen)_2(Hpztr)]^{2+}$. For both the protonated and deprotonated complexes the HOMO and HOMO-1 electron density is based on the Ru metal centre. For the deprotonated complex the LUMO and the LUMO+1 are based on the phen ligands. On protonated the location of the LUMO is seen to switch to the pyrazine – triazole ligand while the LUMO+1 remains on one of the phen ligands. FIGURE 5.30 gives the PDOS diagrams for the phen containing complexes. Again the ground state is Ru based in both protonation states. Protonation results in a reduction of the energy of the molecules, which is shifted by ~ 3 eV. The energy of the phen ligands remain largely unchanged by protonated while the energy of the triazole containing ligand is reduced to an extent that it becomes the location of the LUMO.

The isosurfaces of $[Ru(dpp)_2(pztr)]^+$ and $[Ru(dpp)_2(Hpztr)]^{2+}$ are presented in FIGURE 5.31. These results appear quite similar to those obtained for phen. This is not unexpected due to the similarity of these two ligand structures. Again the HOMO's are Ru(II) based in both protonation states, while the LUMO

are situated on the ligands. In the deprotonated complex the excited state is based solely on the dpp ligand, while for the protonated complex it is seen to switch to the pyrazine ligand. These results are in agreement which the switching of location of excited state energy previously observed for $[Ru(bpy)_2(pztr)]^+$ by Keyes *et al.*[19] and in Chapter 4. However, at this point it is important to note that while the calculations preformed on the biq, phen and dpp containing complexes produce similar results, the experimental data shows clear differences in their excited state structure. This would, therefore, suggest that previously observed dual emission and bi – exponential excited state decay cannot be described solely on the basis of energy differences in the ligands but may also have contributions from the extent of delocalisation in the excited state.

5.4 Discussion.

The steady state electronic spectroscopy measurements of the complexes of interest are presented in TABLE 5.2. These results highlight the ability to control the properties of the complexes with judicious selection of ligand. The emission maxima of the deprotonated complexes are seen to be red – shifted in comparison to corresponding homoleptic $[Ru(LL)_3]^{2+}$ complexes. [7,13,31] This is due to the strong σ – donor ability of the triazole, which raises the energy of the metal orbital and reduces the ^{3}MLCT gap. On protonation the emission energy is blue – shifted. As protonation occurs on the triazole moiety, its donor ability is reduced and the metal orbitals are stabilised. A larger blue shift is observed for the phen and dpp containing complexes than for $[Ru(biq)_2(pztr)]^+$. This is due to the switching of the location of the excited state for the phen and dpp complexes on protonation(*vide infra*). This has been observed for the bipyridine containing complexes[19] and is due to the reduced of electron density on the triazole. Once the triazole is protonated, the energy of the pyrazine moiety is reduced while the energy of the LL ligands remain largely unaffected. The switching of location of the excited state is dependent on the energy of the LL ligand. Protonation of $[Ru(biq)_2(pztr)]^+$ results in a large blue shift in the emission energy. The biquinoline ligand is a strong π – acceptor and hence the emission energy of this complex is lower than that of the phen or dpp based ligands. Protonation again leads to a reduction in the energy of the pyrazine based excited state, however, the biquinoline based ^{3}MLCT remains the lowest energy state.

Only a small difference is apparent in the oxidation energy of $[Ru(phen)_2(pztr)]^+$ and $[Ru(dpp)_2(pztr)]^+$. This is due to the similarity of the σ – donor and π – acceptor properties of the ligands. The oxidation energy of $[Ru(biq)_2(pztr)]^+$ is at higher energy. The reduced σ – donor of the biquinoline stabilises the metal centre and makes it more difficult to oxidise.

The excited state of $[Ru(phen)_2(pztr)]^+$ is seen to deactivate quicker than $[Ru(biq)_2(pztr)]^+$ in agreement with the energy gap law.[32] A reduction in the energy separation between the ground and the excited states reduces the rate of non – radiative deactivation, leading to an increase in the excited state lifetime.

Temperature dependent spectroscopy has been used to further understand the emissive properties of the complexes. Previous studies[19] of $[Ru(bpy)_2(pztr)]^+$ have shown that emission is observed from two excited states in the 140 – 200 K temperature range. The higher energy emission was seen to originate on the pyrazine triazole ligand, while the emission at lower energy is due to the excited state of the bipyridine ligand, as determined by resonance Raman spectroscopy. On protonation of $[Ru(bpy)_2(pztr)]^+$ the emission energy was seen to blue – shift, however, only a single emissive excited state was then observed.

Figure 5.2 gives the temperature dependent emission spectra of $[Ru(biq)_2(pztr)]^+$ in ethanol: methanol (4:1) between 80 and 200K. The spectra on the right highlights the region between 140 and 200 K where dual emission was previously observed. As the temperature is increased the emission maximum is seen to red – shift and decrease in intensity. The red – shift is due to the ability of the matrix to stabilise the excited state as it becomes more fluid at higher temperatures. The decrease in emission intensity is due to the increased rate of non – radiative decay as the energy of emission is red shifted, in agreement with the Energy Gap Law[23] *(vide supra)*. For $[Ru(biq)_2(pztr)]^+$ only a single emission is observed. The energy of this emission suggests that it is due to the biquinoline moiety. Although there is some fluorescence apparent at ~ 600 nm this is not due to emission from the complex. It is seen to be dependent on the excitation wavelength and does not decrease with increasing temperature. It is, therefore, assigned as due to scattering. The emission maxima for this complex is red – shifted compared to that observed for the bipyridine moiety of $[Ru(bpy)_2(pztr)]^+$. This is due to the

strong π – acceptor properties of biquinoline. Therefore, there is a large energy difference between the lowest (biquinoline based) excited state and a second possible emissive state based on the pyrazine. The large energy difference between the two excited states leads to a strong driving force for the THEXI state to be formed solely on the biquinoline ligand.

The temperature dependent emission spectra of $[Ru(biq)_2(Hpztr)]^{2+}$ in the ethanol: methanol matrix between 80 and 180K are shown in Figure 5.3. Again these spectra show a red – shift and decrease in intensity on increasing temperature. The emission maxima are slightly blue – shifted compared to the deprotonated analogue due to the reduced σ – donor of the protonated triazole. For this complex, a single emission is observed at 750 nm representing an excited state based on a single ligand. The emission energy also suggests that this is due to the biquinoline moiety, as with the results above. There is also the presence of a fluorescent signal at ~ 625 nm. Again this is thought to be due to scattering, however, in this case photolability may also be a factor. A previous study[33] on $[Ru(biq)_2(pztr)]^+$ has shown pH dependent photolability due to the ^{3}MLCT – ^{3}MC energy gap. The reduced e_g (^{3}MC) levels in the protonated complex results in photolability while the deprotonated complex was seen to be photostable over long periods. In an effort to reduce the effect of photochemistry, once protonated the complex was kept in the dark and the light source was switched off between measurements. At room temperature, the emission intensity / maximum was unchanged after measurement indicating that minimal photochemistry had occurred.

FIGURE 5.4 gives the temperature dependent emission spectra of $[Ru(phen)_2(pztr)]^+$ in ethanol:methanol between 80 and 200 K. Increasing temperature results in a red – shift and a decrease in intensity, as with the other complexes. For this complex two emissions can be observed at 77K, one centred at 580 nm and the other at 630nm. The relative intensity of these emissions are seen to vary as the temperature is increased which indicates

that the second emission is not due to a vibronic progression (*vide infra*). As the temperature is increased the emission of the low energy emission is seen to increase relative to that of the high energy emission. Figure 5.5 gives the normalised spectra of the complex between 130 and 160K. This highlights the change in intensity between the two emitting states as the temperature increases. Therefore there are two emitting species present in the complex $[Ru(phen)_2(pztr)]^+$ below 200 K. By comparison with the results obtained for $[Ru(bpy)_2(pztr)]^+$ the high energy emission can be assigned to the pyrazine moiety while that observed at the lower energy is due to the phenanthroline based ^{3}MLCT excited state.[19] These results indicate that dual emission based on two ^{3}MLCT non – equilibrated states may be present for complexes containing LL ligands other than bpy.

Figure 5.6 presents the temperature dependent emission spectra of $[Ru(phen)_2(Hpztr)]^{2+}$ in ethanol:methanol between 80 and 200K. As expected the emission maxima are blue – shifted with respect to the deprotonated complexes, due to the reduced σ – donor ability of the triazole. A second band, at lower energy than the main peak, is observed in these spectra at low temperatures. However, as the temperature is increased the intensity of this band is seen to decrease, and by 180 K is no longer present. For the protonated phen complex it therefore appears that there is only a single emitting ligand accompanied by a vibronic progression. Once the triazole is protonated the energy of the pyrazine – triazole ligand is strongly decreased due to a reduction in its electron density. This reduction in energy leads to a switching of excited state from the phen moiety to the pyrazine (*vide infra*). The increased energy gap between the pyrazine and the phen creates a strong driving force for the formation of the THEXI state on a single ligand. The protonation of the triazole also reduces the dipole moment of the complex in the excited state and therefore reduces this barrier to excited state interconversion(*vide infra*).

The temperature dependent emission spectra of $[Ru(dpp)_2(pztr)]^+$ in ethanol: methanol (4:1) between 80 and 200K were also recorded. The spectra show a main emission band with a shoulder at lower energy. However, as the temperature is increased the intensity of the shoulder is seen to diminish and above 140K only a single emission is apparent. Therefore, the $[Ru(dpp)_2(pztr)]^+$ shows "normal" excited state behaviour in which emission occurs from the lowest THEXI state. This is an interesting result as TABLE 5.2 shows that the dpp containing complex has similar photophysical properties to $[Ru(phen)_2(pztr)]^+$. The differences that appear in the temperature dependent behaviour between these two complexes can be put down to inner and outer sphere effects. Inner sphere effects relate to the change in nuclear distances of the bonds on which the excited state is formed. If the excited state is initially formed on the pyrazine moiety energy is required to switch the excited state to the symmetrical LL ligand. These effects are assumed to be a significant contribution to the energy barrier between equilibration of excited states in dual emissive complexes. However, previous studies on the excited state properties of $[Ru(dpb)_3]^{2+}$ (where dpb is 4,4'-diphenyl 2,2'-bipyridine) have shown that the phenyl rings are seen to move to form an elongated conjugated system. The phenyl ring moves from a 23° angle in the ground state to be in plane with the bipyridine moiety in the excited state.[6] The large area of this ligand in the excited state causes the average change in nuclear distance to be reduced and, hence the extent of inner sphere effects to be decreased. This is represented in FIGURE 5.34 as the reduced displacement of the dpp based ^{3}MLCT relative to that of the pyrazine. A second contributing factor are the outer sphere effects. Outer sphere effects relate to the change in dipole moment which occurs when the excited state switches between the two possible ligand sites. In the excited state solvent molecules reorganise so as to stabilise the excited state. In order for the excited state to switch from one ligand based excited state to another, energy is required to modify the solvent configuration. As the electron density on the dpp ligand is spread over a large area the resultant dipole change is not as great as for the phen ligand.

FIGURE 5.8 gives the temperature dependent emission spectra of $[Ru(dpp)_2(Hpztr)]^+$ between 80 and 200K. As with the deprotonated complex only a single emissive state is observed at higher temperatures. Similarly to $[Ru(phen)_2(Hpztr)]^+$, protonation results in the reduction of the energy of the pyrazine based ^{3}MLCT and the switching of the location of the excited state to this moiety (*vide infra*). However, it is also important to note the effects of protonation on the outer sphere / dipole effects. Figure 5.33 shows the dipole moments of $[Ru(bpy)_2(pztr)]^+$ and $[Ru(bpy)_2(Hpztr)]^{2+}$. Bpy has been used as the LL ligand to aid in the clarity of the diagram. The positive charge on the protonated triazole ligand reduces the dipole moment of the complex when the excited state is based on the pyrazine. This, in turn, reduces the barrier to interconversion between the excited states for the protonated complexes. Hence single emission is observed for all protonated pyrazine – triazole containing complexes studied thus far. The effect of dipole formation on the excited state position has been highlighted previously[34] for the mono and di-cationic complexes $[Ru(bpy)_2(CN)_2]^+$ and $[Ru(bpy)_2(i\text{-}biq)]^{2+}$.

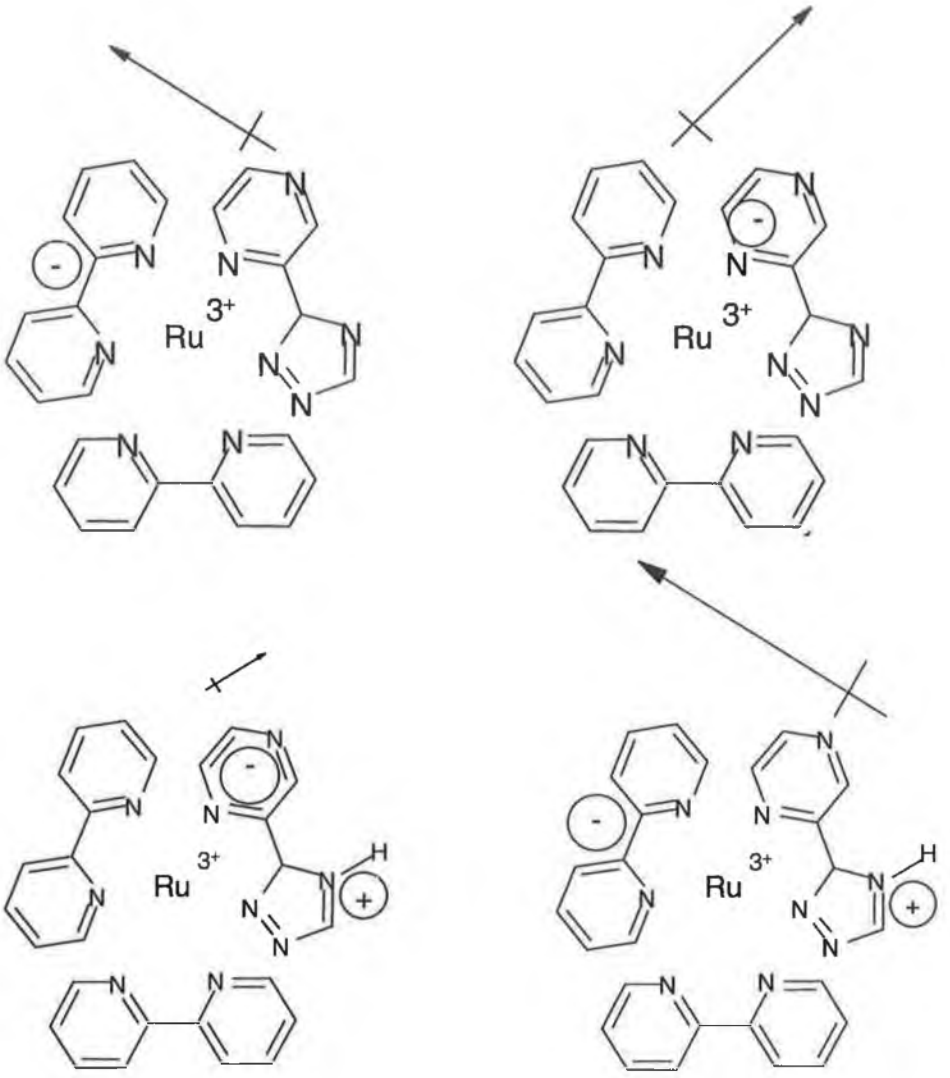

FIGURE 5.33: ESTIMATED DIPOLE MOMENTS OF $[Ru(bpy)_2(pztr)]^+$ AND $[Ru(bpy)_2(Hpztr)]^{2+}$.

As for $[Ru(phen)_2(Hpztr)]^+$, the dpp containing complexes in both protonation states show a band at lower energy than the main emission. This band, however, is seen to gradually reduce as the temperature is increased and disappears at higher temperatures. Previous studies have observed emission of this type from complexes containing a bpy moiety.[35] They were assigned as due to bpy framework vibrations and are emissions from $\nu'_m = 0 \rightarrow \nu_m = 1$ where ν'_m is an excited state vibrational mode and ν_m is the ground state.

Temperature dependent excited state lifetime measurements have been used to calculate the activation energies and prefactors for the deactivation of the excited states formed. The results are presented in Table 5.6. From these the

coupling and deactivation processes can be elucidated. In general the activated processes can be separated into two categories[36]

Category A: Small activation energies (<800 cm^{-1}) and low prefactors (<10^9 s^{-1}).
Category B: Large activation energies (>2000 cm^{-1}) and large prefactors (>10^{11} s^{-1}).

Complexes with activation energies and prefactors in category A are indicative of deactivation via a state that is only weakly coupled to the ^{3}MLCT manifold. This is similar to a state observed by Meyer and co-workers[37] in photostable Ru(II) polypyridyl complexes. It is attributed to the so called "fourth" MLCT state of increased singlet character. The calculated activation energy is, therefore, the energy difference between the ^{3}MLCT and the fourth MLCT. Complexes which fall into category B are deactivated via the ^{3}MC. Deactivation from the ^{3}MC may occur via activated and non – activated decay. These processes are dealt with in Chapter 4. It can be seen from the results presented in TABLE 5.6 that the temperature dependent behaviour of all three complexes are seen to be that of category A. Therefore, all the complexes deactivate via the fourth MLCT state and do not populate the ^{3}MC. These results are in agreement with the photostability observed for deprotonated triazole complexes.[15,33] FIGURE 5.34 presents an overview of the ^{3}MLCT energy levels of the complexes studied.

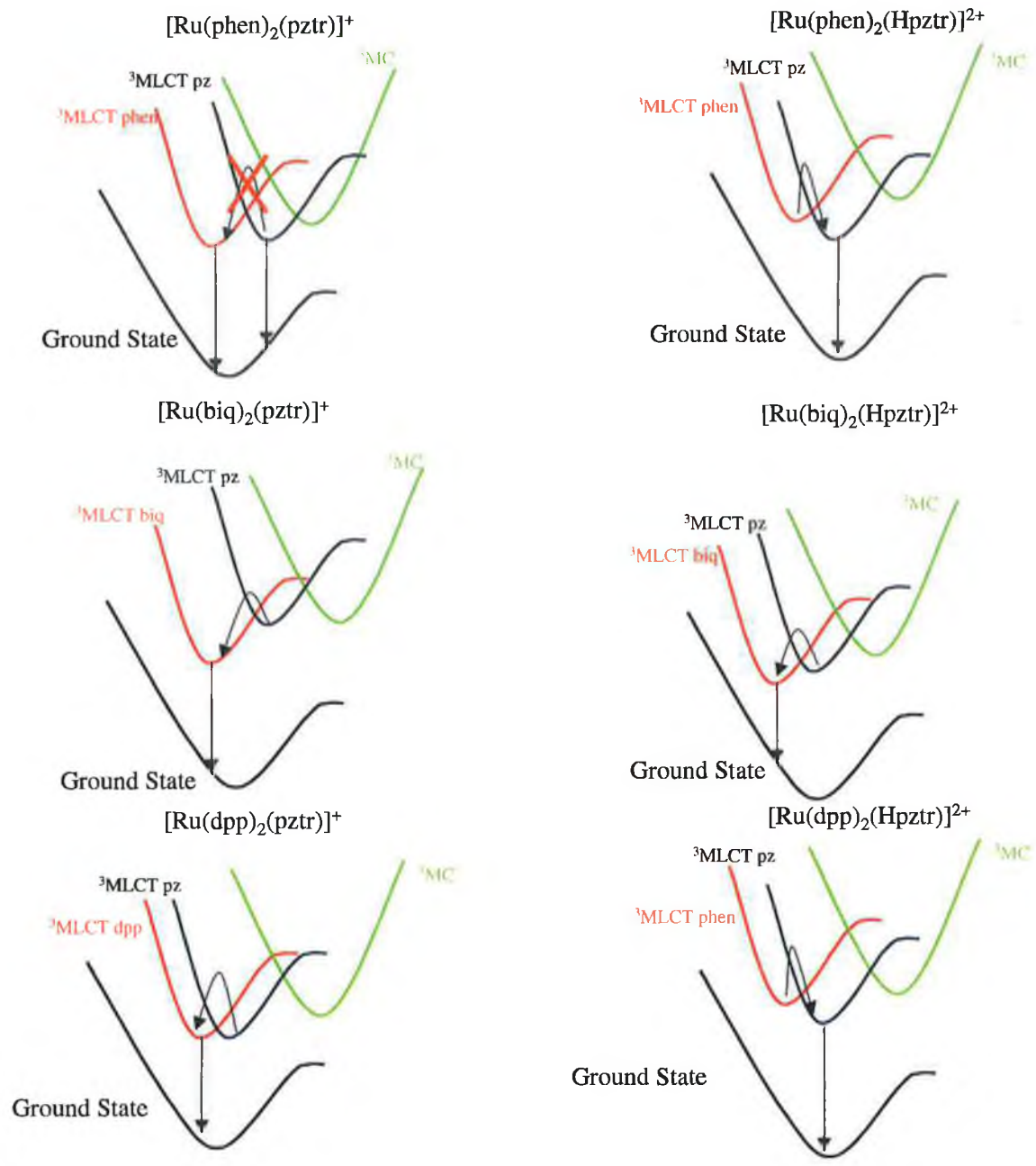

FIGURE 5.34: SCHEMATIC REPRESENTATION OF THE ENERGY LEVELS OF THE COMPLEXES DISCUSSED.

Transient absorption spectroscopy provides information on the excited state of a complex via the depletion of ground state absorption band. It also aids in the interpretation of excited state Raman spectra. In transient Raman measurements, the absence of significant absorption for the excited state at the probe wavelength will result in only ground state bands being observed.

FIGURE 5.13 shows the transient absorption spectra of $[Ru(biq)_2(pztr)]^+$in acetone. The bleach of the ground state bands at 350 and 560 nm are due to the absence of the ^{1}MLCT transition in the excited state. This indicates that the Ru(II) centre is oxidised and is no longer present. The absorptions between 400 – 500 nm are assigned as $\pi \rightarrow \pi^*$ transitions of the biquinoline ligand by comparison with previous results.[27] This is shows that the excited electron localised on one of the biquinoline ligands and that the biquinoline is formally reduced. The LMCT bands observed at longer wavelengths are most likely due to transition from the ligands to the oxidised Ru(III) metal centre. It is important to note the baseline has not fully recovered after 380 ns. This is longer than the excited state lifetime presented in TABLE 5.2 (albeit in acetonitrile) and may indicate some photochemical activity in the complex during the experiment. No absorption is present at 355 nm. This is the probe wavelength used in the transient resonance Raman experiments and, therefore, indicates that the excited state bands of this complex will not undergo resonance enhancement at this energy.

FIGURE 5.14 gives the transient absorption spectra of $[Ru(dpp)_2(pztr)]^+$ in acetone. Ground state bleaching is observable between 400 – 500 nm due to loss of the ^{1}MLCT absorption. This indicates the depletion of the Ru(II) centre. The excited state absorption for the dpp ligand is centred at 370 nm and is due to the $\pi \rightarrow \pi^*$ of the dpp ligand. At higher wavelengths transitions to the Ru(III) centre are also present. The spectra of $[Ru(dpp)_2(pztr)]^+$ appear blue – shifted in comparison to the biq analogue. This reflects the higher energy of the dpp ligand. It is also clear that there is a significant absorption at 355 nm for this complex, indicating that resonance enhancement of the excited state bands is possible. These results highlight the importance of excited state absorption spectra in the interpretation of excited state Raman measurements.

The resonance Raman spectra of the $[Ru(dpp)_2(pztr)]^+$ are presented in section 5.3.4.1 in both protonation states. These spectra are dominated by bands due to the dpp moiety at all wavelengths. These results are interesting

as the transient resonance Raman appears to show a Hpztr based ^{3}MLCT for the protonated complex(*vide infra*). However, the scattering ability of the Hpztr ligand is known to be quite weak and the bands may not be observable in some of the lesser quality spectra.

The results obtained for $[Ru(phen)_2(pztr)]^+$ are somewhat different to those reported above. The deprotonated complex presents bands due to both the phen and pztr ligand upon excitation at 488 nm. As the excitation wavelength is red – shifted contributions from both ligands continue at 514 nm. The quality of the spectra of the protonated complexes are poor in comparison to the deprotonated complexes. The spectral quality may be a reflection of the poor scattering ability of phen ligands and shortened lifetimes of the protonated complexes. For the protonated complexes, bands due to the phen ligand are only observed at 488 nm, while both the pyrazine – triazole and phen ligands contribute at 514 nm. This is due to the shift of the pztr ligand to lower energy on protonation and hence out of resonance with the 488 nm excitation.

Transient resonance Raman spectroscopy is used to investigate the location of the excited state in heteroleptic complexes. It is particularly useful when emission may occur from more than one location or the excited state location may change with experimental conditions, as is the case in the present study.

The transient resonance Raman spectra of $[Ru(biq)_2(pztr)]^+$ and $[Ru(biq)_2(Hpztr)]^{2+}$ show that the excited of these complexes is dominated by the biq moiety. This is unsurprising due to the strong π- acceptor nature of the biq ligand. The spectra of both $[Ru(phen)_2(Hpztr)]^{2+}$ and $[Ru(dpp)_2(Hpztr)]^{2+}$ (in this case $[Ru(bpy)(dpp)(Hbpzt)]^{2+}$) show bands which can be tentatively assigned as due to $Hpztr^{\bullet-}$. Although spectra for the deprotonated complexes were not obtained comparisons with other studies and on the basis of the similarities between the bpy and phen / dpp ligands would suggest that the excited state for $[Ru(phen)_2(pztr)]^+$ and

$[Ru(dpp)_2(pztr)]^+$ is based on the LL ligands. Protonation, therefore, leads to the switching of the location of the excited state as previously observed for pyrazine – triazole containing complexes.[18,19] The switching of the location of the excited state may also be used to explain the reduced effect of protonation on the emission for both $[Ru(phen)_2(pztr)]^+$ and $[Ru(dpp)_2(pztr)]^+$ in comparison to $[Ru(biq)_2(pztr)]^+$ (see TABLE 5.2).

DFT calculations have been employed to aid in the interpretation of the experimental results. The energy and location of the HOMO frontier orbitals can be related to the electrochemical results and the source of an electron in the excited state. The calculated isosurfaces for the LUMO and LUMO+1 have been used to approximate the location of the ^{3}MLCT excited state. There are a number of assumptions which must be borne in mind, namely: that the virtual Kohn-Sham orbitals from the DFT calculations are equivalent to unoccupied orbitals; that the lowest energy transition is to the lowest unoccupied orbitals; and that the ^{1}MLCT is located on the same ligands as the ^{3}MLCT state. The validity of these assumption for the complexes studied will also be discussed. Data for the first 20 HOMO and LUMO frontier orbitals is presented Appendix C.

The electrochemical properties of the complexes are well predicted at the present level of theory. For all complexes the HOMO frontier orbitals are dominated by metal centre. This is in agreement with reversibility of the electrochemical processes and previous studies on Ru(II) complexes containing a triazole moiety.[39] Koopman's theorem predicts that the electron which is most easily oxidation will be promoted on the formation of the excited state. Therefore, the DFT calculations also predict that the metal is also the source of the electron for photoexcitation. Again these results agree well with the transient absorption measurements which show the depletion of the Ru(II) bands on excitation. Protonation of the triazole ligand results in a decrease in its σ – donor properties and in turn in the electron density on the metal

centre. This is reflected in the reduced energy of the metal ligands in all the protonated complexes.

In the present study an attempt is made to predict the location of the ^{3}MLCT based on the LUMO frontier orbitals. It should be noted that the excited state energies of pyrazine – triazole containing complexes are non – facile as highlighted by the dual emissive, bi – exponential excited state decay observed at low temperatures. For the phen and dpp containing complexes, the switching of location of the excited state from the LL ligand in the deprotonated complex to the pyrazine moiety in the protonated complex is well predicted (FIGURE 5.29 and FIGURE 5.31). The isosurfaces and PDOS diagrams for these complexes are quite similar, as is predicted by steady state spectroscopy (TABLE 5.2), and as would be expected on the basis of their structure. This is interesting considering that these complexes show differing low temperature photophysics. Therefore, the contribution of other factors, rather than simply the energy gap between pyrazine and LL ligands, must be considered when attempting to rationalise their low temperature emissive behaviour. At this point, it is appropriate to note that the calculations have been preformed without the inclusion of a solvent shell. This was done due to the extra time required to include solvent effect and due to the number of complexes in the present study. Considering that MLCT states are known to be solvent sensitive and the presence of free nitrogens on both the triazole and pyrazine moiety these effects may be substantial.[38] Previous work in our group compared the calculated Raman spectra of $[Ru(bpy)_3]^{2+}$ with and without solvents effects.[39] Calculations using the Onsager model revealed little change in frequencies, although the intensity showed some differences. Future work may, therefore, concentrate on the effect of solvent on the HOMO and LUMO orbitals for a selection of complexes.

The HOMO and LUMO orbitals of $[Ru(biq)_2(pztr)]^+$ and $[Ru(biq)_2(Hpztr)]^{2+}$ are also similar to those of the other two complexes. This result is surprising considering the lower σ – donor and π – acceptor properties of the biquinoline

ligands result in a reduction in the energy of the absorption and emission bands of these complexes (TABLE 5.2). The metal based HOMO frontier orbitals for the biq containing complexes are in agreement with previous experimental results. However, the switching of the excited state from the biq to the pyrazine moiety on protonated does not agree with experimental results. This again highlights the caution which must be used when using the LUMO orbitals to model the ^{3}MLCT. This also highlights the need to include solvent effects for accurate calculation of the electronic properties of charged complexes.

5.5 Conclusion.

The present work further investigates the phenomenon of dual emission at low temperatures as observed for Ru(II) complexes with a pyrazinyl triazole ligands. The results show that the presence of a deprotonated a pyrazine – triazole does not ensure that the complex will be dual emissive. The lack of dual emission from the complex $[Ru(dpp)_2(pztr)]^+$ also serves to highlight the importance of other factors, such as the extent of delocalisation, which may affect the emission behaviour to the same magnitude as the energy levels of the ligands. This work also uses a variety of techniques and shows the ability to obtain a more complete picture of inorganic photophysics through a multifaceted approach.

One technique which is gaining increasing importance in our own work, and throughout the area of inorganic chemistry, is that of computational studies. The results presented here again show the value of the ability to visualise the location of the ground and excited states, and the overlap between orbitals. The agreement of the calculated results with the steady state spectroscopy increases the confidence in the interpretation of these results although other studies (such as the temperature dependent emission spectra) show the picture to be non – facile. However, the results obtained for $[Ru(biq)_2(Hpztr)]^+$ also emphasise that assumptions about the Kohn – Sham virtual orbitals and the correlation between the ^{1}MLCT and ^{3}MLCT may not be appropriate in all cases. Further study is required, particularly for complexes containing a negative ligand, to increase knowledge on the level of calculation needed to obtain consistently accurate results.

5.6 Bibliography

1 Lehn, J.-M., Supramolecular Chemistry: Concepts and Prespectives, VCH, **1995**.

2 Balzani, V., Scandola, F., Supramolecular Photochemistry, Ellis Horwood, **1991**.

3 Constable, E.C., Handel, R.W., Housecroft, C.E., Morales, A.F., Flamigni, L., Barigelletti, F., *Dalton Trans.*, **2003**, 1220.

4 Calvert, J.M. Casper, J.V., Binstead, R.A., Westmoreland, T.D., Meyer, T.J., *J. Am. Chem. Soc.*, **1982**, *104*, 6620.; Sauvage, J.P., Collin, J.P., Chambron, J.C.Guillerez, S., Coudret, C, Balzani, V., Barigelletti, F., De Cola, L., Flamigni, L., *Chem. Rev.*, **1994**, *94*, 993.

5 Kalyanasundaram, K., Photochemistry of Polypyridine and Porphyrin Complexes, Academic Press, **1996**.

6 Damrauer, N., Boussie, T.R., Devenney, M., McCusker, J.K., *J. Am. Chem. Soc.*, **1997**, *119*, 8253.

7 Juris, A., Barigelletti, F., Balzani, V., Belser, P., von Zelewsky, A., *Isr. J. Chem.*, **1983**, *22*, 2818.

8 Juris, A., Balzani, V., Belser, P., von Zelewsky, A., *Helv. Chim. Acta*, **1981**, *64*, 2175.

9 Mabrouk, P.A., Wrighton, M.S., *Inorg. Chem.*, **1986**, *25*, 526.

10 Giordano,P.J., Bock, C.R., Wrighton, M.S., Interrante, L.V., Williams, R.F.X., *J. Am. Chem. Soc.*, **1977**, *99*, 3187.

11 Juris, A., Balzani, V., Barigelletti, F., Campagna, S., Belser, P., von Zelewsky, A., *Coord. Chem. Rev.*, **1988**, *84*, 85.

12 Watts, R.J., Crosby, G.A., *J. Am. Chem. Soc.*, **1971**, *93*, 3184.

13 Kawanishi, Y., Kitamura, N., Kim, Y., Tazuke, S., *Riken Q.*, **1984**, *78*, 212.

14 Friedman, A.E., Chambron, J.C., Sauvage, J.P., Turro, N.J., Barton, J.K., *J. Am. Chem. Soc.*, **1990**, *112*, 4960.

15 Nieuwenhuis, H.A., Haasnoot, J.G., Hage, R., Reedijk, J., Snoeck, T.L., Stufkens, D.J., Vos, J.G., *Inorg. Chem.*, **1991**, *30*, 48. ; Wang, R., Vos, J.G., Schmehl, R.H., Hage, R., *J. Am. Chem. Soc.*, **1992**, *114*, 1964.

16 O'Connor, C.M., Ph.D. Thesis, Dublin City University, **1999**.

17 Keyes, T.E., Weldon, F., Muller, E., Pechy, P., Grätzel, M., Vos, J.G., *Dalton Trans.*, **1995**, *16*, 2705.

18 Henry, W., Browne, W.R., Ronayne, K.L., O'Boyle, N.M., Vos, J.G., McGarvey, J.J., *J. Mol. Struct.*, **2005**, *735*, 123.

19 Keyes, T., O'Connor, C.M., O'Dwyer, U., Coates, C.G., Callaghan, P., McGarvey, J.J., Vos, J.G., *J. Phys. Chem. A*, **1999**, *103*, 8915.

20 Browne, W.R., Ph.D., Thesis, Dublin City University, **2002**.

21 Kober, E.M., Meyer, T.J., *Inorg. Chem.*, **1984**, *23*, 3877.

22 Damrauer, N.H., McCusker, J.K., *Inorg. Chem.*, **1999**, *38*, 4268.

23 Caspar, J.V., Meyer, T.J., *Inorg. Chem.*, **1983**, 22, 2444.

24 Hage, R., Ph.D. Thesis, Leiden University, **1991**.

[25] Vos, J.G., Polyhedron, **1992**, *11*, 2285.

[26] Nieuwenhuis, H.A., Haasnoot, J.G., Hage, R., Reedijk, J., Snoeck, T.L., Stufkens, D. J., Vos, J.G., *Inorg. Chem.*, **1991**, *30*, 48.

[27] Creutz, C., Chou, M., Netzei, T.L., Okumura, M., *J. Am. Chem. Soc.*, **1980**, *102*, 1309.

[28] Alexander, B.D., Dines,T.J., *Inorg. Chem.*, **2004**, *43*, 342. ; Alexander, B.D., Dines,T.J., *J. Phys. Chem. B*, **2005**, *109*, 3310.

[29] Chang, Y.J., Xiaobing, X., Yabe, T., Soo – Chang, Y., Anerson, D.R., Orman, L.K., Hopkins, J.B., *J. Phys. Chem.*, **1990**, *94*, 729.

[30] Coates, C.G., Keyes, T.E., McGarvey, J.J., Hughes, H.P., Vos, J.G., Jayaweera, P. M., *Coord. Chem. Rev.*, **1998**, *171*, 323.

[31] Lin, C.T., Boettcher, W., Chou, M., Creutz, C., Sutin, N., *J. Am. Chem. Soc.*, **1976**, *98*, 6536.

[32] Casper, J. V., Meyer, T. J., *Inorg. Chem.*, **1983**, *22*, 2444.; Casper, J. V., Meyer, T. J., *J. Am. Chem. Soc.*, **1983**, *105*, 5583.

[33] Keyes, T.E., Vos, J.G., Kolnaar, J.A., Haasnoot, J.G., Reedijk, J., Hage, R., *Inorg. Chim. Acta*, **1996**, *245*, 237.

[34] Barigelletti, F., Juris, A., Balzani, V., Belser, P., von Zelewsky, A., *J. Phys. Chem.*, **1987**, *91*, 1095.

[35] Caspar, J.V., Meyer, T.J., *Inorg. Chem.*, **1983**, *22*, 2444.

[36] Barigelletti, F., Juris, A., Balzani, V., Belser, P., von Zelewsky, A., *Coord. Chem. Rev.*, **1988**, *84*, 85.

[37] Kober, E.M., Meyer, T.J., *Inorg. Chem.*, **1984**, *23*, 3877.

[38] Browne, W.R., O'Boyle, N.M., Henry, W.,Guckian, A.L., Horn, S., Fett, T., Duati, M., De Cola, L., Coates, C.G., Ronayne, K.L., McGarvey, J.J., Vos, J.G., *J. Am. Chem. Soc.*, **2005**, *127*, 1229.

[39] O'Boyle, N.M., Ph.D. Thesis, Dublin City University, **2004**.

Chapter 6

Future Work and Conclusions.

The final chapter provides an overview of the results from the previous chapters and the conclusions drawn. Suggestions are provided for further studies to build on the results already obtained.

6.1 Conclusions.

This work looks at the photophysical properties of Ru(II) complexes over the pico-, nano- and micro – second timescales. A wide range of techniques have been used to obtain a more complete view of the properties, and the factors affecting these properties, of the complexes studied. The experimental techniques range from the standard; steady state fluorescence; to the highly advanced spectroscopic method of picosecond time resolved resonance Raman. Computational studies have also been employed in an attempt to rationalise the observed behaviour and to assess the accuracy of DFT methods for Ru(II) complexes.

Chapter 3 uses picosecond resonance Raman spectroscopy to investigate the grow – in of the steady state spectra of $[Ru(bpy)_3]^{2+}$ (where bpy is 2,2′ – bipyridine) . The steady spectra are thought to represent the formation of the thermally equilibrated excited (THEXI) state of the ^{3}MLCT. These results show that the excited state resonance Raman spectrum is still evolving on the picosecond timescale. It is important to remember that Raman spectroscopy is a vibrational technique and, as such, is best placed to provide information on the vibrational state of the complex. Although these results are somewhat in contradiction with other studies they provide the most direct probe of the vibrational nature of the THEXI state. The results obtained are extended to the heteroleptic complexes $[Ru(bpy)_2(phpytr)]^+$ and $[Ru(bpy)_2(Hdcb)]^+$ (where phpytr is 2,-(5′-phenyl-4′ [1,2,4]triazole-3′-yl)pyridine and dcb is 4,4′-dicarboxy 2,2′-bipyridine). These studies show that the time taken for formation of the THEXI state is not dependent on the symmetry, charge or the ^{3}MLCT – ^{3}MC energy gap of the molecule. The results for $[Ru(bpy)_2(Hdcb)]^+$ are particularly relevant for the development of dye – sensitised solar cells, for which charge injection was proposed to occur from a non – equilibrated state. No changes were observed in the rate of THEXI formation due to ligand deuteriation or solvent.

Chapter 4 further studies the phenomenon of low temperature dual emission, first observed for $[Ru(bpy)_2(pztr)]^{2+}$ (where pztr is 2-(1,2,4-triazol-3-yl)-pyrazine), and in particular the effect of a substituent at the C-5 position. Dual emission, in this case, may be described as the simultaneous emission from two non – thermally equilibrated excited states at low temperature. The results show that emission is observed for both the pyrazine and bpy based ^{3}MLCT's for the deprotonated complex, $[Ru(bpy)_2(thpztr)]^+$ (where thpztr is 2-(5-pyrazin-2'-yl)-1,2,4-triaz-3-yl)-thiophene). By comparison, the protonated complex, $[Ru(bpy)_2(Hthpztr)]^{2+}$, and the pyridine analogue are shown to have singly emissive, mono – exponential excited state decays. Temperature dependent excited state lifetime studies are employed to investigate the route of excited state deactivation for the complexes. These measurements show that the pyrazine based ^{3}MLCT deactivates via high frequency vibrations which lead to the ^{3}MLCT – ^{3}MC crossing region, while the bpy based states deactivate via the 4th MLCT. Resonance Raman studies are used to characterise the ground state absorption, while transient Raman studies show the switching of the location of the excited state for $[Ru(bpy)_2(thpztr)]^+$ upon protonation. The complexes have also been investigated as a model of a simple dyads using Density Functional Theory (DFT) methods, where the metal centre and the thiophene are the sub units. Interaction is observed between the units in the ground but not the excited state. This highlights the care which must be used when extrapolating ground state properties to the excited state and visa versa.

Chapter 5 also deals with temperature dependent dual emission. The complexes $[Ru(LL)_2(pztr)]^+$ (where LL is 1,10-phenanthroline (phen), 2,2' – biquinoline (biq) or 4,7 – diphenyl – 1,10-phenanthroline (dpp)) have been studied. Dual emission is observed for the deprotonated phen containing complex, $[Ru(phen)_2(pztr)]^+$, while a single emission is observed for all other complexes, irrespective of protonation state. The differences in the low temperature emissive properties are attributed to the σ – donor / π – acceptor

properties biq ligand and the increased excited state delocalisation for dpp. Excited state lifetime studies of the deprotonated complexes have shown that the non – radiative decay processes of the LL based states are via the 4th MLCT. Raman studies have been employed to characterise the ground state absorption, while transient studies have tentatively shown pH dependent excited state location for both phen and dpp complexes. DFT studies have been used to further investigate dual emissive behaviour and while satisfactory agreement between experimental and calculated results is obtained, the importance of solvent effects is noted.

6.2 Future Work.

During the course of this work a number of potential areas for further study have become apparent. The suggestions for this future work are outlined below.

6.2.1 Chapter 3.

In order to further understand the ultrafast processes occurring for $[Ru(bpy)_3]^{2+}$ studies of a variety of other complexes would be beneficial. One such complex would be $[Ru(phen)_3]^{2+}$, which would help to establish if the behaviour was isolated to bpy based excited states. In the present work, attempts have been made to obtain anti – Stokes measurements. These bands are due to vibrationally hot molecules and should, therefore, decrease as the THEXI state is formed. It may be possible to obtain these signals by using a combination of pump and probe wavelengths where the overlap with Stokes bands is negligible. Another interesting area of investigation would be that of tetracyano complexes. The nanosecond excited state behaviour of complexes of the type $[Ru(LL)(CN)_4]^{2-}$ (where LL is selectively deuteriated 4,4'-diphenyl-2,2'–bipyridine, 4,7-diphenyl-1,10–phenanthroline and 4,7-dimethyl-1,10-phenanthroline, amongst others) have been thoroughly investigated via Raman (in the Queen's University of Belfast) and time resolved electronic

spectroscopy (in Dublin City University), with a manuscript now in preparation. Measurement of these complexes containing only a single chromophore would allow studies to deal with the issues of electron localisation and inter-ligand hopping.

6.2.2 Chapter 4.

A significant amount of work has been done to characterise the ground and excited state properties of complexes substituted with a thienyl moiety. Although computational studies have been extensively employed, the amount of calculated data on triazole containing complexes remains relatively small. There are a number of areas where this may be improved; specifically using time dependent DFT (TD-DFT) and frequency calculations. TD – DFT calculations are used to investigate excited state properties. The agreement of the present results with those obtained by TD-DFT would allow further light to be shed on one of the initial assumptions made, namely that the virtual Kohn-Sham orbitals from the DFT calculations are equivalent to unoccupied orbitals. Frequency calculations have been carried out on the thienyl substituted complexes. Although they initially show good agreement the ability to accurately calculated the vibrational frequencies for the negative triazole ligand is an area which required further study. The presence of the thienyl moiety also allows the potential for bonding with a gold surface. Although the present geometry would be sterically hindered, complexes bound to the thiophene at a different positions may be able to interact successfully with gold surfaces. This chapter highlights the potential for the thienyl substituted complexes to model simple molecule dyads. The temperature dependent behaviour of the dinuclear complexes based on a thiophene bridging may also be an area for alternative studies. The effect of the second metal centre on the dual emissive behaviour may provide valuable information on the nature of the deactivation processes and also on the role which the bridge plays in mediating interaction between the metal centres. Low temperature excited state resonance Raman studies may also be used to further investigate dual

emission. In the 140 – 170 K temperature region it may be possible to observe excited state bands due to both the pyrazine – triazole and bpy ligands and hence provide further proof of two non – thermally equilibrated excited states.

6.2.3 Chapter 5.

The dual emission process which has been observed for $[Ru(phen)_2(pztr)]^+$ requires further study. As mentioned above low temperature transient resonance Raman studies could be used to investigate the excited states present between 140 and 170K. Further effort is required to study the excited state decay of the protonated complexes. Studies in buytronitrile solutions may be of use due to the increased luminescent intensity observed for non H – bonding solvents. The quantum yield measurements for the complexes studied would provide information on the relative rates of radiative and non – radiative deactivation. This would be particularly interesting for the phen and dpp containing complexes as the excited state structure is expected to be quite similar and, hence, would provide information about the extent of excited state displacement. Further computational studies would also be advantageous. The inclusion of solvent effects may help to further understand the causes of dual emission and the interaction of pyrazine triazole ligands with dipoles. Again TD – DFT may be applied to investigate the excited state properties of the complexes.

Appendix A

Raman Spectra in Support of Chapter 3.

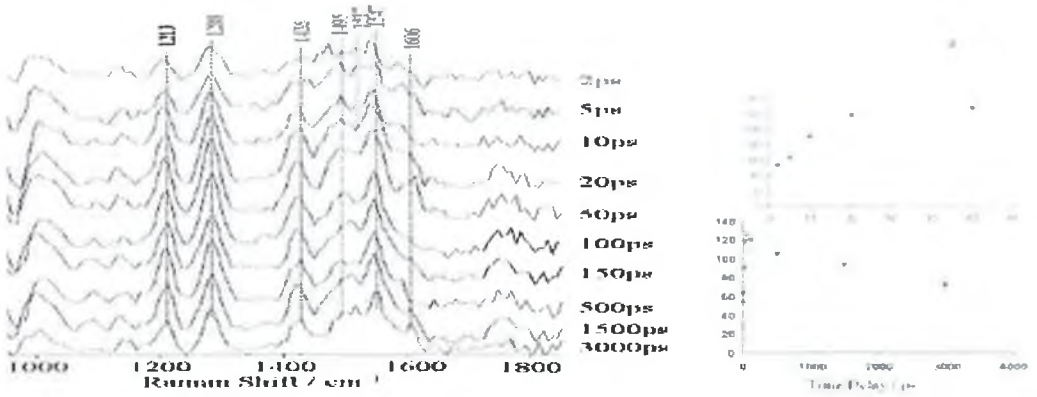

APPENDIX A-1: $[RU(BPY)_3]^{2+}$ IN H_2O WITH 400NM PUMP AND 350 NM PROBE EXCITATION

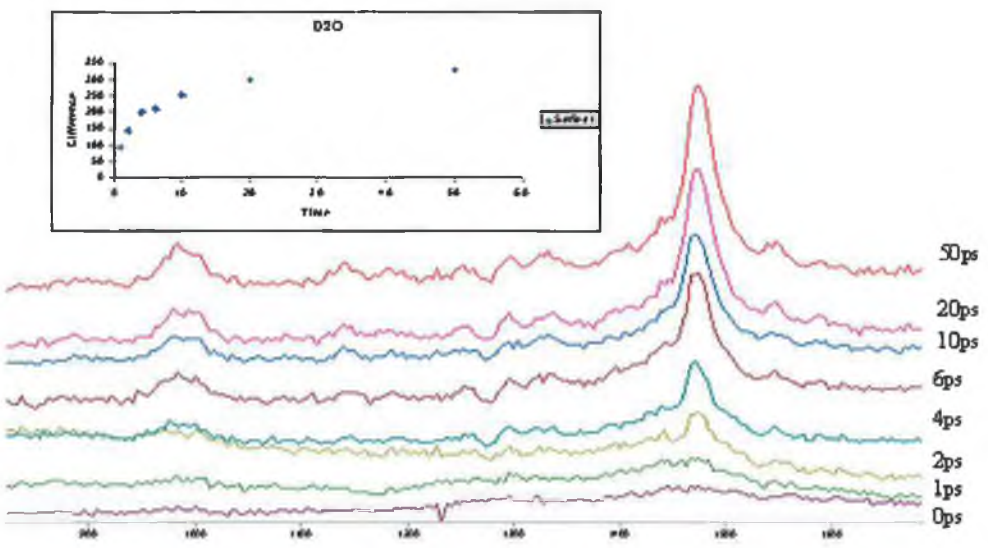

APPENDIX A-2:$[RU(BPY)_3]CL_2$ IN D_2O WITH PUMP AT 410 NM AND PROBE AT 475 NMWITH THE KINETICS OF BAND AT $1475CM^{-1}$.

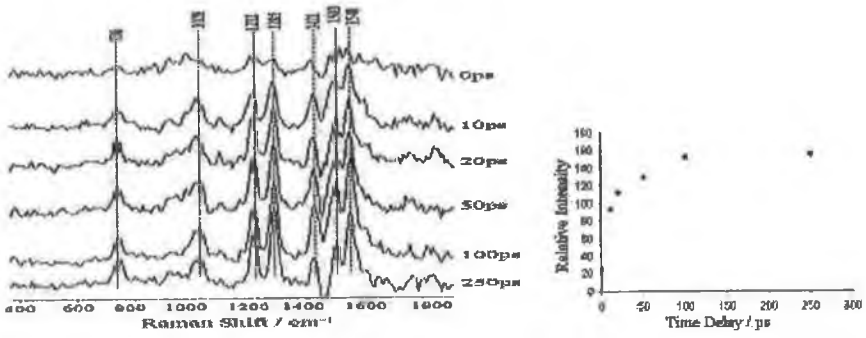

APPENDIX A-3: SPECTRA AND KINETICS OF $[RU(BPY)_3]^{2+}$ IN 1-HEXANOL WITH PUMP AT 400 NM AND PROBE AT 350 NM.

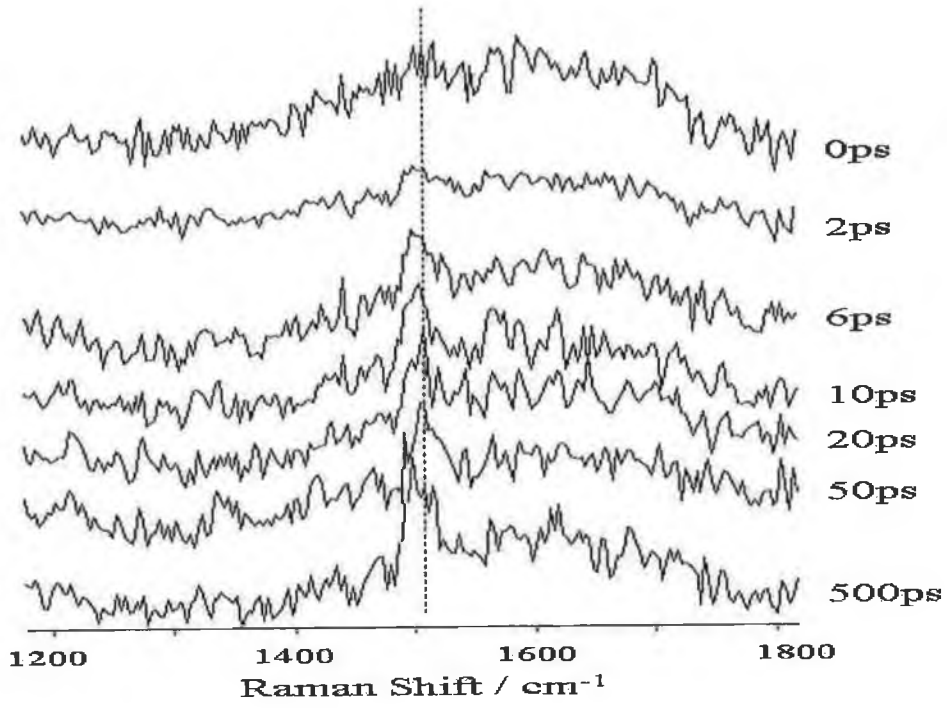

APPENDIX A-4: $[RU(BPY)_3]^{2+}$ IN H_2O WITH 400 NM PUMP AND 530 NM PROBE.

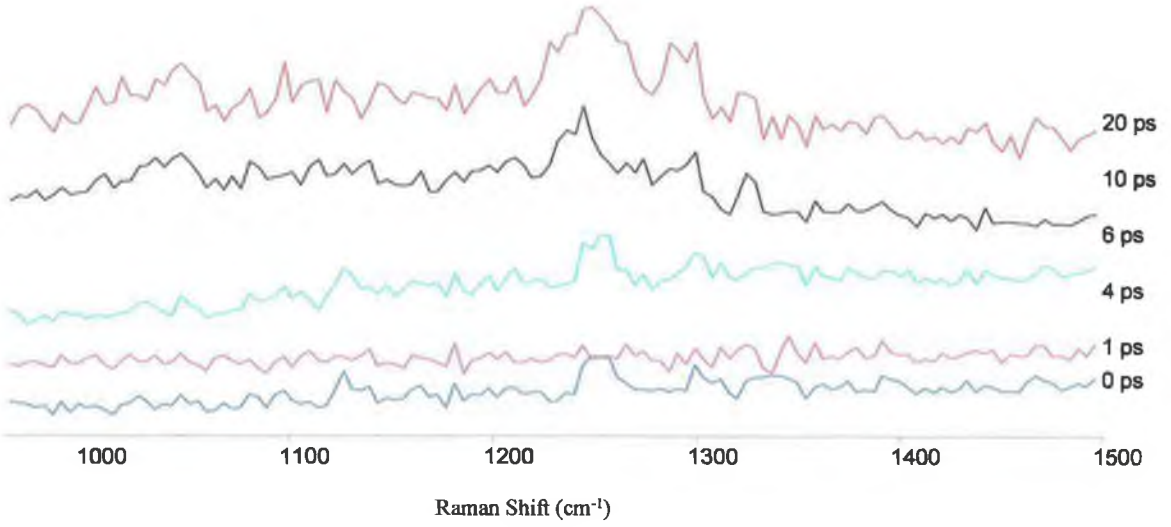

APPENDIX A-5: $[RU(BPY)_3]^{2+}$ IN H_20 PUMP 265NM AND PROBE 400NM.

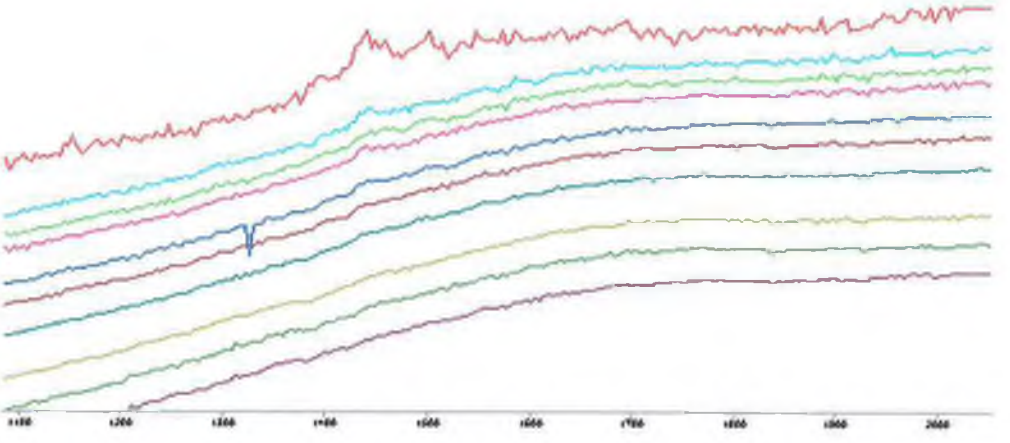

APPENDIX A-6: $[RU(D_8\text{-}BPY)_3]CL_2$ IN D_2O WITH PUMP AT 410 NM AND PROBE AT 470 NM.

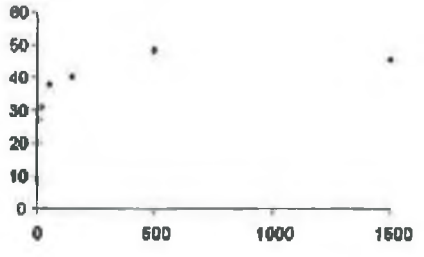

APPENDIX A-7: KINETICS OF $[RU(D_8\text{-}BPY)_2(PHPYTR)]^{1}$ IN CD_3CN WITH PUMP AT 400 NM AND PROBE AT 350 NM.

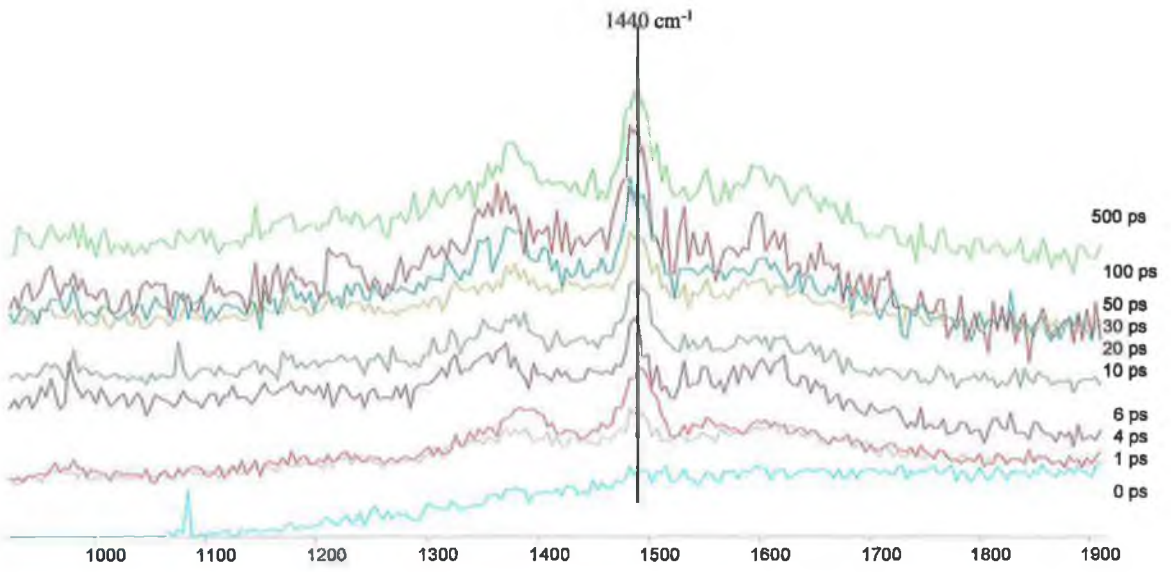

APPENDIX A-8: SPECTRA OF $[RU(BPY)_2(HDCB)]^+$ IN D_2O WITH PUMP 410 NM AND PROBE 470NM.

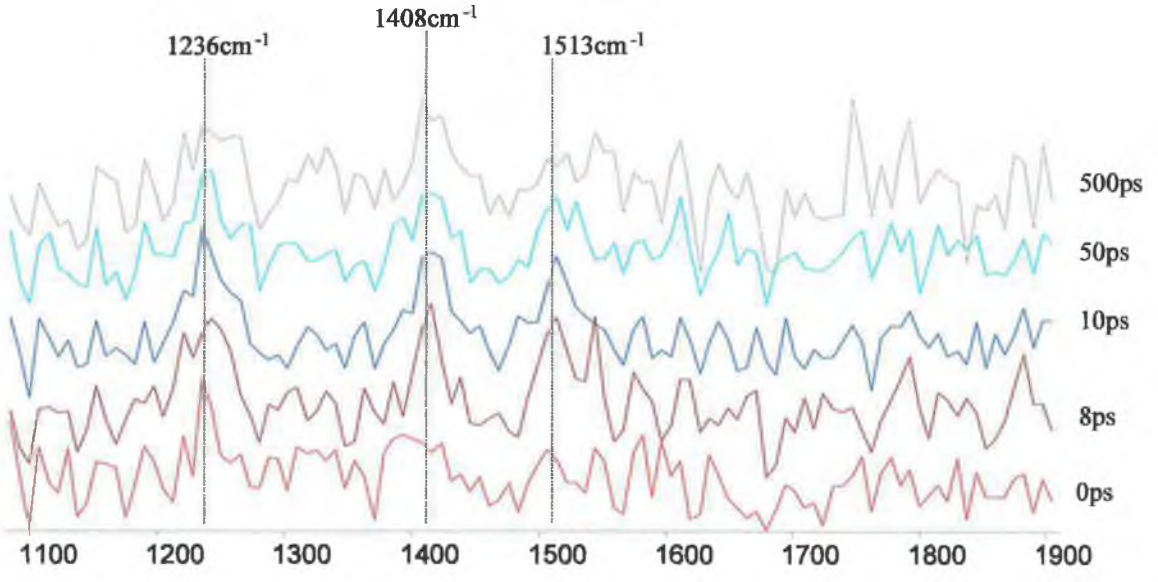

APPENDIX A-9: $[FE(BPY)_3]^{2+}$ IN H_2O PUMP 400 NM / PROBE 350 NM.

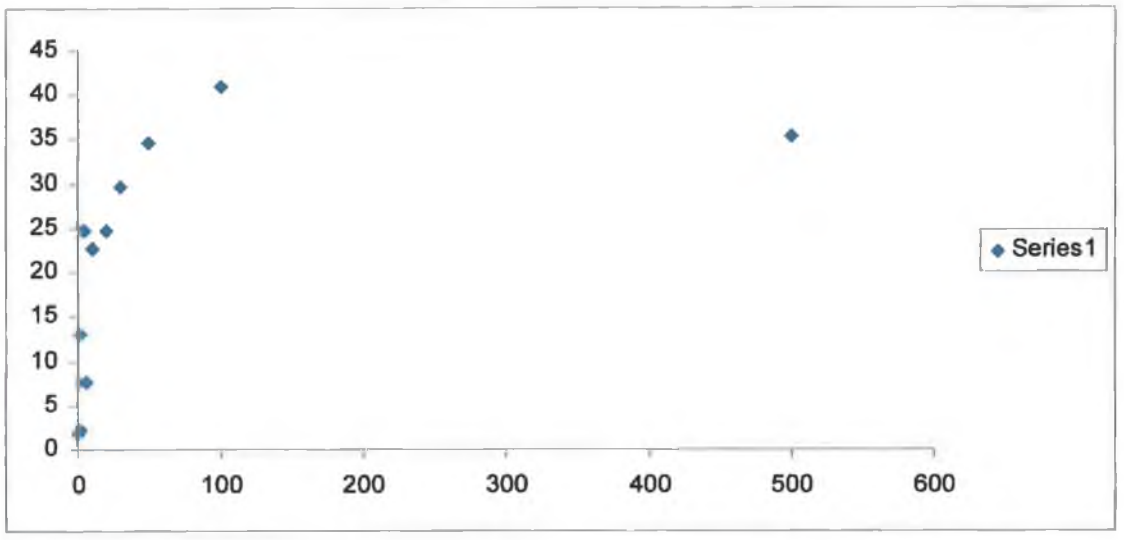

APPENDIX A-10: KINETICS OF BAND AT 1481CM^{-1} FOR $[Os(bpy)_3]^{2+}$ IN D_3-ACN WITH PUMP AT 410 NM AND PROBE AT 470 NM.

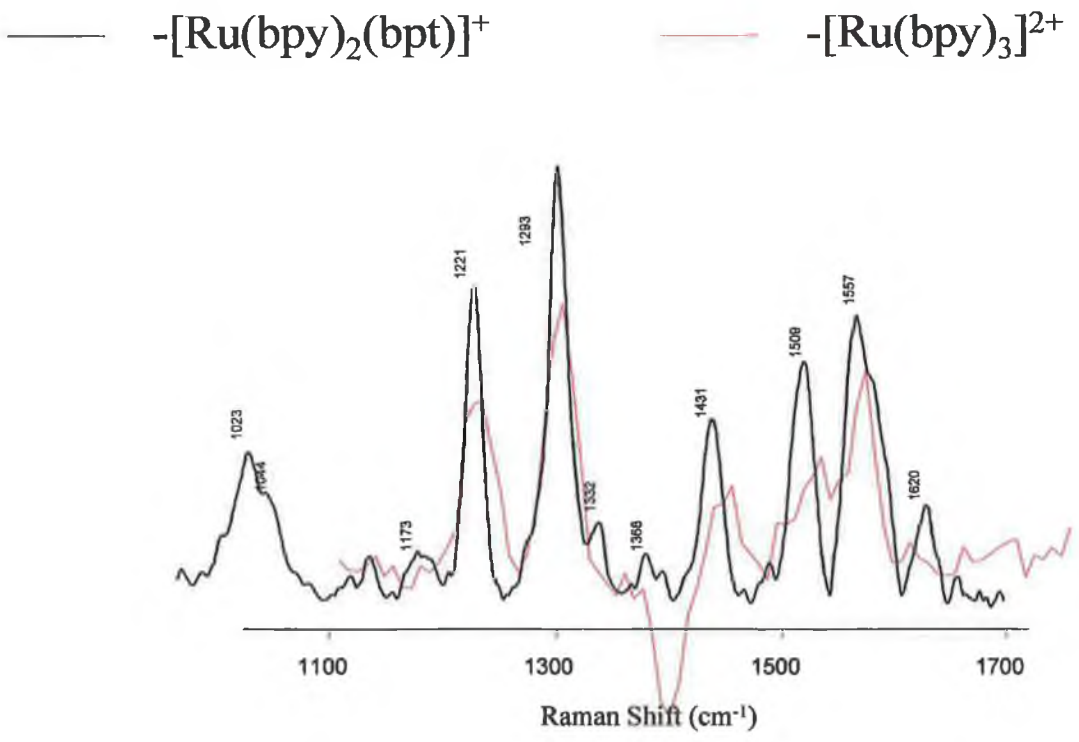

APPENDIX A-11: COMPARISON OF $[Ru(bpy)_3]^{2+}$ IN H_2O WITH PUMP AT 400 NM AND PROBE AT 350 NM AND $[Ru(bpy)_2(bpt)]^{+}$ WITH PUMP AND PROBE AT 355 NM. SPECTRUM OF $[Ru(bpy)_2(bpt)]^{+}$ OBTAINED FROM ROYNANE, K.L., PH.D. THESIS, QUEENS UNIVERSITY OF BELFAST, 2005.

	Raman Shift				
$[Ru(bpy)_2(bpt)]^+$	1557	1509	1431	1293	1221
$[Ru(bpy)_3]^{2+}$	1475	1432	1355	1215	1147
Error	82	77	76	78	74

APPENDIX A-12: COMPARISON OF BANDS FOR $[RU(BPY)_3]^{2+}$ IN H_2O WITH PUMP AT 400 NM AND PROBE AT 350 NM AND $[RU(BPY)_2(BPT)]^+$ WITH PUMP AND PROBE AT 355 NM. NOTE THE BANDS OBSERVED FOR $[RU(BPY)_2(BPT)]^+$ ARE IN AGREEMENT WITH THOSE OBSERVED BY DALLINGER, R.F., WOODRUFF, W.H., *J. AM. CHEM. SOC.*, 1979, *101*, 4391-4393 FOR $BPY^{\bullet-}$.

Appendix B

NMR Spectra, Photophysical and Computational Data in Support of Chapter 4.

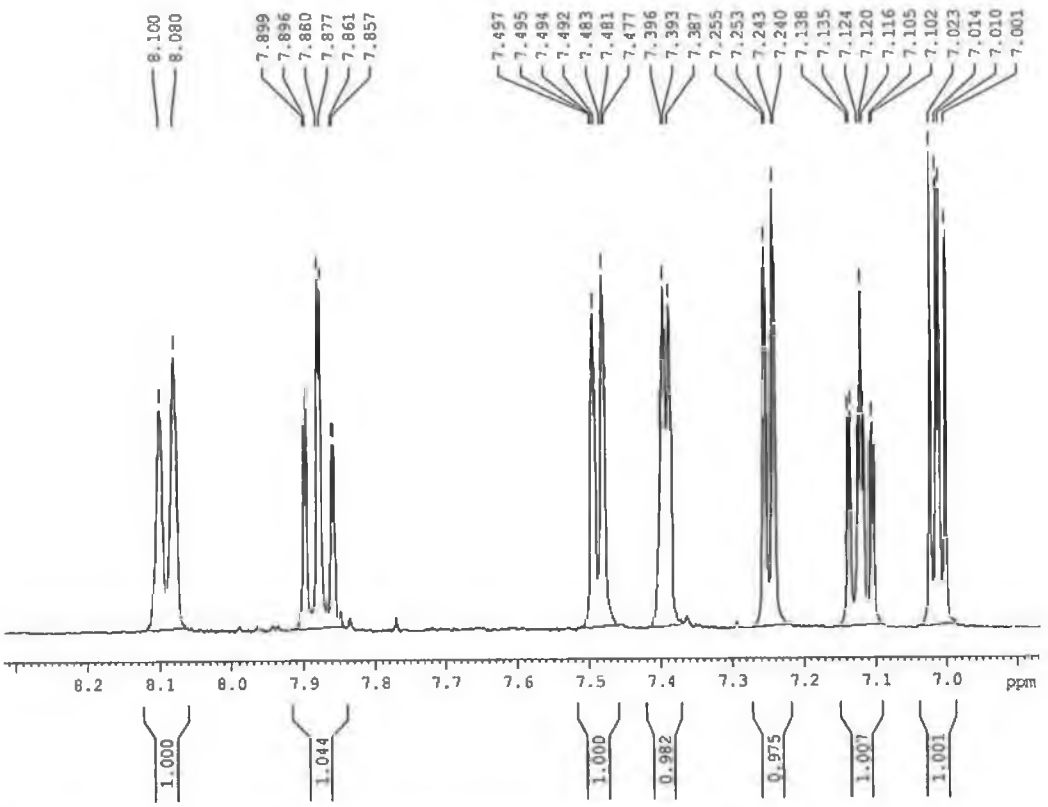

FIGURE B-1: NMR SPECTRUM OF $[RU(D_8\text{-BPY})_2(THPYTR)]$, 1D, IN CD_3CN.

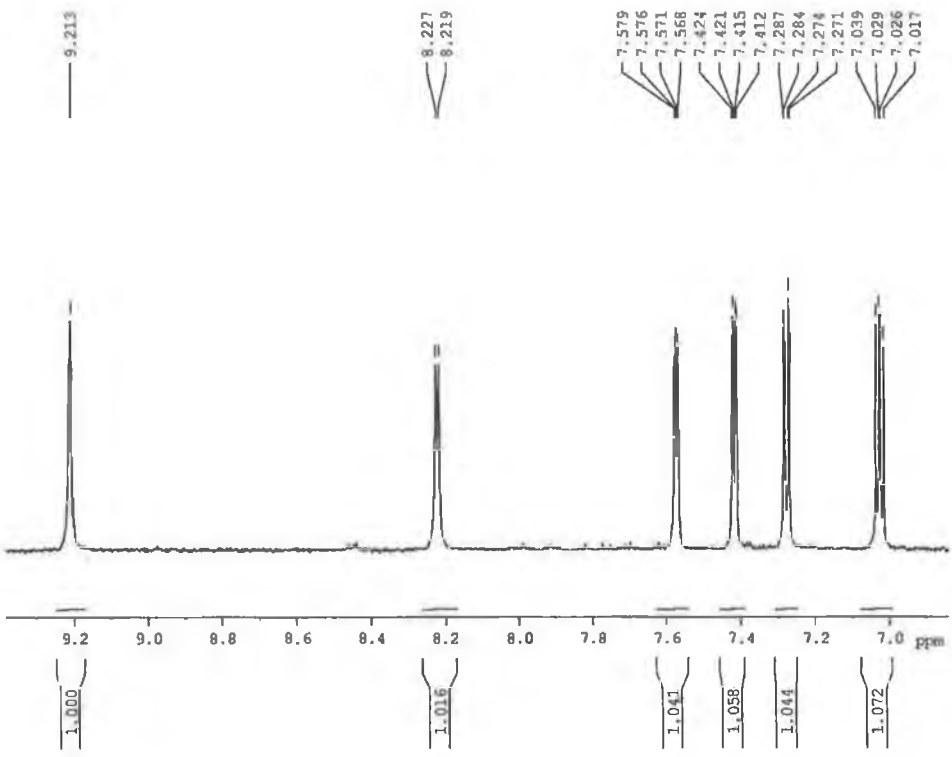

FIGURE B-2: NMR SPECTRUM OF $[RU(D_8\text{-}BPY)_2(THPZTR)]^+$, 2D, IN CD_3CN.

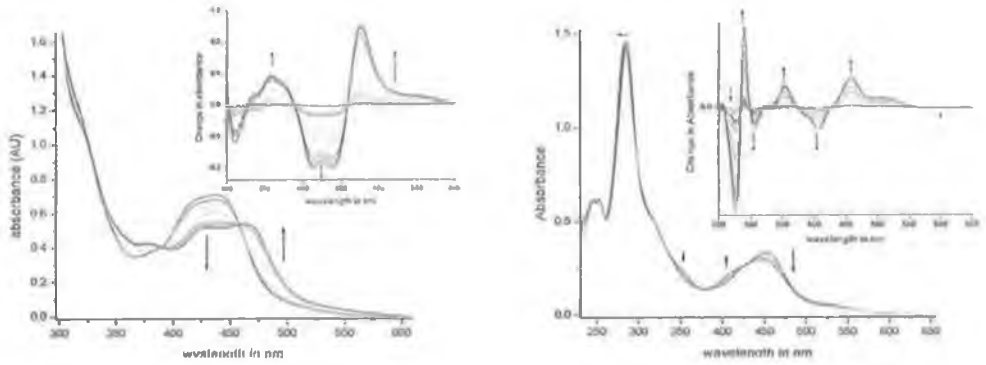

FIGURE B-3: CHANGES IN UV.VIS SPECTRA OF **1A** AND **2A** BETWEEN PH 0.5 AND 10. (INSET DIFFERENCES SPECTRA COMPARED WITH COMPLETELY THE PROTONATED COMPLEXES).

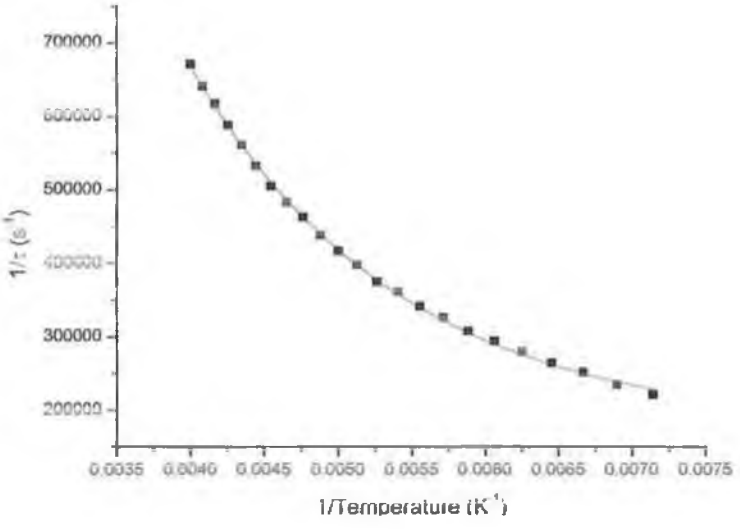

FIGURE B-4: GRAPH OF 1/TEMPERATURE VS RATE FOR 1D.

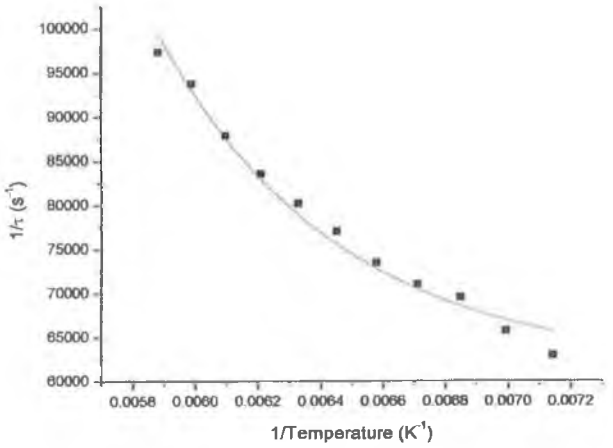

FIGURE B-5: GRAPH OF 1/TEMPERATURE VS RATE FOR H1P.

Temperature	Lifetime (ns)
140	1980
145	1851
150	1784
155	1737
160	1659
165	1585
170	1525
175	1439
180	1388
185	1287
190	1203
195	1130
200	1027
205	927
210	819
215	702
220	594
225	494
230	411
235	334
240	280
245	237
250	204

TABLE B-1: TEMPERATURE DEPENDENT LIFETIMES OF H1D.

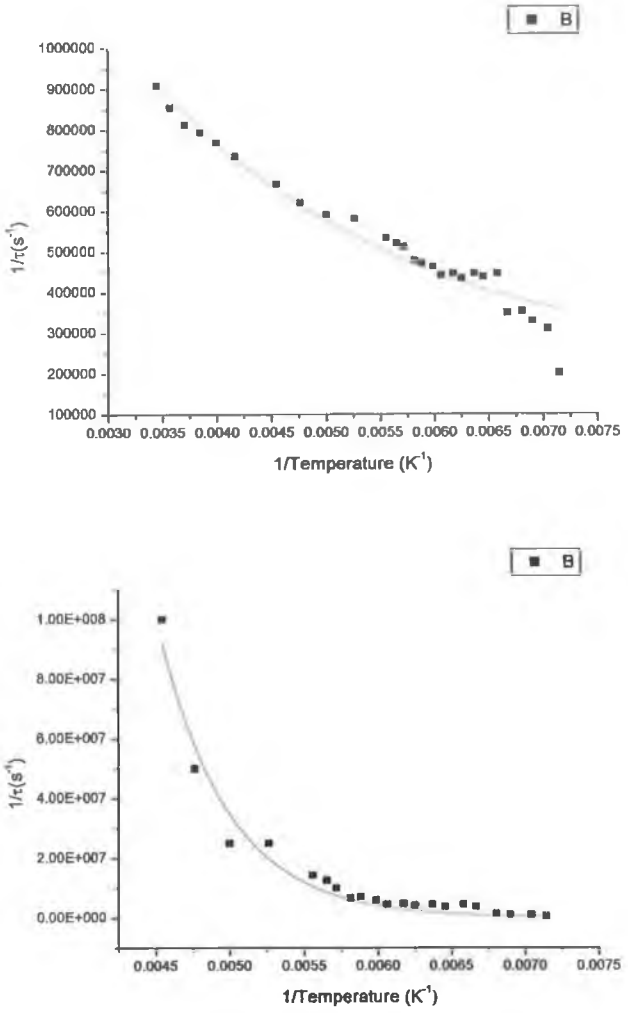

FIGURE B-6: GRAPH OF 1/TEMPERATURE VS RATE FOR 2P: (TOP)LOW ENERGY EMISSION AND (BOTTOM) HIGH ENERGY EMISSION.

Temperature (K)	Lifetime (ns)	Lifetime (ns)
140	127	438
143	118	363
146	133	356
149	134	437
152	117	588
155	97	626
158	40	132
161	39	128
164	38	152
167	37	312
170	31	437

TABLE B-2: EXCITED STATE LIFETIME DATA FOR H2P.

MO		eV	Symmetry	Ru	bpy1	bpy2	py	tr	th
164	L+20	-0.31	A	103	0	0	-6	-2	7
163	L+19	-0.36	A	0	1	12	14	22	50
162	L+18	-0.38	A	8	0	1	0	1	90
161	L+17	-0.43	A	1	4	80	2	4	9
160	L+16	-0.91	A	2	0	1	34	46	17
159	L+15	-1.47	A	109	0	-3	-3	-1	0
158	L+14	-1.53	A	111	-3	-4	0	0	0
157	L+13	-1.7	A	107	-4	-2	0	0	1
156	L+12	-2.03	A	69	5	14	1	11	0
155	L+11	-2.23	A	67	17	6	9	1	0
154	L+10	-2.61	A	0	92	7	1	0	0
153	L+9	-2.63	A	1	0	2	1	32	64
152	L+8	-2.85	A	1	7	91	0	1	1
151	L+7	-3.51	A	1	3	1	87	7	1
150	L+6	-3.92	A	2	92	4	1	0	0
149	L+5	-4.06	A	4	56	17	18	4	0
148	L+4	-4.09	A	3	24	12	51	10	0
147	L+3	-4.11	A	1	5	83	9	1	0
146	L+2	-4.39	A	1	17	78	3	0	0
145	L+1	-4.96	A	5	91	3	0	0	0
144	LUMO	-5.18	A	5	4	91	1	0	0
143	HOMO	-7.28	A	8	1	0	5	30	55
142	H-1	-8.24	A	72	6	5	1	5	11
141	H-2	-8.28	A	11	1	1	1	3	83
140	H-3	-8.34	A	61	9	4	2	6	18
139	H-4	-8.42	A	72	5	12	5	2	3
138	H-5	-8.96	A	3	0	1	28	51	17
137	H-6	-9.04	A	1	1	0	0	97	1
136	H-7	-9.84	A	0	91	1	0	6	1
135	H-8	-9.93	A	4	5	4	2	82	4
134	H-9	-10.04	A	5	4	47	1	34	9
133	H-10	-10.06	A	5	7	52	0	29	7
132	H-11	-10.64	A	0	1	1	67	23	7
131	H-12	-10.65	A	0	0	0	2	4	94
130	H-13	-10.88	A	1	2	13	80	2	1
129	H-14	-11.16	A	1	71	21	5	2	0
128	H-15	-11.28	A	2	76	9	12	1	1
127	H-16	-11.34	A	1	49	6	37	3	3
126	H-17	-11.43	A	2	57	32	4	2	3
125	H-18	-11.51	A	2	12	76	6	0	3
124	H-19	-11.57	A	3	33	58	3	1	1
123	H-20	-11.61	A	-1	45	40	9	3	4

FIGURE B-7: MOLECULAR ORBITAL DATA FOR 1.

MO		eV	Symmetry	Ru	bpy1	bpy2	py	Htr	th
164	L+20	-2.85	A	88	-6	0	0	2	18
163	L+19	-3.36	A	46	-3	-2	7	31	23
162	L+18	-3.87	A	106	0	-3	-2	1	1
161	L+17	-3.99	A	67	-3	-1	0	13	27
160	L+16	-4.03	A	63	-1	0	0	5	37
159	L+15	-4.05	A	47	-1	-2	3	15	40
158	L+14	-4.39	A	28	0	0	2	22	49
157	L+13	-4.52	A	5	0	1	43	49	2
156	L+12	-4.84	A	63	8	16	1	10	1
155	L+11	-4.94	A	66	17	7	9	1	0
154	L+10	-4.94	A	1	86	12	0	0	0
153	L+9	-5.12	A	2	12	86	1	0	0
152	L+8	-6.23	A	2	88	6	1	1	1
151	L+7	-6.35	A	1	11	22	9	25	32
150	L+6	-6.39	A	1	28	39	10	10	11
149	L+5	-6.46	A	2	44	54	0	0	0
148	L+4	-6.55	A	2	13	49	29	4	4
147	L+3	-6.79	A	1	13	26	50	5	5
146	L+2	-7.32	A	5	88	2	3	2	0
145	L+1	-7.44	A	6	0	63	18	10	2
144	LUMO	-7.55	A	1	8	31	37	19	3
143	HOMO	-10.79	A	51	4	2	5	15	23
142	H-1	-11	A	70	9	7	4	4	7
141	H-2	-11.09	A	77	4	12	6	1	0
140	H-3	-11.25	A	38	6	1	1	11	43
139	H-4	-11.74	A	0	0	0	0	1	99
138	H-5	-12.19	A	1	96	2	0	0	0
137	H-6	-12.33	A	1	2	97	0	0	0
136	H-7	-12.8	A	1	1	0	52	28	17
135	H-8	-13.33	A	2	2	4	2	89	1
134	H-9	-13.44	A	1	68	30	1	0	0
133	H-10	-13.62	A	1	10	60	28	1	0
132	H-11	-13.64	A	1	82	7	5	5	0
131	H-12	-13.72	A	1	70	25	1	3	0
130	H-13	-13.84	A	0	19	75	2	2	1
129	H-14	-13.92	A	7	33	41	15	2	1
128	H-15	-13.98	A	0	48	36	14	3	1
127	H-16	-14.06	A	7	5	44	37	5	4
126	H-17	-14.13	A	1	3	4	45	30	18
125	H-18	-14.18	A	-1	57	17	26	1	0
124	H-19	-14.22	A	0	0	0	0	1	98
123	H-20	-14.48	A	0	5	77	1	15	1

FIGURE B-8: MOLECULAR ORBITAL DATA FOR H1.

MO		eV	Symmetry	Ru	bpy1	bpy2	pz	tr	th
164	L+20	-0.47	A	63	1	0	-3	0	41
163	L+19	-0.51	A	47	0	0	-2	0	57
162	L+18	-0.54	A	2	2	28	8	16	44
161	L+17	-0.59	A	1	3	65	4	8	20
160	L+16	-1.25	A	2	0	1	41	46	10
159	L+15	-1.62	A	109	0	-3	-3	0	0
158	L+14	-1.67	A	111	-3	-4	0	0	0
157	L+13	-1.84	A	108	-4	-2	0	0	1
156	L+12	-2.24	A	67	6	14	1	12	1
155	L+11	-2.45	A	67	17	7	9	0	0
154	L+10	-2.77	A	0	92	7	0	0	0
153	L+9	-2.78	A	1	1	1	0	33	63
152	L+8	-3.01	A	1	7	91	0	1	1
151	L+7	-3.86	A	1	5	2	80	11	1
150	L+6	-4.08	A	2	90	4	3	0	0
149	L+5	-4.23	A	3	75	21	1	0	0
148	L+4	-4.27	A	2	9	89	0	0	0
147	L+3	-4.53	A	3	14	70	11	3	0
146	L+2	-4.68	A	3	4	11	72	9	0
145	L+1	-5.13	A	5	91	3	1	0	0
144	LUMO	-5.35	A	4	4	91	1	0	0
143	HOMO	-7.45	A	7	1	0	5	29	58
142	H-1	-8.41	A	2	0	0	0	1	96
141	H-2	-8.46	A	72	6	5	1	5	11
140	H-3	-8.56	A	70	11	4	2	7	6
139	H-4	-8.66	A	73	4	12	6	4	2
138	H-5	-9.21	A	5	0	1	26	52	16
137	H-6	-9.24	A	1	1	0	0	97	2
136	H-7	-9.58	A	2	1	1	89	8	0
135	H-8	-10	A	0	94	1	0	4	1
134	H-9	-10.18	A	4	5	4	7	74	6
133	H-10	-10.21	A	1	1	95	1	2	0
132	H-11	-10.27	A	9	7	3	2	65	14
131	H-12	-10.77	A	0	0	0	0	3	96
130	H-13	-10.96	A	0	1	1	69	23	6
129	H-14	-11.32	A	1	74	23	1	1	0
128	H-15	-11.46	A	2	89	5	0	1	3
127	H-16	-11.51	A	1	8	74	16	1	0
126	H-17	-11.58	A	2	61	26	2	4	5
125	H-18	-11.71	A	0	26	69	2	2	2
124	H-19	-11.74	A	2	53	40	2	1	2
123	H-20	-11.85	A	3	19	48	8	3	20

FIGURE B-9: MOLECULAR ORBITAL DATA FOR 2.

MO		eV	Symmetry	Ru	bpy1	bpy2	pz	Htr	th
164	L+20	-3.03	A	88	-6	0	1	3	16
163	L+19	-3.49	A	46	-3	-2	7	32	23
162	L+18	-4.04	A	104	0	-4	-2	2	2
161	L+17	-4.14	A	65	-2	-1	0	13	28
160	L+16	-4.17	A	65	-1	0	-1	4	36
159	L+15	-4.2	A	50	-2	-1	1	14	40
158	L+14	-4.52	A	32	0	0	1	21	48
157	L+13	-4.87	A	5	1	2	43	49	1
156	L+12	-5.1	A	24	55	13	2	5	0
155	L+11	-5.12	A	39	38	13	2	7	1
154	L+10	-5.19	A	63	17	12	8	0	0
153	L+9	-5.29	A	4	12	82	1	1	0
152	L+8	-6.4	A	2	91	6	0	1	1
151	L+7	-6.52	A	2	18	33	3	20	25
150	L+6	-6.57	A	1	19	31	6	20	23
149	L+5	-6.63	A	2	42	56	0	0	0
148	L+4	-6.78	A	1	24	66	7	1	0
147	L+3	-7.19	A	1	3	6	75	11	5
146	L+2	-7.51	A	4	92	2	1	0	0
145	L+1	-7.65	A	5	2	90	2	1	0
144	LUMO	-7.97	A	5	2	4	64	22	3
143	HOMO	-11.01	A	39	3	2	5	17	34
142	H-1	-11.27	A	70	9	8	3	3	7
141	H-2	-11.4	A	75	4	11	7	1	1
140	H-3	-11.45	A	50	7	2	0	9	31
139	H-4	-11.87	A	0	0	0	0	1	99
138	H-5	-12.36	A	1	96	2	0	0	0
137	H-6	-12.5	A	1	2	92	5	0	0
136	H-7	-12.56	A	1	1	5	91	2	0
135	H-8	-13.07	A	1	2	0	46	33	18
134	H-9	-13.55	A	2	2	4	2	88	2
133	H-10	-13.61	A	1	68	31	0	1	0
132	H-11	-13.82	A	1	84	7	2	5	0
131	H-12	-13.89	A	2	62	33	1	2	0
130	H-13	-13.9	A	3	21	71	4	2	0
129	H-14	-14.02	A	1	20	77	1	2	0
128	H-15	-14.13	A	8	31	56	3	1	1
127	H-16	-14.21	A	0	47	50	1	1	0
126	H-17	-14.34	A	0	0	1	9	7	82
125	H-18	-14.35	A	1	2	4	33	20	40
124	H-19	-14.52	A	1	77	7	15	1	0
123	H-20	-14.67	A	1	5	78	0	15	1

FIGURE B-10: MOLECULAR ORBITAL DATA FOR H2.

Appendix C

Photophysical and Computational Data in Support of Chapter 5.

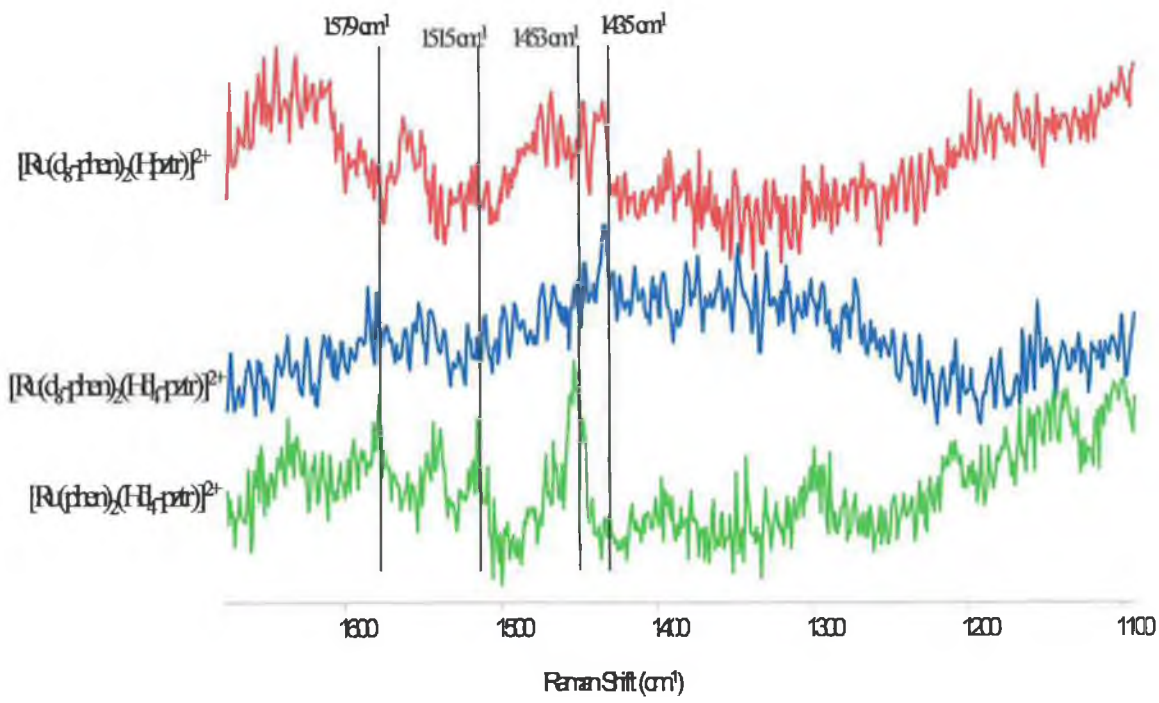

FIGURE C-1: RESONANCE RAMAN SPECTRA OF $[RU(PHEN)_2(HPZTR)]^{2+}$ IN MEOH WITH 488 NM EXCITATION.

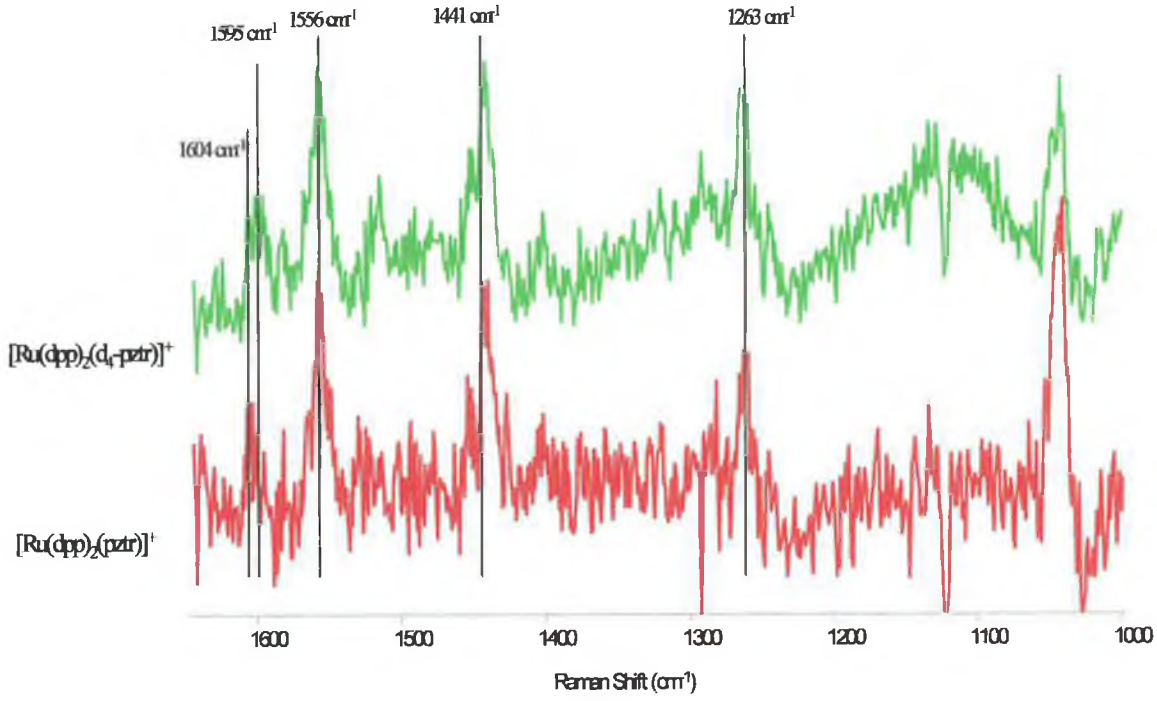

FIGURE C-2: RESONANCE RAMAN SPECTRA OF $[RU(DPP)_2(PZTR)]^+$ IN MEOH WITH 514 NM EXCITATION.

MO		eV	Symmetry	Ru	biq1	biq2	pz	tr
200	L+20	-1.11	A	12	84	1	1	1
199	L+19	-1.14	A	93	1	6	0	0
198	L+18	-1.24	A	25	0	76	0	0
197	L+17	-1.41	A	18	1	1	12	68
196	L+16	-1.49	A	95	0	-1	1	8
195	L+15	-2.11	A	43	7	41	0	8
194	L+14	-2.19	A	15	76	7	2	0
193	L+13	-2.45	A	32	10	49	4	5
192	L+12	-2.62	A	11	84	3	2	0
191	L+11	-2.69	A	12	13	74	1	0
190	L+10	-2.75	A	16	39	44	1	0
189	L+9	-2.91	A	10	86	4	1	0
188	L+8	-2.99	A	1	4	95	0	0
187	L+7	-3.72	A	0	16	3	71	10
186	L+6	-3.84	A	1	82	4	11	2
185	L+5	-4	A	0	2	94	3	0
184	L+4	-4.17	A	2	96	2	0	0
183	L+3	-4.31	A	1	2	96	0	0
182	L+2	-4.55	A	5	2	1	82	10
181	L+1	-5.2	A	6	79	12	2	1
180	LUMO	-5.41	A	6	13	79	1	1
179	HOMO	-8.06	A	63	8	10	3	16
178	H-1	-8.24	A	62	18	9	3	8
177	H-2	-8.46	A	65	4	18	5	8
176	H-3	-8.86	A	12	15	8	18	47
175	H-4	-9.11	A	2	50	9	1	39
174	H-5	-9.19	A	3	18	28	1	50
173	H-6	-9.2	A	6	27	38	4	24
172	H-7	-9.37	A	6	69	10	9	5
171	H-8	-9.43	A	2	85	2	4	7
170	H-9	-9.46	A	3	2	76	16	3
169	H-10	-9.55	A	2	8	37	51	3
168	H-11	-9.57	A	8	5	74	12	1
167	H-12	-9.98	A	14	15	8	0	63
166	H-13	-10.11	A	2	31	5	6	56
165	H-14	-10.3	A	1	60	16	4	19
164	H-15	-10.37	A	1	10	78	2	9
163	H-16	-10.83	A	0	5	5	69	20
162	H-17	-11.06	A	0	58	36	4	2
161	H-18	-11.28	A	2	38	49	11	1
160	H-19	-11.3	A	0	60	31	3	5
159	H-20	-11.36	A	2	69	15	7	8

FIGURE C-3: MOLECULAR DATA FOR $[RU(BIQ)_2(PZTR)]^+$.

MO		eV	Symmetry	Ru	biq1	biq2	pz	tr
200	L+20	-3.54	A	96	-7	11	1	0
199	L+19	-3.87	A	110	-3	-4	-2	2
198	L+18	-4.17	A	70	0	-1	1	32
197	L+17	-4.51	A	4	82	13	0	1
196	L+16	-4.64	A	10	12	74	1	2
195	L+15	-4.88	A	9	77	12	0	2
194	L+14	-4.93	A	3	5	4	43	45
193	L+13	-4.95	A	3	16	80	1	0
192	L+12	-5.13	A	5	80	11	3	2
191	L+11	-5.23	A	32	10	48	2	7
190	L+10	-5.26	A	27	8	58	3	5
189	L+9	-5.41	A	49	30	16	4	0
188	L+8	-5.71	A	1	1	1	1	95
187	L+7	-6.11	A	1	97	1	1	1
186	L+6	-6.26	A	0	2	97	0	0
185	L+5	-6.5	A	2	96	1	0	0
184	L+4	-6.61	A	2	1	97	0	0
183	L+3	-7.13	A	1	1	5	81	12
182	L+2	-7.53	A	8	68	16	7	1
181	L+1	-7.79	A	4	22	68	5	0
180	LUMO	-8.02	A	3	6	7	61	23
179	HOMO	-10.78	A	55	26	17	1	1
178	H-1	-11	A	53	22	18	4	4
177	H-2	-11.16	A	64	12	21	2	1
176	H-3	-11.4	A	3	56	41	0	0
175	H-4	-11.61	A	13	50	34	1	2
174	H-5	-11.68	A	7	79	13	1	0
173	H-6	-11.78	A	26	51	20	1	1
172	H-7	-11.8	A	0	2	98	0	0
171	H-8	-11.86	A	20	20	57	2	1
170	H-9	-12.52	A	1	96	1	1	1
169	H-10	-12.59	A	1	2	43	53	1
168	H-11	-12.64	A	1	1	55	42	1
167	H-12	-12.98	A	2	4	1	50	43
166	H-13	-13.39	A	0	60	35	1	4
165	H-14	-13.6	A	2	54	28	1	16
164	H-15	-13.66	A	1	58	33	1	8
163	H-16	-13.68	A	3	50	38	6	3
162	H-17	-13.79	A	1	28	68	0	3
161	H-18	-13.9	A	3	33	11	1	52
160	H-19	-14.01	A	3	32	61	2	2
159	H-20	-14.06	A	3	24	58	1	14

FIGURE C-4: MOLECULAR DATA FOR [RU(BIQ)2(HPZTR)]2+.

MO		eV	Symmetry	Ru	phen1	phen2	pz	tr
160	L+20	-0.31	A	4	1	94	1	0
159	L+19	-0.44	A	118	-6	0	-4	-5
158	L+18	-0.84	A	0	0	1	34	64
157	L+17	-1.39	A	8	0	0	19	73
156	L+16	-1.55	A	108	0	-7	-1	2
155	L+15	-1.63	A	111	-4	-2	-1	0
154	L+14	-1.74	A	22	76	2	0	0
153	L+13	-1.84	A	89	12	0	0	0
152	L+12	-1.99	A	2	5	92	0	0
151	L+11	-2.19	A	68	5	13	1	12
150	L+10	-2.41	A	67	17	7	8	0
149	L+9	-2.95	A	1	98	0	0	0
148	L+8	-3.19	A	1	0	98	0	0
147	L+7	-3.6	A	2	85	12	1	0
146	L+6	-3.77	A	1	3	36	53	7
145	L+5	-3.97	A	1	10	50	34	5
144	L+4	-4.62	A	5	1	1	82	10
143	L+3	-4.9	A	1	97	2	0	0
142	L+2	-5	A	5	89	5	1	0
141	L+1	-5.11	A	1	2	97	0	0
140	LUMO	-5.23	A	4	5	90	1	0
139	HOMO	-8.13	A	59	5	2	5	28
138	H-1	-8.44	A	74	12	8	2	4
137	H-2	-8.56	A	70	3	12	7	9
136	H-3	-8.93	A	19	3	2	21	55
135	H-4	-9.17	A	1	1	0	0	98
134	H-5	-9.55	A	2	3	1	84	11
133	H-6	-9.71	A	2	80	2	5	12
132	H-7	-9.97	A	3	8	87	1	1
131	H-8	-10.02	A	7	53	5	1	34
130	H-9	-10.13	A	4	10	3	10	73
129	H-10	-10.19	A	11	43	5	2	39
128	H-11	-10.32	A	1	2	96	0	0
127	H-12	-10.93	A	0	1	1	76	23
126	H-13	-11.52	A	0	77	18	2	3
125	H-14	-11.58	A	0	57	34	8	2
124	H-15	-11.61	A	2	81	13	2	2
123	H-16	-11.75	A	0	10	80	8	1
122	H-17	-11.81	A	2	33	56	5	3
121	H-18	-11.87	A	0	47	35	17	2
120	H-19	-11.97	A	0	15	54	4	28
119	H-20	-12.1	A	3	4	18	73	2

FIGURE C-5: MOLECULAR DATA FOR $[RU(PHEN)_2(PZTR)]^+$

MO		eV	Symmetry	Ru	phen1	phen2	pz	Htr
160	L+20	-3.09	A	95	-8	-1	7	9
159	L+19	-3.59	A	55	-4	-4	12	43
158	L+18	-4.11	A	51	45	5	-1	0
157	L+17	-4.11	A	58	44	-1	-1	1
156	L+16	-4.27	A	102	-6	6	0	0
155	L+15	-4.29	A	13	8	78	0	0
154	L+14	-4.51	A	86	-1	-1	0	18
153	L+13	-5.11	A	10	1	2	41	46
152	L+12	-5.25	A	56	8	12	8	16
151	L+11	-5.32	A	46	43	5	6	1
150	L+10	-5.37	A	24	69	5	2	0
149	L+9	-5.53	A	2	1	97	0	0
148	L+8	-5.8	A	1	4	0	2	93
147	L+7	-6.02	A	2	74	21	0	3
146	L+6	-6.27	A	1	21	76	1	1
145	L+5	-7.27	A	1	73	4	20	3
144	L+4	-7.35	A	1	24	1	66	8
143	L+3	-7.45	A	2	12	86	0	0
142	L+2	-7.49	A	3	83	12	1	0
141	L+1	-7.63	A	4	3	91	1	1
140	LUMO	-8.15	A	6	1	2	66	24
139	HOMO	-11.29	A	80	8	6	2	4
138	H-1	-11.35	A	66	19	9	2	4
137	H-2	-11.48	A	70	5	14	8	2
136	H-3	-12.13	A	9	84	6	1	1
135	H-4	-12.3	A	9	8	81	1	0
134	H-5	-12.52	A	3	89	7	1	0
133	H-6	-12.67	A	2	3	84	11	0
132	H-7	-12.74	A	1	2	10	86	2
131	H-8	-13.14	A	3	3	0	48	46
130	H-9	-13.86	A	1	3	7	2	87
129	H-10	-13.92	A	1	81	18	1	0
128	H-11	-14	A	1	84	10	1	4
127	H-12	-14.11	A	0	16	79	3	2
126	H-13	-14.19	A	0	43	54	1	2
125	H-14	-14.2	A	3	22	73	2	1
124	H-15	-14.46	A	2	79	7	12	1
123	H-16	-14.61	A	2	7	68	6	17
122	H-17	-14.66	A	1	3	11	47	37
121	H-18	-14.97	A	1	53	14	1	32
120	H-19	-15.04	A	4	39	37	12	8
119	H-20	-15.16	A	3	17	54	15	11

FIGURE C-6: MOLECULAR DATA FOR $[RU(PHEN)_2(HPZTR)]^{2+}$.

MO		eV	Symmetry	Ru	dpp1	dpp2	pz	tr
240	L+20	-1.57	A	3	6	90	0	0
239	L+19	-1.75	A	69	7	13	1	11
238	L+18	-1.87	A	16	81	1	2	1
237	L+17	-1.96	A	54	32	7	7	0
236	L+16	-2.09	A	2	0	98	0	0
235	L+15	-2.34	A	1	96	3	0	0
234	L+14	-2.47	A	0	98	2	0	0
233	L+13	-2.49	A	1	14	85	0	0
232	L+12	-2.49	A	1	90	10	0	0
231	L+11	-2.57	A	1	0	99	0	0
230	L+10	-2.66	A	0	0	100	0	0
229	L+9	-2.96	A	0	98	1	0	0
228	L+8	-3.14	A	1	1	99	0	0
227	L+7	-3.28	A	1	87	11	1	0
226	L+6	-3.45	A	1	4	45	44	6
225	L+5	-3.63	A	1	8	42	42	6
224	L+4	-4.3	A	6	2	1	81	10
223	L+3	-4.52	A	2	96	2	0	0
222	L+2	-4.6	A	5	89	5	1	0
221	L+1	-4.73	A	1	2	97	0	0
220	LUMO	-4.82	A	3	6	88	2	0
219	HOMO	-7.72	A	62	8	2	4	24
218	H-1	-7.94	A	68	17	11	1	3
217	H-2	-8.08	A	68	3	17	6	5
216	H-3	-8.55	A	10	10	3	21	56
215	H-4	-8.83	A	3	42	5	1	49
214	H-5	-8.89	A	3	33	6	1	57
213	H-6	-9.02	A	3	68	24	1	4
212	H-7	-9.08	A	9	29	59	2	2
211	H-8	-9.16	A	0	100	0	0	0
210	H-9	-9.17	A	0	100	0	0	0
209	H-10	-9.21	A	2	3	79	13	3
208	H-11	-9.25	A	0	0	97	3	0
207	H-12	-9.28	A	4	5	15	69	8
206	H-13	-9.34	A	0	0	100	0	0
205	H-14	-9.52	A	0	94	1	1	4
204	H-15	-9.68	A	5	59	6	1	30
203	H-16	-9.69	A	1	12	87	0	1
202	H-17	-9.78	A	5	23	5	8	59
201	H-18	-9.83	A	9	18	7	6	61
200	H-19	-9.93	A	1	1	97	0	0
199	H-20	-10.62	A	0	1	1	76	22

FIGURE C-7: MOLECULAR DATA FOR $[Ru(dpp)_2(pztr)]^+$.

MO		eV	Symmetry	Ru	dpp1	dpp2	pz	Htr
240	L+20	-4.02	A	69	12	0	0	18
239	L+19	-4.15	A	5	93	1	0	1
238	L+18	-4.18	A	7	89	3	0	1
237	L+17	-4.23	A	2	87	11	0	0
236	L+16	-4.24	A	3	10	87	0	0
235	L+15	-4.27	A	2	2	95	0	0
234	L+14	-4.28	A	3	2	95	0	0
233	L+13	-4.53	A	47	5	12	13	23
232	L+12	-4.63	A	46	11	10	17	16
231	L+11	-4.63	A	38	8	4	26	23
230	L+10	-4.98	A	1	97	2	0	0
229	L+9	-5.11	A	1	2	96	0	1
228	L+8	-5.3	A	1	11	1	2	85
227	L+7	-5.42	A	2	67	23	0	9
226	L+6	-5.64	A	1	22	75	1	2
225	L+5	-6.64	A	1	92	4	3	1
224	L+4	-6.8	A	3	50	29	16	2
223	L+3	-6.82	A	0	10	64	23	3
222	L+2	-6.83	A	3	39	8	45	6
221	L+1	-6.95	A	4	5	90	1	1
220	LUMO	-7.62	A	8	1	2	66	24
219	HOMO	-10.36	A	32	47	19	1	1
218	H-1	-10.51	A	45	35	15	1	4
217	H-2	-10.56	A	37	14	46	3	1
216	H-3	-10.78	A	11	47	40	1	0
215	H-4	-10.84	A	0	100	0	0	0
214	H-5	-10.92	A	0	99	0	0	0
213	H-6	-10.95	A	1	0	99	0	0
212	H-7	-10.96	A	1	3	96	0	0
211	H-8	-10.96	A	24	45	27	1	3
210	H-9	-11.06	A	36	16	42	4	2
209	H-10	-11.1	A	38	18	41	2	1
208	H-11	-11.56	A	4	93	2	0	1
207	H-12	-11.69	A	5	4	91	0	0
206	H-13	-11.88	A	2	91	6	0	0
205	H-14	-12.04	A	2	3	94	1	0
204	H-15	-12.26	A	1	1	1	95	2
203	H-16	-12.61	A	3	3	0	48	46
202	H-17	-13.05	A	1	82	16	1	0
201	H-18	-13.15	A	1	91	5	1	2
200	H-19	-13.21	A	1	11	86	1	0
199	H-20	-13.23	A	1	23	68	1	7

FIGURE C- 8: MOLECULAR DATA FOR $[RU(DPP)_2(HPZTR)]^{2+}$.

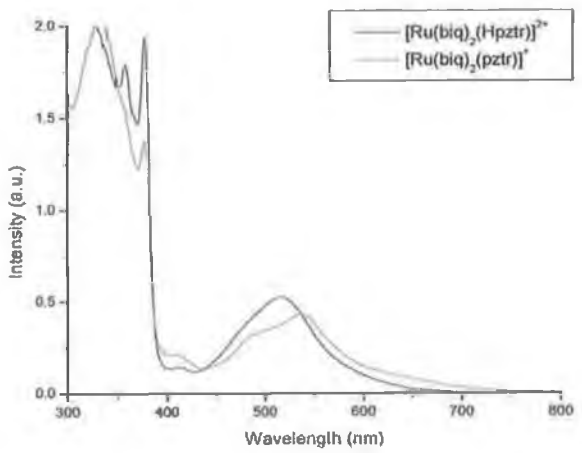

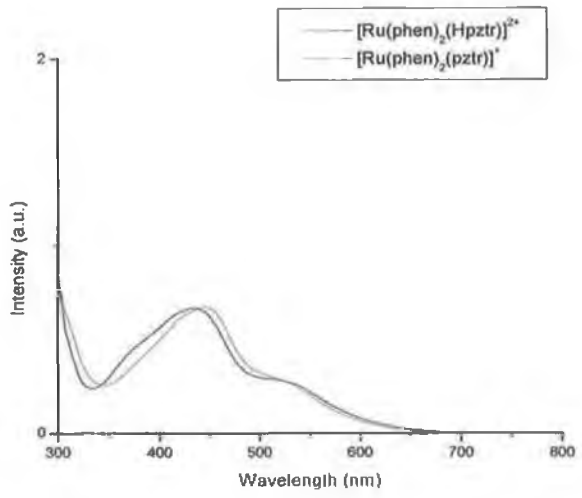

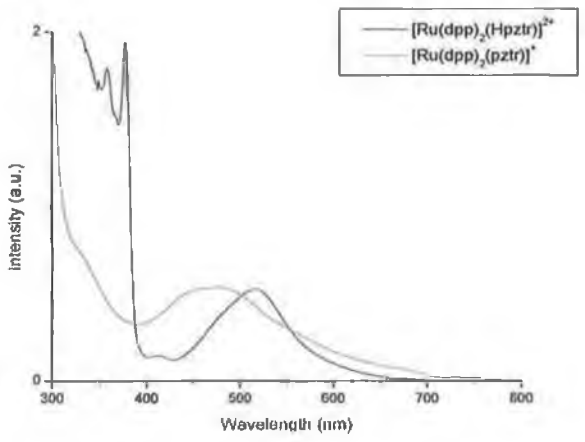

APPENDIX C-9: UV/VIS SPECTRA IN H_2O OF COMPLEXES DISCUSSED IN CHAPTER 5.

Appendix D

Calculated Vibrational Spectra.

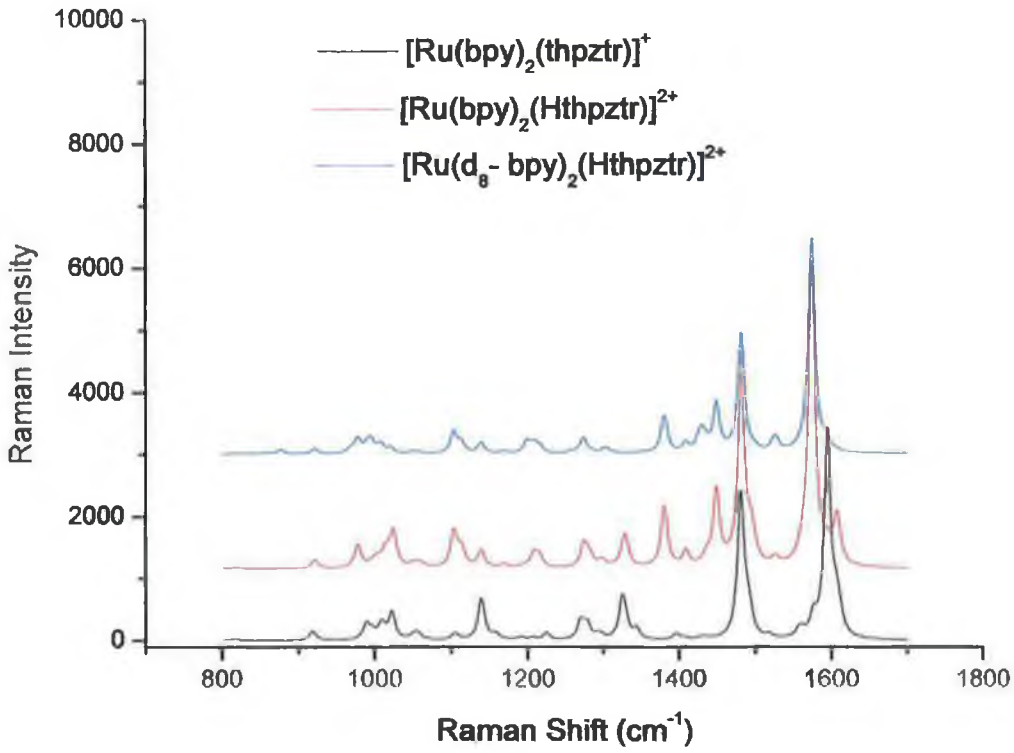

FIGURE D.1: CALCULATED RAMAN OF $[RU(BPY)_2(THPZTR)]^+$, $[RU(BPY)_2(HTHPZTR)]^{2+}$ AND $[RU(D_8BPY)_2(HTHPZTR)]^{2+}$.

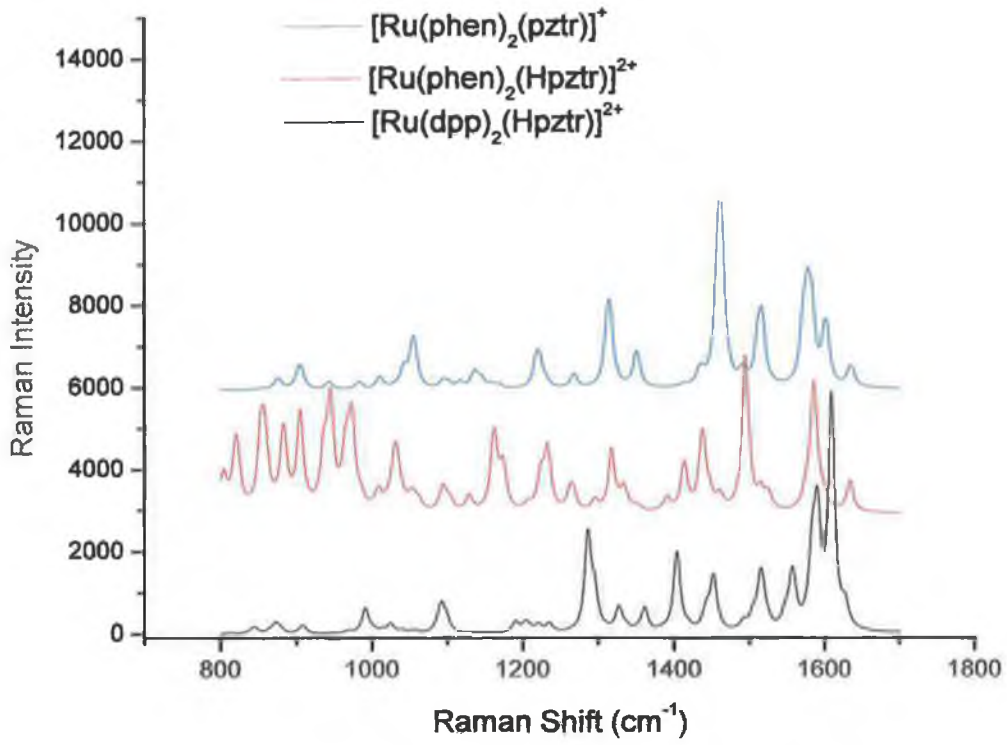

FIGURE D.2: CALCULATED RAMAN SPECTRA OF $[Ru(phen)_2(pztr)]^+$, $[Ru(phen)_2(Hpztr)]^{2+}$ AND $[Ru(dpp)_2(Hpztr)]^{2+}$.

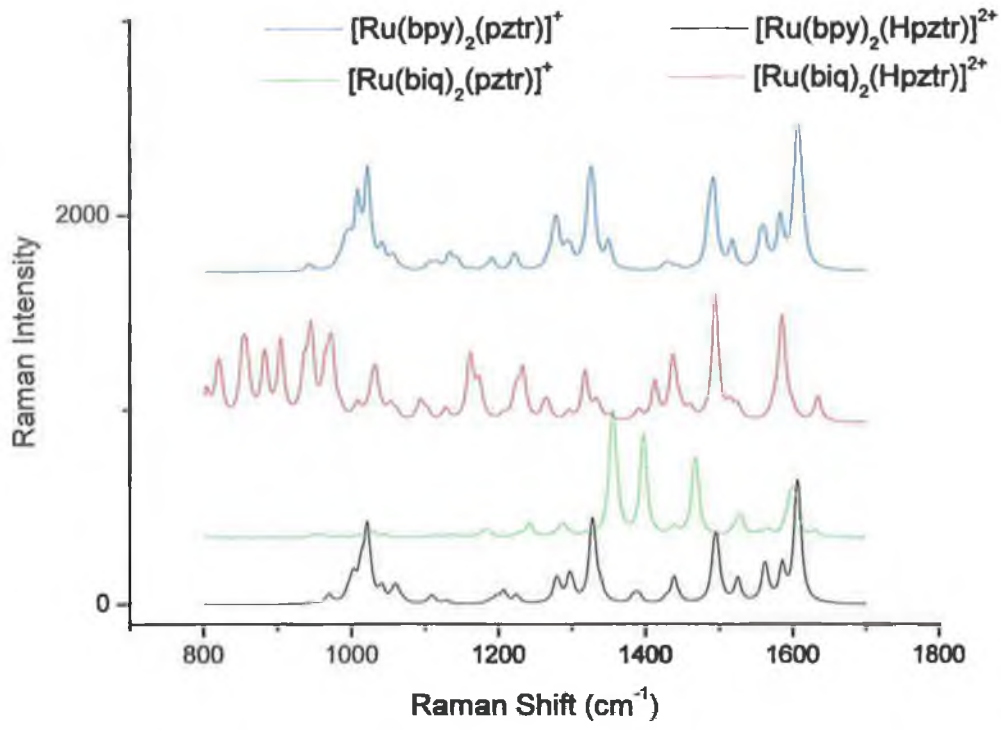

FIGURE D.3: CALCULATED RAMAN SPECTRA OF $[Ru(bpy)_2(pztr)]^+$, $[Ru(bpy)_2(Hpztr)]^{2+}$, $[Ru(biq)_2(pztr)]^+$ AND $[Ru(biq)_2(Hpztr)]^{2+}$.

	Experimental		Predicted		Linear scaling		Wavelength linear scaling	
	P1	**P2**	**P1**	**P2**	**P1**	**P2**	**P1**	**P2**
Bpy	1606	1574	1643	1610	1597	1566	1616	1573
	1562	1526	1594	1552	1550	1509	1562	1514
	1493	1425	1526	1461	1484	1421	1488	1420
	1318	1302	1358	1331	1320	1294	1308	1288
	1174	1006	1218	1020	1184	992	1161	976
phpztr	1598	1598	1617	1618	1572	1573	1587	1582
	1527	1526	1562	1562	1519	1519	1527	1524
	1372	1373	1427	1451	1387	1411	1382	1410
	1289	1289	1355	1355	1317	1318	1305	1313
	1195	1195	1252	1252	1217	1217	1197	1208
	RMSD		43.86	43.92	16.43	20.13	9.18	19.04

FIGURE D.4: CALCULATED AND EXPERIMENTAL RAMAN BANDS FOR $[Ru(bpy)_2(phpztr)]^+$ (P1) AND $[Ru(D_8\text{-}bpy)_2(PHPZTR)]^+$ (P2).

Appendix E

Publications and Presentations.

Publications.

Regioselective Functionalization Of Tetrabromophenanthroline-Ruthenium Complexes
Rau, S., Fischer, R., Jager, M., Schafer, B., Meyer, S., Kreisel, G., Gorls, H., Rudolf, M., Henry, W., Vos, J.G., Eur. J. Inorg. Chem., **2004**, 2001-2003.

Assessment Of Intercomponent Interaction In Phenylene Bridged Dinuclear Ruthenium And Osmium Polypyridyl Complexes.
Guckian, A.L., Doering, M., Ciesielski, M., Walter, O., Hjelm, J., O'Boyle, N.M., Henry, W., Browne, W.R., McGarvey, J.J., Vos, J.G., Dalton Trans., **2004**, 3943-3949.

Ground and Excited-State Electronic Structure Of An Emissive Pyrazine Bridged Ruthenium-Dinuclear Complex.
Browne, W.R., O'Boyle, N.M., Henry, W., Guckian, A.L., Horn, S., Fett, T., O'Connor, C.M., Duati, M., DeCola, L., Coates, C.G., Ronayne, K.L., McGarvey, J.J., Vos, J.G., J. Am. Chem. Soc., **2005**, *127*, 1229-1241.

Ground vs. Excited-State Interactions In Ruthenium-Thienyl Dyads: Implications For Through Bond Interaction In Multicomponent Systems.
Henry, W., Browne, W.R., Ronayne, K.R., O'Boyle, N.M., Vos,J.G., McGarvey, J.J., J. Mol. Struct., **2004**, *735-736*, 123-134.

Microscopy And Spectroscopy Of Interactions Between Metallopolymers And Carbon Nanotubes.

Frehill, F., in het Panhuis, M., Young, N.A., Henry, W., Hjelm, J., Vos, J.G., J. Phys. Chem. B., **2005**, *109*, 13205.

A Heterodinuclear tpphz Complex Capable Of Photocatalytically Producing Hydrogen. Schafer, B., Gleich, D., Rudolph, M., Friedrich, M., Gorls, H., Henry, W., Vos, J.G., Angew. Chem. Int. Eng. Ed. (Copy attached). Accepted

Derivatives of dipyrido[3,2-*a*:2_,3_-*c*]phenazine and its ruthenium complexes, influence of arylic substitution on photophysical properties†
Schafer, B., Gorls, H., Presselt, M., Schmitt, M., Popp, J., Henry, W., Vos, J.G., Rau, S. Dalton Trans., **2006**, *18*, 2225.

Posters.

Tuning Of The Photophysical And Photochemical Properties Of Ruthenium (II) Polypyridyl Complexes Containing 1,2,4 Triazoles By Variation Of Ligand, pH And Solvent.
Presented at European Photochemistry Association Summer School, 28th June to 2nd July 2003, Egmond Aan Zee, The Netherlands.

Application Of Deuteration In Raman Spectroscopy And Its Agreement With Computational Studies.
Presented at Infra Red and Raman Discussion Group: 9th & 10th September 2004, The Queen's University of Belfast, Ireland.
Also presented at Electronic Structure: Principles and Application: 15th to 17th September 2004, Valladolid, Spain.

Microscopy and Spectroscopy of Interactions between Metallopolymers and Carbon Nanotubes

Fiona Frehill,[†] Marc in het Panhuis,*[‡] Nigel A. Young,[‡] William Henry,[†] Johan Hjelm,[†] and Johannes G. Vos[†]

National Centre for Sensor Research, School of Chemical Sciences, Dublin City University, Dublin 9, Ireland, and Department of Chemistry, The University of Hull, Hull, HU6 7RX, United Kingdom

Received: March 21, 2005; In Final Form: May 24, 2005

The interaction between redox polymers, based on Ru- or Os-bis(2,2′-bipyridyl)-poly(4-vinylpyridine), and carbon nanotubes was investigated by spectroscopic and microscopic techniques. These metallopolymers were found to be excellent dispersants for nanotubes, as a result of a good wetting interaction between polymer and nanotubes. The results obtained show that well-coated individual nanotubes can be obtained. In addition, interactions between nanotubes and polymers did not significantly affect the electronic and electrochemical properties of the metallopolymers. On the basis of the electrochemical properties of the polymers this opens the possibility of adding functionality through interaction with nanotubes, either as redox active materials with enhanced mechanical properties or by using these modified nanotubes as nanosized electrochemical sensors.

1. Introduction

Since their discovery in 1991[1] carbon nanotubes have attracted considerable attention, mainly because their unique combination of mechanical, thermal, optical, and electrical properties may form the basis of many potential applications.[2−4] However, processing and manipulation of carbon nanotubes is limited by their lack of solubility in most solvents. Therefore, successful incorporation of nanotubes into materials requires the development of methods for their effective dispersion. Decreasing nanotube aggregation in solution and improving solubility are areas of intensive research. Compounds such as saccharides,[5,6] surfactants,[7−10] ceramics,[11] biological entities,[12,13] synthetic polymers,[14−25] and chemically modified soy oil[26] have been used to disperse single-walled (SWNT) and multiwalled (MWNT) carbon nanotubes through noncovalent functionalization. Polymers are attractive materials since they may be easily processed and fabricated into solid-state forms such as thin films required in most applications.[27] In addition to acting as efficient nanotube dispersing agents, employing polymers in composites is of interest because they allow for a novel combination of nanotube and polymer properties. Previous work established that the formation of stable polymer−nanotube composites depends on a good wetting interaction between polymers and nanotubes.[14,16] This in turn has been found to be dependent in particular on the polymer chain conformation.[16,19] In addition it was determined that certain polymers form crystalline layers around nanotubes thereby increasing polymer backbone−nanotubes interactions.[23,24]

Composite materials from nanotubes and conducting polymers have been investigated.[19,21,22,25] The electrochemical activity in these polymers is based on the electronic and electrochemical properties of the polymer backbone. On the other hand, for redox polymers such as materials of the type $[M(bpy)_2(PVP)_{10}Cl]Cl$ (see Figure 1), where M = Ru or Os, bpy is 2,2′-bipyridine, and PVP is poly(4-vinyl)pyridine, considered in this paper, the electrochemically active moieties are not related to the backbone but are based on pendent groups of the type $M(bpy)_2-$, which are covalently linked to the polymer backbone.[28−30] The polymers are of interest since their electrochemistry is extremely reversible and the materials are very stable in several oxidation states. They have therefore been used extensively as redox catalysts for the sensing of analytes such as Fe(II)/Fe(III), nitrite, and ascorbic acid and have been applied in biosensor assemblies.[31−35] In addition, there is a well-developed synthetic chemistry for these redox metallopolymers containing poly(pyridyl) complexes of ruthenium(II) and osmium(II) and their redox potential can be varied systematically.[36]

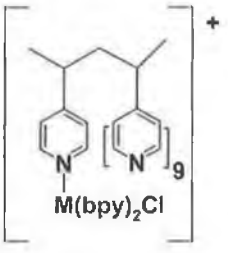

Figure 1. Structure of metallopolymers $[M(bpy)_2PVP_{10}Cl]Cl$, with M = Ru or Os.

In this contribution, (noncovalent) interactions between two redox metallopolymers and single-walled and multiwalled carbon nanotubes are investigated, using a range of microscopic and spectroscopic techniques.

2. Experimental Details

SWNT[37] were prepared by high-pressure decomposition of carbon monoxide (HiPco) obtained from Carbon Nanotechnologies, Inc. (Houston, USA, batch no. P0-185). Catalytic chemical vapor deposition (CVD) produced MWNT were

* To whom correspondence should be addressed. E-mail: M.Panhuis@hull.ac.uk.
[†] Dublin City University.
[‡] The University of Hull.

10.1021/jp051459o CCC: $30.25
Published on Web 06/18/2005

obtained from Nanocyl S.A. (Belgium, batch no. NFL60). The metallopolymers $[Ru(bpy)_2PVP_{10}Cl]Cl$ and $[Os(bpy)_2PVP_{10}Cl]Cl$ where bpy is 2,2′-bipyridine and PVP is poly(4-vinyl)pyridine were prepared as described previously.[36]

Nanotube dispersions were prepared by sonicating SWNT or MWNT in a 0.5% (weight per volume) methanolic solution of the polymer until a dense black dispersion had formed. The resulting composites are the following: $[Ru(bpy)_2PVP_{10}Cl]Cl$–MWNT **1**, $[Ru(bpy)_2PVP_{10}Cl]Cl$–SWNT **2**, $[Os(bpy)_2PVP_{10}Cl]Cl$–MWNT **3**, and $[Os(bpy)_2PVP_{10}Cl]Cl$–SWNT **4**.

UV–vis absorption spectra (accuracy ±2 nm) were recorded in 10 mm quartz cuvettes on a Shimadzu UV–vis–NIR 3100 spectrophotometer interfaced with an Elonex PC466, using a UV–vis data manager. Raman spectra were collected in 180° scattering geometry with a Bruker FRA 106/S Raman module mounted on a Bruker Equinox55 FTIR bench with a cw Nd:YAG 1064 nm laser at ca. 100 mW, a CaF_2 beam splitter, and a liquid nitrogen cooled Ge detector. Transmission electron microscopy (TEM) images were obtained on a JEOL 2011 TEM. Diluted composite solutions were evaporated onto Cu 300 mesh grids. Tapping mode atomic force microscopy (TM-AFM) was carried out in an air environment with use of a Digital Instruments Nanoscope IIIa. Laser alignment was performed manually, and cantilever tuning and drive frequency selection was automatically performed by the DI software. The cantilevers used are made of silicon and have a triangular pyramid shape, a tip radius <10 nm, a force constant of 25–60 N/m, and a resonant frequency of 150–190 kHz. The carbon nanotube polymer composites for TM-AFM analysis were prepared on native oxide-covered Si(111) substrates. Initially a SiO_2 wafer was cleaned by sonication in acetone and ethanol for 5 min each, and then gently boiled in piranha solution (H_2O_2:NH_4:H_2O (1:1:5)) for 25 min (to remove any form of organic contaminants and trace metals). The wafers were rinsed with Milli-Q water and dried under argon. A 1% (v/v in Milli-Q water) solution of 3-(aminopropyl)triethoxysilane (APS, Aldrich) was dropped onto a cleaned wafer and allowed to react for up to 10 min. The wafers were rinsed with Milli-Q water and dried under argon. The various carbon nanotube polymer composite solutions (in methanol) were drop-cast onto the silanized wafer. In one set of samples the silanized wafers coated with the polymer solution were allowed to stand for 10 min. The wafers were then rinsed with Milli-Q water and dried under argon after which TM-AFM analysis was carried out. In the second set of samples no washing with water was carried out and the polymer-coated surfaces were allowed to stand for 24 h until the methanol evaporated and subsequently TM-AFM analysis was carried out.

3. Results and Discussion

Absorption spectroscopy has proved useful in the characterization of ruthenium- and osmium-based polymers[36,38] and to examine the effects of interaction with nanotubes on polymers.[15,16] UV–visible absorption spectra for the $[Ru(bpy)_2PVP_{10}Cl]Cl$ polymer and its polymer–nanotube composites are shown in Figure S1 in the Supporting Information (composite **1**) and Figure 2 (composite **2**). The spectrum for the Ru-metallopolymer is dominated by two characteristic bands at 350 and 498 nm attributed to a single metal-to-ligand charge-transfer (^{1}MLCT) transition. The analogous osmium metallopolymer exhibits similar MLCT bands at 364 and 481 nm and an additional broad feature with a maximum at about 700 nm (see Figure S2 in the Supporting Information). The latter has been assigned to a spin-forbidden ^{3}MLCT transition, which is partly allowed by the considerable spin–orbit coupling present in the Os metal ion.[36]

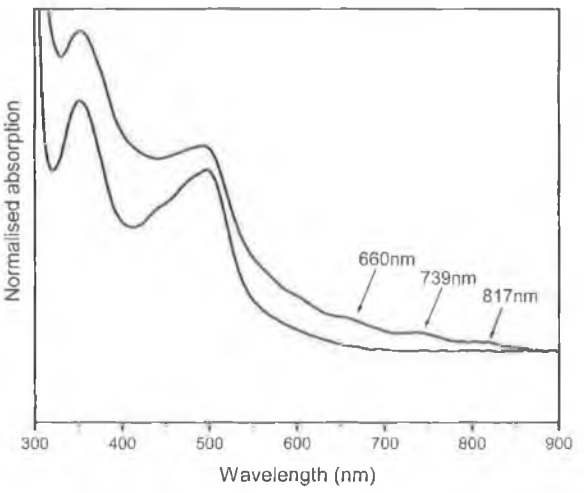

Figure 2. UV–visible absorption spectra of $[Ru(bpy)_2PVP_{10}Cl]Cl$ (top line), and composite **2** (bottom line, SWNT) normalized to 900 nm.

In comparison to the metallopolymers no significant changes are observed in the positions of the spectroscopic features for the composite materials. However, the relative intensity of the band associated with MCLT transitions is significantly reduced in the composite material. In addition, broad features at 660, 739, and 817 nm in the absorption spectrum of composite **2** (see Figure 2) confirm the presence of nanotubes. These bands can be attributed to transitions between van Hove singularities in SWNT aggregates similar to our previous observations.[19] The UV–vis spectral features indicate that the overall structure of the metallopolymers is not significantly changed. This is confirmed by electrochemical studies (not shown), which show that the redox potentials of the composites are very close to those observed for the polymers themselves. The spectroscopic data do, however, indicate the presence of both carbon nanotubes and polymer.

Raman spectroscopy is a spectroscopic tool used to probe carbon nanotubes in polymer composites and can provide insight into the interaction between polymer and nanotubes.[18,19] Raman spectra of HiPco SWNT have been extensively studied and are well understood.[39] Figure S3 (in the Supporting Information) shows the room-temperature Raman spectra of HiPco SWNT and composite **2** for laser excitation at 1064 nm (1.17 eV). The observed features for SWNT are assigned as follows: low-frequency radial breading modes (RBM, below 400 cm^{-1}), the disorder induced D band (around 1275 cm^{-1}), tangential C–C stretching mode features (G bands, near 1590 cm^{-1}), and two-phonon-scattering processes (between 1600 and 3000 cm^{-1}).[39] It has been noted that the various modes in the range 500–1200 cm^{-1} are only observed for this particular excitation wavelength and were attributed to enhancement of Raman cross-section for small-diameter (below 1.0 nm) SWNT.[39] Carbon nanotube features dominate the Raman spectrum of the composite (Figure S3, black line). The intertube interaction in SWNT bundles is dominated by van der Waals interactions. It is well-known that noncovalent sidewall functionalization of nanotubes results in an upshift of the radial breathing modes features.[6,12,15,18,19,26] The magnitude of the upshift depends on the degree of (partial) intercalation of the dispersant between nanotubes in bundles and coating of bundles. In comparison with the HiPco spectrum, the upshifts for the composite are as follows: RBM features by up to 4 cm^{-1}, D-band by 5.8 cm^{-1}, and G-bands by 2.1 cm^{-1}. Therefore, the observed shifts in nanotube features suggest that the Ru-metallopolymer interacts

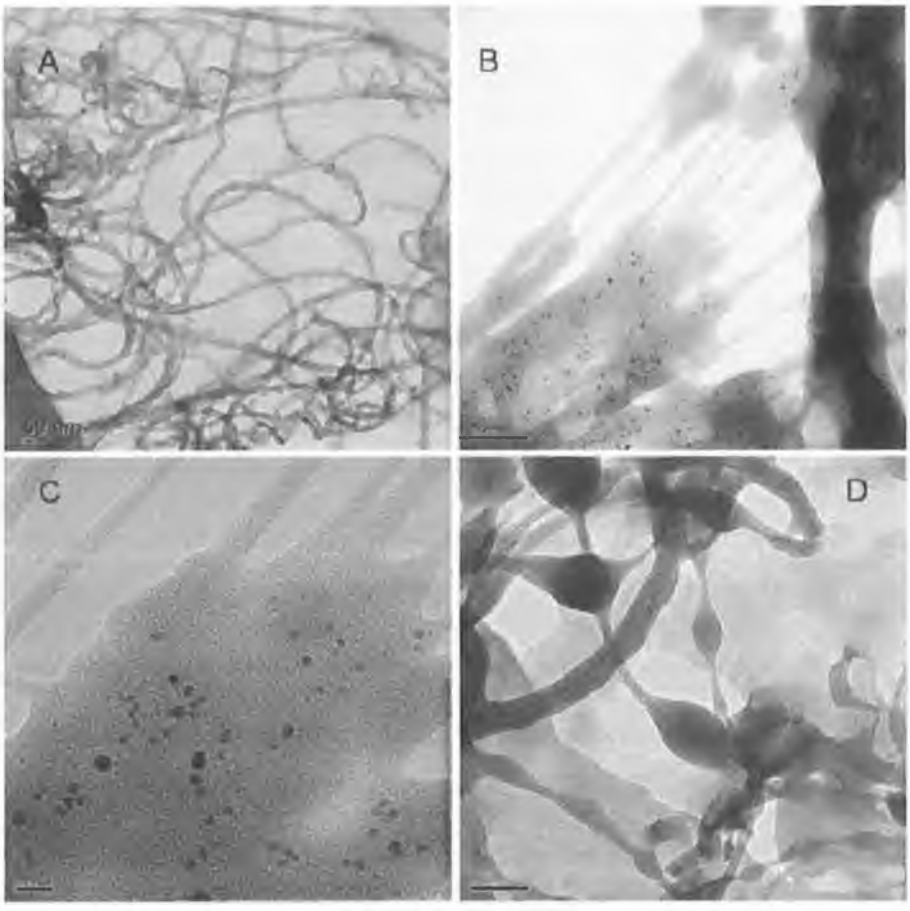

Figure 3. Transmission electron microscopy (TEM) images: (A) Low-resolution images of composite **1** showing wetting of MWNT by Ru-metallopolymers (scale bar 50 nm). (B) Low-resolution image of composite **2** (scale bar 100 nm) and (C) high-resolution image of composite **2** (scale bar 20 nm) showing bundles of SWNT wetted by the Ru-metallopolymer. Dark spheres are Fe catalyst particles used in HiPco synthesis. (D) Low-resolution images of composites **3** showing wetting of MWNT by Os-metallopolymers (scale bar 200 nm).

with nanotubes. Similar observations were made for the other composites (not shown).

Electron microscopy is an excellent technique for investigating the wetting between polymers and nanotubes as both can be readily identified in the images. Figure 3 shows TEM images of composites **1**−**3**. The nanotubes are visible as the darker thin lines, with the hollow core of the nanotube visible within. Nanotubes produced by CVD (Figure 3A,D) and HiPco (Figure 3B,C) techniques are structurally different as is evident from the images. CVD-produced tubes contain structural defects resulting in bends in the nanotube bodies. HiPco tubes contain fewer defects and therefore appear as mainly straight lines. In addition, as CVD tubes are MWNT (consisting of multiple carbon shells) they are thicker and longer compared to the SWNT (consisting of a single carbon shell) produced by the HiPco process. It is evident from the images that both types of nanotubes are nicely and completely covered by metallopolymer. In particular, composites **1** and **3** consist of individual MWNT coated by a thick layer of polymer. Whereas in composites **2** and **4** (not shown), SWNT appear in bundles (or aggregates) coated in polymer. This is indicative of good binding as the nanotubes support a large amount of polymer.

TM-AFM was used to investigate the difference in surface topography between MWNT and polymer−nanotube composites. Height analysis of unmodified MWNT (Figure S4 in the Supporting Information) suggests a nanotube thickness of 50−60 nm, in good agreement with the manufacturer's specification. Height analysis with AFM is only approximate due to surface interactions and flattening of the tube on the surface. Images of composite **1** drop-cast from solution on a wafer can be observed in Figure 4. Ru-metallopolymer covered MWNT (straight lines) and free polymer (spherical objects) can be clearly identified. Subsequently, a sample of composite **1** was prepared by allowing the composite solution to react with the amino-functionalized surface for 10 min, after which the substrate was washed with a small quantity of Milli-Q water. The resulting images (Figure 5) show that the nanotubes are noncovalently bound to the surface whereas free polymer (evidently present in Figure 4) is washed from the substrate. This allows for more reliable height analysis. $[Ru(bpy)_2PVP_{10}Cl]Cl$ does not readily dissolve in water but may be removed from the surface as the methanolic solution has not evaporated. Thus aggregates of composite **1** are now readily identified (in Figure 5), without the presence of excess polymer. Height analysis suggests a thickness of 165−200 nm for the polymer-coated MWNT. Similar observations may be made for the polymer−tube composites **2**, **3**, and **4** (see Figures S5−S7 in the Supporting Information). This coating method incorporating a washing cycle provides a technique for forming aggregates of polymer−nanotube composites without the presence of free polymer.

In previous studies on polymers such as poly(*p*-phenylene vinylene-*co*-2,5-dioctyloxy-*m*-phenelyne-vinylene) (PmPV)[16,40] and electroactive polyaniline[19] it was shown that optimum

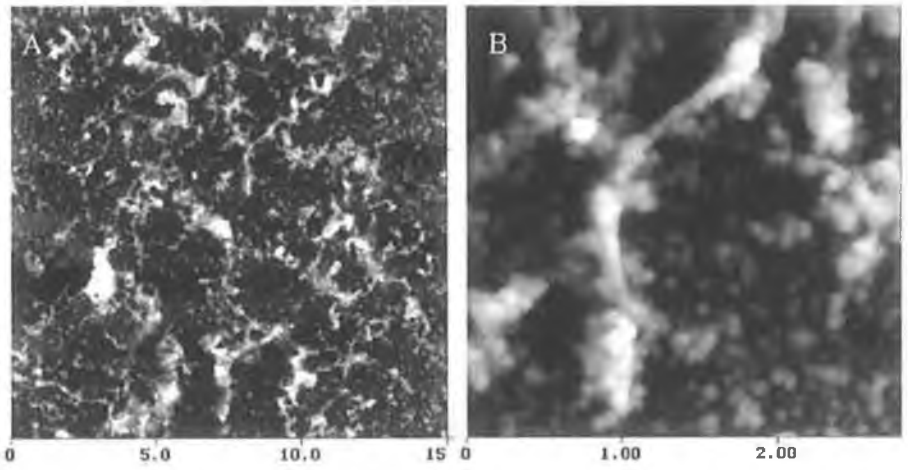

Figure 4. TM-AFM imaging on composite **1** drop-cast onto SiO_2 wafer and allowed to evaporate for 24 h. Image dimensions: (A) 15.0 × 15.0 μm^2, z-range = 200 nm and (B) 2.798 × 2.798 μm^2, z-range = 175 nm.

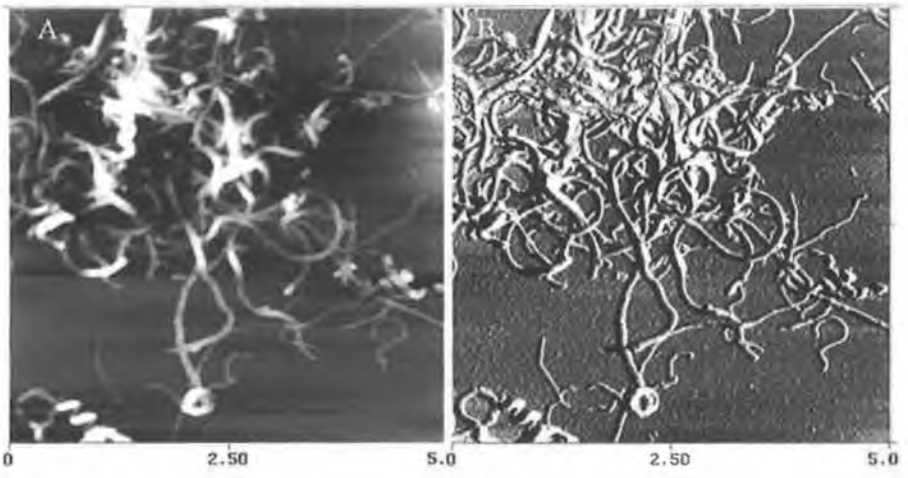

Figure 5. TM-AFM imaging on composite **1** drop-cast onto SiO_2 wafer after washing treatment. (A) AFM image with dimensions 5.0 × 5.0 μm^2 and z-range 175 nm and (B) corresponding amplitude data.

interaction with nanotubes can be linked to backbone exposure in the polymer. These polymers share an important characteristic, e.g., the presence of double bonds in the polymer backbone, which makes them ideal for noncovalent (attractive) interactions with the nanotube surface. This has generally been referred to as π-stacking of the polymer backbone on the nanotube surface. Changes in the optical spectroscopy can be directly linked to changes in the polymer conformation due to the presence of these double bonds. Double bonds are absent in the backbone of our metallopolymers and thus the attractive interaction will be different compared to that of conjugated polymers. Most important, functionalization of nanotubes with metallopolymers will not be facilitated by π-stacking of the polymer backbone (onto the nanotube surface), but by π-stacking of the ligands. One would expect that the π-system of (metallopolymers') ligands would facilitate a strong interaction with the nanotube surface and a significant effect on the MLCT transitions. However, as the MLCT transitions only reduce in intensity it is suggested that steric issues probably prevent a strong interaction (with nanotubes). This would suggest that the polymer conformation itself is not significantly affected. The spectroscopic data agree well with this suggestion as the most observable change is the reduction in intensity of MLCT transitions. Further theoretical work on the interaction between metallopolymers and carbon nanotubes and the morphology of metallopolymers absorbed onto the nanotubes' surface is necessary to fully understand the conformational changes in these metallopolymers (for examples of such investigations see refs 16, 41, and 42).

4. Conclusions

This work has shown that SWNT and MWNT can be stabilized in redox metallopolymers containing poly(pyridyl) complexes of ruthenium(II) and osmium(II). Microscopy (AFM and TEM) analysis has shown excellent wetting of the nanotubes with metallopolymers, thus demonstrating an attractive interaction between polymers and nanotubes. Spectroscopic analysis has shown that interactions with nanotubes do not significantly affect the metallopolymers' electrochemical properties. It is suggested that the resulting composite materials are likely to exhibit redox properties similar to that of free polymer. The interaction with nanotubes then adds functionality, as combining nanotubes and metallopolymers into composites could result in redox active materials with enhanced mechanical properties. The fact that in the polymer−nanotube assemblies the electrochemical and electronic properties of the polymers are maintained opens the possibility for their application of the assemblies as

nanosized electrochemical sensors for a range of both chemical and biological analytes, with the polymer coating acting as a redox catalyst. Further studies are currently in progress.

Acknowledgment. F.F., W.H., J.H. and J.G.V. would like to thank Enterprise Ireland for financial assistance. M.i.h.P. and N.A.Y. acknowledge support from EPSRC and The University of Hull. Mrs. J. Halder of the University of Hull Microscopy Facility is thanked for electron microscopy images.

Supporting Information Available: UV−vis absorption spectra of Ru- and Os-metallopolymers, Raman spectra of HiPco SWNT and **2**, and tapping mode AFM images of MWNT, **2**, **3**, and **4**. This material is available free of charge via the Internet at http://pubs.acs.org.

References and Notes

(1) Iijima, S. *Nature* **1991**, *354*, 58.

(2) Huang, W. Z.; Zhang, X. B.; Tu, J. P.; Kong, F. Z.; Ma, J. X.; Liu, F.; Lu, H. M.; Chen, C. P. *Mater. Chem. Phys.* **2002**, *78*, 144.

(3) Sun, Y.-P.; Zhou, B.; Henbest, K.; Fu, K.; Huang, W.; Lin, Y.; Taylor, S.; Carroll, D. L. *Chem. Phys. Lett.* **2002**, *351*, 349.

(4) Sander, S. J.; Tans, J.; Verschueren, A. R. M.; Dekker, C. *Nature* **1998**, *393*, 49.

(5) Chen, J.; Dyer, M. J.; Yu, M.-F. *J. Am. Chem. Soc.* **2001**, *123*, 6201.

(6) Chambers, G.; Carroll, C.; Farrell, G. F.; Dalton, A. B.; McNamara, M.; Cummins, E.; in het Panhuis, M.; Byrne, H. J. *Nano Lett.* **2003**, *3*, 843.

(7) O'Connell, M. J.; Bachilo, S. M.; Huffman, C. B.; Moore, V. C.; Strano, M. S.; Haroz, E. H.; Rialon, K. L.; Boul, P. J.; Noon, W. H.; Kittrell, C.; Ma, J.; Hauge, R. H.; Smalley, R. E. *Science* **2002**, *297*, 593.

(8) Richard, C.; Balavoine, F.; Schultz, P.; Ebbesen, T. W.; Mioskowski, C. *Science* **2003**, *300*, 775.

(9) Wenseleers, W.; Vlasov, I. I.; Goovaerts, E.; Obraztsova, E. D.; Lobach, A. S.; Bouwen, A. *Adv. Funct. Mater.* **2004**, *14*, 1105.

(10) Moore, V. C.; Strano, M. S.; Haroz, E. H.; Hauge, R. H.; Smalley, R. E.; Schmidt, J.; Yeshayahu, T. *Nano Lett.* **2003**, *3*, 1379.

(11) Hwang, G. L.; Hwang, K. C. *J. Mater. Chem.* **2001**, *11*, 1722.

(12) in het Panhuis, M.; Salvador-Morales, C.; Franklin, E.; Chambers, G.; Fonseca, A.; Nagy, J. B.; Blau, W. J.; Minett, A. I. *J. Nanosci. Nanotechnol.* **2003**, *3*, 209.

(13) Lin, Y.; Taylor, S.; Li, H.; Fernando, K. A. S.; Qu, L.; Wang, W.; Gu, L.; Zhou, B.; Sun, Y.-P. *J. Mater. Chem.* **2004**, *14*, 527.

(14) Ajayan, P. M.; Stephan, O.; Colliex, C.; Trauth, D. *Science* **1994**, *256*, 1212.

(15) McCarthy, B.; Coleman, J. N.; Czerw, R.; Dalton, A. B.; in het Panhuis, M.; Maiti, A.; Drury, A.; Byrne, H. J.; Carroll, D. L.; Blau, W. J. *J. Phys. Chem. B* **2002**, *106*, 2210.

(16) in het Panhuis, M.; Maiti, A.; Dalton, A. B.; van den Noort, A.; Coleman, J. N.; McCarthy, B.; Blau, W. J. *J. Phys. Chem. B* **2003**, *107*, 478.

(17) Rouse, J. H. *Langmuir* **2005**, *21*, 1055.

(18) Dalton, A. B.; Stephan, C.; Coleman, J. N.; McCarthy, B.; Ajayan, P. M.; Lefrant, S.; Bernier, P.; Blau, W. J.; Byrne, H. J. *J. Phys. Chem. B* **2000**, *104*, 10012.

(19) in het Panhuis, M.; Kane-Maguire, L. A. P.; Moulton, S. E.; Innis, P. C.; Wallace, G. G. *J. Nanosci. Nanotechnol.* **2004**, *4*, 976.

(20) Kymakis, E.; Amaratunga, G. A. J. *Synth. Met.* **2004**, *142*, 161.

(21) Chen, G. Z.; Shaffer, M. S. P.; Coleby, D.; Dixon, G.; Zhou, W. Z.; Fray, D. J. *Adv. Mater.* **2000**, *7*, 522.

(22) Maser, W. K.; Benito, A. M.; Callejas, M. A.; Seeger, T.; Martinez, M. T.; Schreiber, J.; Muszynski, J.; Chauvet, O.; Osvath, Z.; Koos, A. A.; Biro, L. P. *Mater. Sci. Eng. C* **2003**, *23*, 87.

(23) Keogh, S. M.; Hedderman, T. G.; Rüther, M. G.; Lyng, F. M.; Gregan, E.; Farrell, G. F.; Chambers, G.; Byrne, H. J. *J. Phys. Chem. B* **2005**, *109*, 5600.

(24) Ryan, K. P.; Lipson, S.; Drury, A.; Cadek, M.; Ruether, M.; O'Flaherty, S. M.; Barrow, V.; McCarthy, B.; Byrne, H. J.; Blau, W. J.; Coleman, J. N. *Chem. Phys. Lett.* **2004**, *391*, 329.

(25) Sainz, R.; Benito, A. M.; Teresa Martinez, M.; Galindo, J. F.; Sotres, J.; Baro, A. M.; Corraze, B.; Chauvet, O.; Maser, W. K. *Adv. Mater.* **2005**, *17*, 278.

(26) in het Panhuis, M.; Thielemans, W.; Minett, A. I.; Leahy, R.; Le Foulgoc, B.; Blau, W. J.; Wool, R. P. *Int. J. Nanosci.* **2003**, *2*, 185.

(27) Marder, S. R.; Perry, J. W. *Proceedings of the SPIE: Organic, Metallorganic, and Polymeric Materials for Non-Linear Optical Applications*; *SPIE*: Los Angles, CA, 1994.

(28) Forster, R. J.; Vos, J. G. *Electrochim. Acta* **1992**, *37*, 159.

(29) Hogan, C. F.; Forster, R. J. *Anal. Chim. Acta* **1999**, *396*, 13.

(30) Forster, R. J.; Figgemeir, E.; Lees, A. C.; Hjelm, J.; Vos, J. G. *Langmuir* **2000**, *16*, 7867.

(31) Doherty, A. P.; Forster, R. J.; Smyth, M. R.; Vos, J. G. *Anal. Chim. Acta* **1991**, *255*, 45.

(32) Doherty, A. P.; Forster, R. J.; Smyth, M. R.; Vos, J. G. *Anal. Chem.* **1992**, *64*, 572.

(33) Doherty, A. P.; Vos, J. G. *J. Chem. Soc., Faraday Trans.* **1992**, *88*, 2903.

(34) Doherty, A. P.; Stanley, M. A.; Vos, J. G. *Analyst* **1995**, *120*, 2371.

(35) Rajaopolan, C. R.; Aoki, A.; Heller, A. *J. Phys. Chem.* **1996**, *100*, 3719.

(36) Forster, R. J.; Vos, J. G. *Macromolecules* **1990**, *23*, 4372.

(37) Nikolaev, P.; Bronikowski, M.; Bradley, R.; Roymund, F.; Colbert, D.; Smith, K.; Smalley, R. *Chem. Phys. Lett.* **1999**, *313*, 91.

(38) Geraty, S. M.; Vos, J. G. *J. Chem. Soc., Dalton Trans.* **1987**, 3073.

(39) Chen, G.; Sumanaskera, G. U.; Pradhan, B. K.; Gupta, R.; Eklund, P. C.; Bronikowski, M. J.; Smalley, R. E. *J. Nanosci. Nanotechnol.* **2002**, *2*, 621.

(40) in het Panhuis, M.; Munn, R. W.; Blau, W. J. *Synth. Met.* **2001**, *121*, 1187.

(41) Grujicic, M.; Gao, G.; Roy, W. N. *Appl. Surf. Sci.* **2004**, *227*, 349.

(42) Yang, M.; Koutos, V.; Zaiser, M. *J. Phys. Chem. B* **2005**, *109*, 10009.

Available online at www.sciencedirect.com
SCIENCE DIRECT®
Journal of Molecular Structure 735–736 (2005) 123–134
Journal of MOLECULAR STRUCTURE
www.elsevier.com/locate/molstruc

Ground vs. excited state interaction in ruthenium-thienyl dyads: implications for through bond interactions in multicomponent systems

William Henry[a], Wesley R. Browne[a,1], Kate L. Ronayne[b], Noel M. O'Boyle[a], Johannes G. Vos[a], John J. McGarvey[b,*]

[a]*National Centre for Sensor Research, School of Chemical Sciences, Dublin City University, Glasnevin, Dublin 9, Ireland, UK*
[b]*School of Chemistry, The Queen's University of Belfast, Belfast BT9 5AG, Northern Ireland, UK*

Received 1 October 2004; revised 28 October 2004; accepted 29 October 2004
Available online 13 December 2004

Abstract

The vibrational and photophysical properties of mononuclear ruthenium(II) and ruthenium(III) polypyridyl complexes based on the ligands 2-(5′-(pyridin-2″-yl)-1′H-1′,2′,4′-triaz-3′-yl)-thiophene, 2-(5′-(pyrazin-2″-yl)-1′H-1′,2′,4′-triaz-3′-yl)-thiophene, are reported. The effect of the introduction of the non-innocent thiophene group on the properties of the triazole based ruthenium(II) complex is examined. The pH sensitive 1,2,4-triazole group, although influenced by the electron withdrawing nature of the thiophene group, does not facilitate excited state interaction of the thiophene and Ru(II) centre. Deuteriation and DFT calculations are employed to enable a deeper understanding of the interaction between the two redox-active centres and rationalise the difference between the extent of ground and excited state interaction in this simple dyad. The results obtained provide considerable evidence in support of earlier studies examining differences in ground and excited state interaction in multinuclear thiophene-bridged systems, in particular with respect to HOMO- and LUMO- mediated superexchange interaction processes.

Keywords: Ruthenium; Charge transfer states; LMCT; Thienyl; Raman

1. Introduction

The well-defined spectroscopic, photophysical, photochemical, and electrochemical properties of Ruthenium(II) polypyridyl complexes underlie their potential as building blocks in supramolecular assemblies. Of particular interest is their incorporation into the design of multinuclear structures capable of directing and modulating electron and energy transfer processes [1]. The ability to tune the excited state properties of these complexes is key to their potential for practical applications. Central to the development of photonic devices based on multicomponent systems is a detailed understanding of the nature of interaction between molecular components. In the present work the differences in the extent of interaction of molecular components, in the ground electronic state and in the thexi (thermally equilibrated excited) state, are investigated.

In previous studies of dinuclear Ru(II) complexes which incorporate 1,2,4-triazole ligands in the bridging unit, the importance of the triazole bridge in mediating electron and energy transfer was demonstrated in the pH dependence of the interaction strength. In these systems a relatively strong ground state interaction between the metal centres was effective over considerable distances (typically, ~12 Å), whilst excited state interaction was found to be much weaker [2]. While the ground state interaction is very sensitive to the nature of the bridging unit, it appears that the excited state interaction is predominantly a through space (Förster) interaction [3].

To investigate further the ability of the 1,2,4-triazole to permit effective control over intercomponent communication, we have extended our study to include 'dyads' based

* Corresponding author. Tel.: +44 2890 975450; fax: +44 2890 382117.
E-mail address: j.mcgarvey@qub.ac.uk (J.J. McGarvey).
[1] Present address: Organic and Molecular Inorganic Chemistry, Faculty of Mathematics and Natural Sciences, Royal University Groningen, Nijenborgh 4, Groningen, The Netherlands.

0022-2860/$ - see front matter © 2004 Elsevier B.V. All rights reserved.
doi:10.1016/j.molstruc.2004.10.114

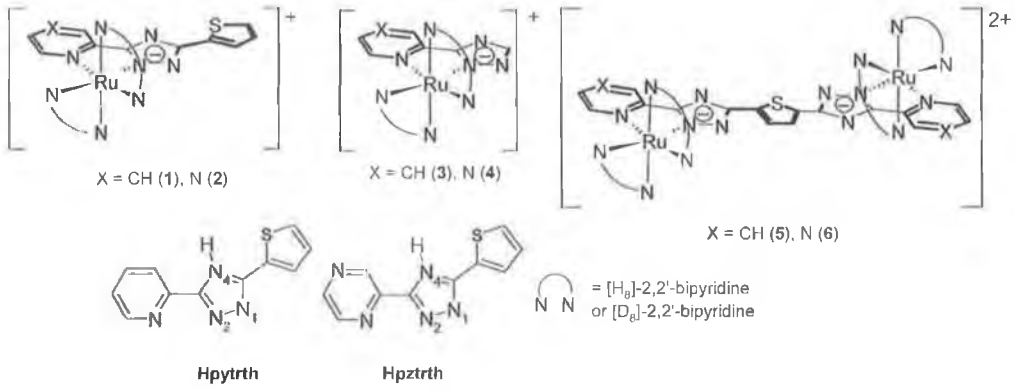

Fig. 1. Structure of complexes and ligands.

on the ligands 2-(5′-(pyridin-2″-yl)-1′H-1′,2′,4′-triaz-3′-yl)-thiophene (Hpytrth) and 2-(5′-(pyrazin-2″-yl)-1′H-1′,2′,4′-triaz-3′-yl)-thiophene (Hpztrth). The electrochemical and spectroelectrochemical properties of these complexes have been reported in an earlier contribution [2], together with the properties of the non-substituted monomers and the dimeric complexes in which thiophene bridges between two Ru(II)-triazole units (see Fig. 1). In the present investigation the mononuclear complexes and their deuteriated isotopologues based on these ligands have been examined by Raman, electronic and emission spectroscopy both in the Ru(II) and Ru(III) oxidation states. The experimental data are supplemented by DFT calculations. The results obtained are compared with our earlier studies on related mononuclear complexes and on the thiophene/triazole-bridged dinuclear complexes (**5** and **6**), with particular reference to the degree of interaction between the ruthenium(II) triazole and the thienyl moieties in the ground and thexi states.

2. Experimental

2.1. Materials

All solvents employed were of HPLC grade or better and used as received unless otherwise stated. For all spectroscopic measurements Uvasol (Merck) grade solvents were employed. All reagents employed in synthetic procedures were of reagent grade or better. $[Ru([D_8]\text{-bpy})_2Cl_2]$ was obtained from Complex Solutions (Dublin, Ireland) and used as received. The complexes $[Ru([H_8]\text{-bpy})_2(pytrth)]PF_6$ (**1a**) and $[Ru([H_8]\text{-bpy})_2(pztrth)]PF_6$ (**2a**) were available from earlier studies [2]. $[Ru([D_8]\text{-bpy})_2(pytrth)]PF_6$ (**1b**) and $[Ru([D_8]\text{-bpy})_2(pztrth)]PF_6$ (**2b**) were prepared by similar procedures to **1a** and **2a** respectively. Deuteriation was >99.5% by ^1H NMR (see Fig. S1, supplementary information).

2.2. Physical measurements

NMR spectra were recorded on a Bruker Avance 400 (400 MHz) NMR Spectrometer All measurements were carried out in $[D_3]$-acetonitrile for complexes. Peak positions are relative to residual solvent peaks. UV/Vis absorption spectra (accuracy ± 2 nm) were recorded in 10 mm quartz cuvettes on a Shimadzu UV/Vis-NIR 3100 spectrophotometer interfaced with an Elonex PC466 using UV/Vis data manager. Molar absorption coefficients are $\pm 10\%$. Emission spectra (accuracy ± 5 nm) were recorded at 298 K using a LS50B luminescence spectrophotometer, equipped with a red sensitive Hamamatsu R928 PMT detector, interfaced with an Elonex PC466 employing Perkin–Elmer FL WinLab custom built software. Emission and excitation slit widths were 10 nm. Emission spectra are uncorrected for photomultiplier response. pH titrations of **1** and **2** were carried out in Britton-Robinson buffer (0.04 M H_3BO_3, 0.04 M H_3PO_4, 0.04 M CH_3CO_2H) (pH was adjusted using concentrated sulfuric acid or sodium hydroxide solution) and followed by monitoring the pH dependence of absorption and emission spectra. pH_i refers to the inflection point of the emission titration curve. The appropriate isosbestic point from the absorption spectra was used as the excitation wavelength for emission titrations. Luminescence lifetime measurements were made using an Edinburgh Analytical Instruments (EAI) Time-Correlated Single-Photon Counting apparatus (TCSPC) as described previously [4]. Samples were deoxygenated by bubbling for 20 min using Ar gas before measurements were carried out, followed by periodic de-aeration to maintain oxygen exclusion. Emission lifetimes were calculated using a single exponential fitting function, involving a Levenberg–Marquardt algorithm with iterative reconvolution (Edinburgh instruments F900 software) and are $\pm 10\%$. The χ^2 and residual plots were used to judge the quality of the fits.

Ground state resonance Raman spectra of the complexes were recorded at 457.9, 488 and 514.5 nm using an Argon ion laser (Spectra Physics model 2050) as the excitation source

[5]. The laser power at the sample was typically 30–40 mW. The Raman backscatter was focused onto the entrance slit of a single stage spectrograph (JY Horiba HR640), which was coupled to a CCD detector (Andor Technology DV420-OE). Spectra generated at an excitation wavelength of 532 nm were recorded using an Andor Technology Raman Station. The spectra were run in quartz cuvettes. Solid state spectra at 785 nm were obtained on a JY Horiba Labram HR800 Raman microscope with a 300 groove grating. Transient resonance Raman spectra were recorded using the single-colour pump and probe method in which the leading edge of the pulse excites the molecules and the trailing edge probes the resultant Raman scattering [6]. The excitation source was a pulsed laser (Spectra Physics Q-switched Nd:YAG, GCR-3) at 354.7 nm with a typical pulse energy of approx 3 mJ at the sample. The Raman backscatter was focused onto the entrance slit of a double-stage spectrograph (Spex 1870), which was coupled to an ICCD (Andor Technology DH501). Typically, spectra were collected as a summation of 6000 accumulations.

2.3. Density functional theory calculations

Density functional calculations were carried out with Gaussian 03W [7] using Becke's three-parameter hybrid functional [8] with the LYP correlation functional [9] (B3LYP). The LanL2DZ basis set was used. This uses the Dunning–Huzinaga double-ζ basis functions [10] (DZ) for carbon, nitrogen, and hydrogen atoms, the Los Alamos effective core potential for the Ru core electrons, and DZ functions for the Ru valence electrons [11]. An ultrafine integration grid was used. Raman frequency calculations were carried out at the optimised geometry. GaussSum 0.8 [12] was used to calculate group contributions to the molecular orbitals and to prepare the partial density of states (PDOS) spectra. The contribution of a group to a molecular orbital was calculated using Mulliken population analysis. The PDOS spectra were created by convoluting the molecular orbital information with Gaussian curves of unit height and FWHM of 0.3 eV.

3. Results

The visible absorption and emission data for complexes **1a/1b** and **2a/2b** are listed in Table 1, with data for related complexes included for comparison. The lowest energy absorption feature for all complexes is assigned to several overlapping singlet metal-to-ligand-charge-transfer (^{1}MLCT) transitions (log ε ~4.2), by comparison with other ruthenium polypyridyl complexes and on the basis of resonance Raman analysis (vide infra) [13]. All compounds show strong absorptions (log ε ~5) at ~ 280 nm, which are π–π* in nature [14] Overall the electronic properties are typical for pyridyl and pyrazine triazole complexes by comparison with complexes **3** and **4** [15]. For the pyridine-1,2,4-triazole based complex, **1a**, the absorption spectra of the protonated and deprotonated species are very different, with a substantial blue shift in the λ_{max} occurring upon protonation (~40 nm) (see Fig. 2). However, for the pyrazine-1,2,4-triazole based complex, **2a**, only a small blue shift in the λ_{max} of the ^{1}MLCT absorption bands occurs upon protonation (~ 10 nm) (Fig. 2). Difference spectra (see supplementary information, Fig. S2) show the changes more clearly, with a blue-shift in the visible absorption bands upon protonation and a red-shift in the $\pi\pi^*_{bpy}$ transition in the UV region. The effect of protonation on the pyridine and pyrazine bound isomers are similar to those of related mononuclear complexes (see Table 1). In strongly acidic solution (conc. H_2SO_4), complex **1a** shows relatively minor changes in its absorption spectrum, whilst in contrast very dramatic changes in the absorption spectrum of **2a** are observed, with a blue-shift in the ^{1}MLCT absorption bands and the appearance of a very strong absorption at ~550 nm. For the mononuclear complexes a progressive modification of the absorption spectrum was observed ± 1 pH unit either

Table 1
Photophysical and redox properties (lifetimes for deuteriated complexes in parentheses)

	λ_{Abs} /nm[a]	$E_{1/2}$ (V vs SCE)[a]	λ_{lum} /nm[c]	pK_a[b]	$\tau_{298\ K}$/ns[a]	$\tau_{77\ K}$ /μs[a]	Ref.
1a	245, 291, 480	0.86 (1.62 irr)	683	3.05	110 (135)	3.01 (4.00)	[c]
H1a	242, 286, 439	1.19 (1.67 irr)	613	–	15 (6)	5.76 (7.62)	[c]
1a$^+$	570, 1050[b]	–	–	–	–	–	[2a]
2a	244, 289, 455	0.95 (1.55 irr)	664	2.15	82 (184)	7.85 (8.75)	[c]
H2a	245, 284, 438	1.23 (1.55 irr)	672	–	312 (320)	7.34 (7.56)	[c]
$H_2$2a	361, 543	–	–	–	–	–	[c]
2a$^+$	570, 1060[b]	–	–	–	–	–	[2a]
3	465	0.83	650	4.1	145 (183)	–	[15]
H3	437	1.14	620	–	–	–	[15]
4	445	1.01	668	3.7	230 (283)	4.45 (7.03)	[15]
H4	441	1.25	658	–	230 (230)	4.77 (6.00)	[15]

[a] In CH_3CN.
[b] In H_2O.
[c] This work.

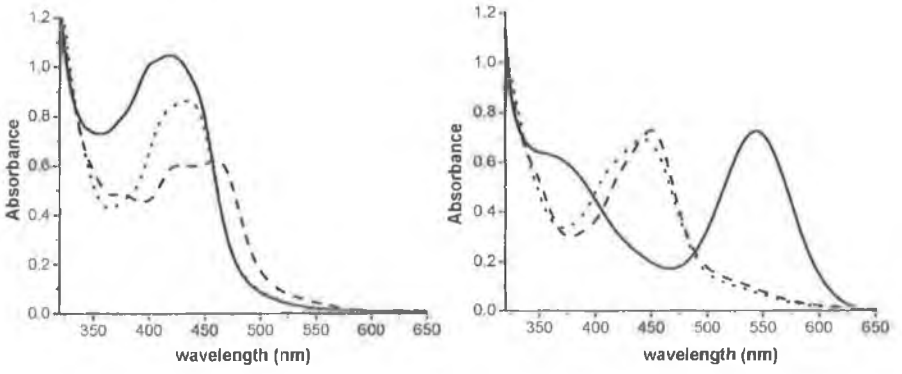

Fig. 2. Absorption Spectra for **1a** (left) and **2a** (right) in conc. H_2SO_4 (solid line), pH 1.5 (dotted line) and pH 7 (dashed line).

side of the pK_a point, with isosbestic points being maintained throughout the titration.

The acid dissociation constants (pK_a) for all complexes are given in Table 1. The values were obtained from the change in the absorption spectra of the complexes with changing pH (see Fig. S2). The behaviour observed can be rationalised by protonation/deprotonation of the triazole moiety. The acidity of the coordinated triazole ring has been found to be dependent on the nature of the non-coordinated substituent in the C3 position of the 1,2,4-triazole. This dependence is reflected in the change in pK_a, with respect to the unsubstituted C–H analogues **3** and **4**, Table 1 [16]. Protonation of the coordinated pyrazine ring, in **2a** and **4**, although possible, occurs at only at negative pH [2].

All complexes examined are luminescent in acetonitrile and, weakly, in aqueous solution, at room temperature and in EtOH/MeOH glass at 77 K. The complexes emit in the 600–700 nm region and a large blue shift is observed between 300 and 77 K, typical for ^{3}MLCT emission [13]. Emission lifetimes at 77 and 298 K measured at the emission maxima indicated are collected in Table 1. As for the absorption spectra, the emission maxima of **1a** and **2a** are close to those of the related complexes **3a** and **4a** respectively. Protonation of **1a** results in a blue shift in the emission and a reduction in emission lifetime, while for **2a**, protonation results in a modest red-shift in the emission spectrum with an increase in emission lifetime. The effect of deuteriation of the bpy ligands on the emission lifetime of **1a** and **H1a** is not very significant at 298 K (Table 1). However at 77 K in alcoholic glass a more pronounced deuteriation effect is observed for both the protonated and deprotonated species. In contrast, for **2a** a larger deuteriation effect is observed at 298 K and (but less so at) 77 K (+12%). For the protonated pyrazine based complexes **H2a**, no deuteration effect is observed at either temperature. A notable feature for complex **4**, is the occurrence of a dual emission between 120 and 180 K [15]. A similar effect was observed (Fig. S4) for **2a** suggesting that the excited state electronic structure in both complexes is similar.

3.1. Raman spectroscopy

Resonance Raman spectroscopy is widely employed in elucidating the ground and excited state properties of Ru(II) polypyridyl complexes, due to the selective enhancement of vibrational modes that are coupled to allowed spectroscopic transitions [17]. Such selective enhancement may assist in elucidating the nature of particular transitions, for instance the extent to which they are centred or localised on specific orbitals of individual ligands in the molecule. This level of detail in the assignment of the transitions leading to population of the lowest excited states is of particular importance in the development and study of photoactive and luminescent transition metal complexes [1].

Non-resonant Raman spectra of **1a/1b** and **2a** (powder samples) were recorded at 785 nm to provide a general overview of the (Raman-active) vibrational modes and are shown in Fig. 3. Deuteriation enables direct assignment of bpy based vibrational bands (at 1600, 1484, 1317, 1269, 1171, 1057, 1033, 761 and 642 cm^{-1})[18] and the pytrth$^-$ (at 1606, 1552, 1514, 1462, 1435, 1388, 1344, 1299, 1184, 1147, 1100, 1014, 949, 761, 646 cm^{-1}) and pztrth$^-$ (1552, 1460, 1418, 1356, 1168, 1143, 1102, 945, 651 cm^{-1}) based vibrational bands.

Resonance Raman (rR) spectra were recorded for **1a/b**, **H1a/b**, **2a/b** and **H2a/b** in aqueous solution at 457.9 and 488 nm and at 514.5 nm for **$H_2$2a/b**. For **1a/1b** and **H1a/H1b** only [H_8]-bpy and [D_8]-bpy based vibrational features respectively were observed at 457.9 and 488 nm (see Figs. S5 and S6, supplementary information), confirming the ^{1}MLCT$_{bpy}$ character of the lowest absorption bands and the absence of transitions associated with the pytrth$^-$ and Hpytrth ligands. In contrast, for **2a/b**, **H2/b**, although vibrational features associated with [H_8]-bpy and [D_8]-bpy are observed, additional bands associated with pztrth$^-$ and Hpztrth are observed also (Figs. 4 and 5). For **2a/b**, additional

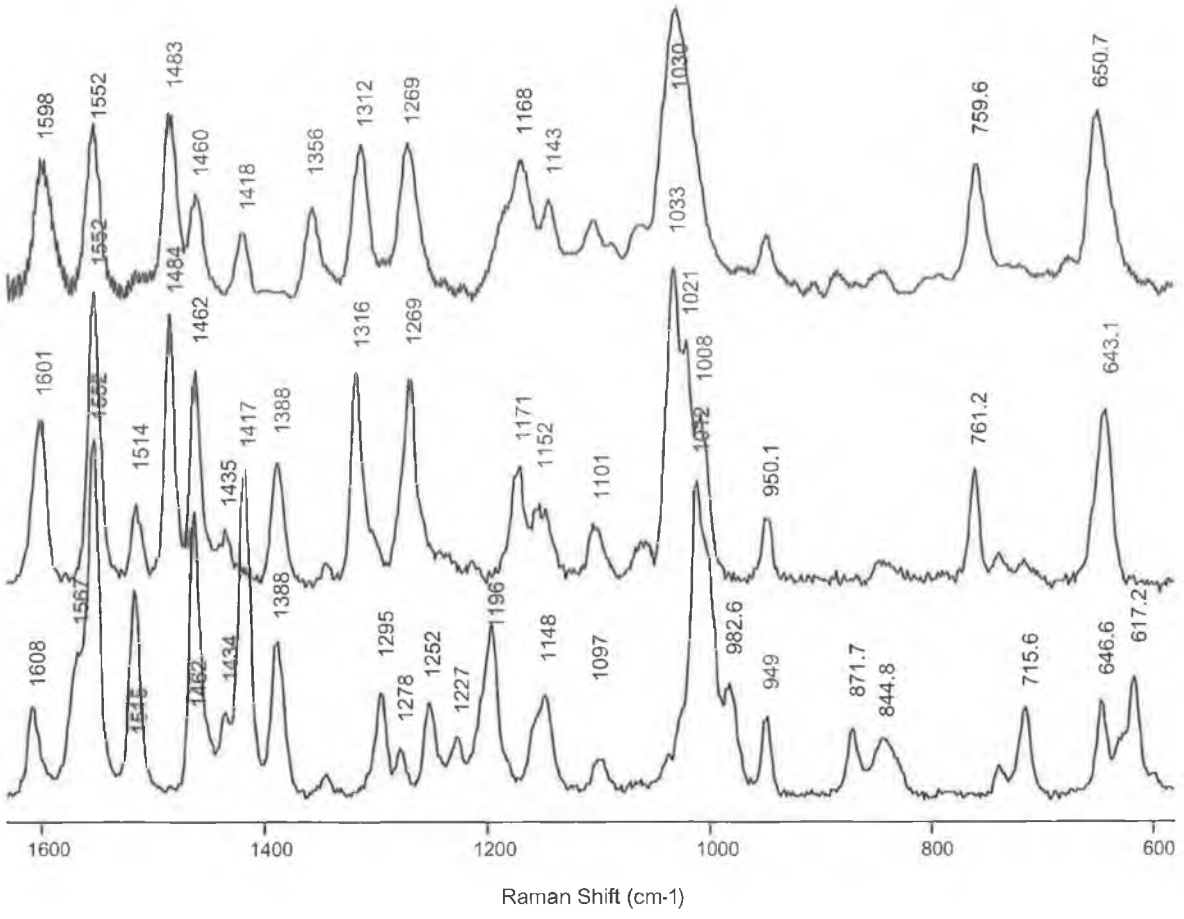

Fig. 3. (Solid state) Raman spectra of **2a** (upper), **1a** (middle) and **1b** (lower) at 785 nm.

vibrational bands at 1602, 1516, 1373 and 1194 cm^{-1} are observed at both 457.9 and 488 nm excitation.

For **H2a/b**, in addition to bpy features, bands assigned to the Hpztrth ligand are present at 1587, 1549, 1513, 1440, 1387, 1293, 1206, 1187 and 1073 cm^{-1}. For **$H_2$2a/b** no vibrational features assignable to $[H_8]$-bpy/$[D_8]$-bpy are observed at either 457.9 or 488 nm. Bands at 1634, 1544, 1494 and 1472 cm^{-1} are insensitive to deuteriation and are assigned to the doubly protonated H_2pztrth ligand.

Resonance Raman spectra of the oxidised complexes **1a**$^+$ and **2a**$^+$, in H_2O, (Fig. 6) in contrast to those of **1a/2a**, show no characteristic $[H_8]$-bpy features. The excitation wavelength used is resonant with a strong absorption assigned as a ligand to metal charge transfer (LMCT) band. The absence of vibrational bands assignable to bpy ligand vibrations is not unexpected since the oscillator strength of LMCT absorptions has been shown to be dependent on the electron donor properties of the ligands [19]. In the present case the electron rich triazole-thiophene ligand results in a much more intense LMCT absorption band than expected for this class of complex and hence the observation of vibrational bands not assignable to the bpy ligand supports the assignment of the absorption to a py(z)trth-to-metal charge transfer band.

3.2. Transient resonance Raman spectroscopy

Transient resonance Raman spectra of **1a** and **2a** in CD_3CN, both in a deprotonated and protonated state, are shown in Fig. 7. The observation of strong bands at 1212 and 1285 cm^{-1} in the spectra of **1a/H1a** and **2a**, readily attributable to the bpy anion radical, confirm the assignment of the lowest emissive state as being from a bpy-based ^{3}MLCT. In the case of **H2a**, there is a notable absence of these bands. On the basis of transient absorption spectra of the related complexes **3** and **4**, the absence of excited state resonance in the spectrum of **H2a**, due to a shift in the excited state absorption out of resonance with the 355 nm excitation line may be discounted. Based on earlier transient Raman studies of **4** [15], it can be concluded that for **H2a** the lowest excited state is pyrazine-based. In aqueous solution, a similar situation is observed.

In the spectra of **1a** and **2a** bands assigned to the 1,2,4-triazole based ligands are also observed, suggesting

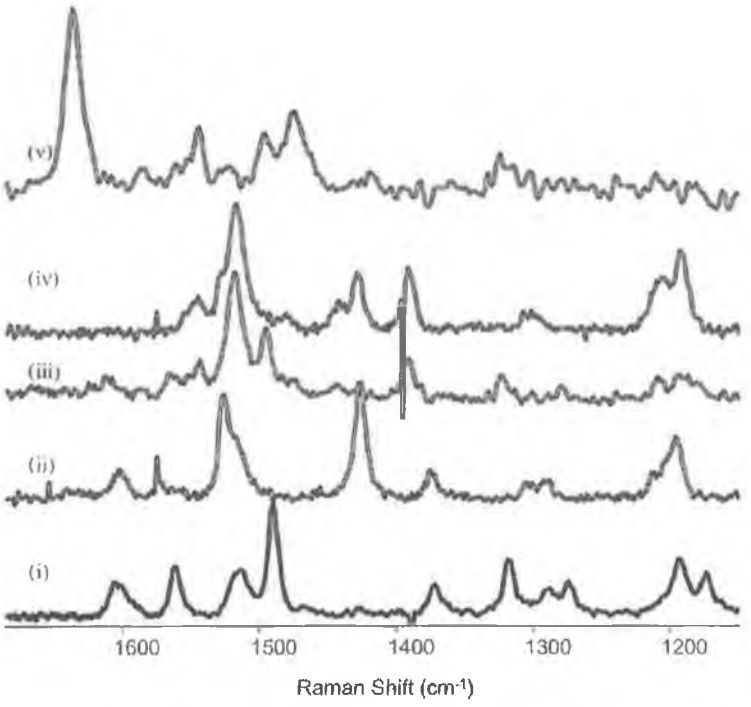

Fig. 4. Resonance Raman Spectra of (i) **2a** (ii) **2b** (iii) **H2a** (iv) **H2b** (v) **$H_2$2a** at 457.9 nm excitation.

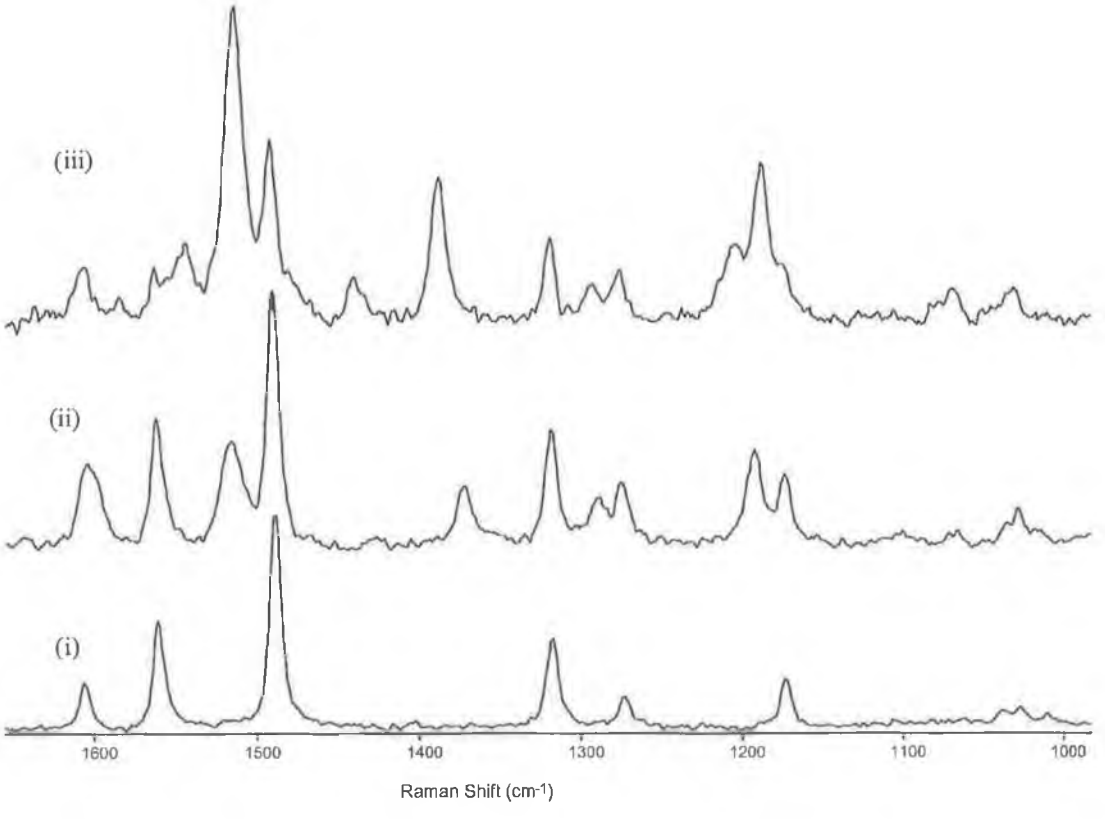

Fig. 5. resonance Raman spectra of (i) **1a** (ii) **2a** and (iii) **H2a** 488 nm excitation.

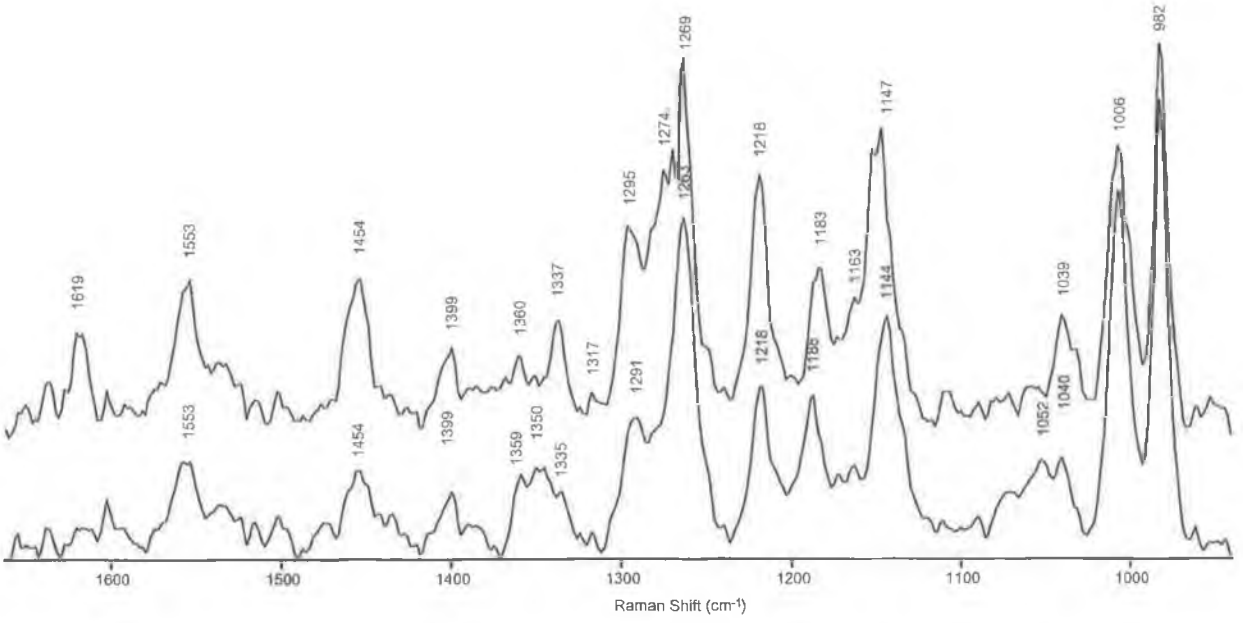

Fig. 6. Resonance Raman spectra of (a) $\mathbf{1a}^{+}$ and (b) $\mathbf{2a}^{+}$, in basic/H_2O at 785 nm.

contributions from pytrth- and pztrth-based absorptions at 355 nm [20].

3.3. Density functional theory

In order to gain more insight into the electronic properties of the complexes **2a/H2a** and **2b/H2b**, DFT calculations were carried using the B3LYP functional and the LanL2DZ basis set. For the protonated complex a complication arises in regard to the point of protonation, whether it is at N1 or N4 (Fig. 1). Previous studies on the relative reactivity of the uncoordinated nitrogen ligands of the 1,2,4-triazole ring have indicated that the N1 position is slightly less acidic than the N4 position. However, due to

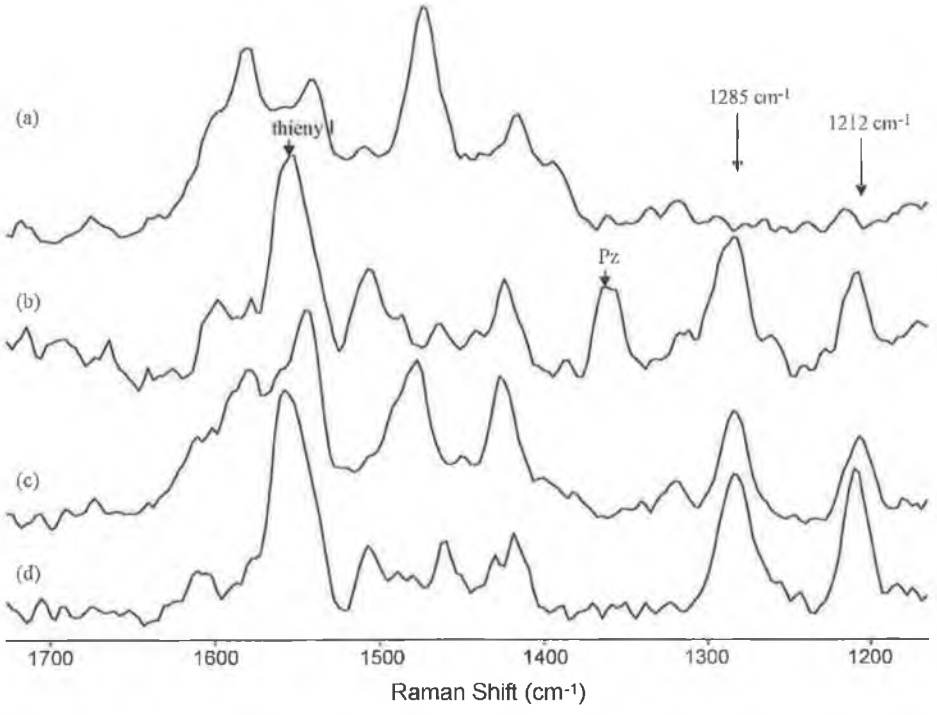

Fig. 7. Transient Raman spectra of (a) **H2a**, (b) **2a**, (c) **H1a** and (d) **1a** in CD_3CN (λ_{exc} 355 nm).

the potential of introducing additional steric interactions in protonation at the N1 position, in the present study, the N4 position of the 1,2,4-triazole was protonated for the DFT calculations of **H2a/b**.

After geometry optimization with an ultrafine integration grid, the molecular orbitals were described in terms of contributions from various groups in the molecule for **2a** and **H2a**: *Ru*—the Ru atom, *pz*—the pyrazine ring, *tr*—the triazole moiety; *th*—the thiophene moiety; *bpy1* and *bpy2*—the two bipyridines. These data are shown in Fig. S7 of the supplementary information. The isosurfaces for the HOMO-1, HOMO, LUMO and LUMO+1 of **2a** and **H2a** are shown in Fig. 8. In the frontier region, neighboring orbitals are often closely spaced. In such cases, consideration of only the HOMO and LUMO may not yield a realistic description of the frontier orbitals. For this reason, partial density of states (PDOS) diagrams, which incorporate a degree of overlap between the curves

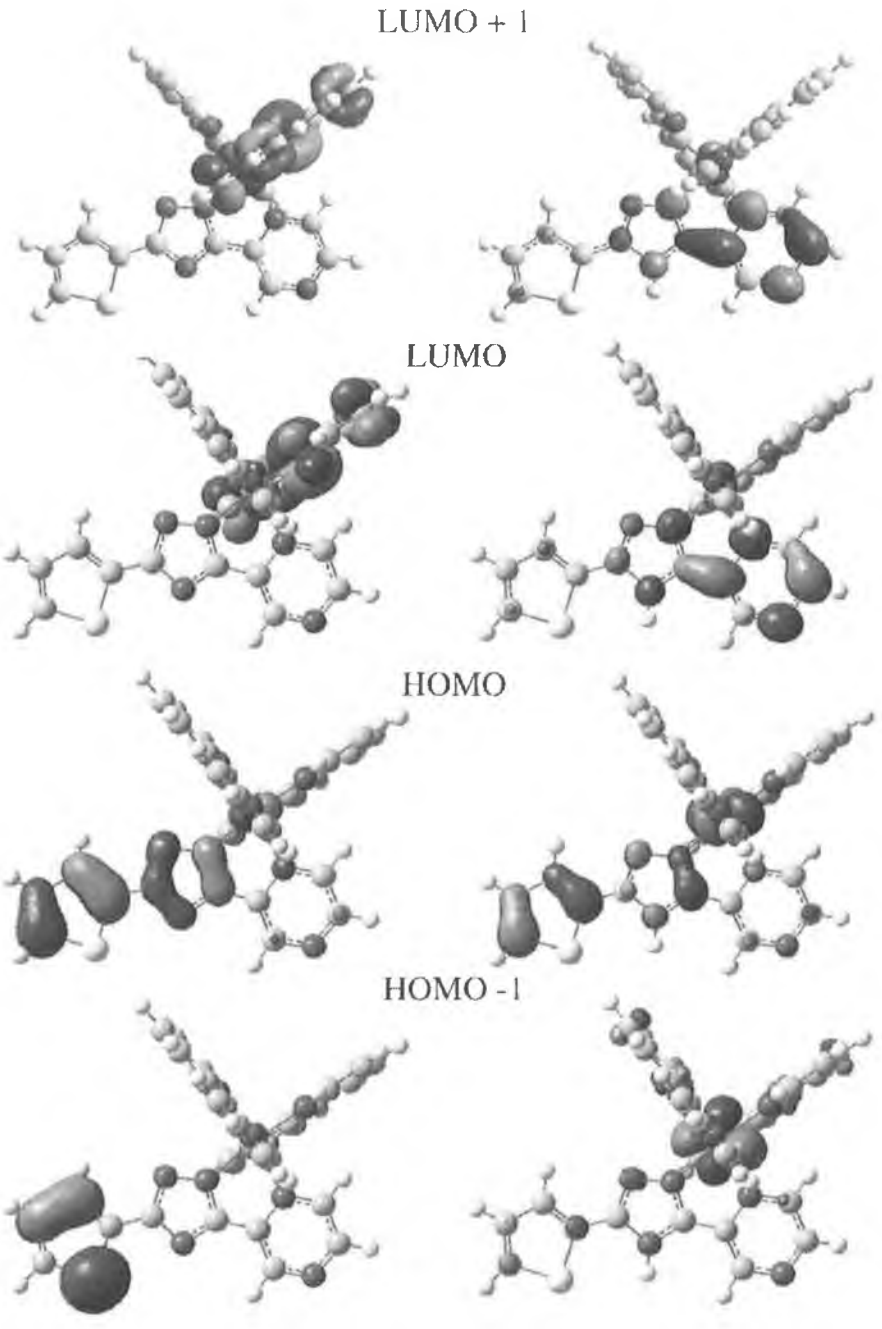

Fig. 8. Isosurfaces of HOMO-1, HOMO, LUMO and LUMO+1 orbitals for **2a** (left) and **H2a** (right).

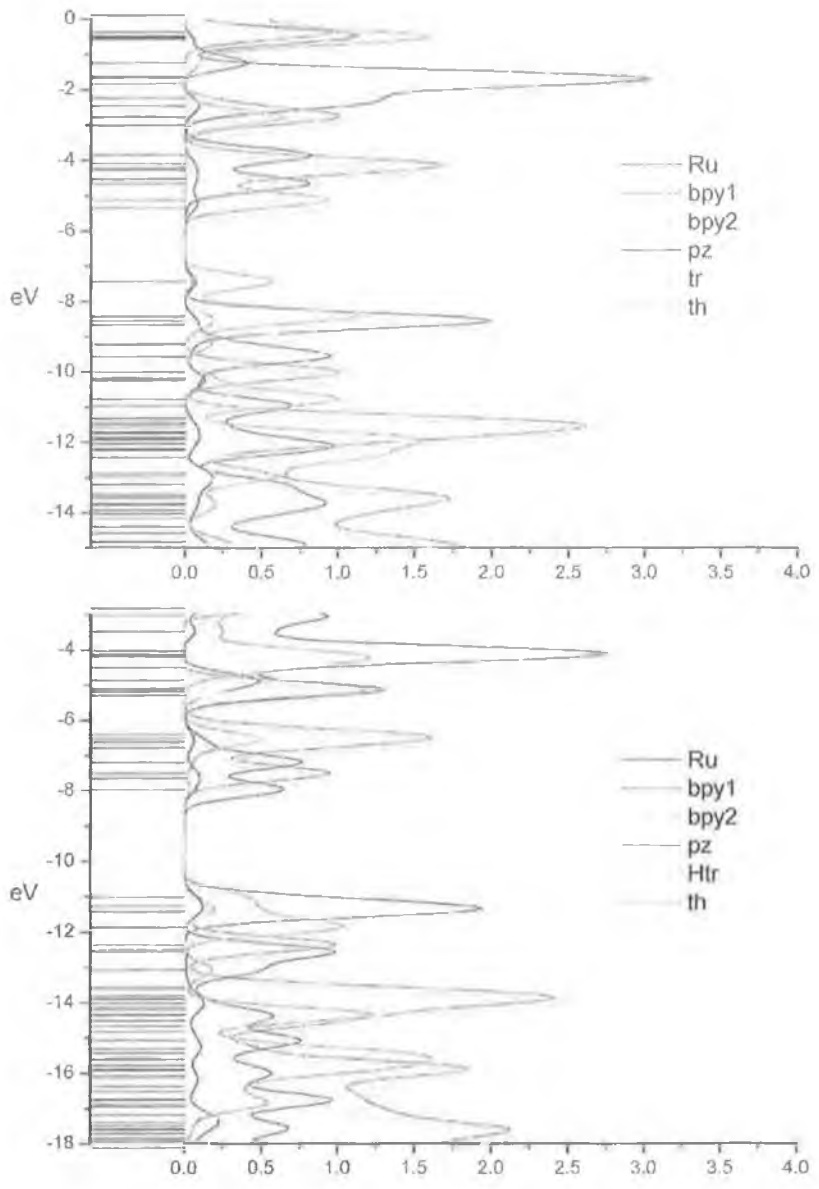

Fig. 9. PDOS diagrams for **2a** (top) and **H2a** (bottom).

convoluted from neighboring energy levels, can give a more representative picture of the nature of the frontier orbitals. The PDOS diagrams obtained are shown in Fig. 9.

DFT calculations were used to predict the Raman spectrum of **2a/H2a** and **2b/H2b** (Table 2). A systematic error occurs in the calculation of vibrational frequencies due to the consistent underestimation of bond length, for example, and the neglect of anharmonicity. To compensate a scaling factor is used. The 'Solver' module of Microsoft™ Excel™ was used to achieve the best fit of the experimental peaks with those obtained from the calculations. The spectra of the perprotio and deuterio complexes were compared, with the bands which were sensitive to bpy deuteration being assigned as bpy-based. The isotope shift observed upon deuteriation in the calculated spectra is demonstrated in Fig. 10.

4. Discussion

The UV·Vis absorption and emission properties of the mononuclear complexes show a close comparison with those of the analogous complexes **3** and **4**, but are slightly red shifted. Upon protonation for both complexes a blue shift in the absorption spectra is observed. For **1a** protonation results in large blue shift (~70 nm), in agreement with observations on other mononuclear pyridyl-1,2,4-triazole complexes. For **2**, protonation results, first in a very minor red shift,

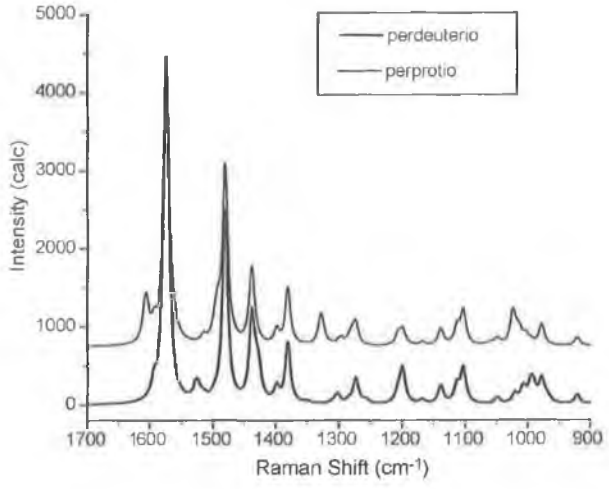

Fig. 10. Calculated Raman Spectra for **H2a** (upper trace) and **H2b** (lower trace).

followed by a blue shift in the emission λ_{max}, with a concomitant reduction in intensity. Again the acid-base emission properties bear close comparison with related systems. The pK_a values determined for both complexes are lower than for **3** and **4**. This confirms the electron withdrawing nature of the thienyl group. As is typical, the pyrazine complex is more acidic than the analogous pyridine complex, due to the greater electron withdrawing nature of the pyrazine ring [16].

The results obtained in the present study provide a basis for a more detailed understanding of the nature of the interaction between the thienyl and ruthenium(II) -based components of these simple dyads. Although it is tempting to consider the thienyl group as an innocent part of the Hpytrth and Hpztrth ligands, in electronic terms such a simplification is not appropriate for understanding the overall properties of the systems. Our intention in this study was to build on the extensive body of data available on 1,2,4-triazole based systems, to explore in a fundamental way the extent to which different moieties in relatively simple dyads can be viewed as distinct groups. It is clear from examination of the properties of the complexes in their ground and thexi electronic states that the degree of interaction between the components is critically dependent on the electronic state (i.e. ground or excited) and that extrapolating conclusions based on study of ground state interaction to excited state systems is not always justified. In the present contribution, extensive resonance Raman spectroscopic investigations of both the ground and lowest excited electronic states together with computational analysis (DFT) are employed to help understand the excited state electronic structure of these systems.

For the complex containing the pyridyl-triazole moiety only the bpy ligands are involved in the absorption process, in both of the protonation states. Pyrazine is a better π-acceptor than pyridine. For **2**, therefore, the π* level is reduced, leading to an overlap in the triazole and bpy absorption bands. Protonation of the triazole leads to a reduction of the electron density on the metal centre. This is reflected in an increase in the oxidation potential, however it does not change the overlap of bpy and Hthpztr in the ^{1}MLCT state. Transient Resonance Raman studies agree with the results from both the DFT and excited state lifetime measurements. Bpy anion radical peaks observed in **2** indicate that the excited state is localised on the bpy moiety while in the protonated complex no bpy radical peaks are observed.

For **2a**, the HOMO is based on thiophene and triazole (Fig. 8). The LUMO is on one of the bpy ligands. The same information is shown in the PDOS spectrum in Fig. 9. In addition, the PDOS spectrum for **2a** shows that the π* orbital of the pyrazine ligand is at higher energy than that of the bpy (Fig. 9). The metal-based frontier orbitals are the HOMO-2 to HOMO-4 (Fig. S7).

In contrast, the HOMO of **H2a** has an increased contribution from the Ru center (Fig. 8). The location of the LUMO has changed from bpy to pyrazine. The PDOS spectrum shows the overall changes in electronic structure. In the protonated complex, the metal center has a large contribution to the first four occupied orbitals (Fig. S7). The PDOS spectrum of **H2a** is shifted to lower energy by about 3.5 eV, compared to that of **2a**. This indicates the increased difficulty in removing an electron from the HOMO of **H2a**, which is due to the increased charge on the complex. A comparison of the PDOS spectra of **2a** and **H2a** shows that the π* orbital of the pyrazine is shifted to lower energy on protonation, so that the LUMO is now pyrazine-based.

The main point to emphasise is the contrast in the degree of interaction between the metal center and the thienyl moiety in the ground and excited states. In the ground state, **2a** shows contributions from both the thienyl and the Ru in the levels H-4 to HOMO, which may be considered the occupied frontier orbitals. However in the excited state the unoccupied frontier orbitals, LUMO to LUMO+4, show increased contributions from the bpy moieties but little or no contributions from the Ru and thienyl. A similar picture emerges for **H2a**. This suggests appreciable delocalisation of the HOMO and is also consistent with the proposal [2] that the significant interaction in the mixed valence thienyl bridged dimers **5** and **6** is indeed due to HOMO assisted superexchange.

The absence of any contribution from the pyrazine ring for **2a** and **H2a** is in agreement with the similarity of the spectra for $\mathbf{1a}^+$ and $\mathbf{2a}^+$ at 514 nm (LMCT bands).

The calculated isosurfaces for the LUMO and LUMO+1 have been used to approximate the location of the ^{3}MLCT excited state in **2a** and **H2a**. There are a number of assumptions which must be borne in mind, namely: that the virtual Kohn-Sham orbitals from the DFT calculations are equivalent to unoccupied orbitals; that the lowest energy transition is to the lowest unoccupied orbitals; and that the ^{1}MLCT is located on the same ligands as the ^{3}MLCT state. In previous studies deuteration has been used to investigate the location of the excited state [21]. If the excited state is

Table 2
Calculated and experimental Raman frequencies for bpy and triazole vibrations in **H2a**

Experimental bpy (cm^{-1})	Calculated bpy (cm^{-1})	Experimental Hthpztr (cm^{-1})	Calculated Hthpztr (cm^{-1})
1608	1606	1517	1526
1561	1563	1440	1449
1492	1492	1394	1408
1320	1328	1210	1215
1175	1187	1194	1208

A scaling factor of 0.978 was used.

located on the ligand, which has been deuterated then the excited state lifetime is seen to increase. In **2a**, deuteration of the bpy ligands leads to an increase in lifetime from 82 to 184 ns (Table 1), indicating that the excited state is bpy-based. This is consistent with the location of the LUMO and LUMO + 1 electron density suggested by the calculations. For **H2a**, computational studies predict that the excited state will be based on the pyrazine-triazole ligand. As would be expected, deuteration of the bpy ligands in this complex has no effect on the excited state lifetime in this case (Table 1).

5. Conclusions

Resonance Raman spectroscopic investigations of the complexes in both the ground and lowest excited electronic states, coupled with photophysical measurements as a function of pH, have been employed to help understand the excited state electronic structure of these simple thienyl dyad systems. The influence of deuteriation on the emission lifetimes provided further evidence as to the nature of the lowest emissive excited state/s involved. DFT calculations have been used to supplement the experimental data, representing the first example of DFT work on Ru(II) monomer complexes containing the 1,2,4-triazole moiety. The overall pattern of results, which emerge from this joint theoretical/experimental approach underlines the fact that the degree of interaction between the components depends very much on the electronic state, i.e. ground or excited, under consideration. The results suggest that the extrapolation of conclusions based solely on the study of ground state interaction between molecular components to the interaction in the corresponding excited state is not necessarily justifiable.

Acknowledgements

The Authors acknowledge Invest Northern Ireland, grant no. RTD COE 40 and Andor Technology Ltd for financial support (to KLR). WH and NMOB would like to thank Enterprise Ireland for financial support. Ligand for the synthesis of **2b** was provided by Claire Brennan.

Appendix. Supplementary Material

Supplementary data associated with this article can be found, in the online version, at doi:10.1016/j.molstruc.2004.10.114

References

[1] (a) L.A. Worl, G.F. Strouse, J.N. Younathan, S.M. Baxter, T.J. Meyer, J. Am. Chem. Soc., 112 (1990) 7571.
(b) V. Balzani, Tetrahedron, 48 (1992) 10443.
(c) V. Balzani, S. Campagna, G. Denti, A. Juris, S. Serroni, M. Venturi, Acc. Chem. Res., 31 (1998) 26.
(d) V. Balzani, F. Scandola, Supramolecular Photochemistry, Horwood, Chichester, UK, 1991;
(e) F. Scandola, M.T. Indelli, C. Chiorboli, C.A. Bignozzi, Top. Curr. Chem., 158 (1990) 73.
(f) P.D. Beer, F. Szemes, V. Balzani, C.M. Salà, M.G.B. Drew, S.W. Dent, M. Maestri, J. Am. Chem. Soc., 119 (1997) 11864.
(g) F. Barigelletti, L. Flamigni, J.-P. Collin, J.-P. Sauvage, Chem. Commun.(1997) 333.
(h) O. Waldmann, J. Hassmann, P. Müller, G.S. Hanan, D. Volkmer, U.S. Schubert, J.-M. Lehn, Phys. Rev. Lett., 78 (1997) 3390.
(i) E. Zahavy, M.A. Fox, Chem. Eur. J., 4 (1998) 1647.
(j) V. Balzani, A. Credi, M. Venturi, Curr. Opin. Chem. Biol., 1 (1997) 506.
[2] (a) W.R. Browne, F. Weldon, A. Guckian, J.G. Vos, Coll. Czech. Chem. Commun. 68 (2003) 1467;
(b) A.C. Lees, C.J. Kleverlaan, C.A. Bignozzi, J.G. Vos, Inorg. Chem. 40 (2001) 5343.
[3] F. Weldon, L. Hammarstrom, E. Mukhtar, R. Hage, E. Gunneweg, J.G. Haasnoot, J. Reedijk, W.R. Browne, A.L. Guckian, J.G. Vos, Inorg. Chem. 43 (2004) 4471.
[4] W.R. Browne, C.M. O'Connor, C. Villani, J.G. Vos, Inorg. Chem. 40 (2001) 5461.
[5] D.S. Jones, A.F. Brown, A.D. Woolfson, A.C. Dennis, L.J. Matchett, S.E.J. Bell, J. Pharm. Sci. 89 (2000) 563.
[6] (a) C.G. Coates, L. Jacquet, J.J. McGarvey, S.E.J. Bell, A.H.R. Al-Obaidi, J.M. Kelly, J. Am. Chem. Soc. 119 (1997) 7130;
(b) C.G. Coates, J. Olofsson, M. Coletti, J.J. McGarvey, B. Onfelt, P. Lincoln, B. Norden, E. Tuite, P. Matousek, A.W. Parker, J. Phys. Chem. B 105 (2001) 12653.
[7] M.J. Frisch, G.W. Trucks, H.B. Schlegel, G.E. Scuseria, M.A. Robb, J.R. Cheeseman, J.A. Montgomery, Jr., T. Vreven, K.N. Kudin, J.C. Burant, J.M. Millam, S.S. Iyengar, J. Tomasi, V. Barone, B. Mennucci, M. Cossi, G. Scalmani, N. Rega, G.A. Petersson, H. Nakatsuji, M. Hada, M. Ehara, K. Toyota, R. Fukuda, J. Hasegawa, M. Ishida, T. Nakajima, Y. Honda, O. Kitao, H. Nakai, M. Klene, X. Li, J.E. Knox, H.P. Hratchian, J.B. Cross, C. Adamo, J. Jaramillo, R. Gomperts, R.E. Stratmann, O. Yazyev, A.J. Austin, R. Cammi, C. Pomelli, J.W. Ochterski, P.Y. Ayala, K. Morokuma, G.A. Voth, P. Salvador, J.J. Dannenberg, V.G. Zakrzewski, S. Dapprich, A.D. Daniels, M.C. Strain, O. Farkas, D.K. Malick, A.D. Rabuck, K. Raghavachari, J.B. Foresman, J.V. Ortiz, Q. Cui, A.G. Baboul, S. Clifford, J. Cioslowski, B.B. Stefanov, G. Liu, A. Liashenko, P. Piskorz, I. Komaromi, R.L. Martin, D.J. Fox, T. Keith, M.A. Al-Laham, C.Y. Peng, A. Nanayakkara, M. Challacombe, P.M.W. Gill, B. Johnson, W. Chen, M.W. Wong, C. Gonzalez, J.A. Pople., Gaussian 03, Revision B.04, Gaussian, Inc., Pittsburgh PA, 2003.
[8] A.D. Becke, J. Chem. Phys. 98 (1993) 5648.
[9] C. Lee, W. Yang, R.G. Parr, Phys. Rev. B 37 (1988) 785.
[10] T.H. Dunning Jr., P.A. Hay, in: H.F. Schaefer III (Ed.), Modern Theoretical Chemistry vol. 3, Plenum, New York, 1977, p. 1.

[11] (a) P.J. Hay, W.R. Wadt, J. Chem. Phys. 82 (1985) 270;
(b) W.R. Wadt, P.J. Hay, J. Chem. Phys. 82 (1985) 284;
(c) P.J. Hay, W.R. Wadt, J. Chem. Phys. 82 (1985) 299.
[12] N.M. O'Boyle, J.G. Vos., 2003, GaussSum 0.8, Dublin City University.
[13] (a) R. Hage, R. Prins, J.G. Haasnoot, J. Reedijk, J.G. Vos, J. Chem. Soc., Dalton Trans. 1987; 1389;
(b) H.A. Nieuwenhuis, J.G. Haasnoot, R. Hage, J. Reedijk, T.L. Snoeck, D.J. Stufkens, J.G. Vos, Inorg. Chem. 30 (1991) 48;
(c) B.E. Buchanan, R. Wang, J.G. Vos, R. Hage, J.G. Haasnoot, J. Reedijk, Inorg. Chem. 29 (1990) 3263;
(d) W.R. Browne, C.M. O'Connor, C. Villani, J.G. Vos, Inorg. Chem. 40 (2001) 5461;
(e) R. Hage, J.G. Haasnoot, H.A. Nieuwenhuis, J. Reedijk, D.J.A. De Rider, J.G. Vos, J. Am. Chem. Soc. 112 (1990) 9245;
(f) J.M. de Wolf, R. Hage, J.G. Haasnoot, J. Reedijk, J.G. Vos, New J. Chem. 15 (1991) 501.
[14] M. Milkevitch, E. Brauns, K.J. Brewer, Inorg. Chem. 35 (1996) 1737.
[15] T.E. Keyes, C.M. O'Connor, U. O'Dwyer, C.G. Coates, P. Callaghan, J.J. McGarvey, J.G. Vos, J. Phys. Chem. A 103 (1999) 8915.
[16] W.R. Browne, C.M. O'Connor, H.P. Hughes, R. Hage, O. Walter, M. Doering, J.F. Gallagher, J.G. Vos, J. Chem. Soc., Dalton Trans. 2002; 4048.
[17] (a) K. Maruszewski, K. Bajdor, D.P. Strommen, J.R. Kincaid, J. Phys. Chem. 99 (1995) 6286;
(b) P.K. Mallick, G.D. Danzer, D.P. Strommen, J.R. Kincaid, J. Phys. Chem. 92 (1988) 5628;
(c) D.P. Strommen, P.K. Mallick, G.D. Danzer, R.S. Lumpkin, J.R. Kincaid, J. Phys. Chem. 94 (1990) 1357.
[18] [D8]-bpy vibrational bands at 1561, 1417, 1294, 1251, 1226, 1196, 1012, 982, 871.5, 845, 716, 617 cm^{-1}.
[19] (a) M.K. Nazeeruddin, S.M. Zakeeruddin, K. Kalyananundaram, J. Phys. Chem. 97 (1993) 9607;
(b) K. Kalyananundaram, S.M. Zakeeruddin, Md. K. Nazeeruddin, Coord. Chem. Rev. 132 (1994) 259.
[20] A.L. Guckian, M. Doering, M. Ciesielski, O. Walter, J. Hjelm, N.M. O'Boyle, W. Henry, W.R. Browne, J.J. McGarvey, J.G. Vos., J. Chem. Soc., Dalton Trans. (2004) 3943.
[21] W.R. Browne, J.G. Vos, Coord. Chem. Rev. 219 (2001) 761.

FULL PAPER

Dalton
www.rsc.org/dalton

Assessment of intercomponent interaction in phenylene bridged dinuclear ruthenium(II) and osmium(II) polypyridyl complexes†

Adrian L. Guckian,[a] Manfred Doering,[b] Michael Ciesielski,[b] Olaf Walter,[b] Johan Hjelm,[a] Noel M. O'Boyle,[a] William Henry,[a] Wesley R. Browne,[a] John J. McGarvey[c] and Johannes G. Vos*[a]

[a] *National Centre for Sensor Research, School of Chemical Sciences, Dublin City University, Glasnevin, Dublin 9, Ireland. E-mail: han.vos@dcu.ie; Fax: 00353-1-7005503; Tel: 00353-1-7005307*

[b] *ITC-CPV, Forschungszentrum Karlsruhe, PO Box 3640, 76021, Karlsruhe, Germany*

[c] *School of Chemistry, Queen's University Belfast, Belfast, Northern Ireland, UK BT9 5AG*

Received 16th June 2004, Accepted 11th October 2004
First published as an Advance Article on the web 3rd November 2004

The synthesis and characterisation of $[Ru(bipy)_2(\mathbf{L1})]^{2+}$ and the homodinuclear complexes $[M(bipy)_2(\mathbf{L1})M(bipy)_2]^{4+}$ (where M = Ru or Os), employing the ditopic ligand, 1,4-phenylene-bis(1-pyridin-2-ylimidazo[1,5-*a*]pyridine) (**L1**), are reported. The complexes are identified by elemental analysis, UV/Vis, emission, resonance Raman, transient resonance Raman and ^{1}H NMR spectroscopy, mass spectrometry and electrochemistry. The X-ray structure of the complex $[Ru(bipy)_2(\mathbf{L1})(bipy)_2Ru](PF_6)_4$ is also reported. DFT calculations, carried out to model the electronic properties of the compounds, are in good agreement with experiment. Minimal communication between the metal centres is observed. The low level of ground state electronic interaction is rationalized in terms of the poor ability of the phenyl spacer in facilitating superexchange interactions. Using the electronic and electrochemical data a detailed picture of the electronic properties of the **RuRu** compound is presented.

Introduction

The design and synthesis of polynuclear transition metal complexes containing electro-active and photo-active units are topics of continuing interest due to their potential usage as building blocks for supramolecular assemblies and molecular devices.[1] Ruthenium(II) and osmium(II) polypyridine complexes are playing a key role in the development of compounds capable of performing photo- and/or redox-triggered useful functions in charge separation devices for photochemical solar energy conversion[2] and information storage.[1,3] In particular, species featuring photophysical properties and redox behaviour, which can undergo controlled modification with external stimuli, are of interest.[3,4] For example, reversible electrochemical switching of emission energy shows potential in applications such as electronic displays.[5] The role played by the bridging ligand in determining intercomponent interaction is well recognised.[6,7] Since the late 1970s, ground and excited state intercomponent interactions in dinuclear Ru(II) complexes containing polytopic bridging ligands employing imidazoles,[8] triazoles,[9] pyrazine,[10] 4,4′-bipyridyl,[11] 2,2′-bipyrimidine,[12] tetrazine,[13] have received considerable attention. The incorporation of spacer units (*i.e.*, phenylene,[14] dimethoxyphenyl,[9b] thienyl,[9c] *etc.*) has allowed for further control over the degree of interaction between metal centres in multinuclear complexes.

In this contribution the structural, photophysical and electrochemical characterisation of two symmetrical, phenylene bridged complexes of the form $[M(bipy)_2(\mathbf{L1})M(bipy)_2](PF_6)_4$ (where M = Ru(II) or Os(II) and **L1** = 1,4-phenylene-bis(1-pyridin-2-ylimidazo[1,5-*a*]pyridine)) are reported (see Fig. 1). Selective deuteriation is employed to facilitate interpretation of ^{1}H NMR, luminescence and resonance Raman spectra. DFT calculations are described for **RuRu**. A detailed description of the electronic properties of this compound is presented based on these calculations and the results obtained are compared with experimental data. Furthermore, the results obtained are discussed in the context of earlier studies on related complexes.

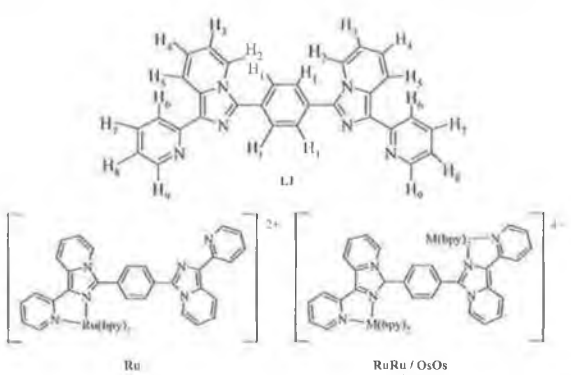

Fig. 1 Structure of the mononuclear and dinuclear complexes and **L1**.

Experimental

All reagents were of HPLC grade or better and used as received. Spectroscopic grade (UVASOL) solvents were employed for all spectroscopic measurements. d_8-2,2′-bipyridyl (d_8-bipy) (Complex Solutions, Dublin, Ireland) was used as received, *cis*-$[Ru(bipy)_2Cl_2]\cdot 2H_2O$, its deuteriated analogue *cis*-$[Ru(d_8\text{-bipy})_2Cl_2]\cdot 2H_2O$ [15] and *cis*-$[Os(bipy)_2Cl_2]\cdot 2H_2O$[16] were prepared by previously reported procedures.

Syntheses

$[Ru(bipy)_2(L1)](PF_6)_2\cdot 2H_2O$ (Ru). **L1** (102 mg, 0.219 mmol) was heated at reflux in 300 cm^3 of a 1 : 1 EtOH/H_2O mixture. *cis*-$[Ru(bipy)_2Cl_2]\cdot 2H_2O$ (114 mg, 0.219 mmol) in 20 cm^3 EtOH

† Electronic supplementary information (ESI) available: Fig. S1: ^{1}H NMR spectra of **Ru** and **RuRu**. Fig. S2: Resonance Raman spectra of ***d*Ru*d*Ru**, **RuRu** and **OsOs**. Fig. S3: Reductive and oxidative electrochemistry of **Ru**. Fig. S4: Frontier orbitals of **RuRu**. Table S1: ^{1}H NMR spectra of L^1 and L^1 in ***d*Ru*d*Ru**. Table S2: Selected bond distances. Table S3: Selected bond angles. Table S4: Calculated data for the frontier orbitals of **RuRu**. See http://www.rsc.org/suppdata/dt/b4/b409189b/

DOI: 10.1039/b409189b

was added over 90 min. After 3 h the reaction was allowed to cool and the volume reduced *in vacuo*. The solution was filtered to remove unreacted ligand. 10 cm^3 of a saturated aqueous solution of ammonium hexafluorophosphate was added to the filtrate yielding an orange–brown precipitate, which was isolated by filtration, washed with 25 cm^3 of water, 25 cm^3 of diethyl ether and air-dried. The compound was purified by column chromatography (silica gel, 0.05 M KNO_3 acetonitrile–water (80/20 v/v)). The first orange band eluted, yielded the desired product. The acetonitrile was removed *in vacuo* and an excess of NH_4PF_6 added to precipitate the product. The precipitate was filtered, washed with 25 cm^3 cold water and 25 cm^3 diethyl ether. Yield 95 mg (37%). Mass spectrometry: *m/z* calculated for $[Ru](PF_6)^{1+}$: 1023.2. Found: 1023.3. ^1H NMR spectrum (400 MHz, d_6-DMSO) δ 6.95 (dd, 1H), 7.24 (m, 4H), 7.44 (m, 2H), 7.60 (m, 7H), 7.78 (d, 1H), 7.82 (d, 1H), 7.88 (m, 2H), 7.97 (d, 1H), 8.14 (m, 7H), 8.29 (d, 1H), 8.53 (m, 5H), 8.66 (d, 1H), 8.74 (m, 3H). Elemental analysis for $C_{50}H_{40}N_{10}Ru_1O_2P_2F_{12}$: Calc. C 50.04, H 3.17, N 11.68. Found C 49.45, H 3.01, N 11.19%.

$[Ru(bipy)_2(L1)Ru(bipy)_2](PF_6)_4\cdot 4H_2O$ (RuRu). **L1** (200 mg, 0.43 mmol) and *cis*-$[Ru(bipy)_2Cl_2]\cdot 2H_2O$ (492 mg, 0.946 mmol) were heated at reflux in 30 cm^3 (1 : 1) EtOH–H_2O for 16 h. The solution was cooled to r.t., reduced *in vacuo* and filtered to remove unreacted ligand. 5 cm^3 of a saturated aqueous solution of ammonium hexafluorophosphate was added to the filtrate to yield an orange–brown precipitate, which was filtered off, washed with 25 cm^3 water and 25 cm^3 diethyl ether. The compound was purified by column chromatography (as for **Ru**). The second orange band to elute yielded the desired product. Yield 650 mg (81%). Mass spectrometry: *m/z* calculated for $[RuRu](PF_6)_3^+$: 1727.15. Found: 1727.3. ^1H NMR spectrum (400 MHz, d_6-DMSO) δ 6.75 (dd, 1H), 6.94 (dd, 1H), 7.24 (m, 8H), 7.43 (m, 7H), 7.60 (m, 10H), 7.80 (d, 1H), 7.90 (d, 1H), 8.16 (m, 12H), 8.40 (d, 1H), 8.63 (m, 6H), 8.75 (m, 4H). Elemental analysis for $C_{70}H_{60}N_{14}Ru_2O_4P_4F_{24}$: Calc.: C 43.43, H 2.90, N 10.13. Found: C 43.11, H 3.08, N 10.01%.

$[Ru(d_8\text{-bipy})_2(L1)Ru(d_8\text{-bipy})_2](PF_6)_4\cdot 4H_2O$ (*d*Ru*d*Ru). As for **RuRu** except **L1** (50 mg, 0.107 mmol) and *cis*-$[Ru(d_8\text{-bipy})_2Cl_2]\cdot 2H_2O$ (127 mg, 0.237 mmol) were heated at reflux in 20 cm^3 of 1 : 1 EtOH–H_2O. Yield 112 mg (55%). Mass spectrometry: *m/z* calculated for $[dRudRu](PF_6)_3^+$: 1759.2. Found: 1758.3 $[M^+]$. ^1H NMR spectrum (400 MHz, d_6-DMSO) δ 7.27 (m, 3H), 7.41 (d, 2H), 7.60 (m, 2H), 8.05 (dd, 1H), 8.63 (m, 2H). Elemental analysis for $C_{70}H_{28}N_{14}D_{32}Ru_2O_4P_4F_{24}$: Calc.: C 42.73, H 2.85, N 9.97. Found C 43.21, H 2.98, N 9.51%.

$[Os(bipy)_2(L1)Os(bipy)_2](PF_6)_4\cdot 4H_2O$ (OsOs). As for **RuRu** except **L1** (200 mg, 0.43 mmol) and *cis*-$[Os(bipy)_2Cl_2]\cdot 2H_2O$ (523 mg, 0.946 mmol) were heated at reflux in 20 cm^3 of 1 : 1 ethylene glycol–H_2O for 72 h. Yield 549 mg (62%). Mass spectrometry: *m/z* calculated for $[OsOs](PF_6)_3^+$: 1907.3. Found: 1908.1 $[M^+]$. ^1H NMR spectrum (400 MHz, d_6-acetone) δ 6.81 (dd, 2H), 7.06 (dd, 1H), 7.25 (m, 7H), 7.53 (m, 13H), 7.74 (d, 1H), 7.94 (m, 14H), 8.26 (d, 1H), 8.40 (d, 1H), 8.46 (m, 2H), 8.65 (m, 10H). Elemental analysis for $C_{70}H_{60}N_{14}Os_2O_4P_4F_{24}$: Calc.: C 39.77, H 2.65, N 9.28. Found C 39.44, H 2.39, N 9.41%.

X-Ray crystallography

Data for **RuRu** were collected on a Siemens SMART 1000 CCD-diffractometer fitted with a molybdenum tube (Mo-Kα, λ = 0.71073 Å) and a graphite monochromator. A full sphere of data was collected with the irradiation time of 4 s per frame. The structures were solved with direct methods and all non hydrogen atoms refined anisotropically with the SHELX-97 program[17] (refinement by least-squares against F^2). *Crystal data*: **RuRu**: $[Ru(bipy)_2(L1)Ru(bipy)_2](PF_6)_4$, $C_{75.1}H_{52}F_{24}N_{14}P_4O_{1.7}Ru_2$; M_r = 1959.73; monoclinic, $P2_1/c$, a = 15.0193(15), b = 24.332(3), c = 21.810(2) Å, β = 96.956(2), V = 7911.9 $Å^3$; D_c = 1.645 Mg m^{-3}, data collection range: h −20 to 19, k = −30 to 32, l = −26 to 28; reflections collected: 85840, reflections unique: 19449, reflections observed ($I > 2\sigma I$): 8985, final R-values: $R1 = 0.054$ ($I > 2\sigma I$), $wR2 = 0.156$ (all data).

CCDC reference number 230287.

See http://www.rsc.org/suppdata/dt/b4/b409189b/ for crystallographic data in CIF or other electronic format.

Physical methods

^1H NMR spectra were recorded on a Bruker Avance 400 (400 MHz) instrument. The chemical shifts are relative to residual solvent peaks. UV/Visible spectra were recorded using a Shimadzu UV3100 UV-Vis-NIR spectrophotometer interfaced with an Elonex PC433 personal computer (Molar absorptivities (ε) ±5%). Emission spectra were recorded on a Perkin-Elmer LS50-B spectrofluorimeter equipped with a red-sensitive Hamamatsu R928 detector, interfaced to an Elonex PC466 personal computer employing Perkin Elmer FL Winlab custom built software. Excitation and emission slit widths were 10 nm. The spectra are not corrected for photo multiplier response. Luminescence lifetime measurements were obtained using an Edinburgh Analytical Instruments Time Correlated Single Photon Counting apparatus.[9d] Excitation employed the 337 nm N_2 emission line of the nanosecond flashlamp. Cyclic voltammetry (100 mV s^{-1}) and DPV (step height: 50 mV, increment: 4 mV, pulse duration: 60 ms, sampling interval: 20 ms, frequency: 5 Hz were carried out in acetonitrile with 0.1 M $TBABF_4$. A conventional three-electrode cell was used. A 2 mm Pt disk electrode sealed in Kel-F (purchased from CH Instruments) was used as the working electrode, the counter (auxiliary) electrode was a coiled Pt-wire, and a Ag/Ag^+ (10 mM $AgNO_3$, 0.1 M $TBABF_4$ in acetonitrile) half-cell was used as reference electrode. The solutions were deoxygenated with argon and a blanket of argon was maintained over the solutions during the experiments. Glassware used was dried in a vacuum oven at 80 °C overnight or flamed using a Bunsen burner prior to preparing solutions. The $TBABF_4$ salt was dried in the vacuum oven overnight at 80 °C. The electrodes were polished on a soft polishing pad (Struers, OP-NAP) with an aqueous slurry of 0.3 micron alumina (Buehler) and sonicated for at least 5 min in MQ-water to remove any remaining polishing material from the surface of the electrode. The working electrodes were rinsed thoroughly with acetone and dried in air before insertion into the cell. The reference electrode was calibrated externally by carrying out cyclic voltammetry (also at 100 mV s^{-1}) in solutions of ferrocene of similar concentration as that of the complexes (0.4–2 mM) in the same electrolyte at the end of each day of experiments. Bulk electrolysis was carried out in a three-compartment, three-electrode cell. The reference electrode was Ag/Ag^+, the working electrode was a cylinder of Pt gauze, 1 cm × 1 cm (52 mesh) and the counter electrode used was a coiled Pt wire. Spectroelectrochemistry[18] was carried out in 0.1 M TEAP acetonitrile (anhydrous, Aldrich). The potential was controlled using a EG&G PARC Model 362 scanning potentiostat. A platinum/rhodium gauze working electrode, Ag/Ag^+ reference electrode (calibrated against the Fc/Fc^+ standard prior to each experiment) and platinum wire counter electrode was employed. All references are quoted relative to Fc/Fc^+ using the relevant conversion factor.[19,20] Absorption spectra of the species generated in the optically transparent thin layer electrode (OTTLE) cell were recorded on a Shimadzu 3100 UV-Vis/NIR spectrophotometer (*vide supra*). Elemental analysis was carried out by the Microanalytical Laboratories at University College Dublin.

Ground-state resonance Raman spectra of the complexes were recorded at 457.9, 488 and 514 nm using an argon ion laser (Spectra Physics model 2050) as the excitation source.[21] The laser power at the sample was typically 30–40 mW. The Raman backscatter was focused onto the entrance slit of a single stage spectrograph (JY Horiba HR640), which was coupled to a CCD

detector (Andor Technology DV420-OE). The spectra were run in quartz cuvettes and were not corrected for detector response. Transient resonance Raman spectra were recorded using the single-colour pump and probe method in which the leading edge of the pulse excites the molecules and the trailing edge probes the resultant Raman scattering.[22] The excitation source was a pulsed laser (Spectra Physics Q-switched Nd:YAG, GCR-3) at 354.7 nm with a typical pulse energy of approx. 3 mJ at the sample. The Raman backscatter was focused onto the entrance slit of a double-stage spectrograph (Spex 1870), which was coupled to an ICCD (Andor Technology DH501). Typically, spectra were collected as a summation of 6000 accumulations.

Density functional theory (DFT) calculations were carried out using Gaussian03.[23] Becke's 3-parameter hybrid functional[24] was used with the correlation functional of Lee, Yang and Parr[25] (B3LYP). The effective core potential basis set LanL2DZ[26] was used for all atoms. Although the crystallographic structure of the dimer was of C_1 symmetry, due to the size of the system it was necessary to reduce the computational cost by imposing C_2 symmetry during the geometry optimisation. The homochiral ΔΔ isomer was studied. The resulting electronic structure is not expected to differ significantly for the other stereoisomers. GaussSum[27] was used to calculate the contributions from groups of atoms to each molecular orbital and to convolute the molecular orbital data to create a partial density of states (PDOS) spectrum. The contributions were calculated within the framework of a Mulliken population analysis. The PDOS was convoluted with Gaussian curves of FWHM of 0.3 eV and unit height.

Results and discussion

The very low solubility of **L1** in comparison with the mononuclear complex (**Ru**) results in the rapid formation of the binuclear complex once the mononuclear complex forms. To overcome this, **Ru** was prepared by slow addition of *cis*-$[Ru(bipy)_2Cl_2]$ to a large volume of solvent saturated with **L1**, heated at reflux. **RuRu** and **OsOs** were prepared by direct reaction of two equivalents of *cis*-$[M(bipy)_2Cl_2]$ (where M = Ru(II) or Os(II)) with one equivalent of **L1** in ethanol–water and ethylene glycol–water, respectively.

X-Ray crystallography

The molecular structure of **RuRu** is shown in Fig. 2. Selected bond angles and lengths are listed in Tables S1 and S2 (ESI†). **RuRu** co-crystallized with 1.7 molecules of acetone per unit cell and four hexafluorophosphate counter anions, (three of which are disordered). From the crystal structure it is clear that **L1** is coordinated to Ru1 *via* the N1 and N3 atoms and the Ru2 atom *via* the N4 and N6 atoms. The bite angle of the N(1)–Ru(1)–N(3) is 78.65(16)° and N(4)–Ru(2)–N(6) is 78.63(16)° which corresponds well with the bite angle of 77.9(1)° obtained by Hage *et al.* for $[Ru(bipy)_2(3\text{-}(2\text{-hydroxyphenyl})\text{-}5\text{-}(pyridin\text{-}2\text{-}yl)\text{-}1,2,4\text{-}triazole)]PF_6{\cdot}CH_3COCH_3$.[28] Bite angles of between 79.35(16) and 78.86(17)° for bipyridine ligands and Ru–N distances of 2.045(4)–2.068(4) Å are also comparable to those found in other complexes.[9,14,28] One factor contributing to the increased length of the Ru(1)–N(1) and Ru(2)–N(4) bond lengths (2.080(4) and 2.086(4) Å, respectively) is the limited π-backbonding to the electron rich bridging ligand from the metal centre. The N1–Ru1–N8, N3–Ru1–N10 and N7–Ru1–N9 angles are 174.81(15), 175.85(16) and 176.44(16)°, respectively, while the *trans* angular bond angles around the Ru2 atom are 169.22(16), 175.74(16) and 172.83(17)° for N4–Ru2–N12, N6–Ru2–N14 and N11–Ru2–N13, respectively. This deviation from octahedral geometry is due to the acute bite angles of both the 2,2′-bipyridyl and the **L1** ligand. The internuclear (Ru···Ru) separation is 9.06 Å and the orientation of the phenyl ring of **L1** is distorted from planarity (by 61.1°) with respect to the imidazole rings.

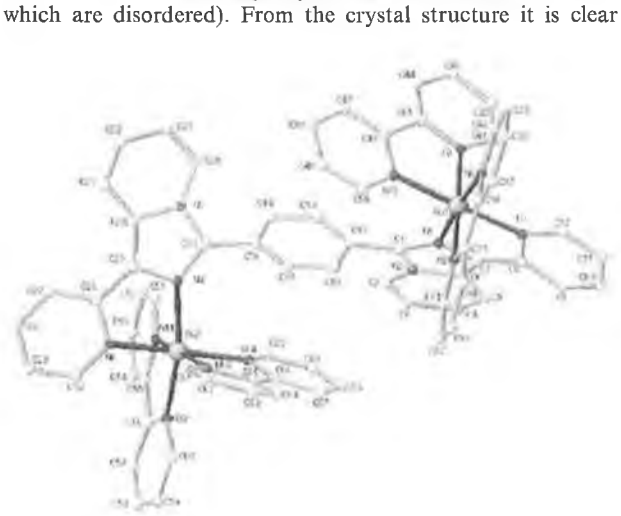

Fig. 2 X-Ray crystal structure of **RuRu** showing the atomic numbering used. The PF_6^- ions, acetone molecules and hydrogen atoms have been omitted for clarity.

^{1}H NMR Spectroscopy

The ^{1}H NMR spectroscopic data of all the complexes are given in the Experimental section (see Table S3 and Fig. S1, ESI†). As expected the protons of the **L1** ligand are shifted downfield upon coordination. The symmetry of **L1** is retained upon addition of the two equivalent metal centres, which greatly simplifies the spectra of the homonuclear (**RuRu** and **OsOs**) complexes.[29] Deuteration of the bipy ligands allowed for the identification of the **L1** protons in the *d***Ru***d***Ru** complex.[30]

Electronic and photophysical properties

The absorption spectra of **Ru** and **RuRu** are similar, differing only in that the molar absorptivity of the dinuclear compound is almost twice that of the mononuclear complex (Table 1). The electronic data of **L1** are shown in Fig. 3(c). The ligand shows a number of features in the visible part of the spectrum, with absorption maxima at 277, 330 and 372 nm. At room temperature an emission is observed at 455 nm. The UV/Vis absorption spectra of the complexes (Fig. 3) are reminiscent with those observed for related Ru(II) and Os(II) imidazole and benzimidazole based complexes reported by Haga and co-workers.[8] The visible region of the spectra is dominated by $d\pi\rightarrow\pi^*$ MLCT transitions, while $\pi\rightarrow\pi^*$ (bipy) and $\pi\rightarrow\pi^*$ (**L1**) transitions are located at *ca.* 290 and 350 nm, respectively (*vide infra*). The metal-to-ligand-charge-transfer (^{1}MLCT) bands for the Ru(II) complexes are close in energy to the transition observed for $[Ru(bipy)_3]^{2+}$ and are assigned as $d\pi\rightarrow\pi_{bipy}^*$ ^{1}MLCT, based on electrochemical and resonance Raman data (*vide infra*). In the mixed-metal complex, **OsOs**, absorption bands between 580 and 700 nm are assigned to formally spin forbidden $d\pi\rightarrow\pi^*$ (bipy) (^{3}MLCT) transitions. Comparison of the spectroscopic properties of the binuclear complexes with the parent $[M(bipy)_3]^{2+}$ (where M = Ru or Os) indicates that transitions involving the bridging ligand **L1** are responsible for the absorption features at around 350 nm. The nature of this band is further discussed in the resonance Raman section.

All compounds are luminescent in acetonitrile at room temperature and in butyronitrile glass at 77 K. As for the absorption spectra only a modest (~15 nm) red shift in the emission spectrum with respect to $[M(bipy)_3]^{2+}$ (M = Ru or Os) is observed (Table 1) and, typical of ^{3}MLCT emission, the emission undergoes a blue shift on cooling to 77 K.[31] The luminescence lifetimes of **Ru** (690 ns) and **RuRu** (506 ns) in deaerated acetonitrile are comparable to the luminescence lifetimes of related complexes (*e.g.*, benzimidazoles, triazoles *etc.*).[8,32] Deuteriation of the bipyridyl ligands leads to an increase

Table 1 Photophysical and electrochemical data in CH_3CN

	Abs, λ_{max}/nm ($10^{-4}\varepsilon$/M^{-1} cm^{-1})[a]	Lum. λ_{max}/nm 298 K (τ/ns)[b]	Lum. λ_{max}/nm 77 K (τ/μs)[b]	Oxid.[c]/V	Red.[c]/V
Ru	290 (7.73), 365 (3.67), 454 (1.135)	628 (690)	598	0.79, 1.42 *irr*[d]	−1.78, −2.01
RuRu	290 (12.97), 357 (4.62), 457 (1.95)	625 (506)	602	0.79, 1.41 *irr*[d]	−1.76, −2.03
***d*Ru*d*Ru**		625 (940)	602		
OsOs	293 (13.5), 359 (4.73), 484 (1.79), 624 (0.72)	753 (39)	738	0.36, 1.41 *irr*[d]	−1.77, −1.99
$[Ru(bipy)_3]^{2+}$[e]	452	620 (1000)	590 (5100)	0.88	−1.82, −2.01, −2.26
$[Os(bipy)_3]^{2+}$[f]	640	723 (62)	940	0.45	−1.65

[a] In CH_3CN. [b] In butyronitrile. [c] *vs.* Fc/Fc^+. [d] Ligand oxidations are sensitive to conditions. [e] Ref. 36. [f] Ref. 37.

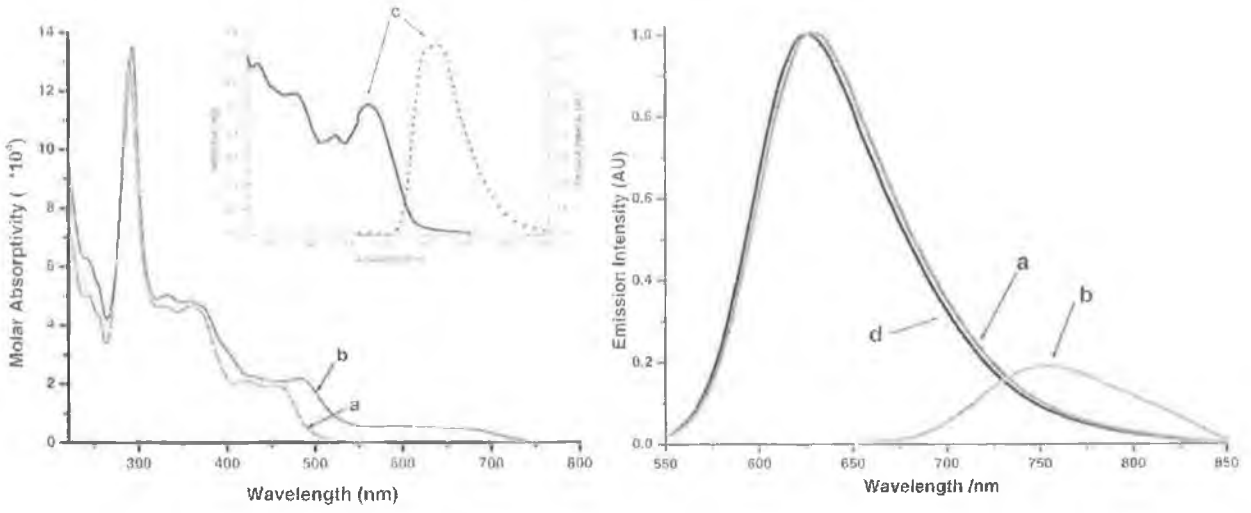

Fig. 3 Absorption (left) and emission (right) spectra in acetonitrile: (a) **RuRu**, (b) **OsOs** and (d) **Ru** [inset: absorption and emission spectra of (c) **L1**].

in the emission lifetime of the **RuRu** complex from 506 to 940 ns (185%), suggesting that the lowest emissive excited state is ^{3}MLCT(bipy) in nature and not ^{3}MLCT (L1).[33]

Resonance Raman and transient Resonance Raman spectroscopy

Resonance Raman (rR) spectroscopy enables the assignment of the optical transitions in the visible region of the absorption spectrum. Using excitation wavelengths coincident with absorption bands results in resonant enhancement of vibrational modes of the chromophore by several orders of magnitude. This allows for assignment of optical transitions. The ground and excited state rR spectra of the **L1** based complexes are complicated by the overlap of resonant chromophores in the visible region, *e.g.* the M(dπ) or **L1**(π) → **L1**(π*) and M(dπ) → bipy(π*) MLCT transitions. In the case of the Os(II) based complexes the spectra are further complicated by the presence of formally spin forbidden ^{3}MLCT transitions. Resonance Raman spectra recorded at 457.9 and 488 nm excitation for all complexes reveal only vibrational modes associated with M(dπ)→bipy(π*) ^{1}MLCT absorption bands, this conclusion is confirmed by isotopic shift observed for ***d*Ru*d*Ru**, as shown in Fig. S2, ESI.† It would be anticipated therefore that emission is ^{3}MLCT(bipy) based, an assignment supported by the observation that, upon deuteriation of the bipy ligands, the emission lifetime observed almost doubles.

Excited state (or transient) resonance Raman spectroscopy (TR^2) proves to be an invaluable tool in confirming the nature of the emissive ^{3}MLCT state. The observation of features characteristic of bipy$^-$* anion radical (*i.e.* bands at 1212 and 1285 cm^{-1}) in the TR^2 spectrum at 354.67 nm excitation, indicate a bipy-based ^{3}MLCT excited state is present.[34] However, as shown in Fig. 4 the presence of a strong **L1** based transition at 350 nm complicates the transient rR spectrum obtained at 354.5 nm excitation, with **L1** ligand modes being observed. The presence of vibrational features due to **L1** raises the possibility that the bands at 1212 and 1285 cm^{-1} are **L1** bands. It is in assigning vibrational modes that deuteriation becomes invaluable. Upon deuteriation the principle marker bands for bipy$^-$* (1212 and 1285 cm^{-1}) disappear and a feature at 1186 cm^{-1} tentatively assigned to d_8-bipy$^-$* is observed (the 1334 cm^{-1} band of d_8-bpy$^-$* is masked by **L1** vibrations), confirming that these bands are bipy based. Since the **L1** based 350 nm absorption is independent of the nature of the metal, it has been assigned as an interligand π−π* transition.

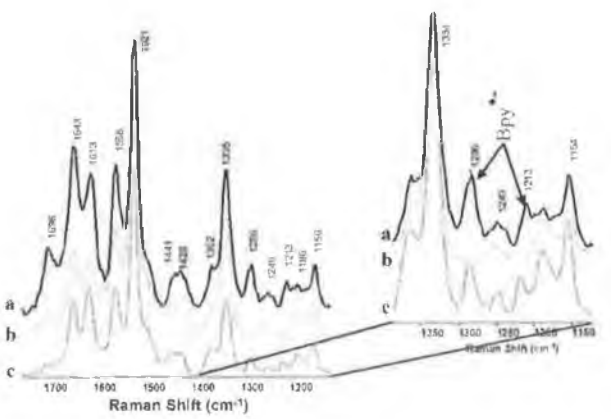

Fig. 4 TR^2 spectra at 354.67 nm of (a) **RuRu**, (b) ***d*Ru*d*Ru** and (c) **OsOs** in H_2O–acetone (95/5 v/v) (spectra normalized to the 1521 cm^{-1} band).

These results demonstrate that excitation of the complexes results in vibrational features which can be assigned to excited state bipy, and hence support the assignment of the lowest emitting ^{3}MLCT state as being bipy based.

Electrochemical properties

The oxidation and reduction potentials of **Ru**, **RuRu** and **OsOs** are presented in Table 1, differential pulse and cyclic voltammograms for the dinuclear complexes are shown in Fig. 5 (for **Ru** see Fig. S3, ESI†). The assignment of the oxidation processes observed is not straightforward due to the presence of the **L1** ligand, which undergoes irreversible oxidation. Assignment of the metal based redox processes is, however, possible by comparison with $[Ru(bipy)_3]^{2+}$ and $[Os(bipy)_3]^{2+}$. The fact that **L1** is oxidised at relatively low anodic potentials suggests that it is electron rich and is supported by the DFT calculations (*vide infra*). The **OsOs** complex displays a single oxidation wave at 0.36 V *vs.* Fc/Fc^+ which is 90 mV lower than that observed for $[Os(bipy)_3]^{2+}$. The stabilisation of the Os(III) oxidation state in this compound with respect to $[Os(bipy)_3]^{2+}$ is indicative of the presence of a stronger electron donating ligand (relative to bipy) in the inner coordination sphere of the Os ion. Similarly, for **Ru** and **RuRu** the metal redox potentials are 90 mV more cathodic than $[Ru(bipy)_3]^{2+}$. The two equivalent Os centres undergo simultaneous one electron oxidations which indicates that any metal–metal interactions are relatively weak. This is further supported by the absence of mixed valence charge transfer transitions (*vide infra*). Attempts to resolve the metal centred redox wave of the **OsOs** compound using differential pulse voltammetry were unsuccessful (Fig. 5). The value of $n = 1.92$ determined by bulk electrolysis carried out on the **OsOs** compound confirms the bielectronic nature of the first oxidation wave. **RuRu** behaves similarly with a single metal oxidation wave being observed at 0.79 V and an irreversible feature at 1.42 V. The absence of separation between the first and second metal oxidation steps in the dinuclear complexes, is in agreement with other systems of similar internuclear separation and is due to the minimal electrostatic interactions observed over these distances.[9c,35]

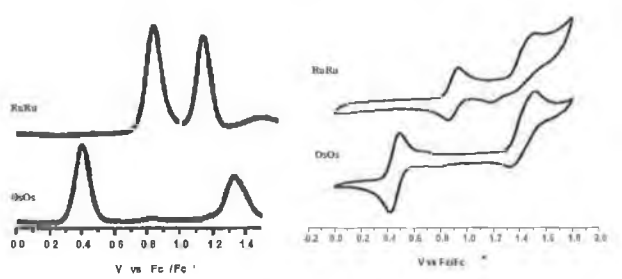

Fig. 5 DPV (left) and cyclic voltammograms (right) of **OsOs** and **RuRu** *vs.* Fc/Fc^+ with 0.1 M $TBABF_4$ in CH_3CN.

Based on the difference in formal potential of $[Ru(bipy)_3]^{2+}$ and $[Os(bipy)_3]^{2+}$, a potential difference of *ca.* 430 mV is expected between analogous Ru and Os metal centres. This compares well with the observed potential difference for the compounds reported of 430 mV.[36,37] The irreversible processes observed at more anodic potentials are attributed to oxidation of the bridging **L1** ligand. These redox processes are ill defined and their potential is very dependent on the conditions employed, with variation in the anodic potentials of up to 200 mV being observed. The reasons for this are at present not fully understood. The reduction potentials are as expected and are in agreement with a bipy based LUMO.

Spectroelectrochemistry

Electrochemical studies discussed above indicate that for **RuRu** and **OsOs** communication between the metal centres in the ground state is, at best, weak (comproportionation constant, $K_c \sim 4$).[38] To gain a better understanding of the true strength of the delocalisation of the SOMO in the mixed valence complex ($M^{II}M^{III}$) and hence internuclear communication, the spectroscopic properties of mixed valence dinuclear complexes were investigated. For the homonuclear complexes the single bielectronic metal oxidation process makes generation of the mixed valence species more difficult. Nevertheless spectroelectrochemistry has proven useful in determining the degree of intercomponent interaction in related dinuclear systems exhibiting single bielectronic metal redox processes.[35] A typical example of such spectroelectrochemical studies is shown in Fig. 6 for the compound **RuRu**. For the dinuclear complexes reversible spectral changes were observed at potentials below 1 V, however, bulk electrolysis at higher potentials results in irreversible spectral changes, which were not investigated further. Oxidation at 0.7 V *vs.* Fc/Fc^+ results in a gradual disappearance of the MLCT bands and a decrease in the intensity and red-shift in the $\pi \rightarrow \pi^*$ transition around 280 nm. Bleaching of the MLCT band continues at potentials higher than 0.7 V *vs.* Fc/Fc^+. At these potentials a concurrent increase in the intensity of band in the region 500 to 800 nm, which can is expected to be ligand-to-metal-charge-transfer (LMCT) in nature. Importantly, neither complex show any evidence for the presence of an intervalence band in the mixed valence state, indicating little or no communication between the two metal centres in the ground state.

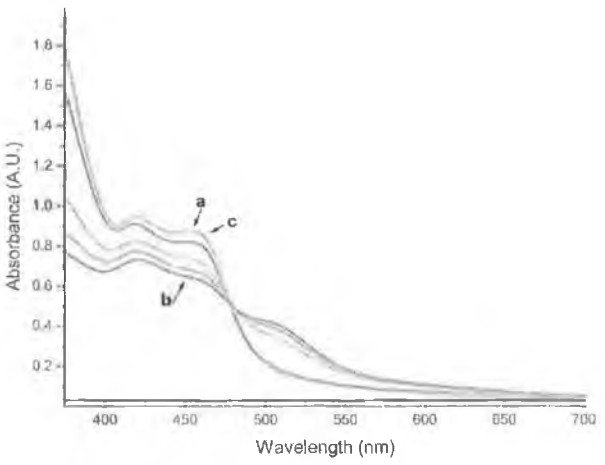

Fig. 6 Spectroelectrochemistry of the mixed metal complex **RuRu** in MeCN with 0.1 M TEAP at intervals from (a) 0 V to (b) 0.9 V and (c) after re-reduction at 0 V (*vs.* Fc/Fc^+)

DFT Calculations

The geometry optimisation of the dimer gave results in good agreement with the crystal structure. B3LYP has a tendency to overestimate the Ru–N bond length[39] (typically by 0.05 Å for the Ru–N_{bipy} bonds). From crystallographic data (*vide supra*) it is seen that for **RuRu** the Ru–N_{py} bond is longer than the Ru–N_{imid} bond (see Table S2. ESI†) but in the calculated structure the reverse is found (with the Ru–N_{imid} bond overestimated by 0.07 Å). The distortion from planarity of the phenyl ring with respect to the imidazole rings is reproduced by the calculations, although the dihedral angle is also overestimated by 7°. The calculated energies of the frontier orbitals are shown in Table S4 (ESI†). Each molecular orbital has been broken down in terms of a percentage contribution from the metal centres, *Ru*, the bipyridine ligands, *bipy*, the central phenyl ring of the **L1** ligand, *L1-ph*, and a moiety comprising the pyridine and fused rings of the **L1** ligand, *L1-py*. These data have been plotted in the form of a PDOS spectra in Fig. 7.[40]

4 (*a*) P. D. Beer, F. Szemes, V. Balzani, C. M. Salá, M. G. Drew, S. W. Dent and M. Maestri, *J. Am. Chem. Soc.*, 1997, **119**, 11864; (*b*) O. Waldmann, J. Hassmann, P. Müller, G. S. Hanan, D. Volkmer, U. S. Schubert and J.-M. Lehn, *Phys. Rev. Lett.*, 1997, **78**, 3390; (*c*) E. Zahavy and M. A. Fox, *Chem. Eur. J.*, 1998, **4**, 1647; (*d*) V. Balzani, A. Credi and M. Venturi, *Curr. Opin. Chem. Biol.*, 1997, **1**, 506.

5 S. Welter, K. Brunner, J. W. Hofstraat and L. De Cola, *Nature*, 2003, **421**, 54.

6 Y. Kim and C. M. Lieber, *Inorg. Chem.*, 1989, **28**, 3990.

7 F. Barigelletti, L. Flamigni, V. Balzani, J.-P. Collin, J.-P. Sauvage, A. Sour, E. C. Constable and A. M. W. C. Thompson, *J. Chem. Soc., Chem. Commun.*, 1993, 942.

8 (*a*) M. Haga, M. M. Ali, H. Sato, H. Monojushiro, K. Nozaki and K. Kano, *Inorg. Chem.*, 1998, **37**, 2320; (*b*) M. A. Haga, M. Ishizuya, T. Kanesugi, T. Yubaka, D. Sakiyama, J. Fees and W. Kaim, *Indian J. Chem., Sect. A*, 2003, **42**, 2290; (*c*) M. Haga, T. Takasugi, A. Tomie, M. Ishizuga, T. Yamada, M. D. Hossain and M. Inoue, *Dalton Trans.*, 2003, 2069; (*d*) M. D. Hossain, M. Haga, B. Gholamkhass, K. Nozaki, M. Tsushima, N. Ikeda and T. Ohno, *Collect. Czech. Chem. Commun.*, 2001, **66**, 307; (*e*) M. D. Hossain, R. Ueno and M. Haga, *Inorg. Chem. Commun.*, 2000, **3**, 35; (*f*) M. M. Ali, H. Sato, M. A. Haga, K. Tanaka, A. Yoshimura and T. Ohno, *Inorg. Chem.*, 1998, **37**, 6176.

9 (*a*) R. Hage, J. G. Haasnoot, H. A. Nieuwenhuis, J. Reedijk, D. J. A. De Ridder and J. G. Vos, *J. Am. Chem. Soc.*, 1990, **112**, 9245; (*b*) P. Passaniti, W. R. Browne, F. C. Lynch, D. Hughes, M. Nieuwenhuyzen, P. James, M. Maestri and J. G. Vos, *J. Chem. Soc., Dalton Trans.*, 2002, 1740; (*c*) W. R. Browne, F. Weldon, A. L. Guckian and J. G. Vos, *Collect. Czech. Chem. Commun.*, 2003, **68**, 1467; (*d*) W. R. Browne, C. M. O'Connor, C. Villani and J. G. Vos, *Inorg. Chem.*, 2001, **40**, 5461.

10 (*a*) C. H. Braunstein, A. D. Baker, T. C. Strekas and H. D. Gafney, *Inorg. Chem.*, 1984, **23**, 857; (*b*) Y. Fuchs, S. Lofters, T. Dieter, W. Shi, R. Morgan, T. C. Strekas, H. D. Gafney and A. D. Baker, *J. Am. Chem. Soc.*, 1987, **109**, 2691; (*c*) W. R. Murphy, K. J. Brewer, G. Gettliffe and J. D. Petersen, *Inorg. Chem.*, 1989, **28**, 81; (*d*) K. Kalyanasundaram and Md. K. Nazeeruddin, *Inorg. Chem.*, 1990, **29**, 1888; (*e*) R. M. Berger, *Inorg. Chem.*, 1990, **29**, 1920; (*f*) G. Denti, S. Campagna, L. Sabatino, S. Serroni, M. Ciano and V. Balzani, *Inorg. Chem.*, 1990, **29**, 4750.

11 C. Creutz, *Prog. Inorg. Chem.*, 1963, **30**, 1.

12 (*a*) E. V. Dose and L. J. Wilson, *Inorg. Chem.*, 1978, **17**, 2660; (*b*) R. Sahai, D. P. Rillema, R. Shaver, S. van Wallendael, D. C. Jackman and M. Boldaji, *Inorg. Chem.*, 1989, **28**, 1022.

13 (*a*) W. Kaim, *Coord. Chem. Rev.*, 2002, **230**, 127; (*b*) W. Kaim, A. Klein and M. Glöckle, *Acc. Chem. Res.*, 2000, **33**, 755; (*c*) B. Sarker, W. Kaim, A. Klein, B. Schwederski, J. Fiedler, C. Duboc-Toia and G. K. Lahiri, *Inorg. Chem.*, 2003, **42**, 6172.

14 (*a*) J. M. de Wolf, R. Hage, J. G. Haasnoot, J. Reedijk and J. G. Vos, *New J. Chem.*, 1991, **15**, 501; (*b*) H. E. B. Lempers, J. G. Haasnoot, J. Reedijk, R. Hage, F. Weldon and J. G. Vos, *Inorg. Chim. Acta.*, 1994, **225**, 67; (*c*) F. Barigelleti, L. Flamigni, V. Balzani, J-P. Collin, J. P. Sauvage, A. Sour, E. C. Constable and A. M. W. Cargill Thompson, *J. Am. Chem. Soc.*, 1994, **116**, 7692; (*d*) M. T. Indelli, F. Scandola, J-P. Collin, J-P. Sauvage and A. Sour, *Inorg. Chem.*, 1996, **35**, 303; T. Ohno, K. Nozaki and M. Haga, *Inorg. Chem.*, 1992, **31**, 4256; (*e*) M. Haga, M. M. Ali, S. Koseki, K. Fujimoto, A. Yoshimura, K. Nozaki, T. Ohno, K. Nakajima and D. J. Stufkens, *Inorg. Chem.*, 1996, **35**, 3335; (*f*) D. P. Rillema, R. Sahai, P. Matthews, A. K. Edwards, R. J. Shaver and L. Morgan, *Inorg. Chem.*, 1990, **29**, 167.

15 B. P. Sullivan, D. J. Salmon and T. J. Meyer, *Inorg. Chem.*, 1978, **17**, 3334.

16 D. A. Buckingham, F. P. Dwyer, H. A. Goodwin and A. M. Sargeson, *Aust. J. Chem.*, 1964, **17**, 325.

17 G. M. Sheldrick, *SHELX-97*, Universität Göttingen, 1997.

18 W. R. Heineman, *J. Chem. Educ.*, 1983, **60**, 4.

19 J. P. Chang, E. Y. Fung and J. C. Curtis, *Inorg. Chem.*, 1986, **25**, 4233.

20 N. G. Connelly and W. E. Geiger, *Chem. Rev.*, 1996, **96**, 877.

21 D. S. Jones, A. F. Brown, A. D. Woolfson, A. C. Dennis, L. J. Matchett and S. E. J. Bell, *J. Pharm. Sci.*, 2000, **89**, 563–571.

22 (*a*) C. G. Coates, L. Jacquet, J. J. McGarvey, S. E. J. Bell, A. H. R. Al-Obaidi and J. M. Kelly, *J. Am. Chem. Soc.*, 1997, **119**, 7130; (*b*) C. G. Coates, J. Olofsson, M. Coletti, J. J. McGarvey, B. Onfelt, P. Lincoln, B. Norden, E. Tuite, P. Matousek and A. W. Parker, *J. Phys. Chem. B*, 2001, **105**, 12653–12664.

23 *Gaussian 03, Revision B.04*, M. J. Frisch, G. W. Trucks, H. B. Schlegel, G. E. Scuseria, M. A. Robb, J. R. Cheeseman, J. A. Montgomery, Jr., T. Vreven, K. N. Kudin, J. C. Burant, J. M. Millam, S. S. Iyengar, J. Tomasi, V. Barone, B. Mennucci, M. Cossi, G. Scalmani, N. Rega, G. A. Petersson, H. Nakatsuji, M. Hada, M. Ehara, K. Toyota, R. Fukuda, J. Hasegawa, M. Ishida, T. Nakajima, Y. Honda, O. Kitao, H. Nakai, M. Klene, X. Li, J. E. Knox, H. P. Hratchian, J. B. Cross, C. Adamo, J. Jaramillo, R. Gomperts, R. E. Stratmann, O. Yazyev, A. J. Austin, R. Cammi, C. Pomelli, J. W. Ochterski, P. Y. Ayala, K. Morokuma, G. A. Voth, P. Salvador, J. J. Dannenberg, V. G. Zakrzewski, S. Dapprich, A. D. Daniels, M. C. Strain, O. Farkas, D. K. Malick, A. D. Rabuck, K. Raghavachari, J. B. Foresman, J. V. Ortiz, Q. Cui, A. G. Baboul, S. Clifford, J. Cioslowski, B. B. Stefanov, G. Liu, A. Liashenko, P. Piskorz, I. Komaromi, R. L. Martin, D. J. Fox, T. Keith, M. A. Al-Laham, C. Y. Peng, A. Nanayakkara, M. Challacombe, P. M. W. Gill, B. Johnson, W. Chen, M. W. Wong, C. Gonzalez, and J. A. Pople, Gaussian, Inc., Pittsburgh PA, 2003.

24 A. D. Becke, *J. Chem. Phys.*, 1993, **98**, 5648.

25 C. Lee, W. Yang and R. G. Parr, *Phys. Rev. B*, 1988, **37**, 785.

26 (*a*) T.H. Dunning, Jr. and P. J. Hay, in, *Modern Theoretical Chemistry*, ed. H. F. Schaefer III, Plenum, New York, 1976, vol. 3, p. 1; (*b*) P. J. Hay and W. R. Wadt, *J. Chem. Phys.*, 1985, **82**, 270; (*c*) P. J. Hay and W. R. Wadt, *J. Chem. Phys.*, 1985, **82**, 284; (*d*) P. J. Hay and W. R. Wadt, *J. Chem. Phys.*, 1985, **82**, 299.

27 N. M. O'Boyle and J. G. Vos, *Gauss Sum 0.8*, Dublin City University, 2004. Available at http://gausssum.sourceforge.net.

28 (*a*) R. Hage, J. G. Haasnoot, J. Reedijk, R. Wang, E. M. Ryan, J. G. Vos, A. L. Spek and A. J. M. Duisenberg, *Inorg. Chim. Acta*, 1990, **174**, 77; (*b*) D. P. Rillema, D. S. Jones, C. Woods and H. A. Levy, *Inorg. Chem.*, 1992, **31**, 2935; (*c*) R. Hage, J. P. Turkenburg, R. A. G. de Graaf, J. G. Haasnoot, J. Reedijk and J. G. Vos, *Acta Crystallogr., Sect. C*, 1980, **45**, 381; (*d*) D. P. Rillema, D. S. Jones and H. A. Levy, *J. Chem. Soc., Chem. Commun.*, 1979, 849.

29 F. Weldon, L. Hammarström, E. Mukhtar, R. Hage, E. Gunneweg, J. G. Haasnoot, J. Reedijk, W. R. Browne, A. L. Guckian and J. G. Vos, *Inorg. Chem.*, 2004, **43**, 4471.

30 W. R. Browne, C. M. O'Connor, H. P. Hughes, R. Hage, O. Walter, M. Doering, J. F. Gallagher and J. G. Vos, *J. Chem. Soc., Dalton Trans.*, 2002, 4048.

31 (*a*) W. J. Vining, J. V. Caspar and T. J. Meyer, *J. Phys. Chem.*, 1985, **89**, 1095; (*b*) M. Wrighton and D. L. Morse, *J. Am. Chem. Soc.*, 1974, **96**, 996; (*c*) A. Juris, V. Balzani, F. Barigelletti, S. Campagna, P. Belser and A. von Zelewsky, *Coord. Chem. Rev.*, 1988, **84**, 85.

32 S. Fanni, F. Weldon, L. Hammarström, E. Muktar, W. R. Browne, T. E. Keyes and J. G. Vos, *Eur. J. Inorg. Chem.*, 2001, 529.

33 W. R. Browne and J. G. Vos, *Coord. Chem. Rev.*, 2001, **219**, 761, and references therein.

34 (*a*) K. Maruszewski, K. Bajdor, D. P. Strommen and J. R. Kincaid, *J. Phys. Chem.*, 1995, **99**, 6286; (*b*) P. K. Mallick, G. D. Danzer, D. P. Strommen and J. R. Kincaid, *J. Phys. Chem.*, 1988, **92**, 5628; (*c*) D. P. Strommen, P. K. Mallick, G. D. Danzer and R. S. Lumpkin, *J. Phys. Chem.*, 1990, **94**, 1357.

35 (*a*) A. C. Ribou, J.-P. Launay, K. Takahashi, T. Nihira, S. Tarutani and C. W. Spangler, *Inorg. Chem.*, 1994, **33**, 1325; (*b*) P. Laine, V. Marvaud, A. Gourdon, J.-P. Launay, M. L. Sachtleben, H. Li and C. W. Spangler, *Inorg. Chem.*, 1996, **35**, 3735.

36 E. Krausz, G. Moran and H. Riesen, *Chem. Phys. Lett.*, 1990, **165**, 401.

37 E. M. Kober, B. P. Sullivan, W. J. Dressick, J. V. Caspar and T. J. Meyer, *J. Am. Chem. Soc.*, 1980, **102**, 7385.

38 D. E. Richardson and H. Taube, *Inorg. Chem.*, 1981, **20**, 1278.

39 S. I. Gorelsky and A. B. P. Lever, *J. Organomet. Chem.*, 2001, **635**, 187.

40 This representation gives a better overview of the nature of the frontier orbitals, especially where neighbouring orbitals are closely-spaced.

Derivatives of dipyrido[3,2-*a*:2′,3′-*c*]phenazine and its ruthenium complexes, influence of arylic substitution on photophysical properties†

Bernhard Schäfer,[a] Helmar Görls,[a] Martin Presselt,[b] Michael Schmitt,[b] Jürgen Popp,[b] William Henry,[c] Johannes G. Vos[c] and Sven Rau*[a]

Received 8th September 2005, Accepted 18th January 2006
First published as an Advance Article on the web 14th February 2006
DOI: 10.1039/b512773d

The synthesis and photophysical properties of a series of substituted dipyridophenazine (dppz) ruthenium complexes of the type $[(tbbpy)_2Ru(dppz\text{-}R_2)]^{2+}$ (where tbbpy = 4,4-*tert*-butyl-2,2-bipyridine and dppz = dipyrido[3,2-*a*:2′,3′-*c*]phenazine and R represents substitution at the 11 and 12 position with: Br, phenyl, 4-*tert*-butyl-phenyl and *para*-biphenyl) are described. The ligands could be obtained in high yields using Suzuki-type coupling reactions, an approach which also has been successfully applied to the analogous dppz-Br_2 ruthenium complex. All compounds are fully characterised by NMR, MS and UV-vis spectroscopy. The solid state structures of dppz-bi-*para*-biphenyl and the ruthenium complex $[(tbbpy)_2Ru(dppz\text{-}Br_2)]^{2+}$ are also reported. The investigation of the free ligands reveals a pronounced effect of the arylic substitution on absorption and emission properties. These properties are mirrored in the corresponding complexes, which possess emission lifetimes of up to 900 ns. The resonance Raman investigation of the complex $[(tbbpy)_2Ru(dppz\text{-}Br_2)]^{2+}$ supports the assumption that the excited state properties of the substituted complexes are related to the parent $[(bpy)_2Ru(dppz)]^{2+}$ compound, but that important differences may be expected based on the differences observed in the lowest energy absorption band.

Introduction

Ruthenium complexes with dipyrido[3,2-*a*:2′,3′-*c*]-phenazine (dppz) are intensively investigated due to their potential as luminescent DNA sensors[1–11] or as reversible electron carriers.[12] Both functions strongly depend on the role of the phenazine part of the dppz ligand as electron acceptor. In addition to this electronic role structural features of the ligand are equally important. For instance the planar geometry of the dppz ligand allows efficient intercalation with helical DNA which is observed with high equilibrium binding constants for Ru–DNA of up to 10^6 M^{-1}.[5] In view of these potential applications substantial efforts have been directed towards the design of new dppz-type ligand structures.[13–16]

To rationally design such new ligands it is helpful to consider the course of events following photoexcitation with visible light. For ruthenium dppz complexes an electron, formally originating from a d orbital on the ruthenium centre, is transferred to a π^* orbital of the dppz ligand and this results in the formation of a long lived ^{3}MLCT state.[10,17–20] A currently discussed detailed mechanism for the population of this ^{3}MLCT involves initial population of the ^{1}MLCT localised on the bipyridine part of the dppz ligand with subsequent intraligand electron transfer to the phenazine based pyrazine moiety where the ^{3}MLCT is finally localised. It is generally accepted that it is this state that is responsible for the unique photophysical properties of these complexes.[21–23] The aim of this contribution is the preparation of novel ligands that will lead to metal complexes with significantly improved excited state properties, such as longer excited state lifetimes. This may be achieved by delocalisation of the charge in the final triplet state. One way of achieving this is by the introduction of phenyl-type substituents.

In this contribution we present a series of substituted dppz ligands and their corresponding ruthenium polypyridyl complexes, see Fig. 1. The reasons for their selection is outlined above but we also wish to emphasise that the development of an efficient synthetic method for introducing substituents in the dppz frame using organometallic reactions is also a major point in this study.

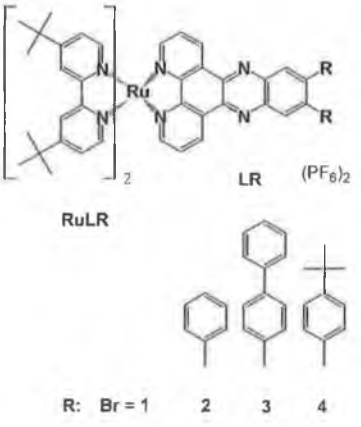

Fig. 1 Naming of ruthenium complexes and corresponding ligands.

[a]*Institut für Anorganische und Analytische Chemie, Friedrich-Schiller-Universität, Lessingstr. 8, 07743, Jena, Germany. E-mail: sven.rau@uni-jena.de; Fax: +49 3641 948102; Tel: +49 3641 948113*
[b]*Institut für Physikalische Chemie, Helmholzweg 4, Friedrich-Schiller-Universität, 07743, Jena, Germany*
[c]*National Centre for Sensor Research, School of Chemical Sciences, Dublin City University, Dublin 9, Ireland*

† Electronic supplementary information (ESI) available: Detailed NMR spectra of the ligands **LR** and complexes **RuLR**. See DOI: 10.1039/b512773d

To avoid solubility problems we utilised *tert*-butyl substituted complexes since this ensures high solubility in organic solvents. Since it has recently been emphasised that the substitution of the ancillary ligands may have an influence on the entantioselectivity of the interaction of the complexes with DNA,[24,25] we were also interested in obtaining more detailed structural information on substituted dppz–ruthenium complexes.

The novel ligands **L1** to **L4** have been prepared to illustrate the potential of the building block approach utilising organometallic C–C coupling reactions.

Experimental

Unless otherwise noted, all Pd catalyzed cross coupling reactions were conducted under an atmosphere of dry, deoxygenated argon using standard Schlenk techniques. $Ru(tbbpy)_2Cl_2$,[26] $phenO_2$[5] and 4,5-dibromo-*ortho*phenylendiamine[27] were prepared using literature methods. Acetonitrile was distilled from CaH_2. Toluene was distilled from sodium benzophenone ketyl under an argon atmosphere prior to use. All other solvents were used as received.

Infrared spectra were recorded using a Perkin-Elmer 2000 FT-IR; ^{1}H NMR spectra were recorded on a Bruker 400 MHz/200 Mhz spectrophotometer. The mass spectra were obtained using a SSQ 170, Finnigan MAT at the Friedrich Schiller University Jena. Electrospray-Mass spectra were recorded on a Finnigan MAT, MAT 95 XL. The positive ES mass spectra were obtained with voltages of 3–4 kV applied to the electrospray needle. The microwave assisted reactions were carried out using the Microwave Laboratory Systems MLS EM-2 microwave system.

Synthesis of Br_2dppz (L1)

Phendione (2 g, 9.5 mmol) and 4,5-dibromo-*ortho*phenylendiamine (2.534 g, 9.5 mmol) were refluxed in absolute EtOH (300 ml) for 8 h. The volume of the solvent was reduced to 50 ml and cooled in a refrigerator over night. $dppzBr_2$ was collected by filtration. Yield 90%. ^{1}H NMR (ppm; $CDCl_3$) 7.730 phen(2H, dd); 8.559 H4(2H, s); 9.233 phen(2H, d(lc)); 9.529 phen(2H, d(lc));EI-MS $m/z = 440$ (100%) matching isotopic pattern.

Typical procedure for preparation of L2 from uncoordinated Br_2dppz (L1)

A Schlenk vessel was charged with $dppzBr_2$ (0.250 g, 0.568 mmol) and the corresponding boronic acid (1.136 mmol), $Pd(PPh_3)_4$ (0.013 g, 0.0113 mmol (1.0 mol %)) in 50 ml dry toluene and 15 ml of oxygen free solution of 2 M aqueous Na_2CO_3. The suspension was refluxed under argon for three days. After cooling to room temperature the reaction mixture was taken up in 100 ml water followed by extraction with chloroform. The solvent of the combined organic layers was removed and the crude product dried under vacuum.

Column chromatography (using silica and a gradients eluent system starting with $CHCl_3$ and changing to $CHCl_3$/MeOH (9 : 1). The fluorescent main band was collected and yields pure **L2**. Yield 60–80%.

L2 ^{1}H NMR (ppm; $CDCl_3$) 7.305 phenyl (10H, s); 7.808 H2-phen (2H, dd); 8.363 H4 (2H, s); 9.300 H3-phen (2H, d); 9.626 H1-phen (2H, d); MS (DEI, EI+ Q1MS) $m/z = 434$ (100%) (M^+).

L3 ^{1}H NMR (ppm; d_6-DMSO) 7.43 H7, H8, H9 (10H, m); 7.70 H6, H5 (8H, m); 7.91 H2(2H, dd); 8.31 H4(2H, s); 9.19 H3(2H, d(lc)); 9.44 H1(2H, d(lc)). MS (DEI, EI+ Q1MS) $m/z = 586$ (100%) (M^+).

L4 ^{1}H NMR (ppm, CD_2Cl_2) 1.321 CH_3 (*tert*-butyl, 18H, s); 7.325 H6, H5(8H, m); 7.794 H3 (2H, dd); 8.361 H4 (2H, s); 9.215 H3 (2H, d(lc)); 9.622 H1 (2H, d(lc)); MS (DEI, EI+ Q1MS) $m/z =$ 546 (30%) (M^+), $m/z = 531$ (35%) ($M^+ - CH_3$).

Complexation of L1–L4

$Ru(tbbpy)_2Cl_2$ (0.1 g, 0.14 mmol) and the corresponding ligand (0.14 mmol) were suspended in DMF/H_2O (80 ml/10 ml) and heated at reflux for 3 h using microwave irradiation (150 W). The solvent was removed under reduced pressure. The complexes were recrystallized from an ethanol/aqueous NH_4PF_6 mixture and further purified using chromatography using a gradient changing from EtOH to EtOH/H_2O/KNO_3. Yield 80–85%. For a detailed assignment of the chemical shifts to the corresponding atom see the electronic supplementary information (ESI).†

RuL1 (ppm CD_3CN) 1.347 (18H, s); 1.441 (18H, s); 7.233 (2H, d); 7.466 (2H, d); 7.565 (2H, d); 7.659 (2H, d); 7.888 (2H, dd); 8.143 (2H,d); 8.476 (2H, s); 8.515 (2H, s); 8.844 (2H, s); 9.556 (2H, d) MS (ESI, MeOH,): $m/z = 1223.2$ ($[M - (PF_6)]^+$, 100%).

RuL2 (ppm CD_3CN) 1.327 (18H, s); 1.434 (18H, s); 7.256 (2H, d(lc)); 7.353 (10H, m); 7.475 (2H, d(lc)); 7.620 (2H, d); 7.694 (2H, d); 7.896 (2H, dd); 8.146 (2H, d(lc)); 8.422 (2H, s); 8.512 (2H, s); 8.551 (2H, s); 9.589 (2H, d) MS (ESI, MeOH,): $m/z = 1217.5$ ($[M - (PF_6)]^+$, 100%); $m/z = 536.4$ ($[M - 2(PF_6)]^{2+}$).

RuL3 (ppm CD_3CN) 1.277 (18H, s); 1.471 (18H, s); 7.412 (10H, m); 7.211 (4H, d); 7.272 (4H, d); 7.348 (2H, d); 7.522 (2H, d); 7.772 (4H, d); 7.799 (2H, dd); 7.968 (2H, s); 8.241 (2H, d); 8.571 (2H, s); 8.639 (2H, s); 9.175 (2H, d); MS (ESI, MeOH): $m/z = 1369.2$ ($[M - (PF_6)]^+$, 69%); $m/z = 611.9$ ($[M - 2(PF_6)]^{2+}$, 100%).

RuL4 (ppm CD_3CN) 1.312 (18H, s); 1.329 (18H, s); 1.468 (18H, s); 7.228 (8H, m); 7.328 (2H, d(lc)); 7.505 (2H, d(lc)); 7.703 (2H, d); 7.736 (2H, d); 7.774 (2H, dd); 8.031 (2H, s); 8.161 (2H, (lc)); 8.517 (2H, s); 8.566 (2H, s); 9.268 (2H, d(lc)) MS (ESI, MeOH): $m/z = 1329.0$ ($[M - PF_6]^+$, 100%), $m/z = 531$ ($[M - 2PF_6]^{2+}$, 20%).

Suzuki-reaction at the complex (RuL1)

$RuL1(PF_6)_2$ (0.150 g, 0.11 mmol), phenyl boronic acid (0.028 mg, 0.23 mmol) and $Pd(PPh_3)_4$ (12 mg, 8.8×10^{-6} mol (4 mol%)) were suspended in 50 ml acetonitrile and 15 ml of a oxygen free solution of 2 M aqueous Na_2CO_3 and refluxed for 3 days. After cooling to rt 100 ml of water were added followed by extraction with dichloromethane. The organic layers were collected, the solvent was removed under reduced pressure and the residue was cleaned by column chromatography collecting the main band (using silica, EtOH, EtOH/H_2O, KNO_3). Yield 67%. Analytical data obtained are identical to those observed for the sample obtained from complexation of **L2** to the ruthenium precursor.

Crystal structure determination

The intensity data for the compounds were collected on a Nonius Kappa CCD diffractometer, using graphite-monochromated

Mo-K_α radiation. Data were corrected for Lorentz and polarization effects, but not for absorption effects.[28,29]

The structures were solved by direct methods (SHELXS[30]) and refined by full-matrix least squares techniques against Fo^2 (SHELXL-97).[31] The hydrogen atoms (without the disordered toluene molecules of **L3**) were included at calculated positions with fixed thermal parameters. All non-hydrogen atoms were refined anisotropically.[31] XP (SIEMENS Analytical X-ray Instruments, Inc.) was used for structure representations. X-Ray suitable crystals of **RuL1** were grown from acetonitrile/hexane solutions.

Crystal data for RuL1. $C_{54}H_{56}Br_2F_{12}N_8P_2Ru{\cdot}2C_2H_3N$, M_r = 1450.01 g mol^{-1}, red-brown prism, size 0.03 × 0.03 × 0.02 mm^3, triclinic, space group $P\bar{1}$, a = 12.7435(3), b = 15.0747(3), c = 16.6350(4) Å, α = 91.617(1), β = 97.359(1), γ = 98.611(1)°, V = 3129.9(1) Å^3, T = −90 °C, Z = 2, ρ_{calcd} = 1.539 g cm^{-3}, μ(Mo-K_α) = 16.6 cm^{-1}, F(000) = 1464, 22044 reflections in h(−16/14), k(−19/18), l(−21/21), measured in the range 3.91° ≤ Θ ≤ 27.49°, completeness Θ_{max} = 98.5%, 14161 independent reflections, R_{int} = 0.031, 10601 reflections with $F_o > 4\sigma(F_o)$, 760 parameters, 12 restraints, $R1_{obs}$ = 0.067, wR^2_{obs} = 0.169, $R1_{all}$ = 0.096, wR^2_{all} = 0.192, GOOF = 1.032, largest difference peak and hole: 2.672/−1.039 e Å^{-3}.

Crystal data for L3. $C_{42}H_{26}N_4{\cdot}C_7H_7$, M_r = 677.79 g mol^{-1}, colourless prism, size 0.06 × 0.06 × 0.05 mm^3, triclinic, space group $P\bar{1}$, a = 11.3762(6), b = 12.7563(7), c = 13.6865(5) Å, α = 97.221(3), β = 102.933(3), γ = 110.078(2)°, V = 1773.1(1) Å^3, T = −90 °C, Z = 2, $\rho_{calcd.}$ = 1.270 g cm^{-3}, μ(Mo-K_α) = 0.75 cm^{-1}, F(000) = 710, 12620 reflections in h(−14/14), k(−15/16), l(−17/17), measured in the range 2.08° ≤ Θ ≤ 27.46°, completeness Θ_{max} = 98.8%, 8025 independent reflections, R_{int} = 0.033, 4464 reflections with $F_o > 4\sigma(F_o)$, 451 parameters, 0 restraints, $R1_{obs}$ = 0.089, wR^2_{obs} = 0.243, $R1_{all}$ = 0.152, wR^2_{all} = 0.293, GOOF = 1.027, largest difference peak and hole: 0.779/−0.488 e Å^{-3}.

CCDC reference numbers 290998 and 290999.

For crystallographic data in CIF or other electronic format see DOI: 10.1039/b512773d

Electronic spectroscopy

UV-vis absorption spectra (accuracy ±2 nm) were recorded on a Varian Cary 50 Scan spectrometer interfaced with a Dell optiplex GXI PC using Win UV Scan Application 2.00 and on an Analytikjena Specord S 600 spectrometer with standard software based tools. Emission spectra (accuracy ±5 nm) were recorded at 298 K using a Perkin-Elmer LS50B luminescence spectrophotometer, which was equipped with a red sensitive Hamamatsu R298 PMT detector and interfaced with an Elonex PC466 employing Perkin-Elmer Fl WinLab custom built software. Emission and excitation slit widths were 10 nm. Emission spectra for the ligands **L2** to **L4** were recorded at only 1% transmission due to large emission intensities. Emission spectra are uncorrected for photomultiplier response. 10 or 2 mm path length quartz cells were used for recording spectra.

Emission lifetime measurements

Luminescence lifetime measurements were obtained using an Edinburgh Analytical Instruments (EAI) time-correlated single-photon counting apparatus (TCSPC) comprised of two model J-yA monochromators (emission and excitation), a single photon photomultiplier detection system model 5300, and a F900 nanosecond flashlamp (N2 filled at 1.1 atm pressure, 40 kHz or 0.3 atm pressure, 20 kHz) interfaced with a personal computer *via* a Norland MCA card. A 410 nm cut off filter was used in emission to attenuate scatter of the excitation light (337 nm); luminescence was monitored at the λ_{max} of the emission. Data correlation and manipulation was carried out using EAI F900 software version 6.24. Samples were deaerated for 30 min using argon prior to measurements followed by repeated purging to ensure complete oxygen exclusion. Emission lifetimes were calculated using a single-exponential fitting function, Levenberg–Marquardt algorithm with iterative deconvolution (Edinburgh instruments F900 software). The reduced χ^2 and residual plots were used to judge the quality of the fits. Lifetimes are ±5%.

Resonance Raman spectroscopy

The Fourier transform off resonance FT-Raman spectrum of the solid complex **RuL1** was recorded with a Bruker IFS 120 HR spectrometer with an integrated FRA 160 Raman module and liquid nitrogen cooled germanium detector. The 1064 nm radiation of a Nd:YAG laser was employed for excitation. The non-resonant Raman spectra of the solid complex $[Ru(tbbpy)_3]^{2+}$ excited at 830 nm was taken with a micro Raman setup (LabRam invers, Jobin–Yvon–Horiba). The spectrometer has a focal length of 800 mm and is equipped with 300 lines/mm grating. The applied laser power was about 8 mW. The scattered light was detected by a CCD camera operating at 220 K. An Olympus MLPlanFL 50 objective focused the laser light on the solid samples.

The resonance Raman spectra were recorded with a conventional 90°-scattering arrangement. The excitation lines at 514.5, 488 and 458 nm provided by an argon ion laser (Spectra Physics Model 2085) served for resonant excitation in the range of the MLCT absorption band (see Fig. 7 later). To avoid the heating of the samples a rotating cell was utilized. No changes in the absorption spectra of the complexes could be observed after exposure to the resonant laser light. Moreover, the spectral lines observed under resonant conditions were also present in the off-resonant spectrum of the solid complexes, which was obtained with excitation at 830 nm. These findings indicate that the scattering due to possible photoproducts was minimal. The scattered light was collected with a photo objective (f = 50 mm, 1 : 0.7) and analysed with a Spex 1404 double monochromator. The dispersed Raman stray light was detected with a Photometrics model RDS 200 CCD Raman detector system. The concentration of the solutions was optimized to obtain a maximum signal-to-noise ratio and was in the millimolar range.

Results and discussion

Synthesis

All complexes under investigation are based on 4,4′-di-*tert*-butyl-2,2′-bipyridine (tbbpy) to increase the solubility of the ruthenium complexes in less polar organic solvents. This is helpful during the development of new synthetic methods which rely on organometallic reactions.[32,33] The new ligands **L1** to

L4 rely on the accessibility of 4,5-diamino-1,2-dibromobenzene which was conveniently prepared using literature methods[27] and coupled to phenanthrolin-5,6-dion resulting in 11,12-dibromo-dipyrido[3,2-*a*:2',3'-*c*]-phenazine (**L1**) in nearly quantitative yield. Both bromine functions in **L1** are easily substituted by aromatics using conventional Suzuki-reactions utilising $\{Pd(P(Ph)_3]_4\}$ as catalyst yielding **L2–L4** in good yields (see Fig. 2).

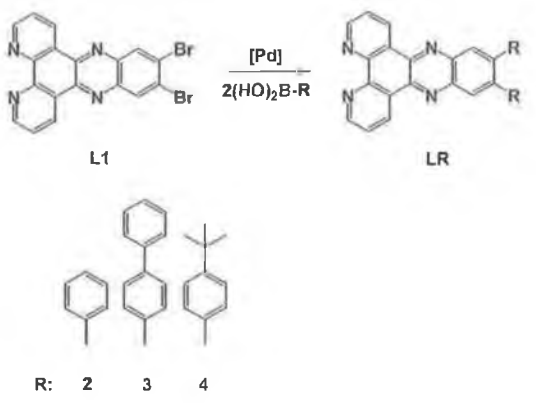

Fig. 2 Synthetic route to aryl substituted dppz ligands.

The nature of the products was unambiguously identified using multidimensional NMR methods, MS and UV-vis/emission spectroscopy. In addition the X-ray structure of **L3**, is shown in Fig. 3. The dppz frame is nearly ideally planar (deviation from planarity 0.038 Å) whereas the two biphenyl substituents are twisted out of the dppz plane by 47° (C16, C17, C19, C24) and 39° (C17, C16, C31, C36).

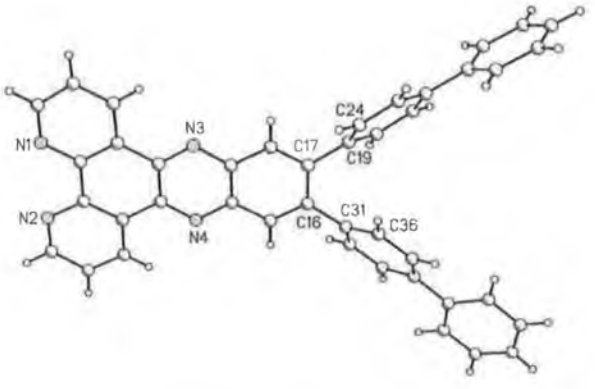

Fig. 3 Solid-state structure of **L3**.

Complexation of **L1–L4** to $(tbbpy)_2Ru^{2+}$ fragments [Ru] is achieved using microwave irradiation.[26] The full characterisation of all complexes with multidimensional NMR methods, MS and UV-vis/emission spectroscopy is outlined in the experimental part and in Table 1. In addition the solid-state structure of **RuL1** has been determined and is shown in Fig. 4. In the solid state structure of **RuL1** the deviation from planarity within the Br_2dppz ligand is 0.038 Å which is negligible. That there is a significant π–π interaction between neighbouring Br_2dppz moieties is apparent in the solid state with a distance of 3.54 Å between the centroid of the pyrazine ring and the plane of the C13–C18 aromatic ring in the ligand of the neighbouring complex at $(1 - x, 2 - y, 1 - z)$ as can be seen in Fig. 4. This arrangement is very similar to 11,12-dicyano-dppz ruthenium complexes.[34]

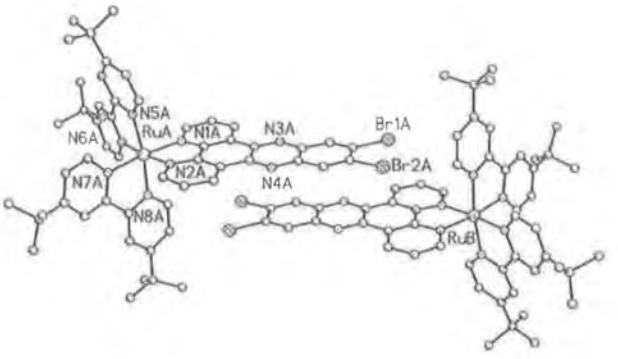

Fig. 4 Solid-state structure of **RuL1** relevant bond length in Å: Ru–N1 2.063(4), Ru–N2 2.065(4), Ru–N5 2.051(4), Ru–N6 2.052(4), Ru–N7 2.053(4), Ru–N8 2.056(4), Br1–C15 1.880(5), Br2–C16 1.894(5); and angles in °: N1–Ru–N2 79.16(16), N5–Ru–N6 78.61(16), N7–Ru–N8 78.17(17); additional "A" letter indicates symmetry equivalent position of the complex at $(1 - x, 2 - y, 1 - z)$.

The successful transformation of the cationic ruthenium complex **RuL1** using the Suzuki-protocol into **RuL2**, with 70% yield, illustrates the potential of organometallic coupling reactions (see Fig. 5) to selectively modify precursor complexes.[32,33] No significant advantages were identified when comparing the organometallic coupling reactions starting from **L1** or **RuL1**. Suzuki coupling of the complexed ligand opens however the route towards the introduction of substituents representing potential coordination sites, such as different pyridines, which would interfere with complexation if introduced into the free ligand.

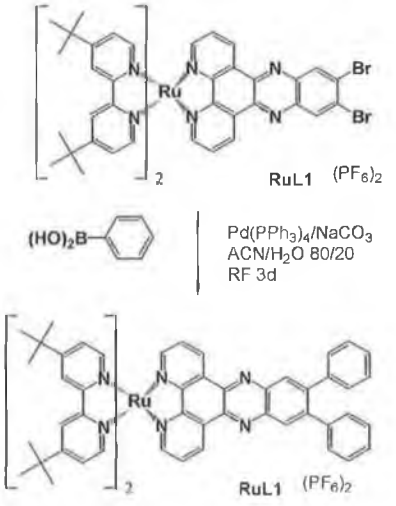

Fig. 5 Complex based Suzuki-reactions.

Electronic properties

All four ligands display absorption maxima around 400 nm. A clear influence of the peripheral substitution pattern on the shape

Table 1 Photophysical properties of **L1**–**L4** and **RuL1** to **RuL4**[a]

Complex	Emission-DCM	Emission-ACN	Absorption in DCM $\lambda_{max,abs}$/nm	Absorption in ACN $\lambda_{max,abs}$/nm	τ-DCM-aerated/ns	τ-DCM-deaerated/ns	τ-ACN-aerated/ns	τ-ACN-deaerated/ns
L1(Br_2)	420	—	237 (sh 297), 373, 392	—	[b]	—	—	—
L2(Ph)	433	—	(sh 374), 394	—	0.59	—	—	—
L3(BPh)	470	—	233, 297, 408	—	2.22	—	—	—
L4(TBPh)	455	—	229, 286, 406	—	1.65	—	—	—
RuL1	645	—	287, 374, 390, 444	287, 370, 386, 442	258	453	—	—
RuL2	631	654	290 (sh 320), 405 (sh 450)	288 (sh 317), 399 (sh 440)	406	779	129	201
RuL3	630	654	291, 424 (sh 480)	288, 414 (sh 480)	452	807	118	180
RuL4	625	650	290 (sh 338), 418 (sh 475)	288 (sh 328), 411 (sh 468)	502	929	129	245

[a] ACN acetonitrile, DCM dichloromethane. [b] Emission intensity was too weak to obtain an accurate lifetime using our set-up.

of the long wavelength maxima is observed. For example, **L1** features two distinct maxima at 393 nm and 374 nm (shoulder at 381 nm). similar to unsubstituted dppz.[13] The introduction of aromatic substituents leads to a red shift of the absorption maxima and loss of the band at around 370 nm. The bathochromic shift is most pronounced for the bi-biphenyl substituted **L3**. This ligand shows only a single broad absorption at 408 nm. All three aromatically substituted ligands (**L2** to **L4**) show relatively strong emission signals between 433 (**L2**) nm and 470 (**L3**) nm in dichloromethane, see Fig. 6, whereas **L1** displays only very weak emission at 420 nm. The largest stokes shift (>60 nm) is observed for the biphenyl substituted **L3**.

Fig. 6 Absorption and emission spectra of **L2** in dichloromethane solution (c(**L2**) = 8.6×10^{-6} mol l^{-1}).

The excited state lifetimes of **L2**–**L4** have been determined. They range from 0.6 to 2 ns, (see Table 1). The absorption and emission data of **L1** to **L4** indicate that the substitution of the dppz frame with aromatic moieties results in very significant changes in the electronic properties of the ligands. It is important at this stage to note that since the ligand based electronic transitions of the LR ligands are at least partly in the visible range of the spectrum and therefore in the same range as those expected for ruthenium polypyridyl-type MLCT the lowest energy transition in a corresponding complex may contain significant π–π* character.

All four complexes show absorption properties which are common for this class of ruthenium polypyridyl compounds. Their oxidation potential is not affected by the peripheral substitution at the dppz ligand and is observed at 0.82 V *vs* Fc/Fc$^+$. This suggests that the introduction of the substituents has no significant influence on the metal based ground state. The absorption spectra in acetonitrile are depicted in Fig. 7. The absorption spectrum of **RuL1** is very similar to the related compound $[Ru(bpy)_2dppz]^{2+}$ showing a MLCT band at 444 nm and a dppz based π–π* transition at shortly below 400 nm.[15] Introduction of more extensive aromatic substituents leads to a red shift of the π–π* transition, which ultimately overlaps increasingly with the Ru-π* MLCT band. This results in an increase of the extinction within the MLCT region from 17 000 for **RuL1** at 444 nm to 26 000 for **RuL3** at 414 nm.

The luminescence data for all four complexes could be obtained in acetonitrile and dichloromethane. A profound influence of the solvent on emission wavelength is evident by the *ca.* 20 nm red shift of the emission wavelength upon going from dichloromethane to acetonitrile. Similar solvent dependencies have been reported for related ruthenium–dppz complexes.[37,38] The most obvious impact of substitution at the dppz core is observed for **RuL1**, which is non-emissive even in CaH_2 dried acetonitrile, whereas relatively

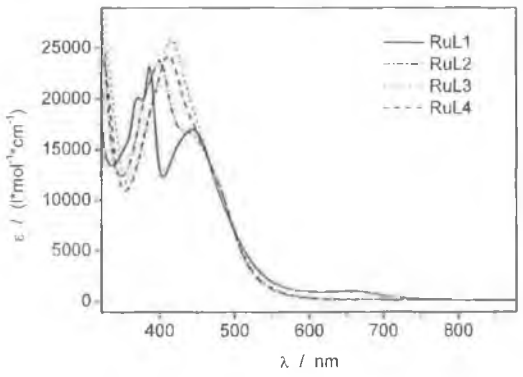

Fig. 7 Absorption spectra of **RuL1** to **RuL4** in acetonitrile.

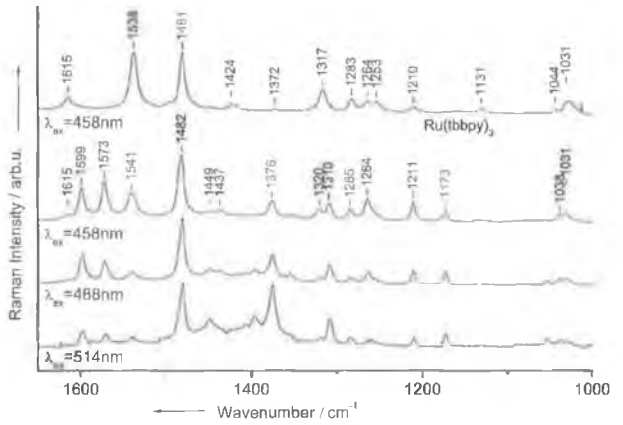

Fig. 8 Resonance Raman spectra of **RuL1** dissolved in acetonitrile excited at three different wavelength (514, 488, 458 nm) lying within the first absorption band of **RuL1**(see Fig. 7). The resonance Raman band of $[Ru(tbbpy)_3]^{2+}$ dissolved in dichloromethane excited at 458 nm in resonance close to the maximum of the first absorption and is shown for comparison. For details see text.

strong luminescence is observed in dichloromethane. A trend of prolonged lifetimes for the aryl substituted complexes **RuL2–RuL4** is evident with the longest lifetime of 929 ns observed for **RuL4** in dichloromethane. The investigation of the lifetimes of the excited state of all complexes in both solvents reveals also a strong solvent dependency. All lifetimes in acetonitrile are only about 25% of the values obtained in dichloromethane. The lifetime of the excited states of **RuL1** in dichloromethane is comparable with literature values obtained for the monobromo-dppz ruthenium complex.[15] Detailed photophysical data are compiled in Table 1.

Resonance Raman of RuL1

Resonance Raman spectroscopy is an extremely capable tool to characterise the molecular degrees of freedom involved in the initial structural changes of photochemically active systems *i.e.* to characterise the Franck–Condon-Point of an electronic transition. The resonance condition arises when the wavelength used to excite the Raman scattering lies within the electronic absorption band, causing the vibrational modes involved in the electronic transition to be selectively enhanced (by a factor of 10^6 compared to non-resonant excitation). Resonance Raman spectroscopy is therefore the method of choice for investigating the location of the initially formed MLCT in heteroleptic complexes where two different ligand sites are possible.

Fig. 8 shows the resonance Raman spectra of **RuL1** excited at three different wavelengths within the first MLCT transition. The vibrational modes at 1599, 1573, 1330 and 1173 cm^{-1} grow in intensity when the excitation wavelength is shifted from 514 nm at the red edge of the absorption band to 458 nm near the maximum of the lowest energy absorption feature and these modes can be assigned to the **L1**-ligand. This is confirmed by the comparison between the resonance Raman spectrum of **RuL1** with that of $[Ru(tbbpy)_3]^{2+}$. The main modes enhanced in the resonance Raman spectrum of **RuL1** are not observed in the spectrum of the latter compound and must therefore be due to **L1**. This assignment is further supported by looking at the off resonance Raman spectra of both molecules plotted in Fig. 9. The fact that the modes which are enhanced most belong to the **L1**-ligand leads us to the conclusion that exciting **RuL1** within the MLCT transition at 458 nm involves mainly the **L1**-ligand rather than tbppy.

Importantly, however, other modes seen in the resonance Raman spectrum at 1615, 1541, 1376, 1320 and 1211 cm^{-1} might

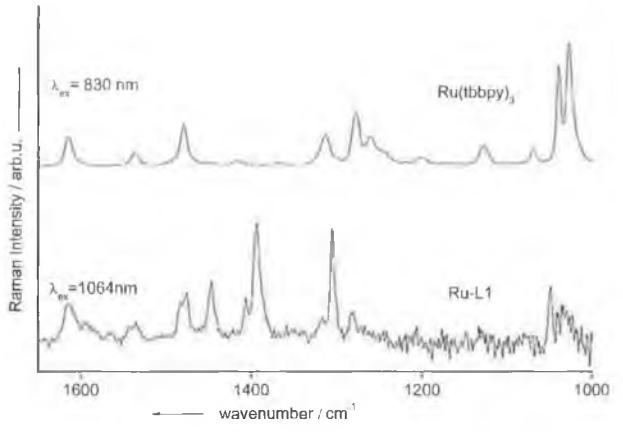

Fig. 9 Off resonance Raman spectra of **RuL1**(λ_{exc} = 1064 nm) and $[Ru(tbbpy)_3]^{2+}$ (λ_{exc} = 830 nm).

be due to tbbpy. The fact that possibly also tbbpy-modes may be enhanced suggests that Ru-to-tbbpy-type MLCT transitions may also contribute to the absorption envelop. This assignment is based on literature values from Meyer *et al.*[39] and McGarvey *et al.*[20] Theoretical calculations which are currently under way may help to shed more light on this issue.[40]

Conclusion

In conclusion we have shown that it is possible to obtain ruthenium polypyridyl-type complexes containing substituted dppz-type ligands using Suzuki coupling reactions starting either from the free ligand dibromo-dppz, **L1**, or from its ruthenium complex **RuL1**. For the compounds reported in this contribution the results obtained from both synthetic approaches are very similar. However, the use of a metal complex rather than the free ligand offers significant advances when the substituents to be introduced either have coordinating properties or would not be stable at

the high temperature conditions needed to prepare the metal compounds.

The second important observation is that the absorption spectra of the free ligands are very dependent on the substitution pattern. Importantly, with increasing aryl character the ligand centred π–π^* transition of the LR ligand moves to lower energy and overlaps considerably with the MLCT transition. This effect has two potentially important consequences; one relates to the application of the ruthenium dppz complexes as luminescent sensors, in that higher extinction coefficients in the visible region will result in a better sensor (ruthenium complex) to analyte (for instance DNA) ratio.

In addition this shift may affect the so called "dark state" of the dppz molecule.[35] The importance of intraligand electron transfer, from the initially populated bpy ^{1}MLCT to the phenazine based ^{3}MLCT for explaining the unusual light switch mechanism observed for the ruthenium dppz complexes has recently been emphasised by Batista and Martin.[36] Expansion of the aromatic frame as evident in **L2** to **L4** may be expected to influence the rate constants for this process and therefore lead to new insights into this phenomenon.

Acknowledgements

Financial support by the DFG (SFB 436) is gratefully acknowledged. S.R. acknowledges financial support by the DFG (RA 1017/1-1 and 1-2). W.H. would like to thank Enterprise Ireland (Grant Number SC/2003/74) for financial support. We would like to thank Professor D. Walther for helpful discussions and encouragement.

References

1 J. K. Barton, A. T. Danishefsky and J. M. Goldberg, *J. Am. Chem. Soc.*, 1984, **106**, 2172.
2 J. M. Kelly, A. B. Tossi, D. J. McConnell and C. OhUigin, *Nucleic Acids Res.*, 1985, **13**, 6017.
3 J. K. Barton, J. M. Goldberg, C. V. Kumar and N. J. Turro, *J. Am. Chem. Soc.*, 1986, **108**, 2018.
4 C. Hiort, B. Nordén and A. Rodger, *J. Am. Chem. Soc.*, 1990, **112**, 1971.
5 A. E. Friedman, J. C. Chambron, J.-P. Sauvage, N. J. Turro and J. K. Barton, *J. Am. Chem. Soc.*, 1990, **112**, 4960.
6 B. Lincoln, A. Broo and B. Nordén, *J. Am. Chem. Soc.*, 1996, **118**, 2644.
7 C. G. Coates, L. Jacquet, J. J. McGarvey, S. E. J. Bell, A. H. R. Al-Obaidi and J. M. Kelly, *J. Am. Chem. Soc.*, 1997, **119**, 7130.
8 I. D. Greguric, J. R. Aldrich-Wright and J. G. Collins, *J. Am. Chem. Soc.*, 1997, **119**, 3621.
9 Y. Jenkins, A. E. Friedman, N. J. Turro and J. K. Barton, *Biochemistry*, 1992, **31**, 10809.
10 C. G. Coates, J. Olofsson, M. Coletti, J. J. McGarvey, B. Önfelt, B. Lincoln, B. Nordén, E. Tuite, P. Matousek and A. W. Parker, *J. Phys. Chem. B*, 2001, **105**, 12653.
11 G. Pourtois, D. Beljonne, C. Moucheron, S. Schumm, A. Kirsch-De Mesmaeker, R. Lazzaroni and J.-L. Bredas, *J. Am. Chem. Soc.*, 2004, **126**, 683.
12 D. A. McGovern, A. Selmi, J. E. O'Brien, J. M. Kelly and C. Long, *Chem. Commun.*, 2005, 1402.
13 W. Chen, C. Turro, L. A. Friedman, J. K. Barton and N. J. Turro, *J. Phys. Chem. B*, 1997, **101**, 6995.
14 P. Aguirre, R. López, D. Villagra, I. Azocar-Guzman, A. J. Pardey and S. A. Moya, *Appl. Organomet. Chem.*, 2003, **17**, 36.
15 N. J. Lundin, P. J. Walsh, S. L. Howell, J. J. McGarvey, A. G. Blackman and K. C. Gordon, *Inorg. Chem.*, 2005, **44**, 3551 and references cited therein.
16 M. K. Kuimova, W. Z. Alsindi, J. Dyer, D. C. Grills, O. S. Jina, P. Matousek, A. W. Parker, P. Portius, X. Zhong Sun, M. Towrie, C. Wilson, J. Yang and M. W. George, *Dalton Trans.*, 2003, 3996.
17 P. Y. Chen and T. J. Meyer, *Chem. Rev.*, 1998, **98**, 1439.
18 E. Amouyal, A. Homsi, J.-C. Chambron and J.-P. Sauvage, *J. Chem. Soc., Dalton Trans.*, 1990, (6), 1841.
19 E. M. Kober and T. J. Meyer, *Inorg. Chem.*, 1982, **21**, 3967.
20 C. G. Coates, P. Callaghan, J. J. McGarvey, J. M. Kelley, P. E. Kruger and M. E. Higgins, *J. Raman Spectrosc.*, 2000, **31**, 283.
21 J.-C. Chambron and J.-P. Sauvage, *Chem. Phys. Lett.*, 1991, **182**, 603.
22 J. Olofsson, B. Önfelt, B. Lincoln, B. Nordén, P. Matousek, A. W. Parker and E. Tuite, *J. Inorg. Biochem.*, 2002, **91**, 286.
23 V. W.-W. Yam, V. W.-M. Lee, F. Ke and K.-W. M. Siu, *Inorg. Chem.*, 1997, **36**, 2124.
24 J. K. Barton, L. A. Basile, A. Danishefsky and A. Alexandrescu, *Proc. Natl. Acad. Sci. U. S. A.*, 1984, **81**, 1961.
25 P. P. Pellegrini and J. R. Aldrich-Wright, *Dalton Trans.*, 2003, 176.
26 S. Rau, B. Schäfer, A. Grüßing, S. Schebesta, K. Lamm, J. Vieth, H. Görls, D. Walther, M. Rudolph, U. W. Grummt and E. Birkner, *Inorg. Chim. Acta*, 2004, **357**, 4496.
27 G. W. H. Cheeseman, *J. Chem. Soc. C*, 1962, 1170.
28 *COLLECT, Data Collection Software*, Nonius B.V., Netherlands, 1998.
29 Z. Otwinowski and W. Minor, Processing of X-Ray Diffraction Data Collected in Oscillation Mode, in *Methods in Enzymology, vol. 276. Macromolecular Crystallography, Part A*, ed. C. W. Carter and R. M. Sweet, Academic Press, 1997, pp. 307–326.
30 G. M. Sheldrick, *Acta Crystallogr. Sect. A*, 1990, **46**, 467.
31 G. M. Sheldrick, *SHELXL-97 (Release 97-2)*, University of Göttingen, Germany, 1997.
32 R. Passalacqua, F. Loiseau, S. Campagna, Y.-Q. Fang and G. S. Hanan, *Angew. Chem., Int. Ed.*, 2003, **42**, 1608.
33 C. J. Aspley and J. A. Gareth Williams, *New J. Chem.*, 2001, **25**, 1136.
34 J. Rusanova, S. Decurtins, E. Rusanov, H. Stoeckli-Evans, S. Delahaye and A. Hauser, *Dalton Trans.*, 2002, 4318.
35 Matthew K. Brennaman, T. J. Meyer and J. M. Papanikolas, *J. Phys. Chem. A*, 2004, **108**, 9938.
36 E. R. Batista and R. L. Martin, *J. Phys. Chem. A*, 2005, **109**, 3128.
37 K. O'Donoghue, J. C. Penedo, J. M. Kelly and P. E. Kruger, *Dalton Trans.*, 2005, 1123.
38 R. S. Nair, B. M. Cullum and C. J. Murphy, *Inorg. Chem.*, 1997, **36**, 962.
39 J. R. Schoonover, W. D. Bates and T. J. Meyer, *Inorg. Chem.*, 1995, **34**, 6421.
40 See for instance S. Fantacci, F. DeAngelis, A. Sgamellotti and N. Re, *Chem. Phys. Lett.*, 2004, **396**, 43–48.

Regioselective Functionalization of Tetrabromophenanthroline–Ruthenium Complexes

Sven Rau,*[a] Reinald Fischer,[a] Michael Jäger,[a] Bernhard Schäfer,[a] Susann Meyer,[b] Günter Kreisel,[b] Helmar Görls,[a] Manfred Rudolf,[a] William Henry,[c] and Johannes G. Vos[c]

Keywords: Ruthenium / Nucleophilic substitution / Phenanthroline

Structural, photophysical and photochemical characterization and reactivity of a novel polypyridyl ruthenium complex based on 3,5,6,8-tetrabromophenanthroline are discussed.

Signal storage at a molecular level is a great challenge for chemistry.[1] The possibility of connecting different functionalities selectively to one ligand of a metal complex may open the route towards higher integrated molecular units capable of processing various external stimuli in a predesignated order. The implementation of this concept demands ligands with a multitude of potential connecting groups which can selectively be transformed.[2] 3-bromo- and 3,8-dibromophenanthrolines have proved useful for the preparation of mononuclear[3] and multiheteronuclear complexes.[4] These systems have found applications ranging from DNA photoprobes,[5] to metalloligands in catalysis.[6] A very useful and well-established feature of these bromophenanthroline–ruthenium complexes is their susceptibility towards nucleophilic aromatic substitution.[7]

We have improved the bromination reaction of phenanthroline first published by Dénes and Chira,[8] which allows for the selective formation of 3,5,6,8,-tetrabromophenanthroline (Br_4phen) in a one-step multigram reaction, Figure 1.[8]

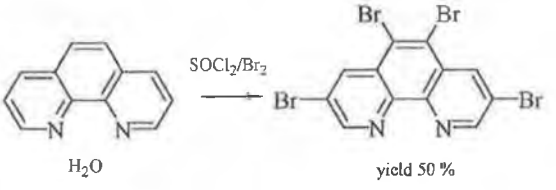

Figure 1. Improved preparation of 3,5,6,8-tetrabromophenanthroline (Br_4phen)

Br_4phen readily forms a complex with $[tbbpy]_2RuCl_2$ resulting in $[(tbbpy)_2Ru(Br_4phen)]^{2+}$, **1**. The structural characterization using two-dimensional NMR spectroscopy suggests that a symmetrical complex is formed as indicated by the presence of only two signals for the four phenanthroline-based protons. ^{13}C, HSQC, and HMBC spectroscopy allows the complete assignment of all signals in the ^1H- and ^{13}C NMR spectra, which together with mass spectroscopy suggests that Br_4phen coordinates in a similar fashion as the unsubstituted phenanthroline. The X-ray crystallographic characterization confirms this assumption, and as seen from Table 1 shows no significant differences compared with the parent complex $[(tbbpy)_2Ru(phen)]^{2+}$, **2** (see Supporting Information). The molecular structure is depicted in Figure 2.

Table 1. Bond lengths (Å) and angles (°)

	1	2
Ru–N1	2.046(5)	2.055(4)
Ru–N2	2.060(5)	2.056(5)
Ru–N3	2.064(5)	2.053(4)
Ru–N4	2.052(5)	2.055(4)
Ru–N5	2.047(5)	2.060(4)
Ru–N6	2.071(5)	2.074(4)
C2–Br1	1.891(6)	–
C5–Br2	1.883(6)	–
N1–Ru–N2	79.27(19)	79.9(2)
N3–Ru–N4	78.21(19)	77.88(16)
N5–Ru–N6	78.25(19)	78.99(16)

[a] Institut für Anorganische und Analytische Chemie, Friedrich-Schiller-Universität,
07743 Jena, Germany
E-mail: Sven.Rau@uni-jena.de
[b] Institut für Technische Chemie und Umweltchemie, Friedrich-Schiller-Universität,
07743 Jena, Germany
[c] National Centre for Sensor Research, School of Chemical Sciences, Dublin City University,
Dublin 9, Ireland

Supporting information for this article is available on the WWW under http://www.eurjic.org or from the author.

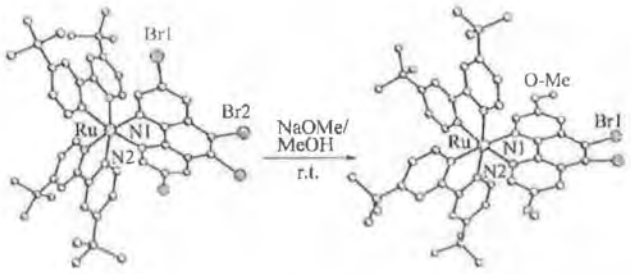

Figure 2. Regioselective nucleophilic substitution of **1** with NaOMe leading to **3**; molecular structure of **1**; anions and hydrogen atoms omitted, and the structural motif of **3** confirming the regioselective substitution

Reaction of **1** with NaOMe at room temperature in methanol leads to the selective formation of one product that contains two bromine and two new methoxy functions, as confirmed by ESI-MS. The fact that the positions of all the bipyridine-based signals in the ^{1}H NMR spectra did not change, together with the presence of only one new signal at $\delta = 4.15$ ppm for the methoxy function, suggests the formation of a symmetrical species where substitution at the phenanthroline moiety has taken place. The regioselective formation of the 5,6-dibromo-3,8-dimethoxyphenanthroline ruthenium complex **3** could be confirmed by a structural motive depicted in Figure 2.

Photophysical investigation of compounds **1** to **3** suggests that tetrabromo substitution lowers the electron density of the phenanthroline ligand considerably. The absorption and emission wavelength of **1** are red-shifted relative to **2**, see Table 2. This finding correlates well with the data obtained for the oxidation potential of $Ru^{II/III}$, which clearly shows that the four bromine substituents significantly decrease the electron density at the metal center (difference of 137 mV). Introduction of the methoxy groups increases the electron density, as expected.[9] The introduction of two methoxy groups has a pronounced influence on the photophysical properties, and this is in agreement with an electron-donating substituent.

Table 2. Photophysical and electrochemical properties of complexes **1**–**3** in acetonitrile

Compound	$E_{1/2}$ ox in V (vs. Fc/Fc^+)	λ_{max} in nm	λ_{em} in nm
1	0.92	470	680
2	0.783	444	610
3	0.845	450	615

In conclusion, rutheniumpolypyridyl complexes based on the ligand Br_4phen are readily obtainable. Most importantly a regioselective nucleophilic substitution with NaOMe at the 3,8-position is possible. It is evident from the conventional reactivity of bromine-substituted aromatics that **1** and **3** are potentially very interesting synthons in itself, opening the possibility to derivatise the previously not easily accessible 5,6-position. Initial investigations on the photochemical reactivity of **3** using ion exchange HPLC suggest that Br_2OMe_2phen is very photolabile.

Experimental Section

All solvents used for spectroscopic measurements were of Uvasol (Merck) grade. All other reagents were of HPLC grade. *cis*-$[Ru(tbbpy)_2Cl_2]\cdot 2H_2O$,[10] was prepared by standard procedures. All reagents for synthesis, $RuCl_3\cdot 3H_2O$ (Chempur), 1,10-phenanthroline (Aldrich) and all other materials were commercially available and of reagent grade.

3,5,6,8-tetrabromophenanthroline (Br_4phen): 1,10-phenanthroline monohydrate (4.0 g, 20 mmol) was dissolved in $SOCl_2$ (200 mL). Freshly distilled Br_2 (9.3 g, 120 mmol) was carefully added. This mixture was refluxed for 31 h and cooled to room temperature, and the bright yellow precipitate was filtered off (3,5,6,8,-tetrabromophenanthroline). The precipitate was washed with aqueous NH_3 until a colorless solution was obtained. The white solid was recrystallized from toluene. ^{1}H NMR ($CDCl_3$): $\delta = 9.16$ (2 H, d), 8.91 (2 H, d) ppm. ^{13}C NMR ($CDCl_3$): $\delta = 122.0, 125.1, 129.6, 139.0, 143.6, 152.4$ ppm. MS (DCI with H_2O): 497 [$M + H^+$] 417 ($M - Br + H^+$), 338 ($M - Br_2 + H^+$), 257 ($M^+ - Br_3$). Yield 5.22 g (52% based on phen).

Synthesis of $[(tbbpy)_2Ru(Br_4phen)](PF_6)_2$ (1): 3,5,6,8-Tetrabromo-1,10-phenanthroline (1.15 g, 2.32 mmol) and $[(tbbpy)_2RuCl_2]$ (1.5 g, 2.11 mmol) were refluxed in a mixture of ethanol (80 mL) and H_2O (20 mL) for 8 hours. The crude reaction mixture was filtered, washed twice with ethanol/H_2O (80:20), and the combined filtrate was concentrated to the half volume. On addition of NH_4PF_6 and stirring at room temperature for 1 hour, the crude product precipitated. Recrystallization from acetone/water gave the desired product. Crystals suitable for X-ray analysis were obtained from acetone/water. ^{1}H NMR ([D$_6$]DMSO): $\delta = 8.997$ [4,7, 2 H, s (lc)], 8.792 [3'', 2 H, s (lc)], 8.788 [3', 2 H, s (lc)], 8.055 [2,9, 2 H, s (lc)], 7.599 [5'', 2 H, d (lc)], 7.527 (6',6'', 4 H, m), 7.310 [5', 2 H, d (lc)], 1.391 [CH_3(*tert*-butyl), 18 H, s], 1.362 [CH_3(*tert*-butyl), 18 H, s] ppm. MS (Micro-ESI in $CHCl_3$ + methanol); *m/z* (relative intensity) with matching isotope pattern: 1279 (100) (**1** + PF_6), 1201 (34) (**1** − Br + PF_6), 567 (51) (1^{2+}). Crystal data for **1**: $[C_{48}H_{52}Br_4N_6Ru]^{2+}\cdot 2\,[PF_6]^-$, $M = 1423.61$ g mol^{-1}, bordeaux-red prism, size 0.02 × 0.02 × 0.01 mm, tetragonalic, space group $I4_1/a$, $a = b = 32.5281(3)$, $c = 20.5151(4)$ Å, $V = 21706.6(5)$ Å^3, $T = -90$ °C, $Z = 16$, $\rho_{calcd.} = 1.742$ g cm^{-3}, μ (Mo-K_α) = 33.74 cm^{-1}, psi-scan, trans(min): 0.5565, trans(max): 0.7367, $F(000) = 11264$, 20023 reflections in $h(-42/42)$, $k(-29/29)$, $l(-19/26)$, measured in the range $2.66° \le \Theta \le 27.49°$, completeness $\Theta_{max} = 99.8\%$, 12423 independent reflections.

Synthesis of $[(tbbpy)_2Ru(phen)](PF_6)_2$ (2): 1,10-phenanthroline (0.018 g, 0.09 mmol) and $[(tbbpy)_2RuCl_2]$ (0.06 g, 0.085 mmol) were reacted and purified according to **1**. Yield 96 mg (95%). Crystals suitable for X-ray analysis were obtained from acetone/water. ^{1}H NMR ([D$_3$]acetonitrile): $\delta = 8.613$ [4,7, 2 H, s (lc)], 8.504 [3', 2 H, s (lc)], 8.456 [3'', 2 H, s (lc)], 8.299 (5,6, 2 H, s), 8.058 [2,9, 2 H, s (lc)] 7.753 (3,8, 2 H, m), 7.705 (6', 2 H, d), 7.463 [5', 2 H, d (lc)], 7.405 (6'', 2 H, d), 7.200 [5'', 2 H, d (lc)], 1.437 [CH_3(*tert*-butyl), 18 H, s], 1.322 [CH_3(*tert*-butyl), 18 H, s] ppm. MS FAB in nba *m/z* (relative intensity) with matching isotope pattern: 980 (22) (**2** + PF_6); 834 (15) (**2**). Crystal data for **2**: $[C_{48}H_{56}N_6Ru]^{2+}\cdot 2\,[PF_6]^-\cdot 2\,C_3H_6O$, $M = 1224.15$ g mol^{-1}, red-brown prism, size 0.12 × 0.10 × 0.09 mm, triclinic, space group $P\bar{1}$, $a = 12.1999(7)$, $b =$

13.3243(7), c = 18.989(1) Å, α = 76.854(2), β = 74.819(3), γ = 78.206(3)°, V = 2866.3(3) Å^3, T = −90 °C, Z = 2, $\rho_{calcd.}$ = 1.418 g cm^{-3}, μ (Mo-K_α) = 4.13 cm^{-1}, psi-scan, trans(min): 0.9521, trans(max): 0.9637, F(000) = 1264, 19624 reflections in h(−15/15), k(−17/14), l(−24/24), measured in the range 2.11° ≤ Θ ≤ 27.44°, completeness Θ_{max} = 97.4%, 12753 independent reflections.

Synthesis of [(tbbpy)$_2$Ru(OMe$_2$Br$_2$phen)](PF$_6$)$_2$ (3): 1 (200 mg, 0.14 mmol), was dissolved in a solution of freshly prepared NaOMe (1 M) in MeOH (100 mL). The solution was stirred for 6 h and H_2O (200 mL) was added. The pH of the solution was slowly adjusted to 7 by adding dilute HCl. The resulting opaque orange solution was extracted with CH_2Cl_2 until colorless, and the solvent was removed from the combined organic phases. The precipitate was dissolved in a minimal amount of EtOH and concentrated aqueous NH_4PF_6 added. The precipitate was recrystallized from acetone/water. Yield 170 mg (90%). ^{1}H NMR ([D$_6$]acetone): δ = 8.879 [3′, 2 H, s (lc)], 8.844 [3″, 2 H, s (lc)], 8.174 [4,7, 2 H, s (lc)], 7.939 (6′, 2 H, d), 7.845 [2,9, 2 H, s (lc)], 7.828 (6″, 2 H, d), 7.618 [5′, 2 H, d (lc)], 7.397 [5″, 2 H, d (lc)], 4.156 [CH$_3$(OMe), 6 H, s], 1.428 [CH$_3$(*tert*-butyl), 18 H, s], 1.367 [CH$_3$(*tert*-butyl), 18 H, s] ppm . MS FAB in nba *m/z* (relative intensity) with matching isotope pattern: 1181 (5) (3 + PF_6); 1035 (5) (3). Crystal data for 3: $C_{52}H_{61}Br_2F_{12}N_6O_2P_2Ru$, M = 1304.72 g mol^{-1}, red prism, size 0.02 × 0.02 × 0.01 mm, monoclinic, space group $P2_1/n$, a = 13.983(3), b = 39.063(5), c = 10.4711(15) Å, β = 100.945(13)°, V = 5615.4(17) Å^3, T = −153 °C, Z = 4, $\rho_{calcd.}$ = 1.543 g cm^{-3}, μ(Mo-K_α) = 6.22 cm^{-1}, F(000) = 2654, 21731 reflections in h(−15/13), k(−45/45), l(−12/12), measured in the range 1.52° ≤ Θ ≤ 14.56°, completeness Θ_{max} = 72.1%, 6903 independent reflections.

CCDC-216455 and -216456 contain the supplementary crystallographic data for this paper. These data can be obtained free of charge via www.ccdc.cam.ac.uk/conts/retrieving.html (or from the Cambridge Crystallographic Data Centre, 12 Union Road, Cambridge CB2 1EZ, UK; Fax: + 44-1223-336-033; E-mail: deposit@ccdc.cam.ac.uk).

Acknowledgments

Financial support for this work from the Deutsche Forschungsgemeinschaft SFB 436 and a grant to S.R. is gratefully acknowledged. We would like to thank Prof. D. Walther for helpful discussions and encouragement.

[1] V. Balzani, A. Credi, M. Venturi, *Molecular Devices and Machines*, Wiley-VCH, Weinheim, **2003**.
[2] A. C. Laemmel, J. P. Collin, J. P. Sauvage, G. Accorsi, N. Amaroli, *Eur. J. Inorg. Chem.* **2003**, 467.
[3] Y. Tor, *Synlett* **2002**, *7*, 1043, and references cited therein.
[4] P. J. Connors, D. Tzalis, A. L. Dunnick, Y. Tor, *Inorg. Chem.* **1998**, *37*, 1121.
[5] D. J. Hurley, Y. Tor, *J. Am. Chem. Soc.* **2002**, *124*, 13231.
[6] M. Osawa, M. Hoshino, Y. Wakatsuki, *Angew. Chem. Int. Ed.* **2001**, *113*, 3580.
[7] D. Tzalis, Y. Tor, *Angew. Chem. Int. Ed., Engl.* **1997**, *36*, 2666.
[8] V. Dènes, R. Chira, *J. Prak. Chem.* **1978**, *320*, 172.
[9] The electrochemical investigation shows different currents for oxidation and reduction of the ruthenium center of 3 suggesting an involvement of the methoxy function as observed previously: L. O'Brien, M. Duati, S. Rau, A. L. Guckian, T. E. Keyes, N. M. Boyle, A. Serr, H. Görls, J. G. Vos, *Dalton Trans.* **2004**, 514.
[10] S. Rau, M. Ruben, T. Büttner, C. Temme, S. Dautz, H. Görls, M. Rudolph, D. Walther, A. Brodkorb, M. Duati, C. O'Connor, J. G. Vos, *J. Chem. Soc., Dalton Trans.* **2000**, 3649.

Received February 27, 2004

A heterodinuclear tpphz complex capable of photocatalytically producing hydrogen

Bernhard Schäfer[a], Dieter Gleich[b], Manfred Rudolph[a], Manfred Friedrich[a], Helmar Görls[a], William Henry[c], Johannes G. Vos[c], Sven Rau*[a]

[a] *Institut für Anorganische und Analytische Chemie, Friedrich-Schiller-Universität, 07743 Jena, Germany*

[b] *Institut für Organische und Makromolekulare Chemie, Friedrich-Schiller-Universität, 07743 Jena, Germany*

[c] *National Centre for Sensor Research, School of Chemical Sciences, Dublin City University, Dublin 9, Ireland*

RECEIVED DATE (automatically inserted by publisher); sven.rau@uni-jena.de

Metal complexes with bridging ligands containing a central phenazine moiety, such as tetrapyridophenazine (tpphz), have shown outstanding properties in photoredox systems.[1] The combination of a reversible photoinduced storage of up to 4 electrons exploiting ultrafast intraligand electron transfer steps,[2] combined with lifetimes of more than 1.3 µs [3] for the charge-separated states opens the possibility to efficiently split water into hydrogen and oxygen.[4] However, to the best of our knowledge no systems based on these principles which are capable of performing processes such as photocatalytic hydrogen production have been reported. We are at present involved in a systematic investigation on the design of mixed metal dinuclear complexes capable of photoinduced catalysis. Because of the well documented catalytic properties of palladium complexes we are particularly interested in $[(tbbpy)_2Ru(tpphz)PdCl_2](PF_6)_2$,[Ru-Pd] type heteronuclear complexes. In this contribution the synthesis and photocatalytic properties of a tpphz based ruthenium-palladium complex [RuPd], (see Figure 1) will be described. Headspace GC strongly indicates that upon irradiation of the [RuPd] complex photoinduced hydrogen production is taking place. This observation is supported by spectroscopic and electrochemical measurements and by DFT calculations.

In contrast to the stepwise preparation of mononuclear tpphz complexes,[5] we employed the direct synthesis of the mononuclear target complex $[(tbbpy)_2Ru(tpphz)](PF_6)_2$,[Ru] utilising microwave-activated reactions.[6] The heterodinuclear complex [RuPd] was prepared starting from [Ru] by simple ligand exchange reactions with $(CH_3CN)_2PdCl_2$ in refluxing CH_2Cl_2. The nature of the products was confirmed using ^{1}H-/^{13}C-NMR, HSQC/HMBC, and ESI-MS. Details are presented as Supplementary Material. Both [Ru] and [RuPd] show concentration-dependent ^{1}H-NMR spectra indicative of aggregation in solution. The X-ray structural investigation of [Ru] supports this assumption with interplanar distances between neighbouring coplanar complexes of 3.742 Å (Figure 1). The intramolecular bond angles and distances are comparable to other investigated ruthenium polypyridyl complexes, see Figure 1 and supporting information. The deviation of the tpphz ligand from planarity is much smaller compared to the data obtained for the dinuclear [RuRu] complex (0.023 Å and 0.570 Å, respectively).[5]

DFT calculations were carried out on corresponding Ru(II) model complexes with polypyridyl ligands without *tert*-butyl substituents. Both compounds $[(bpy)_2Ru(tpphz)]^{2+}$ ([Ru-m]) and $[(bpy)_2Ru(tpphz)PdCl_2]^{2+}$ ([Ru-m-$PdCl_2$]) were fully optimized on DFT level I.[7] Due to the planarity of the (tpphz)$PdCl_2$ fragment, both model complexes belong to the same point group (C_i). The geometry of [Ru-m] is in a similar good agreement with the molecular structure obtained from x-ray data. Similar results were obtained for the corresponding phenanthroline dipyridophenazine (dpphz) complex $[(phen)_2Ru(dpphz)]^{2+}$ (see Figure 1 and Supplementary Material).[8] In [Ru-$PdCl_2$] the coordinated $PdCl_2$ moiety causes only minute geometrical changes on the Ru(II) unit.

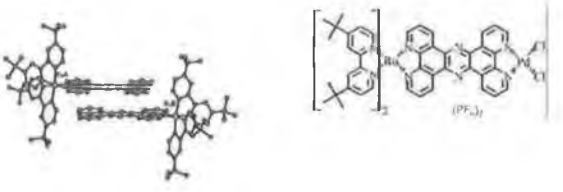

Figure 1. a) π-Stack association between [Ru] and schematic representation of [RuPd].

The photophysical data obtained for both complexes are depicted in Table 1. They are in agreement with literature values on related mono- and dinuclear tpphz complexes.[9] The data show that the presence of the $PdCl_2$ moiety has no major influence on the absorption spectra in comparison with the mononuclear complex, however, the emission intensity is lower and the lifetime of the excited state of [RuPd] is significantly shorter than observed for [Ru]. This is generally observed for dinuclear complexes of this type.[1] This suggests that the Pd centre is able to quench the emitting state originating from excitation of the ruthenium polypyridyl moiety. To obtain information concerning the location of a photoinduced charge separated state EPR experiments were carried out using a suitable irradiation source (selective irradiation at 436 nm) and TEA as a reducing agent. For [Ru]$^•$ as well as [RuPd]$^•$ an EPR active species was detected which could be identified as the radical localised on the pyrazine ring of tpphz (hyperfine coupling depicted in Figure 2c). This signal is very similar to the results obtained by Kaim et al. in electrochemical studies of structurally related dpphz complexes.[10]

Table 1. Photophysical characterisation of [Ru] and [RuPd].

	$\lambda_{max,\ abs}$ [nm]	$\lambda_{max,\ em.}$ [nm][a]	$\lambda_{max,\ em}$ [nm][b]	τ_{aer} [ns]	τ_{77K} [µs]
[Ru]	445 nm	642	600	154	3.8
[RuPd]	445 nm	745	640	27	2.23

[a](293K, CH_3CN) [b](77K, EtOH:MeOH 4:1)

Electrochemical experiments show that the ruthenium centres in [Ru] and [RuPd] are oxidised at 0.8 V vs (Fc/Fc^+) indicating no significant ground state interaction between both metal centres in the dinuclear compound. Whereas the reduction of [Ru] exhibits a very complex set of steps with a broad reduction feature at around –0.7 V [RuPd] displays a relatively simple reduction behaviour (Figure 2). The same broad feature as in [Ru] is visible and has been assigned to the pyrazine reduction.[9]

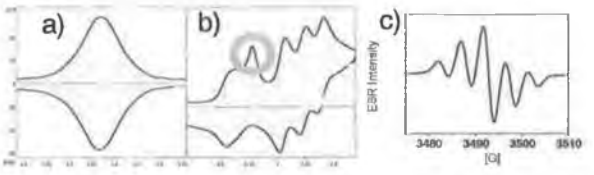

Figure 2 a) Square wave potentiometric oxidation (left) picture shows also reduction process of [RuPd], E(Ru(II)/Ru(III)) = 0.802 V; at 50, 100, 200, 400, 800 Hz scanning frequency; b) Cyclic voltammogram of [RuPd] All potentials vs. (Fc/Fc^+) (1.052 V; 1.235 V; 1.393 V broad feature at around 0.6 V allocated to tpphz reduction, red circle indicating Pd reduction c) EPR signal for the radical anion located at the pyrazine ring of tpphz

Three fully reversible steps which are most likely based on the bpy ligands and the bpy part of the tpphz ligand bound to the ruthenium centre. In addition an, even at high scan rates, irreversible step is observed at –0.78 V. By comparison with literature values for the reduction potential of Pd(II) [11] and the data obtained for [Ru] we assigned this feature to a Pd(II/I) reduction. These data yield a few important points. Firstly, although interaction between the Ru and Pd centres is at best weak in the ground state, the introduction of the Pd centre has a significant effect on the excited state properties of the ruthenium polypyridyl centre. This is an important observation since excited state interaction between the two metal centres is a necessary component from the photocatalytic point of view. Secondly, EPR data clearly identify the pyrazine moiety as the location of this excited state, this suggests that the single-occupied highest molecular orbital (SOMO) is tpphz-pyrazine based. Thirdly, the reduction potentials of the pyrazine moiety and the Pd centre are very similar, this opens the possibility for a photoinduced electron transfer process from the ruthenium to the pyrazine and subsequently from the pyrazine to the Pd metal.

To investigate the potential photocatalytic properties of the mixed metal dinuclear compound both [Ru] and [RuPd] solutions were irradiated at 470 nm in the presence of triethylamine (TEA), which is a known reductive quencher. Reaction mixtures were analysed with headspace gas chromatography (See Table 2) and UV/VIS spectroscopy. The UV/VIS spectra of both complexes change under irradiation with the most notable band growing in at 600 nm. Similar spectroscopic data obtained by MacDonnell et al. [4] and others [1,5] for mono and homodinuclear complexes have been assigned to the presence of a reduced species. Headspace gas chromatography was used to investigate the composition of the gas phase above each solution. For the dinuclear species the presence of hydrogen was verified and moreover the concentration of H_2 exceeds the molarity of [RuPd] by at least a factor of 6 (Table 2, run 2). If no TEA is present or the solution is not irradiated (run 0) no H_2 can be detected. The presence of protons can be explained by decomposition of TEA into protons and other photoredox products subsequent to its participation in the reductive quenching of the photoinduced Ru(III) centre.[12] Another important observation is that addition of tetrabutylammonium chloride as auxiliary chloride source leads to a dramatic decrease in the amount of produced hydrogen (run 4a/b). For the mononuclear [Ru] no production of H_2 is observed.

Table 2. Photocalalytic behavior of [RuPd] under various conditions [13]

Run	Complex 5 x 10^{-5} mol/l	Solvent	c_{TEA} [mol/l]	c_{TBACl} [mol/l]	n(H_2): n([RuPd])	$t_{irrad.}$ [min]
1	[RuPd]	CH_2Cl_2	0.07	0	0	105
2a	[RuPd]	CH_3CN	0.14	0	0.75	45
2b	[RuPd]	CH_3CN	0.14	0	6.5	310
3	[RuPd]	CH_3CN	0.014	0	0.16	45
4a	[RuPd]	CH_3CN	0.16	0.16	0	45
4b	[RuPd]	CH_3CN	0.16	0.16	0.038	150
5	[Ru]	CH_3CN	0.16	0	0	45

The data shown in Table 2 indicate that [RuPd] is capable of catalytic photoinduced hydrogen production. These data together with the earlier mentioned spectroscopic and electrochemical results suggest that this process is driven by a photoinduced electron transfer from the ruthenium to the Pd centre. To obtain further evidence for such a process DFT calculations (level II[7,14]) were carried out and these proved to be extremely useful in identifying the nature of the photocatalytic process. They indicate that in agreement with the EPR data the SOMO in both [Ru-m]$^•$ and [Ru-m-$PdCl_2$]$^•$ is localised on the pyrazine ring of tpphz (Figure 3a). Mulliken [15] and natural population [16] spin densities assign a major part of the radical electron to the two pyrazine nitrogen atoms (Table 3, rows 1 and 2).

As pointed out above, the addition of chloride ions prevents the formation of hydrogen. This suggests that dissociation of chloride may be an important component of the photocatalytic process. To investigate this further the dissociation energies of

(i) [Ru-m-$PdCl_2$] → [Ru-m-PdCl]$^+$ + Cl^-

(ii) [Ru-m-$PdCl_2$]$^•$ → [Ru-m-PdCl]$^{+•}$ + Cl^-

were calculated. Level II [7] gives +91 kJ·mol^{-1} for (i) and –34 kJ·mol^{-1} for (ii), which states that chloride dissociation will be considerably facilitated after reduction of [RuPd].[7] This change in coordination is expected to have consequences for the excited state behavior of the compound. Importantly the calculations show (See Figure 3b) that the SOMO of [Ru-PdCl]$^{+•}$ is localised on the palladium unit. Spin density analyses clearly confirm the electron shift (Table 3, row 3).

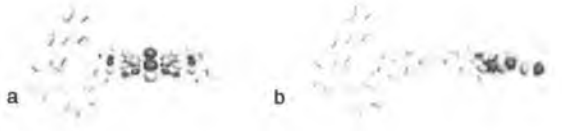

Figure 3. a) SOMO of [Ru-m-$PdCl_2$]$^•$ b) SOMO of [Ru-m-PdCl]$^{+•}$

Table 3. Mulliken and natural population spin densities of [Ru-m]$^•$, [Ru-m-$PdCl_2$]$^•$, and [Ru-m-PdCl]$^{+•}$ (see text).

	$N_{Pyrazine}$	$N'_{Pyrazine}$	Pd	Cl	Cl'
[Ru-m]$^{+•}$	0.27 / 0.27	0.27 / 0.27	- - - -	- - - -	- - - -
[Ru-m-$PdCl_2$]$^{+•}$	0.27 / 0.27	0.30 / 0.29	–0.00/ –0.00	0.00 / 0.00	0.00 / 0.00
[Ru-m-PdCl]$^{2+•}$	0.00 / 0.00	0.00 / 0.00	0.81 / 0.79	0.05 / 0.05	- - - -

Ruthenium based tpphz type complexes have long been identified as potential photocatalysts. In this contribution the first example of such a photocatalytic system is reported. The

combined results of experimental and theoretical investigations suggest the photoinduced generation of hydrogen gas after reduction of the coordinated palladium centre by a photogenerated electron originating from the ruthenium centre. This process is only energetically possible after chloride dissociation. When this exchange process is prevented by additional chloride in solution the SOMO remains pyrazine based and consequently no hydrogen formation is observed. These results show that tpphz based complexes and similar systems have indeed considerable potential as photocatalysts. Moreover, the detailed tuning of the electronic levels of both metal centres is needed to allow for the necessary photoinduced electron transfer process to be efficient. In this respect it is quite surprising that the loss of a chloride anion has such a considerable effect. Further investigations aimed at expanding the scope of this concept are underway.

ACKNOWLEDGMENT JGV and WH thank Enterprise Ireland for financial support (Grant Number SC/2003/0074). BS, SR and DG thank the DFG for financial support (DFG grant RA1017/1 and SFB 436). We are deeply indebted to Prof. D. Walther who encouraged us along this path.

Supporting Information Available: Stating details on synthesis and theoretical investigation is available.

[1] Chiorboli C., Rodgers M. A. J., Scandola F. J. Am. Chem. Soc. 2002, 125, 483-491.
[2] Konduri, R.; Ye, H.; MacDonnell, F. M.; Serroni, S., Campagna, S.; Rajeshwar, K.Angew. Chem. 2002, 114, 3317-3319.
[3] Chiorboli, C; Fracasso, S.; Scandola, F.; Campagna, S.; Serroni, S.; Konduri, R.; MacDonnell, F. M. Chem. Commun. 2000, 1185-1186.
[4] Konduri, R.; de Tacconi, N.R.; Rajeshwar, K.; MacDonnell, F. M. J. Am. Chem. Soc. 2004, 126, 11621-11629.
[5] Bolger, J.; Gourdon, A.; Ishow, E.; Launay, J.-P. J. Chem. Soc. Chem. Commun. 1995, 1799-1800.
[6] Rau, S.; Schäfer, B.; Grüßing, G; Schebesta, S.; Lamm, K.; Vieth, J.; Görls, H.; Walther, D.; Rudolph, M.; Grummt, U. W., Birkner, E. Inorg. Chim. Acta 2004, 357(15), 4496-4503.
[7] for details on the theoretical investigations see supporting information
[8] S. Fantacci, F. De Angelis, A. Sgamelotti, N. Re, Chem. Phys. Lett. 2004, 396, 43-48.
[9] a) Bolger, J.; Gourdon, A.; Ishow, E.; Launay, J.-P. *Inorg. Chem* 1996, *35*, 2937-2944.b) Chiorboli, C.; Bignozzi, C. A.; Scandola, F.; Ishow, E.; Gourdon, A.; Launay, J. P. *Inorg. Chem.* 1999, *38*, 2402-2410.
[10] Fees, J.; Ketterle, M.; Klein, A.; Fiedler, J.; Kaim, W.; *J. Chem. Soc., Dalton Trans.* 1999, 2595-2599.
[11] Arca, M.; Blake, A. J.; Casabò, J.; Demartin, F.; Devillanova, F. A.; Garau, A.; Isaia, F.; Lippolis, V.; Kivekas, R.; Muns, V.; Schröder, M.; Verani, G. *J. Chem. Soc. Dalton Trans.* 2001, 1180-1188.
[12] DeLaive, P. J.; Lee, J. T.; Sprintschnik, H. W.; Abruña, H.; Meyer, T. J.; Whitten, D. G. *J. Am. Chem. Soc.* 1977, *99*, 7094-7097.
[13] Example for run 3. A Schlenk vessel was charged with a solution of complex and TEA in acetonitrile under argon as inert gas. A sample of the gas atmosphere was examined by head-space GC and no H_2 was detected. The atmosphere was replaced by argon and adjusted to normal pressure. The Schlenk vessel was placed next to a LED lamp and irradiated for 45 minutes. During this time the solution was mixed by a magnetic stirrer. After interruption of the irradiation a sample of the gas atmosphere was studied by head-space GC and H_2 was detected.
[14] The optimised structures of $[Ru\text{-}m]^{+}$ / $[Ru\text{-}m\text{-}PdCl_2]^{+}$ are nearly identical to those of $[Ru\text{-}m]^{2+}$ / $[Ru\text{-}m\text{-}PdCl_2]^{2+}$ (levels I and II, cf. supp. info.). The single electron of $[Ru\text{-}m]^{+}$ / $[Ru\text{-}m\text{-}PdCl_2]^{+}$ occupies the LUMO of $[Ru\text{-}m]$ / $[Ru\text{-}m\text{-}PdCl_2]$.
[15] R. S. Mulliken, *J. Chem. Phys.* 1955, *23*, 1833-1840.
[16] A. E. Reed, L. A. Curtiss, F. Weinhold, *Chem. Rev.* 1988, *88*, 899-926.
[17] Values without zero-point and thermal corrections. The calculation of radical cation dissociation energies is a difficult task for density functional theory but here we aim at trends rather than at exact values. J. Gräfenstein, E. Kraka, D. Cremer, *J. Chem. Phys.* 2004, *120*, 524-539.

Insert Table of Contents artwork here

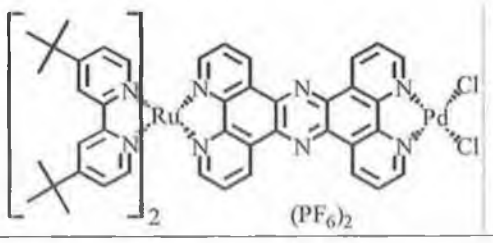

The photocatalytic production of hydrogen as a result of a directional photoelectron transfer within a heterodinuclear complex is reported. The sequential electron transfer steps are investigated using EPR, UV/VIS, electrochemistry, and DFT methods.

J|A|C|S
ARTICLES
Published on Web 00/00/0000

Ground- and Excited-State Electronic Structure of an Emissive Pyrazine-Bridged Ruthenium(II) Dinuclear Complex

Wesley R. Browne,[†,‖] Noel M. O'Boyle,[†] William Henry,[†] Adrian L. Guckian,[†] Sabine Horn,[†] Thomas Fett,[†] Christine M. O'Connor,[†] Marco Duati,[§] Luisa De Cola,[§] Colin. G. Coates,[⊥] Kate L. Ronayne,[⊥] John J. McGarvey,[⊥] and Johannes G. Vos*[,†]

Contribution from the National Centre for Sensor Research, School of Chemical Sciences, Dublin City University, Dublin 9, Ireland, School of Chemistry, Dublin Institute of Technology, Kevin Street, Dublin 8, Ireland, HIMS, Universiteit van Amsterdam, Nieuwe Achtergracht 166, 1018 WV Amsterdam, The Netherlands, and School of Chemistry, Queen's University Belfast, Belfast BT9 5AG, Northern Ireland

Received July 3, 2004; E-mail: Johannes.vos@dcu.ie

Abstract: The synthesis, characterization, and electrochemical, photophysical, and photochemical properties of the binuclear compounds $[(Ru(H_8\text{-bpy})_2)_2((Metr)_2Pz)](PF_6)_2$ (**1**) and $[(Ru(D_8\text{-bpy})_2)_2((Metr)_2Pz)](PF_6)_2$ (**2**), where bpy is 2,2′-bipyridine and $H_2(Metr)_2Pz$ is the planar ligand 2,5-bis(5′-methyl-4′*H*-[1,2,4]triaz-3′-yl)-pyrazine, are reported. Electrochemical and spectro-electrochemical investigations indicate that the ground-state interaction between each metal center is predominantly electrostatic and in the mixed-valence form only a low level of ground-state delocalization is present. Resonance Raman, transient, and time-resolved spectroscopies enable a detailed assignment to be made of the excited-state photophysical properties of the complexes. Deuteriation is employed to both facilitate spectroscopic characterization and investigate the nature of the lowest excited states.

Introduction

Since the first report on the paradigm pyrazine (pz)-bridged binuclear ruthenium(II) complex ($[(NH_3)_5Ru)_2pz]^{2+}$), by Creutz and Taube,[1] pyrazine-bridged multinuclear complexes have received considerable attention.[2] Investigations have focused predominantly on the electrochemical and spectroelectrochemical properties of these complexes, in particular toward the measurement of the degree of delocalization in the mixed-valence ($Ru^{II}Ru^{III}$) species.[2,3] The many structural analogues of the Creutz−Taube (CT) ion, involving substitution of the monodentate amine groups with pyridyl, bipyridyl, chloro, and/or aquo groups, have provided considerable insight into the factors that control internuclear interaction in the Ru(II)Ru(III) state.[4,5] An alternative approach to the perturbation of the ground-state properties of the CT ion has been to modify the bridging pyrazine unit by substitution in the 2,3-, 2,5-, or 2,3,5,6-positions.[6] Many of these systems are especially suited for study by techniques such as electrochemistry, spectro-electrochemistry,[7] and infrared,[8] Mössbauer,[9] and UV−vis absorption

† Dublin City University.
‡ Dublin Institute of Technology.
§ Universiteit van Amsterdam.
⊥ Queen's University Belfast.
‖ Present address: Organic and Molecular Inorganic Chemistry, Rijksuniversiteit Groningen, Nijenborgh 4, Groningen, The Netherlands.

(1) Creutz, C.; Taube, H. *J. Am. Chem. Soc.* **1969**, *91*, 3988−3989.
(2) (a) Chen, P.; Meyer, T. J. *Chem. Rev.* **1998**, *98*, 1439−1477. (b) Brunschwig, B. S.; Creutz, C.; Sutin, N. *Chem. Soc. Rev.* **2002**, *31*, 168−184. (c) Demadis, K. D.; Hartshorn, C. M.; Meyer, T. J. *Chem. Rev.* **2001**, *101*, 2655−2685.
(3) (a) Londergan, C. H.; Kubiak, C. P. *J. Phys. Chem A.* **2003**, *107*, 9301−9311. (b) Braun-Sand, S. B.; Wiest, O. *J. Phys. Chem. A* **2003**, *107*, 285−291.
(4) (a) Callahan, R. W.; Brown G. M.; Meyer, T. J. *J. Am. Chem. Soc.* **1974**, *96*, 7829−7830. (b) Callahan, R. W.; Brown, G. M.; Meyer, T. J. *Inorg. Chem.* **1975**, *14*, 1443−1452. (c) Tom, G. M.; Creutz, C.; Taube, H. *J. Am. Chem. Soc.* **1974**, *96*, 7827−7829. (d) Meyer, T. J. *Acc. Chem. Res.* **1978**, *11*, 94−100. (e) Meyer, T. J. *Chem. Phys. Lett.* **1979**, *64*, 417−420.
(5) (a) Callahan, R. W.; Keene, F. R.; Meyer, T. J.; Salmon, D. J. *J. Am. Chem. Soc.* **1977**, *99*, 1064−1073. (b) Powers, M. J.; Meyer, T. J. *J. Am. Chem. Soc.* **1980**, *102*, 1289−1297. (c) Demadis, K. D.; Neyhart, G. A.; Kober, E. M.; White, P. S.; Meyer, T. J. *Inorg. Chem.* **1999**, *38*, 5948−5959. (d) Powers, M. J.; Meyers, T. J. *Inorg. Chem.* **1978**, *17*, 2955−2958.
(6) (a) Sarker, B.; Laye, R. H.; Mondal, B.; Chakraborty, S.; Paul, R. L.; Jeffery, J. C.; Puranik, V. G.; Ward, M. D.; Lahiri, G. K. *J. Chem. Soc., Dalton Trans.* **2002**, 2097−2101. (b) Brady, I.; Loane, D.; Hughes, H. P.; Forster, R. J.; Keyes, T. E. *J. Chem. Soc., Dalton Trans.* **2004**, 334−341. (c) Braunstein, C. H.; Baker, A. D.; Strekas, T. C.; Gafney, H. D. *Inorg. Chem.* **1984**, *23*, 857−864. (d) Richter, M. M.; Jensen, G. E.; Brewer, K. J. *Inorg. Chim. Acta* **1995**, *230*, 35−40. (e) Sherborne, J.; Scott, S. M.; Gordon, K. C. *Inorg. Chim. Acta* **1997**, *260*, 199−205. (f) Su, H. Q.; Kincaid, J. R. *J. Raman Spectrosc.* **2003**, *34*, 907−916 and references therein. (g) Marcaccio, M.; Paolucci, F.; Paradisi, C.; Roffia, S.; Fontanesi, C.; Yellowlees, L. J.; Serroni, S.; Campagna, S.; Balzani, V. *J. Am. Chem. Soc.* **1999**, *121*, 10081−10091. (h) Loiseau, F.; Serroni, S.; Campagna, S. *Collect. Czech. Chem. Commun.* **2003**, *68*, 1677−1686. (i) Marcaccio, M.; Paolucci, F.; Paradisi, C.; Carano, M.; Roffia, S.; Fontanesi, C.; Yellowlees, L. J.; Serroni, S.; Campagna, S.; Balzani, V. *J. Electroanal. Chem.* **2002**, *532*, 99−112. (j) Campagna, S.; Serroni, S.; Puntoriero, F.; Loiseau, F.; De Cola, L.; Kleverlaan, C. J.; Becher, J.; Sørenson, A. P.; Hascoat, P.; Thorup, N. *Chem. Eur. J.* **2002**, *8*, 4461−4469. (k) Swavey, S.; Brewer, K. J. *Inorg. Chem.* **2002**, *41*, 4044−4050. (l) Baudin, H. B.; Davidsson, J.; Serroni, S.; Juris, A.; Balzani, V.; Campagna, S.; Hammarström, L. *J. Phys. Chem. A* **2002**, *106*, 4312−4319. (m) Seneviratne, D. S.; Uddin, J.; Swayambunathan, V.; Schlegel, H. B.; Endicott, J. F. *Inorg. Chem.* **2002**, *41*, 1502−1517. (n) Constable, E. C.; Eriksson, H.; Housecroft, C. E.; Kariuki, B. M.; Nordlander, E.; Olsson, J. *Inorg. Chem. Commun.* **2001**, *4*, 749−752. (o) Canino, M.; Ceroni, P.; Fontanesi, C.; Marcaccio, M.; Paolucci, F.; Paradisi, C.; Roffia, S. *Electrochim. Acta* **2001**, *46*, 3199−3206. (p) Puntoriero, F.; Serroni, S.; Licciardello, A.; Venturi, M.; Juris, A.; Ricevuto, V.; Campagna, S. *J. Chem. Soc., Dalton Trans.* **2001**, 1035−1042. (q) Goldsby K. A.; Meyer, T. J. *Inorg. Chem.* **1984**, *23*, 3002−3010.
(7) (a) Yeomans, B. D.; Kelso, L. S.; Tregloan, P. A.; Keene, F. R. *Eur. J. Inorg. Chem.* **2001**, 239−246. (b) D'Alessandro, D. M.; Kelso, L. S.; Keene, F. R. *Inorg. Chem.* **2001**, *40*, 6841−6844.

10.1021/ja046034e CCC: $30.25

spectroscopies. The majority of these studies have focused on the relative delocalization of the SOMO, in the mixed-valence form, over the metal centers and the mechanism for interaction in systems where direct overlap of the metal orbitals is not possible (i.e., superexchange processes mediated via either the HOMO or the LUMO of the bridging ligand). The results of these studies can be extended, albeit tentatively, as a guide to the level of excited-state communication between the molecular components in large systems in their homovalent states (i.e., $Ru^{II}Ru^{II}$), and while this extrapolation may give an indication of the level of excited-state interaction, it assumes that the bridging ligand provides the same contribution toward internuclear interaction in the mixed-valence state as in the homovalent excited state. This assumption fails, however, when the LUMO of the bridging ligand provides a significant contribution to the lowest excited states, or the dominant mechanism for energy transfer is via a through-space (Förster) rather than a through-bond (Dexter) energy-transfer mechanism.[10] It is surprising then that, despite such a significant level of interest, the photochemical and excited-state properties of pyrazine-bridged complexes have received relatively little attention, with the notable exception of the dipyridopyrazine (dpp)-based family of complexes.[6,11]

In the present contribution, the effect of the introduction of a pH-sensitive 1,2,4-triazole moiety on the ground- and excited-state properties of a pyrazine-bridged binuclear Ru(II) complex is examined in the synthesis and characterization of the binuclear complexes $[(Ru(H_8\text{-bpy})_2)_2((Metr)_2Pz)](PF_6)_2$ (**1**) and $[(Ru(D_8\text{-bpy})_2)_2((Metr)_2Pz)](PF_6)_2$ (**2**), where bpy is 2,2′-bipyridine and $H_2(Metr)_2Pz$ is 2,5-bis(5′-methyl-4′*H*-[1,2,4]triaz-3′-yl)pyrazine (Figure 1). Recently, a series of ditopic ligands containing both pyrazine and 1,2,4-triazole moieties have been reported (Figure 2).[10] The primary interest in such mixed electron acceptor/electron donor ligands is in the ability to tune, independently, ground- and excited-state properties in multinuclear complexes.[10] In addition, the acid−base chemistry of the bridging triazole moiety influences strongly the properties of the complexes.[10,12−14]

Of particular interest in the present study is the effect of the protonation state of the nonbridging 1,2,4-triazole on the degree

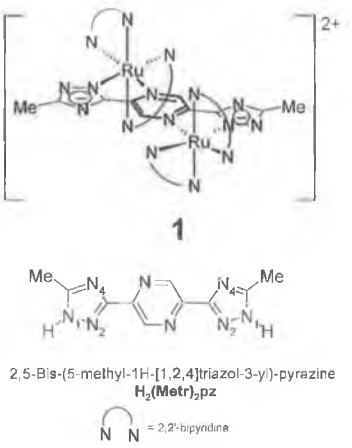

Figure 1. Structure of the ligand $H_2(Metr)_2pz$ and complex **1**.

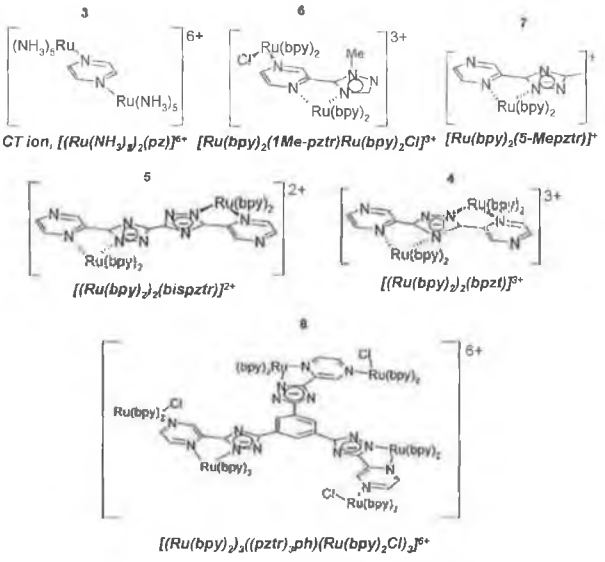

Figure 2. Structure of some of the complexes discussed in the text.

of internuclear communication and on photophysical properties. Extensive resonance Raman spectroscopic investigations of both the ground and lowest excited electronic states, together with computational analysis (DFT), enable a detailed model of the excited-state electronic structure to be developed. The results obtained are compared with those reported for related ligand systems, e.g., Hbpzt[15] and H_2bisztr,[10b] where Hbpzt is 2-(3-pyrazin-2-yl-1*H*-1,2,4-triazol-5-yl)pyrazine and H_2bispztr is 5,5′-dipyrazin-2-yl-1*H*,1′*H*-3,3′-bi-1,2,4-triazole (Figure 2). A de-

(8) (a) Daltelbaum, D. M.; Hartshorn, C. M.; Meyer, T. J. *J. Am. Chem. Soc.* **2002**, *124*, 4938−4939. (b) Crayston, J. A.; Cupertino, D. C.; Dines, T. J. *J. Chem. Soc., Dalton Trans.* **1991**, 1603−1608. (c) Toma, H. E.; Santos, P. S. *Can. J. Chem.* **1977**, *55*, 3549−3553. (d) Londergan, C. H.; Salsman, J. C.; Ronco, S.; Kubiak, C. P. *Inorg. Chem.* **2003**, *42*, 926−928.
(9) Fürholz, U.; Bürgi, H.-B.; Wagner, F. E.; Stebler, A.; Ammeter, J. H.; Krausz, E.; Clark, R. J. H.; Stead, M. J.; Ludi, A. *J. Am. Chem. Soc.* **1984**, *106*, 121−123.
(10) (a) Browne, W. R.; Weldon, F.; Guckian, A.; Vos, J. G. *Collect. Czech. Chem. Commun.* **2003**, *68*, 1467−1487. (b) Di Pietro, C.; Serroni, S.; Campagna, S.; Gandolfi, M. T.; Ballardini, R.; Fanni, S.; Browne, W. R.; Vos J. G. *Inorg. Chem.* **2002**, *41*, 2871−2878. (c) Weldon, F.; Hammarström, L.; Mukhtar, E.; Hage, R.; Gunneweg, E.; Haasnoot, J. G.; Reedijk, J.; Browne, W. R.; Guckian, A. L.; Vos J. G. *Inorg. Chem.* **2004**, *43*, 4471−4481.
(11) (a) Fuchs, Y.; Lofters, S.; Dieter, T.; Shi, W.; Morgan, R.; Strekas, T. C.; Gafney, H. D.; Baker, A. D. *J. Am. Chem. Soc.* **1987**, *109*, 2691−2697. (b) Scott, S. M.; Gordon, K. C. *Inorg. Chim. Acta* **1997**, *254*, 267−272. (c) Cooper, J. B.; MacQueen, D. B.; Petersen, J. D.; Wertz, D. W. *Inorg. Chem.* **1990**, *29*, 3701−3705.
(12) (a) Hage, R.; Prins, R.; Haasnoot, J. G.; Reedijk, J.; Vos, J. G. *J. Chem. Soc., Dalton Trans.* **1987**, 1389−1395. (b) Nieuwenhuis, H. A.; Haasnoot, J. G.; Hage, R.; Reedijk, J.; Snoeck, T. L.; Stufkens, D. J.; Vos, J. G. *Inorg. Chem.* **1991**, *30*, 48−54. (c) Buchanan, B. E.; Wang, R.; Vos, J. G.; Hage, R.; Haasnoot, J. G.; Reedijk, J. *Inorg. Chem.* **1990**, *29*, 3263−3265. (d) Browne, W. R.; O'Connor, C. M.; Villani, C.; Vos, J. G. *Inorg. Chem.* **2001**, *40*, 5461−5464. (e) Hage, R.; Haasnoot, J. G.; Nieuwenhuis, H. A.; Reedijk, J.; de Ridder, D. J. A.; Vos, J. G. *J. Am. Chem. Soc.* **1990**, *112*, 9245−9254. (f) de Wolf, J. M.; Hage, R.; Haasnoot, J. G.; Reedijk, J.; Vos, J. G. *New J. Chem.* **1991**, *15*, 501−507. (g) Hage, R.; Dijkhuis, A. H. J.; Haasnoot, J. G.; Prins, R.; Reedijk, J.; Buchanan B. E.; Vos, J. G. *Inorg. Chem.* **1988**, *27*, 2185−2189.
(13) (a) Barigelletti, F.; De Cola, L.; Balzani, V.; Hage, R.; Haasnoot, J. G.; Reedijk, J.; Vos, J. G. *Inorg. Chem.* **1989**, *28*, 4344−4350. (b) van Diemen, J. H.; Hage, R.; Haasnoot, J. G.; Lempers, H. E. B.; Reedijk, J.; Vos, J. G.; de Cola, L.; Barigelletti, F.; Balzani, V. *Inorg. Chem.* **1992**, *31*, 3518−3522. (c) Barigelletti, F.; De Cola, L.; Balzani, V.; Hage, R.; Haasnoot, J. G.; Reedijk, J.; Vos, J. G. *Inorg. Chem.* **1991**, *30*, 641−645. (d) Passaniti, P.; Browne, W. R.; Lynch, F. C.; Hughes, D.; Nieuwenhuyzen, M.; James, P.; Maestri, M.; Vos, J. G. *J. Chem. Soc., Dalton Trans.* **2002**, 1740−1476. (e) Hage, R.; Lempers, H. E. B.; Haasnoot, J. G.; Reedijk, J.; Weldon, F. M.; Vos, J. G. *Inorg. Chem.* **1997**, *36*, 3139−3145.
(14) (a) Coates, C. G.; Keyes, T. E.; Hughes, H. P.; Jayaweera, P. M.; McGarvey, J. J.; Vos, J. G. *J. Phys. Chem. A* **1998**, *102*, 5013−5018. (b) Hage, R.; Haasnoot, J. G.; Stufkens, D. J.; Snoeck, T. L.; Vos, J. G.; Reedijk, J. *Inorg. Chem.* **1989**, *28*, 1413−1414. (c) Keyes, T. E.; O'Connor, C. M.; O'Dwyer, U.; Coates, C. G.; Callaghan, P.; McGarvey, J. J.; Vos, J. G. *J. Phys. Chem. A* **1999**, *103*, 8915−8920.
(15) Hage, R.; Haasnoot, J. G.; Reedijk, J.; Wang, R.; Vos, J. G. *Inorg. Chem.* **1991**, *30*, 3263−3269.

tailed picture of the excited-state electronic structure is described, and the influence of energy states lying higher than the lowest emissive state is discussed.

Experimental Section

Materials. All solvents employed were of HPLC grade or better and used as received. For all spectroscopic measurements, Uvasol (Merck)-grade solvents were employed. All reagents employed in synthetic procedures were of reagent grade or better. 2,2′-Bipyridine (Aldrich) and [*cis*-[Ru([D_8]-bpy)$_2$Cl$_2$]·2H$_2$O (Complex-Solutions, Dublin, Ireland) were used as received. *cis*-[Ru(bpy)$_2$Cl$_2$]·2H$_2$O,[16] pyrazine-2,5-dicarbonitrile,[17] and tetraethylammonium perchlorate (TEAP)[18] were prepared by previously reported procedures. The synthesis of the ligand, 2,5-bis(5′-methyl-4′*H*-[1,2,4]triaz-3′-yl)pyrazine {H_2(Metr)$_2$pz}, was carried out according to literature methods.[12] ^{1}H NMR in DMSO-d_6: δ 9.41 (2H, s), 2.79 (6H, s). Preparation of the dinuclear complexes was by direct reaction of the ligand with 2 equiv of *cis*-[Ru(bpy)$_2$Cl$_2$] or *cis*-[Ru([D_8]-bpy)$_2$Cl$_2$], with purification by column chromatography on neutral alumina. Both complexes gave satisfactory mass spectra, which showed isotopic patterns in agreement with calculated spectra. Detailed synthetic procedures are available as Supporting Information.

[(Ru(bpy)$_2$)$_2$((Metr)$_2$Pz)](PF$_6$)$_2$·3H$_2$O (1). This compound was recrystallized from neutral solution, and therefore the triazole units are deprotonated. ^{1}H NMR spectroscopy (in CD$_3$CN/NaOD): δ 8.52 (m, 3H), 8.44 (m, 5H), 8.175 (d, 1H), 8.12 (m, 4H), 8.05 (d, 1H), 7.99 (m, 6H), 7.89 (d, 1H), 7.75 (d, 1H), 7.68 (d, 1H), 7.64 (m, 2H), 7.51 (m, 5H), 7.35 (m, 3H), 7.175 (dd, 1H), 2.18 (s, methyl, 3H), 2.175 (s, methyl, 3H). Mass spectroscopy: Mol^{2+} (calcd for $C_{50}H_{40}N_{16}Ru_2$, 534) found, 534 *m/z*. Elemental analysis (calcd for $C_{50}H_{40}N_{16}RuP_2F_{12}$·3H$_2$O): C 42.64 (42.55), H 2.75 (3.05), N 15.64 (15.89).

[(Ru([D_8]-bpy)$_2$)$_2$(H$_2$(Metr)$_2$Pz)](PF$_6$)$_4$ (2). This compound was obtained from acidic solution, and therefore the triazole groups are protonated. ^{1}H NMR spectroscopy (in CD$_3$CN/NaOD): δ 7.98 (s, 1H), 7.92 (s, 1H), 2.18 (s, methyl, 3H), 2.175 (s, methyl, 3H). Mass spectroscopy: Mol^{2+} (calcd for $C_{50}D_{32}H_8N_{16}Ru_2$, 550) found, 550 *m/z*. Elemental analysis (calcd for $C_{50}H_{10}D_{32}N_{16}RuP_4F_{24}$): C 36.10 (35.71), H 2.38 (2.5), N 13.00 (13.33).

Physical Measurements. ^{1}H NMR, UV−vis, emission and mass spectra, luminescence lifetime, electrochemical and spectro-electrochemical measurements,[12d] transient differential absorption spectroscopy,[19] resonance Raman, and transient and time-resolved resonance Raman (TR^2 and TR^3)[14c,20] were carried out as reported elsewhere and are described in detail in the Supporting Information. Photolysis experiments were carried out at room temperature in acetonitrile using visible light with a 400-W tungsten filament light source. Elemental analysis was carried out at the Micro-analytical Laboratory at University College Dublin.

Density Functional Theory Calculations. Density functional calculations were carried out with Gaussian 03W[21] using Becke's three-parameter hybrid functional[22] with the LYP correlation functional[23] (B3LYP). The LanL2DZ basis set was used. This uses the Dunning−Huzinaga double-ζ basis functions[24] (DZ) for carbon, nitrogen, and hydrogen atoms, the Los Alamos effective core potential for the Ru core electrons, and DZ functions for the Ru valence electrons.[25] An ultrafine integration grid was used. The structures of the heterochiral isomers of **1** and **H$_2$1** were constrained to C_i symmetry during the geometry optimization. The energies and intensities of the 35 lowest energy singlet−singlet electronic transitions were calculated at the optimized geometry using TD-DFT. GaussSum 0.8[26] was used to calculate group contributions to the molecular orbitals, to prepare the partial density of states (PDOS) spectra, to convolute the calculated UV−vis spectrum, and to prepare the electron density difference maps (EDDMs). The contribution of a group to a molecular orbital was calculated within the framework of Mulliken population analysis. The PDOS spectra were created by convoluting the molecular orbital information with Gaussian curves of unit height and fwhm of 0.3 eV. The UV−vis spectrum was convoluted with Gaussian curves of fwhm of 3000 cm^{-1}.

Results

^{1}H NMR Spectroscopy. ^{1}H NMR data are given in the Experimental Section and in the Supporting Information, Figure S1. For **1**, two methyl resonances at 2.175 and 2.18 ppm and a total of 34 aromatic resonances are observed, while for the [D_8]-bpy analogue **2** only the resonances due to the methyl groups and pyrazine ring are observed, as expected. The observation of two methyl and two pyrazine singlet resonances is explained by the presence of two diastereoisomeric forms for both compounds (i.e., $\Delta\Delta/\Lambda\Lambda$ and $\Lambda\Delta$) and confirms that the coordination mode of each of the 1,2,4-triazole rings is the same (i.e., N2N2 or N4N4 and not N2N4, see Figure 1).[12d,27]

The incorporation of a methyl substituent in the C5 position of the 1,2,4-triazole ring is known to inhibit coordination via the N4 of the 1,2,4-triazole ring, resulting in almost exclusive formation of the N2-bound isomer (>90%).[12a,13,28] The methyl ^{1}H NMR resonance of the 1,2,4-triazole ring is particularly sensitive to the coordination mode of the ring. In the related mononuclear complexes, [Ru(LL)$_2$(5-Mepztr)]$^+$ (where LL = bpy, phen, or dmbpy, Figure 2),[28] a resonance at 2.15−2.35 ppm is indicative of N2 coordination, while for N4 coordination an upfield shift in the methyl resonance to 1.1−1.3 ppm is observed, due to through-space interaction with a neighboring polypyridyl ligand. The methyl resonance observed at 2.18 ppm for the compounds reported in this contribution, therefore, confirms the N2N2 coordination mode to the 1,2,4-triazole rings.

(16) Sullivan, B. P.; Salmon, D. J.; Meyer, T. J. *Inorg. Chem.* **1978**, *17*, 3334−3341.
(17) Suenaga, Y.; Kamiya, T.; Kuroda-Sowa, T.; Maekawa, M.; Munakata, M. *Inorg. Chim. Acta* **2000**, *308*, 17−21.
(18) Wang, R.; Vos, J. G.; Schmehl, R. H.; Hage, R. *J. Am. Chem. Soc.* **1992**, *114*, 1964−1970.
(19) (a) Kleverlaan, C. J.; Stufkens, D. J.; Clark, I. P.; George, M. W.; Turner, J. J.; Martino, D. M.; van Willigen, H.; Vlček, A., Jr. *J. Am. Chem. Soc.* **1998**, *120*, 10871−10879. (b) Stellfians, M.; Peter Belser, P.; Hartl, F.; Kleverlaan, C. J.; Luisa De Cola, L. *J. Phys. Chem. A* **2002**, *106*, 9242−9250.
(20) (a) Coates, C. G.; Jacquet, L.; McGarvey, J. J.; Bell, S. E. J.; Al-Obaidi, A. H. R.; Kelly, J. M. *J. Am. Chem. Soc.* **1997**, *119*, 7130−7136. (b) Coates, C. G.; Olofsson, J.; Coletti, M.; McGarvey, J. J.; Önfelt, B.; Lincoln, P.; Norden, B.; Tuite, E.; Matousek, P.; Parker, A. W. *J. Phys. Chem. B* **2001**, *105*, 12653−12664.
(21) Frisch, M. J.; Trucks, G. W.; Schlegel, H. B.; Scuseria, G. E.; Robb, M. A.; Cheeseman, J. R.; Montgomery, J. A., Jr.; Vreven, T.; Kudin, K. N.; Burant, J. C.; Millam, J. M.; Iyengar, S. S.; Tomasi, J.; Barone, V.; Mennucci, B.; Cossi, M.; Scalmani, G.; Rega, N.; Petersson, G. A.; Nakatsuji, H.; Hada, M.; Ehara, M.; Toyota, K.; Fukuda, R.; Hasegawa, J.; Ishida, M.; Nakajima, T.; Honda, Y.; Kitao, O.; Nakai, H.; Klene, M.; Li, X.; Knox, J. E.; Hratchian, H. P.; Cross, J. B.; Adamo, C.; Jaramillo, J.; Gomperts, R.; Stratmann, R. E.; Yazyev, O.; Austin, A. J.; Cammi, R.; Pomelli, C.; Ochterski, J. W.; Ayala, P. Y.; Morokuma, K.; Voth, G. A.; Salvador, P.; Dannenberg, J. J.; Zakrzewski, V. G.; Dapprich, S.; Daniels, A. D.; Strain, M. C.; Farkas, O.; Malick, D. K.; Rabuck, A. D.; Raghavachari, K.; Foresman, J. B.; Ortiz, J. V.; Cui, Q.; Baboul, A. G.; Clifford, S.; Cioslowski, J.; Stefanov, B. B.; Liu, G.; Liashenko, A.; Piskorz, P.; Komaromi, I.; Martin, R. L.; Fox, D. J.; Keith, T.; Al-Laham, M. A.; Peng, C. Y.; Nanayakkara, A.; Challacombe, M.; Gill, P. M. W.; Johnson, B.; Chen, W.; Wong, M. W.; Gonzalez, C.; Pople, J. A. *Gaussian 03*, Revision B.04; Gaussian, Inc.: Pittsburgh PA, 2003.
(22) Becke, A. D. *J. Chem. Phys.* **1993**, *98*, 5648−5652.
(23) Lee, C.; Yang, W.; Parr, R. G. *Phys. Rev. B* **1988**, *37*, 785−789.
(24) Dunning, T. H., Jr.; Hay, P. A. In *Modern Theoretical Chemistry*; Schaefer, H. F., III, Ed.; Plenum: New York, 1977; Vol. 3, p 1.
(25) (a) Hay, P. J.; Wadt, W. R. *J. Chem. Phys.* **1985**, *82*, 270−283. (b) Wadt, W. R.; Hay, P. J. *J. Chem. Phys.* **1985**, *82*, 284−298. (c) Hay, P. J.; Wadt, W. R. *J. Chem. Phys.* **1985**, *82*, 299−310.
(26) O'Boyle, N. M.; Vos, J. G. *GaussSum 0.8*; Dublin City University, 2003.
(27) Baitalik, S.; Bag, P.; Flörke, U.; Nag, K. *Inorg. Chim. Acta* **2004**, *357*, 699−706.
(28) Ryan, E. M.; Wang, R.; Vos J. G.; Hage, R.; Haasnoot, J. G. *Inorg. Chim. Acta* **1993**, *208*, 49−58.

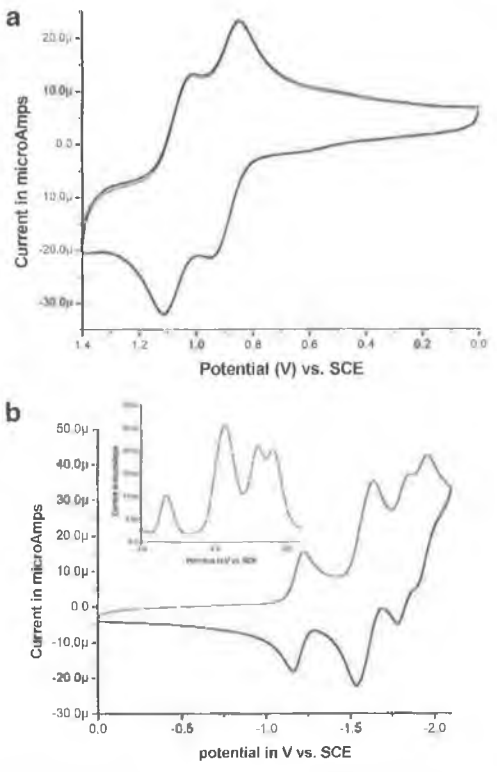

Figure 3. (a) Metal-based oxidation. (b) Ligand-based processes for **1** in 0.1 M TEAP/CH_3CN (CV scan rate 200 mV s^{-1}; inset, DPV scan rate 40 mV s^{-1}).

Redox, Electronic, Photochemical, and Acid−Base Properties. Reversible metal-based oxidation processes are observed at 0.875 and 1.05 V (vs SCE, Figure 3) for **1** and at 1.28 and 1.45 V for $\mathbf{H_21}$. The first oxidation process occurs at potentials comparable with those observed for related 1,2,4-triazole-based complexes but at a considerably higher potential than observed for the Creutz−Taube ion (see Table 1). For **1**, four reversible reduction processes are observed between −1.0 and −2.0 V. Due to the electron-deficient nature of the pyrazine ring, the first reduction process is expected to be pyrazine-based, followed by bpy-based reductions.[11c]

The separation of the first and second oxidation processes facilitates the preparation of the mixed-valence and fully oxidized complexes by bulk electrolysis, and although the complex becomes unstable in the II/III and III/III oxidation states,[6c,29] useful information may still be obtained using this technique. For $\mathbf{H_21}$ only a very weak band is observed at ~850 nm upon oxidation at 1.0 V. Oxidation at a potential above the second oxidation wave results in a depletion of this feature, which suggests that it is an intervalence (IT) band. For **1**, evidence for the presence of an IT band (between 400 and 2500 nm) was not obtained by either spectroelectrochemistry or chemical oxidation.

The absorption spectrum of **1** shows strong absorption features at ~550 and ~450 nm (Figure 4), which are assigned to metal-to-ligand-charge-transfer transitions (^{1}MLCT). An equally intense absorption feature at ~350 nm (vide infra) and a very intense absorption band at ~280 nm are assigned as intraligand ($\pi-\pi^*$) transitions (Table 1).[30] Figure 4 shows that there are two different protonation steps, indicating significant interaction between the two triazole rings, and as a result the formation of the singly protonated **H1** is observed at intermediate pH values. Protonation results in a red shift of the lowest absorption band from 530 to 565 nm, while the higher energy band undergoes a blue shift from 467 to 424 nm. The intraligand ($\pi-\pi^*$) transition at ~280 nm undergoes only a relatively minor blue shift on protonation; however, the absorption band at ca. 350 nm is more strongly blue-shifted. The pK_a values for the two protonation steps are $pK_{a1} = 2.7$ and $pK_{a2} = 4.7 \pm 0.1$.

$$\mathbf{H_21} \overset{pK_{a1}=2.7}{\rightleftharpoons} \mathbf{H1} \overset{pK_{a2}=4.7}{\rightleftharpoons} \mathbf{1}$$

The absorption and the emission spectra of $\mathbf{1}/\mathbf{H_21}$ exhibit solvatochromic behavior. Interestingly, the effects of solvent on each of the absorption bands are different. For both **1** and $\mathbf{H_21}$, the lowest energy band undergoes a red shift with increasing solvent polarity, while the bands at ca. 450 and 350 nm are blue-shifted. Both **1** and $\mathbf{H_21}$ are emissive at room temperature and at 77 K (Table 1), and although the emission spectra are unaffected by deuteriation of the bpy ligands, deuteriation has a noticeable effect on the emission lifetime of the complexes (Table 1). At 298 K, deuteriation results in an increase in emission lifetime of ca. 17%, while at 77 K, the effect is more pronounced, with an increase in emission lifetime of 30%. Upon protonation of **1** to form **H1** and subsequently to form $\mathbf{H_21}$, the emission spectrum of the complex undergoes a red shift from 748 nm to >800 nm (in CH_3CN),[31] and the decrease in emission lifetime is observed for $\mathbf{H_21}$ compared to **1**, in agreement with the energy gap law.[32]

The photochemical stability of **1** and $\mathbf{H_21}$ was examined in H_2O, methanol, ethanol, acetone, acetonitrile, THF, DMF, DMSO, and dichloromethane by monitoring changes in their UV−vis absorption and emission spectra during photolysis.[33] Surprisingly, for $\mathbf{H_21}$ no evidence for photodecomposition was observed after extended photolysis (4 h) in any of the solvent systems examined. Similarly, **1** was found to be photostable in protic solvents and in most aprotic solvents. However, in acetonitrile and DMSO, **1** was found to be photochemically unstable, with changes (a collapse of the absorption at 550 nm and modification of the absorption at ~350 nm; see Supporting Information, Figure S2) observed over several minutes of irradiation.

Resonance Raman Spectroscopy.[34] Ground-state resonance Raman (rR) spectra were obtained for $\mathbf{1}/\mathbf{H_21}$ at λ_{ex} = 457.9, 488, 514.5, and 532 nm. Assignment of the spectra is facilitated greatly by the availability of the deuterated analogue $\mathbf{2}/\mathbf{H_22}$. Figure 5 shows the excitation wavelength dependence of the rR spectra between 457.9 and 532 nm for **1** in basic aqueous solution. At all wavelengths examined, features are observed at 1603, 1508, 1477, 1401, 1283, 1244, and 1165 cm^{-1}. These

(29) Adeyemi, S. A.; Braddock, J. N.; Brown, G. M.; Ferguson J. A.; Miller, F. J.; Meyer, T. J. *J. Am. Chem. Soc.* **1972**, *94*, 300−301.

(30) Milkevitch, M.; Brauns, E.; Brewer, K. J. *Inorg. Chem.* **1996**, *35*, 1737−1739.

(31) Between 800 and 850 nm the detector response drops off, and hence the true λ_{max} of emission <800 nm is not determinable.

(32) Kober, E. M.; Caspar, J. V.; Lumpkin R. S.; Meyer, T. J. *J. Phys. Chem.* **1986**, *90*, 3722−3734.

(33) Examination of the photochemistry of the monoprotonated complex was not attempted due to the small separation between the first and second protonation steps, which might have resulted in the photochemistry of any of three protonation states being observed in this pH region.

(34) Strommen, D. P.; Nakamoto, K. *J. Chem. Educ.* **1977**, *54*, 474−478.

Table 1. Redox and Spectroscopic Data for **1**/**H$_2$1** and **2**/**H$_2$2** and Related Complexes in CH_3CN (Protonation with CF_3CO_2H)

	absorption λ_{max}/nm (log ϵ)	emission λ_{max}/nm τ/ns at 298 K	τ/μs at 77 K[a]	M(II)/M(III) $E_{1/2}$/V vs SCE	ligand red. $E_{1/2}$/V vs SCE	energy of IT band/ cm^{-1} (ϵ)	ref
1	241 (4.56), 290 (4.89), 467 (4.22), 530 (4.38)	748 (191)	697 (2.32)	0.875 [1], 1.05 [1]	−1.18 [1], −1.58 [2], −1.80 [1], −1.91 [1]	11 760 (<100)	
H$_2$1	282 (4.88), 424 (4.21), 565 (4.34)	780 (124)	756 (1.65)	1.28 [1], 1.45 [1]			
2	241(4.64), 290 (4.98) 467 (4.25), 530 (4.35)	749 (220)	700 (3.15)	0.875 [1], 1.05 [1]	−1.18 [1], −1.58 [2] −1.80 [1], −1.91 [1]		
H$_2$2	282 (4.80), 424 (4.24) 565 (4.33)	779 (142)	750 (2.23)	1.28 [1], 1.45 [1]			
$[(bpy)_2ClRu_2(pyrazine]^{2+}$	292 (4.96), 339 (4.08), 497, 513 (4.41)			0.89 [1], 1.02 [1]		7690 (455)	5a
4 $[((bpy)_2Ru)_2bpzt]^{3+}$	449 (4.42)	670 (106)	610 (6.4)	1.16 [1], 1.46 [1]	−1.26, −1.39, −1.55, −1.63, −1.85	5405 (2200)	15
5 $[((bpy)_2Ru)_2(bispztr)]^{2+}$	455	670 (214)		0.92 [1], 1.09 [1]		5580 (1120)	10b
H$_2$5 $[((bpy)_2Ru)_2H_2bispztr]^{4+}$	430	678 (1000)		1.13 [2]			10b
6 $[Ru(bpy)_2(1Me\text{-}pztr)\text{-}Ru(bpy)_2Cl]^{3+}$	440 (4.23), 530 (4.28)	730	705	0.92 [1], 1.41 [1]	−0.97 [1], −1.51 [1] −1.57 [1], −1.76 [1]	10 400 (480)	12c
8 $[(Ru(bpy)_2)_3((pztr)_3ph)\text{-}(Ru(bpy)_2Cl)_3]^{6+}$	465 (6.72), 515 (6.72)	775	685	0.94, 1.16	−1.14, −1.50, −1.71		49
H$_3$8 $[(Ru(bpy)_2)_3((Hpztr)_3ph)\text{-}(Ru(bpy)_2Cl)_3]^{9+}$	445 (6.35), 530 (6.50)	769	695	0.97, 1.35			49
7 $[(bpy)_2Ru(5\text{-}Mepztr]^{+}$	458 (1.21)	670	627	0.92 [1]	−1.44, −1.66, −1.80		12b
H7 $[(bpy)_2Ru(H5\text{-}Mepztr]^{2+}$	441 (1.27)	665	620	1.29 [1]	−1.22, −1.52, −1.77		12b
$[Ru(bpy)_3]^{2+}$	452 (4.1)	620 (1000)	582 (4.8)	1.23 [1]	−1.36, −1.54, −1.79		37
$[Ru(bpz)_3]^{2+}$	440 (4.1)	610 (740)	573	1.93 [1]	−0.74, −0.92, −1.18		35

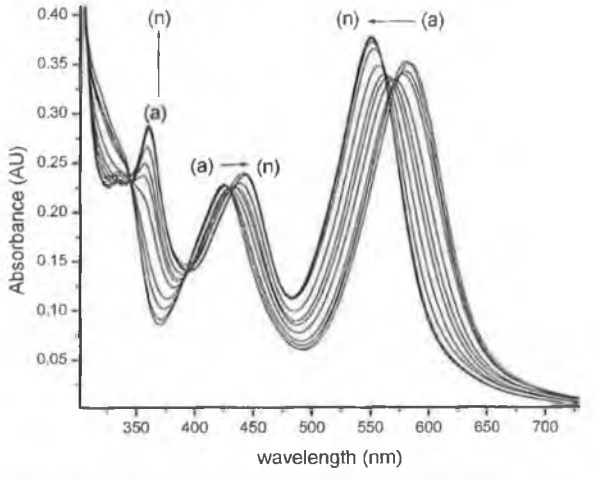

Figure 4. Absorption spectra of **1** at pH (a) 1.02, (b) 1.34, (c) 2.17, (d) 2.44, (e) 3.04, (f) 3.38, (g) 3.61, (h) 4.03, (i) 4.62, (j) 5.3, (l) 6.01, (k) 6.98, (m) 9.41, and (n) 12.98 in Britton−Robinson buffer (pH was adjusted using concentrated sulfuric acid or sodium hydroxide solution).

are assigned to pyrazine-based vibrations, based on comparison with $[Ru(bpz)_3]^{2+}$ [35] (1596, 1517, 1484, 1410 (w), 1347, 1277, 1194, 1164 cm^{-1}).[36] At 457.9 nm, and to a lesser extent at 488 nm, additional bands are observed at 1605 {1574}, 1560 {1523}, 1487 {1418}, 1318 {1255}, 1275, and 1176 cm^{-1}, which are readily assigned as bpy modes on the basis of the isotope shift observed in **2** ($[D_8]$-bpy band energies in { }) and by comparison with the spectrum of $[Ru(bpy)_3]^{2+}$.[37,38] A similar trend is observed for the fully protonated complex (**H$_2$1**), with bands at 1612, 1510, 1494, 1425, 1318, 1291, 1196, and 1151 cm^{-1} assigned to the protonated pyrazine ligand. Shorter-wavelength excitation shows some diminution of these bands, in parallel with the appearance of vibrational bands at 1565, 1493, 1425, 1320, and 1278 cm^{-1}, again assigned as bpy vibrations (see Supporting Information, Figure S3). It is interesting that the 1612 cm^{-1} pyrazine band retains its relative intensity at shorter-wavelength excitation, indicating that there is a significant contribution of pyrazine-based ^{1}MLCT at 457 nm.[39]

The solvent dependence of the absorption spectra and in particular the opposite dependence of the ~450 and ~530 nm absorption features (vide supra) has implications for the resonance Raman experiments. rR spectra recorded at 457.9 nm in CD_3CN show enhancement of the vibrational features assigned to bpy relative to those of pyrazine, compared with the spectrum obtained in H_2O (see Supporting Information, Figure S4). This is in accordance with the red shift observed in the ~450 nm absorption band in acetonitrile relative to water, which brings the transition into better resonance with the 457.9 nm excitation line (see Figure 6 and Supporting Information, Figure S4).

Excited-State Transient Absorption and Transient Resonance Raman Spectroscopy.[40] The nanosecond transient differential absorption (ΔA) spectra of both **1** and **H$_2$1** are shown in Figure 7. For both, upon excitation at 450 nm, a pronounced bleaching of the ground-state absorption spectrum is observed, with excited-state absorption bands appearing for **1** at 380 and 480 nm and for **H$_2$1** at 365 and 475 nm. The relatively small differences in the transient absorption spectra between **1** and

(35) Allan, G. H.; White, R. P.; Rillema, D. P.; Meyer, T. J. *J. Am. Chem. Soc.* **1984**, *106*, 2613−2620.
(36) Danzer, G. D.; Kincaid, J. R. *J. Phys. Chem.* **1990**, *94*, 3976−3980.
(37) Juris, A.; Balzani, V.; Barigelletti, F.; Campagna, S.; Belser, P.; von Zelewsky, A. *Coord. Chem. Rev.* **1988**, *84*, 85−277.
(38) (a) Maruszewski, K.; Bajdor, K.; Strommen, D. P.; Kincaid, J. R. *J. Phys. Chem.* **1995**, *99*, 6286−6293. (b) Mallick, P. K.; Danzer, G. D.; Strommen, D. P.; Kincaid, J. R. *J. Phys. Chem.* **1988**, *92*, 5628−5634. (c) Strommen, D. P.; Mallick, P. K.; Danzer, G. D.; Lumpkin, R. S.; Kincaid, J. R. *J. Phys. Chem.* **1990**, *94*, 1357−1366.
(39) Gardner, J. S.; Strommen, D. P.; Szulbinski, W. S.; Su, H.; Kincaid, J. R. *J. Phys. Chem. A* **2003**, *107*, 351−357.
(40) (a) Terner, J.; El-Sayed, M. A. *Acc. Chem. Res.* **1985**, *18*, 331−338. (b) Schoonover, J. R.; Strouse, G. F. *Chem. Rev.* **1998**, *98*, 1335−1355. (c) Morris, D. E.; Woodruff, W. H. In *Spectroscopy of Inorganic Based materials*; Clark, R. J. H., Hester, R. E., Eds.; John Wiley & Sons: New York, 1987.

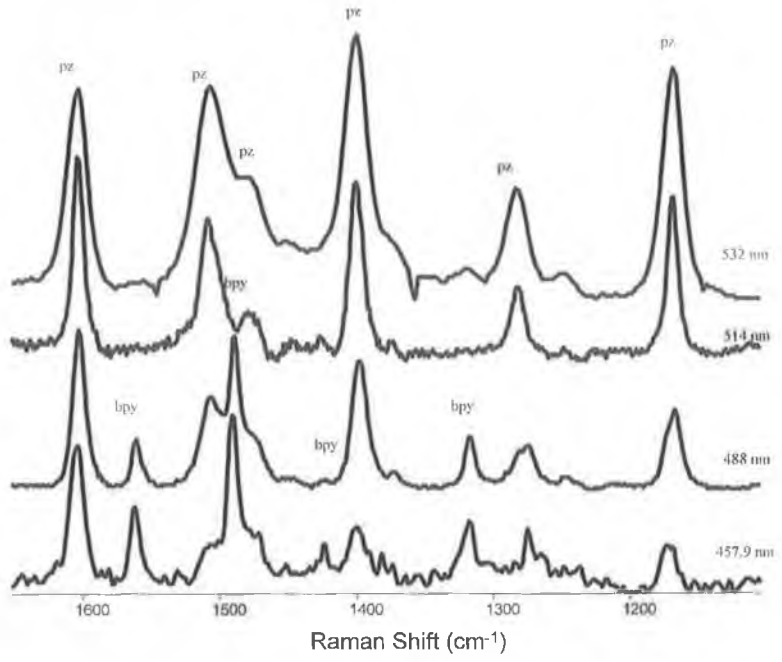

Figure 5. Resonance Raman spectra of **1** in H_2O at 457.9, 488, 514, and 532 nm probe wavelengths.

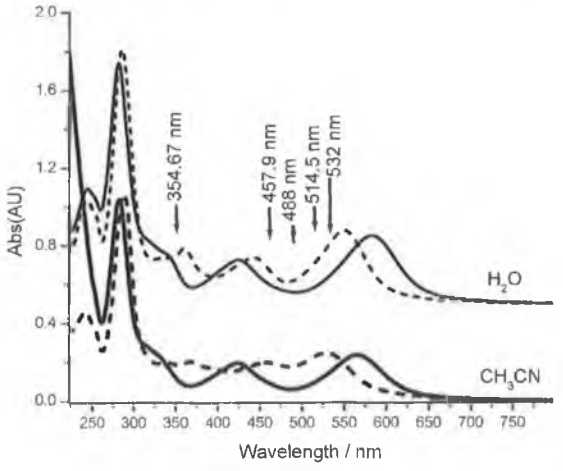

Figure 6. Absorption spectra of **1** (dashed line) and $\mathbf{H_21}$ (solid line) in H_2O (top) and CH_3CN (bottom). Spectra in H_2O are offset by 0.5 AU for clarity. λ_{exc} values used in recording ground- and excited-state resonance Raman spectra are indicated.

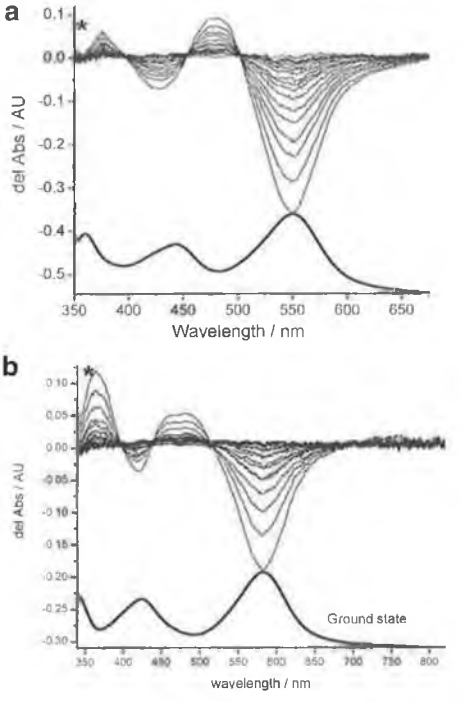

Figure 7. Ground-state and transient absorption spectra of (a) **1** (10 ns increment) and (b) $\mathbf{H_21}$ (5 ns increments), λ_{exc} = 450 nm. The asterisk indicates the 354.67 nm excitation line used in TR^2 and TR^3 experiments.

$\mathbf{H_21}$ are surprising, considering the larger differences observed in the ground-state spectra (Figure 6). The ground-state recovery time in each case is in close agreement with luminescence lifetimes, and the evolution of the spectra with time shows only a change in intensity, indicating that in both cases only a single excited-state species is present over the time range examined.

The combination of strong ground-state absorption at 350 and 530 nm and the presence of an excited-state absorption band at ~350 nm facilitates the study of **1** and $\mathbf{H_21}$ by transient (TR^2) and time-resolved resonance Raman spectroscopy (TR^3). Single-colored transient resonance Raman spectra were recorded in H_2O at both 354.67 and 532 nm for $\mathbf{1}/\mathbf{H_21}$ and $\mathbf{2}/\mathbf{H_22}$.

As shown in Figure 8, the presence of a significant ground-state as well as excited-state absorption (for both **1** and $\mathbf{H_21}$) at 354.67 nm enables the use of variation in the excitation laser pulse energy to differentiate between ground- and excited-state features. At low photon flux, the spectra are almost entirely composed of ground-state features at 1604, 1504, 1476, 1399, 1332, 1283, 1149, and 1016 cm^{-1} for **1** and at 1613, 1514, 1494, 1426, 1327, 1116, and 1005 cm^{-1} for $\mathbf{H_21}$. Excited-state resonance Raman spectra were obtained at higher photon flux.[41] Vibrational features typical of a bpy radical anion (at 1285 and

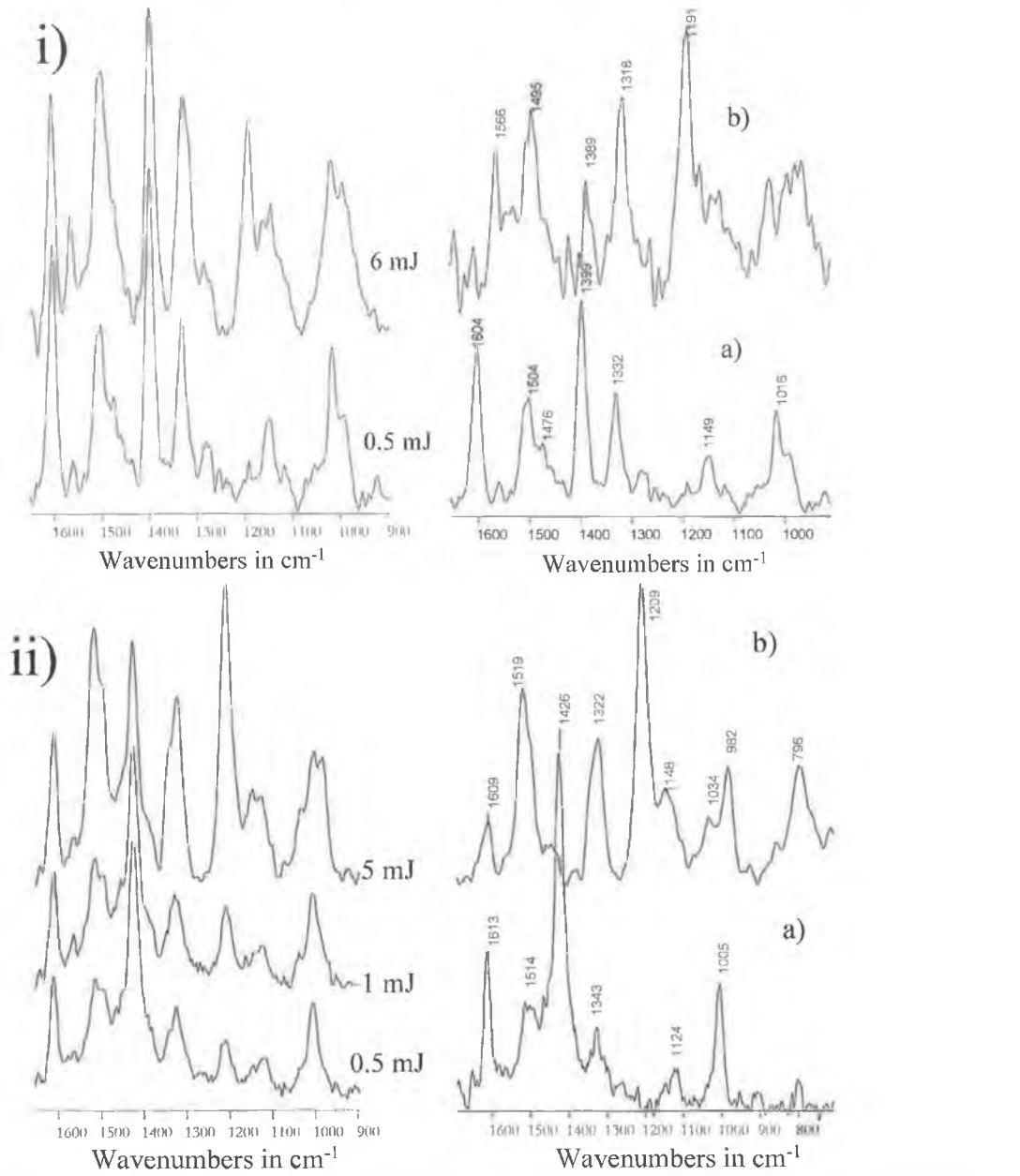

Figure 8. TR^2 spectra of (i) **1** and (ii) **H$_2$1** (in H_2O/HCl), single color pump and probe, λ_{exc} = 354.67 nm. Left: energy-resolved spectra normalized to ground-state feature. Right: (a) pure ground and (b) pure excited state.

1212 cm^{-1}) are notably absent in the high-energy TR^2 spectra of both **1** and **H$_2$1**. For **1**, excited-state bands are observed at 1566, 1495, 1389, 1318, and 1191 cm^{-1}. In the case of **H$_2$1**, the vibrational features appear at 1609, 1519, 1322, 1209, 1148, 982, and 796 cm^{-1}. Almost identical spectra were obtained for the deuterated analogues (**2**/**H$_2$2**), confirming that the peaks observed are pyrazine- rather than bpy-based. TR^2 spectra of **1** recorded at 532 nm show predominantly ground-state features, which are essentially identical to those obtained in the ground-state rR studies (vide supra). At high photon flux, bands at 1562, 1490, 1389, and 1320 cm^{-1} similar to those obtained at high photon flux at 354.67 nm are observed. For **H$_2$1**, only ground-state features are found, identical to rR spectra obtained by excitation at the same wavelength using a continuous-wave laser. This is in agreement with excited-state absorption spectra (vide supra), which indicates that insignificant excited-state absorption is present at 532 nm. Spectra recorded in acetonitrile-d_3 are in good agreement with the results obtained in aqueous solution. TR^3 spectra were recorded for both **1** and **H$_2$1** (λ_{pump} = 532 nm, λ_{probe} = 355 nm in H_2O; see Supporting Information, Figure S5). The time-resolved spectra obtained indicate, in agreement with the transient absorption spectra in Figure 7, the involvement of a single excited-state species (in the nanosecond time regime) in each case.

(41) Excited-state resonance Raman spectra: the resonance Raman spectra of the complex in its excited state with contributions to the spectra from the complex in the ground-state removed by spectral subtraction (see Figure 8).

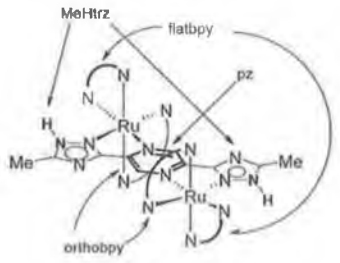

H_21

Figure 9. Nomenclature used in DFT calculations.

DFT Calculations. The complexes **1** and H_21 were studied using the B3LYP/LanL2DZ functionals. As discussed above, both **1** and H_21 are formed as homo- and heterochiral diastereoisomers; however, in the present study only the heterochiral stereoisomers are examined due to the significant simplification the presence of a center of symmetry brings to the calculation (Figure 9). For H_21, an additional complication arises upon protonation. Previous studies on the relative reactivity of the uncoordinated nitrogen ligands of the 1,2,4-triazole ring have indicated that the N1 position is less acidic than the N4 position (Figure 1). Hence, the N1 position of each of the 1,2,4-triazoles was protonated for the DFT calculations of H_21. After geometry optimization with an ultrafine integration grid, the molecular orbitals were broken down in terms of contributions from various groups in the molecule: *Ru*, the two Ru atoms; *pz*, the pyrazine ring; *Metrz*, the methyltriazole moieties (*MeHtrz* in the case of H_21); *flatbpy*, the two equivalent bipyridines, which lie in the same plane, including the Ru−pz−Ru axis; and *orthobpy*, the remaining two bipyridines (Figure 9). The results obtained for the frontier orbitals of **1** and H_21 are listed in Table S1 (Supporting Information).

In the frontier region, neighboring orbitals are often closely spaced. In such cases, consideration of only the HOMO and LUMO may not yield a realistic description. For this reason, partial density of states (PDOS) diagrams, which incorporate a degree of overlap between the curves convoluted from neighboring energy levels, can give a more representative picture. The PDOS diagrams for **1** and H_21 are shown in Figure 10. Using the time-dependent density functional theory (TD-DFT) approach, the 35 lowest energy singlet transitions of **1** and H_21 were calculated and are listed in Table S2 (Supporting Information). The results are simplified due to the presence of a center of symmetry, and the molecular orbitals of the complexes are either symmetric (A_g) or antisymmetric (A_u) with respect to the inversion center. Electronic transitions between orbitals of the same symmetry (labeled A_g in Table S2) are forbidden and have a calculated oscillator strength of 0; hence, only the A_u transitions arising from transitions between orbitals with differing symmetries contribute to the calculated UV−vis spectra (Figure 11). Electron density difference maps (EDDMs) corresponding to five electronic transitions discussed below are shown in Figure 11. These maps show the change in charge density associated with a particular electronic transition.

Discussion

The importance of the structure of the bridging ligand in determining the extent of intercomponent interaction in multinuclear transition metal polypyridyl complexes is well established.[2] Factors such as the distance between the metal centers, the nature of the bridge, and the electronic properties of the nonbridging components are of interest. In this contribution, the title compound has been designed to provide a closely related analogue for both the bpzt$^-$-type dimers (e.g., compound **4**, Figure 2) we have investigated in the past and the Creutz−Taube ion-type complexes. In the former case, the two metal centers are bridged by a ligand containing two pyrazine rings and directly bridging 1,2,4-triazole(s), while in the latter case the bridge is provided by a single pyrazine ring. The separation between the two metal centers is similar for the CT ion, **4**, and $1/H_21$, which allows examination of how the differences in the composition of the bridging ligand affect the electronic and electrochemical properties of the compounds. Of particular interest is the electron delocalization in the mixed-valence state and the effect that the protonation state of the triazole rings has on the electrochemical and electronic properties of the compound.

Redox Properties. The redox processes observed at anodic potentials for both **1** and H_21 are assigned to sequential oxidation of each of the metal centers, and the separation (ΔE (**1**) = 175 mV, ΔE (H_21) = 170 mV) is typical for complexes containing bridging pyrazine rings, such as $[(Ru(bpy)_2Cl)_2pz]^{2+}$ (ΔE = 130 mV)[5a] and $[(Ru(bpy)_2)_2dpp]^{2+}$ (ΔE = 200 mV).[6c] The ΔE value provides a measure for the stability of the mixed-valence compound toward disproportionation, as shown in eq 1, which yields values for the comproportionation constant, K_c, of 910 for **1** and 750 for H_21.[42]

$$K_c = e^{\Delta E(mV)/25.69} \quad \text{at } T = 298 \text{ K} \qquad (1)$$

The separation observed contains contributions from electrostatic interactions as well as electron delocalization.[43] The importance of the latter can be determined from a detailed analysis of the spectroscopic properties of the mixed-valence complexes. The observation of a very weak absorption band at 850 nm for H_21 and the absence of an IT band in **1** indicates that, despite the proximity of the two metal centers, the electronic delocalization between the metal centers in the ground state is at best very weak and that the separation between the first and second redox processes is predominantly due to electrostatic contributions. Indeed, the strength of the effect is comparable with the electrostatic effect of protonation on the redox potentials of **1** and H_21.[4c,44]

The electrochemical studies yield two unexpected results. First, while for both the CT ion and **4** electronic interaction (in terms of delocalization of the SOMO) is relatively strong, for $1/H_21$ electron delocalization is not significant. Second, it is unexpected that the value of ΔE obtained for $1/H_21$ is independent of the protonation state of the triazole ring. For other triazole-based dinuclear systems such as compound **5** (Figure 2), very different behavior is observed. In the depro-

(42) Richardson, D. E.; Taube, H. *Inorg. Chem.* **1981**, *20*, 1278−1285.
(43) Evans, C. E. B.; Naklicki, M. L.; Rezvani, A. R.; White, C. A.; Kondratiev, V. V.; Crutchley, R. J. *J. Am. Chem. Soc.* **1998**, *120*, 13096−13103.
(44) The effect of protonation can be viewed as a "double oxidation" in terms of the change in charge; therefore, the increase in the first and second redox potentials of **1** upon protonation to H_21 would be expected to be equivalent to twice ΔE (i.e., 350 mV). The actual increase upon protonation is 400 mV, and the larger effect of protonation of the 1,2,4-triazole is probably due to the closer proximity of the increase in charge (and hence electrostatic effect) compared with oxidation of one metal center (cf. distance dependence of columbic interactions).

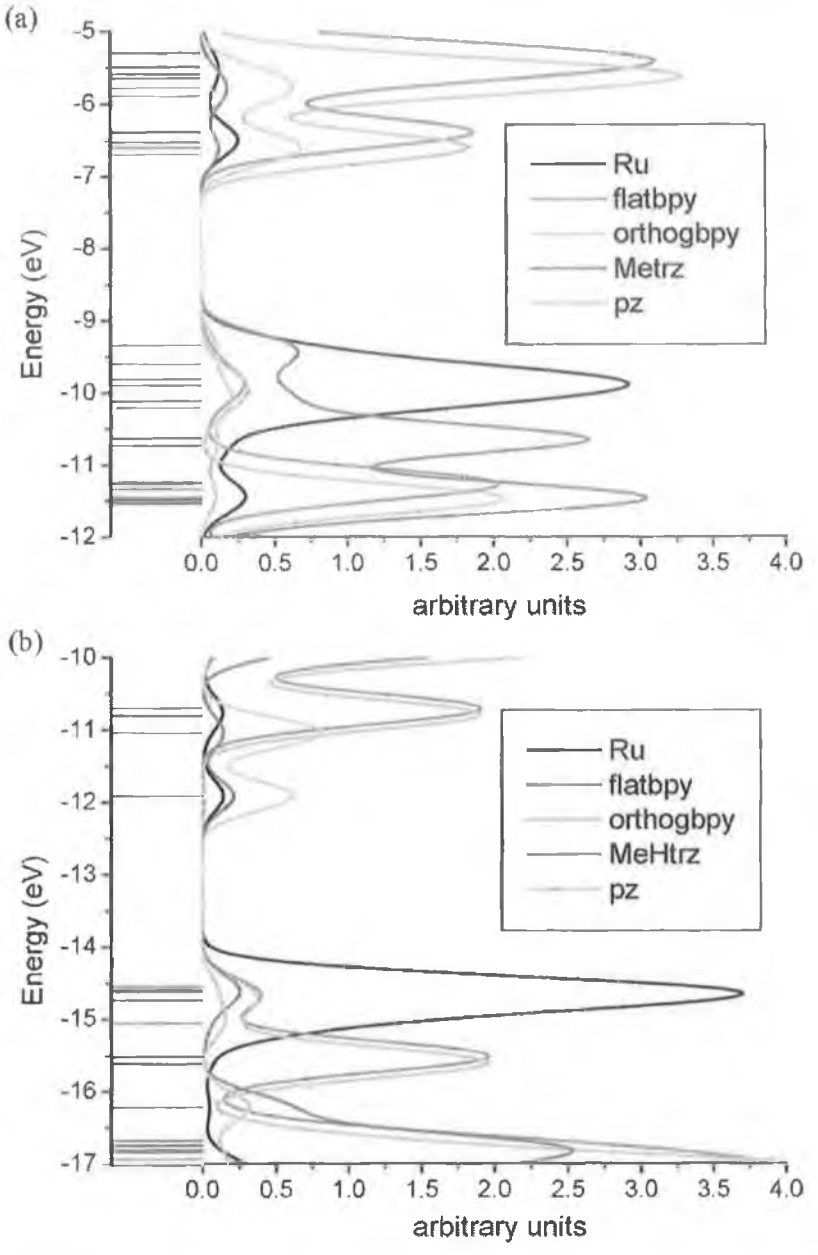

Figure 10. Partial density of states diagram for (a) **1** and (b) $\mathbf{H_21}$. See text for description of the groups.

tonated state **5** shows a ΔE value of **170** mV, while for its protonated analogue a single two-electron wave is observed. In addition, for **5** the deprotonated analogue shows an intervalence band, while for the protonated species no intervalence features are observed. The pH-dependent behavior is typical of interaction via a hole-transfer mechanism[13] and is observed for related imidazole-based systems also.[45] It is, therefore, surprising that the ΔE values obtained for **1** and $\mathbf{H_21}$ are the same and that evidence for electron delocalization, in the form of an intervalence feature, is observed only for $\mathbf{H_21}$. These observations make it very unlikely that hole transfer is an appropriate mechanism to describe the nature of the interaction between the two metal centers. However, the experimental observations may be explained by considering the strong coupling observed for the CT ion, which is rationalized by assuming a LUMO-mediated superexchange mechanism.[5] An important parameter, which determines the efficiency of such a mechanism, is the HOMO−LUMO energy gap. Meyer and co-workers have demonstrated that pyrazine-bridged binuclear complexes with better π-acceptor properties than NH_3 (e.g., $[(bpy)_2ClRu\text{-}(\mu\text{-pyrazine})\text{-}RuCl(bpy)_2]^{2+}$) exhibit a weaker IT band at much higher energy than the CT ion (Table 1).[5] The presence of good π-acceptor ligands, such as bpy, decreases the metal-based HOMO energy and hence increases the barrier to electron transfer between the Ru(II) and

(45) (a) Haga, M.; Ano, T.; Kano K.; Yamabe, S. *Inorg. Chem.* **1991**, *30*, 3843−3849 (b) Haga, M.; Ali, Md. M.; Koseki, S.; Fujimoto, K.; Yoshimura, A.; Nozaki, K.; Ohno, T.; Nakajima, K.; Stufkens, D. J. *Inorg. Chem.* **1996**, *35*, 3335−3347. (c) Haga, M.; Ali, Md. M.; Arakawa, R. *Angew. Chem., Int. Ed. Engl.* **1996**, *35*, 76−78.

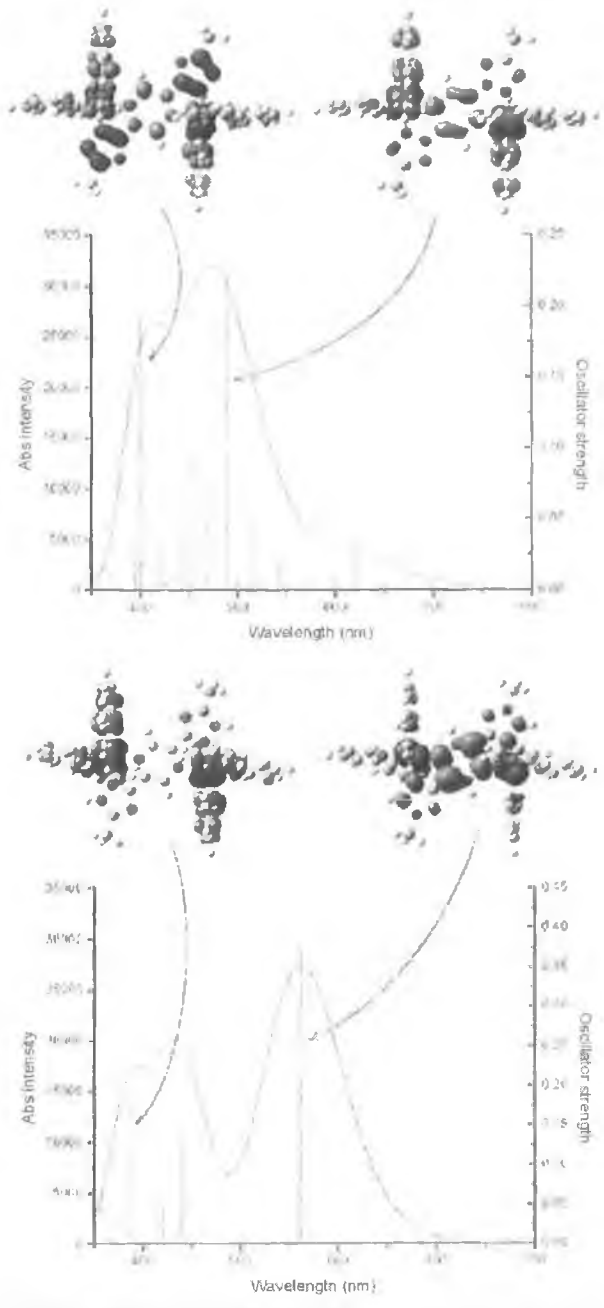

Figure 11. **Convoluted calculated UV−vis spectrum of 1 (top) and H_21 (bottom). The green lines are the individual electronic transitions. Also shown are three electron density difference maps corresponding to transitions 1, 13, and 30 (1) and 5, 8, and 25 (H_21) (green indicates an increase in the charge density, and red indicates a decrease).**

Ru(III) centers. As a result, the oxidation of the first metal center affects the second metal center, but the barrier to electron "hopping" between the Ru(II) and Ru(III) centers is increased and the mixed-valence complex may be viewed as valence-trapped or localized.[4,46] Overall, the high energy barrier to optical electron transfer and the localization of the SOMO on a single metal center result in a lower oscillator strength and higher energy of the IT band than for the CT ion. If a LUMO-mediated exchange mechanism determines the intercomponent interaction in **1** and H_21, then the absence of a clear IT band in the mixed-valence state is not unexpected.

Reductive Processes. Assignment of the first reduction process observed at cathodic potentials as being pyrazine-based is made by comparison with closely related pyrazine-bridged binuclear complexes (Table 1). The subsequent reduction waves observed are assigned as bpy-based reductions, the first of which is a poorly resolved (ΔE < 60 mV) bielectronic redox wave corresponding, at least approximately, to a single bpy reduction of each metal center.[47] The third bpy reduction is at 200 mV more negative potential than the first/second bpy reduction. The third and fourth bpy reductions, which are again assigned to a single bpy reduction at each metal center, are separated by ~110 mV.

The observation that the first and second bpy reductions occur at almost the same potential, while there is a 110 mV separation between the third and fourth bpy reduction steps, may be rationalized on the basis that the first three bpy reduction steps are stabilized by delocalization over the remaining unreduced bpy ligands. For the fourth bpy reduction process, such stabilization is not available; hence, the separation (ΔE) between the third and fourth bpy reduction processes is larger than that between the first and second bpy reductions.[47]

The delocalization of charge in the reduced state is unexpected, considering the very low level of delocalization in the mixed-valence {Ru(II)Ru(III)} complexes (vide supra). If the "interaction" strength is a fixed parameter and is independent of the redox state of the complex, then four separate bpy reduction processes would be expected due to electrostatic factors, with the separation between the four bpy reductions being approximately equal.[48] The first two reductions are delocalized over eight pyridyl rings, and hence electrostatic interactions will be reduced significantly from those observed during oxidation where oxidation is localized on the ruthenium centers. The increased separation between the third and fourth reduction processes (100 mV) cannot be rationalized on the basis of a single reduction at each metal center since the electrostatic effect, and hence separation (ΔE), would be similar to that between the first and second bpy reduction processes. The increased separation can be explained by considering that the third reduction process is stabilized by delocalization over the two centers, while the last reduction does not benefit from such stabilization through delocalization. A similar reductive electrochemistry is seen in the related binuclear complexes $[(Ru(bpy)_2)_2bpt]^{3+}$ [14b] and $[(Ru(bpy)_2)_2bpzt]^{3+}$ [15] and indicates that there is significant interaction/delocalization between the bpy ligands on both metal centers. The results obtained suggest that the communication between the $Ru(bpy)_2^{2+}$ units is increased when the bpy-based reductions are considered, and this can be explained by the fact that the bpy-based reductions take place in a complex containing a negatively charged (reduced) pyrazine

(46) (a) Hupp, J. T. *J. Am. Chem. Soc.* **1990**, *112*, 1563−1565. (b) Piepho, S. B. *J. Am. Chem. Soc.* **1990**, *112*, 4197−4206. (c) Petrov, V.; Hupp, J. T.; Mottley, C.; Mann, L. C. *J. Am. Chem. Soc.* **1994**, *116*, 2171−2172.

(47) Ghosh, B. K.; Chakravorty, A. *Coord. Chem. Rev.* **1989**, *95*, 239−294.

(48) The $E_{pc} - E_{pa}$ of the first bpy reduction peak is 120 mV and not the 29.5 mV expected for a double-electron-transfer process; 120 mV is twice that expected for an electrochemically reversible 1 e⁻ transfer. The third and fourth bpy reductions are electrochemically reversible ($E_{pc} - E_{pa}$ < 70 mV), and hence it is probable that the first and second reductions are also reversible, suggesting a separation of 60 mV between the first and second bpy reduction processes.

bridge and not a neutral bridge as is the case with oxidation processes.

Electronic Properties. The absorption spectra of **1**/**H$_2$1** contain three main absorption features in the visible region and are reminiscent of the spectra exhibited by related pyrazine-bridged binuclear complexes based on the ligands dpp[6c] and bpz (where bpz is 2,2′-bipyrazine).[36] Comparison of the absorption spectra of these compounds with those of **1**/**H$_2$1** suggests that the 550 nm band (Figure 4) is predominantly ^{1}MLCT (t_{2g} to pz) and the 450 nm band is ^{1}MLCT (t_{2g} to bpy) in character. This assignment is confirmed by resonance Raman spectroscopy and electrochemical data (vide supra). For **1**, a red shift in the 530 nm band to 565 nm and a blue shift of the 467 nm band to 424 nm are observed upon protonation.[13b] The red shift of the 530 nm band is most likely due to the stabilization of the pyrazine, which is supported by the DFT calculations (vide infra). Finally, the 350 nm absorption band is assigned, tentatively, as a pyrazine$-^1$IL ($\pi-\pi^*$) transition on the basis of the expected lower energy of the pyrazine$-\pi^*$ relative to the bpy$-\pi^*$. This assignment is supported by the pH dependence of the absorption band, which undergoes a blue shift on protonation (due to the concomitant lowering of electron density on the adjacent 1,2,4-triazole rings), and observation of pyrazine-based vibrational modes in the ground-state resonance Raman spectra obtained during TR^2 studies (vide supra) at $\lambda_{exc} = 355$ nm for both **1** and **H$_2$1**.

DFT Calculation. One of the central aims of the present study is to examine the effectiveness of DFT calculations in elucidating ground- and excited-state features in multinuclear complexes. The picture emerging from the spectroscopic and electrochemical measurements is that the LUMO in both **1** and **H$_2$1** is based on the pyrazine ligand and that, as expected, the HOMO is metal-based. The data indicate that both HOMO and LUMO are stabilized upon protonation. In this section the results obtained from the DFT calculations are compared with the experimental data.

The PDOS diagrams shown in Figure 9 suggest that for **1** the HOMOs are mainly *Ru*- and *Metrz*-based and the LUMOs are based on the bipyridines and *pz*. In contrast, the HOMOs of **H$_2$1** are almost completely *Ru*-based and the LUMOs are primarily based on *pz*, although there are also contributions from *MeHtrz* and *Ru*.

This can be visualized by the EDDM pictures shown in Figure 10a for **1**, which indicate that the lowest energy absorption (of significant oscillator strength) at 490 nm (transition 13, Table S2a; major contributions, H-4 → LUMO and H-2 → LUMO) corresponds to a transfer of electron density from *Ru* to *orthobpy* and *pz* (Figure 9). At ~400 nm there is another electronic transition, also with high oscillator strength (transition 30). The major contributions are HOMO → L+7 and H-1 → L+6, and the change in charge density is similar to that calculated for transition 13. The energies observed for these main bands, as well as the absorption envelope, are quite different from the experimental results. Also, the results indicate a significant mixing of bpy and pz orbitals, in contradiction to resonance Raman data (vide supra). This apparent contradiction may be explained by consideration of the different environments for which the data are obtained. In the DFT calculations the complex is isolated (i.e., no solvation), while the rR experiments were carried out in aqueous solution. It is clear from the solvent dependence of the energy of the absorption bands at ~400 and ~550 nm that increasing solvent polarity (vide supra) also serves to increase the separation of the absorption bands (see Figure 6 and Figure S4).

In contrast, the calculated UV−vis spectrum of **H$_2$1** is in excellent agreement with experiment (Figure 11). For the protonated species, the lowest energy transition with a significant oscillator strength (transition 5, mainly H-1 → LUMO) corresponds to a transfer of electron density mainly from *Ru* to *pz*. Two transitions of similar oscillator strength contribute to the absorption band around 440 nm. The two transitions (transitions 7 and 8, containing different ratios of H-1 → L+1 and HOMO → L+1) correspond to very similar movements of electron density from *Ru* to *pz*. Another transition with a strong oscillator strength occurs at 385 nm. This transition (transition 25 in Table S2b) has a number of contributions, the largest of which are H-3 → L+3 and H-4 → L+2 and *Ru* to bipyridyl (mainly *orthobpy*) in nature. The DFT calculations for the protonated species therefore support the spectroscopic data. The lowest singlet excited state is pyrazine-based, and protonation of **1** leads to a decrease in the energy of the lowest ^{1}MLCT band.

The DFT calculations also support both the electrochemical observations and the mechanism proposed for the interaction between the metal centers in the mixed-valence state. They indicate that, for **1** and **H$_2$1**, the pyrazine moiety provides only very minor contributions to the HOMO and a large contribution to the LUMO, while the 1,2,4-triazoles provide a significant contribution to the HOMO. It is clear that the LUMO energy is stabilized to a greater extent than the metal-based HOMO levels upon protonation from **1** to **H$_2$1**. If the internuclear interaction is dominated by a LUMO-based superexchange mechanism, then an increase in the internuclear interaction would be expected, and although protonation has little effect on ΔE, the tentative observation of an IT band for **H$_2$1** and not for **1** suggests that a small increase in interaction occurs upon protonation.[4c]

Excited-State Electronic Structure and Properties. Although pyrazine-bridged complexes have been the focus of considerable attention for over half a century, the majority of the systems are nonemissive. It is generally accepted that the lowest excited states in those pyrazine-bridged systems, which are emissive (e.g. the dipyridopyrazine family of complexes), are pyrazine-based; however, few detailed studies have been carried out to confirm this.[6f] The emission spectra of **1** and **H$_2$1** are comparable with those reported for the related complexes (see Figure 2 and Table 1) [Ru(bpy)$_2$(μ-1Mepztr)Ru(bpy)$_2$Cl]$^{3+}$ (**6**)[13c] and [(Ru(bpy)$_2$)$_3$((pztr)$_3$ph)(Ru(bpy)$_2$Cl)$_3$]$^{6+}$ (**8**).[49] The red shift observed upon protonation is in agreement with the stabilization of the pyrazine-based LUMO; however, assignment of the emitting state as pyrazine-based is not so clear since a significant isotope effect on the emission lifetimes for **1** and **H$_2$1** (at 298 and 77 K) is observed upon deuteriation of the bpy ligands (Table 1). In previous studies of heteroleptic complexes, deuteriation of the ligands on which the lowest excited state is based results in an increase in emission lifetime.[50] It would be expected, therefore, for **1** and **H$_2$1** that deuteriation of the bpy ligands should have no effect on the emission lifetime,

(49) Lempers, H. E. B.; Haasnoot, J. G.; Reedijk, J.; Hage, R.; Weldon, F. M.; Vos, J. G. *Inorg. Chim. Acta* **1994**, *225*, 67−74.
(50) Browne, W. R.; Vos, J. G. *Coord. Chem. Rev.* **2001**, *219*, 761−787 and references therein.

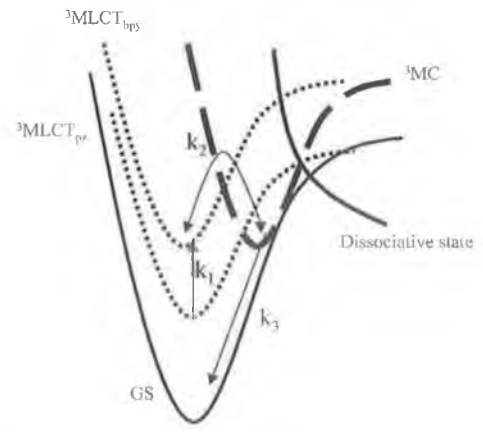

Figure 12. Excited-state internal conversion (IC).

as TR[2] and TR[3] studies strongly indicate that, for **1** and $\mathbf{H_21}$, the lowest excited state is pyrazine-based (i.e. the observation of features attributed to vibrations of the pyrazine group and the absence of the signature bands of the bpy anion radical 1212 and 1285 cm^{-1}).[37] The observation of a pronounced increase in the emission lifetime upon deuteriation of the bpy ligands is therefore somewhat surprising[50] but may be related to interaction between neighboring electronic states, one of which is bpy-based.

Interaction between close-lying, weakly coupled states is dominated by high-energy vibrational modes.[50,51] Hence, if the deactivation of the pyrazine-based ^{3}MLCT state via population of the higher bpy-based ^{3}MLCT state (Figure 12) is an important deactivation route, then the observation of a bpy deuteriation effect is possible. It is clear from the photochemical reactivity of **1** that the ^{3}MC state (thermal population of which is responsible for most ruthenium(II) polypyridyl photochemistry)[37] is accessible, and hence it is not unreasonable to assume that the higher energy ^{3}MLCT$_{bpy}$ states undergo rapid deactivation via this state. Considering Figure 12, if $k_1 \ll k_2 < k_3$, then the rate-determining step is the IC between the ^{3}MLCT$_{pz}$ state and ^{3}MLCT$_{bpy}$, in which, for weakly coupled states (i.e., with a Huang–Rhys factor $S < 1$), high-energy vibrational modes are important.[50,51] The absence of bpy anion radical features in the excited-state Raman data suggests that the lowest pyrazine ^{3}MLCT state is the only state that achieves a significant population at 298 K, and hence the bpy ^{3}MLCT state, if populated, must undergo rapid deactivation (e.g., via the ^{3}MC state, Figure 12). The rate of nonradiative decay of an excited state is the sum of several competing processes ($k_{obs} = k^3_{MLCT-GS} + k_1 + k_2 + k_3 + ...$), such as direct relaxation to the ground state and thermal population of a higher energy state. At 77 K, thermal population of the ^{3}MC state (k_2 in Figure 12) is not observed, and deactivation of the emissive ^{3}MLCT$_{pz}$ state via the weakly coupled ($S < 1$) ^{3}MLCT$_{bpy}$ state provides a proportionally larger contribution to k_{obs}; hence, the isotope effect would become larger.

Conclusions

Ground- and excited-state resonance Raman[41] and electrochemical data enable a detailed assignment to be made of the electronic absorption and emission spectra of **1** and $\mathbf{H_21}$. From the wavelength dependence of the rR spectra and electrochemistry, the absorption band at ca. 530 nm can be assigned as a

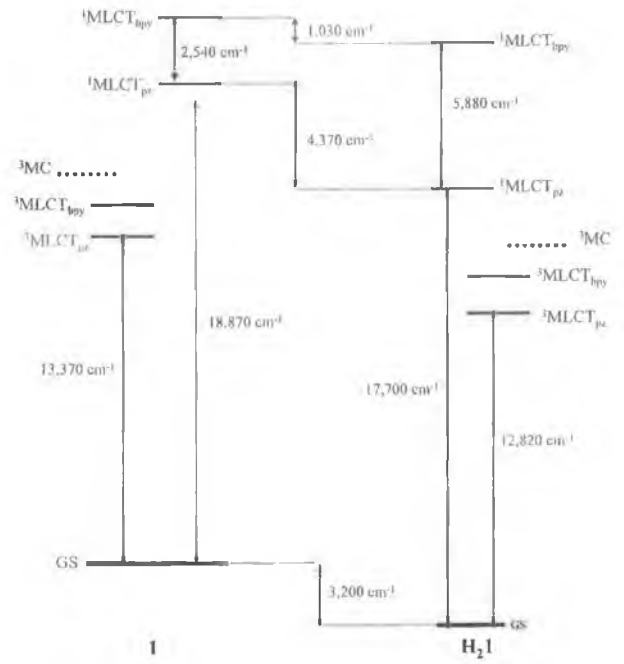

Figure 13. Diagram showing relative position of electronic states for **1** (left) and $\mathbf{H_21}$ (right). Energy differences are estimated from spectroscopic and redox data.

$t_{2g}-\pi^*_{pz}$ ^{1}MLCT transition, the ca. 450 nm band is attributable to a $t_{2g}-\pi^*_{bpy}$ ^{1}MLCT transition, and the emission is assigned as arising from a pyrazine-based relaxed ^{3}MLCT state. A simplified electronic structure of both **1** and $\mathbf{H_21}$ is represented in Figure 13. It is clear that, upon protonation, the lowest pyrazine-based ^{1}MLCT and ^{3}MLCT states are stabilized. In addition, due to the reduction in the σ-donor strength of the two triazole moieties, stabilization of the metal-based (t_{2g}) ground state and the photochemically active ^{3}MC (e_g) state also occurs. The electrochemical data suggest ground-state (HOMO) stabilization (Ru(II)/Ru(III) redox potential) by 3200 cm^{-1}, upon protonation, while electronic spectroscopy suggests that, upon protonation, the energy of the ^{1}MLCT$_{pz}$ band (and hence LUMO) is reduced by 4370 cm^{-1} and that of the ^{3}MLCT$_{pz}$ band is lowered by 3750 cm^{-1}.

In contrast to the ground state, which is stabilized by 3200 cm^{-1}, the bpy-based ^{3}MLCT states are relatively unaffected by protonation (stabilized by only 1030 cm^{-1}), and hence the effective GS-to-^{3}MLCT(bpy) energy gap is increased (Figure 13). It would be expected that a lowering in the energy of the ^{3}MC state would result in an increase in photochemical reactivity; however, the reverse is observed, with the deprotonated complex exhibiting photochemistry while the protonated complex is photochemically inert. Lowering of the ^{3}MC upon protonation reduces the energy gap between the ^{3}MC and ground state and hence leads to an increase in the rate of nonradiative

(51) (a) Hutchinson, C. A., Jr.; Mangum, B. W. *J. Chem. Phys.* **1960**, *32*, 1261–1262. (b) Wright, M. R.; Frosch, R. P.; Robinson, G. W. *J. Chem. Phys.* **1960**, *33*, 934–935. (c) Robinson, G. W.; Frosch, R. P. *J. Chem. Phys.* **1962**, *37*, 1962–1973. (d) Robinson, G. W.; Frosch, R. P. *J. Chem. Phys.* **1963**, *38*, 1187–1203. (e) Siebrand, W. *J. Chem. Phys.* **1967**, *46*, 440–447. (f) Siebrand, W. *J. Chem. Phys.* **1996**, *44*, 4055–4057. (g) Gelbart, W. M.; Freed, K. F.; Rice, S. A. *J. Chem. Phys.* **1970**, *52*, 2460–2473. (h) Jortner, J.; Rice, S. A.; Hochstrasser, R. M. *Adv. Photochem.* **1969**, *7*, 149–309. (i) Freed, K. F.; Jortner, J. *J. Chem. Phys.* **1970**, *52*, 6272–6291. (j) Englman, R.; Jortner, J. *Mol. Phys.* **1970**, *18*, 145–148.

deactivation from the ^{3}MC to the ground state. This increase inhibits thermal population of a dissociative state from the ^{3}MC and hence inhibits photochemistry (Figure 12).

The incorporation of the acid−base chemistry of the 1,2,4-triazole moiety into the well-known Ru−pyrazine−Ru system has enabled the investigation of a pyrazine-bridged system which can undergo quite dramatic changes in both its ground- and excited-state properties, controllable by both solvent and pH. It is clear that the application of multiple techniques in a concerted manner to the elucidation of excited-state structure holds particular advantages, especially in determining the relative contributions of different ligand-based excited states to the electronic properties observed.

Acknowledgment. The authors thank Enterprise Ireland, the EU Framework 5 IHP Training Network Susana, Contract HPRN-CT-2002-00185, and the EPSRC (UK) GR/M45696 for financial support. K.L.R. acknowledges ANDOR Technology Ltd. for financial support. The authors thank Mr. Maurice Burke (DCU) for assistance in the recording of mass spectra.

Supporting Information Available: Detailed synthesis and experimental procedures; ^{1}H NMR spectrum of **1**; UV−vis spectra during photolysis of **1** in CH_3CN; rR spectra of $\mathbf{H_21}$ in H_2O; rR spectrum of **1** in CH_3CN; TR^3 spectra of **1**; eigenvalues, symmetry, and percent contribution of various groups (see text) for the frontier molecular orbitals of **1** and $\mathbf{H_21}$; calculated wavelengths and oscillator strength of the electronic transitions of **1** and $\mathbf{H_21}$. This material is available free of charge via the Internet at http://pubs.acs.org.

JA046034E

Appendix F

Structures Discussed in the Text

Chapter 3

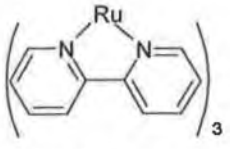

$[Ru(bpy)_3]^{2+}$

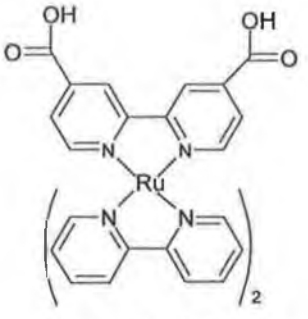

$[Ru(bpy)_2(H_2dcb)]^{2+}$

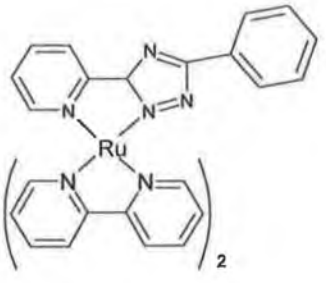

$[Ru(bpy)_2(phpytr)]^{+}$

Chapter 4

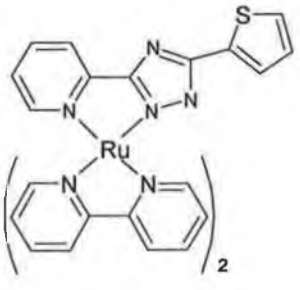

$[Ru(bpy)_2(thpytr)]^{+}$ - 1

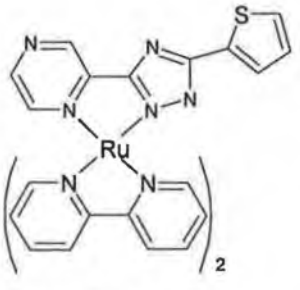

$[Ru(bpy)_2(thpytr)]^{+}$ - 2

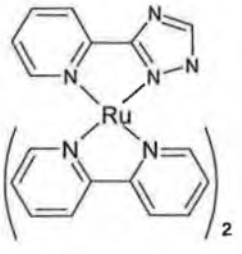

$[Ru(bpy)_2(pytr)]^{+}$ - 3

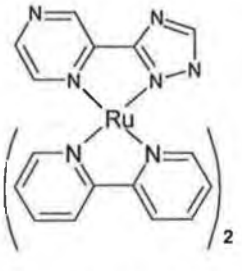

$[Ru(bpy)_2(pztr)]^{+}$ - 4

Chapter 5

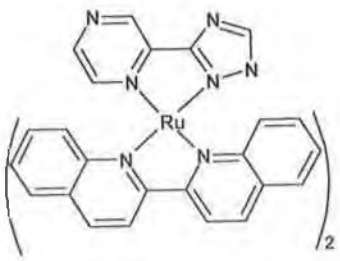

$[Ru(biq)_2(pztr)]^+$

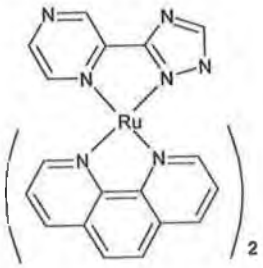

$[Ru(phen)_2(pztr)]^+$

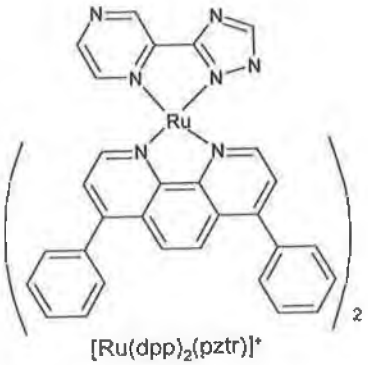

$[Ru(dpp)_2(pztr)]^+$